Distribution, petrology, geochemistry and geochronology of carbonate assemblages at the Olympic Dam deposit

by

Olga B. Apukhtina

M.Sc. Honours (University of Tübingen, Germany)

Submitted in fulfilment of the requirements for the

degree of Doctor of Philosophy

University

of **Tasmania**

July 2016

Declaration

This thesis contains no material which has been accepted for a degree or diploma by the University or any other institution, except by way of background information and duly acknowledged in the thesis, and to the best of my knowledge and belief no material previously published or written by another person except where due acknowledgement is made in the text of the thesis, nor does the thesis contain any material that infringes copyright.

Date: 07.07.2016

Signature:

Olga Apukhtina

Authority of Access

The publisher of the paper comprising Chapter 3 (Contributions of Mineralogy and Petrology) holds the copyright for that content, and access to the material should be sought from the respective journal. The remaining non published content of the thesis may be made available for loan and limited copying and communication in accordance with the Copyright Act 1968.

Front cover image: Carbonate vein in the middle shows oscillatory zoning and crosscuts an older carbonate generation which is highly porous and displays patchy zoning. Sample OD106 (backscattered electron image).

Statement of Co-Authorship

The following people and institutions contributed to the publication of work undertaken as part of this thesis:

Olga B. Apukhtina, University of Tasmania = **Candidate**

Vadim S. Kamenetsky, University of Tasmania = **Author 1**

Kathy Ehrig, BHP Billiton = **Author 2**

Maya B. Kamenetsky, University of Tasmania = **Author 3**

Jocelyn McPhie, University of Tasmania = **Author 4**

Roland Maas, University of Melbourne = **Author 5**

Sebastien Meffre, University of Tasmania = **Author 6**

Karsten Goemann, University of Tasmania = **Author 7**

Thomas Rodemann, University of Tasmania = **Author 8**

Nigel J. Cook, University of Adelaide = **Author 9**

Cristiana L. Ciobanu, University of Adelaide = **Author 10**

Author details and their roles:

Paper 1 (published), Postmagmatic magnetite-apatite assemblage in mafic intrusions: a case study of dolerite at Olympic Dam, South Australia:

Candidate was the primary author (60%), and with authors 1-10 contributed to the idea, its formalisation and development (40%).

Located in chapter 3

Signed: _____ _____

Vadim S. Kamenetsky

Primary supervisor

CODES, ARC Centre of

Excellence in Ore Deposits

University of Tasmania

John Dickey

Head of School, Mathematics and Physics

University of Tasmania

Date: 07/07/2016

11/07/2016

Abstract

The supergiant Olympic Dam Cu-U-Au-Ag deposit in South Australia is the type example of the iron-oxide copper-gold (IOCG) deposit family. Hosted entirely within heterogeneous breccia zone developed within 1.593 Ga Roxby Downs Granite (RDG) the deposit contains a volumetrically important and mineralogically diverse component of carbonate minerals. Carbonate minerals are almost always associated with ore minerals (e.g., Cu-Fe sulfides, uraninite, coffinite, brannerite), implying a genetic relationship. A study of the gangue carbonates may therefore help improve our understanding of ore genesis at Olympic Dam, yet there is very little published data. Most earlier workers favoured a broadly single-stage genetic model, with deposition of metals (and gangue minerals, including carbonates) in the same magmatic-hydrothermal cycle at ~1.59 Ga. In contrast, recent radiometric dating indicates that mineralization and gangue minerals formed episodically over a long period, requiring a re-evaluation of observed parageneses, mineral ages, depositional mechanisms and sources of metals and other components (e.g., carbon).

This study provides the first detailed and comprehensive petrographic, geochemical (e.g., major, minor and trace elements and stable C-O isotopes) and geochronological study of Olympic Dam gangue carbonates. The study is based on a large (totalling 197) set of samples representative of the entire deposit and includes samples from lithologies for which very limited or no drillcore was available for the studies carried out in the late 1980s and early 1990s.

Carbonate minerals are observed in all lithologies present at Olympic Dam: weakly to strongly brecciated granite, mafic to ultramafic dykes of various ages, felsic volcanics and clastic and carbonate sediments. Carbonates (Ca-Fe-Mg-Mn) occur as matrix in breccia, conglomerates and sediment, as breccia clasts, in veins crosscutting ore-rich breccia and other rock types, in amygdales and oolites, and in the form of massive laminated carbonate. Siderite and siderite-rhodochrosite-magnesite solid solution are by far the most common carbonate types, while calcite, dolomite-ankerite solid solution and REE-fluorocarbonates are locally abundant. Individual carbonate grains typically show some form of compositional zoning (simple or oscillatory) and replacement textures (including mutual replacement of carbonates with other carbonates and with hematite) are common. The complexity of the breccia zone prevented compilation of a paragenetic sequence; instead the carbonates were assigned to 7 associations based on the host rock lithology, mineralogy and texture: (1) coarse-grained calcite veins in weakly-brecciated granite and rhyolite, (2) carbonates in strongly-brecciated granite, (3) carbonate veins in bedded sediments, (4) carbonates in mafic and ultramafic igneous rocks, (5) massive barite-fluorite-dominated veins with minor carbonate, (6) laminated siderite, and (7) carbonate matrix in a conglomerate-breccia and sandstone.

Strong textural evidence for the multistage nature of Olympic Dam carbonates is supported by radiometric dating (Rb-Sr, Sm-Nd, Pb-Pb, and Lu-Hf) of Ca-Fe-Mg-Mn carbonates and other minerals which indicates carbonate formation in at least 3 stages (~1.59-1.55, ~0.8 and ~0.6-0.5 Ga), possibly more. Sr-Nd isotope systematics in carbonate minerals are consistent with carbonate- and ore-bearing fluids being derived in large part from the host 1.593 Ga granite and associated polygenetic breccia.

Stable isotope (C-O) data for carbonates are difficult to interpret. $\delta^{13}C$ values (-6.5 ‰ to -2 ‰) show a relatively limited range while $\delta^{18}O$ is more variable (+9.4 ‰ to +20.9 ‰). The data overlap the fields of several major carbon-oxygen reservoirs (magmatic, sedimentary) suggestive of mixed fluid sources possibly including recycling of older carbonate for which there is abundant textural evidence. Carbon sources in local granite, felsic volcanics, older banded

iron-formations (BIFs) and sedimentary rocks (including Nuccaleena Dolomite related to the Cryogenian Marinoan glaciation, part of the *'Snowball Earth'* event, e.g., Kendall et al., 2004) are all possible at different stages of carbonate deposition.

The detailed petrographic-geochemical work on gangue carbonates was augmented by two in-depth case studies. One of these focussed on magnetite-apatite veins hosted in dolerite dykes, the local equivalent of the regional 825 Ma Gairdner Dyke Swarm (GDS), which cut the mineralized Olympic Dam Breccia Complex (ODBC). Magnetite-apatite assemblages are a characteristic of many IOCG deposits, notably the well-known iron-oxide apatite (IOA) or Kiruna-type style. Several genetic models have been proposed to explain large-scale IOA-style mineralization but there appears to be no agreement. At Olympic Dam, there are many examples of dolerite dykes with intensive magnetite-apatite veining, without subsequent overprinting. U-Pb dating shows the magnetite-apatite assemblages formed very soon after the host dolerite, and the vein components (e.g., Fe, P) have been derived from an external fluid and from alteration of the dolerite along vein margins. The setting and spectacular colloform magnetite textures limit the range of metal transport and depositional processes for this IOA assemblage, providing a possible template for magnetite-apatite assemblages in magnetite-apatite-bearing IOCG systems and other occurrences in disparate geological settings.

The second case study focussed on a large-scale magnetite-apatite assemblage discovered in drillhole RD2773 deep within only weakly brecciated host granite and a rhyolitic unit and below the ODBC. By analogy with other IOCG prospects in the region, initial mineralization at Olympic Dam had been expected to be ~1.59 Ga magnetite-apatite-pyrite-siderite, without uraninite. Due to reaction with oxidized fluids, such early magnetite assemblages, if they ever existed at Olympic Dam, were replaced by hematite, with associated deposition of uraninite. In contrast, the magnetite-apatite (IOA) assemblage in RD2773 contains pyrite and quartz as major components, and U mineralization is present as uraninite whereas siderite is completely absent. U-Pb dating of magmatic zircon in the host rhyolite unit, and of hydrothermal apatite, uraninite and hematite (partially replaces magnetite) in the IOA assemblage shows consistent ages near 1.59 Ga. Sm-Nd dating of crosscutting calcite veins suggests these may have formed up to 50 Ma later. The results of this case study suggest that the deep root of the IOCG system is represented by ~1.59 Ga old IOA-type mineralization which was later modified and upgraded to a hematite-rich, highly mineralized paragenesis at shallower levels of the deposit.

The present work has helped to place diverse gangue carbonates and associated minerals within an emerging chronology for this multistage deposit. Carbonates appear to have formed at nearly every stage of the host deposit's evolution, and their development and replacement history parallels that of other gangue minerals, and of the ore minerals themselves. The carbonates formed initially with the texturally earliest hydrothermal magnetite and apatite (~1.59-1.55 Ga) soon after emplacement of the host granite, followed by further periods at ~1.4-1.1 (REE-fluorocarbonates), ~0.8 and ~0.6-0.5 Ga. Thus, deposition of carbonates at Olympic Dam spans a period of more than 1 Ga. This chronology suggests that carbonate deposition and other aspects of the Olympic Dam deposit were related to major tectonic-magmatic events, beginning with the effects resulting from the breakup of Columbia (~1.6 Ga), followed by the tectonic, hydrologic and magmatic effects of the amalgamation and breakup of Rodinia (~1.3-1.1 and ~0.8 Ga, respectively), and renewed reworking, mineralization and mineral formation during amalgamation of Gondwana (~0.5 Ga). Carbonate gangue has been reported from many polymetallic IOCG deposits but few detailed

studies have been published. Comparison with these studies suggests that carbonates at Olympic Dam are unique in their complexity and protracted depositional history. This could be the key to the formation of a supergiant IOCG deposit such as Olympic Dam.

Acknowledgments

First of all, it has been a great pleasure working in the friendly and caring environment of the Centre of Excellence in Ore Deposits (CODES). I would like to thank those people who contributed greatly to this thesis and without whom it would have been impossible to complete this thesis.

My family is thanked for their endless love, belief in me and their constant positive mood which I appreciate very much. It is impossible to describe in words how much I love my family members and how thankful I am for their support especially during the writing period of my thesis just prior to submission. **I dedicate my PhD thesis to my mother.** I would also like to thank my wonderful partner, my love and my ironman, Leslie, who I met at the final stage of my PhD; I owe many hours of love and attention.

My intensive research on the genesis of Olympic Dam for three and a half years has involved the contribution of a large number of people which I would like to thank in particular:

- BHP Billiton Olympic Dam is thanked for giving financial and material support, and providing access to the mine during the two field trips.
- My primary supervisor Vadim (Dima) Kamenetsky, who I met in a nice small city Tübingen on a carbonatite conference, which had been organized by my former research group (with Gregor Markl as a leader of the group). At that time, I was about to finish my Master thesis and was heading to work in Ghana thereafter. However, an offer to spend some more time doing research - research on the largest ore deposit in the world - tempted me to move to Australia, an unknown continent for me those days. Right after arrival I felt like I was at home as Dima Kamenetsky and his family (wife Maya and daughter Sunny) welcomed me to their family, helped me to find accommodation and supported me through the entire PhD. Importantly, having Dima Kamenetsky as my primary supervisor was a great pleasure as he has been always incredibly open-minded towards all my new (and sometimes crazy) ideas, gave feedback almost every day and fortified completing research successfully. Dima Kamenetsky encouraged me at every stage to finish this challenging thesis where for almost every single sample a separate thesis could be completed.
- My four supervisors Dima Kamenetsky, Kathy Ehrig, Roland Maas, and Jocelyn McPhie are gratefully thanked for giving me an opportunity to become a part of the Olympic Dam research team and investigate an important aspect of this deposit - carbonate minerals and their associations. Our long, after hours discussions (in Dima's office or on the mine site) of various aspects of the genesis of the Olympic Dam were very fruitful for my thesis, incredibly interesting, exciting, motivating, and intensive. These people gave me lots of constructive criticism and motivated me to use creativity when proposing new ideas. I have to emphasize that it was a great honour to work with all of these supervisors who became my friends. Kathy Ehrig, a highly professional geologist who has been working at Olympic Dam for nearly 25 years, is gratefully thanked for her endless support from the very beginning, for her readiness to answer every question with great detail, for providing all necessary maps and figures and for creating a perfect working atmosphere in our Olympic Dam team. Roland Maas is particularly thanked for his patience in teaching me the procedures of isotope dilution and providing other everyday support (e.g., finding accommodation) during the time I spent doing my research at the University of Melbourne. Jocelyn

McPhie is thanked for sharing her knowledge about the preparation of detailed but simple and information-rich geological logs of the drillcore and for a comprehensive revision of my manuscripts.

- Maya Kamenetsky is thanked for preparation of numerous samples and her overall help with the analytical work and data reduction.
- Further PhD students of the Olympic Dam PhD team (Qiuyue Huang and Alex Cherry) are thanked for their support and warm atmosphere. Alex Cherry is additionally thanked for his talent in baking delicious cakes which we all ate with great pleasure.
- The team of highly qualified analysts of the Central Science Laboratory at the University of Tasmania is thanked for their help with numerous analyses using diverse analytical techniques. In particular, Karsten Goemann and Sandrin Feig assisted in the work on electron microscopy and X-Ray microanalysis; Christine Cook and Christian Dietz assisted in the work on Isotope Ratio Mass Spectrometry; and Thomas Rodemann assisted with vibrational spectroscopy.
- The CODES analytical research team (Jay Thomson, Sebastien Meffre, Paul Olin, Sarah Gilbert, and Leonid Danyushevsky) for helping in various LA-ICPMS analyses.
- Former and present geologists of the Olympic Dam mine (e.g., Tom Ho, Sabelo Charles Nzama, Glen Diemar) who I was pleased to meet during the two field trips for their interest in my research and for answering my questions. Sabelo Charles Nzama is particularly thanked for the unforgettable underground trip!
- Mike Backer for thoughtful comments about some paragraphs in Chapter 1 and Garry Davidson for general discussions on the IOCG systems.
- Leaders of the "Fox" group (Nigel Cook and Cristiana Ciobanu) from the University of Adelaide for being very helpful in correcting manuscripts and providing lots of useful criticism. PhD students Alkis Kontonikas-Charos and Sasha Krneta from the same group are thanked for discussions which we had during a group meeting in 2014 and SEG conference in 2015 in Hobart.
- Scientists and technical support at CODES, University of Melbourne (Alan Greig and Warrick Joe), University of Adelaide, and University of Cologne (Peter Sprung).
- Current and past office members and some other current and past PhD students at CODES.
- CODES lapidary technician, Alexander Cuison, is thanked for his help in the preparation of thin sections.
- Gregor Markl for his contribution to discussions about the project at the very beginning of it.
- Richelle Pascual for providing some useful material on colloidal genesis and for sharing an amazing time during the Goldschmidt conference (2013) in Florence.
- Douglas Haynes, one of the discoverers of the supergiant Olympic Dam deposit, whom I met at the SEG conference in Hobart (2015) and provided a positive feedback to my work and wished me good luck in finishing this exciting research.
- James Johnson, one of the pioneers of the Olympic Dam research team, whom I met at the CODES Science Planning Meeting and at the SEG conference in Hobart (2015) for his interest in my research and for very useful tips for my future career.

- Hobart unigym instructors (Trudy, Tom, Emilie, Michelle, Nicole, and Ej), and Hobart unigym members who have been spending at least an hour every day exercising together and having lots of fun.

Table of Contents

List of Tables

Table A.1: Major, minor and trace elements of spot analyses of carbonates and anhydrite performed on Q-ICPMS in Melbourne.

Table A.2: Results of the stable isotope analysis (S) of anhydrite.

All Tables are located in the appendix.

List of Figures

Appendices

General abbreviations

Tables 3.1 - 6.3 and A.1 - A.2.

Fig. A.1: Comparison of the trace element data (REY) of carbonates analyzed in Hobart and in Melbourne.

Fig. A.2: REY patterns of carbonates ordered after different carbonate associations.

Fig. A.3: (A) Drillcore images of the three anhydrite-bearing samples. (B) Spectra of the analysed anhydrite.

Fig. A.4: Transmitted and BSE images of anhydrite and several maps for the two selected areas in the studied samples.

Fig. A.5: Results of the stable isotope study of $\delta^{34}S$ in anhydrite, compared with the literature data for barite and diverse sulfides from the Olympic Dam deposit and with the potential S reservoirs.

Chapter 1: Introduction

1.1 Preamble

The supergiant U-Cu-Au Olympic Dam deposit in South Australia, containing approximately 9,5 Gt resources (Ehrig et al., 2012), is nowadays the world's largest U, third largest Au, fifth largest Cu resource with significant economic accumulation of Ag. The discovery of this world-class polymetallic deposit prompted the establishment of a new ore deposit class, namely the IOCG clan, with Olympic Dam (located in the Olympic Fe-oxide Cu-Au province) as a type locality (Hitzman et al., 1992). The basis for the fundamental genetic distinction from other deposit types was the major Cu sulfide mineralization with plentiful Fe-oxides (mainly hematite) inside the anorogenic granite body.

Geologists have been studying the genesis of the supergiant IOCG Olympic Dam deposit for about 40 years (since its discovery in 1975) (e.g., Roberts and Hudson, 1983; Reeve et al., 1990; Oreskes and Einaudi, 1990, 1992; Haynes et al., 1995; McPhie et al., 2011; Ehrig et al., 2012). However, there still exist many issues regarding its formation. Presently, about two million meters of a drillcore has been drilled to date at Olympic Dam. Consequently, previously unknown rock and mineral textures can now be studied. These new features may be critical to our understanding of the deposit formation, and as a result, new genetic models for the formation of the deposit may be necessary. Olympic Dam is not only one of the world's most profitable mineral deposits, but is also one of the most geologically complex, due to multiple stages of ore formation. Therefore, it is necessary to employ a number of analytical methods to adequately characterise the mineral associations present in the deposit and meet the goals of this project.

1.2 Aims and significance

Olympic Dam contains more than 90 minerals in addition to common minerals like Fe-oxides, Cu-sulfides, fluorite, barite, quartz and carbonates (Ehrig et al., 2012). These minerals were observed in different associations in a multistage breccia that makes the genesis of Olympic Dam very difficult to decipher. Previous studies on the Cu-U-Au-Ag Olympic Dam deposit resulted in a number of different genetic models evolved from the strata-bound sediment-hosted deposition (Roberts and Hudson, 1983) through explosive maar-related volcanism, accompanied by magmatic-hydrothermal activity (Reeve et al., 1990) and fluid-mixing of deep magmatic reducing brines with oxidized meteoric fluids (Oreskes and Einaudi, 1990, 1992; Haynes et al., 1995) back to more recent model that involves formation of a deposit syngenetic with the deposition of the bedded sedimentary facies (McPhie et al., 2011).

After the re-assaying of numerous drillcore samples drilled prior to 1997 for many additional elements, combined with the drillcore data from the drilling program in 2003-2008 (Ehrig et al., 2012), it became clear that Olympic Dam bears a large amount of carbonates that were previously thought to occupy only a small volume. The carbonate minerals (ranging in composition from Ca-Mg-Fe- to REE-F-dominated carbonates) represent the second largest after hematite gangue mineral at Olympic Dam, but only limited data are available for carbonates in the deposit, including a few fluid inclusion and stable (C,O) isotope studies of siderite only (Oreskes and Einaudi, 1992). The significance of carbonates has not been recognized in existing genetic models listed above. Moreover, all carbonate formation was assumed to belong to one genetic episode (the earliest pre-mineralization magnetite-pyrite-apatite-chlorite stage; Reeve et al., 1990; Oreskes and Einaudi, 1992; Hitzman et al., 1992; Haynes et al., 1995). Furthermore, compared to ubiquitous hematite in the ODBC (term first used by Reeve et al., 1990), both mineralized and barren zones, carbonates are restricted to the

parts of the deposit that are also rich in economic elements like Cu and U and, therefore, might provide important information about the genesis of the ore.

1.3 Structure of thesis and objectives of each chapter

Chapter 2 provides a general overview of the geology and mineralogy of the Olympic Dam deposit, including its regional and local geological setting, district geology, and lithological units within the deposit. Chapter 2 also contains information about the structural geology, mineralogical zonation, alteration and mineralization features of the deposit. This overall description is followed by a literature review on the geochronological studies of various minerals and studies conducted on carbonates in the deposit. The main genetic models of the deposit proposed by various researchers are discussed in the final part of Chapter 2.

A case study of the magnetite-apatite-bearing vein hosted by Gairdner Dyke Swarm (GDS)-type dolerite dykes is presented in Chapter 3. An assemblage of magnetite and apatite is common worldwide in different ore deposit types, including disparate members of the IOCG clan. The Kiruna-type IOA deposits, a subtype of the IOCG family, are recognized as economic targets as well. A wide range of competing genetic models exists for magnetite-apatite deposits, including magmatic, magmatic-hydrothermal, hydrothermal (-metasomatic), and sedimentary(-exhalative). The sources and mechanisms of transport and deposition of Fe and P remain highly debatable. This study reports petrographic and geochemical features of the magnetite-apatite-rich vein assemblages in the dolerite dykes of the GDS (~0.82 Ga) that intruded the RDG (~1.59 Ga), the host of the supergiant Olympic Dam IOCG deposit.

The ODBC has undergone multiple stages of hydrothermal activity and texturally destructive brecciation and alteration. Chapter 4 focuses on the mineralization within the deepest diamond drillhole to date (RD2773, EOH at ~2325 m). The goal of this chapter is to describe the texture and mineralogy of the *in situ* preserved early mineralization at Olympic Dam. A secondary goal is to use a combination of the dating and radiogenic isotope studies to prove the temporal relationship of the early mineralization and of the two host rocks (RDG and felsic unit) and to decipher the Sr and Nd sources of some minerals comprising this mineralization. Conclusions made in Chapter 4 have considerable relevance for further studies both on the early and on all postdating events within the ODBC. Furthermore, this study discusses the genetic link between IOCG and IOA deposits in general.

The Olympic Dam deposit has been recently recognized to contain not only a huge amount of ore but also carbonate minerals. However, only limited data exist on petrography, geochemistry and geochronology on carbonates at Olympic Dam. Chapter 5 presents the first part of the broad studies of carbonates at Olympic Dam. The objective of Chapter 5 is, firstly, to present recent resource maps which clearly indicate that both ore and carbonate minerals are distributed throughout the deposit in a similar manner (vastly abundant at the edges and at depth), which implies their genetic relationship. A second aim is to provide a detailed petrographic description of a large set of carbonates samples collected from all over the deposit. As investigated samples are very complex in a detail (great diversity of host rocks, textures, mineral relationships, and compositions of major elements), have features which may strongly differ from sample to sample and show evidence of a multistage nature, general systematization was proposed for all carbonate

occurrences at Olympic Dam. This grouping of carbonates represents the basis for further studies done in this chapter and in Chapter 6. The third objective of Chapter 5 is to quantify carbonate compositions using EPMA. This chapter also delivers a large number of results on the stable isotope (C-O) systematics of carbonates analyzed using IRMS. These data increase significantly the range of C-O compositions firstly studied by Oreskes and Einaudi (1992), and provide good foundation for further discussions on the sources of carbon which is one of the enigmas in the overall study of the Olympic Dam genesis. Thus, this research facilitated the understanding of the previously not fully appreciated, complex carbonate nature at Olympic Dam. All results of this study were used in this chapter in order to compare different IOCG deposits in terms of their carbonate characteristics worldwide.

The second part on the carbonate study is described from Chapter 6. This chapter compares in Chapter 5 those established carbonate groups in terms of their trace element contents (using Q-ICPMS) and various radiogenic isotope compositions (using MC-ICPMS). Numerous geochemical investigations of carbonates and some associated minerals (e.g., fluorite, anhydrite) represent pioneer studies which have the objective to determine the sources of some trace elements (e.g., Sr, Nd, Pb, Hf) and to estimate the stages of the precipitation of carbonates and associated minerals. This research indicates the suitability of several radiogenic isotope systems (Rb-Sr, Sm-Nd, Lu-Hf, Pb-Pb) in resolving the ages of carbonates. Chapter 6 provides a comprehensive description of geochemical work, which largely contributes to a further discussion of the Olympic Dam genesis in the context of its multistage evolution of some gangue and associated ore minerals.

Chapter 7 presents the overall conclusions for the work presented in this thesis. Appendices contain some data of analyses which were not included in Chapters 3-6.

1.4 Statement of authorship

Chapter 3 represents the only published paper from the current thesis. I was the primary author (60%) and designed the experiments with the goal of my supervisors Vadim Kamenetsky, Kathy Ehrig, Roland Maas and Jocelyn McPhie. I performed all analyses myself except for the bulk analysis on dolerite and radiogenic isotopes of dolerite and apatite in Chapter 3 which were performed by co-authors Kathy Ehrig (5 %) and Roland Maas (5 %), respectively. U-Pb dating of apatite and titanite was partially undertaken by Maya Kamenetsky (5 %), Vadim Kamenetsky (5 %) and Sebastien Meffre (5 %). EPMA analyses of apatite, magnetite and calcite and EBSD studies of magnetite and quartz have been conducted under strong supervision of Karsten Goemann (5 %). LA-ICPMS studies of apatite and magnetite have been conducted under supervision of Maya Kamenetsky and Sebastien Meffre. Thomas Rodemann (5 %) has helped in Raman study of magnetite and quartz. Careful proofreading has been made by Nigel Cook and Christiana Ciobanu (both 5 %).

Comments and edits for Chapter 3 were provided by Jay Thompson, Paul Olin, Qiuyue Huang, Alex Cherry, Richelle Pascual, and reviewers of the journal Contributions to Mineralogy and Petrology (Adam Simon, Christian Ballhaus, and an anonymous reviewer).

1.5 Statement of publication

A version of Chapter 3 is published in the Journal Contributions to Mineralogy and Petrology (doi. 10.1007/s00410-015-1215-7).

Chapter 2: Geology and Mineralogy of Olympic Dam

2.1 Regional and local geological setting

The Gawler craton is one of the four major cratons in central South Australia (Fig. 2.1) and was assembled episodically over a period spanning more than 1 Ga, from the Late Archaean to the late Paleoproterozoic-early Mesoproterozoic (Hand et al., 2007). The oldest granites in the Gawler craton, located on the Eyre Peninsula, are of a Mesoarchean age (~3150 Ma) and were recently discovered by Fraser et al. (2010). Neoarchean (2550-2500 Ma) is characterized by the creation of the complex basin with coeval arc-like magmatism which produced a range of magmatic rocks, from felsic through mafic to ultramafic (Hand et al., 2007). The latter include komatiites (2520 Ma) in the Harris domain (Hoatson et al., 2005). The period from ~2480-2420 Ma is marked by a collisional deformation which was followed by 400 Ma of tectonic inactivity. The next significant tectonic active phase occurred in the Proterozoic between 2000 and 1450 Ma (Hand et al., 2007). The largest basin sequence in the E Gawler craton, called the Hutchinson Group, formed after ~2000 Ma and most probably before ~1845 Ma on an inactive margin to the E of the Archean nucleus (Parker and Lemon, 1982; Hand et al., 2007). This complex contains quartzite and massive dolomite which are overlain by carbonates, interlayered pelitic units, and iron ore-hosting iron formations which are in turn covered by pelitic rock types and felsic volcanic and volcaniclastic units of the 1866±10 Ma Bosanquet Formation (Parker and Lemon, 1982; Fanning et al., 2007; Hand et al., 2007). Short-lived pulse wise deformation and granitic magmatism (on a batholith scale) occurred 1850±3.5 and 1860±4 Ma (Jagodzinski, 2005) and caused in the Olympic Dam district and SE Gawler craton emplacement of the capacious Donington Suite granites (Mortimer et al., 1988). Most of the E Gawler craton was covered during the period ~1765-1740 Ma (Cowley et al., 2003) by a next basinal sequence named Wallaroo Group. The sediments (metasiltstones, metacarbonate rocks, metavolcanic rocks of greenschist to amphibolite facies, and minor BIF) in this group are significant as they are host rocks for several IOCG prospects. The development of a large basin was hindered during the Kimban Orogeny (1730-1690 Ma) which led to granitic magmatism, crustal-scale shearing and metamorphism (up to a high grade). This was followed by an extensional period, confined magmatism and sediment deposition from 1680 to 1640 Ma which is coetaneous with the 1650 Ma Ooldean metamorphic event in the W Gawler craton. The S Gawler craton was intruded by arc-related St Peters Suite granitic magmas at 1620 Ma. Thereafter, the active plate margin developed to a continental interior system which led to the production of the coexistent intrusive Hiltaba Suite (1595-1575 Ma) and the equivalent extrusive Gawler Range Volcanics (GRV, 1595-1590 Ma). The Hiltaba Suite formed by high temperature fractionated felsic magmatism with lesser coeval mafic magmas. These mafic magmas are said to confirm a mantle component to the magma source (Hand et al., 2007 and references therein). The Hiltaba Suite granites, which are related to IOCG style mineralization in the Olympic Domain (Jagodzinski, 2005) in the eastern Gawler craton, are compositionally different to those located outside of this Domain (Hand et al., 2007). In the N part of the Olympic Domain, the Mesoproterozoic RDG (part of the Hiltaba Suite, Creaser, 1989) contains the Olympic Dam deposit (Fig. 2.1). The widespread Kararan Orogeny affected the Gawler craton at 1570-1540 Ma (Hand et al., 2007). Although the RDG remained undeformed during this period, this event might have influenced formation of the post-GRV sedimentary basin which surrounds Olympic Dam and has been described by McPhie et al. (2011). The Coorabie Orogeny 1470-1450 Ma (Hand et al., 2007) caused reactivation

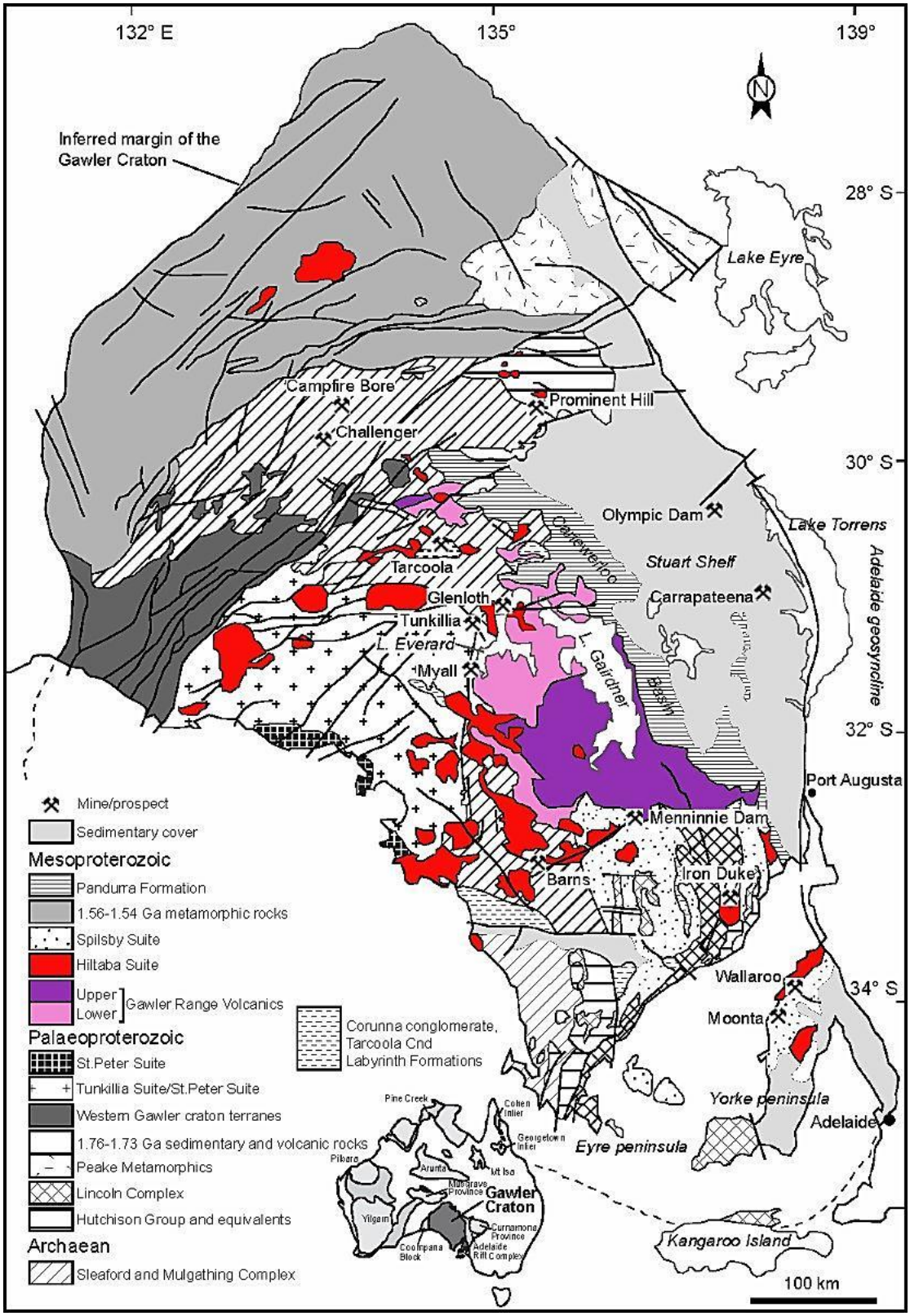

Fig. 2.1: Geology of the Gawler Craton (after Daly et al., 1998; Betts and Giles, 2006, Hand et al., 2007). Note the location of the Olympic Dam deposit.

of regional shear zones in the W Gawler craton, which resulted in a metamorphism (greenschist to amphibolite facie, e.g., Teasdale, 1997; Swain et al., 2005). Besides these periods, localised magmatism has been mentioned in the literature. The Coorabie Orogeny may have commenced the weathering of the source rocks to deposit the Pandurra Formation (~1.4 Ga, Drexel et al., 1993; Fanning, 2003) which unconformably overlays the Paleoproterozoic basement and early Mesoproterozoic igneous rocks in the E Gawler craton. The Pandurra Formation is composed of quartz-feldspathic fluviatile sandstones with minor shale bands (Mason et al., 1978). The Beda Volcanics cover unconformably this formation and represent a quite small package of subaerial basalt located in the far E margin of the Gawler craton and represent the last documented event in the Mesoproterozoic. These basalts superimpose the Pandurra Formation and are overlain by the Tapley Hill. Nevertheless, the age of Beda Volcanics is not well constrained yet with an assumed age between 1425 and 750 Ma (Drexel et al., 1993) and with the most widely accepted age of 1076 Ma (Webb and Coats, 1980). The latter age is similar to the age which has been derived from the dating of ~1.6 Ga old zircons and has been interpreted as a Grenvillian-aged reworking/resetting (1130 Ma) of the older Paleoproterozoic crust in Central Australia (Wong et al., 2015). Besides Central Australia, there is also evidence of this resetting in the Gawler craton (e.g., hydrothermal zircon at Olympic Dam, ~1.1 Ga, Jagodzinski, 2014). Importantly, many of the described tectonic processes are related to the assembly and breakup of the supercontinent named Columbia which may have enclosed nearly all of the earth's continental blocks at a period between 1.9 and 1.3 Ga (~1.6-1.3 Ga, Srivastava and Rao, 2007; Rogers and Santosh, 2009).

A further supercontinent assembly and break-up which affected the Gawler craton (Wingate et al., 1998) have happened during a relative long period of time, starting with amalgamation of Rodinia (~1.3-0.9 Ga). The activity of the superplume was triggered 40 to 60 Ma after amalgamation by thermal insulation from the thick continental crust which finally led to the breakup of Rodinia from ~0.8 to 0.5 Ga. The destruction of the large supercontinent led to the formation of the smaller supercontinents such as Gondwana (in a period between ~0.6 and 0.3 Ga, Veevers, 2004) and by this time already formed Laurasia (Li et al., 1999, 2008). The Gawler craton experienced some of the initial widespread plume activity which was caused by intra-continental, NW-SE rifting. In the time of this extensional event, mafic to ultramafic intrusions of the GDS were formed. These dyke intrusions have been emplaced at ~0.82-0.83 Ga (Wingate et al., 1998; Li et al., 2008; Huang et al., 2015). Beda Volcanics are possibly extrusive equivalents of the GDS.

2.2 Olympic Dam district geology

The Olympic Dam deposit is located on the E edge (former active arc environment, Hand et al., 2007) of the Gawler craton in South Australia (Fig. 2.1) and is hosted by a crystalline basement which is situated in a 60 km wide passage in the Olympic Domain, between the Torrens Hinge Zone to the E and the Elizabeth Creek fault to the W (Hayward and Skirrow, 2010). Felsic to ultramafic igneous rocks of the Donington Suite (1855-1845 Ma, Hand et al., 2007), Hiltaba Suite (1595-1575 Ma, Hand et al., 2007), the GRV (~1591 Ma for lower and upper GRV intrusives, erupted over a very short period of time, Fanning et al., 1988; Blissett et al., 1993; Hand et al., 2007), and GDS (~0.82-0.83 Ga, Zhao and McCulloch, 1993; Zhao et al., 1994; Huang et al., 2015) build the basement. The particular region of the crystalline basement around Olympic Dam is forming a paleotopographic high which is possibly formed by a horst thrust. The RDG appears to have been rapidly unroofed as the extrusive GRV rests nonconformably on coeval intrusive RDG (Creaser, 1989). The RDG is nonconformably overlain by ~350 m of flat-lying sedimentary cover sequence of Lower

Proterozoic shale and sandstone and Cambrian limestone (Sugden and Cross, 1991). This cover begins with the Pandurra Formation (~1.4 Ga, Drexel et al., 1993; Fanning, 2003), and overlain by the undeformed Stuart Shelf Facies. These include Adelaidean (Tregolana Formation, Arcoona Quartzite, and related facies) and Cambrian (Andamooka Limestone) sediments (Creaser, 1989).

2.3 Olympic Dam deposit

The detailed features of the Olympic Dam deposit have been documented by various authors since the deposit's discovery (e.g., Roberts and Hudson, 1983; Reeve et al., 1990; Oreskes and Einaudi, 1990, 1992; McPhie et al., 2011; Ehrig et al., 2012; Huang et al., 2015, 2016). The deposit is hosted by the ODBC (Fig. 2.2, Reeve et al., 1990) which is, in turn, entirely surrounded by the pink, undeformed, medium- to coarse-grained, equigranular alkali A-type RDG, which was emplaced at ~1.59 Ga (1588±4 Ma, Creaser, 1989; 1593.1±5.6 Ma, Jagodzinski, 2014). RDG belongs to the Hiltaba Suite granites which intruded both the Gawler craton and Curnamona Province (Hand et al., 2007). The granite has gone through multiple brecciation and alteration events, which are connected with the introduction of Fe, Cu and other metals and elements by hydrothermal fluids into the ODBC which at the end stage produced an IOCG deposit. The brecciation of the major host led to the development of one of the most pronounced zonation patterns across the deposit (Fig. 2.2), starting by continuum from unaltered unbrecciated granite on the peripheries, through granite-rich breccias (‘biotite out’ zone, biotite completely altered to chlorite, hematite alteration of magnetite, sericite alteration of plagioclase), to hematite-dominant breccias towards the centre of the deposit (i.e., barren hematite-quartz core, Figs. 2.2 and 2.3 A). Apart from the deposit-wide progressive brecciation and Fe-alteration of the granite, other several deposit-wide zoning patterns can be recognized at Olympic Dam and include orthoclase-sericite-hematite, siderite-fluorite-barite and pyrite-chalcopyrite-bornite-chalcocite zoning (listed by increasing abundance towards the centre of the deposit, e.g., Ehrig et al., 2012). It is assumed that this zonation was caused by an increase in both mechanical energy and hydrothermal fluid flux in the direction of the core of the deposit (Oreskes and Einaudi, 1990). It can be distinguished between several discrete minor (granite- and hematite-rich breccias) and major (felsic unit, various sedimentary facies, and two generations of mafic to ultramafic igneous rocks) lithological units within the ODBC which are briefly described below.

2.3.1 Granite-rich breccias

There is a wide range of granite-rich breccias (Fig. 2.3 A) which are usually comprised more of granite than hematite and are defined by a slight Fe alteration marked by the ‘5% Fe’ on Fig. 2.2. The extension of such breccias is wide and there is a range of breccia textures, implying their multistage nature and the involvement of different intensities and styles of brecciation. Most granitic breccias consist of veined or fractured granite and coarse clast-supported breccia types with occasional crackle and jig-saw textures (especially in matrix-poor granite breccias). Very rarely and on a small scale (a few cm), particularly in breccias with large granite clasts, graded bedding and fluid flow textures are common and resulted from sedimentation after milling. Rounding and milling of some clasts is explained by increased transportation. Hematite can be contained as clasts (usually angular to highly angular), cement and veins. The breccia matrix is composed of granitic and hydrothermal components; the latter are predominantly hematite, siderite, fluorite, chalcopyrite and pyrite (e.g., Roberts and Hudson, 1983; Reeve et al., 1990; Ehrig et al., 2012).

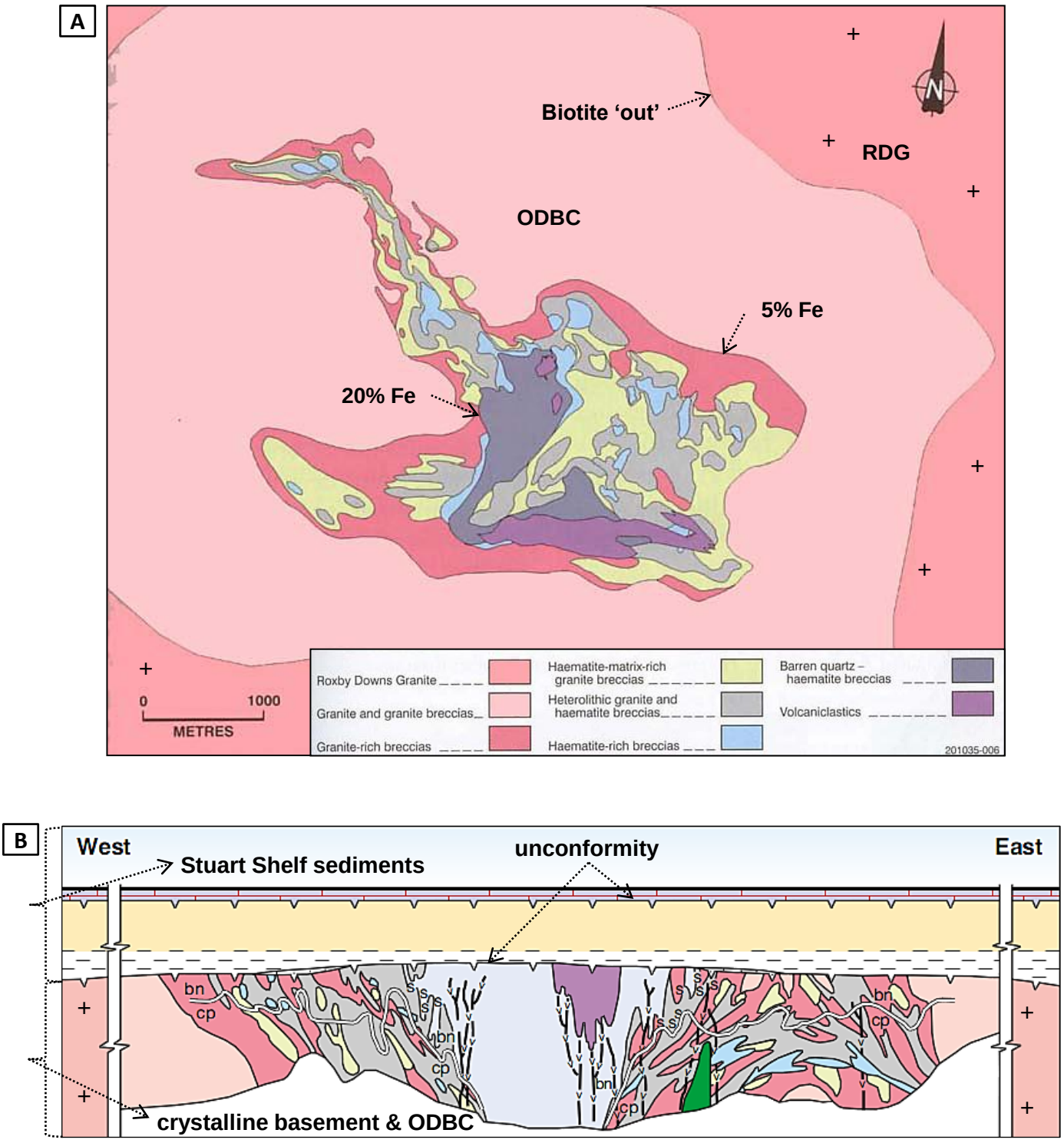

Fig. 2.2: (A) Plan view on the deposit at -350 mRL. Image shows the boundary (biotite 'out zone') between the unaltered RDG and the ODBC. Note the 5% and 20% Fe contours and general distribution of the major breccia units throughout the deposit. (B) Cross section of the ODBC showing the major unconformity separating the ODBC at the bottom a thick sedimentary package of Stuart Shelf at the top. Note the bornite (top) - chalcopyrite (bottom) interface. Images (modified) obtained from Reeve et al. (1990).

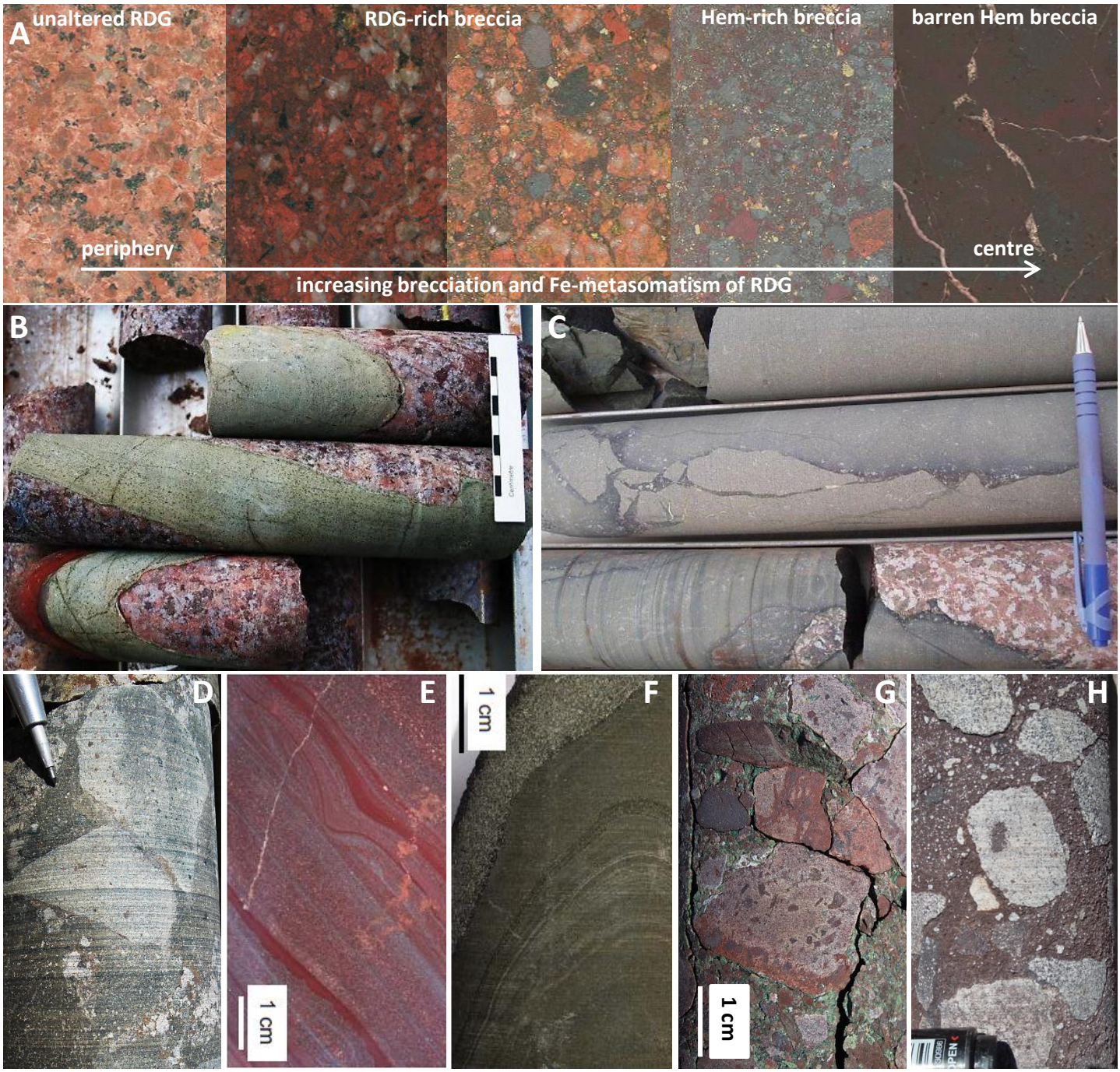

Fig. 2.3: (A) Selection of the most representative images of some of the major lithological units within the ODBC: unaltered and unbrecciated pink RDG on the left side becomes progressively hematite (Hem)-altered and brecciated towards the center of the deposit. Note transition from the altered RDG through RDG-rich breccia and hematite-rich breccias to the barren hematite-quartz-barite breccias. Images are 5 cm wide and obtained from Ehrig et al. (2012). (B) A sample of the light greenish, olivine-loaded picrite (a GRV component) hosted by the RDG; image obtained from Huang et al. (2016). (C) Two greenish GDS-related dyke generations which intruded into the RDG and show dyke-in-dyke texture; image obtained from Huang et al. (2016). (D) Light green felsic unit clasts within the chlorite-sericite- and RDG-rich breccia. (E-H) Sedimentary facies incorporated into the ODBC: (E) bedded red (hematite-rich) sandstone and mudstone, (F) bedded green (chlorite-rich) sandstone and mudstone, (G) polymictic volcanic conglomerate, and (F) clasts of grey (sericite-rich) Pandurra Formation-like sediment within the hematite-loaded breccia. Images (E-G) obtained from McPhie et al. (2011).

2.3.2 Hematite-rich breccias

The original textures of the granite-rich breccias are largely overprinted and, therefore, barely recognizable within the breccia with Fe content over 20% ('20% Fe' contour, Fig. 2.2), implying the dominance of hematite over other breccia components and a transition from granite- to hematite-rich breccias (Fig. 2.3 A). The latter also contain RDG-derived components; however, the RDG is by far more brecciated and altered. On the whole, the granite-rich breccias are more extensive than the hematite-rich breccias, which occur in more discrete and narrower zones. These breccias contain more hydrothermal minerals than the RDG-rich type and represent the major host for the zones where sulfide mineralization is by far the most abundant. Therefore, this breccia type has been assumed to be the main hydrothermal fluid pathway linked to the formation of the IOCG deposit. The hematite-rich breccias exhibit a range of textural variations between the types of clasts, matrix, cement ratios and different hematite colours. The clast size is usually less than 20 cm; however, locally large blocks up to tens of meters in size have been documented. The hematite colour depends on the grain size and is red to red-brown if fine-grained, brown if coarser-grained and grey to black if coarse-grained. Clast-in-clast breccias are common, implying multiple brecciation and cementing stages. Breccia clasts can exhibit highly variable angularity and sphericity but are generally angular and approximately equidimensional. The more hematite contained in the breccia, the more matrix-supported the breccia is. Such matrix-rich breccias are more abundant than a clast-supported type.

According to Reeve et al. (1990), there is a range of hematite-rich breccia subtypes, including hematite breccias, heterolithic hematite breccias and barren hematite-quartz breccias (Fig. 2.3 A). Usually dark grey to black in colour *hematite breccias* are localized to small areas within the deposit, usually within or on the edges of larger hematitic breccia bodies or contained (as narrow vein-like bodies) within the granite-rich breccias. Hematite is the dominant component both in the matrix and in the clasts. In the NW parts of the deposit this breccia type is strongly mineralized; however, when located below the chalcocite-bornite boundary, these breccias contain more pyrite than Cu-Fe sulfides. Porosity of these breccias can be highly variable; thereby, the most porous areas of these breccias appear to have resulted from strong leaching of particular breccia components in these discrete zones. Some exotic features of the hematite breccias include ooids/pisolites (often highly hydrothermally overprinted and mineralized), crustiform hematite, intensely laminated hematite-rich rock fragments, wispy discontinuous layering, and coarse feathery-textured hematite. *Heterolithic hematite breccias* occur as discrete elongate, irregular or lenticular bodies within a wide zone around the central hematite-quartz breccia body and are generally surrounded by granite-rich breccias. These breccias contribute to the largest proportion of the hematite-rich breccias within the deposit, which is the principal host of ore. This breccia type is comprised of clasts of different types where hematite-rich components (usually fine- to medium-grained) predominate. The heterolithic breccias can contain many different components of granite, re-brecciated hematite or granite, sedimentary clasts, volcanic and dyke fragments, and single mineral clasts (e.g., barite, siderite, fluorite, sulfides) in different proportions, depending on the location within the deposit. Matrix is mainly composed of hematite and a variable proportion of RDG-sourced components; hydrothermal gangue and ore minerals are usually disseminated in the matrix. Formation of this breccia type has most likely included significant transport and mixing. *Barren hematite-quartz breccias* are confined to the central parts of the deposit directly underneath the present unconformity, where these breccias occur as an L-shape lens with irregular edges. Clasts are principally hematite and

quartz which swim in a matrix of the same composition. In some parts of these breccia units, GRD-derived quartz can be highly abundant (up to 40% of the volume). However, hematite usually dominates in clasts and matrix. Minor breccia components are barite (disseminations, veins, infill and vein fragments) and rare fluorite. It is assumed that a significant late-stage leaching event produced this breccia type (e.g., Roberts and Hudson, 1983; Reeve et al., 1990; Ehrig et al., 2012).

2.3.3 Mafic to ultramafic igneous rocks

2.3.3.1 Early (~1.59 Ga) generation

Early generation of the mafic to ultramafic lavas and dykes (Fig. 2.3 B) related to the Gawler Silicic Large Igneous Province (SLIP) magmatic event (~1.595 to1575 Ga, in general are comprised of GRV and Hiltaba Suite, Blissett et al., 1993; Jagodzinski, 2005; Allen et al., 2008; Jagodzinski, 2014; Reid and Fabris, 2015) has been recognized at Olympic Dam at a relatively early stage of research (Reeve et al., 1990; Johnson, 1993; Johnson and McCulloch, 1995). The age of these rocks and similar rocks found at Wirrda Well and at Mt Gunson has been confirmed, on the basis of a U-Pb dating of the magmatic apatite, to be correlative with the SLIP event and intruded the RGD and the ODBC (Huang et al., 2016). Occurrence of the old generation of mafic to ultramafic rocks is largely restricted to one area directly beneath the major unconformity between the ODBC and flat-lying sedimentary cover where the thickness of dykes and lavas is ranging from 15 to 45 cm and in a NW-striking direction where the thickness is very small (up to 1 m, Huang et al., 2016). These rocks are basalts, dolerites and picrites which have been extremely altered to sericite, chlorite, quartz, carbonates and hematite. A detailed petrographic work has shown that these rocks were originally composed of plagioclase, clinopyroxene and olivine. The latter usually occurs as a skeletal relict, evenly distributed throughout the rock and can contribute up to ~20 vol.% in picrites (or olivine-phyric basalts) and contain Cr-spinel inclusions (occasionally with melt inclusions). Phlogopite microphenocrysts in groundmass have been largely pseudomorphically replaced by tabular to platy association of fluorite and chlorite (Ehrig et al., 2012; Huang et al., 2016).

The timing of the sericite alteration of these mafic-ultramafic rocks has been placed to ~1.1 Ga (Rb-Sr age, 1059±69 Ma, Creaser, 1989; Rb-Sr systematics, Maas et al., in preparation a). These rocks are fragmented and, therefore, have experienced multiple brecciation and compaction events and, therefore, occur as relicts within the ODBC intersected in a few drillholes. These units have been interpreted to have been formed in a pre-brecciation and pre-mineralization stage of the ODBC evolution (Ehrig et al., 2012; Huang et al., 2016). Many of these dykes are completely replaced by fine-grained hematite; these can be distinguished from other hematite rich lithologies as they are the only facies in Olympic Dam that are devoid of granite clasts. A study of the composition of Cr-spinel inclusions in a former olivine phenocrysts implies a heterogeneous mantle source (probably, modified by subduction) and has been suggested to play a role in the formation of this old mafic generation. This mantle-derived magma itself was most likely of a relatively high temperature which led to the partial melting of both the mantle and crust and the formation of the voluminous silicic magmas of the Gawler SLIP. Thus, the model proposed earlier for the Gawler SLIP (e.g., Giles, 1988; Daly et al., 1998; Hand et al., 2007) appears to be the most promising according to the studies of mafic-ultramafic GRV-related rocks at Olympic Dam (Huang et al., 2016).

2.3.3.2 Late (~0.82-0.83 Ga) GDS-type generation

A number of young mafic dykes (usually medium-grained, equigranular dolerite to fine-grained, porphyritic basalt, Fig. 2.3 C) have been intersected in the ODBC (e.g., Ehrig et al., 2012; Huang et al., 2015). These steeply deeping dykes intruded the mineralized ODBC and the granite but do not propagate into the barren, flat-lying cover sequence (e.g., Sugden and Cross, 1991). Therefore, it has been suggested that these dykes represent a separate and younger suit of dykes (e.g., Reeve et al., 1990; Ehrig et al., 2012). The width of the dykes ranges from several metres to over 100 m but narrow dykes occur as well. The main components in these dykes are plagioclase, pyroxene; rare mineral phases are Ti-magnetite and apatite (Ehrig et al., 2012; Huang et al., 2015). Magmatic apatite found in dolerites yield Neoproterozoic U-Pb ages around 830 to 820 Ma (Huang et al., 2015). Interestingly, these ages are consistent with the age for the intrusion of the GDS in the Gawler craton (E and N parts of it) and the Pandurra Formation at ~825 Ma (Zhao and McCulloch, 1993; Zhao et al., 1994), indicating that the Olympic Dam area was also impacted by the rifting at the time of the dyke emplacement (Huang et al., 2015). In general, the GDS is a NW-striking group of the longest (~1000 km in length) mafic dyke swarm in Australia and intruded at a time of the major crustal extension event at 0.82 Ga (Zhao and McCulloch, 1993; Wingate et al., 1998; Hoatson et al., 2008a; Hoatson, 2008b) as a response to the breakup of the supercontinent Rodinia (Ling et al., 2003; Wang et al., 2010; Sandeman et al., 2014). In addition to the temporal similarities, young mafic dykes at Olympic Dam are also similar to GDS dykes in terms of their composition and radiogenic isotope systematics (Nd, Huang et al., 2015). Contrary, the GDS dykes at Olympic Dam and elsewhere have more distinct geochemical signatures than the dykes of the ~1070 Ma Warakurna Large Igneous Province (LIP) which indicate the early stage of the Rodinia breakup (Huang et al., 2015 and references therein). Nevertheless, the dolerite Rb-Sr isochron age of 1059±69 Ma (Creaser, 1989) points either to the potential presence of this mafic generation at Olympic Dam or solely represents a sericite alteration event (Huang et al., 2015).

At Olympic Dam, these igneous rocks are dominantly dolerites; however, some dyke-in-dyke-textures (Fig. 2.3 C) imply a later impulse of basalt (Ehrig et al., 2012). These young mafic rocks which intruded the ODBC significantly later after the GRV-related mafic-ultramafic rocks and the RDG, are usually only weakly altered and postdate the early brecciation event. However, local syn- to post-intrusion brecciation features can be observed (e.g., Ehrig et al., 2012; Huang et al., 2015). Chilled margins are often found along the contacts between the dykes and both the breccia and RDG (Huang et al., 2015).

Occasionally, these GDS-type mafic dykes are crosscut by usually only a few mm narrow post-magmatic veinlets which have various compositions, including carbonates, quartz, chlorite, barite, fluorite, apatite and some ore minerals. U-Pb dating of titanite (often usually on the vein selvage) and apatite yield ages (821±15 and 817±11 Ma, respectively) which are similar to the intrusion ages of this dyke generation (Huang et al., 2015). The preliminary results on the alteration of the mafic rocks suggest the contribution of mafic rocks to some metal and element components seen within the mineralized breccias (Huang et al., in preparation).

2.3.4 Felsic unit

The *'felsic unit'* termed rock unit at Olympic Dam has been mentioned in one work (Ehrig et al., 2012). This rock has been intersected at a depth of ~1900 to 2300 m in the deepest vertical drillhole (RD2773) which is only located in the SE part of the breccia complex. This rock has been interpreted to have intruded as a dyke into the RDG. The margins

of the dyke have experienced brecciation and the rock has been strongly altered to sericite and recrystallized (Fig. 2.3 D). However, no age data exist in the literature and neither its exact origin (e.g., lava, dyke) nor its genetic and temporal relationship (pre-/syn-/post-RDG) to the weakly brecciated RDG in this particular drillhole could be surely constrained at that time of research. The composition of this highly sericite-altered rock is dominated by quartz (in a groundmass and as phenocrysts, occasionally with melt inclusions) and rare apatite and zircon. This implies a magmatic origin of this rock with a rhyolitic composition.

2.3.5 Sedimentary facies

The deposit incorporates a significant volume of Mesoproterozoic sedimentary rocks with the largest extension at least 1.5 km long, 0.9 km wide and 350 m thick (e.g., McPhie et al., 2011, 2016). Sediments occur immediately below the unconformity with late, flat-lying, barren Neoproterozoic formations and have usually faulted and brecciated to rare gradational contacts between them and the breccia complex. These sediments can be subdivided into five facies based on several characteristics (e.g., composition, grain size and bed forms). These units include interbedded sandstone and red mudstone, well-sorted quartz-rich sandstone, green sandstone and mudstone, polymictic volcanic-clast conglomerate, and thinly bedded green and red mudstone (Fig. 2.3 E-H, McPhie et al., 2016). Beds in green (locally altered to hematite) and red sediments can be both graded and massive and usually contain volcanic quartz. While components (e.g., feldspar, quartz) in the red units are largely granite-derived; green (chlorite-rich) sandstone also comprised of detrital chromite which, together with the volcanic quartz, is supposed to have been sourced not only from the immediate vicinity of the deposit (McPhie et al., 2011; Ehrig et al., 2012; McPhie et al., 2016). Particular beds of the bedded clastic facies may contain features pointing to the hydrothermal alteration. Such features include anomalous concentrations of Mo and As (Ehrig et al., 2012) and as post-depositional interpreted ore components (e.g., pyrite, galena, concentrated along specific beds, Meffre et al., 2010; Kamenetsky et al., 2015; McPhie et al., 2016). Conglomerate-breccia contains mafic to felsic GRV-derived clasts and represents rather a volumetrically minor component of all sedimentary facies within the ODBC and occurs interbedded with red and green sandstones (McPhie et al., 2011; Ehrig et al., 2012; McPhie et al., 2016).

Recent field work completed as a part of this PhD has led to the discovery of the Pandurra Formation-like clasts of the quartz-rich sandstone in one drillhole (Fig. 2.3 H, Kamenetsky et al., 2015; McPhie et al., 2016). This unit has been described as *'well-sorted quartz-rich sandstone'* in McPhie et al. (2016). Dating of zircon found in these clasts yield three age populations (~2.5, ~1.7 and ~1.6 Ga, Kamenetsky et al., 2015; McPhie et al., 2016) which have also been identified in the Pandurra Formation which infills the ~1.4 Ga old Cariewerloo Basin (e.g., Drexel et al., 1993; Fanning, 2003). This implies that older Gawler craton basement rocks also contributed sediment to the bedded clastic facies (McPhie et al., 2016). The founding of the relicts of the largely *'digested'* or reworked by the breccia complex clasts of this Formation is a highly important observation as the Pandurra Formation might have contributed to the element (e.g., C) and metal (e.g., Fe, Cu, U) contents of the Olympic Dam deposit.

There is a continuing debate on the source and timing of these sediments (e.g., Ehrig et al., 2012 and references therein). Earlier researchers explained these massive sedimentary packages within the deposit as slump blocks of subaqueous-subaerial volcanic maar-lake sediments sourced from volcanic processes with some later reworking by surficial processes (Reeve et al., 1990; Oreskes and Einaudi, 1990; Johnson and McCulloch, 1995; Haynes et al., 1995).

This theory was mainly based on the distinction of the five apparently isolated domains of bedded sedimentary units. It is now known from further drilling that the exact architecture of these blocks, which allowed a reinterpretation of the nature of these sediments to being considered as slump block remnants of a sedimentary basin succession (with a provenance which extended beyond the Olympic Dam area). These sediments formed above the RDG pre- to syngenetically with the mineralization (McPhie et al., 2011; Ehrig et al., 2012; McPhie et al., 2016). The structural measurements in the faults within the bedded sediments provided solid evidence that the basin has probably been gently plunged to the NE direction prior to final lithification. Moreover, a new finding of the bubble-wall shards in tuffaceous mudstone facies implies contribution from rhyolitic explosive eruptions located perhaps several km away (McPhie et al., 2016).

2.3.6 Structural geology

The deposit is crosscut by a highly complex array of brittle, mainly steeply-dipping, continuous to discontinuous, multistage faults having diverse orientations and a sense of movement (Fig. 2.4, Sugden and Cross, 1991; Drexel et al., 1993). Thereby, their foremost movement plane seldom lies directly on the lithological contact (Sugden and Cross, 1991). It is evident that "*the ODBC was formed in a dynamic system involving the interaction of hydrothermal fluid flow, brecciation, mineral precipitation, dyke injection and faulting*" (Sugden and Cross, 1991). A structural aspect of one of the world's largest underground mines (400 km of underground development, K. Ehrig, SEG conference talk, 2015) was studied in great detail using different approaches (underground mapping, acoustic televiewer logging, oriented drillcore measurements, and regional geophysical datasets) and can be obtained from several published and unpublished works (e.g., Sugden and Cross, 1991; Widupp et al., 2004; Hayward and Skirrow, 2010), which are summarised in Ehrig et al. (2012). The above described the minor and major lithologies together with the hydrothermal alteration and mineralization show evidence of strong tectonic impact (e.g., Ehrig et al., 2012). This includes shearing, brecciation, milling and movement of blocks in various directions. Five major sets were recognized at Olympic Dam (Fig. 2.4), trending N-S, NW, WNW to E-W, NE and ENE. Discontinuous local-scale structures are represented by N-S and WNW to E-W faults (Ehrig et al., 2012). However, shear zones trending NW (Elizabeth Creek fault, Hayward and Skirrow, 2010), NE (Todds Dam fault, e.g., Drummond and Lyons, 2002; FitzGerald et al., 2004), and a Masher's fault (total length of ~35 km long, Cranswick and Network, 2009) can be tracked over many kilometres and are, therefore, significant on a regional scale. It is hard to define a clear chronological classification scheme for these fault zones; however, there is evidence of reactivation for the majority of these faults. For example, steeply to the N deeping, generally the NW-trending Masher's fault which passes through the middle of Olympic Dam, known as the Jubilee fault in a regional context (Cranswick and Network, 2009; Hayward and Skirrow, 2010), has been active since Neoproterozoic to Delamerian and has offset all other fault sets at Olympic Dam with the exception of the N-S faults (Ehrig et al., 2012).

The complex fault system at Olympic Dam appears to have contributed to the deposit shape, rock unit distribution and ore (pre- and/or synmineralization) and mineral zonation. For instance, it is known that a huge block of bedded sediments near the centre of the ODBC has been transported downwards during the extensional regime (pers. com. with K. Ehrig). Further, hematite and Cu mineralization has been found to be partially associated with N-S, NW and NE fault zones; whereas enrichment in Mo minerals is bound to WNW to E-W array (Ehrig et al., 2012). The relatively late stage

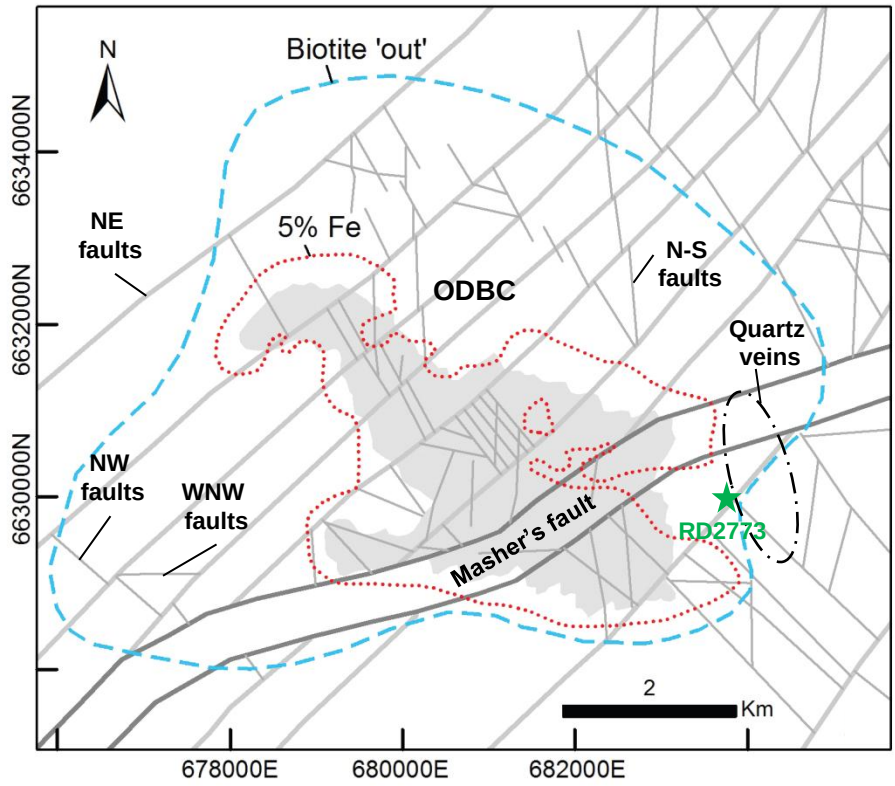

Fig. 2.4: Simplified structural map shows strongly fault-controlled nature of the ODBC. Note different fault directions and their generally discontinuous nature. Also note the location of the quartz veins and the deepest drillhole RD2773. Masher's fault, going through the middle of the deposit, is the widest and lonest among all faults at Olympic Dam. Map modified after Ehrig et al. (2012).

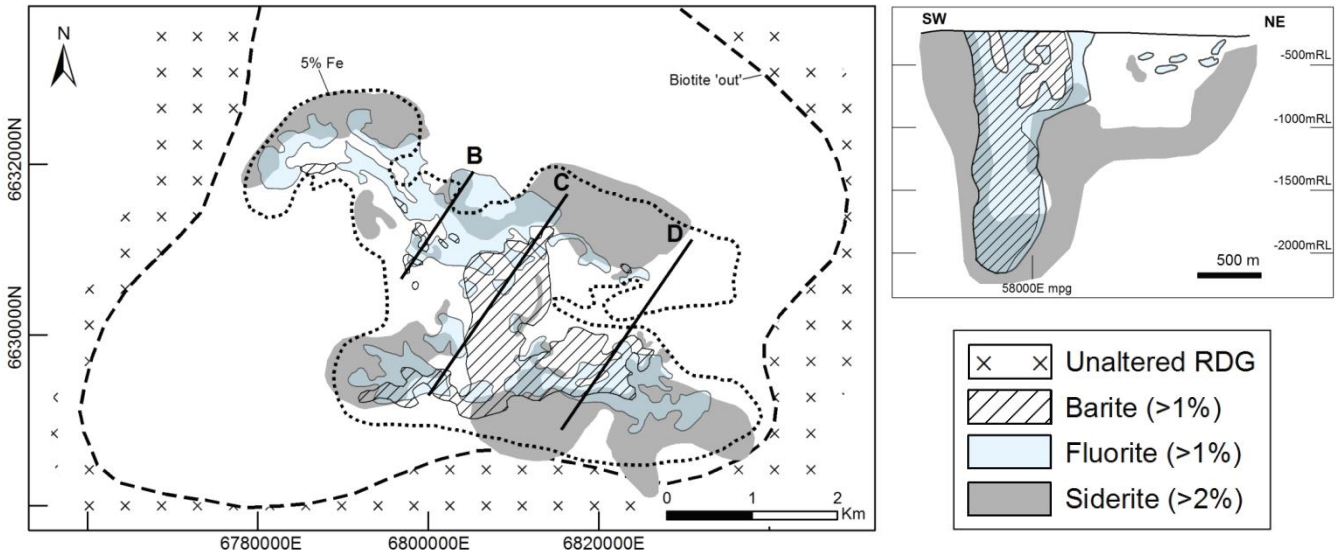

Fig. 2.5: (A) Simplified plan map at -350 m RL illustrating the extent of the hydrothermal alteration caused by siderite, fluorite and barite. Note the gross deposit margin-to-core zonation from siderite through fluorite and to barite in a cross section (right side). Figure obtained from Ehrig et al. (2012).

of the evolution of the ODBC is characterized by an intrusion of dolerite dykes (GDS), emplaced as diffuse swarms, which used mainly NW and locally NE striking faults as structurally preferable zones for their emplacement (e.g., Sugden and Cross, 1991; FitzGerald et al., 2004; Ehrig et al., 2012; Huang et al., 2015). Further, a late-stage event such as the formation of the generally massive barite-fluorite-carbonate-sulfide veins can be interconnected with conjugate NE and E-W striking fault zones which were found to propagate into the cover sequence, indicating Delamerian Orogeny (Preiss, 1987; Sugden and Cross, 1991).

2.3.7 Hydrothermal alteration

The main alteration minerals at Olympic Dam are hematite, sericite (including fine-grained muscovite, illite, phengite and paragonite), carbonates, quartz, barite and fluorite (e.g., Reeve et al., 1990; Ehrig et al., 2012; Tappert et al., 2013). Hematite and sericite are the predominant alteration minerals which can be observed in all alteration assemblages across the deposit. Besides granite, all four alteration minerals also usually overprint other non-granitic lithologies, for instance mafic to ultramafic dykes. Alteration of the matrix is commonly more intense than that of clasts which is a grain-size issue. Often one single lithological unit displays more than one alteration event which implies multistage overprinting of the ODBC by circulating hydrothermal fluids. In some cases, alteration of major and minor host lithologies at Olympic Dam is so pervasive that the initial rock fabric is nearly or completely unrecognizable. These zones with extremely altered rock and breccia units complicate the interpretation of the primary rock distribution and, therefore, hinder the evaluation of the genetic model. Nevertheless, some general features of alteration aspects across the deposit could be figured out:

(1) *Hematite* alteration is zoned across the deposit (Fig. 2.2). The grade of the hematite alteration is used to establish the limits of the alteration (e.g., 5%, 20% contours) within the deposit and to separate some lithological units within the ODBC. Hematite gradually replaces *in situ* brecciated granite at the periphery and strongly replaces brecciated granite components and matrix towards the centre of the deposit. Hematite forms pseudomorphs of former igneous orthoclase but also of some early hydrothermal minerals (e.g., magnetite, siderite, chlorite, sericite, sulfides) as well. The crystal grain-size of hematite varies from very fine (e.g., if pseudomorph after sericite) to large (specular crystals, usually in late veins and fillings).

(2) *Sericite* is widespread across the deposit (see Fig. 6 in Ehrig et al., 2012), similar to hematite. Sericite has completely replaced plagioclase (in areas with Fe concentration up to 5%), most of the orthoclase and some of the hydrothermal chlorite in nearly all ore-bearing zones. This replacement has given rise to the widespread deposit-wide alteration halo and zoning of feldspar-(sericite+feldspar)-sericite margin-to-center zonation. The felsic unit, occurring in the deepest drillhole, is partially to almost completely overprinted by sericite. Tappert et al. (2011, 2013) analysed the phengite composition across the deposit and suggested that the ore zones contain Al-rich phengite, whereas peripheral phengite contains by far less Al, which can be used as a prospecting tool for IOCG deposits.

(3) *Chlorite* alteration of the igneous biotite has been used as a frontier for the unaltered granite and the ODBC. Also the igneous amphibole of the RDG has been partly destroyed by chloritization, particularly at depth. Mafic to ultramafic rocks (and their clasts) are commonly associated with chlorite alteration where chlorite is the main alteration mineral. Away from the contact with mafic to ultramafic rocks, sericite typically replaces chlorite and becomes gradually more abundant towards the mixed granite-hematite breccias.

(3) Ubiquitous silica alteration (*quartz*) is generally limited to localised zones. The deposition of the hydrothermal quartz is most probably a result of the silica released during the sericite alteration of the magmatic feldspar. Quartz is abundant in breccia matrix and often occurs as anhedral to subhedral grains. Narrow (1 to 5 mm thin) quartz (±apatite-magnetite-siderite) veining is a common feature of the altered, unbrecciated granite in the deposit margins. An approximate 200 m wide zone in the SE part of the deposit is characterized by the occurrence of larger (up to 50 m thick, strike length of >800 m) veins in altered RDG (Fig. 2.4). These thick quartz veins are typically barren and their timing cannot be estimated via field relationships.

(4) *Carbonate* alteration is abundant as well and generally restricted to a deposit-wide alteration halo which retraces a vessel-like shape (Fig. 2.5). Siderite is by far the dominant carbonate type, whereas Ca-Mg-rich carbonates are usually associated with mafic-ultramafic igneous rocks. Siderite commonly occurs in a reduced assemblage together with some other minerals such as magnetite, apatite, chlorite, pyrite and quartz. Siderite and magnetite in this assemblage are partially to completely replaced by hematite. Apart from the breccia matrix, siderite is also preserved as vein fragments, late-stage veins and veinlets and some other more exotic textures (e.g., laminations, crusts, vug fills, oolites). Zones with Cu-rich sulfides (e.g., bornite, chalcocite) are by far siderite-depleted compared to the zones where pyrite-chalcopyrite association dominates (periphery and deep parts of the deposit). Neither siderite nor the below discussed fluorite and barite have been observed to replace any preexisting minerals within the ODBC. However, all three minerals show textures (e.g., matrix cement, breccia clasts, veins, amygdales) pointing to their multistage nature (Ehrig et al., 2012).

(5) *Fluorite* is disseminated throughout the whole deposit (Fig. 2.5) and exhibits a range of colours (purple, green, translucent) with the purple variety being the most common among all. The role of fluorine in the generation of the supergiant IOCG Olympic Dam deposit has been emphasized by Agangi et al. (2010). Nearly all breccia units (including the high grade hematite and copper ore) are composed of some localized high grade fluorite, which have precipitated in all and can be associated with. Fluorite forms together with barite late stage (Delamerian, Maas et al., 2011) massive veins which produced a large alteration halo across the deposit.

(6) Similar to fluorite, *barite* is abundant in the ODBC in most breccia facies (Fig. 2.5). The barren hematite-quartz core zone of the deposit is particularly rich in barite (mainly occurring as thick barite-dominated dykes which is also comprised of hydrothermal fluorite, Maas et al., 2011), often reaching concentrations of 15 wt%. Oreskes and Einaudi (1990, 1992) have interpreted the appearance of laminated barite clasts as maar-lake chemical sediments deposited together with REE.

2.3.8 Mineralization

The distribution of the ore components, their abundance, associations and correlations of diverse ore minerals has been detailed documented by numerous workers (e.g., Roberts and Hudson, 1983; Reeve et al., 1990; Oreskes and Einaudi, 1990, 1992; Ehrig et al., 2012). The Olympic Dam deposit is currently mined for Cu, U (U_3O_8), Au and Ag; thereby, Cu sulfides (chalcopyrite, bornite and chalcocite) are the primary economic ore. In addition, the ODBC contains elevated/anomalous concentrations of many other metals and elements (F, S, C, As, Ba, Bi, Cd, Co, Cr, Fe, In, Mo, Nb, Ni, P, Pb, Se, Sn, Sr, Te, V, W, Y, Zn and REE). The vast majority of Cu, U and Au mineralization is found within hematite-rich breccias (which are not always mineralized); however, these metals are present in significant amounts in the granite-rich breccias; whereas other lithological units within the ODBC might contain minor

mineralization. Thus, the ore minerals show a positive correlation with the Fe contents; thereby above 45 wt% Fe the concentrations of precious metals decrease. The distribution of Cu, U and Au at Olympic Dam correlates positively (Fig. 2.6, Ehrig et al., 2012).

Precious metals are incorporated into a variety of different ore minerals at Olympic Dam:

(1) *Copper* occurs mainly as primary interpreted Cu sulfides such as chalcopyrite, pyrite (at least two generations), bornite and chalcocite (listed in the order of decreasing abundances, with chalcopyrite having 50 % abundance). At Olympic Dam, Cu can be also present in relatively minor abundant ore minerals (some of them of a secondary nature) such as fahlore (tennantite-tetrahedrite), enargite, covellite, tenorite-cuprite and native copper. Cu ore minerals are generally small-sized (avg. 100 μm) and occur predominantly disseminated within the breccia. Apart from pyrite, Cu sulfides have usually an interstitial nature with gangue minerals; microveinlets in some other minerals such as hematite are common, whereas sulfide clasts are scarce. Intergrowth with siderite is by far more typical for pyrite and chalcopyrite than for bornite and chalcocite. Massive sulfide mineralization is very rare. One of the important features of Cu sulfides is their deposit-wide margin-to-center zonation of low Cu/S ratio species to high Cu/S ratio species: pyrite → chalcopyrite → bornite→ chalcocite→ (native copper) → native Au. Thereby, the chalcopyrite-bornite boundary is a well-defined interface at Olympic Dam (Roberts and Hudson, 1983; Reeve et al., 1990; Ehrig et al., 2012).

(2) The main *uranium*-containing ore minerals are coffinite, brannerite, and uraninite with relative proportions of 56%, 31% and 13%, respectively. Small amounts of U are present in some other ore, gangue and accessory minerals. U, in general, has a relatively low abundance across the deposit and the grain sizes of U-bearing minerals are usually very small (avg. 20 μm). The highest U grades are often seen disseminated in bornite- in hematite-rich breccias. Microveinlets occur locally and can contain a significant U amount. Textural observations reveal that most U minerals have been remobilized on both a micron and large scale. This might be the reason why the end product of the deposit, as we see it today, does not show zonation of U minerals, which is opposite to sulfides and some other minerals (Roberts and Hudson, 1983; Reeve et al., 1990; Ehrig et al., 2012).

(3) *Gold* is broadly distributed with U and Cu; however the gold grades can vary independently. The dominant Au mineral phase is electrum which has various Au/Ag ratios depending on mineral associations. Other Au-rich minerals are calaverite, petzite and terta-auricuprite. Three main mineralogical and lithological associations bear gold. These include sulfide native gold or electrum locked up as inclusions in sulfides, Au inclusions in some gangue minerals (particularly abundant at edges of the hematite-quartz-barite breccias), and associated with the seritization and silicification of the granite-rich breccias. High grade gold nuggets or bonanza veins can be found inside the margins of the barren hematite-quartz breccia in zones up to several m wide. *Silver* occurs mainly as hessite inclusions in sulfides and is also incorporated in electrum, acanthite, petzite, allargentum and infrequently as native silver. Trace contents of silver are common for bornite, chalcocite and fahlore. Similar to the U mineral distribution, the distribution of different Au minerals does not display any systematic deposit-wide zonation pattern (Ehrig et al., 2012).

The majority of earlier workers (e.g., Roberts and Hudson, 1983; Reeve et al., 1990; Oreskes and Einaudi, 1990, 1992) emphasize that the paragenetic sequence between different ore types is extremely hard to establish. Nevertheless, based on petrographic textures (see above) and the existing chalcopyrite age data (1258±28 Ma, McInnes et al., 2008),

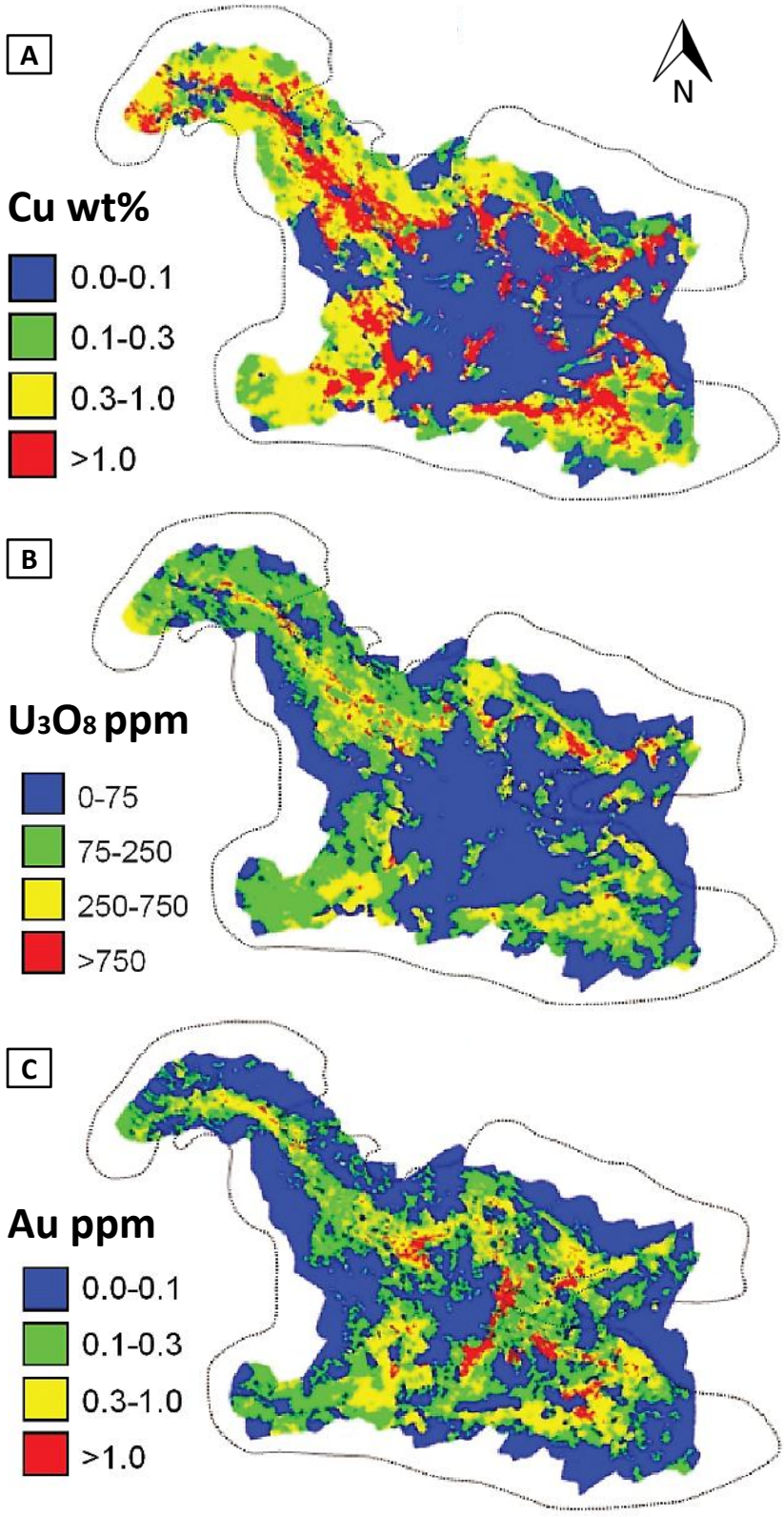

Fig. 2.6: Distribution of Cu (A), U_3O_8 (B) and Au (C) ore (at -350 mRL) is positively correlative. Maps are based on the 2011 resource model. Figure obtained from Ehrig et al. (2012).

Cu sulfides appear to have been deposited fairly late in the cycle of brecciation and deposit evolution. Uraninite is often intimately intergrown with chalcopyrite (rhythmic intergrowths with sulfides+fluorite from core to margin, Ehrig et al., 2012; Macmillian et al., 2015) and the overall occurrence of U minerals is positively correlated with those of Cu minerals (Ehrig et al., 2012). This implies that Cu and U have been precipitated together from F-carrying hydrothermal fluids at least in one stage during the deposit formation. Further, Reeve et al. (1990) suggested that Cu either post-dates most or all of the hematite, or at least is coeval with it. There is no evidence that Cu sulfides have been formed under supergene conditions (i.e., no chalcocite replacements of pyrite or chalcopyrite) in the ODBC; however, it is possible that the erosion has removed this part of the former deposit cap. In general, there are numerous forms of evidence that most ore (e.g., Ehrig et al., 2012; Macmillian et al., 2015; Ciobanu et al., 2015) and gangue (e.g., Wawryk, 1989; Maas et al., 2011, in preparation a and b; Diemar, 2014) minerals have gone through one or several rounds of precipitation, dissolution, and reprecipitation which partially overprinted or completely vanished the initial distribution (and, possibly, zonation) of these minerals.

2.4 Review of Olympic Dam carbonates

As mentioned in Chapter 1.2, carbonate studies at Olympic Dam are limited to a few (e.g., Oreskes and Einaudi, 1992; Lottermoser, 1995; Maas et al., 2011; Ehrig et al., 2012; Diemar, 2014). Understanding of the importance of further studies of carbonates has significantly changed since the discovery of the deposit, particularly after realizing that the Olympic Dam deposit is not only a polymetallic but also a carbon anomaly and carbonates have been observed in associations with ore minerals throughout the entire deposit. The following subchapters provide a detailed literature overview of studies and subsequent interpretations of various carbonates at Olympic Dam. Importantly, Fe-Ca-Mg-Mn- and REE-F-dominated carbonates have very different relative abundances (97.1% and 2.9%, respectively, Ehrig et al., 2012), are distributed not in exactly the same manner throughout the deposit, and appear in many different associations which do not always overlap. It appears that the two distinct carbonate groups have been precipitated both cogenetically and independently from each other during the long-term evolution of the breccia complex. Therefore, Fe-Ca-Mg-Mn- and REE-F-dominated carbonates are discussed separately below.

2.4.1 Fe-Ca-Mg-Mn carbonates

2.4.1.1 Distribution and petrography

Pioneers in the research of the genesis of the Olympic Dam observed that diverse rocks in the Olympic Dam graben have been altered to varying degrees to hematite, sericite, chlorite, silica and carbonates. Thereby, pervasive carbonate alteration was described more as a local feature of the breccia complex (e.g., Roberts and Hudson, 1983). At present, it is known that Fe-Ca-Mg-Mn carbonates (especially siderite) are by far more widespread and, thus, are among the principle hydrothermal alteration minerals (e.g., hematite, magnetite, sericite, quartz, chlorite, fluorite, barite) described at Olympic Dam. Siderite is the dominant carbonate mineral at Olympic Dam (relative abundance is ~88%), whereas ankerite and dolomite-calcite are only locally abundant (5.6% and 4%, respectively, Ehrig et al., 2012). Carbonate associations and textures are diverse. Some carbonate types have been observed to occur in a particular association and to develop a particular texture.

Siderite is enriched at depth and at the outer margins of the deposit (Fig. 2.5) where it appears together with the reduced association containing magnetite, pyrite, apatite, chlorite and quartz. This association is one of the major alteration assemblages in the deposit and has been proven by recent drillcore re-assaying and aggressive drilling program (2003-2008) to be more widespread downward and outward in Olympic Dam than previously described (Ehrig et al., 2012). Siderite is a common inclusion in pyrite in this association (Roberts and Hudson, 1983) which also occurs as microveinlets (1-5 mm) in highly altered but unbrecciated granite (Ehrig et al., 2012). The zones with massive siderite are also rich in some ore components (e.g., Cu, U_3O_8, La, Au, Ehrig et al., 2012; Diemar, 2014). Contrary, zones with Cu-rich minerals such as bornite and chalcocite are siderite-poor (Ehrig et al., 2012). These observations led to the assumption of the genetic relationship of this reduced assemblage and, therefore, their early nature (e.g., Roberts and Hudson, 1983; Oreskes and Einaudi, 1990; Reeve et al., 1990; Hitzman et al., 1992; Haynes et al., 1995; Ehrig et al., 2012). Distractive hematite alteration is one of the main features of the Olympic Dam. A common texture in the Olympic Dam breccia is replacement and rimming of siderite, magnetite, and chlorite by hematite, especially in the central parts and near the top of the deposit where hematite is the most abundant component in the breccia (20% Fe, Oreskes and Einaudi, 1990; Ehrig et al., 2012). In such Fe-rich breccias, clasts of single minerals such as siderite, chalcopyrite, barite, and fluorite may appear randomly distributed throughout the deposit (Oreskes and Einaudi, 1992; Ehrig et al., 2012). The three gangue minerals have been interpreted as pieces of early veins which were fragmented and incorporated into breccia (Oreskes and Einaudi, 1990) and sulfide clasts have been assumed to have formed after preexisting carbonate clasts (Roberts and Hudson, 1983). However, siderite (together with barite and fluorite) was not observed to replace any preexisting primary or hydrothermal minerals (Ehrig et al., 2012). Siderite is also contained within concentric to radial pisoliths and ooliths. Such rocks are variously composed and comprise hematite, fluorite, chlorite, sulfides, and U minerals (Roberts and Hudson, 1983). Crustiform siderite is another rare, briefly described texture in the Olympic Dam texture of siderite (Roberts and Hudson, 1983). Siderite also forms a cavity infill in the breccia complex (Oreskes and Einaudi, 1992).

When going from the periphery inward and upward from depth towards the deposit center, a siderite-rich zone is followed by fluorite and then by barite (Fig. 2.5, Oreskes and Einaudi, 1990; Ehrig et al., 2012). This zoning is caused by later massive barite-fluorite-dominated veins which crosscut the old siderite generation preferably near or in the center of the deposit. The age of these veins, which are propagating into the cover sequence (Sugden and Cross, 1991) and have a stress direction sub-parallel to those inferred by the Delamerian Orogeny in the Willouran Fold Belt (e.g., Preiss, 1987; Sugden and Cross, 1991), was assumed (Wawryk, 1989) and then proven as Delamerian (Sm-Nd age, ~0.5 Ga, Maas et al., 2005, in preparation a). This implies that these veins postdate the granite intrusion by more than 1 Ga. Siderite (and to a lesser extent dolomite and calcite), chlorite, sericite, quartz and various Cu-Fe sulfides (commonly chalcopyrite and rare pyrite, bornite and chalcocite) might be present in these barite-fluorite-dominated veins (e.g., Wawryk, 1989). Thereby, apart from this late association, siderite and barite have not been observed to occur together in a paragenesis, although both minerals occur in multiple generations (e.g., Wawryk, 1989; Oreskes and Einaudi, 1992; Maas et al., 2005; Ehrig et al., 2012; Diemar, 2014). Occasionally, hematite and siderite form narrow veins which have been interpreted as intermediate in nature (Oreskes and Einaudi, 1990).

Ankerite and dolomite-calcite occur locally in predominantly matrix-poor breccias containing basement granite clasts (Roberts and Hudson, 1983) and as hydrothermal impregnation and narrow veining in mafic-ultramafic rocks (Ehrig et al., 2012). Dolomite veins having uncertain (presumably late) age have been briefly described by Oreskes and Einaudi (1990).

2.4.1.2 Analyses

Semi-quantitative results of the major element *composition* of Fe-Ca-Mg-Mn-dominated carbonates are accessible in Ehrig et al. (2012). In order to identify the carbonate species, the authors used automated mineralogy data (Mineral Liberation Analysis, MLA), which is based on matching energy dispersive x-ray spectra patterns of the samples to reference spectra and does not include a full quantification of the data. This study resulted in identification of ankerite, dolomite-calcite solid solutions and siderite. Siderite has been subdivided into Mn-free/poor (relative abundance of 2.65 wt%) and less common Mn-rich siderite (0.24 wt%) based on MLA. No quantitative data on carbonates exist yet.

Fluid inclusion studies on one siderite sample, representing a vein fragment in a breccia, were conducted in the 1990s (Oreskes and Einaudi, 1992). Eighteen isolated (assumed as primary) and secondary (trail-related) inclusions have been analyzed. A wide range in homogenisation temperatures from 110 to 300˚C (Fig. 2.7 A) and no clear clustering have been explained as a common problem of highly cleavable minerals. All inclusions are 2-phase, consisting of vapour and liquid with no clearly observed daughter minerals. Interestingly, no CO_2 clathrates have been observed which authors explain by the presence of dissolved in liquid CO_2 and/or technical difficulties.

In order to make tentative estimates of the origin of the siderite-depositing fluids, Oreskes and Einaudi (1992) conjugated the fluid inclusion study with the analysis of *stable C-O isotope compositions*. Sixteen texturally diverse (ooids, clasts, veins, cavity fill and massive) siderite samples were taken from the siderite-rich zone on the E side of the deposit (with one taken from the NW area). Samples yield $\delta^{13}C$ from -3.5 to -2.3‰ (avg. -2.6‰) and $\delta^{18}O$ from 12.7 to 20.9‰ (avg. 16.6‰). Although the carbon field is relatively tight compared to hydrothermal carbonates worldwide, the data cloud intersects a number of possible carbon reservoirs (Fig. 2.7 B). Thus, a solid conclusion about the source of carbon was impossible to make at that stage. However, the authors assumed that carbon might have been derived from basement carbonates or carbonatites or exsolved magmatic carbon dissolved in hydrothermal waters. The range of $\delta^{18}O$ is larger which might be caused by oxygen isotope fractionation during a progressive cooling of the related hydrothermal fluids. The combined study of fluid inclusions and stable isotopes in various hydrothermal minerals conducted by Oreskes and Einaudi (1992) resulted in the establishment of a 2-stage genetic model, involving precipitation of the reduced siderite-magnetite-pyrite assemblage from hot (~400˚C) hydrothermal fluids with a high $\delta^{18}O$ content (~10‰), followed by a second-stage hematite-ore assemblage deposited from cooler (200-400˚C) fluids with lower $\delta^{18}O$ content (<9‰). Despite proposing the coeval formation of siderite and magnetite, the authors admitted that there is a problem in the siderite stability with the presence of magnetite at such elevated temperatures. The CO_2 pressures required to stabilize siderite should be high which is, however, incompatible with a near-surface milieu of deposition. The authors suggested that enrichment of siderite, in particular thermodynamic components (e.g., Mg, Ce), might solve the problem of the magnetite-siderite coexistence at a relative low depth of formation; unfortunately, no data on carbonate composition were accessible at that stage of the research. Alternatively, this association might not be cogenetic at all.

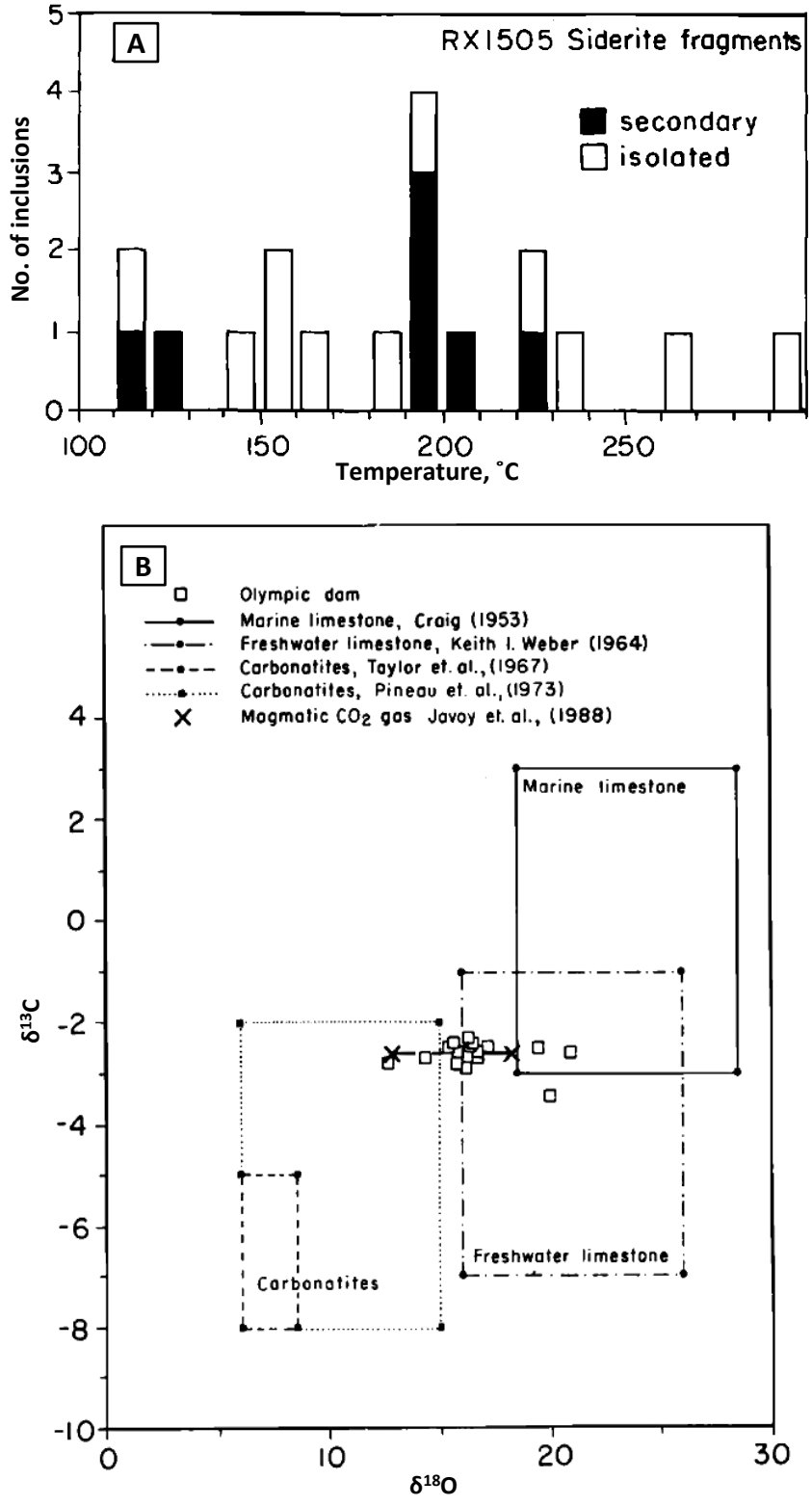

Fig. 2.7: (A) Fluid homogenization temperatures for siderite plotted on a histogram. Note the temperature range from 110 to 300˚C. (B) $\delta^{13}C$ and $\delta^{18}O$ results for the Olympic Dam siderite. Stable isotope values from various carbon reservoirs such as carbonatites (Taylor et al., 1967; Deines and Gold, 1973; Pineau et al., 1973), limestones (Craig, 1953; Keith and Weber, 1964) and CO_2 gas from Oldoinyo Lengai (Javoy et al., 1988) are plotted for comparison. Figures obtained from Oreskes and Einaudi (1992).

Radiogenic isotope ($^{87}Sr/^{86}Sr$) studies have been conducted on two white to pinkish-white dolomite vein samples (collected in the S part of the deposit) as a part of the broad study on the barite-fluorite association at Olympic Dam (Wawryk, 1989). The Sr content of barite and fluorite is generally higher than that of carbonates (Sr^{2+} substitution of Ba and Ca cations of the same charge). Dolomite yield 140 to 204 ppm Sr and no measurable Rb. Compared to co-analyzed barite ($^{87}Sr/^{86}Sr$ = 0.70935 to 0.72593) and fluorite ($^{87}Sr/^{86}Sr$ = 0.71272-0.72725), two dolomite samples show slightly different $^{87}Sr/^{86}Sr$ ratios (0.71387 and 0.71674). The author interpreted the variation in isotopic compositions of the three gangue minerals as a reflection of *"differences in source rock chemistry, to be expected for a proposed source such as the Olympic Dam Suite, the members of which exhibit a range of compositions"*.

2.4.2 REE-fluorocarbonates

2.4.2.1 Distribution and petrography

Olympic Dam contains an anomalous but in a moment subeconomic amount of REE-bearing minerals which have around 0.17 wt % La and 0.25 wt % Ce (Fig. 2.8, Ehrig et al., 2012). It can be distinguished between several REE species. These include minerals with REE as a primary element in the crystal structure (e.g., monazite, florencite, bastnäsite and synchysite) and in solid solution (e.g., apatite, brannerite, coffinite, crandallite, thorinite, thorite, uraninite, uranothorite and zircon, Lottermoser, 1995; Ehrig et al., 2012; Diemar, 2014). The most common REE phase at Olympic Dam is bastnäsite [$(Ce,La)CO_3(F,OH)$]; synchysite [$Ca(REE,Y,Fe,Th,U)(CO_3)_2F$] is another REE-fluorocarbonate which is less widespread (2.5% and 0.4% of all carbonates, respectively, Ehrig et al., 2012). Synchysite has been interpreted as early as it is contained in the RDG as an accessory mineral (Ehrig et al., 2012). Overall petrographic observations (e.g., Oreskes and Einaudi, 1990; Lottermoser, 1995; Ehrig et al., 2012; Diemar, 2014) revealed a large variety of mineral associations observed in REE-fluorocarbonate-bearing samples. Synchysite is by far less documented than bastnäsite. The latter has usually 20-100 μm sizes but can be down to a submicron size (Lottermoser, 1995) and shows anhedral (in groundmass) and euhedral (tabular-elongated-prismatic needles) habits (Diemar, 2014). Euhedral (to subhedral) habit indicates a growth into open spaces and has been interpreted as primary mineral growth which can be assumed to have occurred after the main brecciation events. In contrast, an anhedral habit can be explained in various ways which includes mineral properties, physical milling, interstitial mineral growth or co-precipitation, recrystallization, pseudomorphing (e.g., after sericite), alteration, corrosion, overgrowths and replacement (Diemar, 2014). Bastnäsite is contained within the granite- and hematite-breccias, in breccias comprising mafic to ultramafic rocks, and sericite dykes (Diemar, 2014). In these lithological units bastnäsite occurs as: (1) fine-grained in laminated barite and its fragments (interpreted to have formed in the maar crater lakes); (2) disseminated in orange-peach-coloured, *in situ* brecciated, and as intermediate (temporal aspect) interpreted quartz-sericite-monazite veins; (3) intergrown and/or cementing hematite; (4) disseminated in the quartz-sericite matrix of granitic breccia; (5) interstitially intergrown with bornite; (6) intergrown with fluorite; (7) replacement rims on fluorite; (8) sericite-altered groundmass sericite-altered groundmass; (9) intimately intergrown with florencite; (10) as anhedral inclusion in chalcocite, bornite, quartz, and chlorite; and (11) disseminated in siderite (Roberts and Hudson, 1983; Oreskes and Einaudi, 1990; Lottermoser, 1995; Ehrig et al., 2012; Diemar, 2014). Thus, precipitation of bastnäsite and synchysite has most likely occurred over a substantial period of time, most probably *"during much of the hydrothermal history of the Olympic Dam"* (Oreskes and Einaudi, 1990), including possible remobilization of these

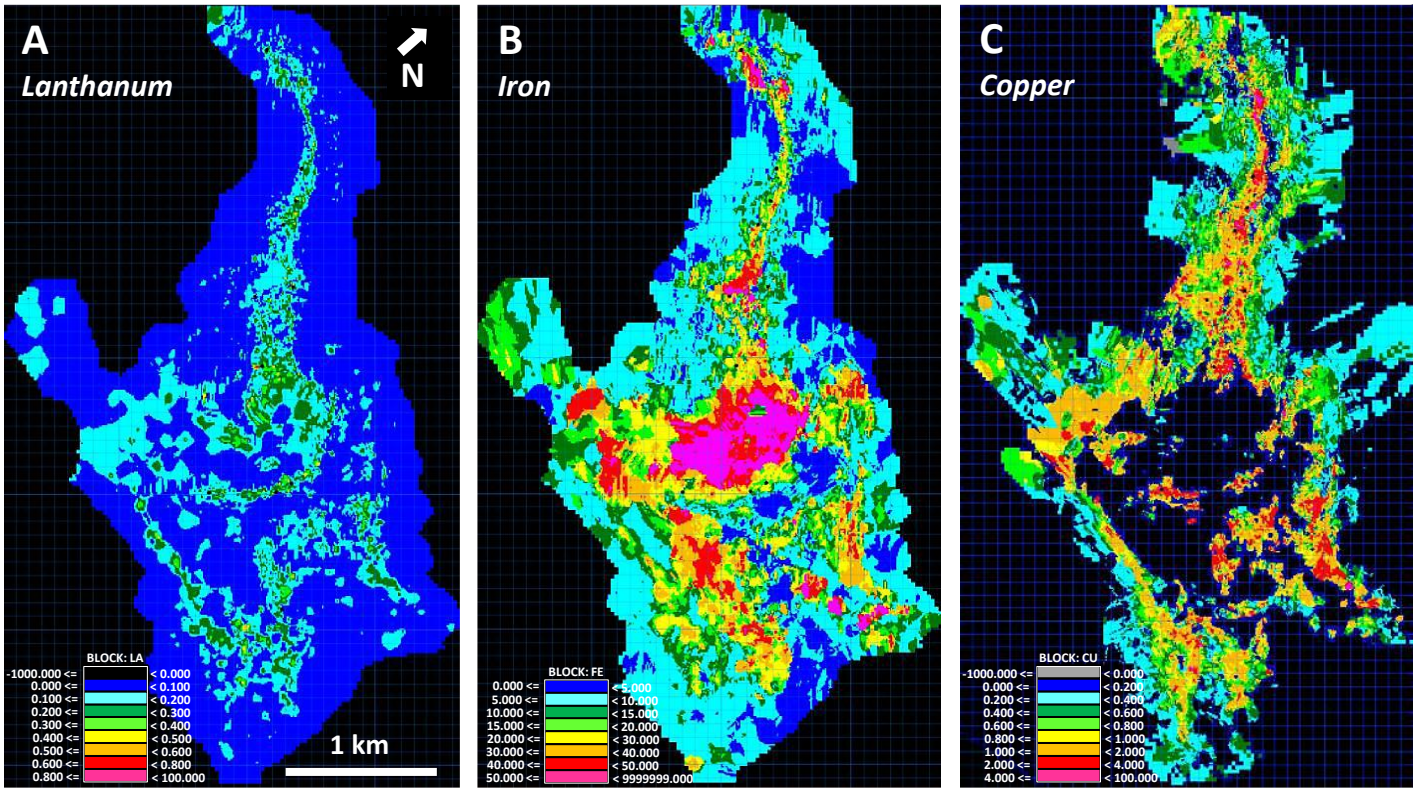

Fig. 2.8: Cross sections at -450 mRL showing the distribution of La (A), Fe (B), and Cu (C, in wt%), based on the 2010 resource block model. Images obtained from Diemar (2014).

carbonates (e.g., Diemar, 2014). Summarizing, bastnasite appears to have been co-precipitated with some other gangue (e.g., fluorite, barite, hematite, quartz, chlorite) and ore (bornite, chalcocite) minerals. Interestingly, there is no description of the association of REE-fluorocarbonates and Ca-Fe-Mg-Mn carbonates apart from siderite association mentioned above. Based on petrographic observations such as intimate intergrowth of U- and REE-bearing minerals with sulfides, hematite and fluorite, researchers stated that besides F, S, P and Fe, carbonate complexes might have played an important role during the deposition of the U-REE mineralization (Roberts and Hudson, 1983).

2.4.2.2 Analyses

A few *semi-quantitative electron microprobe analyses* of bastnäsite combined with those of the main U minerals (uraninite, brannerite, and coffinite) presented in Lottermoser (1995) yield low Y and heavy REE (HREE) contents for bastnäsite compared to U mineral phases. As Y and HREE complexes are generally considered to be more stable in hydrothermal fluids, the authors proposed a certain genetic model for the precipitation of the REE minerals. This model describes precipitation of LREE-rich minerals (bastnäsite, synchysite, florencite and monazite) prior to HREE- and Y-rich minerals (U minerals, xenotime and zircon) at Olympic Dam.

Fifteen *quantitative geochemical analyses*, each representing a separate REE-rich (bastnäsite-dominated) breccia sample, of a large suit of major, minor and trace elements (totalling 75) have been analyzed using 9 different analytical techniques (Diemar, 2014). These studies revealed that La, Ce, and Nd can be count to major elements in these REE-rich bulk samples. REE patterns are generally very similar (excluding one outlier, Fig. 91 in Diemar, 2014) and exhibit very high LREE and HREE enrichment compared to chondrite (McDonough and Sun, 1995) with the LREE enrichment being more pronounced. The REE enrichment and high La/Lu ratios for the samples might be explained by a high degree of brecciation and fluid flow in the sample location areas which has been suggested as a rule for the deposit on the whole (Oreskes and Einaudi, 1990).

A *cathodoluminescence* study of REE-rich samples conducted by Diemar (2014) was aimed to show the growth and possible recrystallization features of the REE-fluorocarbonates and subsequent mapping of trace elements across bastnäsite grains. However, this technique showed little success (no signal).

Radiogenic isotope geochronology (Rb-Sr and Sm-Nd, Fig. 2.9) has been conducted by R. Maas (Maas et al., 2011) on five particular REE-rich breccia samples (one of the samples has been analyzed twice) described in the study of Diemar (2014). The technique used was acid step-leach with five leach steps, which aimed at separating the REE contained in the fluorite from the REE in other minerals (e.g., bastnäsite), which would lower contamination by REE from the fluorite. The produced Sm-Nd results show no random scatter, and, therefore, indicate relatively complete separation of mineral solubilities which, in turn, means reliable data. Results plotted on a Sm-Nd isochron diagram (Fig. 2.9 A) form an elongate cluster with a trend line having a slope at 1300±250 Ma. When adding two results with the extremely low Sm/Nd, the age produced is significantly younger (1115±100 Ma). Another line can be drawn through the two Sm/Nd-poor ratios and four other results coming from leach steps four and five from the three fluorite-poor samples. In this case, the slope is very steep and the corresponding age is ~4.0 Ga which is unrealistic for the particular deposit. Therefore, the steep array has to be treated as a mixing line rather than an isochron. Although being not as reproducible as the Sm/Nd step-leach, the Rb/Sr step-leach results (1390±190 and 1341±320 Ma, Fig. 2.9 B) completed on the same step-leach fractions broadly supports the two Sm-Nd ages. At 1300 Ma, the εNd and $^{87}Sr/^{86}Sr$ values are

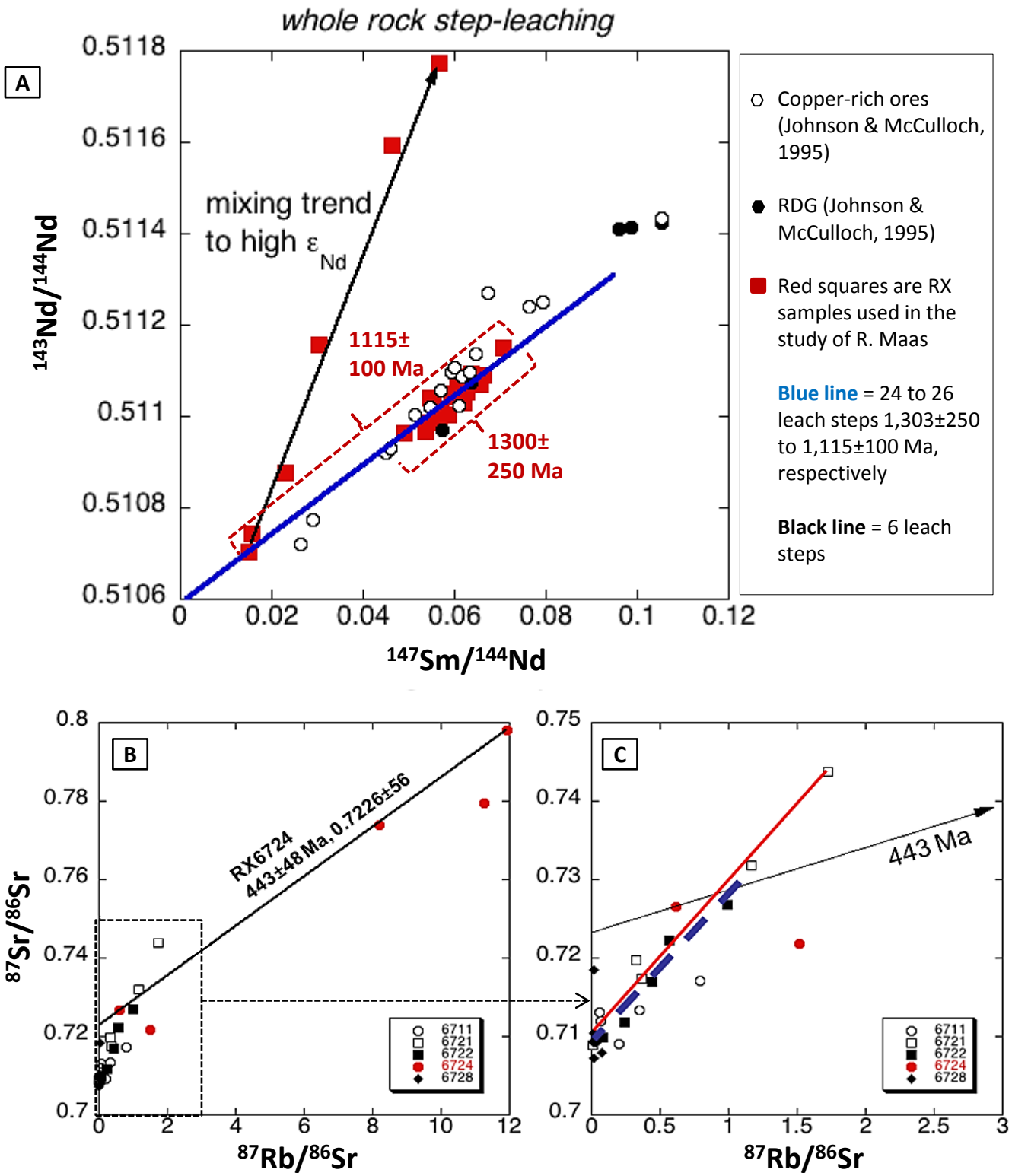

Fig. 2.9: Radiogenic isotope systematics of the five REE-rich breccia samples. (A) The black line defines a mixing, whereas the blue line is a real Sm-Nd isochron (1300±250 and 1115±100 Ma, with/without including of the two results with the lowest Sm/Nd ratios). (B) Rb-Sr isochron (with a close-up in C) produces ages 1390±190 and 1341±320 Ma which largely coincide with the Sm-Nd ages. One sample (white sericite dyke) indicates a much later age (443±48 Ma). Figure produced by R. Maas and obtained from Diemar (2014).

~-7.5 and ~0.708, respectively. Overall, the age of ~1.3 Ga for the REE mineralization confirmed in the study of R. Maas correlates with the ages reported for some Fe-Cu-Pb sulfides (e.g., Re-Os age of chalcopyrite ~1.26 Ga, McInnes et al., 2008; Pb-Pb age of pyrite and galena ~1.4-1.2 Ga, Meffre et al., 2010) and U mineralization (oldest published U-Pb age of uraninite ~1.4 Ga, Johnson, 1993; Trueman, 1986), which implies that much of the metals at Olympic Dam were deposited in the period 1.4-1.1 Ga (Maas et al., 2011).

2.5 Review of Olympic Dam geochronology

The age of the Olympic Dam deposit (e.g., Gustafson and Compston, 1979; Trueman, 1986; Wawryk, 1989; Johnson, 1993; Johnson and Cross, 1995; Johnson and McCulloch, 1995; McInnes et al., 2008; Meffre et al., 2010; Huang et al., 2015, 2016; McPhie et al., 2016) and similar deposits and prospects particularly within the Olympic Cu-Au Province in the E Gawler craton (e.g., Acropolis, Creaser, 1989; Carrapateena, Porter, 2010; Ernest Henry, Marshall et al., 2006; Hillside, Ismail et al., 2014; Conor et al., 2010; Moonta, Morales Ruano et al., 2002; Prominent Hill, Belperio et al., 2007; Wirrda Well, Davidson et al., 2007) is poorly constrained and is, therefore, a highly debatable subject to date. Both dating of various ore, gangue and accessory minerals in the breccias and in various lithologies within the ODBC complex have had and still have crucial effects on the deposit's genetic model which is being constantly updated (see Chapter 2.3).

As Olympic Dam deposit is the largest U deposit in the world, substantial dating on uraninite (or pitchblende) has been carried out. Trueman et al. (1988) recorded uraninite ages of ~1359 Ma and ~533 Ma based on ion microprobe $^{207}Pb/^{206}Pb$ ratios. Johnson (1993) conducted further studies on uraninite and, firstly, verified ages from Trueman et al. (1988) by getting ages of ~1400-1350 and ~570 Ma and, secondly, added some new data (~1.2 and ~0.83 Ga). Thus, the age of ~1.4 Ga has been interpreted as a maximum crystallization time of uraninite and, therefore, the introduction of U into the Olympic Dam system. A similar age of the sericite alteration of the granite has been proven by another researcher (Rb-Sr age of ~1315-1360 Ma, Gustafson and Compston, 1979). A bit younger Rb-Sr age (1059±69 Ma) of the sericite alteration of the dolerite dykes is obtainable from work of Creaser (1989). However, the problem back then was that researchers did not allow the thought of the ~1.6 Ga host granite being not cogenetic with the mineralization. Moreover, as the deposit formation has been considered as one-staged (e.g., Reeve et al., 1990; Oreskes and Einaudi, 1992; Hitzman et al., 1992; Haynes et al., 1995; Johnson and McCulloch, 1995) and no geological events known at that time could explain all the age palette of uraninite, these data has been considered rather as a remobilization phenomenon and have not been published. Further, Johnson and Cross (1995) issued SHRIMP ion microprobe U-Pb zircon results for two felsic dykes (perperites) which have been dated to 1593±7 and 1584±20 Ma. Authors interpreted one of these dykes to cut across sediments and the other to cut across mineralized breccias. Johnson and McCulloch (1995) used the age of ~1.6 Ga as a widely accepted age for the Olympic Dam ore for their calculations of the initial εNd values. The resulted values (avg. ~-2.5) have been interpreted as a result of mixing of fluids supplied by the granites (negative εNd) and mantle derived mafic to ultramafic rocks (positive εNd); thereby, the contribution of the mantle-derived source rock or

magma contribution was ~30%. The chalcopyrite Re-Os age of 1258±28 Ma (McInnes et al., 2008) has been discounted by the authors as unrealistic young (younger than the age of the granite) and should, therefore, mean resetting rather than primary crystallization. Similarly, Hayward and Skirrow (2010) criticized analogous, post-1.6 Ga ages for uraninite (~1.4 Ga, Trueman et al., 1988; Johnson, 1993) and vein galena (^{207}Pb-^{206}Pb ages, ~1.4-1.2 Ga, Meffre et al., 2010) again based on the possible isotopic resetting. Interestingly, the age of ~1.6 Ga has gained popularity in the entire Gawler craton (e.g., Skirrow et al., 2007) and majority of later researchers dismiss their dates if they are not ~1.6 Ga rather than question it. One of the first workers who questioned this syn-RDG age of the ore deposition were Oreskes and Einaudi (1990, 1992). The authors based this suggestion both on the repeating literature results of the post-granite ages for numerous minerals and on the observed field relationships. Latter include hard comprehendible sequence of ~1.6 Ga events such as formation of the RDG at great depth, fast uplift, erosion, and formation of the extended sedimentary rocks prior to deposit formation. However, new drilling completed during the 2003-2008 expansion of the resource model allowed observation of new field relationships and, in particular, the extension of the sedimentary facies. These appear in new models more as a relatively continuous layer rather than discrete occurrences which allowed McPhie et al. (2011) to conclude that *"…hydrothermal system operated beneath and partly within an active sedimentary basin, was not confined to maar craters, and did not vent"*. This implies that there are still substantial uncertainties in the timing of brecciation and mineralization for the Olympic Dam deposit and that the ~1.6 Ga ages derived by earlier workers have to be re-examined for revised conclusions. A stepwise leaching study on REE- fluorocarbonate-rich samples implies formation in a period ~1.4-1.1 Ga with an average at ~1.3 Ga (Maas et al., 2011). Comparable age has also been determined for hydrothermal xenotime rimming magmatic zircon (1343 Ma, Ciobanu et al., 2013). Dating of hematite revealed three generations precipitated at ~1.6 (1590±8 and 1577±5 Ma, Ciobanu et al., 2013), ~1.4 and ~1.2 Ga (Ciobanu et al., 2015). Overall, geochronological dates for different minerals appear to be repetitive and clustered around 1.6, 1.4, 1.3, 1.2, 1.1, 0.8 and 0.5 Ga which infers the multistage nature of the Olympic Dam deposit. However, as noted above, researchers have to be careful in interpreting of the ages of particular minerals because of the potential uncertainties in these dates (possible post-emplacement resetting of the isotopic systems, e.g., Hayward and Skirrow, 2010; Maas et al., 2011). Latest results show a presence of undigested BIF relicts (magnetite selected on deposit edges, 1769±58 Ma, Ciobanu et al., 2015) within the breccia complex. Authors suggest that some ore components might have even been inherited from the pre-granite lithologies. Additionally, Sm-Nd data on fluorite which forms massive barite-fluorite-carbonate-sulfide veins crosscutting the mineralized breccia, revealed that Delamerian event has largely affected the deposit as well (~0.5 Ga, Wawryk, 1989; Maas et al., 2011, in preparation a and b); thereby their age, considering the large error of the Rb-Sr age of the deposit overlaying Tregolana Shale (676±200 Ma, whole-rock Rb-Sr date, samples coming from Woomera bore, Webb et al., 1983) and field observations (veins and related faults propagate into the Tregolana Shale, e.g., Sugden and Cross, 1991), these veins postdate the cover sequence by some Ma.

Summarizing, in a case of the Olympic Dam ores researchers have, on the one hand, a problem of the establishment of the lower age boundary which has been previously widely accepted to be limited by the age of the granite (~1.6 Ga, Creaser and Gray, 1993; Jagodzinski, 2014) but has been challenged by one recent study (Ciobanu et al., 2015). On the other hand, the upper age boundary is problematic as well and might not necessarily be set at the age of the flat-lying covering sequence (676±200 Ma, Webb et al., 1983). All geochronological data produced to date together

unquestionably indicate the multistage evolution of the Olympic Dam ore. This ore had been evolving over a period of more than 1 Ga and undergone multiple stages of brecciation, mechanical intermixing, mineralization, and alteration/remobilization. Apart from the exact timing of the ore at Olympic Dam, researchers are even more challenged and intrigued by attempts to connect a particular age of a certain ore mineral (containing valuable metals such as U, Cu, Au and Ag) with the volume of the metals introduced to the breccia complex at a particular time in the past.

2.6 Existing models for the Olympic Dam genesis

A long-time search for Cu deposits in Australia initiated by Western Mining Corporation (acquired by BHP Billiton in 2005) initiated in 1957 eventually led to the discovery of the supergiant Olympic Dam deposit in 1975. In 1972 Douglas Haynes, being part of the exploration division of the Western Mining Corporation, completed the PhD thesis Haynes (1972) where he developed a model which primarily aimed to find a major sediment-hosted Cu deposit in surroundings of mafic rocks. The exact theory is based on an intensive hydrothermal alteration of mafic rocks and consequent release of Cu (Fig. 2.10 A). Transport of this base metal should have occurred by in hydrothermal fluids migrating through the major lineament with a well-developed fault system towards the overlaying sediments. When contacting the oxidized sediments, Cu is supposed to be reduced and deposited as sulfides parallel to the sediment bedding where the fluid permeability is high. Sediments of the Stuart Shelf have been selected for testing as the most promising target, indicated by the positive gravity and magnetic anomalies which might point to dense mafics below the sedimentary successions. Interestingly, the Olympic Dam deposit has been found not in the overlaying sediments but in the basement granite below the sedimentary cover at ~300 m depth. In addition, the geophysical anomaly is based not so much on mafic component (mafic-ultramafic rocks) but rather on also dense magnetite-hematite which are, as now known, prevalent in the deposit. As the mineralization has been found in a basement and not in the overlying sediments, the host-rock part of the original exploration model had been thrown into doubt and a long history of the still ongoing research started.

At present, there exist two principally distinct genetic models of the breccia complex - sedimentary and magmatic-hydrothermal - where authors debate not only major genetic issues but also smaller and still weighty aspects of these two models (Figs. 2.10 and 2.11). First model developed nearly 10 years after the deposit's discovery has been published in the first paper on Olympic Dam (Fig. 2.10 B, Roberts and Hudson, 1983). The researchers were pioneers in the field of the Olympic Dam deposit and had access to core samples coming from surface drilling only as at there has been no underground exposure back then. The model can be addressed as sedimentary as authors suggested that Olympic Dam is a *"new type of strata-bound sediment-hosted ore deposit"*; thereby the word *"new"* refers to the unusual association of Cu-U-REE-Au minerals. In particularly, researchers suggested that the ore is syn- to syndiagenetic with the graben-fill sediments which have been deposited in flat-lying, sedimentary piles of matrix-rich polymict breccia units in a very high energy, arid subaerial environment during tectonic activity. Local volcanism has been proposed as a possible reservoir of the sulfide components which are partly cogenetic and partly predate the REE-U mineralization. To note, this model was influenced by the original exploration target of strata bound Cu-style mineralization as well. The age of the deposit formation was derived from the absence of deformation of the host granite and the fact that the young dolerite dyke swarm (age has not been constrained at that time of research) did not intrude

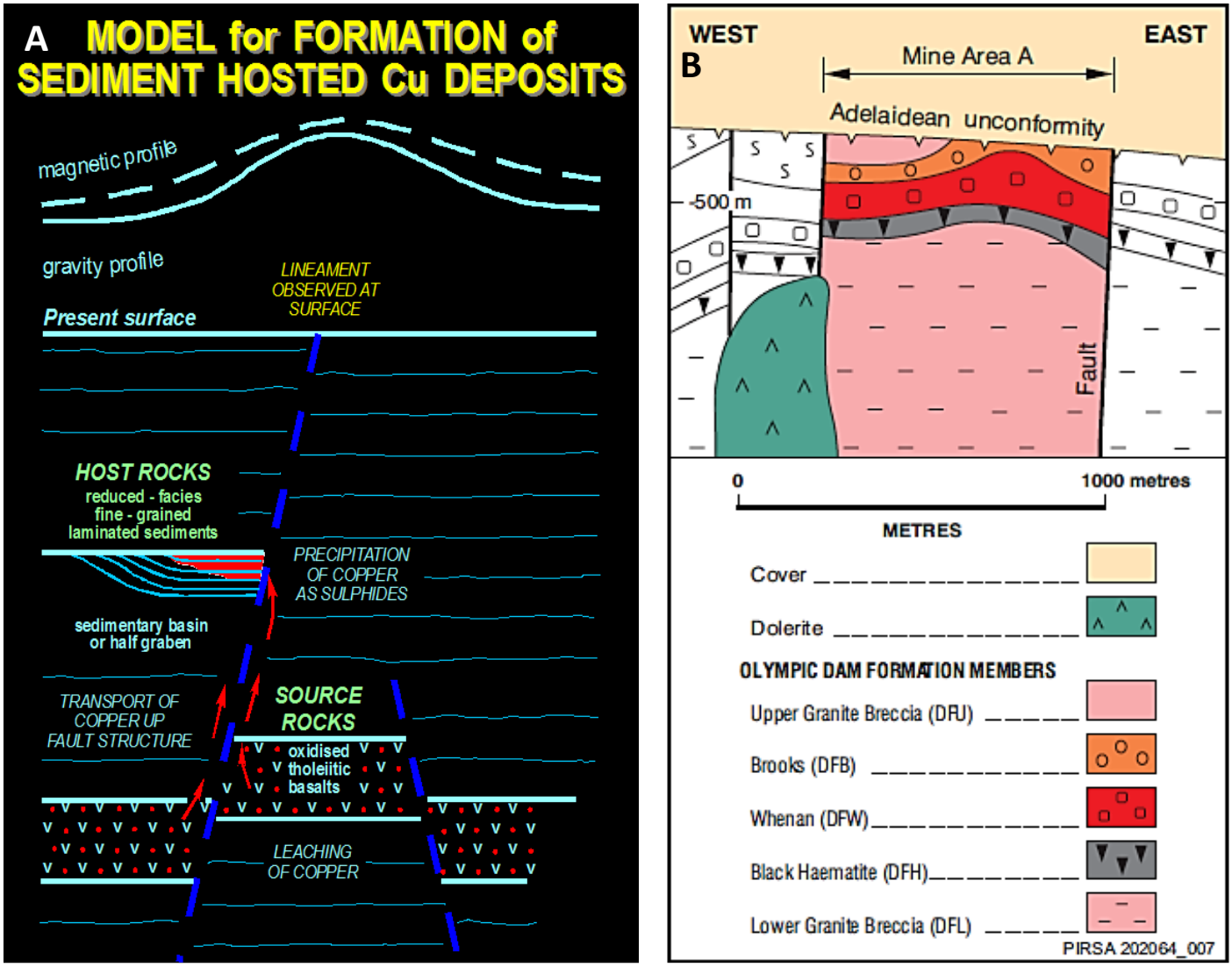

Fig. 2.10: Models of the Olympic Dam formation (part I). (A) The initial exploration model for Cu deposits described in Haynes (1972). Cu is suggested to have been leached out of tholeiitic basalts by oxidized hydrothermal fluids, transported along the fault zones and thereafter concentrated/deposited in the overlaying, reduced sediment facies. Figure obtained from BHP Billiton report (2009). (B) Historic profile of the mining block A. Figure obtained from Roberts and Hudson (1983), modified after Conor (2004).

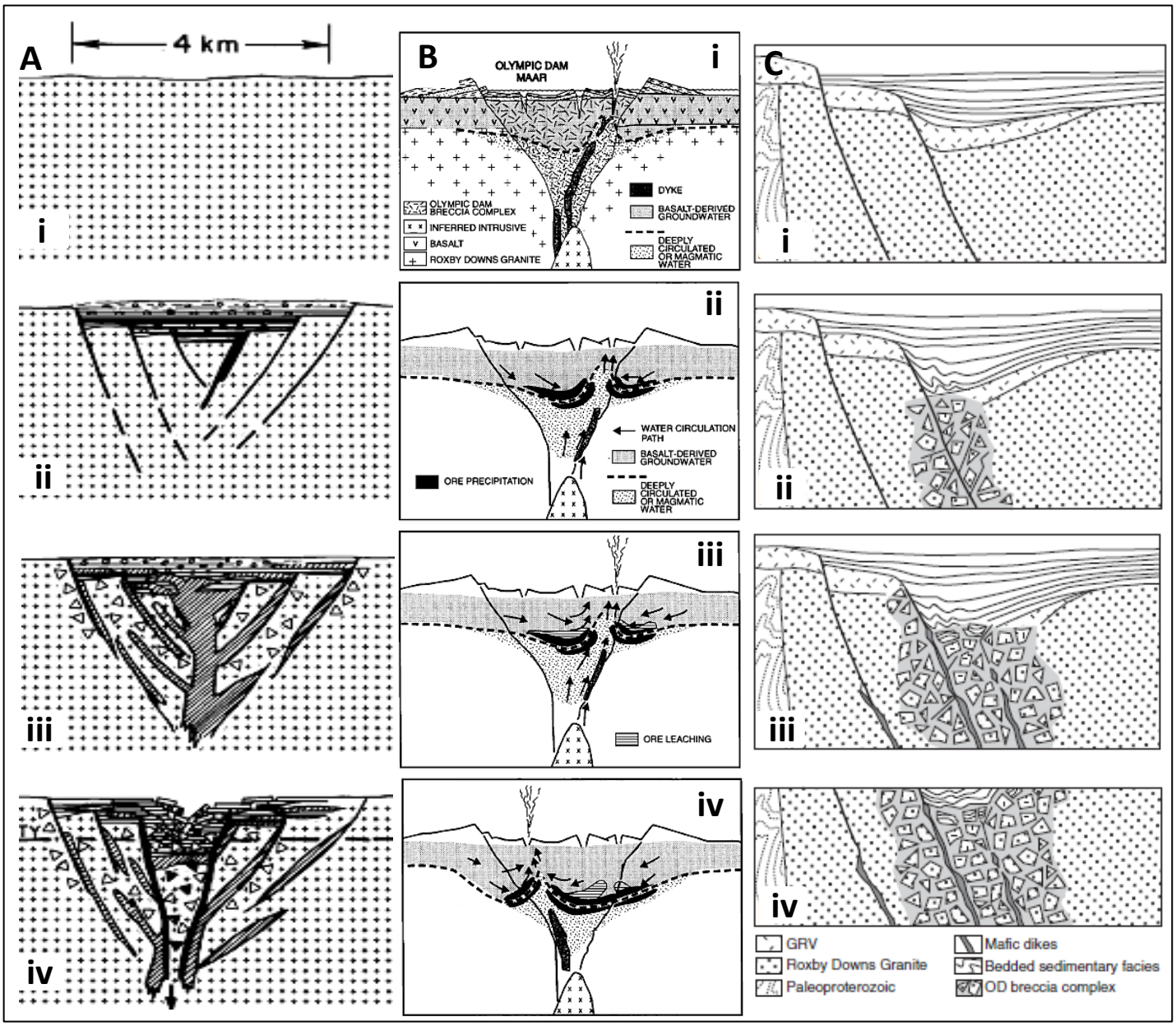

Fig. 2.11: Models of the Olympic Dam formation (part II).

(A) Oreskes and Einaudi (1990) suggested: (i) post-1.59 Ga unroofing and venting of RDG, (ii) extensional faulting, dyke emplacement, volcanism and start of the hydrothermal activity, volcanoclastic sediments are observed in fault basins, (iii) formation of the ODBC along faults, barite-bastnäsite precipitation on paleosurface, hematite alteration of the granite at depth, and (iv) second stage of brecciation and collapse of the central part comprising sediments into the complex; thereafter erosion.

(B) The maar-crater model for the genesis of the ODBC originally suggested by Reeve et al. (1990) and significantly modified presented by Haynes et al. (1995). Scenario of water mixing, ore precipitation events at Olympic Dam (i-iv).

(C) McPhie et al. (2011) suggested: (i) deposition of the sedimentary facies within the basin which has been bound to faults propagating from underlying basement consisting of RDG and GRV; (ii) subsurface fragmentation of the basement and basin sediments along faults and subsequent hydrothermal activity formed the mineralized breccia complex; (iii) mafic dyke emplacement; and (iv) unroofing of the ODBC.

the Adelaidean cover sequence. The workers divided the deposit into two major lithostratigraphic units (Olympic Dam Formation and overlaying Greenfield Formation) which comprised several members (Fig. 2.10 B); thereby the Cu mineralization was defined as a strata-bound type (pyrite-chalcopyrite-bornite) and a younger, overlaying transgressive type (bornite-chalcocite). However, this terminology has never been used in following papers on this deposit as new insights into the drillcore samples did not justify neither the division of the deposit units nor the suggested Cu-styles. Nevertheless, the detailed petrographic and mineralogical description presented in this paper was and still is of a great value for further studies conducted on the Olympic Dam deposit.

Around 10 years thereafter, a series of papers has been published where the involvement of magmatic-hydrothermal processes have been favoured in the formation of the polymetallic mineralization observed at Olympic Dam (e.g., Reeve et al., 1990; Oreskes and Einaudi, 1990, 1992; Hitzman et al., 1992) has been published. Authors suggest a principally new model based both on new drillcore observations and on various geochemical studies. In 1990 Oreskes finished her PhD on the genesis of the Olympic Dam deposit which resulted in the two publications (Oreskes and Einaudi, 1990, 1992). She proposed that the deposit has being formed by a number of events which took place in the period ~1590-1400 Ma (Fig. 2.11 A). In particular, authors emphasize the involvement of extensional faulting, minor late stage volcanism (GRV) and mafic dyke emplacement in the deposit formation around 1.6 Ga. Thereby, tuffaceous sediments and volcanic conglomerates have been interpreted to occur along fault basins. Magnetite-apatite-pyrite-siderite association has been marked as primary and interpreted as have been formed by hot (400˚C), saline, upraising brines. In contrast, introduction of a significant ore component (e.g., Cu, U and REE) into the breccia complex has been suggested to have occurred later due to a major upward flow of cooler (200-400˚C) and less saline hydrothermal fluids which have been circulating at the time of the second major hydrothermal brecciation event at ~1400 Ma, following the uraninite dating results (~1.4 Ga, Trueman et al., 1988; Johnson, 1993). Authors suggest venting of the system at the time of the major ore deposition and involvement of the surficial waters in the late-stage hydrothermal activity. Final stage is marked by the collapse of the sedimentary basin comprising laminated layers of barite intergrown with bastnäsite into the breccia complex, following by erosion to the level of the today's unconformity.

Reeve et al. (1990) added to the model of Oreskes and Einaudi (1990, 1992) considerations regarding the details of the deposit formation and the magmatic processes. These include the initial intensive brecciation of the RDG due to the later magmatic (mafic-felsic) impulse(s) produced by the Burgoyne batholith. Regional faulting, subsurface brecciation, dyke injection, and venting of the system (initially through the GRV which have been suggested to overlay the RDG) all triggered the hydrothermal eruptions and phreatomagmatic activity localized at multiple centres within the breccia complex. These explosions created a maar-crater lake where mixed distal GRV (interpreted to have slumped back into the deposit), laminated sediments and debris flows could have been accumulated. Fumarolic activity has been suggested to supply Ba and Fe into the crater complex. Relicts of the five major fossil maar-diatreme centres or diatreme pipes are, according to the author, still visible on the plan sections of the deposit (see Fig. 2 A in Reeve et al., 1990) and represent separate units which age relationship to the mineralization is unclear. Authors debate that potential sources of the metals might have been mafic-intermediate (Cu, Au, Fe), felsic (U, Ba, REE, F, Au, Ag) igneous rocks and related magmas. Thereby the host granite itself has been left out from this list as chemical leaching of the granite alone has been interpreted not to be able to produce all ore metals and associated elements found at present in the deposit. Although

authors support the deposit formation in period from ~1.59 Ga (estimated RDG emplacement age at that time of research) to ~1.57 Ga (GRV activity, Fanning et al., 1988), the evolution of the deposit is suggested to include *"episodic of brecciation-alteration-precipitation events."* Mineralized breccia penetrating dolerite dykes have been already suggested to relate to the GDS at that time of the research; however, their contribution to the metal contents of the deposit has not been debated at that time. Massive fluorite-barite dominated veins have been also separated from the main mineralizing event as they have been suggested and later proved to belong to the Delamerian event (Wawryk, 1989; Sugden and Cross, 1991; Maas et al., 2011).

Haynes et al. (1995) discuss similar formation processes (magmatic-hydrothermal, Fig. 2.11 B) and timing concepts as suggested by Reeve et al. (1990) and Oreskes and Einaudi (1990, 1992). The work of Haynes et al. (1995) is based on numerical modelling and derives the fluid temperature, salinity and interactions of the parental hydrothermal fluids required to deposit the complex mineral assemblages (three major ore associations) and parageneses observed in the deposit. The main aspect of this model (Fig. 2.11 B) is its formation under a maar lake environment with an involvement of the oxidative leaching of Cu, U, Au and most of the S from overlying basalt which leads partly back to the primary exploration model (Haynes et al., 1995). Thereby, fluid-mixing of the hot reduced magmatic or deeply circulating meteoric water (potential source of Fe, F, Ba and CO_2) with the cooler oxidised surficial water (e.g., from the saline lake) has been suggested as the dominant ore-forming process at Olympic Dam. Chemically, this process means coupled sulfate reduction and oxidation of iron. According to this model, magnetite(±hematite)-dominated and U-Cu-bearing association has been produced at the early stage of the mixing event which has been followed by a precipitation of the hematite-barite-fluorite-dominated and also Cu-U-rich association as the larger part of the cooler fluid mixed with the hotter fluid. Barren hematite-quart-barite-rich association found preferentially in the core of the deposit has been suggested to have formed at the waning stage of the mixing event due to the oxidation of minerals formed in the first two associations. Researchers add that this process has likely occurred repetitive, similar to the brecciation events. However, all these mineralizing and mechanical intermixing events have been nailed to the age of the RDG intrusion at ~1.6 Ga, similarly to the paper of Reeve et al. (1990).

One of the recent publications done by McPhie et al. (2011) updated the genetic model according to new results from the core drilling and geochemical analyses of chromite from the bedded sedimentary facies. Firstly, four of the five bedded sedimentary occurrences which have been interpreted as crater-fill sediments, have been found to *"extend continuously across a 1.5 km × 0.9 km area and are not limited to small separate maar craters, as previously thought"* (Fig. 1 B in McPhie et al., 2011). Thus, this new model (Fig. 2.11 C), which is similar to the model suggested earlier by Oreskes and Einaudi (1990), contradicts the original mafic maar-diatreme milieu with the maar-diatreme crater-lake sedimentary units (Reeve et al., 1990) and magmatic-hydrothermal origin (Reeve et al., 1990; Oreskes and Einaudi, 1990, 1992; Hitzman et al., 1992; Haynes et al., 1995; Johnson and McCulloch, 1995) for Olympic Dam. Instead, McPhie et al. (2011) propose formation of the deposit underneath a large, active sedimentary basin (but after the GRV-related volcanism) with multi-province sources, and sediment deposition below wave-base in a sub-aqueous environment. The large basin contains detrital chromite with a variety of compositions, indicating multi-province sources located within the regionally extensive Gawler SLIP (e.g., RDG, and various units of the GRV) but also possibly outside of the local area of the Olympic Dam. Hydrothermal system is suggested not to have vented and to

operate both beneath and partly within this basin which had an uncompacted sediment thickness of >500 m (McPhie et al., 2011). This view makes sedimentary processes important in the ore genesis of the Olympic Dam again, following back to the first paper on Olympic Dam genesis (Roberts and Hudson, 1983). Large blocks of these sediments were incorporated into the Olympic Dam breccia system due to the basin collapse which altogether places the age of brecciation after the extrusion of the GRV and the formation of the sedimentary basin.

Importantly, all researchers admit that to evaluate a more robust genetic model for the Olympic Dam deposit is a great challenge because of the multistage nature of the ore and mineral precipitation and brecciation stages and incorporation and possible contribution to the metal and element contents of several genetically and chemically distinct lithological units apart from the major host granite. Simplifying of the ore-forming processes and leak of substantial age data for the majority of the hydrothermal minerals within the complex can lead to only partly applicable genetic models. However, all pioneers in the deciphering of the Olympic Dam genesis have undeniably produced highly useful descriptions and data which, together with the data contained in this thesis, help to understand a highly complex nature of the supergiant mineralized ODBC.

Chapter 3: Postmagmatic magnetite-apatite assemblage in mafic intrusions: a case study of dolerite at Olympic Dam*

3.1 Introduction

The discovery and subsequent investigation of the supergiant Olympic Dam Cu-U-Au-Ag deposit in South Australia led to the introduction of a new class of ore deposits, collectively known as IOCG deposits (Meyer, 1988; Hauck, 1990; Hitzman et al., 1992). They were considered to be fundamentally distinct from other deposit types in that polymetallic sulfides are associated with dominant Fe-oxides (magnetite and/or hematite) and related to an extensional tectonic regime (Hitzman et al., 1992). Subsequent investigation of similar deposits around the world has shown that the IOCG clan includes deposits that can be very diverse in terms of their host rock compositions, metal contents, ages, mineralization depths, host rock-ore relationships and fluid sources. This diversity has led to an evolution in both classification and genetic models (Williams et al., 2005; Groves et al., 2010; Barton, 2014).

A characteristic feature of many deposits belonging to the IOCG clan *sensu lato* is the presence of magnetite-apatite accumulations that in some instances are large enough to warrant classification in distinct Kiruna-type deposits. The latter have been assigned by Hitzman et al. (1992) to an end-member category in the IOCG clan. Furthermore, the Kiruna-type deposits have been interpreted as deeper roots of IOCG systems (e.g., Sillitoe, 2003; Knipping et al., 2015). Some authors distinguish between Ti-poor magnetite-apatite (Kiruna-type) and Fe-Ti-oxide apatite (or iron-oxide apatite, IOA, Williams et al., 2005) deposits. The Fe-Ti-oxide systems or *'nelsonites'* (Watson and Taber, 1910), have long been treated separately and are generally accepted to be of magmatic origin (Song et al., 2013; Charlier et al., 2015). The Ti-poor Kiruna types systems are the problematic examples, and differ in fundamental ways from the others and are postulated to be either magmatic (e.g., deposits in Central Sweden, Jonsson et al., 2013) or magmatic-hydrothermal or hydrothermal(-metasomatic) (e.g., El Romeral deposit in Chile, Bookstrom, 1977) or sedimentary(-exhalative) (e.g., Kiruna deposits in Sweden, Parak, 1975, 1984). A recently proposed genetic model for Kiruna-type deposits combines magmatic and related hydrothermal processes (Knipping et al., 2015).

Given a wide range of genetic models, the petrogenesis of magnetite-apatite assemblages is likely to be diverse. On the other hand, competing models have been applied even to single deposits. For example, the Kiruna-type deposits in Sweden have been interpreted as magmatic (Jonsson et al., 2013) and sedimentary-exhalative (Parak, 1975, 1984), and El Laco deposit in Chile have been interpreted as magmatic (Nystroem and Henriquez, 1994) and hydrothermal-metasomatic (Sillitoe and Burrows, 2002; Dare et al., 2015). Understanding large-scale ore deposits is complicated by the variety of processes and metal/fluid sources involved, as well as unknown duration of deposition. Genetic models can be valid, if applied to a certain part (mineral assemblages, mineralized zones etc.) of a single ore deposit; however, other parts of the same deposit may have gone through different processes at different times. In other words, if any particular sample is representative of one or another process/deposition environment, the application of the strategy *'from little things big things grow'* may facilitate understanding of large-scale accumulations of minerals and mechanisms of their formation, e.g., Fe and P in the case of IOCG/IOA deposits.

We applied this approach to samples from Olympic Dam - the flagship IOCG deposit. The Cu-Au-U-mineralized ODBC was intruded by dolerite dykes (Ehrig et al., 2012) that host abundant Kiruna-type mineralization. Our

*Manuscript published in Contributions to Mineralogy and Petrology (2015), volume 171, issue 1, pages 1-15. DOI: 10.1007/s00410-015-1215-7.

mineralogical and geochronological study reveals the source of metals and mineralizing fluids and ultimate origin of Fe oxide-apatite assemblages in a particular environment of mafic intrusions.

3.2 Sample location and methods

3.2.1 The Olympic Dam deposit

Olympic Dam Cu-U-Au-Ag deposit (Ehrig et al., 2012) is located in the NE part of the Gawler craton, approximately 520 km north-northwest of Adelaide, South Australia. The Olympic Dam ore body occurs within the 6 x 8 km large ODBC (Fig. 3.1), which is in turn located within the RDG (1593.1±5.6 Ma, Jagodzinski, 2014), a member of the Hiltaba Supersuite and part of the Gawler SLIP. The breccia complex is strongly heterogeneous and is dominated by relict, variably hematite-altered host granite and other minor lithologies (e.g., mafic and ultramafic intrusions; possible rhyolitic rock, bedded clastic sediments). Although multistage, the ODBC dominant alteration assemblages and ore formed shortly after the ~1593 Ma host granite (Johnson and McCulloch, 1995; Ciobanu et al., 2013).

Both the ODBC and the host granite are intruded by prominent NNW-striking sub-vertical doleritic dykes (Fig. 3.1) which have long been suspected to be much younger than their host rocks (Reeve et al., 1990). The dolerite dykes were recently confirmed as members of the Neoproterozoic GDS (~0.827 Ga, Huang et al., 2015). Although generally much better preserved than other mafic and ultramafic intrusions within the ODBC, the margins of the doleritic dykes are brecciated and the dykes are variably altered, clearly showing that at least some alteration and brecciation occurred long after deposition of the oldest Fe-oxide alteration near 1590 Ma (Ciobanu et al., 2013). The dolerite sample (OD422, drillhole RD222, 759 m) hosting veins with a magnetite-apatite is the subject of this case study. One additional sample collected from the drillhole RD222 and 18 samples from RU65-8337 are also dolerite dykes containing plentiful magnetite-apatite-bearing veins and, in addition, similarly composed accumulations (Table 3.1).

3.2.2 Analytical methods

The case study is based on the sample OD422 which comprises dolerite with magnetite-apatite-bearing veins. Radiogenic isotope analyses of the dolerite, a *'bulk vein'* powder sample and a high-purity concentrate of the apatite were carried out on a Nu Plasma multi-collector (MC)-ICPMS with sample uptake through a CETAC Aridus desolvator and PFA nebulizer (The University of Melbourne). Raman spectroscopy (Renishaw inVia Raman microscope with Streamline) and combined energy dispersive x-ray spectrometry (EDS) and electron backscatter diffraction (EBSD, Hitachi SU-70 field emission scanning electron microscope, SEM) mapping of the vein magnetite and quartz were performed in Central Science Laboratory (CSL, University of Tasmania, UTas) with a goal evaluate their degree of crystallinity. Backscattered electron (BSE) and cathodoluminescence (CL) imaging was performed on a FEI Quanta 600 scanning electron microscope (SEM) fitted with a FEI solid-state BSE detector and a Gatan PanaCL-F panchromatic CL detector with RGB filters (CSL, UTas). Measurement of the compositions of oscillatory zones observed in some vein minerals in BSE and CL images was carried out on an electron probe microanalyzer (EPMA, Cameca SX100 electron microprobe, CSL, UTas) and a laser ablation inductively coupled plasma mass spectrometer (LA-ICPMS, Resonetics M50 Ar-F excimer laser coupled to an Agilent 7500cs, CODES, UTas). The latter was also used for the U-Pb dating on the alteration-related titanite (see below) and vein apatite. A half-core of the sample OD422, containing the vein hosted by dolerite, was sawn into four pieces and cast into 1 inch diameter epoxy blocks. After optical microscopy and Raman

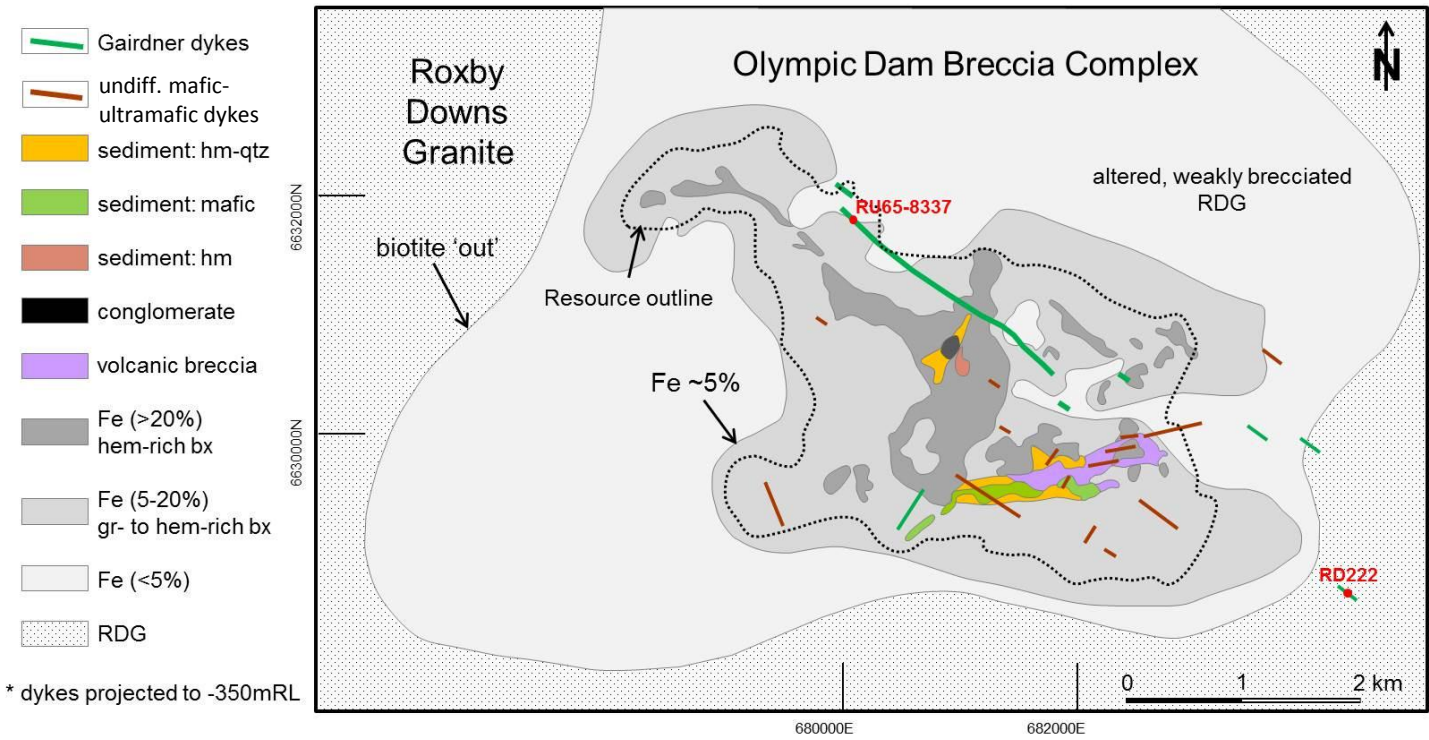

Fig. 3.1: Simplified geologic map at -350 mRL (ODBC under the cover of barren, flat-lying Neoproterozoic to Cambrian sediments). Two generations of mafic-ultramafic rocks (~1.6 and ~0.8 Ga) can be distinguished, only major bodies are shown. The locations of the drillholes RD222 and RU65-8337 studied in this work are marked on the map. Map modified after Ehrig et al. (2012).

spectroscopy, one mount was polished for ~1 h on a Pace GIGA-0900 vibratory polisher with a 0.05 μm colloidal silica suspension and thereafter coated with ~10 nm thin carbon layer for EBSD analysis. After this analysis, the carbon coating was removed and all mounts were coated with ~20 nm of carbon for scanning electron microscopy and electron probe microanalysis. In addition, one polished thin section was prepared for optical and scanning electron microscopy and CL imaging. Full BSE maps were collected for all mounts to aid in selection of representative features for the various analyses. For a sample RD423 (RD222) and further 18 samples (RU65-8337), several polished thin sections and mounts were prepared for optical and scanning electron microscopy purposes.

3.2.2.1 Scanning Electron Microscopy (BSE and EDS: all samples, EBSD and CL: OD422)

BSE and CL imaging were performed on a FEI Quanta 600 scanning electron microscope (SEM) fitted with a FEI solid-state BSE detector and a Gatan PanaCL-F panchromatic CL detector with RGB filters at the CSL, UTas. The acceleration voltage was 15 to 20 kV and the beam current around 3 nA.

Additional BSE imaging, energy dispersive x-ray spectrometry (EDS) and EBSD were carried out on a Hitachi SU-70 field emission scanning electron microscope (SEM) at the CSL, UTas, which is equipped with an Oxford AZTec microanalysis system with X-Max80 SDD EDS detector and HKL NordlysNano EBSD camera. The sample was tilted to 70˚ from the normal. Mapping was performed using an accelerating voltage of 20 keV and a beam current of around 3 nA. Cubic magnetite was used as a reference.

3.2.2.2 Raman spectroscopy (OD422: vein magnetite and quartz)

Raman spectroscopy on magnetite and quartz was conducted under ambient conditions on one uncoated epoxy round using the Renishaw inVia Raman microscope with Streamline at the CSL, UTas. The excitation wavelength was 532 nm. Focussing of the beam was carried out by a 50x object lens (NA 0.75) resulting in a spot size of ~1 μm. Spectra of the colloform magnetite and colloform quartz were recorded from ~100 to 1350 cm^{-1} and from ~100 to 1900 cm^{-1} using a grating of 2400 and 1800 mm/l with a spectral resolution of ~1.2 and ~1.7 cm^{-1} respectively. A diode pumped laser had an adjusted laser power of ~0.05 (magnetite) and ~0.25 mW (quartz) on the sample surface. A second experiment, involving the water peak analyses, was recorded from ~109 to ~3917 cm^{-1} using a grating of 600 mm/l resulting in a spectral resolution of ~3.7 cm^{-1}. The data was collected by a Peltier cooled CCD camera with an exposure time of 1 s using 100 accumulations.

3.2.2.3 Major elements (OD422: vein apatite, calcite and magnetite)

Microprobe measurements were conducted on a Cameca SX100 electron microprobe (CSL, UTas). In addition to spot measurements in calcite (3 spots), apatite (11), and magnetite (30), line profiles were acquired in separate grains of apatite and magnetite to investigate zoning of these minerals. Carbonates were analysed for Ca, Mg, Fe, Mn and Si, apatite for Ca, P, Cl, F, Si and Fe and magnetite for Fe, Si, Ca, Al, Zn, Mg and Mn. Oxygen was calculated by cation stoichiometry. In addition, carbon was also calculated by stoichiometry for calcite. Fe^{2+} and Fe^{3+} in magnetite were calculated using the formula described in Droop (1987). Beam conditions were 15 kV for accelerating voltage, 10 nA for beam current, 10 μm for beam diameter for calcite and apatite, whereas for magnetite, accelerating voltage was 20 kV, the beam current was 20 nA and the beam diameter was ~2 μm. Fluorine intensities were corrected for fluorine accumulation during analysis over time. Low analysis totals of some of the apatite microprobe analyses (Table 3.2) are

likely due to high REE contents, which were only analysed by LA-ICPMS and not EPMA, and can reach up to 7.4 wt% total REE. Including the highest LREE concentrations measured by LA-ICPMS (La 1.24 wt%, Ce 3.40 wt%, Pr 0.41 wt%, Nd 1.49 wt%) as known concentrations in the microprobe matrix correction changes the determined P concentration by around +0.3 wt%, Ca by around -0.5 wt% and F by around -0.2 wt%. A correction of the Ce on F peak interference, which amounts to an overestimation of F by around 0.1 wt% for the highest measured Ce concentration of 3.40 wt%, was also not performed.

The standards used for calibration were the following natural minerals: clinopyroxene (Ca, Si in calcite and Si in apatite), apatite (Ca, P in apatite), wollastonite (Ca, Si in magnetite), dolomite (Mg in calcite), olivine (Mg in magnetite), hematite (Fe in calcite and apatite), magnetite (Fe in magnetite), bustamite (Mn in calcite), rhodonite (Mn in magnetite), gahnite (Al and Zn in magnetite), tugtupite (Cl), and topaz (F).

3.2.2.4 Trace elements (OD422: vein apatite and magnetite)

LA-ICPMS measurements were conducted done using a Resonetics M50 HR ArF excimer laser ablation system coupled to an Agilent 7500cs ICPMS (CODES, UTas). The system operated at a wavelength of 193 nm, a repetition rate of 10 Hz and energy density 3.5 J/cm^2. For magnetite, 3 maps on representative areas were made and data on trace elements from 3 representative profiles from the maps were processed like spot data. A total of 46 analyses of vein apatite were made and 40 trace elements (including REE) were measured. Count rates were measured using the following isotopes for magnetite: ^{24}Mg, ^{27}Al, ^{29}Si, ^{43}Ca, ^{47}Ti, ^{51}V, ^{55}Mn, ^{57}Fe, ^{88}Sr, ^{90}Zr, ^{118}Sn, ^{123}Sb, ^{137}Ba, ^{139}La, ^{140}Ce, ^{146}Nd, ^{147}Sm, ^{163}Dy, ^{172}Yb, ^{232}Th and ^{238}U; and for apatite: ^{7}Li, ^{23}Na, ^{24}Mg, ^{27}Al, ^{29}Si, ^{31}P, ^{43}Ca, ^{51}V, ^{55}Mn, ^{57}Fe, ^{65}Cu, ^{66}Zn, ^{75}As, ^{77}Se, ^{88}Sr, ^{89}Y, ^{90}Zr, ^{93}Nb, ^{137}Ba, ^{139}La, ^{140}Ce, ^{141}Pr, ^{146}Nd, ^{147}Sm, ^{153}Eu, ^{157}Gd, ^{159}Tb, ^{163}Dy, ^{165}Ho, ^{166}Er, ^{169}Tm, ^{172}Yb, ^{175}Lu, ^{178}Hf, ^{181}Ta, ^{197}Au, ^{204}Pb, ^{206}Pb, ^{207}Pb, ^{208}Pb, ^{209}Bi, ^{232}Th and ^{238}U. Count rates were quantified using primary standard reference material GSD-1G for magnetite and NIST 610 for apatite.

The evaluation of REE patterns in apatite, magnetite and dolerite was carried out using values of McDonough and Sun (1995). Calculation of the Eu anomalies was done according to Sun and McDonough (1989) using a formula [$Eu/Eu^* = Eu_n / (0.5*(Sm_n+Gd_n))$].

3.2.2.5 U-Pb dating (OD422: vein apatite and alteration-related titanite)

The procedure is identical to those described in Huang et al. (2015). U-Th-Pb dating of apatite and titanite was carried out using LA-ICPMS (Chew et al., 2014) on polished rock samples mounted in 25 mm diameter epoxy mounts. Apatite and titanite were recognized using a scanning electron microscope. The crystals were analysed using a Coherent Scientific 193 nm Ar-F excimer gas laser coupled with a Resonetics S155 ablation cell and an Agilent 7500cs Q-ICPMS at the UTas. Both apatite and titanite were ablated in a He atmosphere (0.35 l/min) using a 32 μm laser spot (5 Hz, energy density ~2 J/cm^2). Following a 30 second gas blank samples were ablated for 30 seconds. Ablation in the S155 ablation cell is carried out in He, followed by transfer to the ICPMS torch in argon via nylon tubing; a mixing manifold (squid) was applied in this work. The isotopes measured were ^{31}P, ^{49}Ti, ^{43}Ca, ^{56}Fe, ^{140}Ce, ^{202}Hg, ^{204}Pb, ^{206}Pb, ^{207}Pb, ^{208}Pb, ^{232}Th and ^{238}U (5 ms dwell time for the major and trace elements, 20 ms for the Pb isotopes, and 10 ms for Th and U). Downhole fractionation, instrument drift and mass bias in apatite analyses were corrected using an in-house apatite standard, OD306, a coarse-grained apatite from an apatite-magnetite vein at the Acropolis Cu-Au prospect in South Australia. Isotope dilution U-Pb data obtained for 6 mg-sized (1.3-4.5 mg) fragments by MC-ICPMS at the University

of Melbourne (e.g., Woodhead and Pickering, 2012) show modest U contents (15-19 ppm), Th/U ~4.8 and variable but generally low common Pb contents (measured $^{206}Pb/^{204}Pb$ = 336-1556, f_{206} = 0.011-0.051, n = 6, R. Maas, 2012, unpubl. data). After common Pb correction, the data yield concordant to near-concordant (≤2.5% disc.) $^{207}Pb/^{206}Pb$ ages averaging 1598±4 Ma (2 se) and a formal discordia intercept of 1594±7 Ma. At the sampling scale of the laser, the apatite shows a high degree of homogeneity in Pb/U ratios and little evidence of the variable common Pb seen in the bulk analyses. Kovdor and Otter Lake apatite (Amelin and Zaitsev, 2002; Barfod et al., 2005; Chew et al., 2011) were monitored as secondary standards; the ^{207}Pb-corrected $^{206}Pb/^{238}U$ ages obtained for these crystals are well within error of published reference ages (Table 3.3). OD306 apatite was preferred as primary standard over the Otter Lake or Kovdor apatites because it provides more homogeneous Pb/U data on the UTAS laser ablation system (internal precision ±1.1%, n = 10 compared to ±1.4% and ±3.9% for Otter Lake and Kovdor, respectively, each based on n = 10 analyses), has lower common Pb at the laser sampling scale, and its U-Th contents closely match those in the apatites measured here. Recalculation of the data for apatite from OD422 with Otter Lake apatite as primary standard yields a concordia intercept age of 817±3.5 Ma, compared to 821±15 Ma (MSWD = 0.60) if OD306 is used. While these ages overlap within errors, it is clear that LA-ICPMS U-Pb dating of apatite has issues similar to those described for zircon (e.g., Black et al., 2004; Klötzli et al., 2009; Allen and Campbell, 2012).

Titanite raw data were corrected with reference to another in-house standard, AUR100606, a magmatic titanite from a mafic intrusion in North Queensland. ID-TIMS U-Pb isotope data for microgram-sized samples obtained at the University of British Columbia are near concordant and define an age of 432.02±0.64 Ma (Best, 2012). Primary standards were analysed at the beginning of each session and between sets of 15 unknowns (i.e. roughly every 30 minutes). Pb isotopic mass bias was monitored using regular analyses of the NIST610 glass (e.g., Baker et al., 2004; Jochum et al., 2011). Data reduction was done using in-house software (e.g., Halpin et al., 2014), with common Pb corrections based on the techniques of Chew et al. (2011, 2014).

3.2.2.6 Sr and Nd isotopes (OD422: dolerite and vein)

Radiogenic isotope analyses were done on a whole rock powder made from fragments of the least altered section of the OD422 dolerite, and on small (20-30 mg) powder samples obtained with a dental drill from the polished surface of the OD422 drillcore. A *'bulk vein'* powder sample from the magnetite-apatite-quartz-calcite vein was also collected using the hand-held drill. Finally, a high-purity concentrate of the apatite was prepared by handpicking. The isotopic analyses were conducted at the University of Melbourne (Maas et al., 2015). Samples were dissolved in HF/HNO_3 and 5M HNO_3 on a hotplate; the apatite sample (0.31 mg) was dissolved in HNO_3 only. The clear solutions were equilibrated with ^{85}Rb-^{84}Sr and ^{149}Sm-^{150}Nd tracers for isotope dilution work; the small sample of apatite (0.31 mg) was only spiked with the Sm-Nd tracer while Rb and Sr concentrations were obtained by Q-ICPMS on a 10% split of the sample solution. Rb and Sr were extracted using a combination of EICHROM SR resin and AG50-X8 (200-400) cation exchange resin. Sm and Nd were extracted using EICHROM TRU and LN resin. Total analytical blanks were 80 pg for Sr and Nd, with Rb/Sr = 0.3 and Sm/Nd = 0.2, resulting in sample/blank ratios >1000 except for Rb in the apatite sample which was corrected for a 10 pg Rb dissolution blank (resulting in a 3% correction).

Isotopic analyses were carried out on a Nu Plasma MC-ICPMS with sample uptake through a CETAC Aridus desolvator and PFA nebuliser operated at ~0.07 ml/min sample uptake, with sensitivities of 100V/ppm Sr and

150V/ppm Nd. Analyses were carried out in static multi-collection mode with signals near 8V Sr and 15V. Instrumental mass bias was corrected by normalizing to $^{88}Sr/^{86}Sr = 8.37521$ and $^{146}Nd/^{145}Nd = 2.0719425$ (equivalent to $^{146}Nd/^{144}Nd = 0.7219$), using the exponential law as part of an on-line iterative spike-stripping/internal normalization procedure. Data are reported relative to SRM987 = 0.710230 and La Jolla Nd = 0.511860. Typical in-run precisions (2se) are ±0.005-0.008% (Sr) and ±0.002% (Nd); external precision (reproducibility, 2sd) is ±0.006% (Sr) and ±0.004% (Nd). Rb isotope dilution analyses were performed using the Zr-doping method (Waight et al., 2002). External precisions for $^{87}Rb/^{86}Sr$ and $^{147}Sm/^{144}Nd$ obtained by isotope dilution are ±0.5% and ±0.2%, respectively. Results for international standards agree with TIMS reference values. For example, long-term (2011-2014) averages for BCR-2 are 0.704997±42 (2sd, n = 44) and 0.512641±24 (2sd, n = 74), and $^{147}Sm/^{144}Nd$ is 0.1382±0.0002. Decay constants are ^{87}Rb $1.395\ 10^{-11}$/yr and ^{147}Sm $6.54\ 10^{12}$/yr. Modern CHUR has $^{147}Sm/^{144}Nd = 0.1960$, $^{143}Nd/^{144}Nd = 0.512632$ (Bouvier et al., 2008).

3.3 "Gairdner-type" dolerite

Dolerite sample OD422 belongs to a dyke cutting unmineralized RDG on the NE margin of the deposit. OD422 is unusually fresh and composed of well-preserved clinopyroxene, plagioclase, Ti-magnetite and ilmenite (Fig. 3.2 A-C). Euhedral to subhedral clinopyroxene and plagioclase are equidimensional (~2-3 mm) and there is no preferred orientation of plagioclase laths. Cubic to skeletal magnetite carries numerous fine lamellae of ilmenite oriented parallel to the {111} planes. Ilmenite is also present as discrete skeletal grains or rods. The main accessory phases are acicular fluorapatite and irregularly shaped Cu sulfides (chalcopyrite and bornite). The sulfides are interstitial or occur as inclusions in the main minerals.

The bulk composition of dolerite OD422 is within the range of other Olympic Dam GDS-type dolerites (Fig. 3.3; Table 3.4) documented by Huang et al. (2015). Whole rock Sr-Nd isotope data for three samples from the ~20 cm-long drillcore section have a range in initial $^{87}Sr/^{86}Sr$ (at 827 Ma) of 0.7035-0.7052, whereas initial εNd_{827} is homogeneous (+2.7 to +3.0; Table 3.5). The lowest $^{87}Sr/^{86}Sr$ ratio comes from the least-altered section of the specimen while the ratios >0.705 are from more altered sections. The εNd_{827} values are within the range for other GDS -type dolerites at Olympic Dam (+2.7 to +2.9) and elsewhere (-0.2 to +5.7) reported in Huang et al. (2015).

Although generally well preserved, dolerite OD422 contains several fractures. Primary minerals in the dolerite have been progressively modified close to these fractures and within ~4 mm of the fracture margins, magmatic minerals are completely replaced by chlorite, quartz and titanite (Fig. 3.2 B). Ti-magnetite-ilmenite has been converted to titanite (Fig. 3.2 D-E) and apatite is absent. The fractures are filled by an assemblage of magnetite, apatite, calcite, quartz, chlorite and chalcopyrite.

3.4 Magnetite-apatite-bearing vein

One of the magnetite-apatite-calcite-quartz veins in OD422 is particularly well preserved and is the subject of this study (Figs. 3.2 and 3.4). It is about 4 mm wide. Magnetite is the most abundant mineral (~50 to ~95 %), followed by calcite (~5 to ~50 %), apatite, quartz, and chlorite (each up to ~5 %); traces of chalcopyrite (<10 μm, <1%) are scattered throughout the vein. Magnetite is preferentially associated with apatite along the vein-dolerite contact; this assemblage is joined by quartz-calcite in the vein margin whereas magnetite is associated with calcite in the central parts of the vein (Fig. 3.4 B). In places, colloform magnetite extends from both sides of the vein and merges, occupying the entire vein.

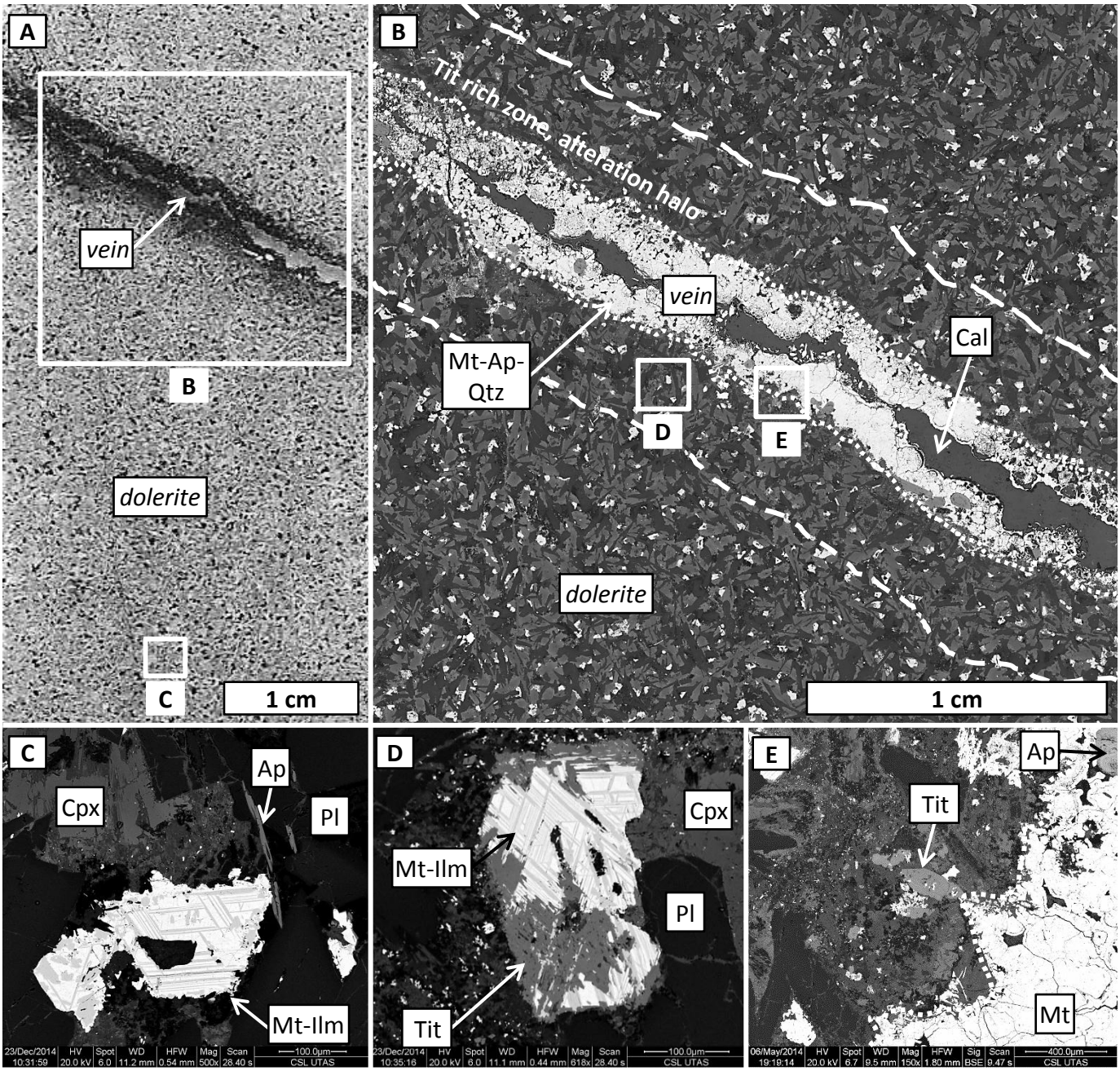

Fig. 3.2: Petrography of the dolerite. (A) Thin section of dolerite and a vein; close-up shown in (B). (B) A symmetrical magnetite (Mt)-apatite (Ap)-quartz (Qtz)-calcite (Cal) vein is surrounded by an alteration halo. (C) Unaltered dolerite consists of clinopyroxene (Cpx), plagioclase (Pl), magnetite-ilmenite (Mt-Ilm) intergrowth and accessory apatite. (D) The most intensely altered zone on the vein selvage is marked by the appearance of titanite (Tit) which has grown at the expense of magnetite-ilmenite. (E) Euhedral titanite on the vein selvage. (B-E) are BSE images.

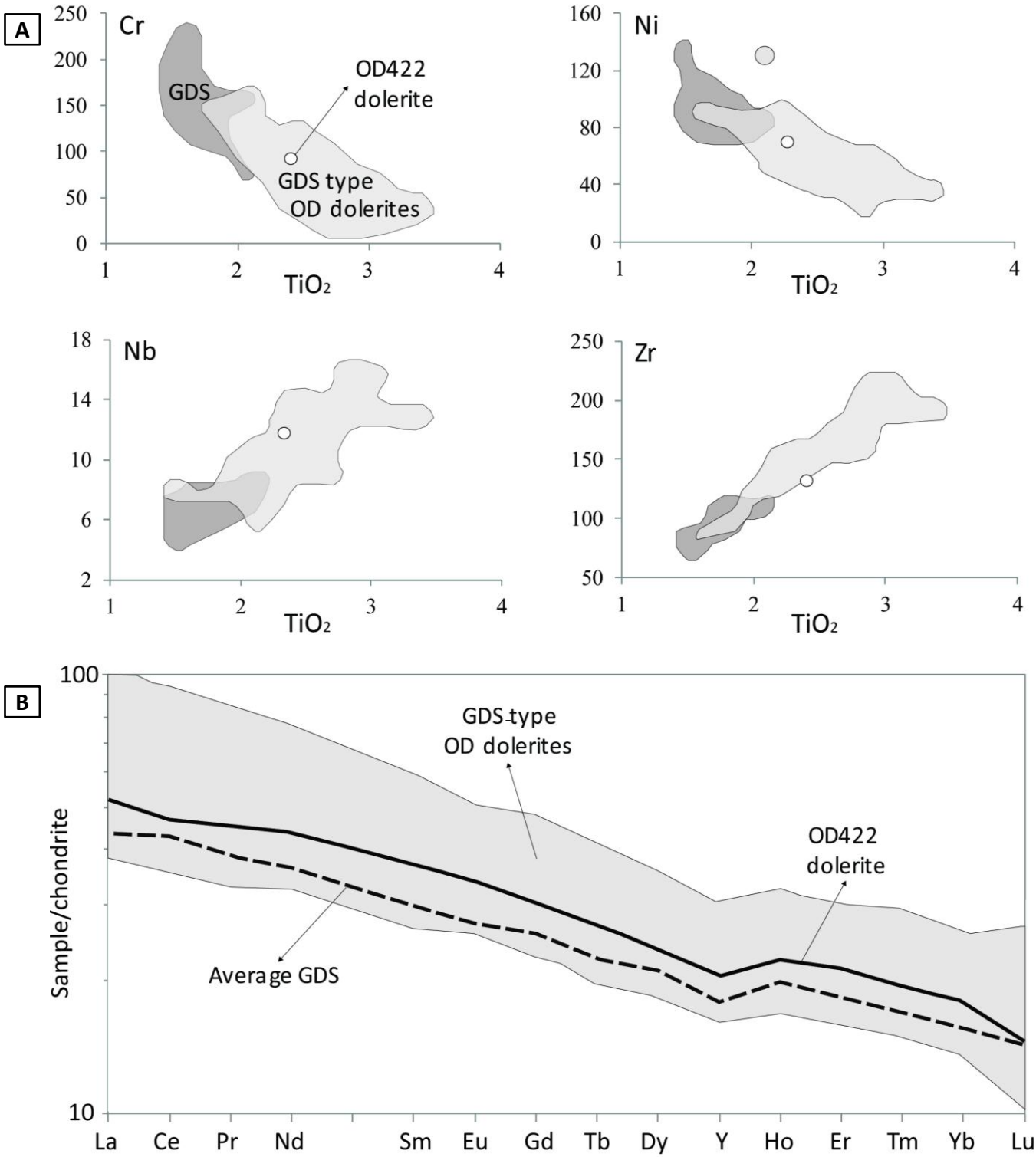

Fig. 3.3: Geochemical comparison of the OD422 dolerite, GDS-type Olympic Dam (OD) dolerite (Johnson, 1993; SARIG database; DMITRE Resources and Energy Group 2014; Huang et al., 2015) and the GDS (SARIG database; Zhao et al., 1994). (A) Plots of Cr, Ni, Nb and Zr (in ppm) plotted against TiO_2 (wt%) revealed similarity of OD422 and the ~0.82 Ga dykes. (B) Chondrite-normalized (after Sun and McDonough, 1989) REE diagram for the OD422 dolerite, GDS-type OD dolerites (modified with additional analyses after Huang et al., 2015) and the average composition of the GDS (Zhao et al., 1994; Wang et al., 2008; Huang et al., 2015; SARIG database).

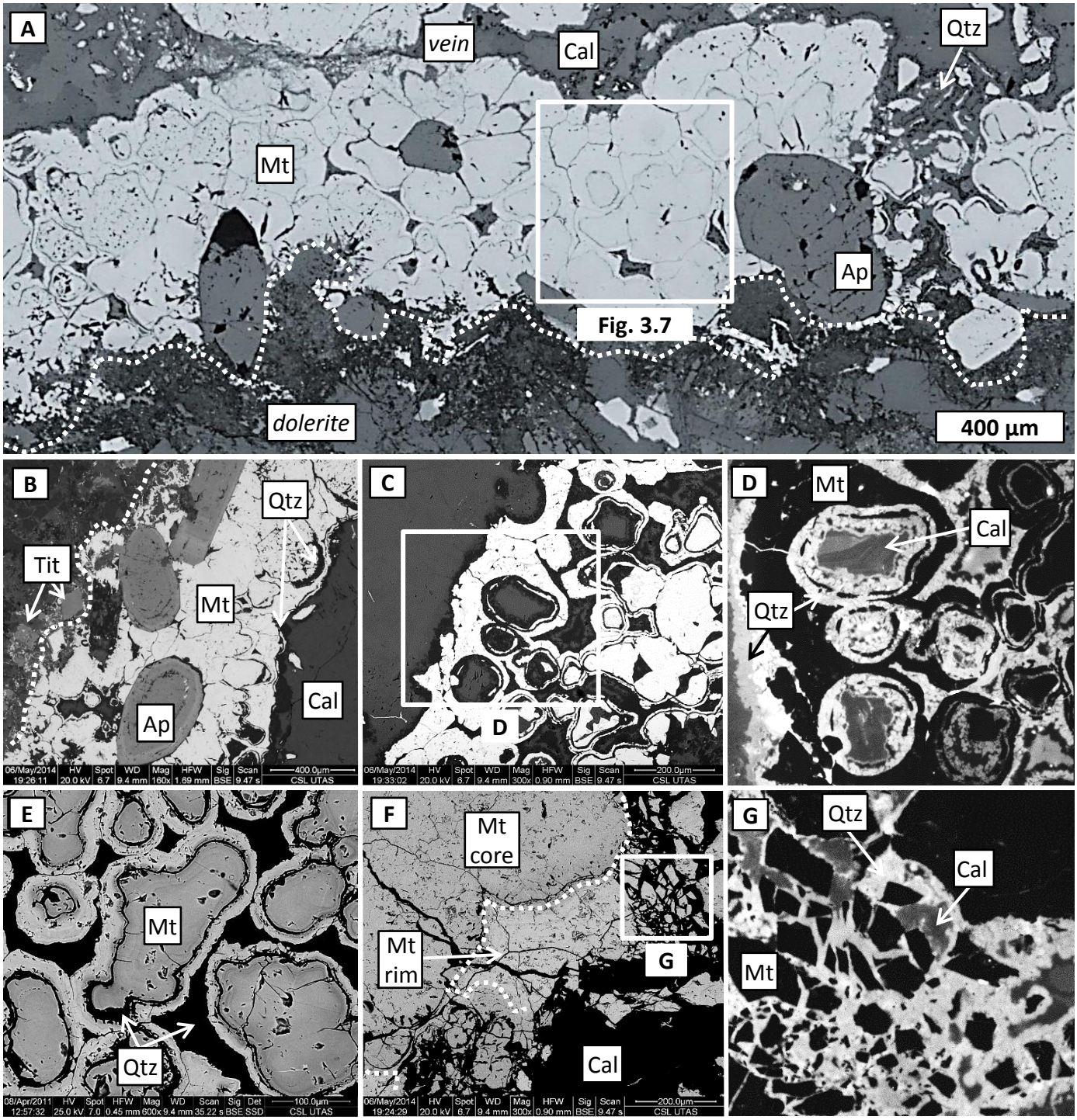

Fig. 3.4: Petrography of the vein. (A) Apatite prisms grow either adjacent to the dolerite or inside the magnetite. The white box shows the LA-ICPMS map area in magnetite (Fig. 3.7). (B) Coarse apatite crystals. (C-E) Colloform magnetite can contain both calcite and quartz. (F-G) Magnetite margin brecciated in situ and fully encapsulated by quartz; magnetite has no direct contact with calcite. Abbr. are the same as in Fig. 3.2. (A) is a RL image, (B-C) and (E-F) are BSE images, (D) and (G) are CL images.

Elongate grains of apatite can be either oriented parallel or perpendicular to the vein walls and vary from ~50 μm to ~1 mm in size. Magnetite has colloform morphology with considerable curvatures (Fig. 3.4 A-F). Thin (~15 μm) bands of quartz, locally intergrown with chlorite, are intergrown with magnetite. Quartz also separates nodules of colloform magnetite from each other and from the coarse-grained (up to ~1 mm) calcite. Some quartz exhibits colloform morphology. Calcite primarily occurs in the central part of the vein but also occupies the space inside the magnetite nodules which are preferably located in the outer part of the magnetite-dominated bands. Calcite commonly encloses aggregates of *in situ* brecciated magnetite (preferably rims) which are ubiquitously framed by irregular quartz layers of variable thickness (Fig. 3.4 F-G).

3.4.1 Mineralogy

3.4.1.1 Magnetite

Magnetite in the vein is colloform (Fig. 3.4). Numerous round intersecting nodules have overgrown each other and range from ~20 μm up to ~1.5 mm in size. The largest are nucleated at the vein margins. Smaller nodules may form coalescing aggregates overgrown by an outer layer of magnetite. Nodules exhibit oscillatory bands and concentric zones but lack observable radiating structures. Single magnetite nodules appear divided into core and rim, which are typically separated by one or two thin, irregular and mostly continuous bands of quartz. Quartz also fills fractures inside the nodules. The two zones in colloform magnetite are characterized by distinct compositions, the cores being darker than the rims in BSE images. Each zone consists of multiple alternating bands, observable in the form of slight changes in BSE intensity. The bands in inner parts of the nodules are generally thicker, prominent, more ordered and display greater contrast than those in the outer parts.

The crystallinity of colloform magnetite was investigated with Raman spectroscopy and EBSD. Raman spectra show three modes at 307, 554, and 673 (strongest band) cm^{-1} (Fig. 3.5 A), consistent with magnetite Raman shifts reported previously (e.g., Shebanova and Lazor, 2003). This result indicates the colloform magnetite has typical magnetite structure and is not maghemite (γ-Fe_2O_3, Chernyshova et al., 2007; Molchan et al., 2014), which is cubic. No spectral differences are noticed between compositionally distinct cores and rims (Fig. 3.5 A-B), indicating crystal orientations are similar in both zones. The absence of Raman bands between ~3000 and 3600 cm^{-1} (Burke, 2001) implies that H_2O is not incorporated into the structure of colloform magnetite.

The results of the EDS-EBSD mapping (Figs. 3.5 C-D and 3.6) are in accordance with those from Raman spectroscopy. Each pixel in the map represents an electron backscatter pattern (EBSP) and a corresponding ED spectrum (Fig. 3.5 B-G). High intensities (brightness) in the band contrast image (Fig. 3.6) indicate good EBSP quality, confirming the crystalline nature of the colloform magnetite; the rim areas show slightly lower band contrast (Fig. 3.6) compared to the cores. The mineral phase map (Fig. 3.5 C) shows that quartz not only surrounds magnetite grains but - like calcite - also forms micro-scale inclusions within host magnetite. The Euler map (Fig. 3.5 D) is a graphical representation of the crystal orientation (as determined from the EBSPs) in a single image. A change in colour corresponds to a change in crystal orientation. The map shows that single magnetite domains in zoned colloform magnetite grains or aggregates have distinct crystallographic orientations relative to neighbouring magnetite domains. Interestingly, there appears to be no correlation between local variations in the BSE intensity (and thus chemical

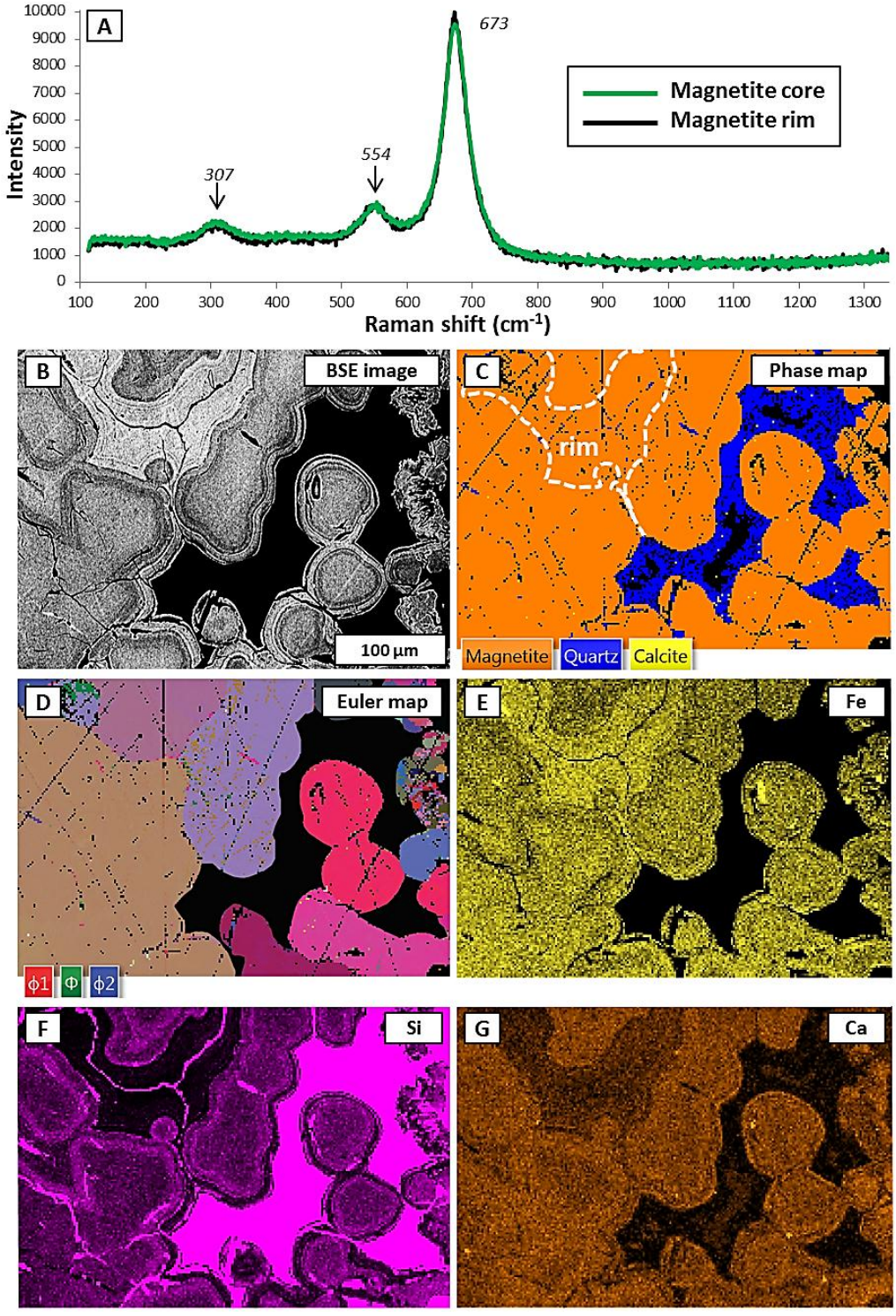

Fig. 3.5: Structural analysis and compositional zones in the vein magnetite. (A) Raman spectra for core and rim of the magnetite show the same patterns. (B) BSE image of the area mapped with EBSD shows clear division of the dark core and bright rim. (C) Phase map based on combined EDS and EBSD data showing magnetite, quartz and calcite as mineral phases. Note numerous calcite and quartz micro-inclusions inside the magnetite. (D) EBSD map representing the orientation of the points in Euler space using colours. Euler map (with the angles φ1-3 which transform the specimen coordinate system onto the crystal coordinate system) shows that the orientation of neighbouring magnetite crystals is distinct but there is no difference within a single domain. Other mineral phases were coloured black in order to emphasize the magnetite grain orientations. (E-G) EDS compositional maps reveal clear zones with respect to Fe, Si and Ca, respectively.

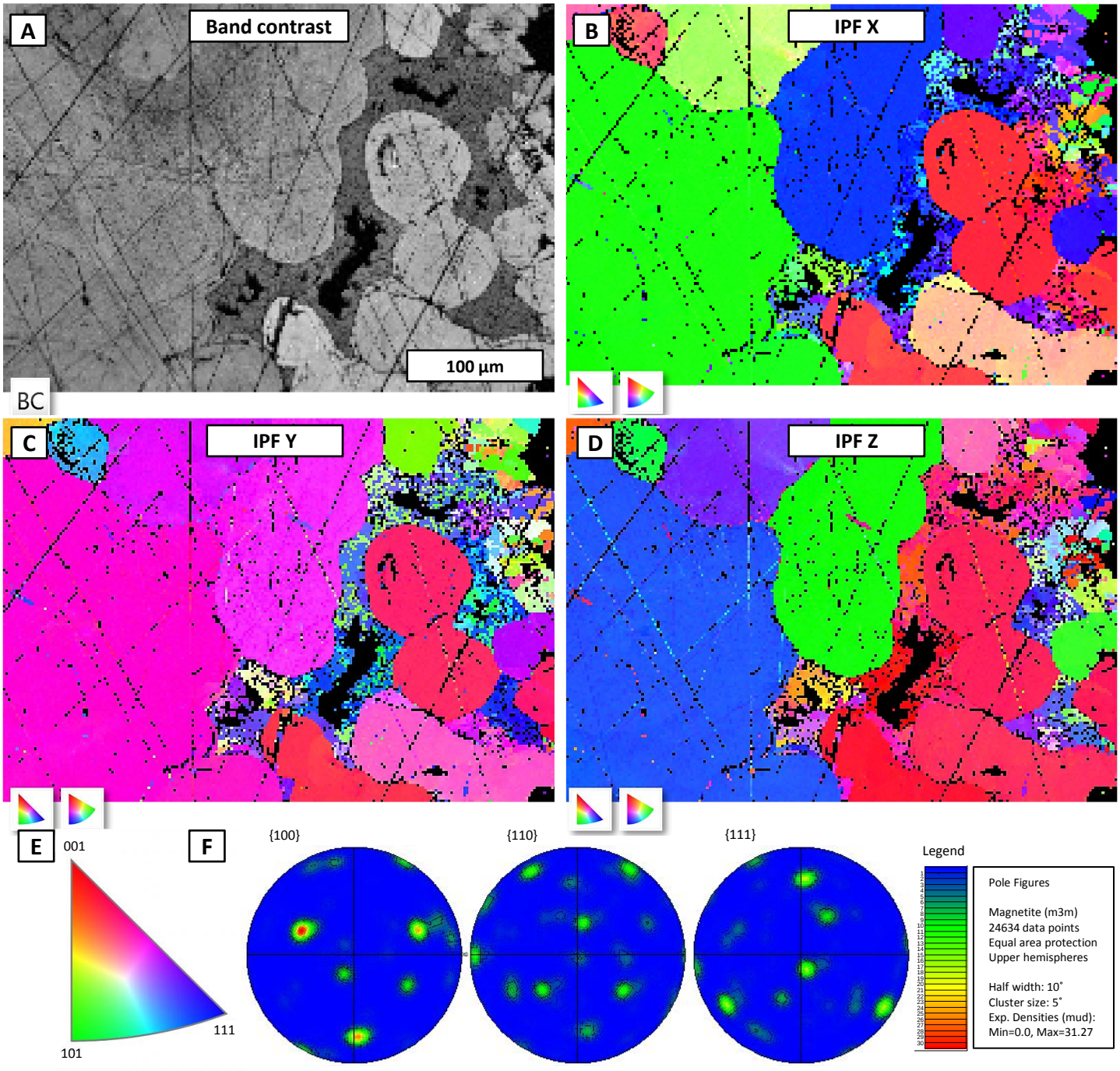

Fig. 3.6: Additional (to Fig. 3.5) results of the EBSD analysis. (A) Band contrast (or pattern quality) map shows that the rim areas have lower band contrast. (B-D) Inverse pole figures (IPFs) for X, Y and Z (B, C, and D, respectively); colour scale in (E) show the crystallographic orientations of single-crystal domains (same colours) relative to the X, Y and Z direction of the image. (F) Pole figures show the three primary sets of planes, {111}, {110} and {100}, in magnetite relative to the sample.

composition, see Fig. 3.5 B) and the orientation of single magnetite nodules. This indicates that the compositional banding is present within individual magnetite crystals.

Compared to stoichiometric magnetite (~72.4 wt%), Fe concentrations in the studied magnetites are noticeably lower (Fig. 3.5 E). The cores of colloform magnetite aggregates which have weaker (darker) BSE intensities, contain 66.2 - 69.4 wt% Fe, whereas the rims, with more intense (brighter) BSE response, have higher Fe concentrations (70.7 - 72 wt% Fe). Minor element contents in colloform magnetite are strongly zoned, e.g. Si (0.4 to 3.8 wt%; Fig. 3.5 F), Ca (up to 0.8 wt%; Fig. 3.5 G), Al, Mn (both up to 0.5 wt%) and Mg (up to 0.2 wt%; EPMA data in Table 3.6 and LA-ICPMS data in Table 3.7). The outer parts of the cores have the highest trace element contents, e.g. Ti (up to 0.03 wt%), V (up to 58 ppm), Zn (up to 0.05 wt%), Sn (up to 29 ppm), and REE (La 127 ppm, Ce 239 ppm, Nd 77 ppm). Trace element contents drop dramatically in the rims of the magnetite nodules (Fig. 3.7), to the extent that rims are virtually pure Fe_3O_4.

3.4.1.2 Apatite

Fluorapatite (avg. 3.8 wt% F and 0.4 wt% Cl, EPMA; Table 3.2) is associated with magnetite but the two minerals are commonly separated by quartz. Numerous sub-micron-sized fluid and magnetite inclusions (Fig. 3.8 A) are scattered within some apatite grains. Euhedral apatite grains display fine concentric growth zones; up to 40 distinct, oscillatory zones are present, and can be further subdivided into numerous narrower zones. In general, zones are thinner towards the crystal margin. The zones are distinct in BSE (Fig. 3.8 A) and panchromatic CL (Fig. 3.8 B) images; bright BSE bands correlate with dark CL response and vice versa. The CL brightness and thickness of single zones can vary as a zone that is traced around the grain. Zone morphology is crystallographically controlled and mostly follows the crystal form. In some cases, zones have smooth edges or are partially irregular and not entirely continuous. In some places, apatite also displays significant sectorial zoning. Despite the alternating zones of variable thickness, brightness and morphology, apatite grains can be roughly divided into cores and rims. The zones in the cores typically lack the fine-scale oscillatory zones, are thicker, and in general darker on the BSE images than the rims. The rims of some apatite grains display concave bands that are typically surrounded by secondary dark patches (Fig. 3.8 A). Quartz fills fine fractures in some grains.

Zones in apatite correlate with variations in minor and trace elements determined by EPMA (Table 3.2) and LA-ICPMS (Table 3.8). The primary control on BSE brightness appears to be the concentration of REE which vary from 1.7 to 7.6 wt% ∑REE. In general, apatite grains are more enriched in REE towards the grain margins. The concentrations of La, Ce, Pr, Nd, and Y in the rim zones can be as high as 1.2, 3.4, 0.4, 1.5, and 0.4 wt%, respectively. Apatite can also contain elevated Si (avg. 0.8 wt%) and Fe (avg. 0.27 wt%) but very low concentrations of Al, Sr, Mn and Na (~500 ppm each).

REE fractionation patterns for apatite (Fig. 3.8 C) are characterized by strong enrichment in light REE (LREE) relative to heavy REE (HREE), and high and variable LREE/HREE (La/Lu_n ~70 and 431). HREE contents are more variable than LREE contents by a factor of 6. Eu/Eu* is also highly variable (0.1 to 1.3), being typically higher in REE-depleted core zones than in rims. Marked Eu depletion seems to be a common feature. In contrast, Ce shows a minor positive anomaly (Ce/Ce* = 0.9 to 1.3, calculated on La-Nd).

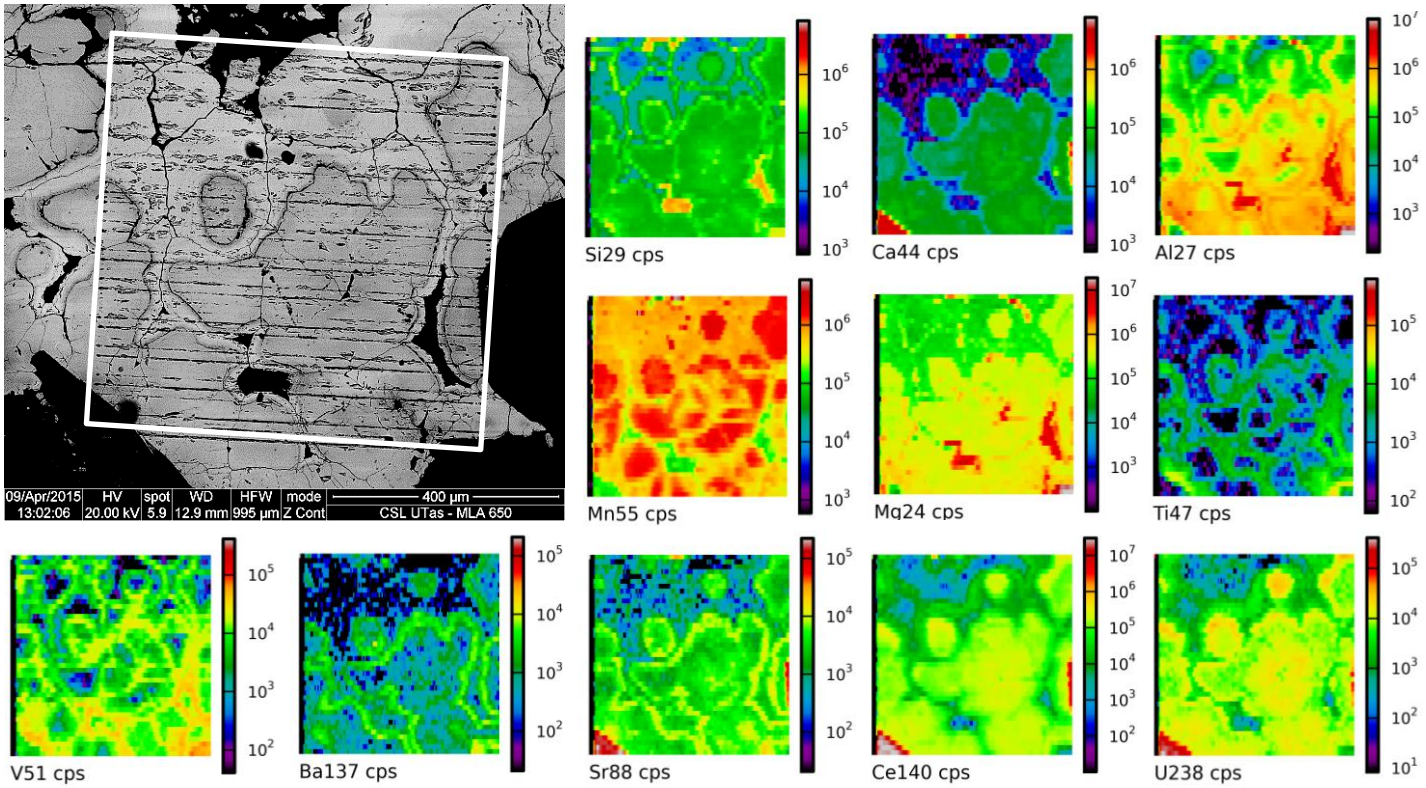

Fig. 3.7: LA-ICPMS maps for the white area marked in the BSE image. The elements such as Si and Ca are present in significant quantities, whereas Mn, Mg, Ti, V, Ba, Sr, Ce and U are present at trace levels.

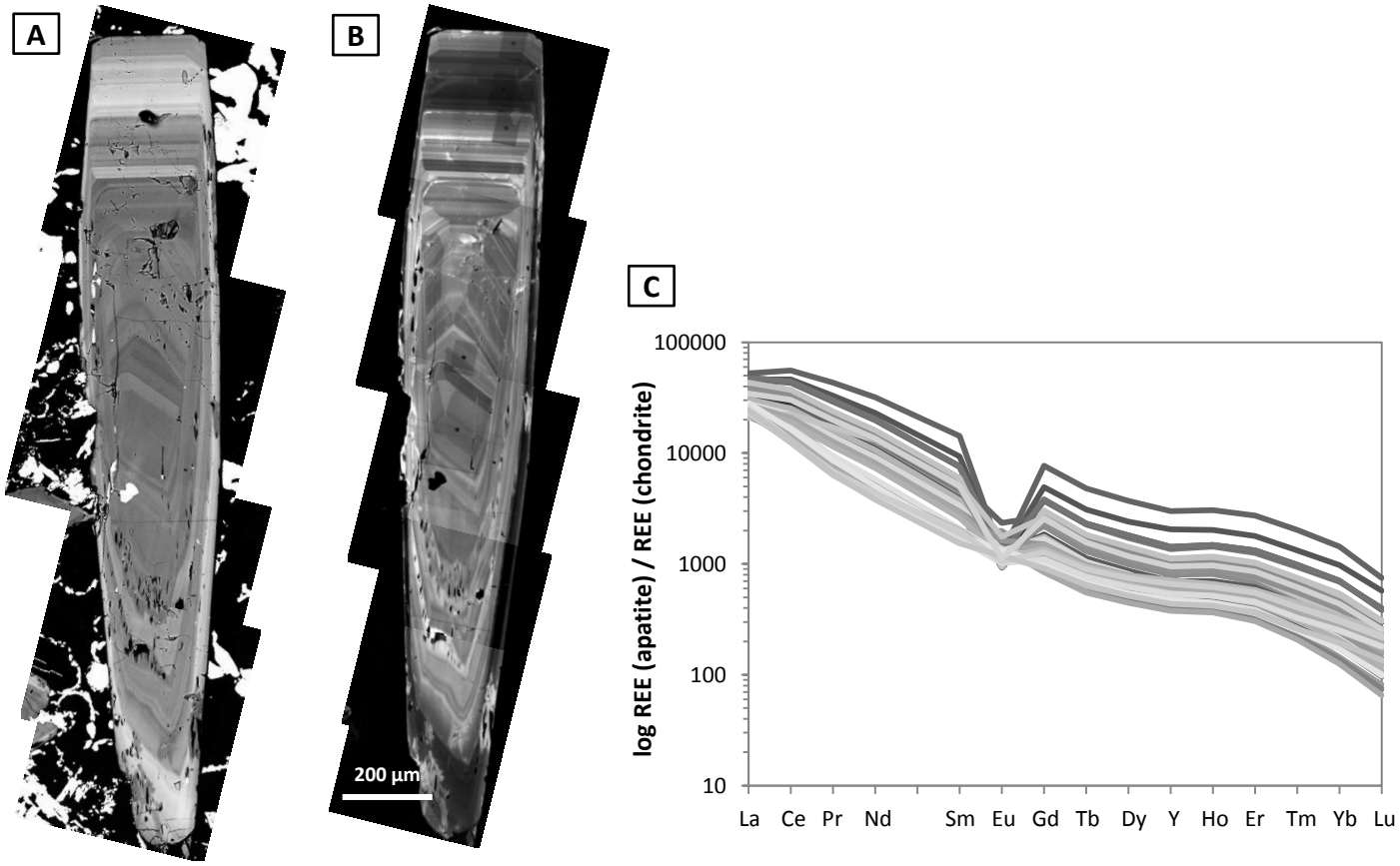

Fig. 3.8: Compositional zones and REE patterns in the vein apatite. BSE (A) and CL images (B) show inverse correlation. Note a large number of the zones having varying width, morphology and brightness. Numerous fluid inclusions concentrated along some growth zones may be secondary. Magnetite inclusions are also present. (C) REE pattern (normalized to chondrite using data from Sun and McDonough, 1989) of all analysed apatites reveals strong LREE enrichment compared to HREE coupled with strong fractionation.

3.4.1.3 Calcite

Euhedral to subhedral calcite ranges in size from a few μm up to ~1 mm and displays a range of habits. Contacts with other minerals are locally irregular. There is no clear general pattern in the orientation of calcite crystals within the vein. In some cases, large aggregates of small calcite crystals occur in the center of the vein, surrounded by radiating calcite crystals (Fig. 3.9). In other cases, large calcite crystals occur at the boundary of the apatite-magnetite-quartz layers located on the margins of the vein and merge elsewhere within the vein.

Calcite crystals of all sizes show well-developed zones which are only slightly visible in BSE images but are pronounced in CL images (Figs. 3.4 D and 3.9). The zones are discrete, have variable thickness, and may be discontinuous. Core and rim zones can be clearly distinguished in CL images. The core mostly comprises a single homogeneous zone which is overgrown by many narrow oscillatory zones. In rare cases, calcite crystals display sectorial zoning. The calcite inside magnetite nodules is distinctly zoned, and the orientation of the zones is dependent on nodule orientation. Microprobe analyses show detectable variations in Fe (1.1 to 2.6 wt%), Mg (0.3 to 0.6 wt%) and Mn (1.2 to 2.4 wt%) contents (Table 3.9). Manganese, in particular, is known as a strong luminescence activator (Götze, 2002) and could be responsible for the strong CL zones. Further trace elements may be present and heterogeneously distributed; however, such analysis is beyond the scope of the present study.

3.4.1.4 Quartz

Quartz is a minor component of the vein and occurs as rims on apatite and magnetite, and as inclusions or in fractures in these minerals. Quartz also displays a colloform habit in the interstices between magnetite nodules (Fig. 3.2). CL images reveal that both quartz rims and colloform quartz are zoned; the outer zones possess less intense colour than interior zones (Figs. 3.9 and 3.10).

Raman spectroscopy and EBSD were conducted to determine the crystallinity of colloform quartz. Both techniques showed that quartz nodules have crystalline features and match the characteristics of α quartz (low-temperature polymorph of quartz). A Raman spectrum of one silica nodule (Fig. 3.10) shows a typical α quartz (e.g., Dumanska-Słowik et al., 2013) spectrum comprising bands at 130, 207, 263, 355, ~400, 465 (strongest peak), 806, and 1160 cm^{-1}.

3.4.2 Geochronology

LA-ICPMS analyses of vein apatite yield highly variable U (17 to 276 ppm) and Th (14 to 129 ppm) concentrations, and Th/U ratios are relatively low for apatite (0.2-5.7; Table 3.10). The common lead content of the apatite is low which has resulted in a clustering of the majority of the data points near the concordia on the Tera-Wasserburg diagram (Fig. 3.11 A). An intercept age of 817±3.5 Ma (MSWD = 0.95) was obtained by means of a least-square regression of the 72 analyses using isoplot. The small age uncertainty (0.4%) is a result of the large number of tightly clustered analyses close to the concordia line.

LA-ICPMS analyses of alteration-related titanite from the zone of intense alteration of dolerite at the contact with the magnetite-apatite vein yield concentrations of U (7 to 21 ppm) and Th (13 to 96 ppm, Th/U 1.2-4.9; Table 3.11). Fifteen spot analyses have variable but generally low common lead contents (Fig. 3.11 B) and provide a lower intercept age of 840±22 Ma (MSWD = 1.13). The U-Pb results for apatite and titanite overlap within the quoted uncertainties and are consistent with U-Pb ages on secondary apatite-titanite association with other dolerite dykes at Olympic Dam

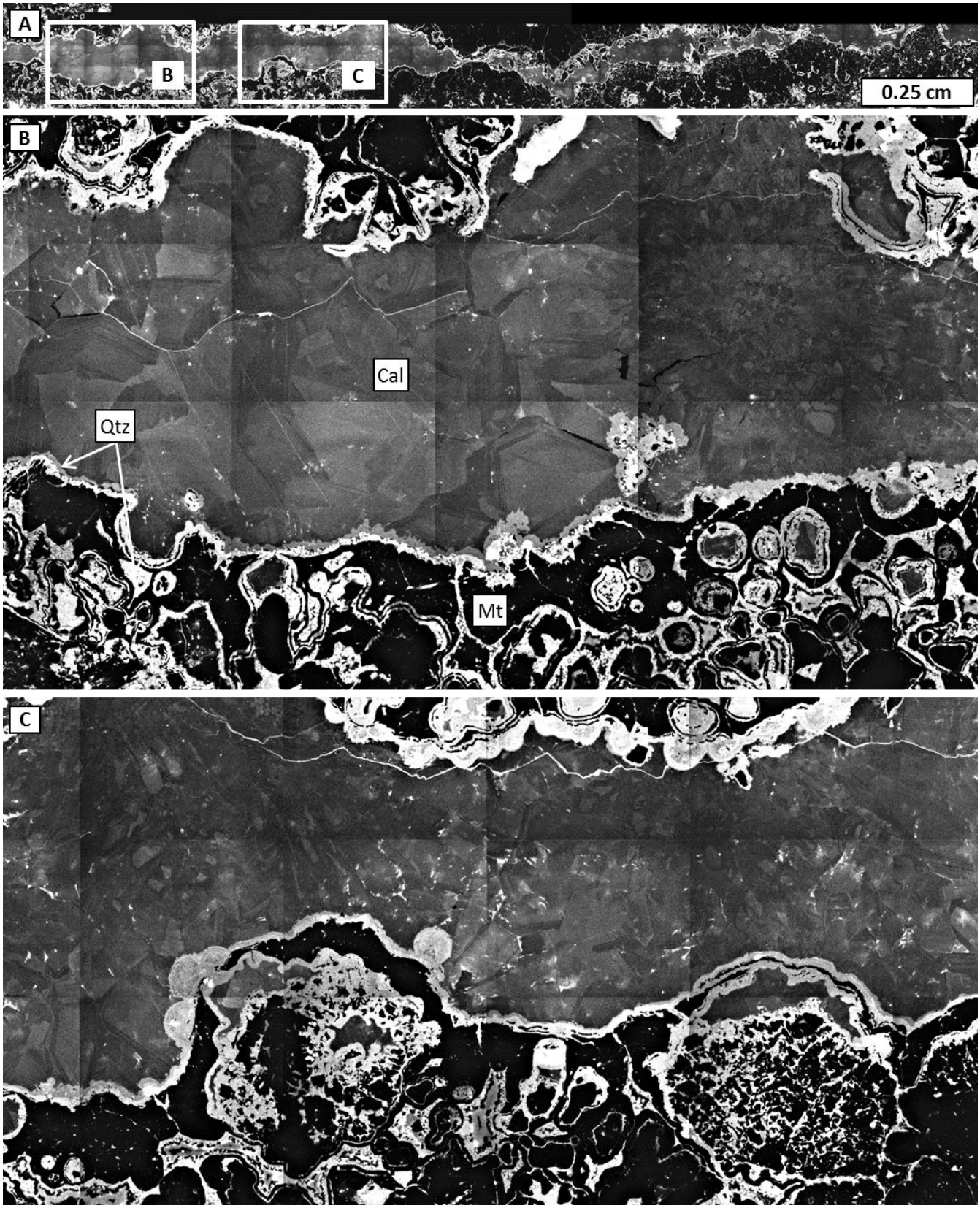

Fig. 3.9: (A) CL map for the vein area with close-ups in (B) and (C). Note zonation patterns in calcite and quartz.

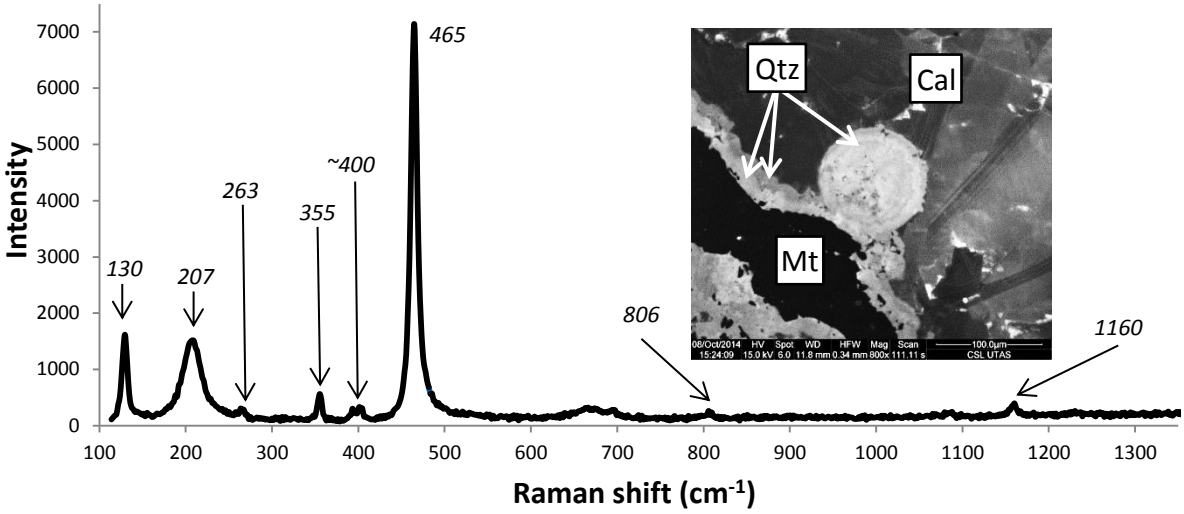

Fig. 3.10: Raman spectrum and BSE image of a quartz nodule inside the vein. Abbr. are same as in Fig. 3.2.

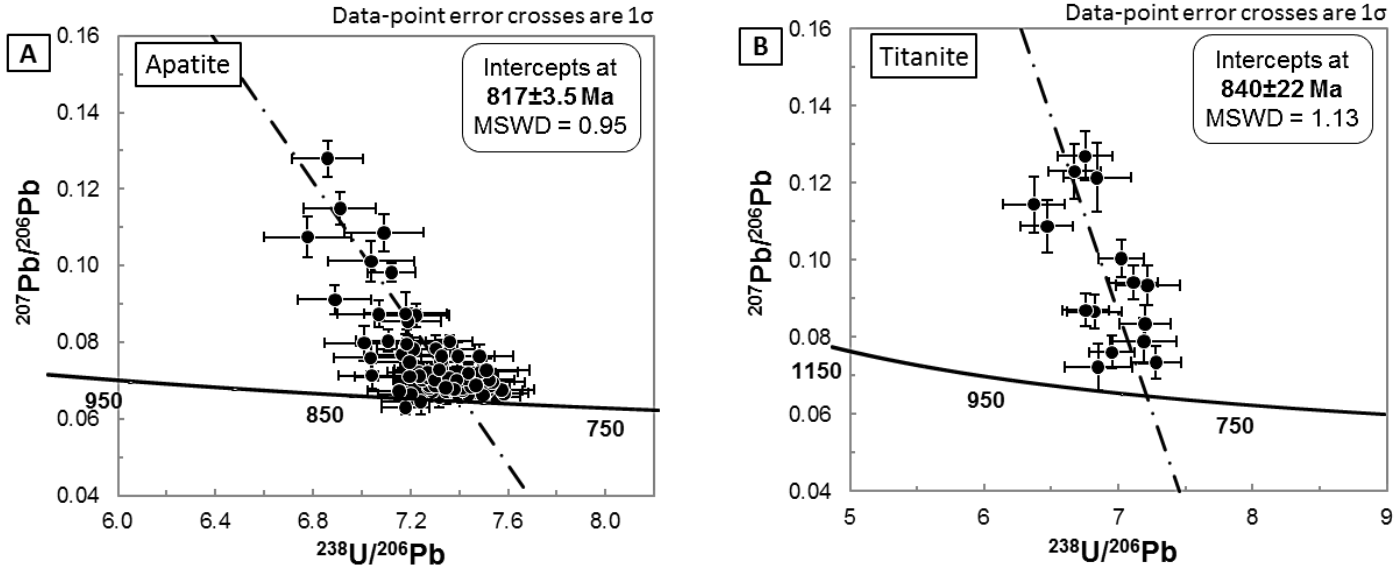

Fig. 3.11: Dating results of the (A) vein apatite and (B) titanite from Olympic Dam. Titanite is located in the dolerite host rock and is related to the alteration during the vein formation.

(secondary apatite 835±16 Ma, secondary titanite 806±13 Ma, Huang et al., 2015) and with reported U-Pb age of baddeleyite in the GDS (827±6 Ma, Wingate et al., 2004).

3.4.3 Sr-Nd isotope results

A high-purity concentrate of vein apatite (vein crushing and separation of apatite grains) measured by isotope dilution contains 4788 ppm Nd and has a low Sm/Nd ratio, consistent with the laser-ablation data in Table 3.8. Present-day $^{143}Nd/^{144}Nd$ is low (εNd = -22.2±0.3) and $^{87}Sr/^{86}Sr$ is high (0.73492±4; Table 3.5). Age correction to 827 Ma (Wingate et al., 2004) yields initial $^{87}Sr/^{86}Sr$ and εNd_{827} of 0.7348 and -9.3, respectively. A bulk vein sample material (statistically representative bulk sample, carefully collected with a ~1 mm diameter dental drill) has much lower trace element concentrations (55 ppm Sr, 51 ppm Nd) and calculated initial $^{87}Sr/^{86}Sr$ and εNd_{827} of 0.7207 and -3.9, respectively (Table 3.5). This indicates considerable inter-mineral disequilibrium. Furthermore, these signatures differ strongly from those in the host dolerite ($^{87}Sr/^{86}Sr$ = 0.7035-0.7052, εNd_{827} = +3).

3.5 Discussion

The magnetite-apatite-quartz-calcite-chlorite-chalcopyrite vein studied here crosscuts dolerite which contains magmatic magnetite and apatite. U-Pb dating of similar dolerite dykes at the Olympic Dam, and compositional features of OD422 (Fig. 3.3) and many other Olympic Dam dolerite dykes, indicate these dykes are correlated with the 827 Ma GDS. The latter are associated with magmatic events, related to the break-up of Rodinia (Zhao and McCulloch, 1993; Wingate et al., 2004). U-Pb ages of vein minerals (apatite 817±3.5 Ma; Fig. 3.11 A and titanite 840±22 Ma; Fig. 3.11 B) are consistent with vein formation shortly after dyke emplacement.

3.5.1 Source of components and fluids

The source of Fe and P is one of the main questions in the debate about the origin of magnetite-apatite deposits (e.g., Treloar and Colley, 1996). In general, numerous studies on mafic systems show that alteration of these rocks can result in a mobilization of a whole range of elements which can form diverse deposit types, including various IOCG (Johnson and McCulloch, 1995; Barton and Johnson, 2000; Barton, 2014), Fe-Ni-Cu (e.g., Namew Lake, Manitoba, Menard et al., 1996), and porphyry copper deposits (e.g., Mount Pinatubo, Philippines, Bingham Canyon, USA, Hattori and Keith, 2001). A purely magmatic origin (e.g., immiscible Fe-oxide liquid or magma-derived aqueous or carbonic fluid) of these components in the vein studied is rejected, because the vein occupies a fracture in already solidified dolerite. However, alteration of dolerite near the vein produced narrow selvages where dolerite was converted to chlorite, quartz and titanite. Alteration destroyed magmatic apatite, and original magmatic magnetite-ilmenite aggregates are partially to completely replaced by titanite (Fig. 3.2 D-E). Part of the vein's Fe and P (and Si and Ca as well) budget could therefore originate from the local alteration zone (Fig. 3.12). The Sr-Nd isotopic results support a mixed source for components in the vein. Samples of *'bulk vein'* and pure vein apatite have initial $^{87}Sr/^{86}Sr$ and εNd (at an assumed age of 827 Ma) of 0.7207/-3.9 and 0.7348/-9.1, respectively (Fig. 3.13). By contrast, several analyses of OD422 dolerite yield $^{87}Sr/^{86}Sr$ of 0.7035-0.7052 and εNd_{827} of ~+2.9 (Table 3.5). These values indicate considerable isotopic heterogeneity within the vein, and between the vein and the host dolerite. Sr and Nd within the vein minerals were derived from a source with low εNd and high $^{87}Sr/^{86}Sr$, most likely the breccia complex intruded by the dolerite dyke. Published Sm-Nd isotope data on Olympic Dam ore indicate an εNd_{827} of -16 (average of 17 samples, Johnson and McCulloch, 1995). This value

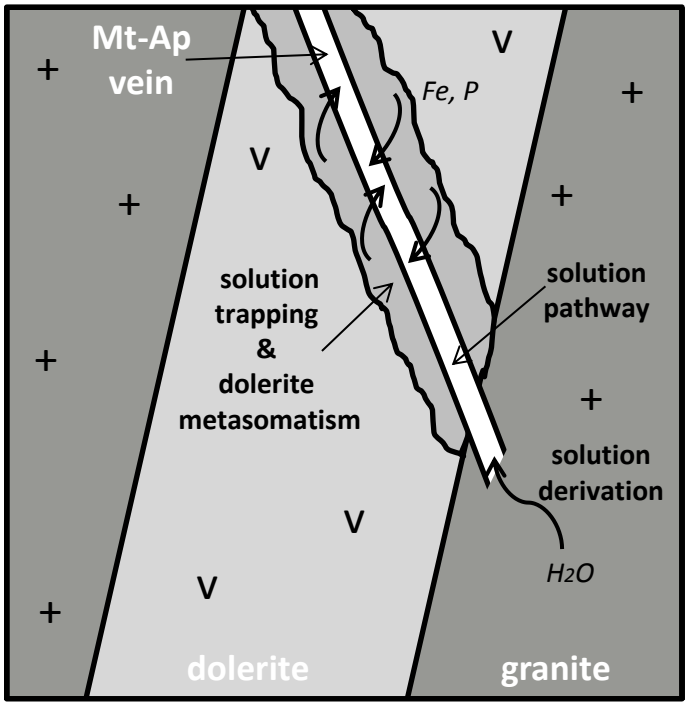

Fig. 3.12: A generalized model for the hydrothermal precipitation of cogenetic magnetite (Mt) and apatite (Ap) in the dolerite-hosted vein. The fluid leached Fe, P, Sr and REE (Nd) from the mafic rock immediately along the crack. Components such as H_2O, Sr and REE (Nd) originated from the granitic source and were trapped in the crack in dolerite. The result is the co-precipitation of magnetite, apatite and other vein minerals.

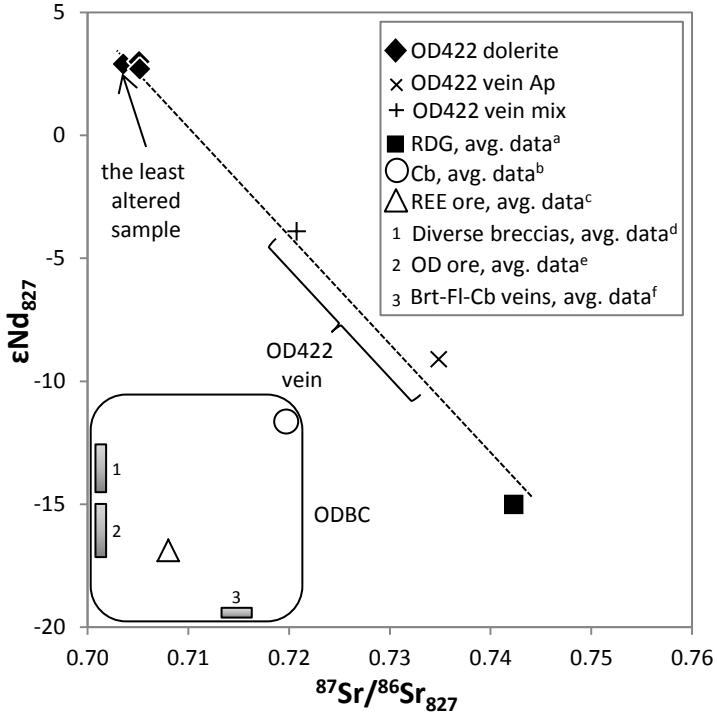

Fig. 3.13: Range of compositions of the radiogenic isotopes in the ODBC. The composition of the vein lies on the trend line between the dolerite and granite, indicating the mixed Nd and Sr sources for vein minerals. For comparison, average values for the ODBC are countered by a black box. All data values are calculated to the age of 0.827 Ga. Abbr.: apatite (Ap), barite (Brt), carbonate (Cb), fluorite (Fl), Olympic Dam (OD). References: [a] εNd data from Johnson and McCulloch (1995), Sr-weighted data from Creaser and Gray (1992); [b] Maas et. al. (2015); [c, d] R. Maas (unpub. data); [e] Johnson and McCulloch (1995); [f] Wawryk (1989).

is comparable to the average εNd_{827} of -14.1 for a large sample set ranging from unmineralized host granite to Cu- and U-mineralized breccia (R. Maas, unpub. data). Sr isotope results for REE ores, fluorite-barite and for various hydrothermal carbonates yield $^{87}Sr/^{86}Sr_{827}$ of 0.7080 (average of 25 analyses; R. Maas, unpub. data), 0.7146 (average of 23 analyses, Wawryk, 1989) and 0.7197 (average of 50 analyses, Maas et al., 2015), respectively, providing a reasonably comprehensive survey of average $^{87}Sr/^{86}Sr$ in the ODBC at 827 Ma. However, the $^{87}Sr/^{86}Sr$ composition of the OD422 vein requires a more radiogenic Sr source, such as the host granite: 13 analyses of Hiltaba Suite granite samples yielded a Sr-weighted average $^{87}Sr/^{86}Sr_{827}$ of 0.7423 (Creaser and Gray, 1992). This $^{87}Sr/^{86}Sr_{827}$ value combined with the average εNd_{827} of -15 for 5 analyses of the RDG (Johnson and McCulloch, 1995), defines a point on the extension of the dolerite-magnetite/apatite vein trend (Fig. 3.13). The $^{87}Sr/^{86}Sr$ and εNd analyses of vein material appear to record mixing of Sr and Nd derived from the local host dolerite, presumably via wall rock alteration at vein margins, and Sr and Nd derived externally, most likely from host granite.

3.5.2 Origin of the magnetite-apatite vein

The studied vein has a symmetrical arrangement of minerals which records successive stages of mineral precipitation. Apatite, present along the vein selvage or directly on the dyke-vein boundary and in the interior of colloform magnetite, appears to have been deposited first. Apatite was followed by successive crystallization of magnetite, magnetite-quartz-calcite and finally calcite toward the center of the vein (Figs. 3.2 B and 3.4 A). Well-preserved delicate features, such as fine bands and the symmetrical distribution of the minerals, suggest a static depositional environment within a narrow fissure. No evidence was found for the operation of a *'crack-seal'* mechanism that indicates multiple injections of the hydrothermal fluid(s). In other words, we are confident that the observed assemblage formed in a closed system. Thus, we consider that all the components that crystallized the vein mineral were confined to the crack in the dolerite, as soon as the fissure formed. In fact, a term *"schlieren"* is more applicable to the aggregate of related minerals enclosed in a limited space and principally different to the surrounding host.

3.5.3 Were colloidal solutions involved?

A salient feature of the vein magnetite is its colloform habit (Fig. 3.4) which is a new occurrence at Olympic Dam. Unlike other isometric minerals such as pyrite, galena and sphalerite, a colloform habit appears to be very unusual for magnetite (Stevenson and Jeffery, 1964). The concentrically zoned colloform magnetite in this study is crystalline (Fig. 3.5), and has structurally identical (Fig. 3.6 A,D) but chemically diverse (Figs. 3.5 B,E-G and 3.6) cores and rims. Other exceptional features of this magnetite are: (1) rhythmic compositional bands (defined by minor and trace element content) of cores and rims; (2) alternating layers of quartz in magnetite nodules (Fig. 3.4); (3) syneresis cracks (filled with quartz; Fig. 3.4) and *in situ* brecciation of the magnetite's rim, both possibly due to spontaneous dehydration; (4) overgrowths of colloform quartz (Fig. 3.10); and (5) incorporation of sporadically distributed calcite and quartz micro-inclusions into magnetite nodules (Fig. 3.5 C). According to this set of attributes, the involvement of hydrocolloids in the vein formation becomes highly possible. However, as the temperature constrains on the origin of the vein assemblage are lacking, the involvement of colloidal media cannot be confidently supported.

Colloform magnetite is a rare feature worldwide, however, it has been found in iron deposits on Vancouver Island, Canada (Stevenson and Jeffery, 1964), at Kurzhunkul, Kazakhstan (Dymkin and Sokolov, 1961), at Kezhma, Russia

(Pavlov, 1961) and at El Laco, Chile (Dare et al., 2015). The deposits on Vancouver Island comprise colloform magnetite (associated with silicates, calcite, and diverse sulfides) which was precipitated due to the gel metasomatism type of replacement of limestone (Stevenson and Jeffery, 1964). In the Kurzhunkul deposit, colloform magnetite (associated with silicates, calcite, apatite and diverse sulfides) was formed during intense brecciation of volcanic (andesite and quartz porphyrite) and sedimentary (limestone) rocks accompanied by abrupt pressure release in the local ore zones which resulted in a formation of a colloidal solution (Dymkin and Sokolov, 1961). The magnetite-maghemite in the Kezhma ores occurs in deep faults and adjacent fault zones and is genetically associated with mafic igneous rocks (Pavlov, 1961). The most renowned example of the colloform magnetite is the El Laco deposit, where it is associated with fluorapatite in veins in andesite and in massive segregations replacing andesite (Dare et al., 2015).

Precipitation from colloidal solutions plays an important role in mineral and ore formation, is empirically confirmed and applicable in our case study. Origin involving colloids has been proposed elsewhere (e.g., Chukhrov, 1966; Baumgartner et al., 2013) but has not found broad acceptance because of problems in explaining the thermodynamic stability and transport of colloids in nature. The coagulation of particles in gel-like media can be achieved in various ways (e.g., cooling, boiling or mixing of hydrothermal solutions, Saunders, 1990, 1994) and, therefore, may take place in a range of geological environments (Wilkinson et al., 1996) at different crustal depths (Chukhrov, 1966). Importantly, colloidal solutions are able to carry large volumes of dispersed metals (e.g., Cu, and Zn, Karathanasis, 1999; Fe, Williams et al., 2005) compared to true solutions. As envisaged in our study, the source of iron and phosphorus is within a few mm from the narrow fissure, which is both a collector and precipitation site for magnetite-apatite. Thus, sustained fluid flow with low abundances of the above elements (true solution) through the fissure is not practical, whereas much more concentrated colloidal matter presents a feasible explanation.

3.5.4 Implications for ore-forming processes

The Olympic Dam is a complex multi-stage deposit, containing anomalous quantities of Fe (mainly incorporated into hematite and subordinate magnetite), Cu, U, REE and many other elements (Ehrig et al., 2012). Occurrences of massive magnetite-apatite in the deeper parts of the deposit hosted by the RDG have been described, and were interpreted as having formed at an early stage of deposit evolution (Ehrig et al., 2012). In the ODBC, this mineralization is largely destroyed by repeated brecciation or replaced during hematitization. The source of Fe has been much debated but remains enigmatic, even if current consensus favors a model for contributions from both felsic and mafic magmas and hydrothermal fluids generated during their emplacement (e.g., Johnson and McCulloch, 1995), as well as a possible role for Fe supplied by sediments of the bedded facies succession occurring within the ODBC (McPhie et al., 2011).

The genesis of the magnetite-apatite veins described here relates to emplacement of the GDS-type dolerites at ~0.82 Ga. These dykes are in general Fe-rich (FeO_t ~14 wt%, Huang et al., 2015) and commonly contain magmatic apatite. As shown above, these mafic rocks can also include a hydrothermal magnetite-apatite association which is considered to be the product of the leaching of Fe and P components from the host dolerite.

Magnetite-apatite-bearing veins such as those in sample OD422 (RD222, Fig. 3.1) are common to other dolerite occurrences within the ODBC. For example, drillhole RU65-8337 (Fig. 3.1) contains GDS-type dolerite which contains not only abundant magnetite-apatite veins within the dyke but also massive aggregates of magnetite-apatite (containing additional minerals such as uraninite, Figs. 3.14 and 3.15; Table 3.1). Based on the U/Pb ratios of uraninite (U/Pb =

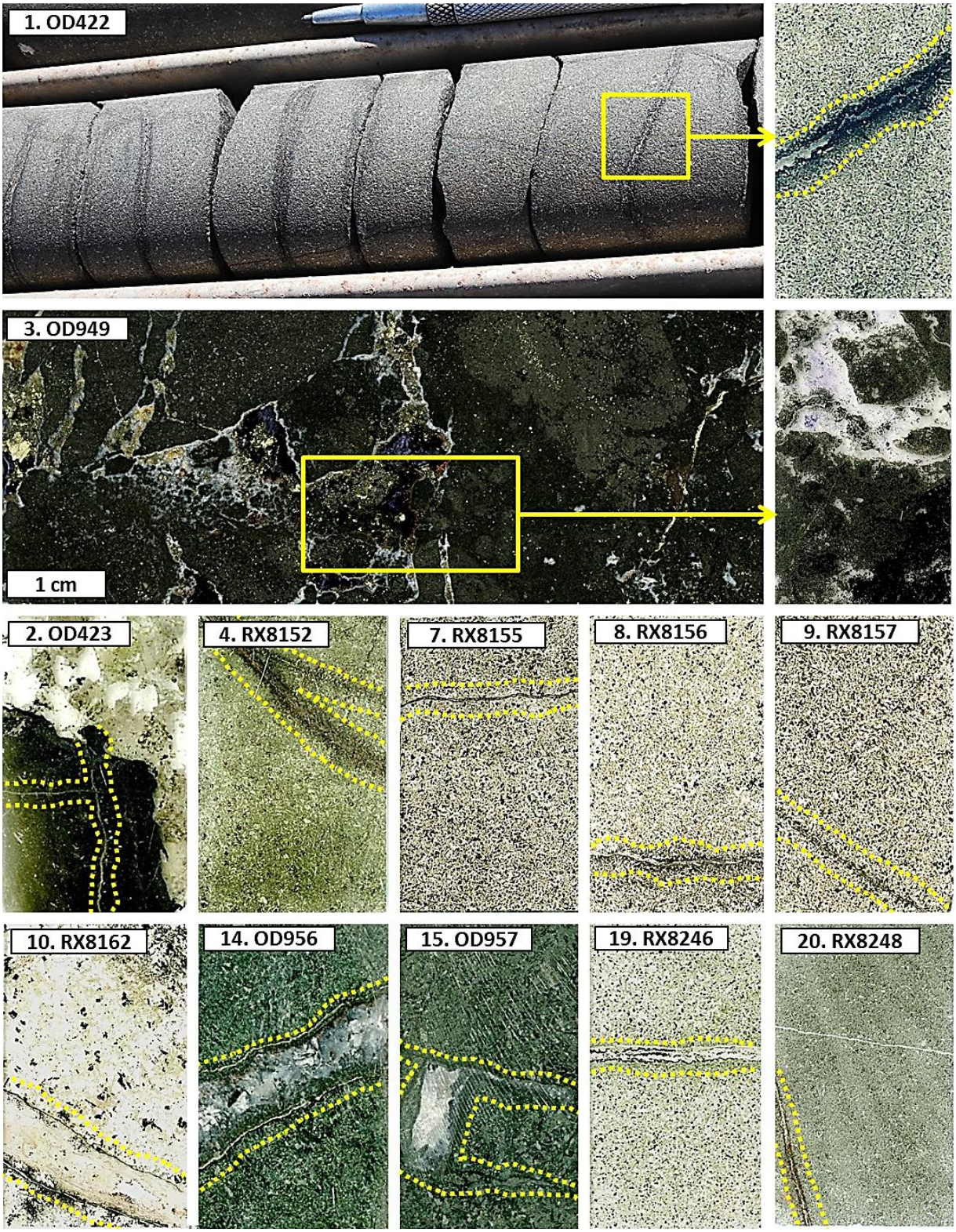

Fig. 3.14: Representative macroscopic images of mafic dykes from the drillholes RD222 and RU65-8337 hosting magnetite-apatite bearing veins of various thicknesses. Numbers of the images are in accordance with those listed in Table 3.1. (1) Drillcore from the drillhole RD222 with the closeup of the sample OD422 (case study of the current work). Note plentiful parallel magnetite-apatite-rich veins within the dolerite. (3) Drillcore from the drillhole RU65-8337 with a close-up of the sample OD949 shows almost complete replacement of the dolerite by the magnetite-apatite-rich assemblage. Later fluorite-barite-carbonate-sulfide veins crosscut the altered dolerite. Images (2, 4, 7-10, 14, 15, 19 and 20; all are ~2 x 4 cm thin section images) show further examples from the magnetite-apatite bearing veins inside mafic rocks within the Olympic Dam deposit.

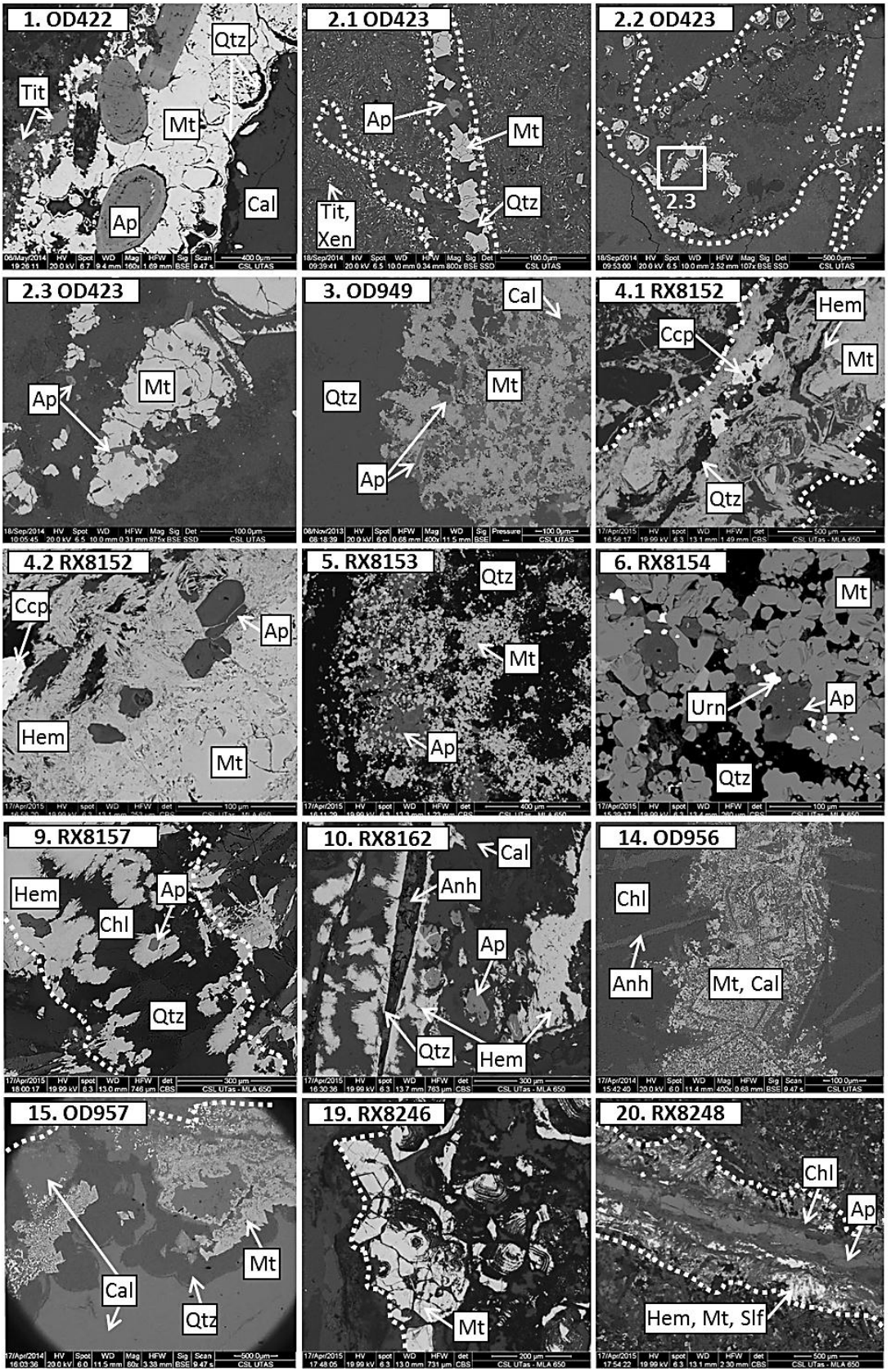

Fig. 3.15: Representative BSE images in addition to Fig. 3.14. Numbers of the images are in accordance with those listed in Table 3.1.

8.59±0.49, corresponding to 780±40 Ma), these zones of massive IOA are coeval with the GDS-type Olympic Dam dolerite. Apatite is present in the majority of such veins together with magnetite which is either colloform or euhedral. Thus, the stable assemblage of these two minerals in mafic rocks within the ODBC constitutes the potential source for Fe and P and possibly also the source of other components.

Researchers have debated and modified existing genetic models in an attempt to identify a holistic model that can be applied to the entire clan of IOCG deposits. However, in many cases, several distinct stages of formation can be recognized, or the deposits have been superimposed during later events (Treloar and Colley, 1996), making unequivocal validation of these models problematic. Olympic Dam illustrates this particularly well, in that careful analysis of prevalent mineral assemblages indicate a complex sequence of events that transition from magmatic to hydrothermal, accompanied by structural reworking, and superimposed by thermally-driven reactivation multiple times over the past 1.6 Ga.

The case study reported here, addressing the products of one of the later events affecting the orebody, and thus unaffected by substantial reworking, represents an unambiguous example of an assemblage formed by hydrothermal activity. The proposed model, involving hydrothermal-metasomatic reaction in a mafic environment, is plausible, and explains the observed petrographic features. Furthermore, we believe that the same process could, potentially, have operated, albeit at a larger scale, during the 1.6 Ga event that formed the OD deposit. Dare et al. (2015), in their study of the El Laco deposit, emphasize that *"if this IOA deposit formed by hydrothermal processes, then the origin of similar deposits will have to be revisited as well"*. Taken with the evidence presented here, we are confident that detailed geological and geochronological studies of IOA deposits will reveal a diversity of genetic models.

3.6 Conclusions and implications

In this study, we demonstrate a possible way to form a magnetite-apatite association. Using an example from the Olympic Dam deposit, it is proposed that deposition of this association was the result of the leaching of Fe and P from a mafic rock, coupled with element migration, trapping and deposition within an open fracture (Fig. 3.12). The metasomatized dolerite dyke described is genetically related to the GDS, emplaced at ~0.82 Ga. The genetic model for this magnetite-apatite assemblage is applicable to a broad spectrum of ore occurrences, including magnetite-apatite-bearing IOCG systems and a range of other deposits in disparate geological settings.

Chapter 4: Deep, early mineralization at the Olympic Dam Cu-U-Au-Ag deposit

4.1 Introduction

The Olympic Dam deposit, ~520 km NNW of Adelaide, South Australia, is the world's largest uranium, third largest gold and fifth largest copper resource; significant accumulations of Ag and REEs are also present (Ehrig et al., 2012). Discovered in 1975, the deposit was classified as an IOCG deposit (Meyer, 1988; Hauck, 1990; Hitzman et al., 1992). Early studies interpreted the deposit as a strata-bound sediment-hosted mineralization (Roberts and Hudson, 1983) or a magmatic-hydrothermal mineralization formed within an subvolcanic (maar) setting (Reeve et al., 1990), involving possible fluid-mixing of deep magmatic reducing brines with surficial colder oxidizing meteoric fluids (Oreskes and Einaudi, 1990, 1992; Haynes et al., 1995).

Recent work at Olympic Dam shows that formation is more complex than previously thought (e.g., McPhie et al., 2011; Maas et al., 2011; Ehrig et al., 2012), and several aspects make clarification of paragenetic and absolute age relationships, and therefore a genetic model, more difficult to establish than at other IOCG deposits in the region and elsewhere. These aspects include: (1) extensive and possibly repeated brecciation within a voluminous and heterogeneous breccia complex (6 x 8 km in plan, at least 1.5 km deep, Reeve et al., 1990; Oreskes and Einaudi, 1992) which is the principal host of polymetallic mineralization at Olympic Dam; (2) a range of lithologies dominated by the ~1.59 Ga RDG (Creaser and Gray, 1993; Jagodzinski, 2014), and lesser GRV, bedded clastic facies (McPhie et al., 2011; Ehrig et al., 2012), and GDS dolerites (Zhao and McCulloch, 1993; Huang et al., 2015); (3) presence of several mineral associations (e.g., Ehrig et al., 2012); (4) strong diversity in ore and mineral textures (e.g., breccia matrix, breccia clasts, veins, microcavity fillings, oolites; Roberts and Hudson, 1983) and uncertainty in the relative and absolute ages of these different mineral assemblages; and (5) pervasive, texture-destructive hematite alteration (Ehrig et al., 2012). It is clear that present-day mineralization at Olympic Dam reflects multiple magmatic, tectonic, sedimentary, hydrothermal and mechanical intermixing events, including (but not limited to) intense bimodal magmatism at ~1.59 Ga (Creaser and Gray, 1993), formation of a sedimentary basin now incorporated and mineralized within the breccia complex (McPhie et al., 2011), intrusion of abundant mafic dykes (GDS dolerites, ~0.8 Ga, Huang et al., 2015) and finally emplacement of barite-fluorite-carbonate-sulfide dominated veins at ~0.5 Ga (Wawryk, 1989; Maas et al., 2011). These events all influenced and strongly overprinted primary textures and mineral assemblages of the early stage of mineralization. Petrographic study and, in particular, recognition of the early mineralizing event is challenging but crucial for an understanding of Olympic Dam, and with application to IOCG systems in general.

In IOCG-style ore deposits, primary ores are expected to carry abundant magnetite (e.g., Hitzman et al., 1992; Williams et al., 2005; Groves et al., 2010). This is indeed the case at other Cu-Au deposits in the Gawler craton (e.g., Acropolis prospect, Paterson, 1986; Hillside deposit, Conor et al., 2010; Oak Dam East deposit, Davidson et al., 2007; Prominent Hill deposit, Belperio et al., 2007; Titan prospect, Bastrakov et al., 2007; and Wirrda Well prospect, Vella, 1997) and is an implicit assumption of previous studies at Olympic Dam (e.g., Hitzman et al., 1992). However, magnetite-dominant assemblages are rare at Olympic Dam, due to pervasive and ubiquitous addition of hematite which was inferred to be related to a hydrothermal overprinting of magnetite at temperatures between 200 and 400˚C (Oreskes

and Einaudi, 1992). If (presumably) early magnetite-dominant Cu-Au-U mineralization still exists at Olympic Dam, it would most likely be preserved at the margins of the deposit, away from the most intense brecciation and hydrothermal overprints (Ehrig et al., 2012). In a search for such mineralization, we examined several deep drillholes located at edges of the ODBC. Drillhole RD2773, the longest drillhole yet completed at Olympic Dam, was selected for detailed study as it contains a ~175 m (maximum thickness) interval of coarse-grained, strongly magnetic mineralization which is only weakly altered and brecciated. In the Olympic Dam context, this type of mineralization is most uncommon and may represent early, perhaps RDG-related, magnetite-dominant mineralization. This paper describes the petrographic and geochronological features of this assemblage.

4.2 Geologic background

The Olympic Dam deposit is the largest ore deposit in the Olympic Cu-Au Province in the eastern Gawler craton. The multistage, brecciated, mineralized complex is entirely surrounded by the Mesoproterozoic RDG, a Hiltaba Suite granite, which, together with the GRV represents the Gawler SLIP (Allen et al., 2008).

Although dominated by clasts of the RDG, the ODBC also contains clasts of other lithologies, including bedded sedimentary facies of various compositions, mafic to ultramafic dykes, and rocks interpretable as porphyritic felsic units (Ehrig et al., 2012). Some of the GDS-type dolerite and basalt dykes intruded the ODBC at ~0.82 Ga (e.g., Huang et al., 2015). The deposit is unconformably overlain by a ~320 m-thick sequence of flat-lying, unaltered and unmineralized Neoproterozoic to Cambrian sedimentary formations (Reeve et al., 1990).

4.3 Cross-section of drillhole RD2773

Diamond drillhole RD2773 (Fig. 4.1) is vertical, and located ~0.5 km E of the ODBC (683689.42 E, 6630026.81 N, see location of the drillhole in Fig. 2 A in Ehrig et al., 2012). While the usual maximum depth of drilling at Olympic Dam deposit is ~1.5 km, RD2773 being the deepest among all holes allows to track the mineralization to larger depths (EOH at 2329 m). Elevated concentrations of Cu (up to 0.7 wt%), U_3O_8 (up to 1450 ppm), and Ce (up to 0.23 wt%) measured over 1 m assay intervals, define the deep mineralization which occur sporadically as concentration spikes from ~1500-2150 m, and nearly continuously from 2150 m to EOH (see positive correlation of Cu, U_3O_8, and Ce with Fe, P, and CO_2 in element plots in Fig. 4.1).

RD2773 intersects four main lithologies (Fig. 4.1). The uppermost 370 m consist of Neoproterozoic sedimentary units which unconformably overlie RDG and ODBC. The granite (RDG) was intersected between ~370 m and the EOH. The RDG is locally brecciated *in situ* and is weakly to moderately altered. Hematite and sericite are abundant in shallower parts of the drillhole, whereas chlorite and sericite are more abundant in deeper zones and adjacent to mafic dykes. A massive GDS dolerite dyke (surrounded by several of smaller dykes) occurs between ~1250 and ~1360 m. This dolerite is variably altered and is itself intruded by a number of narrow basalt dykes which display chilled margins at contacts. From ~2010 to ~2265 m, there is a pale green, quartz-sericite-dominated lithology (common accessories are hematite, fluorapatite, zircon, monazite, rutile, uraninite, thorite-uranothorite and allanite) termed the *'felsic unit'*. This felsic unit is briefly mentioned in Ehrig et al. (2012) and to date has only been encountered in this one drillhole. The felsic unit is highly sericite-altered and the boundary with RGD is brecciated, obscuring their original relationship.

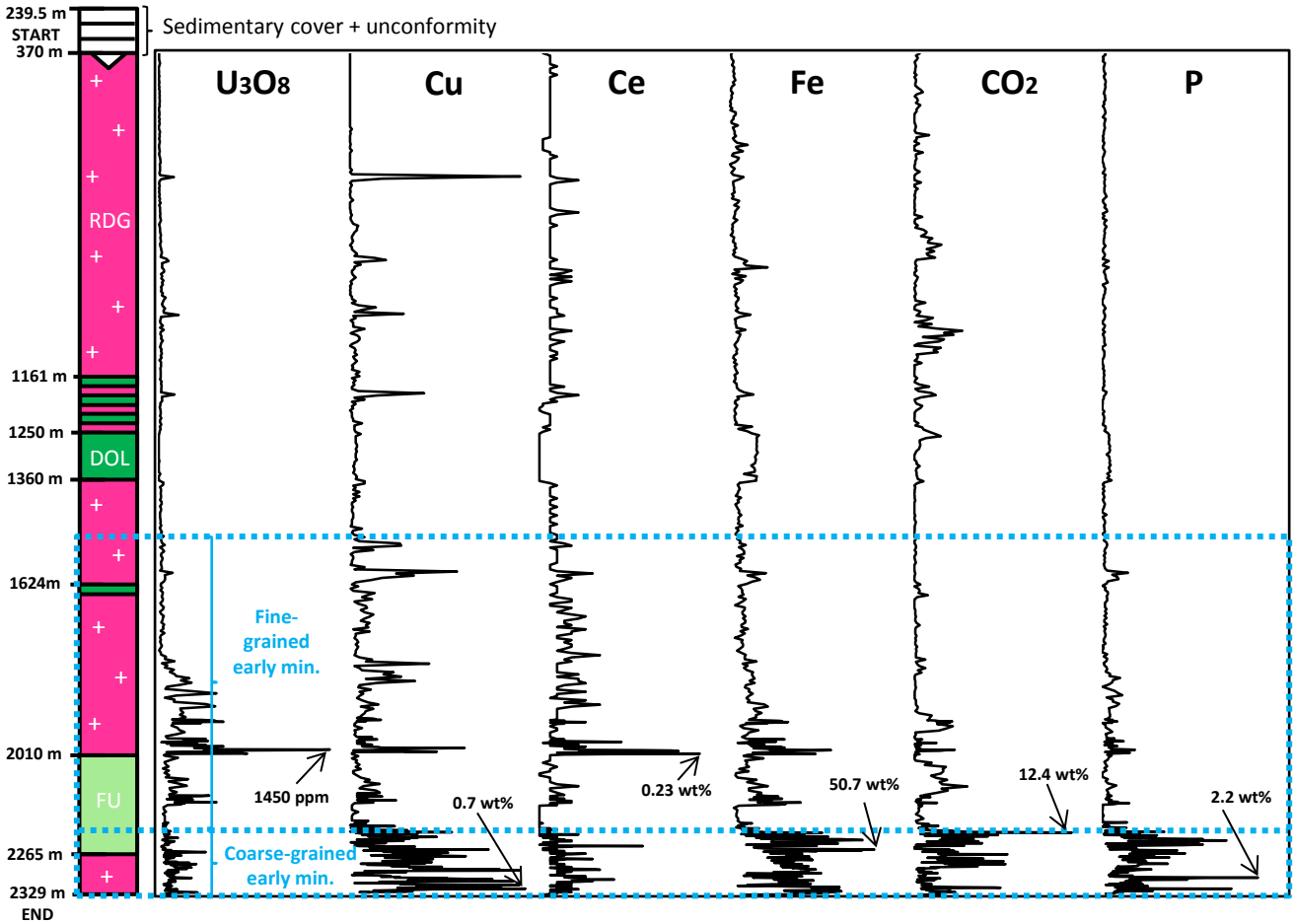

Fig. 4.1: Simplified geological cross section of the drillhole RD2773 which comprises the RDG, felsic unit (FU), and later dolerite (DOL) dykes. Fine-grained mineralization starts at ~1500 m and becomes coarser from ~2150 m to the end of the drillhole. Petrographic observations are in accordance with the concentrations of selected metals and elements which correlate positively and become abundant with increasing depth. Maximum values (i.e. maximum peaks in plots) for Cu, U_3O_8, Ce, Fe, P and CO_2 are about 0.7 wt%, 1450 ppm, 0.23 wt%, 50.7 wt%, 2.2 wt% and 12.4 wt%, respectively.

However, the presence of abundant quartz phenocrysts (containing melt inclusions) and lack of plutonic textures suggest a rhyolitic composition and a volcanic or sub-volcanic origin for the felsic unit.

4.4 Sampling and methods

After petrographic examination on an Olympus BX60 microscope, polished thin sections and epoxy-mounted targets were examined in the Scanning Electron Microscope (SEM, FEI Quanta 600), followed by determination of major element concentrations on an electron microprobe (Cameca SX100) at CSL, UTas. U-Pb ages of magmatic zircon from the felsic unit and various U-bearing minerals (uraninite, fluorapatite and hematite) were determined using LA-ICPMS (Resonetics S-155 Ar-F excimer laser) at the UTas. Uraninite and hematite have been dated using a method similar on Halpin et al. (2014) in terms of data collection, data reduction and error propagation; apatite dating has been done accordingly to method described in Thompson et al. (2016). Sm-Nd and Sr isotope analyses of calcite from the felsic unit were done using solution-mode MC-ICPMS at the University of Melbourne. Descriptions of the samples (n = 23) used in various investigations are summarized in Table 4.1.

4.4.1 SEM

BSE imaging was performed on a FEI Quanta 600 SEM fitted with a FEI solid-state BSE detector at the CSL, UTas. The acceleration voltage was 15 to 20 kV and the beam current around 3 nA. Additional BSE imaging, energy dispersive x-ray spectrometry (EDS) were carried out on a Hitachi SU-70 field emission SEM at the CSL, UTas, equipped with an Oxford AZTec microanalysis system with X-Max80 SDD EDS detector and HKL NordlysNano EBSD camera.

4.4.2 LA-ICPMS (U-Pb dating)

Samples were prepared by cutting out portions of rock or mineral separates and mounting in 1" epoxy rounds. The samples were then polished with fine grit, cleaned, and polished using 0.3 micron alumina polish. Samples were cleaned in DI water in a sonic bath and rinsed several times before being dried thoroughly and placing into the laser ablation cell.

In situ analyses for Pb/U and Pb isotopic compositions were done by LA-ICPMS using a Resonetics Resolution S-155 laser ablation system with a Coherent Compex Pro 110 ArF excimer laser coupled to an Agilent 7900 ICPMS. The laser has a ~20 ns pulse width and was fired at 5 Hz and at ~2.0 J/cm^2, with the energy being measured daily by external meter. Each analysis consisted of a 30 s *'gas blank'* followed by 30 second ablation. Ablation of the various minerals took place in a helium atmosphere (0.35 l/min) and was mixed immediately with argon (~1 l/min). The signal was homogenized in a signal smoothing device (the *'squid'*) and finally sent into the torch of the ICPMS. Small amounts of nitrogen gas (~1.5 ml/min) is added to the gas stream after the ablation cell to improve sensitivity. The ICPMS is tuned daily for maximum sensitivity while keeping oxides below 0.2% (ThO/Th in a line on NIST612).

For all geochronological analyses, the synthetic NIST610 glass was used as a primary standard for mass bias and drift correction for Pb isotopic compositions (from Baker et al., 2004) as well as for trace element concentrations (using values from Jochum et al., 2011). NIST610 was analysed multiple times throughout each session to constrain any drift in the ICPMS.

For all minerals a mineral specific primary standard was analysed in duplicate at the beginning at end of each session as well as after every 15 unknowns for the Pb/U ratio. This primary standard for the Pb/U ratio was used to correct for ICPMS drift, ICPMS mass bias, as well as laser induced element fractionation. The laser induced elemental fractionation was corrected by stacking down hole Pb/U curves from the primary standard and applying a correction based on this curve to the unknowns (Paton et al., 2010).

Specifics for each mineral phase dated are as follows:

Zircon: Analyses for Pb/U geochronology were done at a ~30 μm spot size and masses ^{49}Ti, ^{56}Fe, ^{91}Zr, ^{178}Hf, ^{202}Hg, ^{204}Pb, 2^{06}Pb, ^{207}Pb, ^{208}Pb, ^{232}Th, ^{235}U and ^{238}U measured (Table 4.2). The 91500 zircon (Wiedenbeck et al., 1995) was as a primary standard for the Pb/U ratio. Secondary standard zircons Mudtank (Black and Gulson, 1978), Temora (Black et al., 2003), and Plesovice (Sláma et al., 2008) were monitored to assess accuracy. Trace element concentrations were calculated using ^{91}Zr as the internal standard element using stoichiometric proportions.

Apatite: Analyses for Pb/U geochronology were done at ~30 μm spot size while measuring masses ^{43}Ca, 5^{6}Fe, 1^{39}La, ^{202}Hg, ^{204}Pb, ^{206}Pb, ^{207}Pb, ^{208}Pb, ^{232}Th and ^{238}U (Table 4.3). The primary standard for the Pb/U ratio was an in-house apatite from the Acropolis Cu-Au prospect in South Australia (OD306) which has been characterized bulk digestion and analysis by ID-MC-ICPMS by R. Maas at the University of Melbourne (unpub.data, 2012) as well as *in situ* by LA-ICPMS. This apatite is homogenous for Pb/U, low in common Pb, and is similar in composition to the unknown apatites (U contents). Data is corrected as described above however an additional correction for the common Pb in the primary standard (Chew et al., 2011, 2014). Secondary standard apatites Otter Lake (Barfod et al., 2005), McClure Mountain (Schoene and Bowring, 2006), and Kovdor (Amelin and Zaitsev, 2002). Trace element concentrations are calculated using ^{43}Ca as the internal standard and assuming stoichiometric proportions.

Uraninite: Analysis for Pb/U were done using an 8 μm spot measuring ^{29}Si, ^{43}Ca, ^{49}Ti, ^{202}Hg, ^{204}Pb, ^{206}Pb, ^{207}Pb, ^{208}Pb, ^{232}Th, ^{235}U and ^{238}U (Table 4.4). Ablation was only 20 seconds to minimize signal drop off as the laser drills down. The primary standard for the Pb/U ratio was an in-house uraninite, Kintyre (R. Maas, unpub. data). Data reduction is similar to that of zircon. Trace elements were calculated using ^{238}U as the internal standard and assuming stoichiometric proportions.

Hematite: Analysis for Pb/U was done using a ~30 μm spot measuring ^{29}Si, ^{27}Al, ^{65}Cu, ^{202}Hg, ^{204}Pb, ^{206}Pb, ^{207}Pb, ^{208}Pb, ^{232}Th and ^{238}U (Table 4.5). The 91500 reference standard (Wiedenbeck et al., 1995) was used as the primary standard for the Pb/U ratio in hematite with the same procedure as for zircon. While it is likely there is some matrix effects between the hematite and zircon for the Pb/U element fractionation, we are able to find some concordant grains on the Tera-Wasserburg plot with the ^{207}Pb/^{206}Pb ratio being independently calculated from the NIST610, so matrix effects from use of zircon for the Pb/U ratio are considered minor (Ciobanu et al., 2013).

4.4.3 LA-ICPMS (trace elements)

LA-ICPMS measurements were conducted using a Resonetics S-155 ArF excimer laser ablation system coupled to an Agilent 7700 ICPMS instrument, UTas. The laser operated at a wavelength of 193 nm, had a pulse width of 20 ns and was fired at 5 Hz for all the trace element analyses.

Apatite: A total of 160 analyses from samples OD826, OD829 and OD846 (Table 4.6) were acquired. Spot size was 30 μm with an energy density of 3.5 J/cm^2. Count rates were measured for the following isotopes: ^{7}Li, ^{23}Na, ^{24}Mg, ^{29}Si,

^{31}P, ^{51}V, ^{55}Mn, ^{57}Fe, ^{63}Cu, ^{66}Zn, ^{69}Ga, ^{71}Ga, ^{72}Ge, ^{75}As, ^{85}Rb, ^{88}Sr, ^{89}Y, ^{90}Zr, ^{93}Nb, ^{137}Ba, ^{139}La, ^{140}Ce, ^{141}Pr, ^{146}Nd, ^{147}Sm, ^{151}Eu, ^{153}Eu, ^{157}Gd, ^{159}Tb, ^{163}Dy, ^{165}Ho, ^{166}Er, ^{169}Tm, ^{172}Yb, ^{175}Lu, ^{181}Ta, ^{197}Au, ^{204}Pb, ^{206}Pb, ^{207}Pb, ^{208}Pb, ^{209}Bi, ^{232}Th and ^{238}U. Stoichiometric Ca concentration of 39.74 wt% was used as the internal standard element in calculations. Concentrations were calculated using standard reference materials NIST610 (Jochum et al., 2011) and Durango apatite.

Magnetite: A total of 61 analyses on samples OD826 and OD829 (Table 4.7) were acquired and 41 trace elements were measured. Spot size was 30 μm with an energy density of 2.5 J/cm^2. Count rates were measured for the following isotopes: ^{24}Mg, ^{27}Al, ^{29}Si, ^{31}P, ^{43}Ca, ^{45}Sc, ^{47}Ti, ^{49}Ti, ^{51}V, ^{52}Cr, ^{55}Mn, ^{59}Co, ^{60}Ni, ^{63}Cu, ^{65}Cu, ^{66}Zn, ^{68}Zn, ^{69}Ga, ^{71}Ga, ^{75}As, ^{77}Se, ^{85}Rb, ^{88}Sr, ^{89}Y, ^{90}Zr, ^{93}Nb, ^{95}Mo, ^{107}Ag, ^{109}Ag, ^{111}Cd, ^{118}Sn, ^{123}Sb, ^{137}Ba, ^{139}La, ^{140}Ce, ^{146}Nd, ^{147}Sm, ^{163}Dy, ^{172}Yb, ^{232}Th and ^{238}U. Stoichiometric Fe concentration of 72.36 wt% was used as the internal standard element in calculations. Concentrations were calculated using the standard reference material GDS-1G using GeoReM preferred values.

Hematite: A total of 65 analyses on samples OD826 and OD829 (Table 4.8) were acquired and 46 trace elements were measured. Spot size was 30 μm with an energy density of 2.5 J/cm^2. Count rates were measured for the following isotopes: ^{24}Mg, ^{27}Al, ^{29}Si, ^{31}P, ^{43}Ca, ^{45}Sc, ^{47}Ti, ^{49}Ti, ^{51}V, ^{55}Mn, ^{59}Co, ^{60}Ni, ^{63}Cu, ^{65}Cu, ^{66}Zn, ^{68}Zn, ^{69}Gn, ^{71}Gn, ^{75}As, ^{77}Se, ^{85}Rb, ^{88}Sr, ^{90}Zr, ^{118}Sn, ^{121}Sb, ^{137}Ba, ^{139}La, ^{140}Ce, ^{146}Nd, ^{147}Sm, ^{153}Eu, ^{157}Eu, ^{163}Dy, ^{172}Yb, ^{178}Hf, ^{181}Ta, ^{182}W, ^{197}Au, ^{204}Pb, ^{205}Tl, ^{206}Pb, ^{207}Pb, ^{208}Pb, ^{209}Bi, ^{232}Th and ^{238}U. Stoichiometric Fe concentration of 69.94 wt% was used as the internal standard element in calculations. Concentrations were calculated using the standard reference material GSD-1G using GeoReM preferred values.

Pyrite: A total of 219 analyses from samples RX7986 and RX7987 (Table 4.9) were acquired and 32 trace elements were measured. Spot size was 30 μm with an energy density of 2.5 J/cm^2. Count rates were measured for the following isotopes: ^{27}Al, ^{47}Ti, ^{55}Mn, ^{59}Co, ^{60}Ni, ^{65}Cu, ^{66}Zn, ^{75}As, ^{77}Se, ^{89}Y, ^{90}Zr, ^{95}Mo, ^{109}Ag, ^{111}Cd, ^{118}Sn, ^{121}Sb, ^{140}Ce, ^{157}Gd, ^{172}Yb, ^{178}Hf, ^{181}Ta, ^{182}W, ^{197}Au, ^{204}Pb, ^{205}Tl, ^{206}Pb, ^{207}Pb, ^{208}Pb, ^{209}Bi, ^{232}Th, ^{235}U and ^{238}U. Stoichiometric Fe concentration of 46.55 wt% was used as the internal standard element in calculations. Concentrations were calculated using standard reference materials GSD-1G (GeoReM preferred values) and STDGL2b2 (Danyushevsky et al., 2011).

Chalcopyrite: A total of 33 analyses from sample RX7986 (Table 4.10) were acquired and 34 trace elements were measured. Spot size was 30 μm with an energy density of 2.5 J/cm^2. Count rates were measured using the following isotopes: ^{27}Al, ^{47}Ti, ^{55}Mn, ^{57}Fe, ^{59}Co, ^{60}Ni, ^{66}Zn, ^{75}As, ^{77}Se, ^{89}Y, ^{90}Zr, ^{95}Mo, ^{109}Ag, ^{111}Cd, ^{118}Sn, ^{121}Sb, ^{125}Te, ^{140}Ce, ^{157}Gd, ^{172}Yb, ^{178}Hf, ^{181}Ta, ^{182}W, ^{185}Re, ^{197}Au, ^{204}Pb, ^{205}Tl, ^{206}Pb, ^{207}Pb, ^{208}Pb, ^{209}Bi, ^{232}Th, ^{235}U and ^{238}U. Stoichiometric Cu concentration of 34.63 wt% was used as the internal standard element in calculations. Concentrations were calculated using standard reference materials GSD-1G (GeoReM preferred values) and STDGL2b2 (Danyushevsky et al., 2011).

Calcite: A total of 15 analyses from 14 samples (Tables 4.1 and 4.11) were acquired and 54 trace elements were measured. Spot size was 67 μm with an energy density of 3.5 J/cm^2. Count rates were measured using the following isotopes: ^{23}Na, ^{24}Mg, ^{27}Al, ^{29}Si, ^{31}P, ^{34}S, ^{39}K, ^{47}Ti, ^{51}V, ^{53}Cr, ^{55}Mn, ^{57}Fe, ^{59}Co, ^{60}Ni, ^{65}Cu, ^{66}Zn, ^{68}Zn, ^{85}Rb, ^{88}Sr, ^{89}Y, ^{93}Nb, ^{95}Mo, ^{107}Ag, ^{111}Cd, ^{137}Ba, ^{139}La, ^{140}Ce, ^{141}Pr, ^{143}Nd, ^{146}Nd, ^{147}Sm, ^{151}Eu, ^{153}Eu, ^{157}Gd, ^{159}Tb, ^{163}Dy, ^{165}Ho, ^{166}Er, ^{169}Tm, ^{172}Yb, ^{173}Yb, ^{175}Lu, ^{177}Hf, ^{178}Hf, ^{181}Ta, ^{182}W, ^{184}W, ^{197}Au, ^{204}Pb, ^{206}Pb, ^{207}Pb, ^{208}Pb, ^{232}Th and ^{238}U. Stoichiometric Ca concentration of 40.04 wt% was as the internal standard element used in calculations. Concentrations were calculated standard reference materials NIST612 and GSD-1g using GeoReM preferred values.

4.4.4 MC-ICPMS (Sr-Nd isotopes)

Radiogenic isotope analyses were conducted at the University of Melbourne (Maas et al., 2015) on small samples of felsic unit (~1g, two sub-samples OD820.3 and OD820.5) and calcite (~10 to 100 mg, 7 samples, Table 4.12). Powder samples were obtained with a dental drill from the polished surface and high-purity concentrates were prepared by handpicking. Felsic unit sub-samples were dissolved in HF/HNO_3 and 5M HNO_3 on a hotplate; the calcite samples were dissolved in HNO_3 only. The clear solutions were equilibrated with ^{85}Rb-^{84}Sr and ^{149}Sm-^{150}Nd tracers for isotope dilution work; the small sample of apatite (0.31 mg) was only spiked with the Sm-Nd tracer while Rb and Sr concentrations were obtained by Q-ICPMS on a 10% split of the sample solution. Rb and Sr were extracted using a combination of EICHROM SR resin and AG50-X8 (200-400) cation exchange resin. Sm and Nd were extracted using EICHROM TRU and LN resin. Total analytical blanks were 80 pg for Sr and Nd, with Rb/Sr = 0.3 and Sm/Nd = 0.2, resulting in sample/blank ratios >1000 except for Rb in the apatite sample which was corrected for a 10 pg Rb dissolution blank (resulting in a 3% correction).

Isotopic analyses were carried out on a Nu Plasma MC-ICPMS with sample uptake through a CETAC Aridus desolvator and PFA nebuliser operated at ~0.07 ml/min sample uptake, with sensitivities of 100V/ppm Sr and 150V/ppm Nd. Analyses were conducted in static multi-collection mode with signals near 8V Sr and 15V. Instrumental mass bias was corrected by normalizing to $^{88}Sr/^{86}Sr = 8.37521$ and $^{146}Nd/^{145}Nd = 2.0719425$ (equivalent to $^{146}Nd/^{144}Nd = 0.7219$), using the exponential law as part of an on-line iterative spike-stripping/internal normalization procedure. Data are reported relative to SRM987 = 0.710230 and La Jolla Nd = 0.511860. Typical in-run precisions (2se) are ±0.005-0.008% (Sr) and ±0.002% (Nd); external precision (reproducibility, 2sd) is ±0.006% (Sr) and ±0.004% (Nd). Rb isotope dilution analyses were performed using the Zr-doping method (Waight et al., 2002). External precisions for $^{87}Rb/^{86}Sr$ and $^{147}Sm/^{144}Nd$ obtained by isotope dilution are ±0.5% and ±0.2%, respectively. Results for international standards agree with TIMS reference values. For example, long-term (2011-2014) averages for BCR-2 are 0.704997±42 (2sd, n = 44) and 0.512641±24 (2sd, n = 74), and $^{147}Sm/^{144}Nd$ is 0.1382±0.0002. Decay constants are ^{87}Rb $1.395x10^{-11}$/yr and ^{147}Sm $6.54x10^{-12}$/yr. Modern CHUR has $^{147}Sm/^{144}Nd = 0.1960$, $^{143}Nd/^{144}Nd = 0.512632$ (Bouvier et al., 2008).

4.5 Results

4.5.1 Petrography

Magnetite-bearing mineralization in RD2773 can be detected from ~1516 m (Figs. 4.1 and 4.2) to the EOH at 2329 m, suggesting it extends to greater depths. Mineralization is hosted within the RDG or the felsic unit, or intermixed with breccia fragments of either lithology. It appears to occur preferentially along the brecciated and/or sheared (i.e., structure-controlled) contact between these lithologies where it displays features such as grading, sorting and preferential orientation of grains (Fig. 4.2 A). Discrete mineralized zones are typically several cm wide (up to 1 m) and disseminated throughout the adjacent host rocks, suggesting such zones have remained *in situ*, at least within their local environment. Mineral grain size in the magnetite-rich assemblages varies from ~0.1 to ~7 cm; coarser grains tend to be more abundant at greater depth (Fig. 4.2 B-E) and are present in almost every meter of core from ~2150 m to EOH.

Mineral assemblages remain the same, regardless of grainsize, and are dominated by magnetite (euhedral), pyrite (subrounded), fluorapatite (euhedral) and hematite (various habits) in a matrix of quartz, sericite and chlorite (Fig. 4.3).

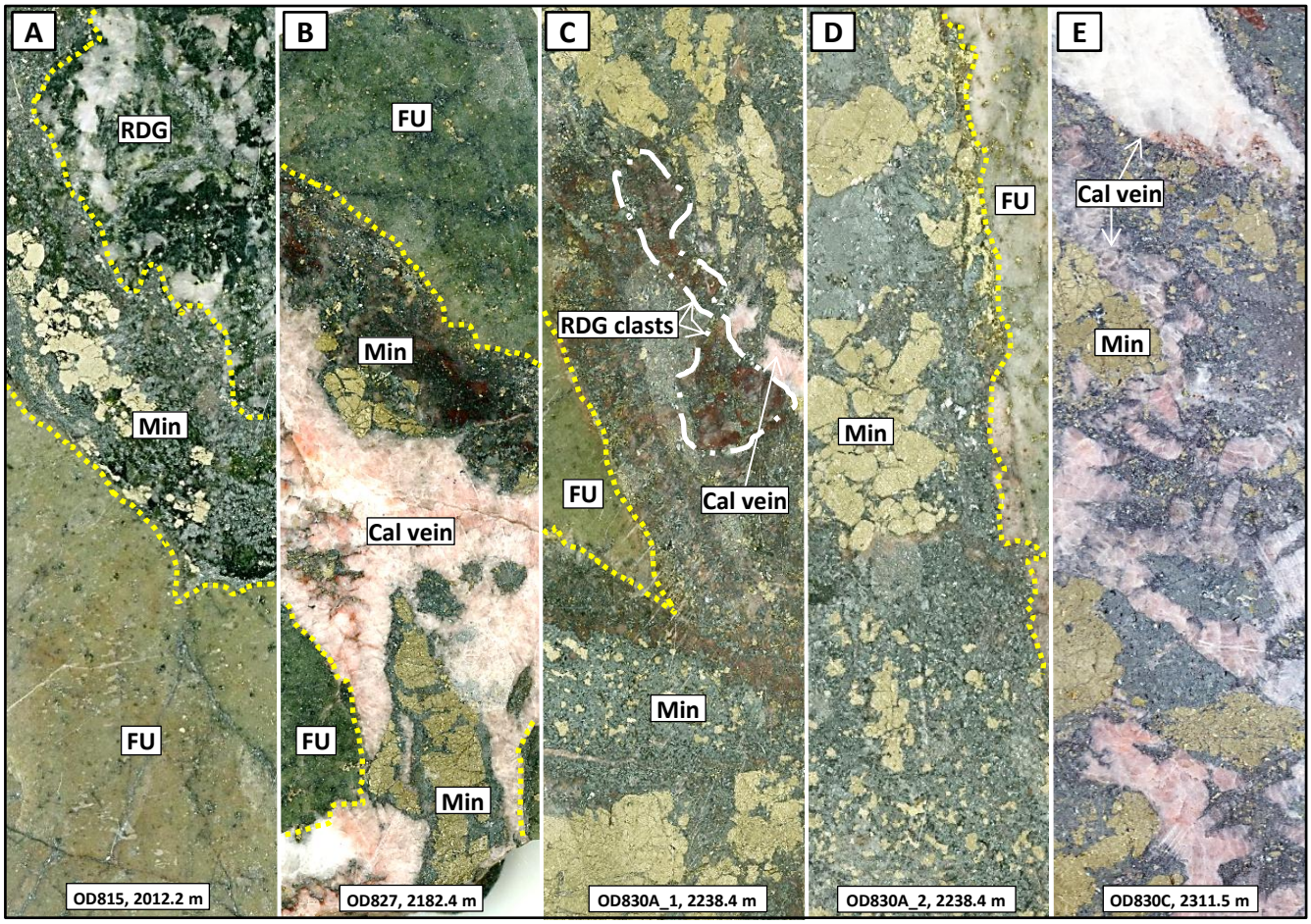

Fig. 4.2: (A-E) Representative ore textures arranged towards the increasing depth (images' width is ~2.5 cm). Fine- (B) and coarse- (C-D) grained mineralization (Min) occurs both on the contact of the RDG and felsic unit (FU) and intermixed with the two lithologies. Later calcite (Cal)-dominated veins crosscut the early mineralization. Microscopic images of the early mineralization are obtainable from Fig. 4.3.

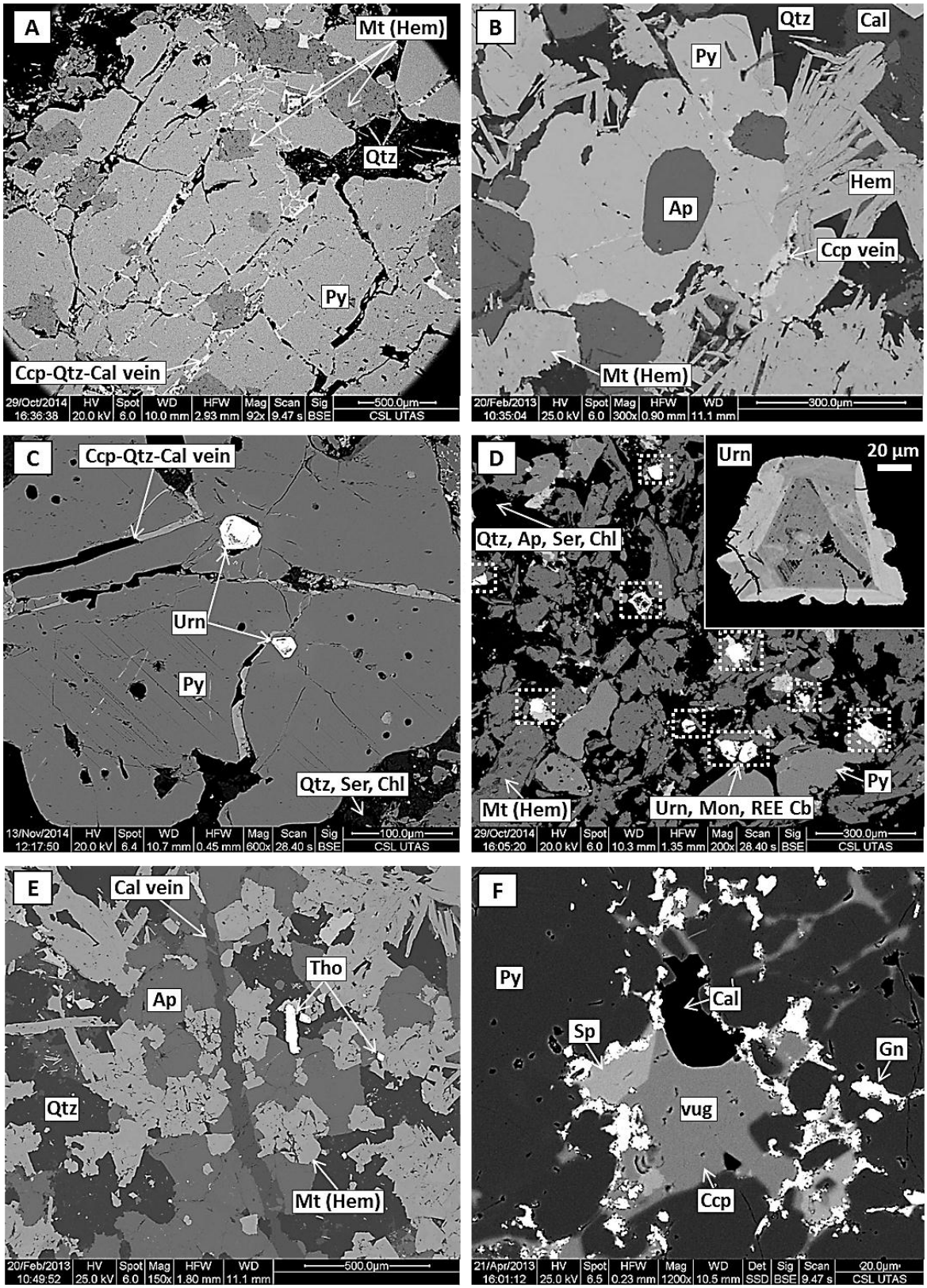

Fig. 4.3: Photomicrographs showing representative textures of the early mineralization. Pyrite (Py) often contains euhedral inclusions of magnetite (Mt, A), apatite (Ap, B) and uraninite (Urn, C) and is intimately intergrown with magnetite (largely converted to hematite, Hem, A-B, D-E), apatite (D, E), quartz (Qtz, A-E), sericite (Ser, C-D), chlorite (Chl, C-D), uraninite (D, close-up displays prominent core-rim zoning), thorite (Tho, E), monazite (Mon, D) and REE-fluorocarbonates (REE Cb, D). Late veins (A-C, E) and vugs (F) mainly composed of chalcopyrite (Ccp)-galena (Gn)-sphalerite (Sp)-calcite (Cal) are commonly localized within early pyrite.

Pyrite contains random or oriented mineral inclusions such as euhedral magnetite (Fig. 4.3 A), fluorapatite (Fig. 4.3 B), quartz and uraninite (Fig. 4.3 C), anhedral pyrrhotite (intergrown with chalcopyrite) and anhydrite. Uraninite also occurs abundantly as single euhedral grains up to 100 μm in size, being statistically larger than typical ~20 μm grains of uraninite in the Olympic Dam ore, (Ehrig et al., 2012), and are intimately intergrown with monazite and REE-fluorocarbonates (synchysite, bastnäsite, Fig. 4.3 D). BSE images commonly show variable major element compositions, expressed as BSE-dark, porous, usually metamict cores surrounded by BSE-bright rims (both discrete grains and inclusions in pyrite); some grains show oscillatory and sectoral zones (close up in Fig. 4.3 D). Magnetite (largely converted to hematite, Fig. 4.3 A-B, D-E) and fluorapatite contain abundant, subhedral thorite inclusions (up to ~200 μm in size, Fig. 4.3 E). Hematite is tabular in shape, zoned and twinned. Some hematite grains contain abundant disseminated, <3 μm small U-W-bearing inclusions. Several cm-size pockets or veins of anhydrite bearing above described mineralization occurs in a short interval from ~2035 to ~2040 m. Orange coloured, fine- to medium-grained anhydrite in this association takes the place of quartz, sericite, chlorite, and calcite as the main phase over this interval. The anhydrite contains abundant euhedral inclusions (usually ~10μm) of hematite, tourmaline and rutile.

The magnetite (reduced) assemblage experienced only minor brecciation and modification. However, the following features are indicative of overprinting of the magnetite-bearing assemblage: (1) numerous veins (~1 to several cm in width) containing abundant pink to locally white, coarse-grained calcite, with trace barite, fluorite and quartz (Fig. 4.2 B,C,E) are particularly abundant from ~2150 m (where mineralization becomes coarse-grained) to the EOH; (2) chalcopyrite and hematite rims on, and replacing, pyrite (Fig. 4.3); (3) veinlets, amygdales (localized in pyrite, Fig. 4.3 A-C, E-F) and cements with the assemblage chalcopyrite-galena-sphalerite-hematite-monazite-calcite-quartz-fluorite-REE-fluorocarbonate; (4) veinlets of sericite-chlorite-REE-fluorocarbonate which crosscut everything; (5) hematite forms pseudomorphs after magnetite; however, locally hematite pseudomorphs after magnetite are themselves replaced by magnetite (*'mushketovite'*); (6) replacements of uraninite by coffinite, brannerite, and REE-fluorocarbonates; (7) secondary (highly irregular) zoning in various minerals (e.g., fluorapatite, uraninite, hematite); (8) metasomatism-related monazite impregnation of some fluorapatite grains (see for comparison, Harlov, 2015; Krneta et al., 2015); and (9) replacement/overgrowth of hematite by a younger hematite generation.

4.5.2 Geochronology

The age of the felsic unit was determined by U-Pb dating of *zircon* on 72 grains from 5 samples and results show a wide range of ages from ~1540 to ~1620 Ma (Fig. 4.4 A, Table 4.2). Many of the grains have very high U and Th contents (>1000 ppm, some >10000 ppm; Th/U 0.09-33.27, mostly around 1), reflecting tiny inclusions of uraninite and/or thorite. A subset of 29 analyses (mostly from sample OD816), with U contents mostly <1000 ppm, yielded a cluster of concordant to near-concordant results which define an upper intercept age of 1591±11 Ma (95% CL, MSWD = 0.64, Fig. 4.4 A, Table 4.2). This result is taken as the magmatic emplacement age of the inferred rhyolitic precursor of the felsic unit.

The age of the magnetite-dominant mineralization in the felsic unit was determined using *in situ* U-Pb dating of hydrothermal fluorapatite, uraninite and hematite in a mineralized interval at 1998.1 m. Like the magmatic zircon, the *fluorapatite* results are heterogeneous (Fig. 4.4 B, Table 4.3). U contents vary from 7 to 1753 ppm (Th/U 0.03-1.18) and the U/Pb ratios scatter widely. However, a subset of 46 analyses with low common Pb contents and homogeneous U

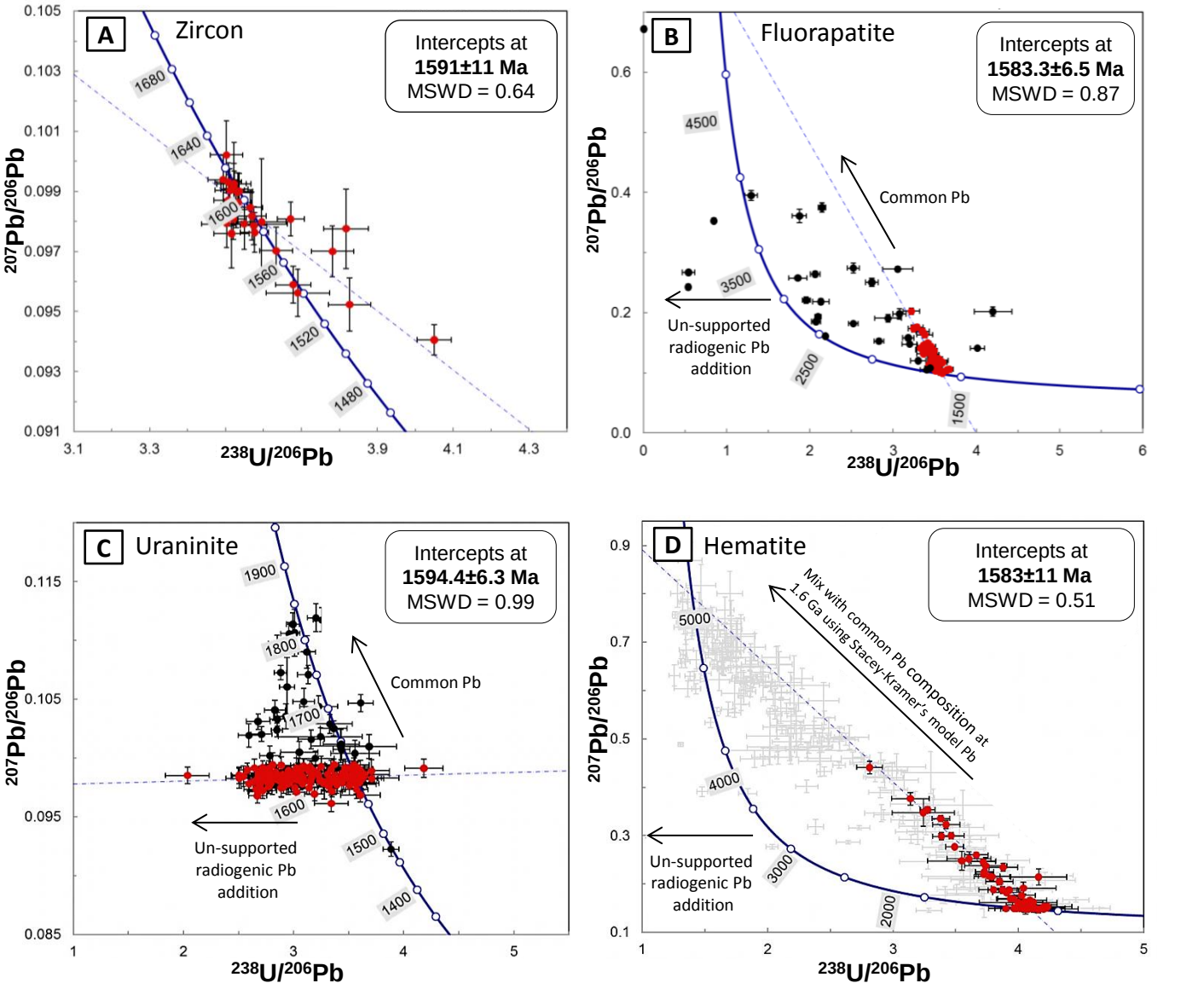

Fig. 4.4: Results of U-Pb dating (Tera-Wasserburg plots, all data-point error crosses are 1σ). A) The intercept age of magmatic zircon in the felsic unit is 1591±11 Ma. Fluorapatite (1583.3±6.5 Ma, intercept age, red points, B), uraninite (1594.4±6.3 Ma, intercept age, red points, C), and alteration-related hematite (1583±11 Ma, intercept age, red points with samples low common Pb, and spectrums indicative of closed system behavior, D) in the early mineralization revealed ages comparable with the felsic unit and the RDG.

concentrations around 40-50 ppm define a coherent trend (red data points in Fig. 4.4 B) which intersects concordia at 1583.3±6.5 Ma (MSWD = 0.87).

Spot analyses on *uraninites* from 4 samples (n = 182, Table 4.4) show concordant to strongly reversely discordant compositions. A subset of these analyses (n = 148, red) yielded a coherent trend of near-constant $^{207}Pb/^{206}Pb$ but variable $^{238}U/^{206}Pb$ (Fig. 4.4 C, Table 4.4), ranging from concordant to strongly reversely discordant, possibly due to U loss and/or redistribution of radiogenic Pb. An age of 1594.4±6.3 Ma (decay constant error used, MSWD = 0.99) was calculated from the intercept of this trend with the concordia.

Spot analyses of *hematite* show highly erratic U-Th concentrations and very low Th/U (Table 4.5). U/Pb data in a very large (>300 data points, not listed) data set covers the entire range from pure common to pure radiogenic Pb (Fig. 4.4 D), with considerable scatter. After rejecting all analyses with >50% common Pb and/or irregular ablation patterns, a set of 60 data points remains (Table 4.5) which plot along a mixing line (MSWD = 0.51) between 1.6 Ga common Pb and a 1583±11 Ma lower intercept. This result is interpreted to give the age of the hematite.

4.5.3 Sr-Nd isotopes

Rb-Sr isotope compositions of coarse-grained calcite from 8 veins within the felsic unit have similar Sr concentrations (84-166 ppm, Table 4.12) and very low Rb/Sr ($^{87}Rb/^{86}Sr$ = 0.001 to 0.052). Present-day $^{87}Sr/^{86}Sr$ varies from 0.71009 to 0.72321. Sm-Nd isotope data for 10 of these calcite samples are well-correlated in the isochron diagram, defining an apparent age of 1537±42 Ma (MSWD = 3.0, εNd_{1593} = -3.9), well within error of the other ages for the magnetite-dominant mineralization, for the felsic unit and for the age of the host RDG (e.g., 1593±5.6 Ma, Jagodzinski, 2014). The calcite Sm-Nd isotope data are collinear with those for anhydrite, the unmineralized felsic unit (Table 4.12) and with data for unaltered RDG (Johnson and McCulloch, 1995). The data for two subsamples of anhydrite from sample OD817 extend the range in Sm/Nd and fit on the same regression line (MSWD = 2.7), producing a more precise age of 1538±32 Ma (εNd_{1593} = -3.9). Data for two subsamples (OD820) of the *'felsic unit'* host rock also plot on this line and change the combined age to 1546±33 Ma (MSWD = 3.2, εNd_{1593} = -4.0). The large errors in these Sm-Nd isochron ages reflect the small dispersion and scatter of the data sets. Initial εNd_i in the felsic unit and the calcite veins (-3.1 to -4.2, Table 4.12) overlaps those in the host RDG (-3.7 to -5.3, n = 5, adjusted from Johnson and McCulloch, 1995; Creaser, 1995) and magnetite-rich mineralization (-4.9 to -4.0, Johnson and McCulloch, 1995). Initial $^{87}Sr/^{86}Sr_{1593}$ in the calcite samples (0.7101-0.7232) is surprisingly variable. The felsic unit is too differentiated (very high Rb/Sr, present-day $^{87}Sr/^{86}Sr$ >1, O. Apukhtina, unpubl. data) for a detailed comparison of initial $^{87}Sr/^{86}Sr$, but all calcites have higher initial $^{87}Sr/^{86}Sr$ than the host RDG at 1593 Ma (0.7084-0.7090, Creaser and Gray, 1992). This relationship suggests that the calcites maybe somewhat younger (by a few Ma to 10s of Ma) than their felsic unit host and the RDG; at that stage, fluids in equilibrium with the felsic unit would have access to mildly radiogenic Sr of the type found in the calcites, without noticeable effects on the Sm-Nd isotope systematics.

4.6 Discussion

Examination of several drillholes on the flanks of the ODBC led to the discovery of the early mineralization in RD2773 (Figs. 4.1 and 4.2). This mineralization is hosted by only weakly altered and mainly *in situ* brecciated RDG and

felsic unit. The mineralized interval is large (~1516 to 2329 m) and indicates extension of mineralization below the depth reached by the drillhole RD2773 (Fig. 4.1).

4.6.1 Timing of magnetite-dominant mineralization

U-Pb dating results on magmatic zircon (1591±11 Ma, Fig. 4.4 A) from the felsic unit overlap within analytical uncertainties with the age of the principal host rock at Olympic Dam (1588±4 Ma, Creaser, 1989; RDG, 1593.1±5.6 Ma, Jagodzinski, 2014). Ages for fluorapatite (1583.3±6.5 Ma, Fig. 4.4 B), uraninite (1594.4±6.3 Ma, Fig. 4.4 C) and alteration-related hematite (1583±11 Ma, Fig. 4.4 D) are comparable with the two host rocks. Moreover, crosscutting coarse-grained calcite veins (1537±42 Ma, Fig. 4.5) were clearly also formed in this early stage. Radiogenic isotope data for calcite suggest the RDG as the main Nd (Fig. 4.5) and Sr reservoir. Together with published geochronological data for ore minerals within the ODBC (hematite $^{207}Pb/^{206}Pb$ ages, 1590±8 and 1577±5 Ma, Ciobanu et al., 2013), the new age data for minerals and various lithologies present in the ODBC indicate a multistage event at ~1.6 Ga that influenced the deposit's ultimate morphology and buildup, and contributed to the overall metal budget.

4.6.2 Components of the early mineral association

The discovery of what appears to be intact magnetite-dominant mineralization formed at or close to the Hiltaba-GRV magmatic event at ~1593 Ma helps to clarify some important aspects of ore genesis at Olympic Dam. It also allows reassessment of various observations published since the discovery of the deposit in 1975. A major conclusion is that minerals such as magnetite, pyrite, fluorapatite, chlorite, quartz and uraninite are indeed part of the earliest IOCG paragenesis at Olympic Dam, as inferred in earlier petrographic studies (e.g., Reeve et al., 1990; Oreskes and Einaudi, 1990, 1992; Ehrig et al., 2012) on the basis of petrography but now we benefit of the direct and robust dating. The following points highlight some other important features and implications of the magnetite-dominant mineralization:

(1) The general style of the early mineralization is both massive and structure-controlled (Fig. 4.2). Early crosscutting calcite veins are stockwork-like in appearance.

(2) Magnetite, pyrite, fluorapatite, and quartz are the major minerals, and sericite, chlorite, chalcopyrite, uraninite, thorite, REE-minerals (monazite and REE-fluorocarbonates), calcite, barite, fluorite, anhydrite, tourmaline, rutile and pyrrhotite are minor minerals in the early magnetite-dominant mineralization (Figs. 4.2 and 4.3). We emphasize the presence of euhedral to subhedral uraninite (similar in its petrographic and geochemical characteristics to the primary uraninite described for other parts of the ODBC, Macmillian et al., 2015) and thorite, strongly associated with other early minerals, and thus defining the early assemblage as U-Th-REE-Fe-Cu-bearing.

(3) The replacement of hematite by magnetite (mushketovite) has not previously been reported from Olympic Dam.

(4) Magnetite and fluorapatite are important components of the early mineralization (Fig. 4.3 B,D,E). It is possible that its rarity in the ODBC reflects fluorapatite breakdown in this environment. This inference is consistent with the assertion of Ehrig et al. (2012) that the two minerals are more widespread both downwards and outwards in the deposit.

(5) Siderite is not observed in the magnetite-dominant mineralization in RD2773 whereas coarse-grained, generally unaltered vein of calcite is very abundant (Fig. 4.2 B,C,E). Elsewhere in the deposit, Fe carbonate is the dominant carbonate (e.g., it comprises ~88% of all carbonates in the ODBC matrix, Ehrig et al., 2012), it is abundant on the flanks of the ODBC and at depth (where it is associated with the early magnetite). Commonly observed replacement of siderite by hematite led to broadly accepted inference that siderite belonged to the earliest paragenesis, which was assigned an

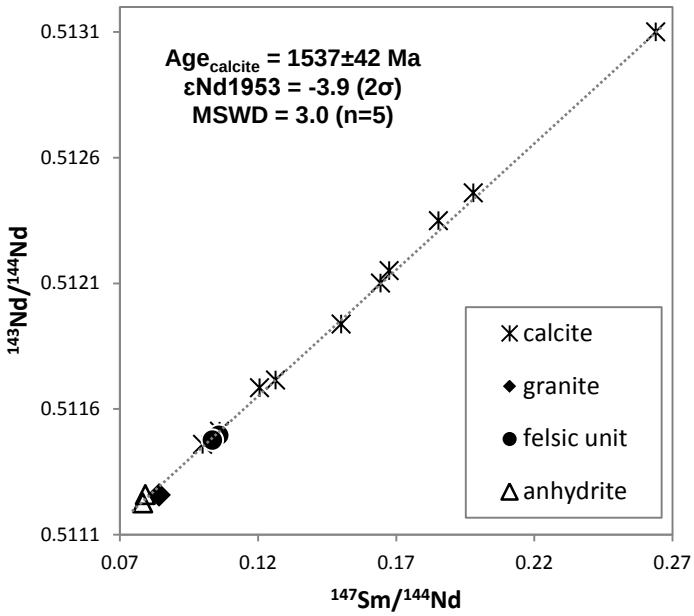

Fig. 4.5: Composition of radiogenic isotopes in calcite, RDG and felsic unit at ~1.59 Ga (Jagodzinski, 2014). A well-established isochron proves the formation of calcite at 1537±42 Ma (εNd_{1953} = -3.9, MSWD = 3.0). The avg. results for the fresh RDG (Johnson and McCulloch, 1995) fall well on the line, implying that the RDG represents the main reservoir for Nd in calcite.

age of ~1.4 Ga (e.g., Oreskes and Einaudi, 1990). However, the reported here ~1.6 Ga mineralization, unlike later paragenesis, is calcite-rich. This suggests that siderite may have formed at the expense of calcite, or has been precipitated later than calcite or both.

(6) Pyrrhotite was briefly mentioned in the mineralogical description in Ehrig et al. (2012). In the magnetite-dominant mineralization in RD2773, pyrrhotite is observed as anhedral micron-sized inclusions (intergrown with chalcopyrite) in many early pyrite grains. This relationship could indicate that pyrrhotite formed as a precursor-stage prior to pyrite and was overgrown and/or replaced by pyrite.

(7) The occurrence of the massive anhydrite associated with the fine-grained mineralization, and the presence of tourmaline and anhydrite inclusions within the early pyrite have not previously been reported from Olympic Dam. The origin of these minerals is enigmatic at this stage. Nevertheless, it implies that the early mineralizing fluid had to be saturated in B and SO_4.

4.6.3 Relationship with the ODBC

Magnetite-dominant ~1580-1590 Ma mineralization in RD2773 extends to > ~2.3 km depth below the surface, implying original formation before erosion at ~4-6 km depth, i.e. similar to estimates for IOCG systems generally (Hitzman et al., 1992). Similar magnetite-dominant mineralization may have extended to considerably shallower depths, possibly into the - now reworked - GRV successions which must have overlain the RDG (e.g., McPhie et al., 2011), but part of this has been eroded and the rest was reworked within the ODBC. In general, the *"upward extensions of IOCG deposits are even less known than their roots"* (Sillitoe, 2003).

Many textural features (mostly on a microscopic scale, Fig. 4.3) of the early magnetite-dominant mineralization are reminiscent of well-known large-scale textures within the ODBC. In particular, we note replacement of magnetite by hematite, pyrite by chalcopyrite, fluorapatite by monazite, and uraninite by coffinite, brannerite and REE-fluorocarbonates. As these mineral reactions tend to increase the grade of the Cu-U-REE-ore, the evolution of the Olympic Dam mineralization as a whole may have followed a path of progressive upgrading of the early stages of mineralization, and recycling of such early stages may have contributed to the contemporary metal budget. The evolution history (for over ~1 Ga) of Olympic Dam, which is not only an iron-oxide gold-copper but also a U, REE, CO_2, S, Ba, F anomaly (Ehrig et al., 2012), has been proven by numerous workers. Multistage events which effected Olympic Dam deposit include besides the early ~1.6 Ga events (age of the RGD, Jagodzinski, 2014; mafic-ultramafic rocks, Huang et al., 2015, 2016; felsic unit and the early mineralization, this chapter) also several other mineralization and rock formation stages at ~1.4 (minimum depositional age of the Pandurra Formation, Fanning, 2003; Kamenetsky et al., 2015), ~1.3 (Cu ore, McInnes et al., 2008; REE ore, Maas et al., 2011), ~1.3-1.1 (galena and pyrite mineralization, Meffre et al., 2010; carbonate formation, Maas et al., 2015), ~1.1 (sericite alteration of mafic-ultramafic rocks, Maas et al., in preparation a), ~0.8 (GDS-type dolerite, Huang et al., 2015; carbonate formation, Maas et al., 2015) and to ~0.5 Ga (massive barite-fluorite-carbonate-sulfide veins, Wawryk, 1989; Maas et al., 2011). Importantly, all new data for various minerals, with exception of the ~1.6 Ga event which is the focus of this study, are entirely in agreement with uraninite ages (interpreted as *"primary mineralization"* at ~1.40-1.35 Ga and younger generations at ~1.22, ~0.83, and ~0.57 Ga, Trueman, 1986; Johnson and McCulloch, 1995). The earlier studies (Trueman, 1986; Johnson, 1993) neither recorded the ~1.6 Ga age of the Olympic Dam uraninite nor found the correlation between the uraninite ages and

regional geological events known at that time. Overall, all above mentioned dates not only prove the multistage nature of the Olympic Dam deposit but also suggest involvement of numerous sources of metals and elements. This hampers researchers from the establishment of the exact genesis of the ODBC which remains unresolved to date.

4.6.4 Similarities with other IOCG deposits

Classification of diverse Cu-Au deposits within the IOCG family is based on features which imply a similar genetic history, particularly at the early stage (e.g., Hitzman et al., 1992; Williams et al., 2005; Groves et al., 2010; Barton, 2014). At Olympic Dam, early features are largely obliterated but the discovery of a pocket of well-preserved, syn- to early post-granite magnetite-dominant mineralization allows more detailed comparison with initial mineralization stages of other IOCG deposits. There are many parallels between this style of mineralization at Olympic Dam and early stages of other IOCG deposits: (1) host rocks of IOCG deposits (ranging in age from Archean to Mesozoic) are generally coeval with the primary phase of deposit formation (e.g., Hitzman et al., 1992; Sillitoe, 2003; Pollard, 2006); (2) the style of mineralization tend to be massive, structure-controlled vein stockworks and disseminated (e.g., Hitzman et al., 1992); (3) presence of a (generally magnetite-rich) iron-oxide nucleus with or without apatite (Hitzman et al., 1992; Williams et al., 2005; Groves et al., 2010; Barton, 2014); (4) the replacement of hematite by magnetite, mushketovite, was also reported at Candelaria deposit (Marschik and Fontboté, 2001); Oak Dam East deposit (Davidson et al., 2007), Titan prospect (Bastrakov et al., 2007); (5) the presence of minor pyrrhotite (e.g., Sillitoe, 2003; Skirrow et al., 2007; Groves et al., 2010); (6) the local occurrence of tourmaline has also been reported in IOCG deposits of the Coastal Cordillera (Sillitoe, 2003) as well as in the Olympic Dam province (Skirrow et al,, 2007); (7) abundant paragenetically late Fe-Cu sulfides (Groves et al., 2010); and (8) occurrence of massive calcite veins in deep parts of the deposit, similar to some IOCG deposits of Coastal Cordillera (Sillitoe, 2003).

In general Cu-poor but locally REE-enriched Kiruna-type magnetite-apatite deposits (e.g., Barton, 2014) which are sometimes called as IOA (Nystroem and Henriquez, 1994; Williams et al., 2005) ores, are considered one of the 6 end-members of the broad IOCG family (e.g., Groves et al., 2010). However, their origin and exact relationship to other IOCG remain contentious. Kiruna-type deposits are generally less brecciated than most other IOCG and are dominated by a well-developed magnetite-apatite paragenesis. Deposits with features that are transitional between Kiruna IOA and IOCG appear to be rare, with suggested examples among the deposits in the Coastal Cordillera (Sillitoe, 2003; Knipping et al., 2015). In the Olympic Cu-Au Province where the magnetite-apatite dominated Acropolis prospect was interpreted as a deeper level analogue of nearby Olympic Dam (Oreskes and Einaudi, 1992). Our study shows that the early mineralization in the lowest parts of Olympic Dam is indeed magnetite-apatite rich which underpins the assumption about the genetic relationship between the typical Kiruna-type assemblage possibly representing a deep root of the highly evolved *sensu stricto* IOCG systems.

4.7 Conclusions

The discovery and characterization (primary texture, mineral association and age) of deep, early (~1.59 Ga) mineralization on the edge of the Olympic Dam Cu-U-Au-Ag deposit is important for further genetic interpretations. The early paragenesis comprises minerals that are both nearly absent (magnetite, fluorapatite, calcite, thorite) and present (pyrite, chalcopyrite, hematite, uraninite, pyrite, monazite, REE-fluorocarbonates) within the strongly altered,

brecciated and mechanically intermixed ODBC. The coexistence of these Fe-, Cu-, U-, Th- and REE-bearing mineral phases, and inferred accumulation of these metals, can be viewed as the embryonic stage in the formation of Olympic Dam. U-Pb dating of fluorapatite, uraninite and hematite shows that the early mineralizing events were coeval or shortly after the crystallization of the host felsic at ~1.59 Ga. We consider that the post ~1.59 Ga events have led to recycling and upgrading of the early minerals and, therefore, contributed to the budget and distribution of metals in the deposit, as seen today.

Chapter 5: Carbonates at the supergiant Olympic Dam deposit. Part II: Carbonate distribution, textures, associations and stable isotopes (C, O) at the supergiant Olympic Dam deposit

5.1 Introduction

The Olympic Dam IOCG deposit in South Australia is one of the largest known ore deposits, with metal contents of 78 Mt of Cu, 95 million ounces of Au and 2.1 Mt of U (Ehrig et al., 2012). Mineralization is hosted almost entirely within a complex, polyphase breccia, ODBC, and is dominated by Fe-oxides (dominantly hematite), Cu-(Fe) sulfides, fluorite, barite, quartz and carbonates (e.g., Reeve et al., 1990; Ehrig et al., 2012). Primary paragenetic relationships have been strongly disrupted by repeated brecciation and multiple alteration events (e.g., Oreskes and Einaudi, 1990, 1992; Ehrig et al., 2012), complicating the development of genetic models. An initial interpretation as a strata-bound sediment-hosted mineralization (Roberts and Hudson, 1983) was superseded by magmatic-hydrothermal model involving phreatomagmatic driven hydrothermal activity (maar crater model, Reeve et al., 1990), with possible mixing of reduced magmatic fluids with colder and oxidized fluids of meteoric origin (Oreskes and Einaudi, 1990, 1992; Haynes et al., 1995).

Assaying of core samples drilled prior to 1997 for total carbon (reported as carbonate), combined with new drillcore data obtained from the 2003-2008 drilling program (Ehrig et al., 2012), revealed that carbonates comprise of a significant, previously underestimated component of the ODBC. It is now known that carbonates, ranging from Ca-Mg-Fe-Mn-dominant to REE-F-enriched in composition, are among the principal gangue minerals (Ehrig et al., 2012). They are present in parageneses across almost all known stages of ore deposition and are thus likely to preserve information on the compositions of carbonate-depositing fluids, their sources, and the timing of mineral deposition. Existing published data on Olympic Dam carbonates is limited and includes semi-quantitative compositions of Ca-Mg-Fe-Mn carbonates (Ehrig et al., 2012), fluid inclusion and stable (C, O) isotope compositions for siderite (Oreskes and Einaudi, 1992), and petrographic and compositional data for REE-fluorocarbonates (e.g., bastnäsite and synchysite, Lottermoser, 1995; Maas et al., 2011; Diemar, 2014). Here we provide a comprehensive documentation of Olympic Dam carbonates, including their overall distribution, paragenetic relations, petrography and geochemistry (major element compositions, C-O isotopes). This study complements ongoing work on Olympic Dam ore minerals (e.g., Cu sulfides, Cook et al., 2015; uraninite, Macmillian et al., 2015), and provides a basis for further studies of Olympic Dam. Many other IOCG deposits in Australia (e.g., Prominent Hill, Belperio et al., 2007; Hillside, Ismail et al., 2014; Conor et al., 2010; Ernest Henry, Marshall et al., 2006; Great Australia, Cannell and Davidson, 1998) and deposits in the IOCG spectrum elsewhere (e.g., Wernecke Breccias in Canada, Hunt et al., 2007; Alvo 118, Torresi et al., 2012; Sossego in Brazil, Monteiro et al., 2008; Rakkurijärvi, Smith et al., 2007; Kiruna, Hitzman et al., 1992 in Sweden) also contain significant carbonates, yet these are sparsely described in the accessible literature. Documentation of carbonates at Olympic Dam, a type example of the IOCG clan (Meyer, 1988; Hauck, 1990; Hitzman et al., 1992), would therefore also benefit future studies of other IOCG deposits.

5.2 Geology of the Olympic Dam deposit

Olympic Dam is located in the NE part of the Gawler craton. Basement comprises late Archean gneisses, Paleoproterozoic metasediments (including metacarbonates and BIFs) and granitoids, and a Mesoproterozoic magmatic succession. The Mesoproterozoic succession is represented by the ~1.6 Ga Gawler SLIP, comprising lavas (GRV) and granite intrusions (Hiltaba Suite) (e.g., Giles, 1988; Creaser and Cooper, 1993; Allen and McPhie, 2002; Ehrig et al., 2012). The latter includes the RDG, the principal host rock for the mineralized breccia complex. Other non-granitic lithologies such as bedded clastic facies rocks (up to ~350 m thick), local conglomerate-breccia-sandstone unit, mafic dykes, picrite lavas, and rhyolitic rock (temporally related to the granite intrusion, *'felsic unit'* in Apukhtina et al., in preparation a; Ehrig et al., 2012) are locally abundant.

The ODBC is 6 x 8 km in plan (Reeve et al., 1990) and typically extends to ~800 m, and locally to more than 1.5 - 2.3 km (Ehrig et al., 2012; Apukhtina et al., in preparation a). The shape and internal structure of the complex is thought to be controlled by five major sets of faults, and both the intensity of brecciation and host rock alteration increase towards the center of the breccia complex (Ehrig et al., 2012). A large number of dolerite dykes, identified as equivalents of the ~0.8 Ga GDS (Zhao and McCulloch, 1993; Wingate et al., 1998; Huang et al., 2015), intruded the breccia complex along NW-striking structures (e.g., Sugden and Cross, 1991; Ehrig et al., 2012). The breccia complex is unconformably overlain by a ~320 m of unmineralized, flat-lying Proterozoic to Lower Cambrian sediments of the Stuart Shelf. At Olympic Dam, the Stuart Shelf sequence is represented by thin discontinuous dolomites which show similarities with the Nuccaleena Dolomite (an Ediacaran cap dolomite in the nearby Flinders Ranges, ~636 Ma, Calver et al., 2013) and by the overlying Tregolana Shale (676±200 Ma, samples coming from Woomera bore, Webb et al., 1983; Preiss, 1987; Reeve et al., 1990).

5.3 Mineralogical zoning patterns

Although most primary features of the mineralization have been overprinted by texturally, mineralogically and chemically destructive alteration and mechanical intermixing, some broad geochemical-mineralogical zonation features have been recognized. From the margins of the breccia complex inwards, granitic host rock is progressively altered to produce a deposit-wide orthoclase-sericite-hematite zoning. Remnants of early, reduced mineral assemblage, with magnetite, siderite, apatite, quartz and chlorite, occur at the margins and in the deepest parts of the deposit (Ehrig et al., 2012; Apukhtina et al., in preparation a). Correlated with this early assemblage are some of the most Cu-U-rich zones (Fig. 5.1) which appear to trace out a bowl-like shape (Ehrig et al., 2012). Perhaps the best-known zonation pattern at Olympic Dam is the margin-to-center and depth-to-top sequence of pyrite, chalcopyrite, bornite and chalcocite described originally in Roberts and Hudson (1983) and later by Oreskes and Einaudi (1992) and Ehrig et al. (2012). Positively correlated ore components such as Cu (chalcopyrite is the most abundant Cu sulfide), U_3O_8 (coffinite is the most abundant U mineral), and Au (Au-Ag-bearing electrum and tellurides) occur dominantly as μm-small scale inclusions mainly in hematite and sulfides in the hematite-rich breccias (Fe > 20 wt%); however, not all hematite breccias are mineralized. Besides the metals recovered from the existing operations (Cu, U, Au and Ag), the deposit is an anomaly for a large suite of other elements (e.g., F, S, C, As, Ba, Bi, Cd, Co, Cr, Fe, In, Mo, Nb, Ni, P, Pb, Se, Sn, Sr, Te, V, W, Y, Zn, REE, Ehrig et al., 2012). Overall mineral relationships are highly complex and there is solid evidence that almost every ore and associated gangue mineral has gone through a number of precipitation and

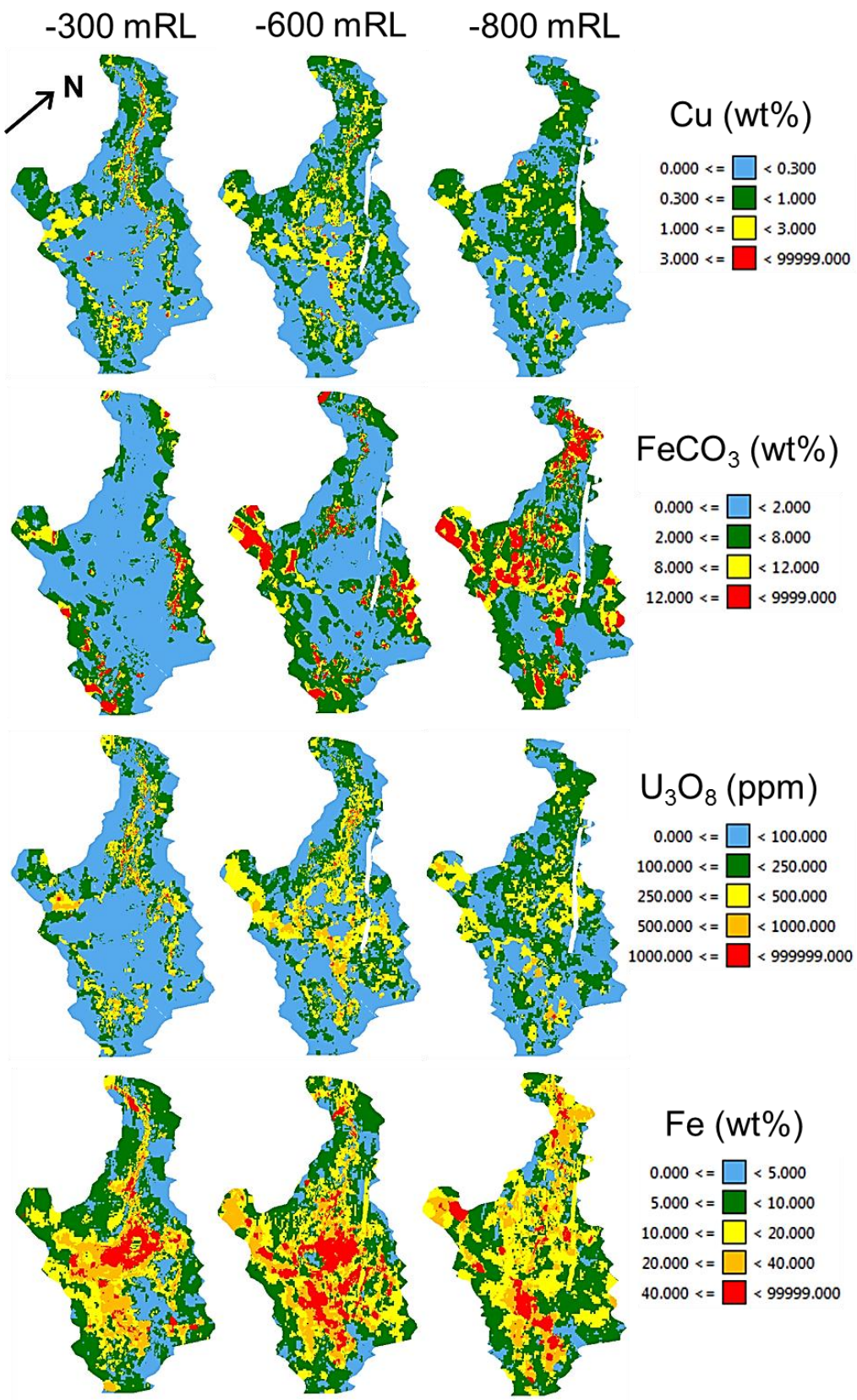

Fig. 5.1: Resource maps for Cu, $FeCO_3$, U_3O_8 and Fe in the Olympic Dam deposit for depths -300, -600 and -800 mRL. Legends (warm colours mean high abundance) are on the right side. Maps provided by K. Ehrig.

dissolution events during the evolution of the deposit (e.g., Cu minerals, Cook et al., 2015; hematite, Ciobanu et al., 2013 and 2015; pyrite, gold, Ehrig et al., 2012; uraninite, Macmillian et al., 2015; REE-fluorocarbonates, Maas et al., 2011; Diemar, 2014).

The center of the breccia complex shows the highest intensity of brecciation and Fe alteration and is dominated by largely unmineralized hematite±quartz-barite assemblage. It is assumed that the core represents a major block of sediments which has been deposited in a fault-controlled environment (McPhie et al., 2011; 2016). Swarms of barite-fluorite-dominated veins (with traces of various carbonates and sulfides) crosscut the deposit. There is a large-scale carbonate to fluorite-barite (margin-to-center) zonation within the breccia complex (see Fig. 15 in Ehrig et al., 2012) which is not related to the swarms of barite-fluorite veins. Sm-Nd dating (Wawryk, 1989; Maas et al., 2011, in preparation a; Diemar, 2014) indicates a ~0.5 Ga age for these structurally late hydrothermal veins.

5.4 Carbonate mineralogy

Siderite is the most abundant carbonate mineral at Olympic Dam, comprising ~88% of total carbonates (based on modal mineralogy of the 10,000-sample MLA data set, Ehrig et al., 2012). It occurs in breccia clasts, in the breccia matrix and in veins, either by itself or together with fluorite and barite. None of these three gangue minerals appears to replace any other hydrothermal mineral. Far less abundant than siderite are Ca-Mg-Fe-Mn-dominated carbonates (calcite, dolomite, ankerite, siderite, and solid solutions of dolomite-ankerite and siderite-rhodochrosite-magnesite) which occur predominantly near mafic dykes (Ehrig et al., 2012). The bulk of the light rare earth elements (LREE) at Olympic Dam is hosted in the carbonates bastnäsite [$(Ce,La)(CO_3)F$], the most abundant REE mineral in the deposit, and synchysite [$Ca(Ce,La)(CO_3)_2F$] which together comprise ~3% of total carbonates and occur jointly or separately in a number of associations (Oreskes and Einaudi, 1990; Lottermoser, 1995; Ehrig et al., 2012; Diemar, 2014).

Based on a wealth of company core logging and our own observations, carbonates at Olympic Dam can be assigned to 7 distinct associations (Tables 1 and 2): (1) coarse-grained calcite veins in weakly-brecciated granite and rhyolite; (2) carbonates in strongly brecciated granite; (3) carbonate veins in bedded sediments; (4) carbonates in mafic and ultramafic igneous rocks; (5) massive barite-fluorite-dominated veins (with minor carbonate); (6) laminated siderite; and (7) carbonate matrix in a conglomerate and sandstone. Carbonates in strongly brecciated granite represent by far the most voluminous and texturally multifaceted group with the Fe-rich carbonate being the dominant carbonate phase. Other groups comprise locally abundant carbonates of mostly highly variable compositions. A representative set of 197 samples (from 54 drill holes and 5 locations in underground exposures, Table 5.1) was selected for study, sample locations are shown in Fig. 5.2. Note that one sample has been collected in the Snake Gully IOCG prospect located nearby the Olympic Dam deposit.

5.5 Analytical methods

Polished thin sections and epoxy mounts for each sample were examined with an Olympus BX60 petrographic microscope and imaged with an EDS (FEI Quanta 600) CSL, UTas. Carbonate major element compositions (Table 5.3) were obtained with a Cameca SX100 electron microprobe at the CSL, using a 15 kV accelerating voltage, 10 nA beam current and 10 µm beam diameter. Clinopyroxene (Ca, Si), dolomite (Mg), hematite (Fe) and bustamite (Mn) were used as standards.

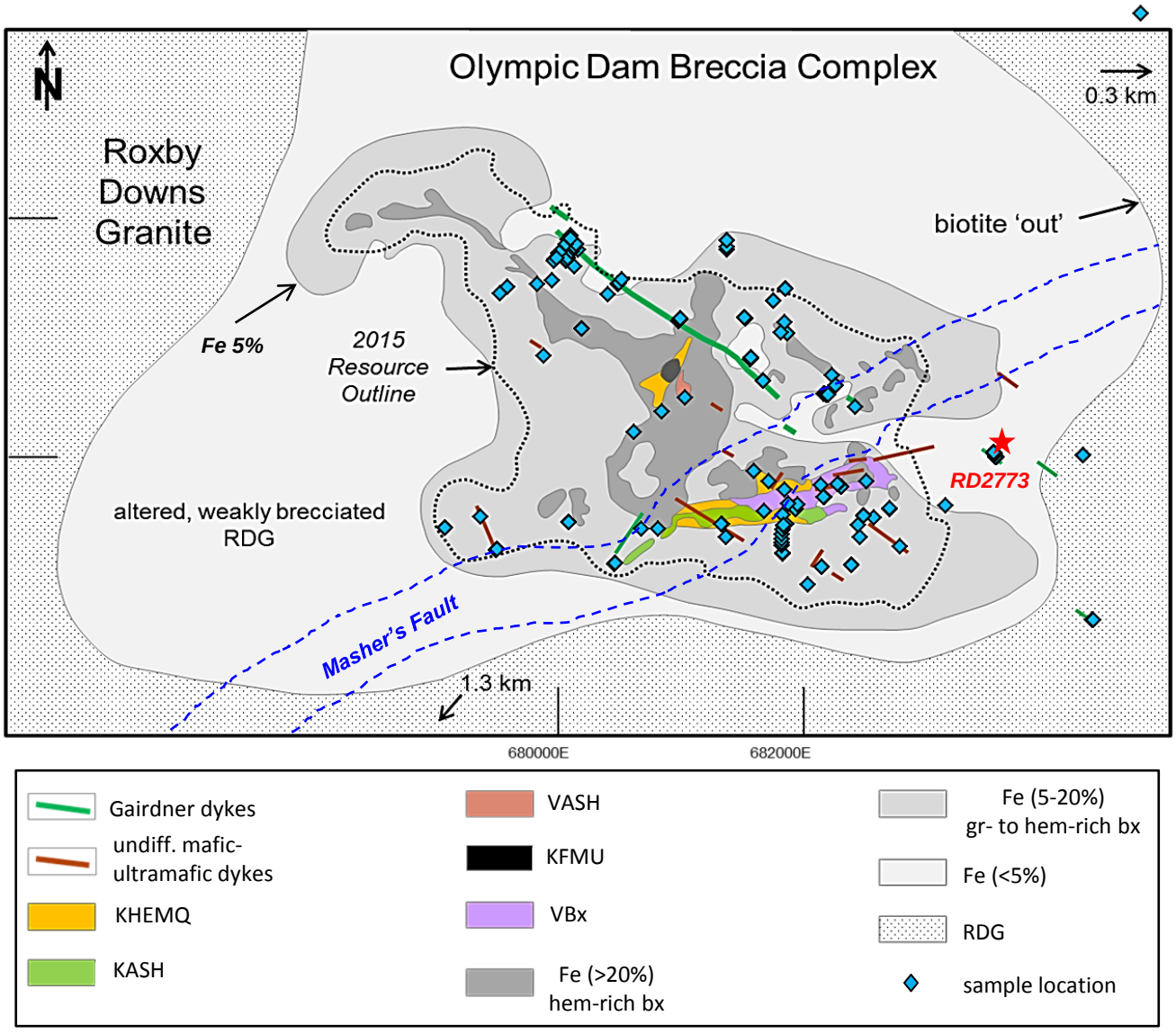

Fig. 5.2: Map with location of samples (blue diamonds), projected at the -350 mRL level. Note boundaries between the breccia complex (marked by biotite 'out' zone), 5% Fe limit, resource outline and position of the deepest diamond drillhole (RD2773) within the breccia complex. Map modified after Ehrig et al. (2012). Position of the undifferentiated mafic-ultramafic (blue) and Gairdner (green) dykes and lavas obtained from Apukhtina et al. (2015). Lithological units: chlorite-bearing, laminated sandstone and mudstone (KASH), well-bedded, hematite-rich sandstone, mudstone, and conglomerate-breccia (KHEMQ), thinly laminated, very hematite-rich mudstones (VASH), polymictic volcanic conglomerate (KFMU), hematite-rich breccias consisting of porphyritic felsic volcanic clasts (VBx).

High-purity carbonate separates for stable isotope (C, O) analysis, typically 7 to 20 mg were pretreated with hypochlorite to remove organic material and weighed into a reaction tube. After digestion in 100% H_3PO_4 (50˚C, 24h), the resulting CO_2 gas was purified using cold traps and measured on VG Optima stable isotope mass spectrometer at CSL. Within-run precision for $\delta^{13}C$ and $\delta^{18}O$ was better than ±0.045‰. NBS19 limestone, NBS18 carbonatite and two calcite standards (ANU-M1, ANU-PRM2) were used for corrections. Acid fractionation factors for digestion at 50˚C (Kim et al., 2007) were chosen based on the dominant carbonate type within each sample. Duplicate measurements were made for 84 of 86 samples. The results in Tables 5.2 and 5.4 are reported relative to V-PDB ($\delta^{13}C$) and V-SMOW ($\delta^{18}O$).

5.6 Results

5.6.1 Sample description and classification

The distribution, parageneses and compositions of carbonates at Olympic Dam are highly variable. Host rocks include weakly brecciated granite, fine-grained breccia, bedded clastic sediments, conglomerate-breccia-sandstone unit, mafic to ultramafic rocks, and a conspicuous unit of strongly altered, possibly rhyolitic rocks. Carbonates occur in breccia and conglomerate-sandstone matrix, breccia clasts, as veins crosscutting ore-rich breccia and various rocks, as amygdale fillings, as massive laminated blocks and as oolites (see simplified schematic drawing in Fig. 5.3). In each of these settings, carbonates are associated with a wide range of different gangue, ore and accessory minerals. Carbonate textures also vary considerably (simple to oscillatory growth zoning, mutual replacements between carbonates and hematite), as does the chemical compositions of each carbonate mineral species. Because of this heterogeneity, it has proven difficult to establish a consistent, deposit-wide paragenetic mineral sequence. Instead, carbonates were assigned to 7 broad associations (Table 5.2) which can, in some cases, be subdivided further. These associations are:

5.6.1.1 Coarse-grained calcite veins in weakly-brecciated granite and rhyolite

Pink to white, coarse-grained, unbrecciated and unaltered calcite veins (Fig. 5.4 A) crosscut texturally early magnetite-pyrite-apatite-quartz-uraninite-dominant mineralization (Fig. 5.4 A-C) near the lower margin of the breccia complex. This assemblage produced U-Pb ages in the range ~1590-1570 Ma and indicates it is a rare remnant of very early (embryonic?) Kiruna-type magnetite-apatite mineralization at Olympic Dam (Apukhtina et al., in preparation a). The calcite veins (up to 5 cm wide) are abundant in a ~180 m interval near the end of a very deep drillhole (RD2773) where they cut the RDG and a rhyolitic unit which have been brecciated *in situ* and show mainly chlorite-sericite alteration. The calcite veins locally carry barite, fluorite, quartz, hematite, synchysite and sulfides (galena, chalcopyrite, and pyrite; ~1 vol.%).

5.6.1.2 Carbonates in strongly-brecciated granite

Coarse- to fine-grained granite-dominant breccias constitute the most important host of carbonates; they contain ~88% of all carbonates (Ehrig et al., 2012). Most of the textural and mineralogical heterogeneity mentioned above is encountered within this association. Carbonates occur in the breccia matrix/cement (Fig. 5.5 A-C), in breccia clasts (Fig. 5.5 D-F), within amygdales (Fig. 5.5 G-I), and as carbonate-bearing oolites (Fig. 5.5 J-L), in order of decreasing abundance. Siderite is by far the most abundant carbonate mineral in this association. In drillcore, siderite-dominated breccia is dark brown in colour (Fig. 5.5 A) and relatively soft, compared to hematite-rich breccia (black, harder).

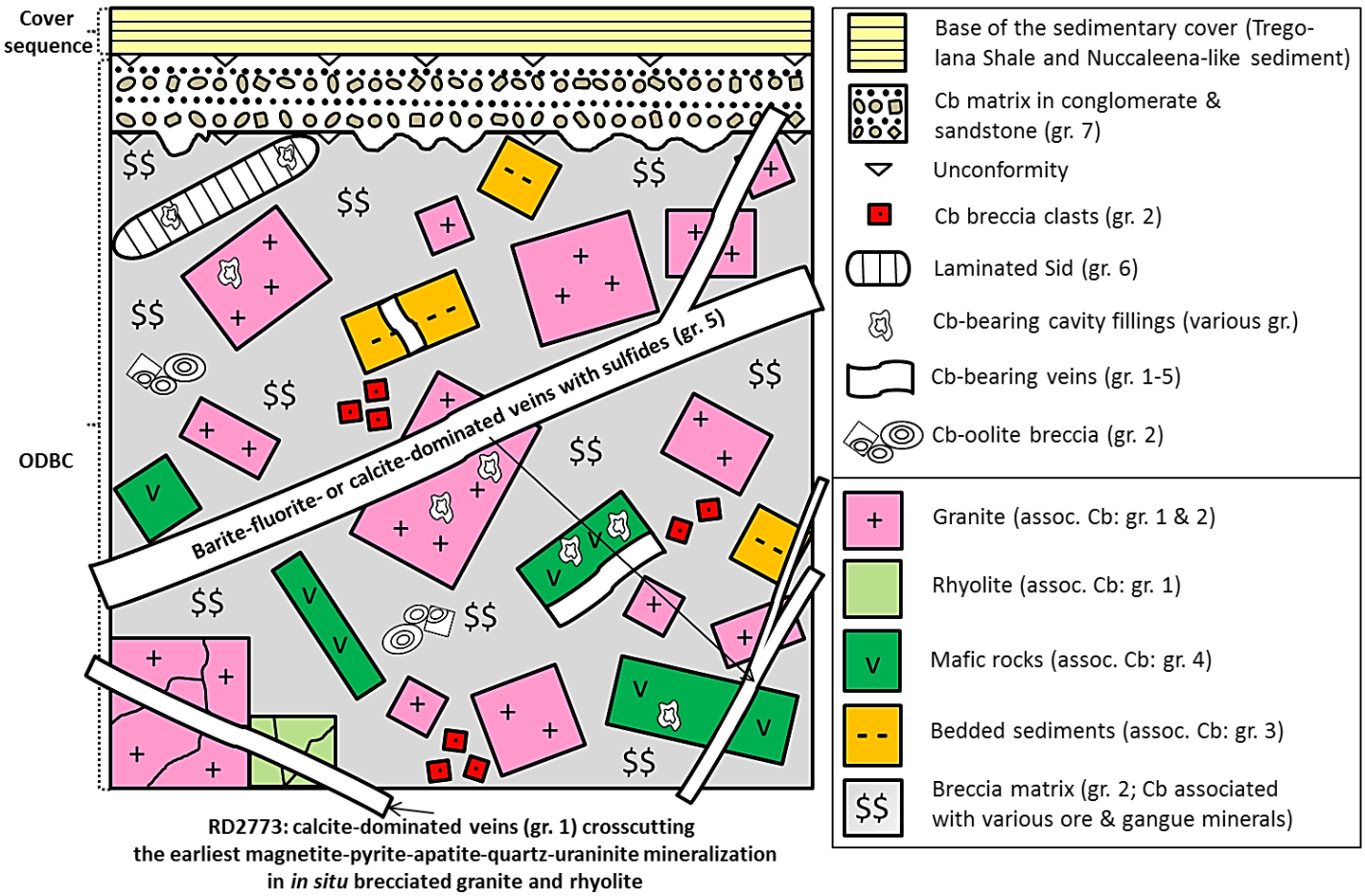

Fig. 5.3: Schematic composite of diverse carbonate (Cb) occurrences within the ODBC. Scale of units is exaggerated. Carbonate veins are hosted by various lithologies (granite, fine-grained breccia, mafic-ultramafic rocks and bedded sediments). Among these, deep early calcite veins (RD2773), late-stage veins (barite-fluorite- or carbonate-dominated, both are usually sulfide-carrying) and blocks of laminated siderite are not brecciated. The number of the appropriate group is marked in brackets. Gr.: group, Sid: siderite.

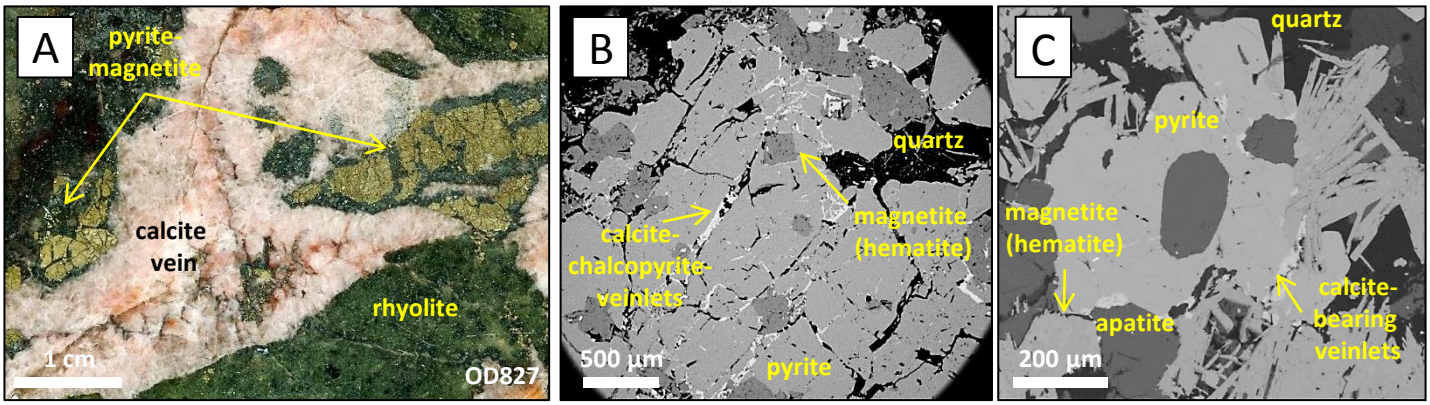

Fig. 5.4: Group 1 carbonates. (A) Massive pink calcite veins crosscutting early stage pyrite-magnetite (largely converted to hematite)-apatite-quartz-uraninite paragenesis (A-C) hosted by the granite and rhyolite (felsic unit). (B-C) Later calcite-sulfide-quartz-barite-fluorite veinlets are often localized in pyrite (BSE images).

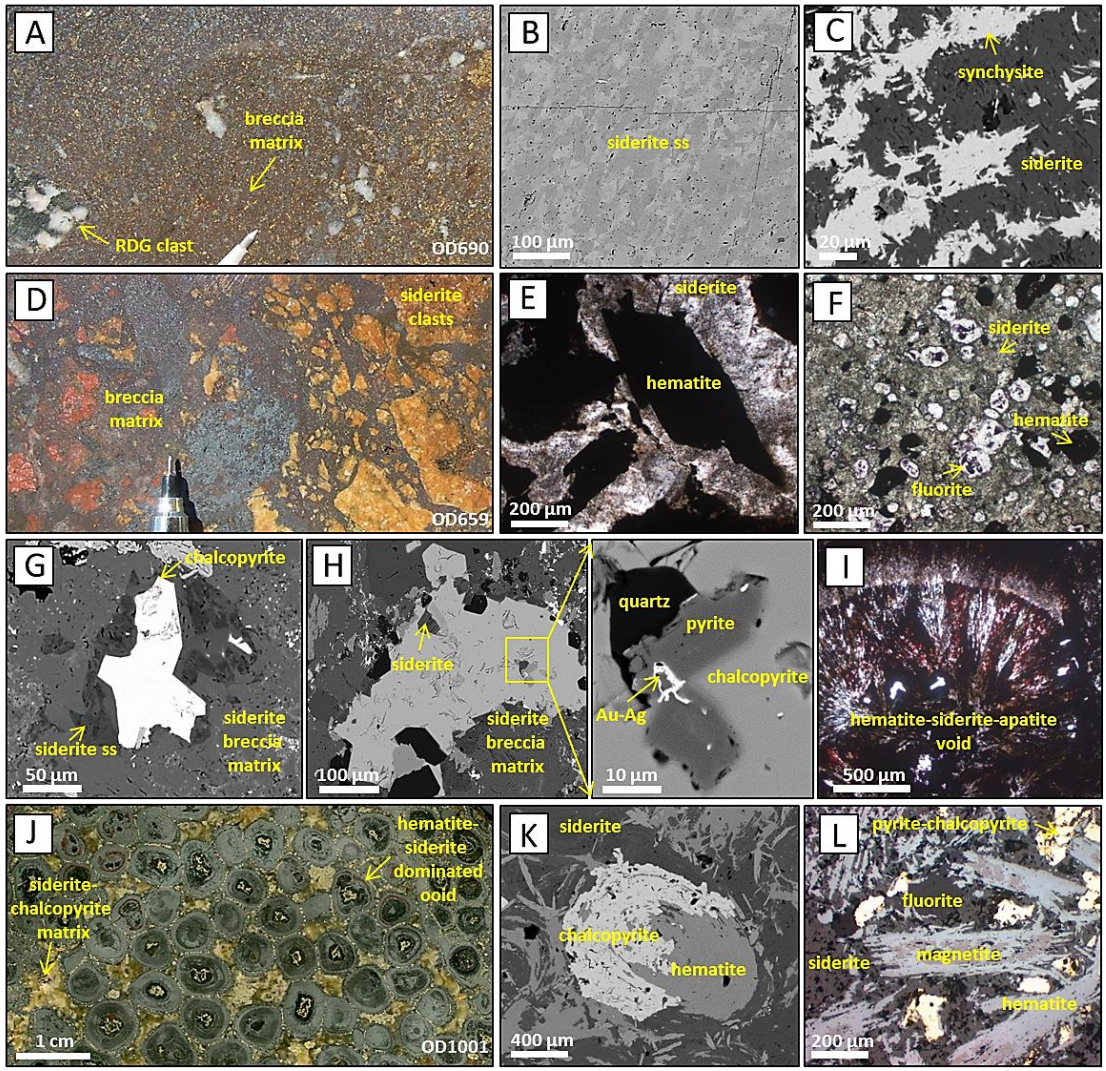

Fig. 5.5: Group 2 carbonates. Carbonate-dominated dark brown breccia matrix (A), commonly show patchy zoning and increased porosity (B), and may contain abundant REE-fluorocarbonates (synchysite, C). Light brown, carbonate-dominated breccia clasts (D) often bear hematite relicts (E), and fine-grained fluorite (F). (G-I) Late stage carbonate-bearing amygdales show a variety of associations. (J-L) Oolites mainly composed of siderite and hematite (J), whereas sulfides (e.g., chalcopyrite) usually replace single ooids (K); mushketovite (magnetite pseudomorph after hematite, L) is a common feature of such rocks. BSE images: B, C, G, H, K; TL images (//P): E, F, I; RL image (//P): L.

Within-grain siderite textures can be complex. Siderites varying in composition between almost pure and Mn-Mg-rich are observed to replace (Fig. 5.5 B) and overgrow (Fig. 5.5 G) each other, and they are the components in simple to oscillatory zoning patterns. With increased alteration particularly towards the center and shallower parts of the breccia complex (where bornite, chalcocite and hematite become highly abundant) growth zoning in siderite becomes patchy and porosity develops (Fig. 5.5 B).

Siderite-bearing breccia matrix carries many relicts of earlier minerals, such as magnetite and siderite which have been partially converted to hematite (sometimes comprising μm-small U-Mo-W-Sn-bearing inclusions, this work and Ciobanu et al., 2013), and pyrite (with apatite inclusions) which has been converted to chalcopyrite. Sometimes, siderite appears to be cogenetic with, or replaces hematite, illustrating its multistage nature. Within siderite-bearing breccia matrix, blebs consisting of barite, quartz, fluorite, diverse sulfides (chalcopyrite, following by rare associations with galena, sphalerite, Co-Fe-As sulfides, fahlore, bornite and chalcocite), diverse Bi-Ag-Au-Pb-Te-Se alloys (often as inclusions in chalcopyrite), U-Th-REE bearing minerals (monazite, florencite and REE-fluorocarbonates, Fig. 5.5 C), sericite and chlorite are common and are considered mostly as late-stage. Disseminated specks of REE-fluorocarbonates, mostly bastnäsite which often replaces or overgrows Ca-dominated synchysite, occur in 50% of all studied siderite-bearing breccia matrix samples.

Siderite-rich breccia clasts, often with associated carbonate vein fragments, can reach several centimetres in size, are recognised by their brown colour, have strongly variable within-clast grainsize and usually occur within a siderite-dominated matrix (Fig. 5.5 D). Siderite within clasts is sometimes cut by Mg-Mn-rich siderite veinlets and can replace (Fig. 5.5 E), or is itself replaced by hematite. Other common minerals in siderite-rich breccia clasts are finely disseminated fluorite (Fig. 5.5 F), barite, quartz, chalcopyrite, and less frequently pyrite, sphalerite, galena, uraninite, coffinite, brannerite, monazite, and REE-fluorocarbonates.

Strongly brecciated granite also contains numerous microscopic amygdales (Fig. 5.5 G-I). Amygdale infill minerals often include carbonates as well as minerals typical of association 5 described below. In rare cases, amygdales filled with a radiate-textured hematite-siderite-apatite assemblage are observed (Fig. 5.5 I).

Carbonate-bearing oolites and (where constituent ooids are coarse-grained, up to 2 cm in diameter) pisoliths (first briefly described by Roberts and Hudson, 1983) occasionally occur within the breccia and where only slightly to not brecciated, they are typically ooid-supported (Fig. 5.5 J). Contacts between adjacent ooids locally show signs of plastic deformation (Fig. 5.5 J). Such examples are usually weakly brecciated and variably altered. The primary concentric banding of individual ooids reflects variable modal proportions of hematite and siderite in alternating bands. The cores of many ooids contain texturally distinct siderite-hematite, with numerous other minor minerals. These include pyrite (with inclusions of pyrrhotite and magnetite), chalcopyrite (Fig. 5.5 K), mushketovite (pseudomorph replacement of hematite by magnetite, Fig. 5.5 L, Ramdohr, 1950) and uraninite. At shallow depths within the deposit, such secondary sulfide assemblages in siderite-hematite oolites and pisolites are themselves partially replaced by bornite, chalcocite, Co sulfides and hematite. Many individual ooids in oolite clasts contain abundant veinlets which contain mineral assemblages similar to those in their host, plus barite, quartz and notronite (?). The oolites are thought to have been present at the time of the earliest IOCG-type mineralization at Olympic Dam (Apukhtina et al., in preparation a).

5.6.1.3 Carbonate veins in bedded sediments

Bedded clastic sediments (e.g., McPhie et al., 2011, 2016) are one of the more conspicuous non-granite clast types within the breccia complex. Many of these sediment clasts contain carbonate veins (typically ~1 cm thick), in particular the green (sericite- and chlorite-rich, Fig. 5.6 A-B) and red (hematite loaded, Fig. 5.6 C-D) varieties. The bedded sediments are usually well-sorted, often show soft-sediment deformation features, and are faulted and *in situ* brecciated on a cm-scale. Green bedded sediment clasts can carry secondary pyrite, chalcopyrite and galena, while red bedded sediment clasts may contain abundant bornite and chalcocite arranged parallel to bedding. The carbonate veins are mostly dolomite-ankerite solid solution, with μm-scale inclusions of calcite and Fe-rich carbonates. Other gangue minerals (typically with internal zoning) are barite, fluorite, quartz, hematite and anhydrite (the latter appears only in green sediments). Sulfide minerals within the carbonate veins mirror those of their host sediments (Fig. 5.6 B,D); carbonate veins in red bedded sediment clasts can additionally carry some fahlore.

5.6.1.4 Carbonates in mafic to ultramafic igneous rocks

Igneous rocks such as olivine-phyric (picritic) lavas (Fig. 5.7 A), basalts (locally with chilled margins and related recrystallization features, Fig. 5.7 B), and dolerite (Fig. 5.7 C) show diverse types and degrees of alteration, resulting in colour changes from dark green through pale green and beige to almost red. The major alteration minerals are chlorite, sericite, hematite, zeolites and carbonate. They are present in the groundmass, as replacement of igneous phenocrysts, in veins and as fillings of drop-shaped amygdales. Multimineral veins are present within mafic to ultramafic rocks and along their contacts with host granite. The veins average ~1 cm in width, are locally brecciated (Fig. 5.7 D) and are either carbonate- (preferably calcite and dolomite-ankerite solid solution, often twinned) or barite-fluorite-dominated. Both vein sub-types also contain quartz, anhydrite, hematite, Ti-oxide and diverse sulfides. The latter (commonly chalcopyrite, pyrite, galena and sphalerite, Fig. 5.7 E; and less commonly safflorite, altaite, fahlore, bornite and chalcocite) often form continuous layers between host and vein. REE-fluorocarbonates and U minerals are very rare and those present may have been inherited from the surrounding breccia.

A characteristic feature of some calcite-dominated veins hosted by ~0.82 Ga GDS-type dolerite dykes (Huang et al., 2015) is the association of calcite with magnetite (often colloform, Fig. 5.7 F) apatite, quartz (usually colloform) and sulfides (Apukhtina et al., 2015). Titanite often marks the boundaries of the calcite-magnetite-apatite-quartz veins against thin but intensely altered selvedges of host dolerite (Fig. 5.7 G, Apukhtina et al., 2015).

5.6.1.5 Massive barite-fluorite-dominated veins (with minor carbonate)

Barite (or solid solution with celestite)-fluorite veins (Fig. 5.8 A-D) were recognised as structurally late in some of the earliest studies of Olympic Dam (e.g., Wawryk, 1989; Sugden and Cross, 1991; Ehrig et al., 2012). They crosscut the breccia complex along NE and E-W arrays (Sugden and Cross, 1991) but are not brecciated themselves (see Fig. 15 in Ehrig et al., 2012); they are also found in the cover sequence of the deposit (Sugden and Cross, 1991). The thickness of these veins ranges from a few mm (Fig. 5.8 B) to ~1 m (Fig. 5.8 A) and vertical extension can be up to ~800 m. Such veins usually display complex zoning expressed by colour variations of barite (white to red) and fluorite (colourless to green and purple). Minor components of such veins are carbonates of all types (Ca-Mg-Fe-Mn- and REE-F-rich), quartz, hematite (occasionally botryoidal), various ore minerals (chalcopyrite, pyrite and traces of bornite, chalcocite, fahlore, safflorite, cobaltite, löllingite, sphalerite, galena, native gold, alloclasite, diverse Bi-Ag-Pb-Se-Te-bearing

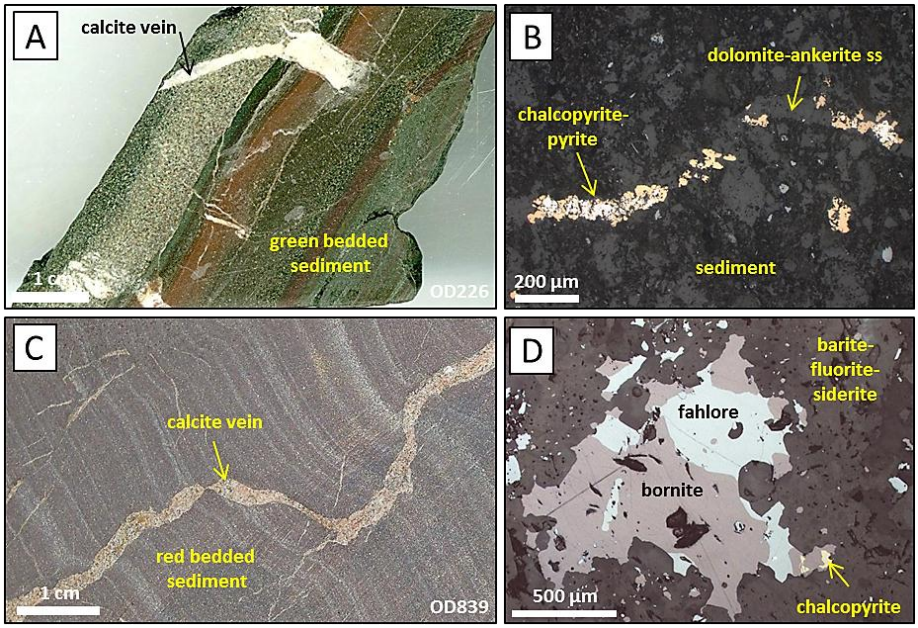

Fig. 5.6: Group 3 carbonates. (A) Green bedded sediment containing a few hematite-rich bands crosscut by mineralized carbonate vein (B). Red bedded sediment (C) is an ironstone and comprises a sulfide-bearing carbonate veins as well (D). TL image (//P): B; RL image (//P): D.

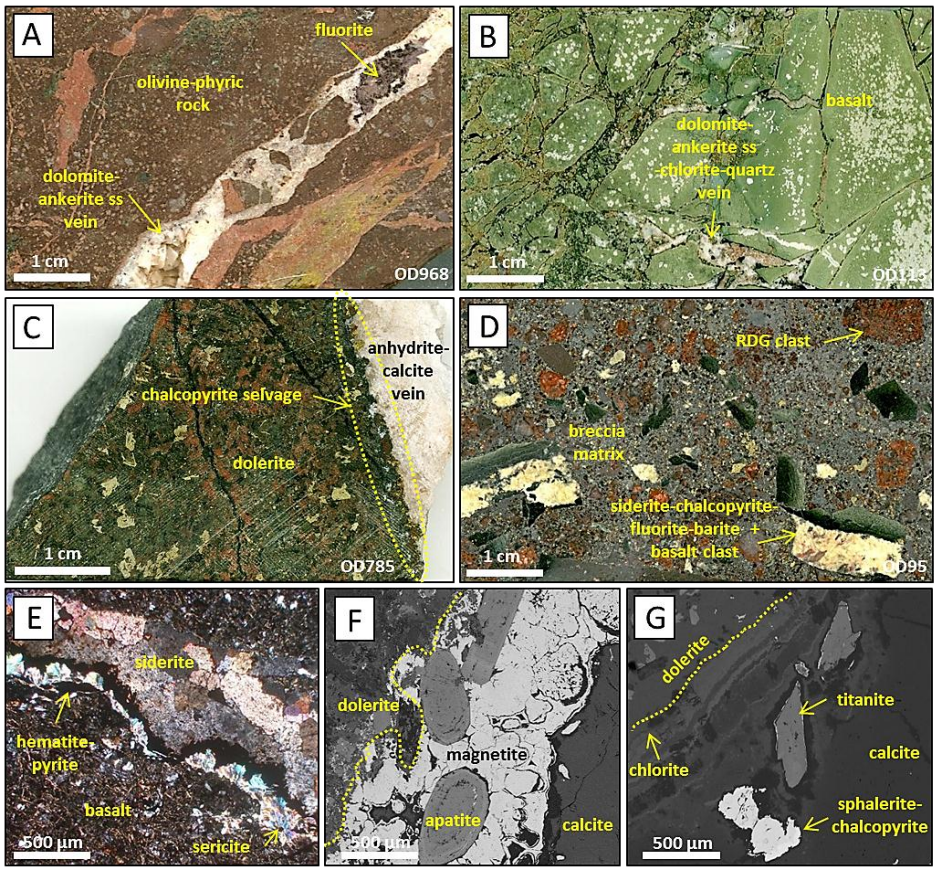

Fig. 5.7: Group 4 carbonates. (A) Brown, strongly-altered olivine-phyric lava with carbonate-fluorite vein. (B) Light green, strongly-altered basalt with recrystallized glass crosscut by carbonate-chlorite-quartz veins. (C) Moderately-altered dolerite hosting an anhydrite-calcite-chalcopyrite vein. (D) Matrix-supported, polymict breccia with clasts of granite and basalt (with carbonate vein relict). Siderite-sericite-hematite-pyrite-carbonate (E) and magnetite (colloform)-apatite-calcite-titanite-bearing veins (F) hosted by dolerite. (G) Titanite and sulfides are often arranged near vein selvedges. BSE images: F, G; TL image (X pol): E.

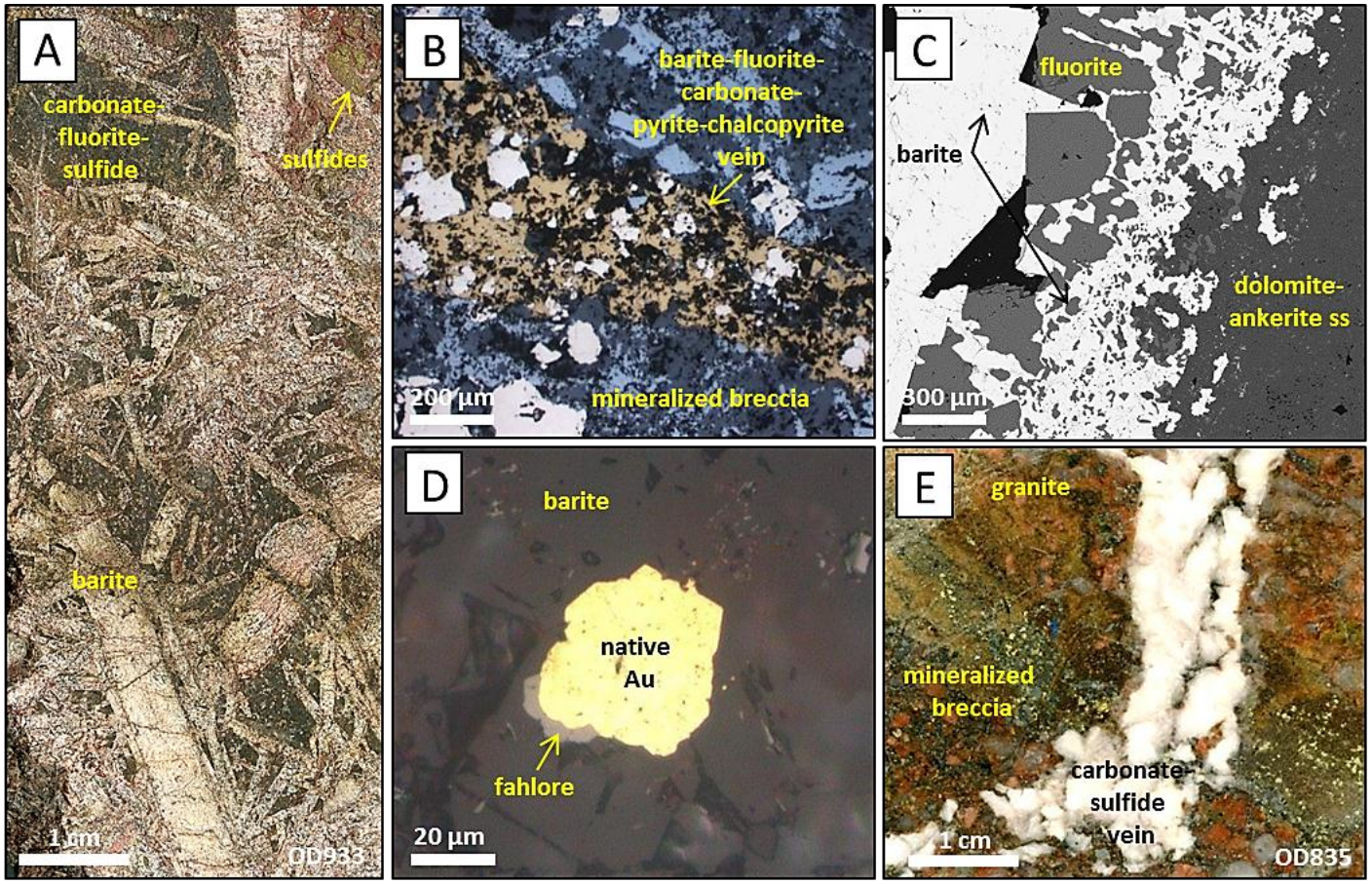

Fig. 5.8: Group 5 carbonates. (A, E) Massive barite (white, brown)-fluorite (purple, green, colourless)-carbonate-dominated veins which may be extremely sulfide-rich (B), zoned (C), and usually carry a range of other minerals such as fahlore and native gold (D). BSE images: B, C; RL images (//P): D.

alloys, Fig. 5.8 D) and U-REE (uraninite, coffinite, brannerite, florencite and REE-fluorocarbonates). In some cases, carbonates are the dominant vein minerals (Fig. 5.8 E). More rarely, uraninite (typically colloform, as *'massive uraninite'* described, Macmillian et al., 2015) is the dominant vein mineral, with associated calcite, barite and Fe-Cu sulfides.

5.6.1.6 Laminated siderite

Numerous drillhole intersections up to 10s of meters thick of beige to brownish siderite (briefly mentioned by Roberts and Hudson, 1983) showing a variety of textures (lamination, druses, cockade structures, crustiform textures), were intersected within the Masher's fault zone (Fig. 5.2). Siderite progressively replaces brecciated blocks (sizes highly variable, up to several cm) composed of hematite-dominant bedded sediments (siderite metasomatism, Fig. 5.9 A). Some fragments are replaced and concentrically overgrown by fine- to coarse-grained siderite to such an extent that primary mineralogy and fabric are unrecognizable (e.g., extensive replacement of the dominant components hematite, quartz, sericite and chlorite). Like the barite-fluorite veins of association 5, the replacement siderite does not appear to be brecciated, suggesting it post-dated brecciation in that part of the orebody. Association 6 siderite is overwhelmingly pure $FeCO_3$ with local replacement by Mg-Mn-rich siderite. Common inclusions in siderite are barite, fluorite, synchysite (Fig. 5.9 B), hematite (Fig. 5.9 C), monazite, uraninite (often rimmed by galena and occasionally colloform), brannerite (replacing Ti-oxide) and sulfides. The latter include sphalerite, galena, and commonly pyrite in epitaxial intergrowths with chalcopyrite (Fig. 5.9 D-E); chalcopyrite often contains up to ~20 μm small, disseminated Au-Ag-Te-rich alloys, clausthalite and uraninite. Hematite shows complex textures, including patchy zoning (Fig. 5.9 C) with bright-BSE inner cores which usually contain abundant μm-small U-W-Pb- and Au-Ag-bearing inclusions, overgrowths of older hematite generation by a younger generation, and hematite replacements of magnetite and chalcopyrite.

5.6.1.7 Carbonate matrix in a conglomerate breccia and sandstone

This group is represented by carbonates which form coarse- to fine-grained matrix in alternating layers of conglomerate-breccia and sandstone (total thickness usually <10 m) found directly at the unconformity and overlain by Nuccaleena Dolomite-like sediment (Fig. 5.10 A-B). Conglomerate-breccia contains spherical to oval-shaped to slightly angular, polymictic clasts up to several cm in size. Despite strong hematitization and clast-in-clast textures, some clasts can be identified as RDG and GRV, others appear to be dropstones associated with Nuccaleena Dolomite-like sedimentary carbonate (Fig. 5.10 B). Fine-grained, well-sorted sandstone is composed of rounded, quartz-dominated (grain size ~3 mm), locally hematite-rich layers which are often cross-bedded. Carbonate matrix in both conglomerate-breccia matrix and sandstone is dominated by dolomite-ankerite grains characterized by Fe-poor interiors and Fe-rich outer zones. Barite, occasionally intergrown with celestite, is commonly associated with the dolomite-ankerite. Sulfide aggregates (pyrite, chalcopyrite, bornite and altaite; up to ~0.5 cm, Fig. 5.10 C) are disseminated throughout the conglomerate clasts and matrix. Sulfide-carbonate veins commonly crosscut individual clasts. The finely-bedded Nuccaleena Dolomite-like sediment at the unconformity is composed of small (~50 μm) dolomite grains intergrown with quartz and possibly granite-derived accessory minerals such as apatite, zircon, and Ti-oxide. The dolomite sediments show evidence of post depositional Fe-alteration of a primary dolomite and are cut by barite-carbonate veins.

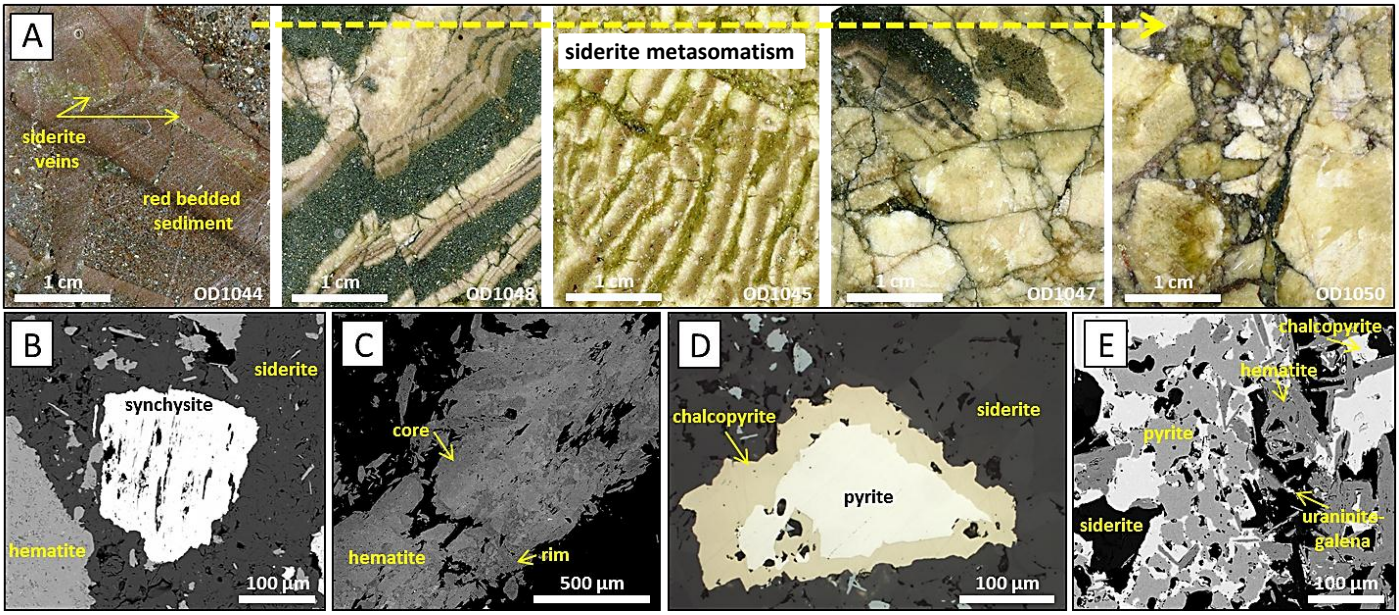

Fig. 5.9: Group 6 carbonates. (A) Successive siderite metasomatism of red-bedded sediments up to a stage where the primary texture becomes unrecognizable. Images are ~2 x 2 cm small. Associated minerals are synchysite (B), hematite (with U-W µm-small inclusions in C) and various sulfides such as epitaxial intergrown pyrite and chalcopyrite (D-E). BSE images: B, C, E; RL image (//P): D.

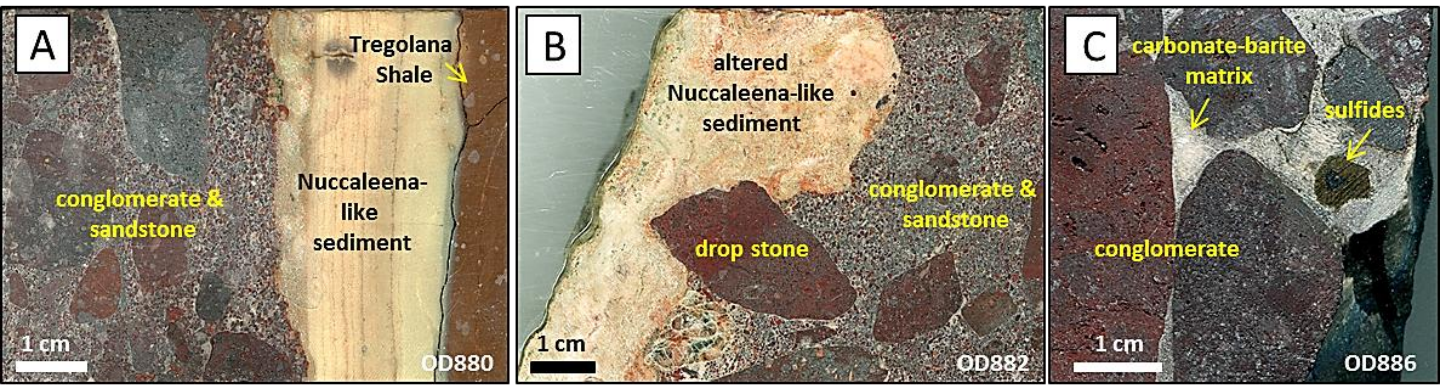

Fig. 5.10: Group 7 carbonates. A range of textures displayed by carbonate-bearing samples found direct on the unconformity (e.g., below the well-bedded Nuccaleena Dolomite-like sediment and overlain Tregolana sediment). Conglomerate in pictures (A-C) is composed of polymictic, strongly hematite-altered clasts having rounded to slightly angular shapes and intermixed sandstone. (B) Shows a dropstone in the highly altered (primary bedding destroyed, Fe metasomatism) Nuccaleena-like sediment. (C) Displays a ~1 cm small sulfide grain within the conglomerate matrix. Coarse- to fine-grained carbonate which is often intergrown with barite builds a matrix of the conglomerate and sandstone.

5.6.2 Carbonate compositions

Based on semi-quantitative SEM analyses (Ehrig et al., 2012), Olympic Dam gangue carbonates are dolomite-calcite solid solution, ankerite and siderite. Mn-free/poor and Mn-rich siderite could be distinguished. The results of 302 fully quantitative electron microprobe data for Ca-Mg-Fe-Mn carbonate samples studied here (Table 5.3) are shown in ternary diagrams (Ca-Fe+Mn-Mg, Mn-Fe-Mg, Fig. 5.11 A-B). Mn was added because it can reach >10 wt% and correlates with Fe. The results show that calcite is almost pure calcite [$CaCO_3$], dolomite [$CaMg(CO_3)_2$] usually forms a complete solid solution series with ankerite [$Ca(Fe,Mg)(CO_3)_2$], and siderites vary extensively in the solid solution system siderite-rhodochrosite-magnesite ($FeCO_3$ - $MnCO_3$ - $MgCO_3$). Fe and Mn in dolomite-ankerite solid solution can reach up to 13.9 and 7.2 wt%, respectively, while siderite solid solution has up to 11.2 wt% Mn and 12.3 wt% Mg. Calcite can contain up to 2.6 wt% Fe and Mn. The distribution of compositions in the various carbonate associations is shown in Fig. 5.11 C.

5.6.3 Stable isotopes (C, O)

Forty six carbonate samples from 22 drillholes covering the range of carbonate types and associations were analysed; the results are given in Tables 5.2 and 5.4. Duplicate analyses were done for almost all samples and generally show good agreement. However, some samples show internal variation in $\delta^{13}C$ and $\delta^{18}O$ values of up to 0.47 ‰ and 1.33 ‰, respectively, well above the typical analytical precision of 0.1 ‰ for $\delta^{13}C$ and $\delta^{18}O$ measurements. This might be explained by heterogeneously distributed, multiple C-O reservoirs, such as secondary fluid inclusions or relicts of replaced carbonates. Hydrothermal alteration of the RDG has been suggested based on fluid inclusion investigations (whole rock and magmatic quartz) to be able to cause a significant shift in $\delta^{18}O$ data of the host granite (Oreskes and Einaudi, 1992), depending on the fluid-rock ratio. Equilibrium temperatures were not calculated because none of the carbonate samples contains two separable cogenetic carbonate generations.

$\delta^{13}C$ varies from -6.5 to -2 ‰ (avg. -3.9 ‰) while $\delta^{18}O$ varies from 9.4 to 20.9 ‰ (avg. 13.6 ‰). Like the data presented in Oreskes and Einaudi (1992, $\delta^{13}C$ -3.5 to -2.3 ‰, $\delta^{18}O$ 12.7 to 20.9 ‰, for siderite only), the new results show a relatively small range in $\delta^{13}C$ compared to $\delta^{18}O$ (Fig. 5.12). Based on the descriptions in Oreskes and Einaudi (1992), their siderites are most similar to those assigned associations 2 and 5 (this work). The C-O isotope data show no clear systematic differences between different carbonate types, although calcite assigned to association 1 (believed to be a result of very early IOCG mineralization, Fig. 5.4, Apukhtina et al., in preparation a) shows tightly clustered $\delta^{13}C$-$\delta^{18}O$ values and has the lowest average $\delta^{18}O$. Dolomite-ankerite from association 3 (veins in bedded sediment clasts, Fig. 5.6) has similarly limited compositions but this may be a result of a small data set. Fe-rich carbonates in strongly brecciated granite (association 2, Fig. 5.5), Ca-Mg-rich carbonates in veins within mafic to ultramafic rocks (association 4, Fig. 5.7) and carbonates in late barite-fluorite veins all show variation across the entire $\delta^{18}O$ range, while association 4 carbonates reaches the lowest $\delta^{13}C$.

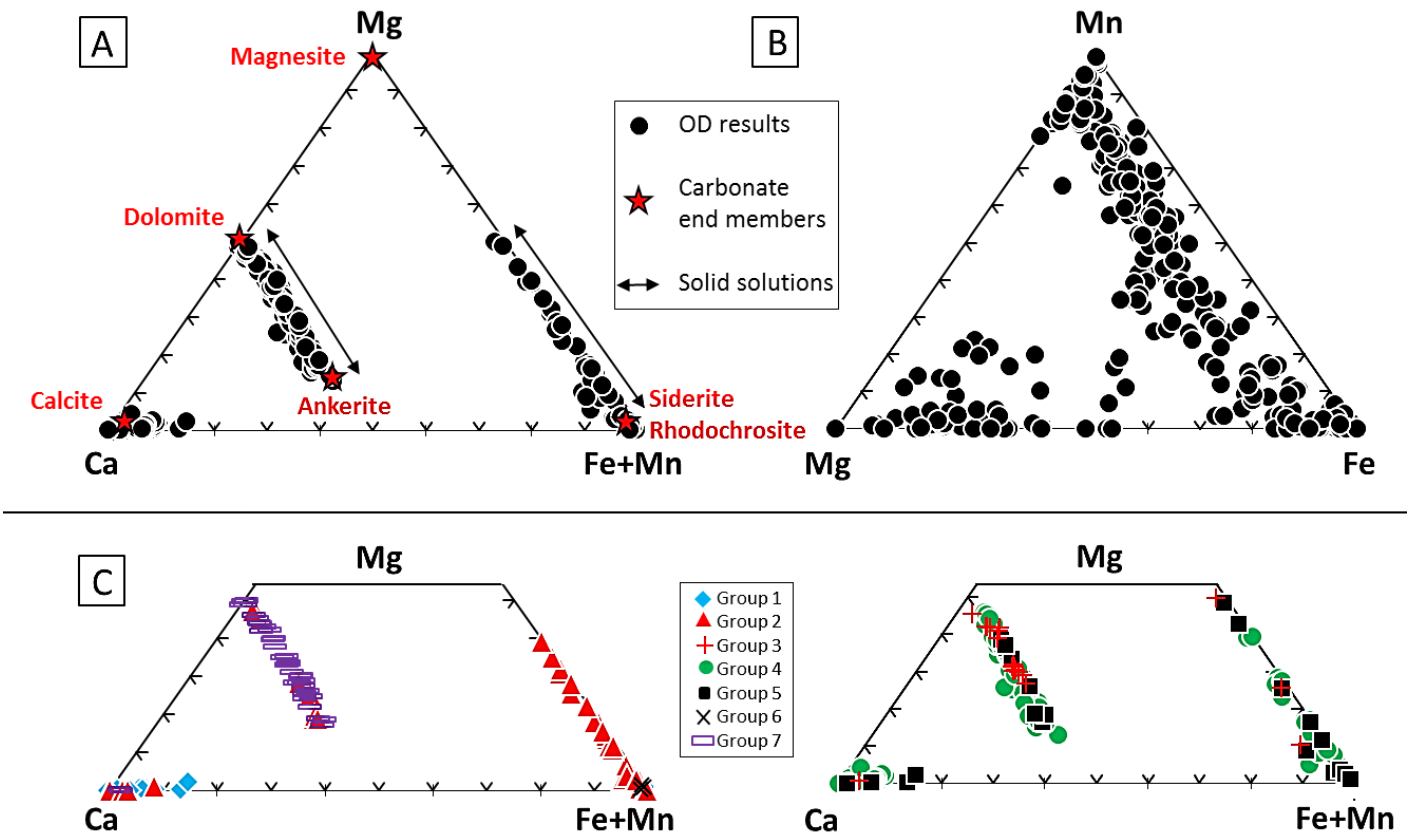

Fig. 5.11: Carbonate compositions expressed on Ca-Mg-(Fe+Mn) and Mn-Mg-Fe plots. (A) Olympic Dam (OD) carbonates compared with ideal (end member) compositions of carbonate minerals (Reeder and Dollase, 1989; Deer et al., 1992). (B) Compositional variations in carbonates from groups 1-7. Note the dominance of some carbonate types in certain carbonate groups (e.g., calcite in groups 1 and 4, siderite solid solution in groups 2 and 6, dolomite-ankerite solid solution in groups 4 and 7).

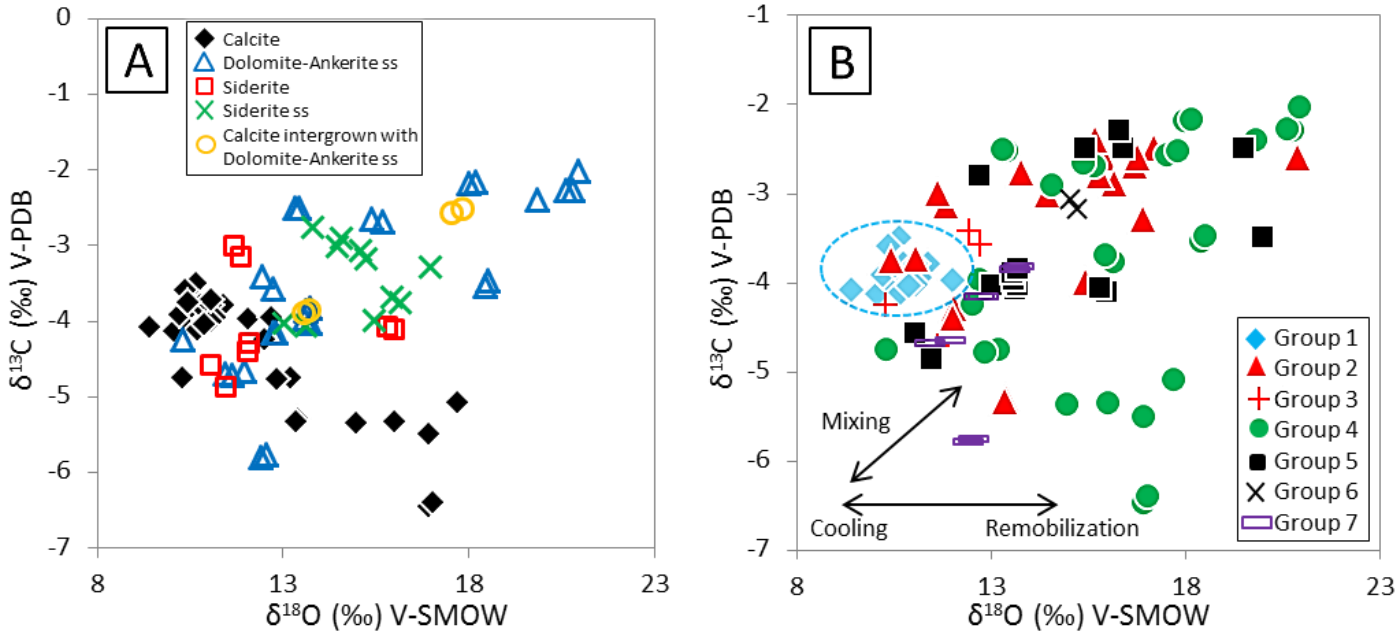

Fig. 5.12: Carbon and oxygen isotopic data for the different carbonate types (A) and groups (B) at Olympic Dam. Note tight clustering of the data for group 1 and overall mixing, cooling and remobilization trends obtained from Schwinn et al. (2006). Ss: solid solution.

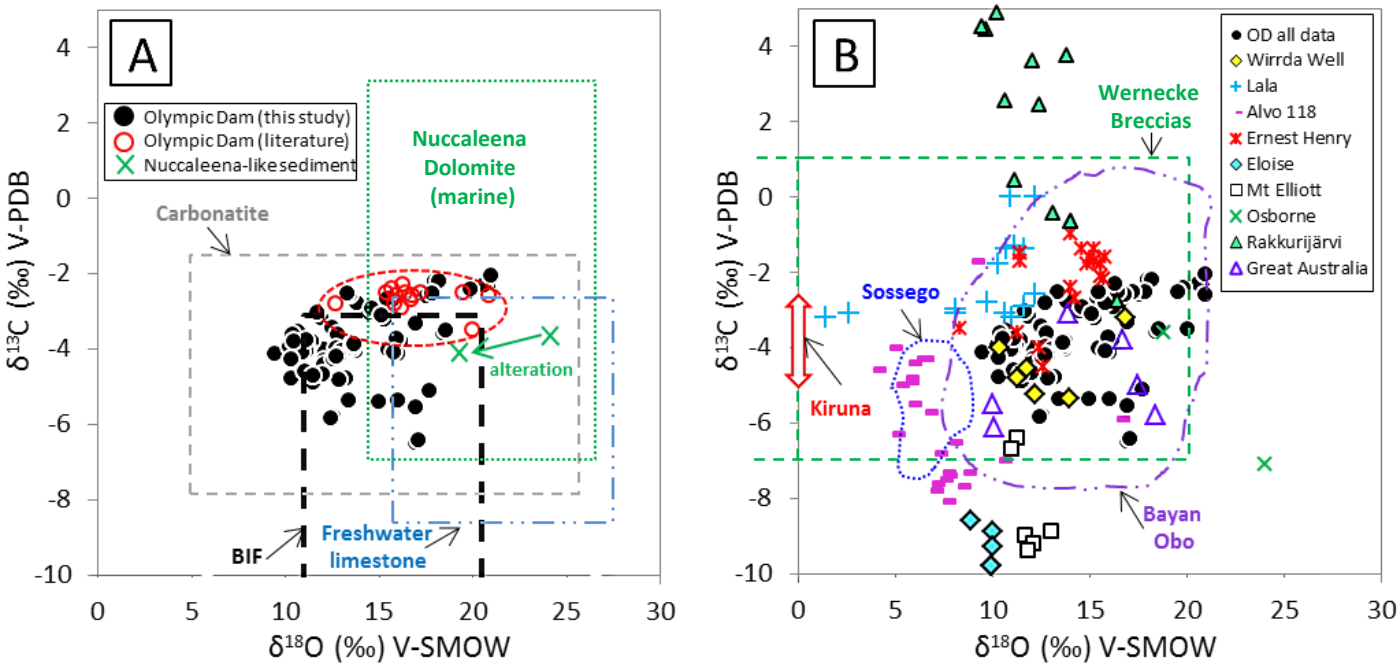

Fig. 5.13: Available carbon and oxygen isotopic data from Olympic Dam (OD, current study and data from Oreskes and Einaudi, 1992) compared with: (A) potential carbon reservoirs such as BIFs (Baur et al., 1985), carbonatites (Santos et al., 1995 and references therein), freshwater limestone (Keith and Weber, 1964), and marine limestone (e.g., Nuccaleena Dolostone, Kennedy et al., 2008; Rose and Maloof, 2010) and Nuccaleena Dolomite-like sediment (unaltered and slightly altered samples, this study), and (B) with various IOCG deposits and prospects such as Alvo 118 (Torresi et al., 2012), Kiruna (Hitzman et al., 1992), Lala (Chen and Zhou, 2012), Bayan Obo (Wu, 2008 and references therein), Wirrda Well (Davidson et al., 2007), Sossego (Monteiro et al., 2008), Rakkurijärvi (Smith et al., 2007), Wernecke Breccias (Hunt et al., 2007) and deposits in the Mt Isa Block (e.g., Eloise, Ernest Henry, Mt Elliott, Osborne, Marshall et al., 2006 and references therein; Great Australia, Cannell and Davidson, 1998). (B) Contains all Olympic Dam (OD) data from this study and study from Oreskes and Einaudi (1992). Ss: solid solution.

5.7 Discussion

Prior to this study, little data existed for carbonates in the ODBC (e.g., Lottermoser, 1995; Oreskes and Einaudi, 1992; Maas et al., 2011; Diemar, 2014) and it was previously assumed that carbonates constitute only a small volume at the breccia complex. Published information consisted of generalised petrographic descriptions and a limited set of fluid inclusion and stable (C-O) isotopic data of siderite (Fig. 5.13 A, Oreskes and Einaudi, 1992). These and other studies (e.g., Roberts and Hudson, 1983; Oreskes and Einaudi, 1990; Reeve et al., 1990; Hitzman et al., 1992; Haynes et al., 1995; Ehrig et al., 2012) led to a broadly-accepted consensus that siderite was formed at the early stage together with magnetite and pyrite. This mineralizing event was attributed to precipitation from ascending, hot (~400 ˚C), saline magmatic-hydrothermal fluids (e.g., Oreskes and Einaudi, 1992).

The present study is based on petrographic studies of drill core collected post the original studies in the early-mid 1990s. Although carbonates are volumetrically minor compared to hematite alteration or quartz gangue (as observed in earlier papers), they are nevertheless widely distributed and the *'carbonate shell'* is coincident with pyrite- and chalcopyrite-bearing ore zones (Fig. 5.1, Ehrig et al., 2012). Carbonates at Olympic Dam are mineralogically diverse, often have wide ranges in chemical compositions (Fig. 5.11), and are characterised by diverse host rocks, textures and parageneses (Figs. 5.3-5.10). As mentioned earlier, the complexity of the deposit greatly complicates the establishment of a robust paragenetic sequence of carbonate and other minerals for the entire deposit, resulting in the carbonate *'association'* approach chosen here, with 7 associations currently recognized (Figs. 5.3-5.10). Based on available and emerging radiometric dating, these associations formed at ~1590 Ma (Johnson and McCulloch, 1995; Apukhtina et al., in preparation a), between ~1.4 to ~1.1 Ga (Maas et al., 2011), at ~825 Ma (Apukhtina et al., in preparation a; Huang et al., 2015), and at about 500 Ma (Wawryk, 1989; Maas et al., 2011). Recent Sm-Nd, Pb-Pb and Lu-Hf dating of carbonates (Maas et al., 2015; Maas et al., in preparation b) supports this chronology and suggests that carbonate deposition at Olympic Dam occurred episodically over a period of 1000 Ma. The local geology at Olympic Dam, and presumably the Stuart Shelf in general, appears to have responded to major geological events: the breakup of supercontinent Columbia (~1.6-1.3 Ga, Rogers and Santosh, 2009; Srivastava and Rao, 2007), amalgamation and breakup of Rodinia (~1.3-0.9 and ~0.8-0.5 Ga, respectively, Li et al., 1999, 2008), and amalgamation of Gondwana (~0.6-0.3 Ga, Veevers, 2004).

5.7.1 Temporal evolution of the Olympic Dam carbonates in time

5.7.1.1 Mesoproterozoic carbonates

Several of the carbonate associations described above have formed in the Mesoproterozoic:

(1) Weakly altered, deep-seated (>2.3 km below surface) mineralization on the eastern flank of the deposit consists mainly of magnetite (±hematite), pyrite, fluorapatite and quartz, reminiscent of typical IOCG assemblages in several other deposits of the Olympic Dam Province (Apukhtina et al., in preparation a). U-Pb dating of several minerals yields ~1590 Ma ages, consistent with the broadly syn-GRV age reported for other IOCG deposits in the region (Skirrow et al., 2007) and for parts of Olympic Dam itself (e.g., Johnson and Cross, 1995; Ciobanu et al., 2013). Association 1 calcite occurs within stockwork-like, unbrecciated veins which crosscut magnetite-pyrite-apatite-quartz-uraninite mineralization (Fig. 5.4). Sm-Nd dating of the calcite indicates the veins could have formed several 10s of Ma after the magnetite-pyrite-apatite-quartz ore (Apukhtina et al., in preparation a).

(2) Siderite (and its solid solutions, Fig. 5.11) of association 2 (granite-dominated breccia, Fig. 5.5) is the most abundant carbonate mineral at Olympic Dam (Ehrig et al., 2012). It is prominent in several carbonate associations (e.g., breccia matrix, association 2, Fig. 5.5), and it correlates with the deposit-wide ore zonation, forming the bowl-shaped *'carbonate shell'* (Ehrig et al., 2012). Siderite was previously thought to be the earliest carbonate at Olympic Dam (e.g., Roberts and Hudson, 1983) although Oreskes and Einaudi (1992) noted that coexistence of siderite with early-stage magnetite at elevated temperatures (~400˚C) and low pressures would require unrealistically high CO_2 pressures. They mooted the possibility that siderite may have formed later than early magnetite IOCG assemblages. This is supported by the lack of magnetite-associated siderite in the recently discovered syn-1590 Ma, magnetite-apatite-quartz-pyrite-uraninite IOCG assemblage described by Apukhtina et al. (in preparation a). Further evidence of the multistage nature of siderite (and its solid solution) is provided by textural observations which indicate multistage deposition, recrystallization, dissolution/leaching, and reprecipitation. Matrix carbonates (the vast bulk being siderite) are observed to mutually replace each other, and similar mutual replacement is observed between Fe carbonates and hematite. No such textures were observed for the abundant calcite present in the relict 1590 Ma magnetite-apatite-quartz-pyrite-uraninite assemblage described in Apukhtina et al. (in preparation a) who argue that some of the siderite forming the breccia cement has been formed by recycling of the early calcite. On a deposit scale, siderite shows increasing porosity towards barren hematite-quartz±barite breccias (see Fig. 4 in Ehrig et al., 2012) and the shallower bornite-chalcocite-hematite-rich parts of the breccia zone (Ehrig et al., 2012). The timing of siderite dissolution in these parts of the deposit is unclear but the process is most likely genetically and temporally correlated with the leaching of various sulfides (abundant pores within the core breccia, e.g., Roberts and Hudson, 1983; Ehrig et al., 2012) from the barren core zone. While most of the evidence from this study suggests a relatively late (significantly post-1590 Ma) origin of siderite, it nevertheless remains possible that some of the siderite in both breccia clasts and matrix (Fig. 5. 5 D-F) formed very early.

(3) Oolite and pisolite clasts largely composed of siderite-hematite are found throughout the breccia complex (association 2, Fig. 5.5 J) and represent a potentially early siderite formation event. The primary siderite-hematite banding is overprinted by later generations of siderite-hematite, with Cu and U minerals (see description as part of association 2). If the secondary sulfide-uraninite assemblages in oolite clasts belong to the 1.59 Ga IOCG mineralization (Apukhtina et al., in preparation a), the oolites may in fact predate the 1.59 Ga event. We suggest they are relicts from BIFs. Siderite (both biotic and abiotic) is known to be an abundant Fe mineral (with hematite and magnetite) in BIFs (Köhler et al., 2013) where it can exhibit a range of depositional textures, including oolite (e.g., Gole and Klein, 1981). BIFs are widespread in the Paleoproterozoic lithologies of the Gawler craton (e.g., Parker, 1987; Oreskes and Einaudi, 1990; Hitzman et al., 1992) and would thus be expected to be available for reworking during emplacement of the Hiltaba Suite granites and initial formation of the breccia complex. This is supported by pre-Hiltaba U-Pb dates for magnetite (1769±58 Ma) at Olympic Dam which were interpreted as evidence for incorporation of pre-existing Fe-rich fragments into the breccia complex (Ciobanu et al., 2015). By contrast, oolites in other IOCG deposits, such as Oak Dam East (Gawler Craton, Davidson et al., 2007), Acropolis (Gawler Craton, Creaser, 1989) and in Southeast Missouri (USA, Nold et al., 2014) were interpreted as *in situ* hydrothermal textures rather than remnants of older BIF.

(4) The age of carbonate-bearing veins in bedded sediments (association 3, Fig. 5.6) is uncertain because there is currently no robust radiometric dating for the host (red and green) sediments or the veins. Geological and petrographic data indicate that the bedded facies sediments may have been deposited soon after the 1.59 Ga GRV/Hiltaba event (McPhie et al., 2016; Cherry et al., in preparation), but common Pb model ages for galena and pyrite found in some of the green sediment are much younger (~1.4 to 1.2 Ga, Meffre et al., 2010; Kamenetsky et al., 2015). By contrast, the presence of barite and fluorite in association 3 carbonate veins is reminiscent of association 5 vein assemblages which formed in the Cambrian. Further work is required to clarify this issue.

(5) Highly altered ultramafic and mafic lavas and dykes (Fig. 5.2) within the breccia complex, thought to be related to the bimodal 1.59 Ga GRV magmatism (Huang et al., 2016), contain abundant but undated carbonate veins (Fig. 5.7 A). Carbonate mineralogy and compositions in these veins are similar to those in the less altered, ~0.82 Ga dolerite dykes, suggesting some host rock buffering of vein fill assemblages. For this reason, we assume that the veins in the older (1.59 Ga) ultramafic-mafic intrusives have been emplaced soon after cooling of their host rocks.

(6) REE-fluorocarbonates (e.g., bastnäsite, synchysite) were studied by Lottermoser (1995) and Diemar (2014). Sm-Nd isotopic results for several REE-rich lithologies with prominent bastnäsite and florencite (Maas et al., 2011, in preparation a) suggest apparent ages between ~1.4 and ~1.1 Ga. The significance of these ages is uncertain. REE patterns and SEM data indicate that REE-rich minerals are present within almost every carbonate association described in this paper, implying that REE-fluorocarbonates could have been formed throughout the history of the deposit.

5.7.1.2 Neoproterozoic (~0.8 Ga) carbonates

Carbonate-bearing veins of association 4 (Fig. 5.7) in ~0.82 Ga GDS-type doleritic dykes (Huang et al., 2015) have been dated directly in several cases, suggesting they formed soon after dyke emplacement (Apukhtina et al., 2015; Huang et al., 2015). The veins are locally brecciated, consistent with this chronology.

5.7.1.3 Ediacaran to Cambrian (~0.64-0.5 Ga) carbonates

(1) Several examples of unbrecciated barite-fluorite-carbonate-sulfide veins of association 5 (Fig. 5.8) have ~0.5 Ga Sm-Nd ages (Wawryk, 1989; Maas et al., 2011, in preparation a), broadly synchronous with the Delamerian Orogeny (~510-490 Ma, Foden et al., 2006) in the Adelaide Fold Belt to the east of the Stuart Shelf.

(2) Laminated siderite (association 6, Fig. 5.9), locally found intersecting Masher's fault (Fig. 5.2), is undated but may be Cambrian in age. It is unbrecciated and therefore likely to have formed very late in the deposit's history. Siderite of this association shows a range of textures which include open space fill and hydrothermal replacement of older breccia clasts. The open space may have been created by deformation along Masher's fault which is known to have been reactivated during the Delamerian (Hayward and Skirrow, 2010; Ehrig et al., 2012). The presence of barite and fluorite in laminated siderite further supports a 0.5 Ga age. However, no direct dating of this carbonate generation is available at this stage of research to support this assumption (see Chapter 6).

(3) The dolomite-ankerite matrix carbonates in thin conglomerate-breccia and sandstone horizons above the unconformity (association 7, Fig. 5.10) are thought to have formed during fluid flow along the unconformity. Minor sulfides in this carbonate-dominated matrix resemble sulfide assemblages in bornite-chalcocite-rich rocks located immediately below the unconformity, perhaps implying both formed during the same fluid flow event(s). A maximum age for association 7 is given by the Neoproterozoic-Cambrian age of the post-unconformity rocks (Ehrig et al., 2012).

One of the lithologies resembles dolomites of the Nuccaleena Formation (Flinders Ranges) which defines the base of the Ediacaran (635-541 Ma).

5.7.2 Fluid sources and characteristics

The complex multistage depositional history of gangue carbonate described here requires modification of the relatively simple, single-stage fluid-mixing models proposed earlier (e.g., Johnson and McCulloch, 1995; Oreskes and Einaudi, 1990, 1992; Haynes et al., 1995). While the oldest carbonates formed during the history of mineralization (association 1), as well as association 4 (basalt-associated) carbonates, probably have magmatic components (Apukhtina et al., 2015, in preparation a), there is no evidence for magmatic activity after ~0.82 Ga, implying that formation of the youngest carbonates (associations, 5-7) involved contribution of meteoric waters, possibly migrating along faults during the Delamerian Orogeny (Clark et al., 2006). Abundant evidence for mineral dissolution and replacement suggests that mineral signatures that are unique to just one type of fluid system would be preserved only in rare cases.

Although the heterogeneity of the carbonates prevents determination of physico-chemical conditions and fluid properties (e.g., temperature, pH, pCO_2 and salinity) for each carbonate association, some general observations may be made from the textural and major element data presented here. Carbonate compositions appear to be buffered by host rock compositions in some cases (Fig. 5.11), such as the Fe-carbonates of association 2 in hematite-rich breccia (Fig. 5.5), or the Ca-Mg-carbonates in weakly-altered granite and rhyolite (association 1, Fig. 5.4) and in mafic to ultramafic magmatic rocks (association 4, Fig. 5.7). Fluid pH of some (particularly early-stage) fluids was probably very low, as inferred from ubiquitous evidence for dissolved/replaced pyrite in the breccia complex. The range in carbonate compositions (including REE-fluorocarbonates), mineral zoning patterns and composition changes during replacement reactions indicate that the carbonate-forming fluids evolved and/or precipitated carbonate minerals under variable physico-chemical condition at different depositional stages. This is consistent with the fluid salinity variations noted in Oreskes and Einaudi (1992). Carbonate-bearing veins often contain fluorite, barite, quartz, hematite and diverse Cu-Co-As-Fe-Pb-Zn sulfides which implies the presence of F-, Cl- and S-bearing species. Almost all the carbonate associations in Table 5.2 include chalcopyrite, the most common sulfide at Olympic Dam (Ehrig et al., 2012), which implies a significant Cu-Fe-S component in the relevant fluids. It is unclear if these metals were recycled or represent new input from an external source. The widespread presence of REE-fluorocarbonates indicates that dissolved REE complexes were present in CO_2-rich fluids which produced the earliest (associations 1 and 2) and youngest (at least associations 5-6) carbonates. By contrast, association 4 carbonates in ~0.82 Ga dolerite dykes do not carry REE minerals, implying an absence of REE enrichment of the relevant fluids. The apparent link between REE-fluorocarbonates and the 1.59 and 0.5 Ga carbonate associations is at odds with Sm-Nd ages of ~1.1-1.4 Ga for REE-rich rocks (see above).

5.7.3 Sources of carbon

The stable isotope (C, O) compositions of Olympic Dam carbonates (Figs. 5.12 and 5.13) do not show obvious clustering with mineral type (calcite, dolomite-ankerite solid solution, siderite and siderite solid solution, Fig. 5.12 B) and there is substantial overlap between C-O isotope ranges in the various carbonate associations. The data plot within, or overlap substantially, the (large) fields for carbonatites and sedimentary carbonates (Fig. 5.13 A) and are not

therefore diagnostic of any particular C- and O-source, such as a carbonatite source debated for some IOCG deposits (Meyer, 1988; Hauck, 1990).

The isotope data for early calcite of association 1 are relatively homogeneous and show consistently low $\delta^{18}O$, consistent with formation at elevated temperatures (O'Neil et al., 1969) which can be attributed to magmatic-hydrothermal processes during RDG emplacement at ~1.59 Ga. The more variable compositions for carbonates in the other associations are more difficult to interpret (Fig. 5.12). Given the heterogeneity of each carbonate association in age, composition and replacement history, isotopic variability could reflect multiple sources of carbon and oxygen, temperature-dependant fluid-rock interaction, salinity-related variation (e.g., Ohmoto, 1972; O'Neil et al., 1969), simple cooling of a fluid (Oreskes and Einaudi, 1992), fluid-mixing, secondary disequilibrium processes (Schwinn et al., 2006), and/or isotopic fractionation (particularly in the case of $\delta^{18}O$ between a number of O-bearing minerals associated with carbonates). Generalised vectors of the better-known processes capable of producing variable C-O isotope compositions (Schwinn et al., 2006) are shown in Fig. 5.12.

While the isotope data alone are difficult to interpret in terms of carbon sources, mass balance indicates that the host granite cannot be the only source of the carbon now present in the ODBC. The average CO_2 content in 49 samples of RDG is 0.27 wt% (736 ppm C) while the modal abundance of carbonates in the breccia complex suggests a C abundance of ~3500 ppm (not adjusted for density contrasts; C contents calculated from data in Ehrig et al., 2012). Additional carbon sources include GRV, mafic-ultramafic dykes, and clastic sediments, such as the bedded facies (McPhie et al., 2011), and inferred clasts of Pandurra Formation (e.g., McPhie et al., 2016; Cherry, in preparation). Pandurra Formation is dominated by fluvial sandstones, quartzite, pebble conglomerate and shale (e.g., Fanning et al., 1983; Cowley, 1993) and contains minor carbonate in form of sediment matrix and local occurring ooids (personal observations on samples of Pandurra Formation obtained from the Emmie Bluff). Carbon contributions from pre-granite BIFs which often contain significant primary siderite (Kholodov and Butuzova, 2008) are also possible (see association 2 oolites/pisolites), as are contributions from Neoproterozoic metacarbonates, as suggested in Oreskes and Einaudi (1990). Dolomite interpreted to be equivalent with dolomites of the Ediacaran Nuccaleena Formation (~0.63 Ga, Calver et al., 2013) is locally present directly above the breccia complex. The dolomite is only a few to 10s of cm thick at Olympic Dam, compared to its average thickness of 18.5 m (Rose and Maloof, 2010). Much of the inferred Neoproterozoic dolomite may have been reworked into the breccia complex, like other sedimentary units now known to have been incorporated (McPhie et al., 2011, 2016). If this is the case, remobilized Nuccaleena-type dolomite would be a potential source of sedimentary carbon for some of the younger carbonate associations, e.g. association 5 siderites and association 7 conglomerate cements, both inferred to be related to tectonic activity during the Cambrian Delamerian Orogeny. Two samples of the Nuccaleena-type dolomitic sediment have among the highest $\delta^{18}O$ measured in this study (Fig. 5.13 A), defining a possible mixing trend between sedimentary carbonate and the Olympic Dam carbonate field.

5.7.4 Carbonates in IOCG systems

Carbonate minerals are present, often in significant volumes, in other IOCG deposits and prospects. In the NE Gawler craton, examples are Acropolis (Creaser, 1989), Carrapateena (Porter, 2010), Hillside (Ismail et al., 2014; Conor et al., 2010), Prominent Hill (Belperio et al., 2007), and Wirrda Well (Davidson et al., 2007). Examples elsewhere include Alvo 118 (Torresi et al., 2012), Bayan Obo (Wu, 2008), Ernest Henry (Marshall et al., 2006), Great Australia

(Cannell and Davidson, 1998), Kiruna (Hitzman et al., 1992), Lala (Chen and Zhou, 2012), Nova Scotia (O'Reilly, 2006), Phalaborwa (Groves and Vielreicher, 2001; Harmer, 2015), Rakkurijärvi (Smith et al., 2007), Sossego (Monteiro et al., 2008), and Wernecke Breccia (Hunt et al., 2007). This suggests that carbonates are a universal feature of the IOCG deposit clan (Hitzman et al., 1992; Williams et al., 2005; Groves et al., 2010), as pointed out by Pollard (2006) who noted that *"fluid inclusion studies in IOCG systems show that carbon dioxide is a key component of the fluids"*. Carbonate composition in IOCG deposits is highly variably with one carbonate usually being the dominant (e.g., siderite in Olympic Dam deposit, Ehrig et al., 2012; dolomite-calcite in Great Australia, Cannell and Davidson, 1998). Rare paragenetic studies show that carbonate deposition in IOCG deposits can occur pre-, syn- and post-ore (e.g., Cannell and Davidson, 1998; Williams et al., 2005; Chen and Zhou, 2012) but "*the behaviour of carbonate rocks in these* (IOCG) *systems is currently not well understood"* (Hitzman et al., 1992). The carbonate data presented here and in companion papers (see above) are likely to represent a particularly complex endmember case characterised by diachronous and heterogeneous carbonate generations.

The stable isotope compositions for Olympic Dam carbonates are very similar to those from the nearby Wirrda Well IOCG prospect (Davidson et al., 2007) and Great Australia located in Mt Isa Block (Cannell and Davidson, 1998) and plot entirely within the much larger compositional field for the Bayan Obo deposit (Wu, 2008 and references therein) and Wernecke Breccias (Hunt et al., 2007, Fig. 5.13 B). $\delta^{13}C$ values around -4 ‰, typical of Olympic Dam carbonates, are also known from the Kiruna iron oxide-apatite deposit (Hitzman et al., 1992). Olympic Dam carbonate $\delta^{13}C$-$\delta^{18}O$ values partly overlap with those for carbonates in Ernest Henry IOCG deposit (Marshall et al., 2006), while the fields for Alvo 118 (Torresi et al., 2012), Eloise (Marshall et al., 2006), Lala (Chen and Zhou, 2012), Mt Elliott (Marshall et al., 2006), Rakkurijärvi (Smith et al., 2007), and Sossego (Monteiro et al., 2008) IOCG deposits show little to no overlap with those for Olympic Dam. Various carbon sources have been suggested, e.g. magmatic (e.g., Kiruna; Hitzman et al., 1992), metamorphic (some deposits in Mt Isa Block, Marshall et al., 2006), sedimentary (e.g., Wernecke Breccias, Hunt et al., 2007) and mixed (e.g., mantle-sedimentary, Bayan Obo deposit, Bai et al., 1996; Wu, 2008; Great Australia deposit, Cannell and Davidson, 1998). From the Olympic Dam perspective, where carbonates and some metals were added and/or redistributed intermittently over a period of 1000 Ma, such interpretations would need to be treated cautiously.

5.8 Conclusions

Although carbonate minerals occur throughout the deposit, they are concentrated in the outer and deeper parts of the ODBC. This implies a genetic link between carbonates and ore minerals. Siderite and other carbonates occur in multiple associations distinguished by mineralogy, paragenesis, texture and host rock. All associations contain ore minerals although their volume, like that of the associated carbonates, varies greatly. Recycling, and replacement of early carbonates by later generations is common, and this is probably also the case for some ore minerals. The available radiometric dating indicates that the various carbonate associations were deposited in at least three stages which broadly overlap significant tectonic events: the break-up of Columbia (~1.6 Ga), amalgamation and breakup of Rodinia (~1.3-1.1 and ~0.8 Ga, respectively), and amalgamation of Gondwana (~0.5 Ga) supercontinents. This statement is in accordance with the results reported for some other gangue and ore minerals at Olympic Dam (Kamenetsky et al., 2015). Further direct dating of carbonates is likely to yield a more complex chronology. This diachroneity implies

multiple fluid sources and depositional settings, consistent with carbon-oxygen isotope data which indicate mixed (magmatic and sedimentary) fluid components. The oldest identified carbonates, calcites in veins crosscutting the ~1.59 Ga magnetite-apatite-pyrite-quartz ore, have the lowest $\delta^{18}O$, consistent with the high temperatures and magmatic-hydrothermal signature of early ore fluids inferred in previous studies. Carbonates in other associations with greater mineralogical, textural, age and isotopic diversity record mixed and increasingly more sedimentary fluid sources, possibly as a result of true fluid diversity but also due to fluid-rock interaction in heterogeneous breccia which incorporated various types of sedimentary lithologies, perhaps over as much as 1000 Ma. The diversity of Olympic Dam carbonates mirrors the diversity in textures, mineral types and mineral ages in the deposit generally and clearly shows that ore-forming models based on a single-stage of hydrothermal-meteoric fluid mixing at ~1.59 Ga, as proposed in previous studies, need to be modified to accommodate the increasing evidence for both the longevity and multistage nature of the mineralization. Olympic Dam carbonates show similarities to carbonate suites in other IOCG deposits, but are likely to represent an endmember case of strong textural and chronological complexity.

Chapter 6: Carbonates at the supergiant Olympic Dam deposit. Part II: Radiogenic isotopes (Sr, Nd, Pb, Hf)

6.1 Introduction

Like many other IOCG deposits, the large Olympic Dam Cu-U-Au-Ag deposit (South Australia) is associated with significant Ca-Fe-Mg-Mn carbonate gangue (e.g., Meyer, 1988; Hauck, 1990; Hitzman et al., 1992; Ehrig et al., 2012). The carbonates have recently been described in Apukhtina et al. (in preparation b) who document their mineralogical-compositional diversity and multistage nature. They distinguish seven associations of carbonates based largely on host rock lithology within and peripheral to the large and complex ODBC which hosts virtually all of the mineralization (Table 5.1). The origin of these carbonates cannot be attributed to a single mineralization-alteration event because recent work has indicated that mineralization at Olympic Dam was formed in a multistage process over perhaps 1000 Ma (Maas et al., 2011; McPhie et al., 2011; Kamenetsky et al., 2015; McPhie et al., 2016), rather than in a geologically short magmatic-hydrothermal event linked to the voluminous Gawler Range-Hiltaba Suite magmatism at ~1.59 Ga as it was proposed previously (Johnson and Cross, 1995; Skirrow et al., 2007). Radiometric dating of the carbonates is therefore required to examine their relationship to the history of their host rocks and their significance to the mineralization process. Furthermore, mass balance calculations indicate that carbon, like the Fe and economic metals (Cu, Au, U, Ag), must largely be sourced from outside the host 1.59 Ga A-type granite in which ODBC is developed (Apukhtina et al., in preparation a). Carbon and oxygen isotopes for the carbonates suggest a range of fluid sources (magmatic, sedimentary) and there is much overlap of $\delta^{13}C$-$\delta^{18}O$ between the various carbonate associations (Apukhtina et al., in preparation b). Interpretation of such data is hindered by the inferred diachronous nature of the carbonate associations.

This paper reports new Sr-Nd isotopic results for samples representing all 7 carbonate associations of Apukhtina et al. (in preparation b), augmented by more limited Pb and Hf isotopic data. It is shown here that many of the carbonates are amenable to Sm-Nd and Lu-Hf isochron dating. Sm-Nd dating has been applied to many ore deposits, notably uranium, fluorite, skarns and gold (e.g., Maas, 1989; Chesley et al., 1994; Brugger et al., 2002; Turner et al., 2003; Li et al., 2004; Reid et al., 2009; Biczok et al., 2012) and generally provides reliable although often imprecise age information. Carbonate minerals, including those in mineralized hydrothermal systems (e.g., Bau and Möller, 1992; Hecht et al., 1999), can show strong and variable REE fractionation (e.g., Stipp et al., 2006), and this has been used to produce chronologies for hydrothermal vein formation in several ore deposits (Peng et al., 2003; Su et al., 2009). Sm-Nd dating of diagenetic calcites in coal measures was used to date basinal fluid flow (Uysal et al., 2007). While rare, these studies demonstrate the potential of hydrothermal carbonates for precise Sm-Nd dating. In contrast, we are not aware of any Lu-Hf isotopic dating studies of ore deposits, even though Lu/Hf fractionation in many hydrothermal minerals far exceeds that of the Sm-Nd system, as has been shown for the carbonate fraction of carbonatites (Bizimis et al., 2003). Hydrothermal garnet, phosphates, fluorite, epidote and carbonates all tend to exclude the high field strength elements and have high Lu/Hf ratios, and are therefore promising targets for Lu-Hf dating in ore deposits and other settings (e.g., Barfod et al., 2005). A major problem in Lu-Hf dating of such minerals are their often very low Hf concentrations which require highly sensitive analytical techniques or large samples. The results presented here show that even highly

complex rocks such as the ODBC, which is characterized by diverse lithologies, heterogeneous replacement and clast-in-clast textures as well as widespread LREE-rich accessory minerals (nuggets), can preserve carbonate Sm-Nd and Lu-Hf isotope systematics which can be used to directly date the various carbonate suites.

Sr isotopic tracing of hydrothermal carbonates, a widely used tool in ore deposit research, was used here because different models of carbonate and ore deposition (single-stage, multi-stage) predict different patterns of carbonate $^{87}Sr/^{86}Sr$. Models which interpret all or most of the carbonate as having formed at or close to 1590 Ma would predict relatively unradiogenic and homogeneous $^{87}Sr/^{86}Sr$, while the protracted history indicated by recent U-Pb dating (e.g., Macmillian et al., 2015) would predict highly heterogeneous $^{87}Sr/^{86}Sr$ (Maas et al., 2015).

6.2 Geological setting and mineralization

The supergiant Olympic Dam Cu-U-Au-Ag deposit is by far the largest of several IOCG-deposits in the Olympic Cu-Au Province on the eastern Gawler Craton, South Australia (e.g., Williams et al., 2005), and is one of the largest known resources of Cu, Au and U (Ehrig et al., 2012). Mineralization is hosted in a voluminous breccia complex, the ODBC, developed entirely within the 1.593 Ga RDG, a member of the Hiltaba granite suite and thus part of the Gawler SLIP (e.g., Allen et al., 2008; Jagodzinski, 2014). The mineralized breccia complex is dominated by granite but non-granitic lithologies are also present and have considerable potential to clarify the history and setting of brecciation. These lithologies include bedded clastic sedimentary rocks (e.g., hematite-rich red ironstones and chlorite-sericite-chromite-rich green sediment), mafic to ultramafic dykes/lavas, and inferred porphyritic rhyolitic rocks (e.g., Ehrig et al., 2012; Apukhtina et al., in preparation a). Additional lithologies are being discovered in ongoing studies of the complex (e.g., McPhie et al., 2016; Cherry et al., in preparation). Although heavily altered, the mafic-ultramafic (picritic) rocks within the breccia complex are believed to be broadly coeval with the host granite and are equivalents of mafic extrusives in the 1.59 Ga lower GRV (Huang et al., 2016). A clearly younger generation of less altered dolerite dykes crosscuts the breccia complex and has been identified as part of the regional 825 Ma GDS (e.g., Huang et al., 2015; Apukhtina et al., 2015). The granite and breccia complex are unconformably overlain by ~320 m of undeformed, unaltered and unmineralized Neoproterozoic to Cambrian sedimentary formations of the Stuart Shelf (Reeve et al., 1990).

The Olympic Dam deposit is mined for Cu, U, Ag and Ag; the substantial REE endowment of the deposit is currently subeconomic (Ehrig et al., 2012). Mineralization is hosted within the breccia complex and is strongly structure-controlled. Nevertheless, mineral zoning is well-developed, with a margin-to-center zoning of Fe-Cu sulfides (pyrite → chalcopyrite → bornite → chalcocite) being the best-known example (Roberts and Hudson, 1983; Reeve et al., 1990). U- (e.g., uraninite, coffinite, brannerite) and Au-rich (e.g., electrum) zones are positively correlated across the deposit (Ehrig et al., 2012). Alteration and gangue minerals also show a margin-to-center zoning with siderite, apatite and magnetite being abundant at the margin of the breccia complex and hematite, barite, fluorite and sericite in the center (Ehrig et al., 2012). U-Pb dating of the marginal magnetite-apatite-pyrite-uraninite assemblage shows it formed during the initial stages of IOCG-style mineralization at 1.59 Ga (Apukhtina et al., in preparation a). Similar U-Pb ages were reported for well-formed hematite (with minute inclusions of uraninite, Ciobanu et al., 2013). Other radiogenic isotope evidence supports continuing, perhaps episodic, brecciation, mineralization and alteration between 1.4 and 1.1 Ga (Gustafson and Compston, 1979; Trueman, 1986; Johnson, 1993; McInnes et al., 2008; Maas et al., 2011;

Kamenetsky et al., 2015), local remobilization of Cu and other elements at the time of dolerite emplacement at 0.82 Ga (Huang et al., 2015), and formation of massive barite-fluorite-dominated veins at about 0.5 Ga (Maas et al., 2011).

6.3 Sample selection and analytical methods

6.3.1 Samples

Based on the carbonate petrographic study of Apukhtina et al. (in preparation b), 56 samples (from 27 drillcores and 2 underground locations) representing the 7 carbonate associations were selected for isotopic study (Maas et al., in preparation b). These selected samples cover the range in carbonate textures (breccia and conglomerate matrix, breccia clasts, veins crosscutting ore-rich breccia and various rock types, amygdales, massive laminated blocks and oolites) and compositions vary from calcite, dolomite, ankerite, siderites to dolomite-ankerite and siderite-rhodochrosite-magnesite (Table 5.1). One sample of anhydrite from early IOCG mineralization at Olympic Dam (1.59 Ga magnetite-apatite-uraninite-pyrite-quartz, drillcore RD2773, Apukhtina et al., in preparation a) was included in this work. Hematite-stained (orange coloured) anhydrite occurs as coarse grains with the early magnetite-apatite-uraninite-pyrite-quartz mineralization, while younger, fine-grained and clear anhydrite occurs massive in the same sample (together with tourmaline, rutile and the minerals of the early assemblage listed above). Carbonates were sampled by handpicking small fragments from crushed material or by removal of fragments from polished drillcore using a small hand-held drill. Where required, fragments were powdered in an agate mortar.

6.3.2 Methods

Rb-Sr, Sm-Nd and U-Th-Pb isotopic and trace element analyses were carried out at the University of Melbourne, following techniques described in Maas et al. (2005) and Maas et al. (2015). Splits (20-50 mg) of calcite and dolomite-ankerite powder were dissolved in dilute nitric acid while siderite and anhydrite were dissolved in 2M HCl; for anhydrite, 10 ml of acid were used to bring the anhydrite in solution. Aliquots of the solutions were used for trace element analysis on an Agilent 7700 Q-ICPMS, using methods adapted from Eggins et al. (1997). The full trace element results are compiled in the senior author's PhD thesis from the UTas (Table A.1, Apukhtina, 2016). Discussion of this highly heterogeneous data set is beyond the scope of this paper (see Appendices). The concentrations of Rb and Sr (and those of Sm and Nd for samples not analysed by isotope dilution) listed in Table 6.1, and concentrations of U, Th and Pb (Table 6.2), were taken from this data set and used to calculate parent/daughter ratios for isochron plots. Because solution-mode trace element analyses were done on splits of the solutions used for Sr (±Nd, ±Pb) isotopic work, these parent/daughter ratios should be directly applicable to the material for which isotopic data are reported. Analytical precision (2sd) for the trace element data is usually better than ±5%, and based on long-term data for rock standards, elemental ratios such as Rb/Sr, Sm/Nd, U/Pb and Th/Pb should have precisions of ±1-2%.

Based on the trace element results, solutions intended for isotope dilution Sm-Nd analysis were equilibrated with a ^{149}Sm-^{150}Nd tracer. Sr and LREE were extracted using Eichrom Sr and TRU resin (Pin et al., 1994) followed by purification of Nd and Sm using Eichrom LN resin (Pin and Zalduegui, 1997). In some Ba-rich (barite-bearing) samples, Sr fractions were passed over the Sr resin up to 3x to reduce Ba/Sr to a safe level (Scher et al., 2014). Where required, Pb was extracted first, using a double pass over 0.1 ml beds of AG1-X8 (100-200 mesh, HBr, HCl technique). Total analytical blanks were <100 pg in all cases, and no blank corrections were required. Isotopic analyses were carried out

on a Nu Plasma MC-ICPMS with sample uptake through a CETAC Aridus desolvator and PFA nebuliser operated at ~0.07 ml/min sample uptake, with sensitivities in the range 100-150 V/ppm. Analyses were conducted in static multi-collection mode with signals near 6 V Sr, 15 V Nd and 10 V Pb, where possible. Instrumental mass bias in Sr and Nd runs was corrected by normalizing to $^{88}Sr/^{86}Sr$ = 8.37521 and $^{146}Nd/^{145}Nd$ = 2.0719425 (equivalent to $^{146}Nd/^{144}Nd$ = 0.7219), using the exponential law as part of an on-line iterative spike-stripping/internal normalization procedure. Data are reported relative to SRM987 = 0.710230 and La Jolla Nd = 0.511860. External precision (reproducibility, 2sd) is ±0.006% (Sr) and ±0.004% (Nd). External precision for $^{147}Sm/^{144}Nd$ obtained by isotope dilution is ±0.2%. $^{87}Rb/^{86}Sr$ ratios for age corrections are based on the trace element results for the same sample solution and have an external precision and accuracy of 1%. Results for international standards agree with TIMS reference values. For example, long-term (2011-2014) averages for BCR-2 are 0.704997±42 (2sd, n = 44) and 0.512641±24 (2sd, n = 74), and $^{147}Sm/^{144}Nd$ is 0.1382±0.0002. Decay constants are $^{87}Rb = 1.395x10^{-11}$/yr and $^{147}Sm = 6.54\ x10^{12}$/yr. Modern CHUR has $^{147}Sm/^{144}Nd$ = 0.1960, $^{143}Nd/^{144}Nd$ = 0.512632 (Bouvier et al., 2008). Mass bias in Pb was corrected using the thallium-doping technique. This produces results which are accurate to within ±0.02-0.06% relative to the reference composition for the SRM981 Pb standard given in Woodhead and Pickering (2002). The long-term average for Broken Hill galena measured with the same technique is $^{206}Pb/^{204}Pb$ = 16.004±0.038%, $^{207}Pb/^{204}Pb$ = 15.388±0.057% and $^{208}Pb/^{204}Pb$ = 35.661±0.076% (n = 73, ±2sd%), consistent with the reference values (e.g., Richards, 1986; Parr et al., 2004). The uncertainties for these averages are a good estimate of the external precision of the method. $^{238}U/^{204}Pb$ and $^{232}Th/^{204}Pb$ ratios are based on the trace element results for the same sample solution and have an external precision and accuracy of 1%.

Lu-Hf isotopic data for a small set of calcites and siderite were acquired at the University of Cologne, Germany. Low Hf concentrations (<1 to several ppb) and extremely high Lu/Hf make analyses of these materials very challenging. The powdered samples (up to 2 g) were dissolved with 3M HCl – 1 vol% H_2O_2 or 3M HNO_3 – 1 vol% H_2O_2 at room temperature and 80˚C, respectively. A ^{176}Lu-^{180}Hf spike optimized for high-Lu/Hf materials was added prior to digestion, and spike and sample were allowed to equilibrate for 24 hours, promoted by heating (HNO_3-H_2O_2 experiments) and ultrasonication. Prior to column chemistry, the sample solutions were adjusted to 1M HCl or 1M HNO_3, respectively, by adding distilled water with 1 vol% H_2O_2. These solutions (10 ml total) were loaded onto column 1 of Bast et al. (2015), in this case rescaled to a 15 ml bed of AG50-X8 (200-400) cation resin within Biorad PolyprepTM columns. Hf and other high field strength elements were collected in the loading solution and 15 ml of 0.1M HCl-0.1M HF or 0.1M HNO_3-0.1M HF (depending on dissolution type), followed by removal of the Ca/Fe matrix and collection of a Lu-rich fraction with 2.5M HCl. Hf was purified using EICHROM LNTM resin (column 2 of Bast et al., 2015). The procedural blank averaged 7 pg Lu and 36 pg Hf ($^{176}Hf/^{177}Hf$ assumed as 0.28216) and Hf blank was significant (0.3-38 mol %) in all analyses. Isotopic data were acquired on a Thermo-Finnigan Neptune MC-ICPMS equipped with standard nickel sampler and H-type skimmer cones as well as two 10-12 Ohm Faraday detectors to record signals on ^{175}Lu and ^{177}Hf during Hf isotope analysis. Hf fractions were picked up in 4% HNO_3-1% HF and aspirated via a PFA nebulizer and Cetac Aridus 2 desolvator (uptake rate 0.1 ml/min). Typical signals were 0.4-0.8 V of total Hf from solution with 0.5-1 ppb Hf. Interference from HREE was mostly negligible, a result of excellent separation of Hf from HREE in the 2-column procedure. Mass bias and spike stripping corrections were done offline, using $^{179}Hf/^{177}Hf$ =

0.7325 for internal normalization, with error propagation based on the Monte Carlo technique outlined in Sprung et al. (2013). Hf extracted from USGS standard BCR-2 was measured at concentrations similar to those obtained for the carbonate samples (0.5-1 ppb) and yielded an average of 0.282872±68 (95% CL, n = 8), in excellent agreement with reference values; the large uncertainty (equivalent to an external precision, 2sd, of ±0.00016, or ±5.8 εHf units) reflects the small Hf signals. Lu isotope dilution runs were done as described in Sprung et al. (2013). The Lu decay constant is $1.867x10^{-11}$/yr.

6.4 Results

6.4.1 Rb-Sr isotope results

Hydrothermal Ca-Fe-Mg-Mn carbonates at Olympic Dam have strongly variable Sr concentrations (2-688 ppm, avg. 98 ppm, Fig. 6.1 A) and Rb/Sr is low in most samples: 58 of 75 samples listed in Table 6.1 have $^{87}Rb/^{86}Sr \leq 0.05$. The remaining 17 samples have $^{87}Rb/^{86}Sr$ from 0.08 to 2.89, and the average for the entire data set is 0.155 (Fig. 6.1 B). With some exceptions, Sr concentrations tend to be lowest in siderite but otherwise there is little systematic difference between the various carbonate minerals. Present-day $^{87}Sr/^{86}Sr$ varies from 0.70769 to 0.75241 with an average at 0.72076; the Sr-weighted average is 0.72834 (Table 6.1, Fig. 6.1 C). In the Rb-Sr isochron diagram (Fig. 6.1 B), most of the data points plot at low Rb/Sr. Points with higher Rb/Sr tend to be associated with high $^{87}Sr/^{86}Sr$ which probably reflects local ^{87}Sr ingrowth. However there are no consistent, well-supported linear arrays that could be interpreted as isochrons. A close-up (Fig. 6.1 B) shows that for samples with low Rb/Sr (say, $^{87}Rb/^{86}Sr \leq 0.2$), local ingrowth over 500-1590 Ma could only produce a fraction of the observed $^{87}Sr/^{86}Sr$ variation. Present-day $^{87}Sr/^{86}Sr$ in such samples is thus a good proxy for initial $^{87}Sr/^{86}Sr$. On this basis, measured $^{87}Sr/^{86}Sr$ in carbonates representing the 7 associations is compared in Fig. 6.1 C. In this compilation, associations 6 and 7 (laminated siderite; conglomerate cement) show relatively limited ranges (~0.715-0.725) while groups 3 and 5 (red and green sandstone; massive fluorite-barite veins) are most diverse. There is no obvious correlation of $^{87}Sr/^{86}Sr$ with association (host rock type) although the lowest ratios (<0.710) only occur in associations 1-3.

Two samples of anhydrite from one of the association 1 calcite veins are rich in Sr (~1500 ppm) and have very low Rb/Sr (Table 6.1). Measured $^{87}Sr/^{86}Sr$ (0.7180-0.7204) is within the range of associated calcite.

6.4.2 Sm-Nd isotope results

Nd concentrations in the carbonates also vary strongly (0.08-177.5 ppm, avg. 25.3 ppm), as do Sm/Nd ratios ($^{147}Sm/^{144}Nd$ = 0.028-0.548, avg. 0.177, Figs. 6.1 D and 6.2 A, Table 6.1). Sample OD675, a siderite of association 2 (granite-dominant breccia) is very rich in LREE (3236 ppm, not included in average). No obvious correlations exist between carbonate association or mineral type and Nd concentration, or between Nd concentration and Sm/Nd (not shown). Sm/Nd shows least variation in associations 3, 5 and 6 (sandstone; fluorite-barite veins, laminated siderite, respectively), and is most variable in association 4 (mafic-ultramafic, Fig. 6.2 A). Consistently high Sm/Nd is observed in association 7 (conglomerate cement). In general, Sm/Nd in Olympic Dam carbonates is high relative to the host granite and the breccia complex (Figs. 6.1 D and 6.2), as reflected in the high average $^{147}Sm/^{144}Nd$ (see above). Two samples of anhydrite from one of the association 1 calcite veins have 41-46 ppm Nd and the lowest Sm/Nd observed in this association.

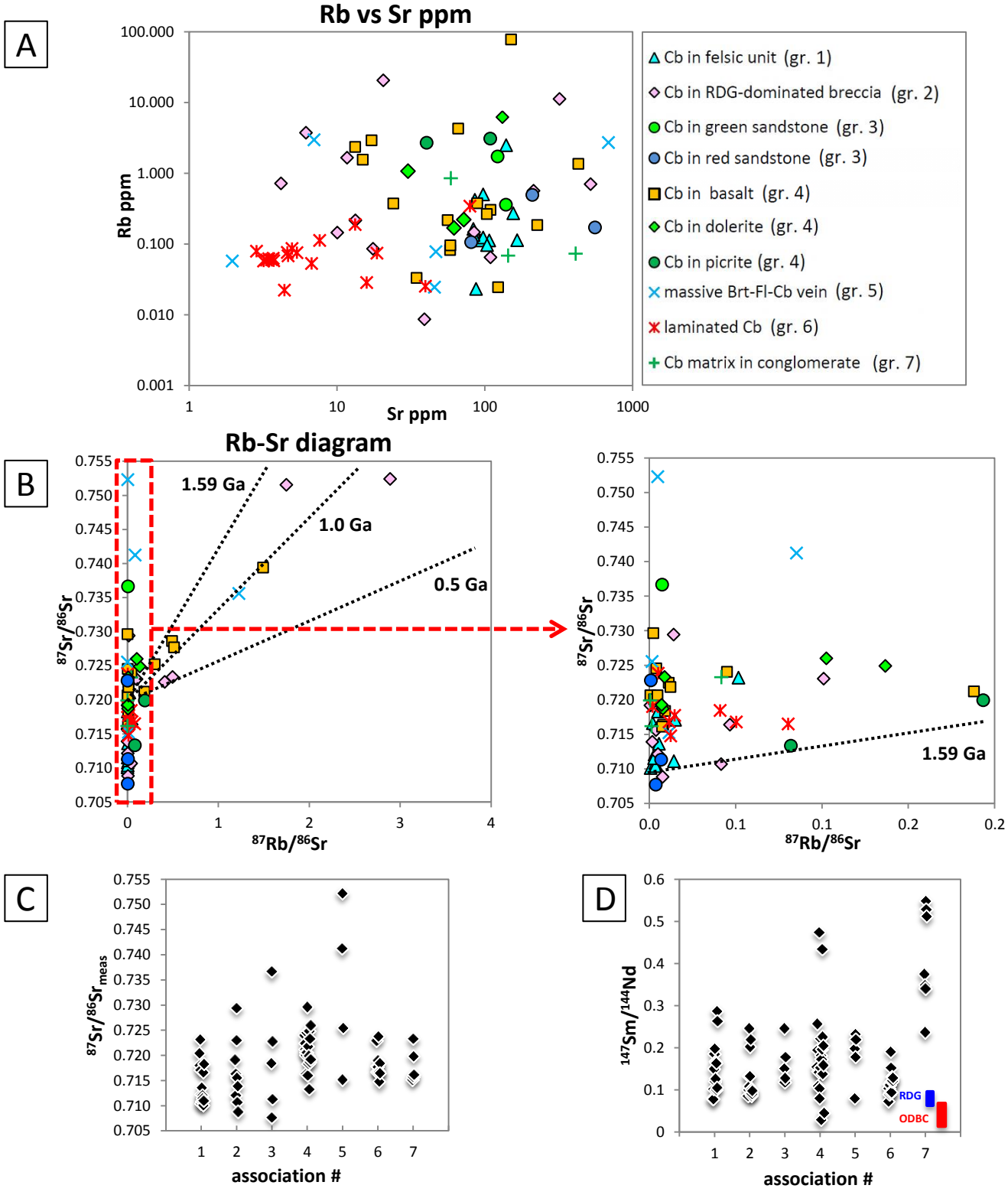

Fig. 6.1: (A) Rb and Sr concentrations for Olympic Dam carbonate (Cb) associations 1-7. (B) Rb-Sr isochron diagram with reference isochrons for 1590, 1000 and 500 Ma anchored at 0.720. Inset shows data with $^{87}Rb/^{86}Sr \leq 0.2$, with reference isochrons for 1590 Ma anchored at 0.710. Legends in (A) and (B) are same. (C) Present-day $^{87}Sr/^{86}Sr$ distinguished by association, with samples $^{87}Rb/^{86}Sr > 0.2$ omitted to avoid large ingrowth effects. (D) Distribution of $^{147}Sm/^{144}Nd$ ratios in Olympic Dam carbonates; fields for host granite (RDG) and Olympic Dam Breccia Complex (ODBC) shown for comparison. Brt: barite, Fl: fluorite.

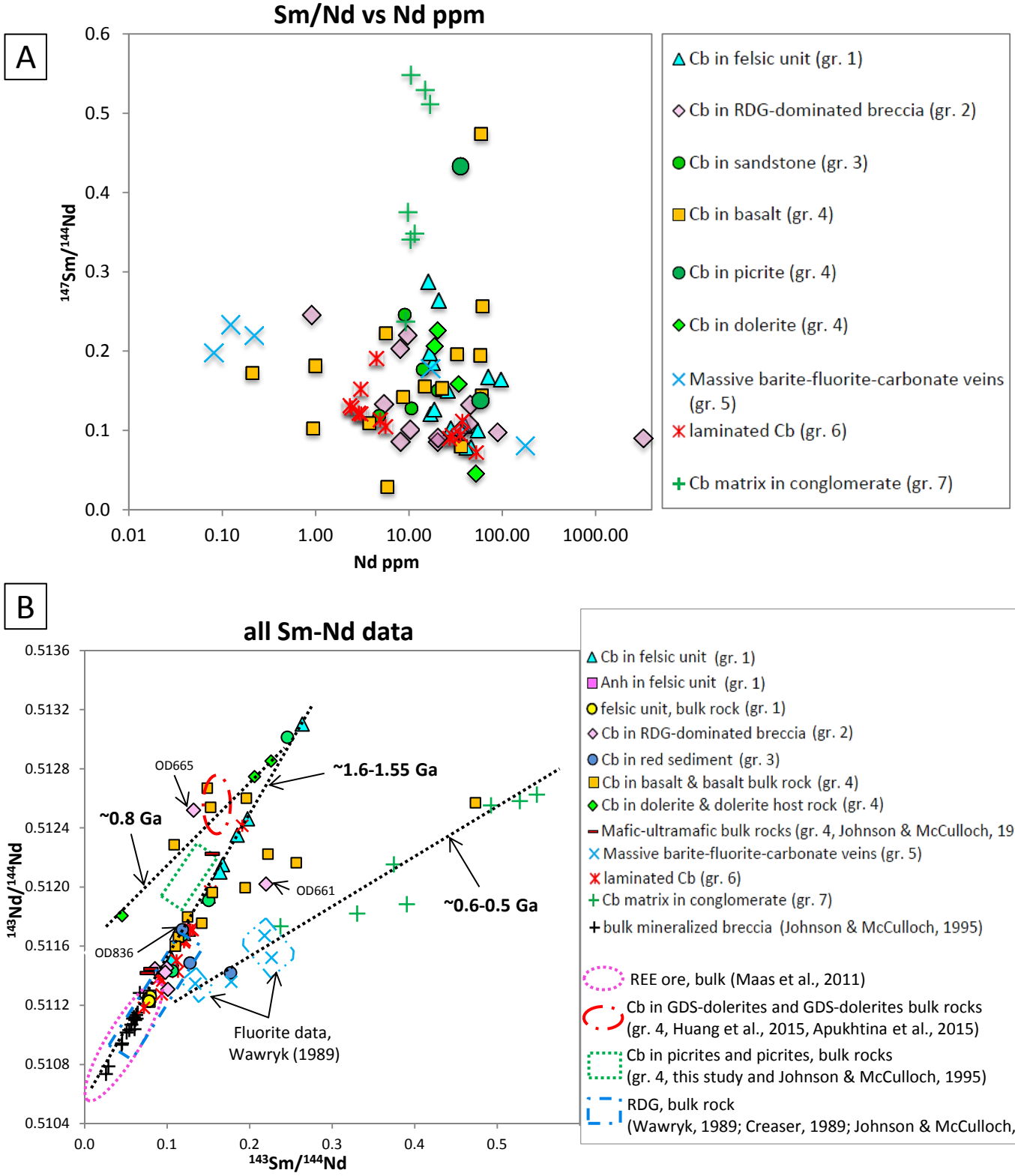

Fig. 6.2: (A) $^{147}Sm/^{144}Nd$ vs. Nd ppm for associations 1-7. (B) Overview of Sm-Nd results of all carbonate (Cb), anhydrite (Anh), and host rock samples. Some literature results (e.g., granite, Creaser, 1989; Johnson and McCulloch, 1995; Wawryk, 1989; fluorite, Wawryk, 1989; Maas et al., in preparation a; diverse mafic-ultramafic rocks, Johnson and McCulloch, 1995; GDS-type dolerites, Apukhtina et al., 2015; Huang et al., 2015; REE-rich breccias, Diemar, 2014) have been plotted in the same diagram. Note the position of the samples OD661 and OD665, see text for explanations. Cb: carbonates.

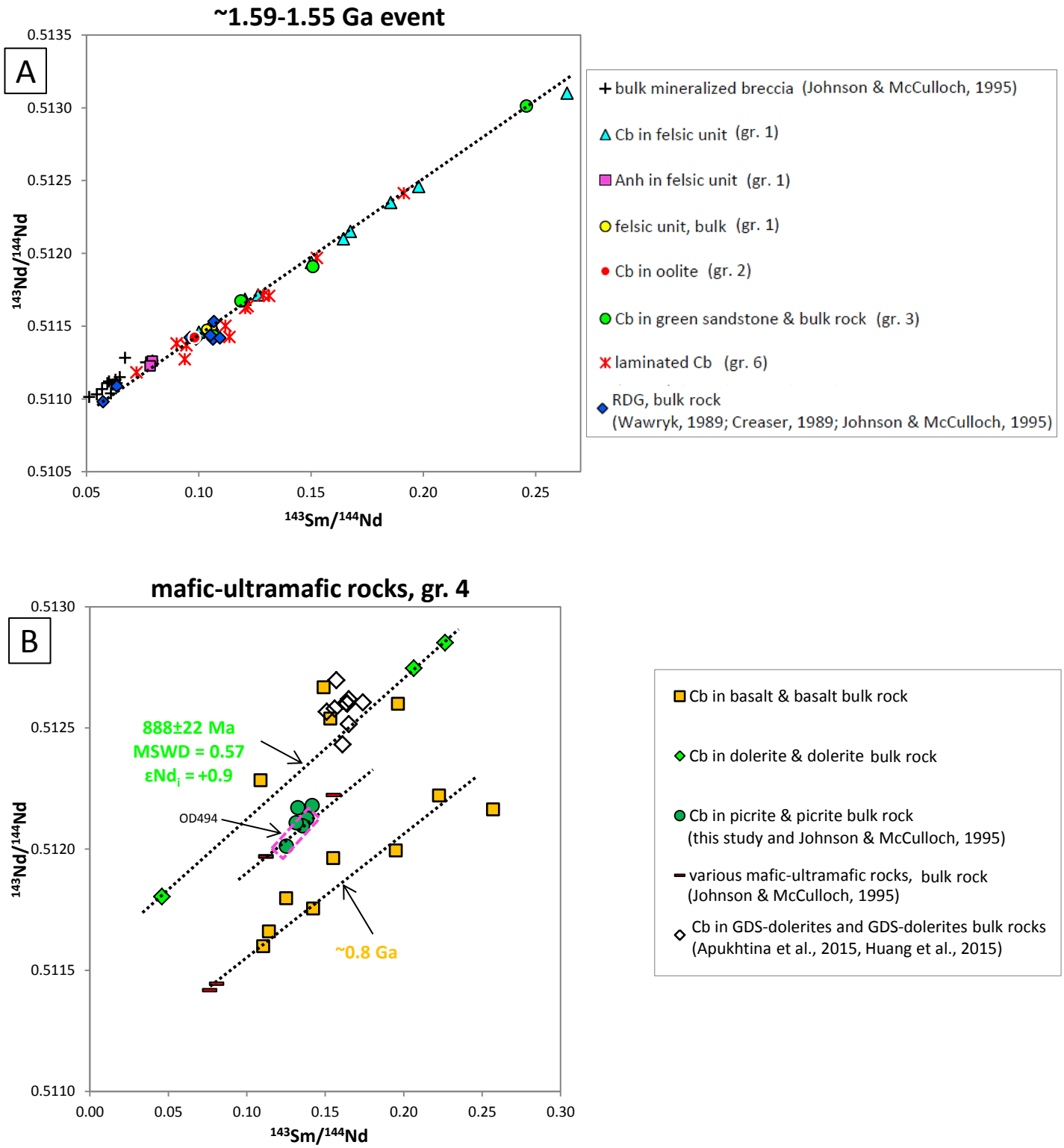

Fig. 6.3: (A) 1.59-1.55 Ga Sm-Nd isotope trend for carbonates (Cb) from association 1 (RD2773, Apukhtina, in preparation a), 6 (laminated siderite), 3 (carbonate in green sediment), and 2 (e.g., sideritic oolites). Results for host granite (Creaser, 1989; Wawryk, 1989; Johnson and McCulloch, 1995), felsic unit, anhydrite (Anh, Apukhtina et al., in preparation a) and ore breccia bulk samples (Johnson and McCulloch, 1995) lie on the same isochron. (B) Sm-Nd isochron diagram for association 4 (carbonate veins in 1.59 and 0.82 Ga mafic-ultramafic rocks); data appear to define three 0.9 to 0.8 Ga sub-parallel trends for picrite, dolerite and basalt and associated carbonates, indicating post-granite (i.e., post-1.59 Ga) magmatic-hydrothermal event(s).

In the Sm-Nd isochron diagram (Figs. 6.2 B and 6.3), the data show a number of more or less distinct trends. Sm-Nd data for calcite and anhydrite from association 1 (Fig. 6.3 A), all from a short interval in drillcore RD2773, define a linear array equivalent to an apparent age of 1546±33 Ma (MSWD = 3.2, εNd_i = -4.0). This age is based on data for 10 calcites, 2 anhydrites and 2 samples of the host rock, a rhyolitic rock referred to as *'felsic unit'* in mine terminology (see also Apukhtina et al., in preparation a; Maas et al., in preparation b). $^{87}Sr/^{86}Sr$ for association 1 minerals ranges from 0.71007 to 0.72321 (Fig. 6.1 C). Sm-Nd data for 4 of 6 carbonates dispersed in granite-dominated breccia (association 2), including oolitic siderite OD1001, cluster close to the composition of the host granite; the two other samples have higher Sm/Nd and more radiogenic Nd (Figs. 6.2 B and 6.3). No direct Sm-Nd age information can be retrieved from these data. Dolomite-ankerite in two carbonate veins within green clastic sediments (association 3) show considerable dispersion in Sm/Nd and $^{143}Nd/^{144}Nd$ and plot within the steep 1546±33 Ma array of association 1 calcites-anhydrites, as does dolomite-ankerite OD836 from red sandstone, suggesting a similar age. Two further vein sample from green sediment plot away from the 1546 Ma trend (Figs. 6.2 B and 6.3 A).

Carbonates of association 4 (Fig. 6.3 B) occur in (i) highly altered mafic-ultramafic rocks including inferred picrites believed to be ~1.59 Ga old (Huang et al., 2016), and in (ii) veins within much better preserved ~0.82 Ga GDS-type dolerite dykes (Huang et al., 2015). Sm-Nd isotope data for carbonates from the older basalts and picrites scatter widely and do not define consistent trends. Some plot with the 1546 Ma association 1 calcites, others plot well above this trend, while a third group defines a much shallower, scattered trend which is subparallel to the ~0.52 Ga trend of the association 7 carbonates, see below. Three analyses of carbonate from veins in 0.82 Ga dolerite dykes define a trend which intersects a cluster of dolerite whole rock analyses (Huang et al., 2015; Apukhtina et al., 2015) and provide an apparent Sm-Nd age of 888±22 Ma (MSWD = 0.57, εNd_i = +0.9). While technically older than the age of the host dolerites, this 3-point age is nevertheless broadly consistent with the dolerite age, as is the positive initial εNd, a characteristic of the 0.82 Ga dolerite dykes.

Sm-Nd data for siderites from laminated carbonate (association 6) consistently plot within the 1546 Ma association 1 trend and thus probably have a similar age. Because so many of the carbonate data points lie within this array, we will refer to the array as *'Main array'* (Figs. 6.2 B and 6.3 A). Regression of the 11 association 6 siderite data points yields an apparent age of 1598±170 Ma (MSWD = 19, εNd_i = -4.2), consistent with early formation during the history of the breccia complex. Finally, siderites and dolomite-ankerite within massive (unbrecciated) fluorite-barite veins (association 5) should be ~500 Ma old, based on fluorite Sm-Nd ages (Wawryk, 1989; Maas et al., in preparation a). A single Sm-Nd isotopic analysis for dolomite-ankerite from one of these veins plots below the 1546 Ma association 1 Sm-Nd trend on an extensive shallow trend populated by association 5 fluorites (not shown), one association 3 (red sandstone) carbonate and one association 4 carbonate from highly altered, possibly 1.59 Ga basalt (see above), and all association 7 (conglomerate cement) carbonates. The latter are characterized by high Sm/Nd ratios (Fig. 6.2 A). Pooling of the data for 9 carbonate samples from four associations produces an apparent Sm-Nd age of 522±83 Ma (MSWD = 94, εNd_i = -22.8).

6.4.3 U-Th-Pb isotope results

Pb isotope data for association 1 calcites have <1 ppm U, Th/U from 0.1 to 1.5, and high Pb contents (6.4-17.3 ppm, Table 6.2); as a consequence, U/Pb and Th/Pb ratios are low. Pb isotope ratios vary strongly ($^{206}Pb/^{204}Pb$ = 17.94-

109.65, $^{208}Pb/^{204}Pb$ = 36.73 to 62.89) but this variation is unsupported by measured U/Pb and Th/Pb ratios. The uranogenic Pb results define straight arrays in the $^{207}Pb/^{204}Pb$-$^{206}Pb/^{204}Pb$ and inverse ^{207}Pb-^{206}Pb diagrams (Fig. 6.4). The former yields a 1585±23 Ma (MSWD = 25) Pb-Pb isochron age.

Association 6 laminated siderites have very different U-Th-Pb systematics. U concentrations are highly variable (0.55-165.6 ppm), Th/U is <0.1, and Pb concentrations are high (27.2-148.1 ppm); as a consequence, U/Pb ratios vary strongly ($^{238}U/^{204}Pb$ = 0.22-116.4) while Th/Pb is low throughout. $^{206}Pb/^{204}Pb$ varies from 16.66 to 19.95 but does not correlate with U/Pb. $^{208}Pb/^{204}Pb$ is uniformly low (36.20-36.42), consistent with low Th/Pb. In the uranogenic Pb isotope diagram (Fig. 6.4 A-B), the data form 2 short arrays, one of which is broadly collinear with the association 1 calcite trend, the other plots below this trend. In the inverse ^{207}Pb-^{206}Pb diagram (Fig. 6.4 C), the association 6 data plot near the upper end of the association 1 trend, possibly indicating a similar age.

6.4.4 Lu-Hf dating of calcite and siderite

Six samples of laminated siderite (association 6) have heterogeneous Lu (7-1686 ppb) and Hf (0.045-9.79 ppb) concentrations (Table 6.3). Within-sample heterogeneity (notably sample OD1051) is almost certainly related to yield problems and incomplete spike-sample equilibration in HNO_3-H_2O_2 experiments. $^{176}Lu/^{177}Hf$ (4.9-98) and $^{176}Hf/^{177}Hf$ (0.349-3.546) ratios are high and variable, and therefore favorable for dating. The highly radiogenic nature of the results means that calculated ages are not strongly affected by blank corrections (e.g., Barfod et al., 2005), and ages were therefore derived from uncorrected data. Regression of all 9 data points in the isochron diagram yields an *'age'* of 1687±150 Ma (MSWD = 2736). After exclusion of the most radiogenic point (OD1045.2), the pooled *'age'* changes to 1460±120 Ma (MSWD = 1944, Fig. 6.5 A). The most precise apparent age (MSWD = 1.8, 1428±3 Ma) is produced by combining the results for OD1047.2, OD1048.2 and OD1051.2, all from HCl-H_2O_2 digests which are considered to produce more reliable siderite data than the HNO_3-H_2O_2 digests. The initial $^{176}Hf/^{177}Hf$ ratios of these regressions are imprecise and strongly variable relative to plausible Hf reservoirs at Olympic Dam, and are therefore not discussed.

Five calcite samples (association 1) have generally higher concentrations of Lu (633-8248 ppb) than the siderites, while Hf concentrations (0.54-6.12 ppb) are broadly similar. $^{176}Lu/^{177}Hf$ (262-26137) and $^{176}Hf/^{177}Hf$ (7.32-847) are therefore much higher than for the siderites. Despite concerns over sample loss during some dissolutions, the data form a near-linear array in the isochron diagram. If OD830C2, the most radiogenic point and a clear outlier, is excluded, the remaining 7 points yield an apparent age of 1482±61 Ma (MSWD = 74, Fig. 6.5 B). The most precise age (MSWD = 0.11, 1472±20 Ma) is obtained for analyses OD826, 829 and 829.2; these are considered the most reliable of the calcite analyses because there was no sample loss during dissolution.

By analogy with isotopic data for other highly radiogenic minerals (e.g., Rb-Sr mica, Re-Os molybdenite, U-Pb zircon), it is possible to derive single sample Lu-Hf model ages for the siderites and calcites. Although the exact composition of the assumed *'common'* Hf anchor used for the calculations has little influence, we chose present-day $^{176}Lu/^{177}Hf$ and $^{176}Hf/^{177}Hf$ ratios of 0.015±0.005 and 0.28216±0.00002, respectively. The Lu/Hf ratio is an often-used estimate for average continental crust while the $^{176}Hf/^{177}Hf$ is based on Hf isotope data for Hiltaba event-derived zircons (Belousova et al., 2009); a very similar independent estimate is obtained from the global Hf-Nd isotope correlation (e.g., Vervoort et al., 1999), when using the average of numerous Sm-Nd isotope analyses for the ODBC (Maas et al., in preparation a) to infer its average $^{176}Hf/^{177}Hf$. Two-point model ages for the siderites range from 1394 to 1870 Ma

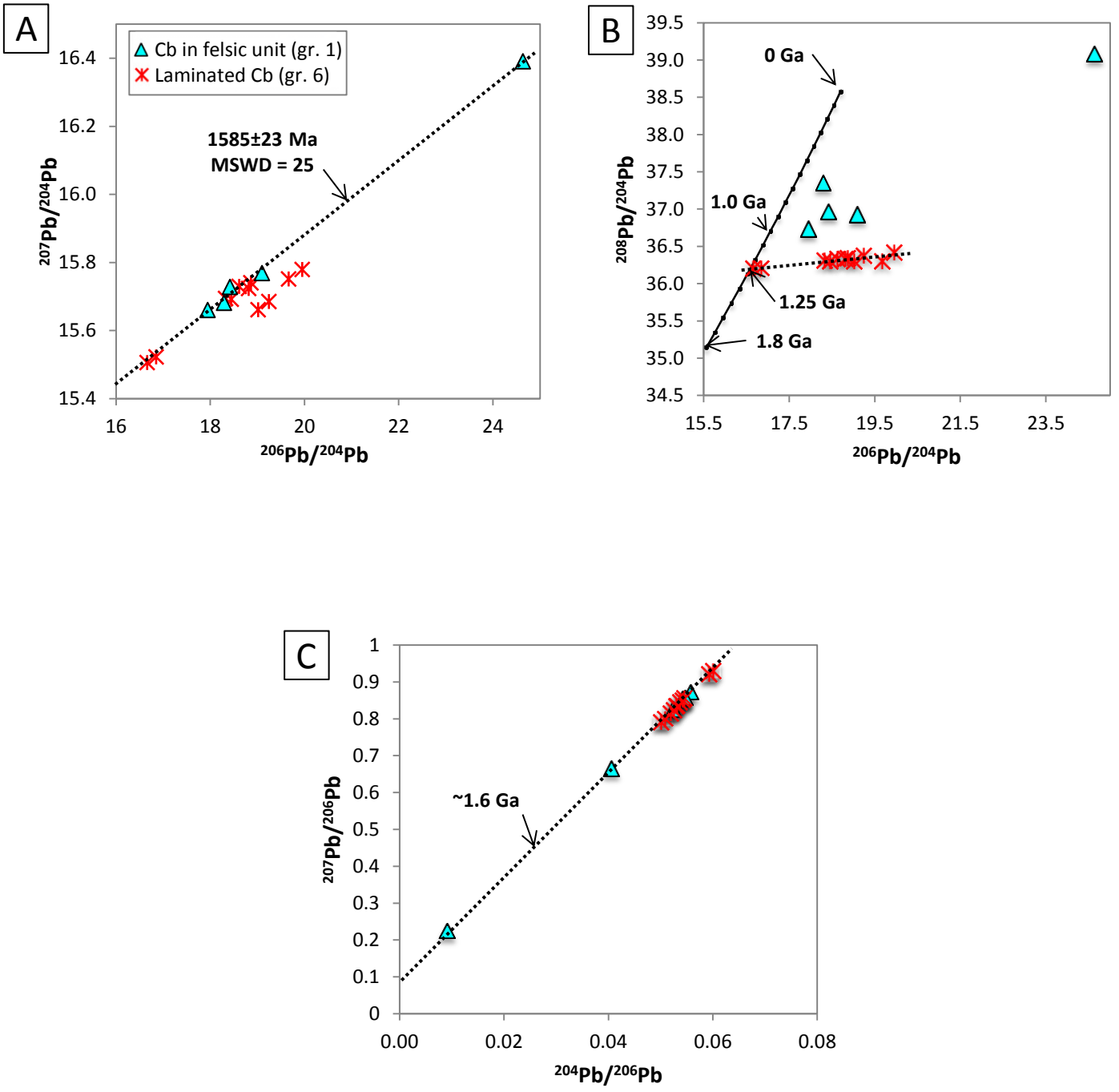

Fig. 6.4: Pb isotope systematics for 1.59-1.55 Ga carbonates (Cb) from association 1 (RD2773, Apukhtina et al., in preparation a) and 6 (laminated siderite). $^{207}Pb/^{204}Pb$ vs $^{206}Pb/^{204}Pb$ (A) data yield a ^{207}Pb-^{206}Pb isochron age of 1585±23 Ma for association 1. $^{208}Pb/^{204}Pb$ in association 6 siderites correlate well with $^{206}Pb/^{204}Pb$ (B), producing a radiogenic-common Pb mixing which intersects the crustal Pb growth curve (Stacey and Kramers, 1975) at ~1.25 Ga which produces a minimum age for the common Pb component (see text). (C) Inverse Pb-Pb ($^{207}Pb/^{206}Pb$ vs $^{204}Pb/^{206}Pb$) plot showing all association 1 and 6 data to lie on same ~1.6 Ga array. Legends in (A-C) are same.

A

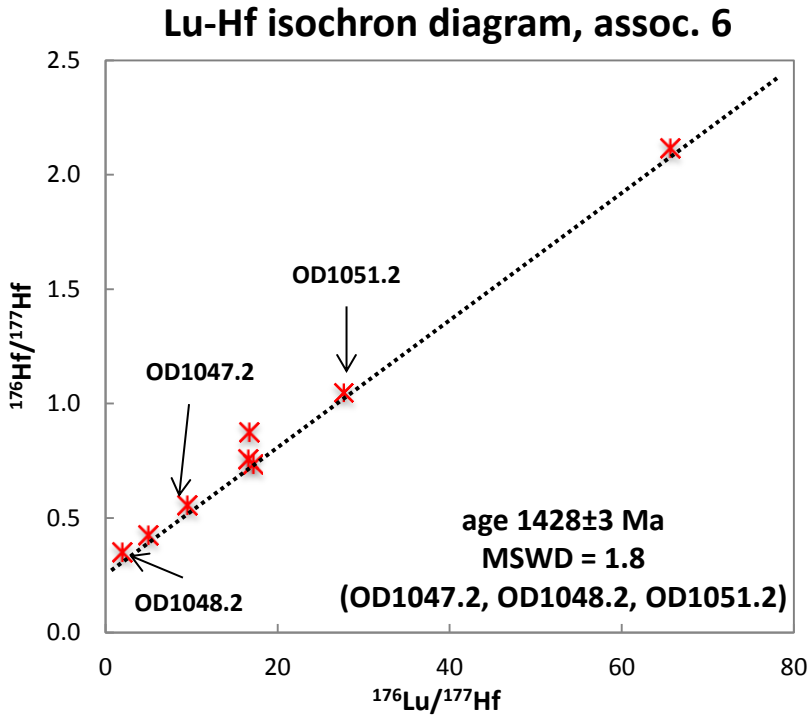

B

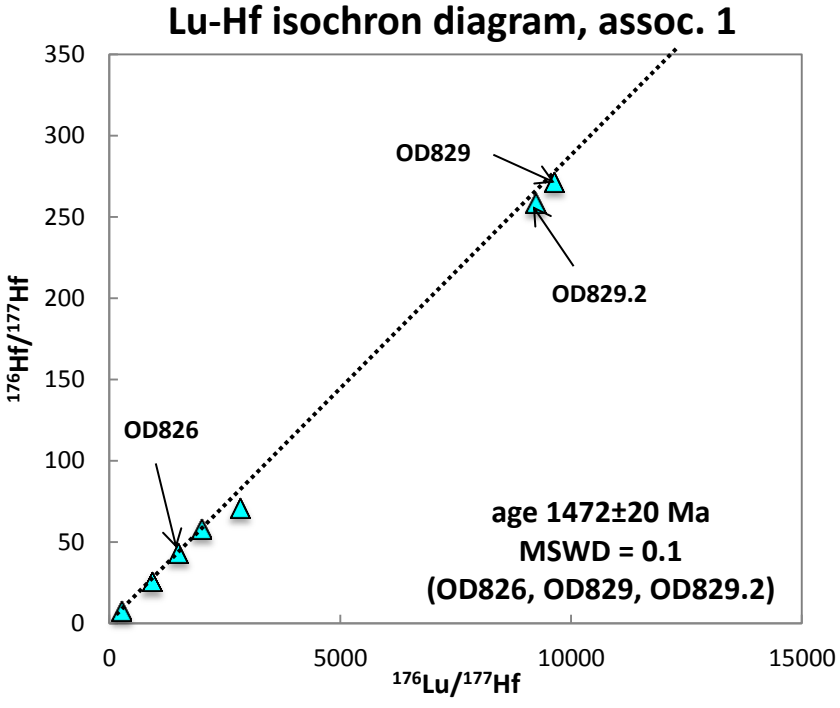

Fig. 6.5: Lu-Hf dating of associations 6 (siderite, A) and 1 (calcite, B); the isochrons and ages given are for subsets of the two data sets.

(average 1593±179 Ma, 1sd), those for the calcites range from 1320 to 1707 Ma (average 1485±111 Ma, 1sd). Model ages for the analyses considered to be the most reliable are 1460-1850 Ma for siderites and 1477-1510 Ma for calcites.

6.5 Discussion

The results from this study substantially increase the radiogenic isotope data available for the Olympic Dam deposit. They add to Sr isotope data for two dolomites (meas. $^{87}Sr/^{86}Sr$ = 0.71387, 0.71674) from fluorite-barite veins which are probably equivalent to the host rocks of association 5 carbonates (Wawryk, 1989). The Sm-Nd data for association 1 calcites (Table 6.1) were also part of an earlier study (Apukhtina et al., in preparation a) and are listed and discussed here for completeness.

6.5.1 Age constraints for carbonates

Calcite veins (association 1) from paragenetically early magnetite-apatite-quartz-pyrite-uraninite IOCG mineralization within an unbrecciated porphyritic facies of the RDG (the '*felsic unit'*) provide age constraints that are broadly consistent with U-Pb ages for apatite (1583±7 Ma) and uraninite (1594±6 Ma) from this assemblage (Apukhtina et al., in preparation a). Calcite isochron ages of 1546±33 Ma (Sm-Nd, Apukhtina et al., in preparation a, Fig. 4.5) and 1585±23 Ma (Pb-Pb, this study, Fig. 6.4) indicate vein emplacement coeval with or within 10s of Ma after formation of the initial IOCG mineralization. The Lu-Hf ages are younger (1472±20 Ma isochron, Fig. 6.5 B, model ages 1477-1510 Ma) which may be a result of slight disturbance of calcite Lu-Hf systems. Hf concentrations are very low (<0.01 ppm) and Lu/Hf ratios are extreme relative to vein host rocks, and small degrees of exchange over ~1500 Ma may have affected the calcites. $^{87}Sr/^{86}Sr$ in the calcites varies from 0.71007 to 0.72321, higher than initial $^{87}Sr/^{86}Sr$ in the host granite as derived from magmatic apatite (0.7088-0.7089, Creaser and Gray, 1992). If the calcite Sr is derived from the felsic unit/host granite and IOCG-assemblage, the difference in $^{87}Sr/^{86}Sr$ implies a substantial age gap prior to emplacement of the calcite veins, to allow the development of higher $^{87}Sr/^{86}Sr$ in the granite. This would be consistent with the nominal difference between the calcite Sm-Nd age and the U-Pb ages for the granite (1593±5.6 Ma), felsic unit (1591±11 Ma) and magnetite-apatite assemblage (1594-1583 Ma, see above Jagodzinski, 2014; Apukhtina et al., in preparation a).

Four of the six analysed carbonates in granite-dominated breccia (association 2) have Sm-Nd isotope compositions that are very similar to those of the host RDG (Fig. 6.2 B) while two further examples, OD661 and OD665, have higher Sm/Nd and more radiogenic Nd. While no age information can be extracted from the granite-like compositions, the position of OD661 and OD665 outside the ~1590-1550 Ma main Sm-Nd isotope array implies they formed from fluids with non-granitic Nd (with distinct initial $^{143}Nd/^{144}Nd$), or they are a different age. For example, OD665 plots close to a cluster defined by the 825 Ma dolerites and to some of the carbonate samples hosted in 1.59 Ga basalts, and could thus be related to basaltic rocks, one of the major non-granite clast components in the breccia, or to carbonate-bearing fluids with basalt-like (relatively radiogenic) Nd. OD661 plots to the right of the Main Array, with other carbonate samples extracted from 1.59 Ga basalt (see above), and on a trend which runs sub-parallel to the ~0.52 Ga association 7 trend. This suggests that OD661 may be 0.5 Ga old. The other carbonates in association 2 are possibly older although it is impossible to be more precise with the available data. Sr isotope data for eight low-Rb/Sr association 2 carbonates are in the range 0.7088-0.7294 while five high-Rb/Sr examples form a broad array with a slope equivalent to 900 Ma. The data

are too scattered to derive any firm age constraints. The $^{87}Sr/^{86}Sr$ of oolitic siderite OD1001 (Fig. 3 A) is within the range of inferred magmatic signatures of the host granite (0.70883 vs 0.7088-0.7089) which supports a near-1.59 Ga age for inclusion of this particular clast. Apukhtina et al. (in preparation b) suggest that oolitic siderite within the breccia complex may be a remnant of older BIF, with implications for the source of metals (Fe) and the geological history of the breccia complex.

Carbonates in the bedded (green and red) sedimentary facies (association 3) plot in both the Main Array and in the ~0.52 Ga association 7 (Figs. 6.2 B and 6.3 A) trend. It is thus possible that carbonate veining in both green and red sandstones is 1.59-1.55 Ga old, with implications for the depositional age of these sediments (e.g., McPhie et al., 2011, 2016). Cambrian carbonates may also be present. All analysed samples from this association have low Rb/Sr, and measured $^{87}Sr/^{86}Sr$ (0.7077-0.7367) is thus close to the initial $^{87}Sr/^{86}Sr$. The lowest $^{87}Sr/^{86}Sr$ in this group is well below the magmatic $^{87}Sr/^{86}Sr$ in the host granite. It occurs in a sample OD836 which lies on the Sm-Nd Main Array. Because it is from a vein in red sandstone, it must post-date the latter which itself postdates the host granite (McPhie et al., 2011, 2016). An influence from basaltic Sr might explain the low $^{87}Sr/^{86}Sr$ but would be unexpected within the hematite-rich, well-bedded sandstone facies (KHEMQ, see Table 2 of Ehrig et al., 2012; Fig. 5.2) which consists of detrital quartz, feldspar, granitic/volcanic fragments and detrital hematite, but lacks basaltic components; furthermore, average K/Ca is high, implying high Rb/Sr. The origin of this low $^{87}Sr/^{86}Sr$ is thus unclear.

Like the Sm-Nd data for associations 2 and 3, those for association 4 carbonates are diverse (Figs. 6.2 B and 6.3). Three of the carbonates extracted from inferred 1.59 Ga basalt plot in the Main Array and may thus be close in age to their host rocks. However, one of these carbonates is from sericite-altered dyke which yields a 1181±3 Ma Rb-Sr age (Maas et al., in preparation a). Two further carbonates, as well as one carbonate from inferred picrite OD 494 plot above the Main Array; no Nd isotope age information can be derived from these. Four more carbonates from 1.59 Ga basalt form a very shallow trend which is subparallel to the ~0.52 Ga trend of the association 7 carbonates, and may thus be of Cambrian age. The situation is less complex for association 4 carbonates collected from the 0.82 Ga dolerites. The three examples form a perfectly aligned array with an apparent age of 888±22 Ma and positive initial εNd, broadly consistent with age of the host dolerite. Carbonate $^{87}Sr/^{86}Sr$ does not correlate with position of the association 4 data points on the Sm-Nd diagram. The few high-Rb/Sr carbonate samples from ~1.59 basalt define a crude ~890 Ma age (not shown) although this is not considered robust. None of the samples has the low $^{87}Sr/^{86}Sr$ expected from a basaltic setting; the $^{87}Sr/^{86}Sr_{1593}$ (0.70587, Table 6.1) of OD82 is most likely an artifact of an inappropriate age correction. This implies that all of the carbonates were formed with variably radiogenic Sr derived from the breccia complex.

Association 5 carbonates are expected to be ~0.5 Ga old (Maas et al., 2011; Diemar, 2014; Apukhtina et al., in preparation b). This is confirmed by the Sm-Nd composition of dolomite-ankerite OD1005 which plots on the shallow ~0.52 Ga Sm-Nd trend defined by fluorite in fluorite-barite veins (association 5) and by association 7 carbonates. We consider this to be strong support for the robust nature of the age constraints derived the Sm-Nd data, not just for this sample but in general.

Like association 1 calcites, association 6 carbonates (laminated siderites) show very coherent Sm-Nd isotope systematics within (and helping to define) the Main Array (Fig. 6.3 A). This implies a 1.59-1.55 Ga age, supported by the rather imprecise formal Sm-Nd age (1598±170 Ma) for the 11 data points. The Pb isotope data show too little

dispersion to derive robust Pb-Pb ages although they appear to be consistent with those for association 1 calcites (Fig. 6.4 A-B). The low and uniform $^{208}Pb/^{204}Pb$ ratios (36.20-36.42) are likely to be close to initial ratios and support a Mesoproterozoic age. Measured $^{208}Pb/^{204}Pb$ and $^{206}Pb/^{204}Pb$ define a well-fitted line which may be a mixing line between unradiogenic initial Pb and a low-Th/U radiogenic component common to all analysed association 6 siderites. It intersects global Pb growth curves at ages between 1200 and 1600 Ma. A more precise model common Pb age would require a robust Pb growth curve for the Gawler craton (see Carr et al., 1995; Parr et al., 2004). Lu-Hf dating yields ages in the range 1400-1500 Ma, the most precise being a 1428±3 Ma 3-point age. As suggested for association 1 calcites, this age deficit relative to Sm-Nd data for the same samples may be related to subtle exchange effects between the extreme siderite Lu-Hf systems and the host rocks. Sr isotope ratios for the laminated siderites are comparatively homogeneous (0.7147-0.7238) and, if Sr was sourced within the breccia complex, require at least a few 10s of Ma age gap between emplacement of the granite and siderite deposition.

Association 6 laminated siderites are interpreted to be former ironstone/Fe-rich sandstones overprinted by hydrothermal siderite (Apukhtina et al., in preparation b). They occur preferentially near Masher's fault, inferred to be a long-lived structure which was remobilized during the Delamerian Orogeny in the Cambrian (Sugden and Cross, 1991). The age constraints presented here do not include any Cambrian signatures of the type inferred for associations 2, 3, 4 and 5.

Association 7 carbonates, like those in fluorite-barite veins (association 5), have the strongest independent age constraints. Dolomite-ankerite (+barite+celestite±Cu-Fe sulfides) form the cement of alternating beds of conglomerate-breccia and sandstone beds which unconformably overlie the eroded breccia complex and are estimated to have a maximum age of ~0.6 Ga old (Apukhtina et al., in preparation b). Their Sm-Nd isotope signatures clearly diverge from the Main Array, amplified by their uniformly high Sm/Nd, and yield a Sm-Nd age of 522±83 Ma. Analyses of members from several other carbonate associations plot within this trend and the same age is assigned to them. $^{87}Sr/^{86}Sr$ in association 7 covers the same range as in association 6 laminated siderites (0.7162-0.7233 vs 0.7147-0.7238), despite a potentially 1000 Ma age difference between these carbonate assemblages (see also Fig. 6.1 C).

6.5.2 Isotopic constraints on fluid sources and pathways

Johnson and McCulloch (1995) reported a small difference between the Nd isotopic signature of the 1593 Ma RDG (εNd_i ~-5) and various styles of Cu mineralization within the granite-hosted ODBC (εNd_i ~-3 to -2, the *'ore envelope'*), with data points for various types of breccia having intermediate compositions. They suggested this difference was consistent with 2-stage models involving two or more contrasting fluids (e.g., Oreskes and Einaudi, 1992) and allowed tracing of the Cu-enriched fluid to isotopically more primitive, perhaps basaltic (i.e. mantle) sources within the breccia complex. In a survey of other, much smaller Cu-Au IOCG prospects of the NE Gawler craton, Skirrow et al. (2007) did not find equivalent Nd isotopic shifts and concluded that a strong mantle influence may have been important in the formation of the unusually large mineralization at Olympic Dam. All of these studies are based on the assumption that ore-forming activity at Olympic Dam was concentrated near 1590 Ma, and all εNd values were corrected to this age. It is now clear that the ore formation and alteration started at ~1593 Ma but continued episodically over a long period, for at least 1 Ga (e.g. Maas et al., 2011; Ciobanu et al., 2013; Diemar, 2014; Kamenetsky et al., 2015), and some of these episodes are recorded in carbonate gangue (this study and Apukhtina et al., in preparation a, b). Furthermore, the Sm-Nd

isotopic systematics of the ODBC are now known to be far more complex than previously thought (Maas et al., in preparation a).

Carbonate εNd values show a large range (~+3 to -26, Table 6.1) but this depends strongly on the assigned ages which are not robust in every case. For example, age assignment is difficult for association 4 carbonates (for samples extracted from inferred 1.59 Ga basalt and picrite). In some cases, a default age of 1593 Ma produces unrealistically high (higher than contemporaneous depleted mantle, εNd_{1590} ~+6.5) or low (εNd_{1590} below -10) εNd values. Such signatures could reflect changes in Sm/Nd (open system behavior) during a mineral's history but for simplicity's sake it is assumed here that unrealistic calculated εNd is related to inappropriate age assignment. The inferred 1.59 Ga mafic rocks show strong Rb-Sr evidence for a 1.15-1.2 Ga sericite alteration event (Maas et al., in preparation a) but it is not clear which, if any, of the association 4 carbonates formed, or had their Sm-Nd systems reset, during this event. This remains a problem. An εNd vs time plot (Fig. 6.6 A) shows that the 1.59-1.55 Ga stages of the deposit produced carbonate εNd from ~-7 to ~0, broadly similar to the range reported for whole rocks of granite, breccia and Cu ore in Johnson and McCulloch (1995). εNd in association 1 calcites, which are the only carbonates clearly related to early single-stage, pre-hematite IOCG ore, clusters at -3.9 (for an age of 1550 Ma, average is -3.6 for 1593 Ma). Association 6 laminated siderites, dated at ~1.6 Ga, show similar signatures (εNd_{1550} = -4.7; εNd_{1590} = -4.3). Association 2 carbonates are more heterogeneous (Fig. 6.2 A) and ages were assigned as described in section 5.1. The samples assigned a 1.59-1.55 Ga age have εNd of -6.5 to -0.6 (n = 4). Carbonates in association 3 assigned 1.59-1.55 Ga ages show a similar range (εNd = -7.4 to -2.5) as do those in association 4 (εNd = -6.1 to -0.7). This suggests that granitic (crustal) Nd (εNd_{1590} = -5 to -3) is prominent in the early stage of the deposit. Some of the early carbonates record slightly higher εNd which may reflect a mantle component, as concluded by Johnson and McCulloch (1995).

Carbonates assigned a 0.82 Ga age are more mantle-like, with εNd mostly from +5 to 0 (Fig. 6.6 A). Tentative assignment of a 0.82 Ga age to some of the association 4 carbonates is based on unrealistic εNd_{1590} and the ~0.9 Ga carbonate Rb-Sr trend mentioned above. High εNd in carbonates of this period reflect the doleritic magmatism at 0.82 Ga and possible remobilization of radiogenic Nd in inferred 1.59 Ga mafic and ultramafic intrusives during that event and earlier.

Carbonates formed during the Cambrian occur in several associations and all show strongly negative εNd (-26 to -10, Fig. 6.6 A). Carbonate εNd_{520} signatures below ~-16 could reflect local crustal sources available at the time but higher εNd_{520} is not typical of the host granite or the breccia complex and appears to require more radiogenic sources, possibly in the basaltic rocks within the breccia complex.

Carbonate $^{87}Sr/^{86}Sr$ is much less dependent on age assignments than εNd because age corrections are small in the majority of analysed samples. On the other hand, Sr is known to be more mobile than Nd in hydrothermal and meteoric fluids, and local isotopic exchange is more likely (e.g., Zhao and McCulloch, 1993). As discussed earlier, the carbonate associations show differences in $^{87}Sr/^{86}Sr$ dispersion but all straddle the interval 0.715-0.725 (Fig. 6.1 C). If plotted against age, there is a broad increase of $^{87}Sr/^{86}Sr$ towards younger ages but a dominant 0.710-0.725 signature persists throughout (Fig. 6.6 B). Given the generally high Rb/Sr in local granite and breccia host rocks (avg. Rb/Sr for samples >80 ppm Sr is 1.09, present-day mean $^{87}Sr/^{86}Sr$ = 0.8088, Creaser and Gray, 1992; Ehrig et al., 2012), successive generations of carbonate would be expected to have ever-increasing $^{87}Sr/^{86}Sr$ if fluid Sr is sourced in local granite or

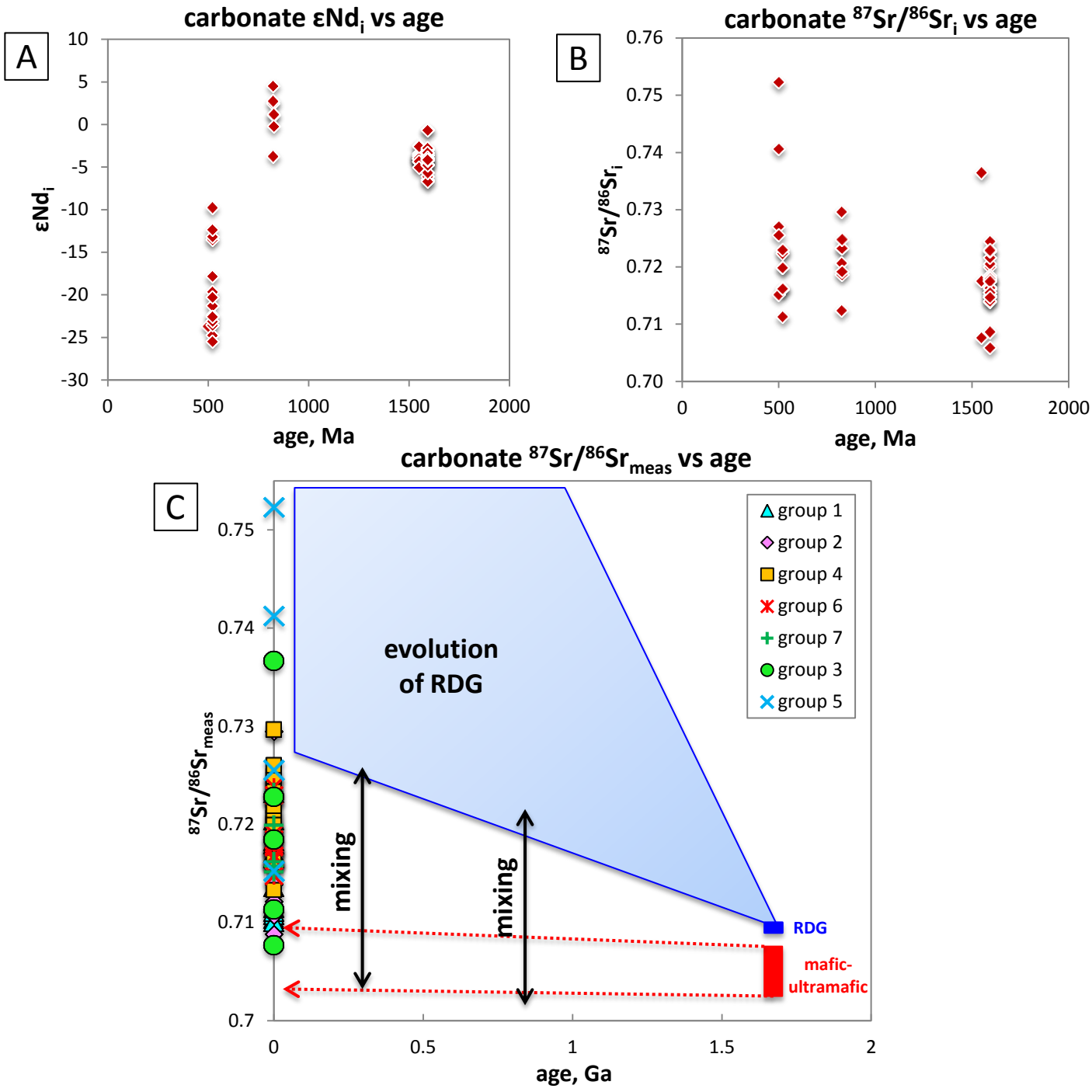

Fig. 6.6: (A) An εNd vs inferred age plot shows that the 1.59-1.55 Ga stages of the deposit produced carbonate εNd$_i$ from ~-7 to ~0, broadly similar to the range reported for whole rocks of granite (RDG), breccia and Cu ore in Johnson and McCulloch (1995). (B) A $^{87}Sr/^{86}Sr_i$ vs inferred age plot illustrates that there is a broad increase of $^{87}Sr/^{86}Sr_i$ towards younger ages but a dominant 0.710-0.725 signature persists throughout. (C) Schematic interpretation of carbonate $^{87}Sr/^{86}Sr$ compositions. Present-day Sr isotope ratios for low-Rb/Sr carbonates ($^{87}Rb/^{86}Sr<0.2$) on left axis, at 0 Ga, compared with the Sr isotopic evolution expected in low-Rb/Sr carbonates (and any other low-Rb/Sr mineral) formed at 1.59 Ga from a hydrothermal fluid in isotopic equilibrium with the host granite or 1.59 Ga mafic/ultramafic rocks (red arrows). Very few carbonate have the low $^{87}Sr/^{86}Sr$ expected in this scenario. Most of the carbonates have substantially higher $^{87}Sr/^{86}Sr$ which require appropriately radiogenic fluid sources. The host granite and breccia derived from it provide a strongly heterogeneous Sr isotope reservoir with rapidly increasing $^{87}Sr/^{86}Sr$, but only after several 10-100s of Ma of ageing. This means that almost all carbonates must be younger than the host granite, i.e. they must be post-1590 Ma even though in some cases the age difference may be small. $^{87}Sr/^{86}Sr$ signatures near 0.720 may have originated by exchange with both granite/breccia and the unradiogenic mafic/ultramafic rocks within the breccia complex (arrows labelled 'mixing').

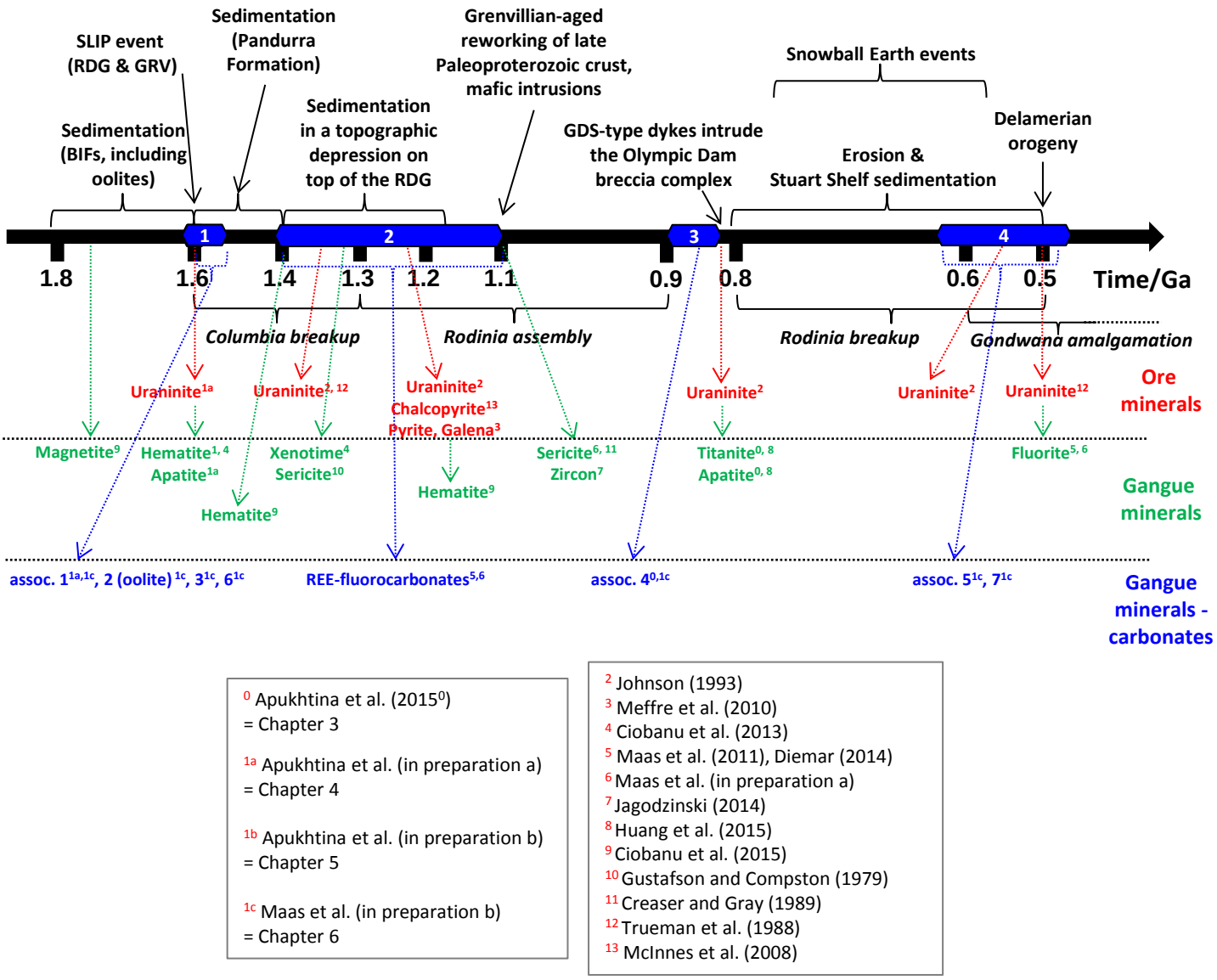

[0] Apukhtina et al. (2015[0]) = Chapter 3

[1a] Apukhtina et al. (in preparation a) = Chapter 4

[1b] Apukhtina et al. (in preparation b) = Chapter 5

[1c] Maas et al. (in preparation b) = Chapter 6

[2] Johnson (1993)
[3] Meffre et al. (2010)
[4] Ciobanu et al. (2013)
[5] Maas et al. (2011), Diemar (2014)
[6] Maas et al. (in preparation a)
[7] Jagodzinski (2014)
[8] Huang et al. (2015)
[9] Ciobanu et al. (2015)
[10] Gustafson and Compston (1979)
[11] Creaser and Gray (1989)
[12] Trueman et al. (1988)
[13] McInnes et al. (2008)

Fig. 6.7: Time chart for the major carbonate forming events within the breccia complex. Precipitation of Ca-Fe-Mg-Mn carbonates is confirmed for 1.59-1.55, ~0.8 and ~0.6-0.5 Ga; published data points to the deposition of REE-fluorocarbonates in an interval ~1.4-1.1 Ga (Maas et al., 2011, in preparation a; Diemar, 2014). Note that all of these carbonate-precipitation events correlate both with the ages for other hydrothermal ore (e.g., uraninite, ~1.59 Ga, Apukhtina et al., in preparation a; uraninite, ~1.40-1.3, ~1.22, ~0.83 and ~0.57 Ga, Johnson, 1993; uraninite, ~1.4 and ~0.5 Ga, Trueman et al., 1988; pyrite and galena, Meffre et al., 2010; chalcopyrite, McInnes et al., 2008) and gangue minerals (e.g., hematite, Ciobanu et al., 2013, 2015; Apukhtina, in preparation a; apatite, titanite, Huang et al., 2015; Apukhtina et al., 2015; Apukhtina et al., in preparation b; fluorite, Maas et al., 2011, in preparation a; xenotime, Ciobanu et al., 2015; zircon, Jagodzinski, 2014; sericite, Maas et al., in preparation a; Gustafson and Compston, 1979; Creaser and Gray, 1989).

All mineral precipitation stages presently known at Olympic Dam (1.59-1.55, ~1.4-1.1, ~1.1, ~0.8 and ~0.6-0.5 Ga) show a correlation with the some of the younger tectonic events in the Gawler craton. These are related to supercontinent cycles over an interval of nearly 1.3 Ga, including the breakup of supercontinent Columbia (~1.6-1.3 Ga, Rogers and Santosh, 2009; Srivastava and Rao, 2007), Grenville-resetting of some ~1.6 Ga old rocks (Wong et al., 2015), amalgamation and breakup of Rodinia (~1.3-0.9 and ~0.8-0.5 Ga, respectively, Li et al. 1999, 2008) and amalgamation of Gondwana (~0.6-0.3 Ga, Veevers, 2004).

breccia host rocks. The persistence of the 0.710-0.725 signature is reminiscent of the unexpected constancy of low initial $^{87}Sr/^{86}Sr$ in Phanerozoic shales observed by Goldstein (1988). This was interpreted in terms of buffering of radiogenic upper crustal clastic detritus by sedimentary carbonates and exchange with mantle Sr in marine hydrothermal environments. $^{87}Sr/^{86}Sr$ in Cambrian carbonates (and fluorites+barite in the same veins) may likewise be buffered by unradiogenic Sr from marine carbonates and basaltic rocks. Overall, $^{87}Sr/^{86}Sr$ in Olympic Dam carbonates is too high and too variable to have formed in a single stage at 1.59 Ga, as implied in all earlier models (Fig. 6.6 B).

6.6 Summary and conclusions

The data presented here, in combination with other recent radiogenic isotope work, allow the following conclusions to be drawn:

(1) Sm-Nd isotope studies of gangue carbonates document a diversity of likely formation ages, from 1.60-1.55 Ga to about 0.52 Ga. Pb isotope data support the oldest ages. The carbonate-based chronology is consistent with that for other minerals, including some other gangue minerals (fluorite, apatite, titanite, zircon) as well as ore minerals (e.g., Kamenetsky et al., 2015), providing additional evidence for the previously unrecognized multistage history of this large and unusual mineralization. Our study also provides yet another example of the utility of Sm-Nd dating for ore deposits. A first attempt at Lu-Hf dating of hydrothermal calcite and siderite with extremely high Lu/Hf ratios yielded results of adequate precision although the obtained ages were some 70-100 Ma younger than those from other techniques. It is suggested that this may be a result of cryptic exchange of the extremely radiogenic carbonate Lu-Hf systems (with ≤0.01 ppm Hf) with host rocks. Further work is necessary to explore this technique as a dating tool for carbonates.

(2) The post-1.59 Ga carbonate ages obtained here might be interpreted as a result of multiple or semi-continuous resetting in the long-lived thermal anomaly of the large U deposit. For example, complex radiometric age patterns have been reported from numerous U deposits. However, similar ages were obtained for minerals with a wide range of closure characteristics, and with different isotopic techniques. Furthermore, most of the Olympic Dam ages, in both carbonates and other minerals, correspond to a large-scale pattern of regional tectonic events (Fig. 6.7), confirming that Olympic Dam responded to most, if not all, regional geological events, presumably through changes in hydrology brought on by changing crustal stress regimes, or through magmatically-driven hydrothermal activity.

(3) Qualitative support for a protracted, multistage evolution of the carbonate minerals comes from $^{87}Sr/^{86}Sr$ ratios which tend to be much higher and more variable than expected if all carbonates (and associated ore minerals) formed near 1.59 Ga and remained undisturbed to the present day.

(4) A multistage history of gangue carbonate deposition is also consistent with their mineralogical, textural and compositional diversity. The low precision of the ages reported here almost certainly masks the true extent of complexity in carbonate depositional history, as observed in textures. Multiple reactivation of the breccia complex is also supported by the presence of lithologies that are younger than the host granite (McPhie et al., 2011, 2016).

(5) Nd isotopic tracing of the oldest (1.59-1.55 Ga) carbonates indicates fluids with isotopic signatures (εNd = -5 to -3.5) similar to those in the host granite. Higher εNd (to -1) in some carbonates may indicate a mildly radiogenic component. A similar isotopic range was observed in Johnson and McCulloch (1995); however, their *'ore envelope'* of εNd values slightly above those of the host granite is based on Cu ore whole rocks which would now be

suspected to be composites of multiple mineral generations and should therefore be viewed cautiously. Carbonates inferred to have formed at 0.82 Ga (1.0-0.8 Ga) have largely positive εNd, clearly showing a basaltic component, while the youngest known carbonate generation (0.52 Ga) has strongly negative and variable εNd (-26 to -10). The lower part of this range overlaps with the isotopic evolution for the host granite and the breccia complex, and the fluids involved in Cambrian carbonate deposition probably sourced LREE in such rocks, or externally in surrounding crustal rocks and/or overlying sedimentary basins. More radiogenic 0.52 Ga carbonates may have formed from fluids which had interacted with older basaltic rocks in the breccia complex.

(6) $^{87}Sr/^{86}Sr$ in almost all carbonates is higher than the 0.7088-0.7090 range for the host granite, requiring more radiogenic fluid Sr sources. $^{87}Sr/^{86}Sr$ in the range 0.710-0.725, common to the early carbonates, would be available in the granite within 10-200 Ma after emplacement. There is no evidence in the carbonates for mantle-like Sr ($^{87}Sr/^{86}Sr$~0.703-0.705), even in carbonate veins within basaltic/doleritic rocks, suggesting that Sr was dominantly derived from the host granite and breccia complex. The persistence of $^{87}Sr/^{86}Sr$ in the range 0.710-0.725 in 0.52 Ga carbonates (and in barites and fluorite, Wawryk, 1989; Maas et al., in preparation a), when fluid sources involved in pre-1.5 Ga carbonate formation would have evolved much higher $^{87}Sr/^{86}Sr$, suggests a different mix of fluid source rocks.

(7) Gangue and ore minerals at Olympic Dam formed diachronously, and distinct generations are known to occur in the same vein or hand specimen. This implies that interpretations of fluid inclusion, stable isotope or whole rock chemical data obtained without radiometric dating should be treated with caution.

(8) We speculate that the multistage nature of ore and gangue mineral deposition at Olympic Dam appears to be critical to the formation of a supergiant, polymetallic mineralization. Each mineralization stage had a distinct evolution, producing a large variety of gangue and ore minerals within the multiply reactivated breccia complex. The evolving breccia complex gradually incorporated diverse clast populations, ranging from possible BIF fragments to remnants of clastic sedimentary sequences of different ages, inheriting their metal endowment in the process. A process of the stepwise recycling and upgrading (Apukhtina et al., in preparation a) therefore appears to be a significant aspect of the deposit's evolution.

(9) Carbonates occur together with ore minerals in most IOCG deposits (Apukhtina et al., in preparation b). Typically, there is little detailed information on carbonate petrography and virtually no radiogenic isotope data. Our results from Olympic Dam show that carbonates are a rich source of information on the chronology and geochemical evolution of IOCG deposits.

Chapter 7: Conclusions

Prior to this study, very little published data existed for carbonates in the ODBC, and the information available consisted of generalised petrographic descriptions and a limited set of fluid inclusion and stable (C-O) isotopic data for siderite. For nearly 40 years since discovery of the Olympic Dam deposit, siderite was thought to have formed during an initial stage of IOCG mineralization, together with magnetite and pyrite. This mineralizing event was attributed to precipitation from ascending, hot (~400˚C), saline magmatic-hydrothermal brines. The diversity of carbonate compositions, textures and relationships with ore minerals, as well as the sources of carbon, timing of carbonate precipitation and the role of carbonates in the formation of the ODBC had remained unconstrained.

The current study documents the first detailed examination of the carbonate mineralogy at Olympic Dam. New resource maps show that the ODBC is both a polymetallic and a carbon anomaly. Moreover, the deposit-wide distribution of carbonates positively correlates with the distribution of ore minerals, implying a temporal and genetic relationship between carbonates and ore (Fig. 5.1). The most common carbonate mineral is siderite and siderite-rhodochrosite-magnesite solid solution, followed by calcite, dolomite-ankerite solid solution and REE-fluorocarbonates. Carbonate minerals occur in a range of host lithologies (variably brecciated RDG, bedded clastic sediment, mafic and ultramafic rocks of different ages, late fluorite-barite veins, and in conglomerate above the breccia complex), display a large variety of intergrowth and grain-internal textures, and are associated with many other gangue and ore minerals (almost all carbonate associations are ore-bearing, Fig. 5.3). Carbonate minerals represent *'snap shots'* of the deposit's evolution through time.

This study has shown that carbonate minerals are the result of multiple cycles of deposition, dissolution (partial or complete), recrystallization and reprecipitation (hence, continuous recycling and new input of carbonate material). The source of carbon in the carbonate minerals is difficult to determine but could plausibly include pre-granite BIF, the local host granite, clastic sedimentary rocks of the 'bedded facies', Pandurra Formation sediments, Neoproterozoic metacarbonates, mafic-ultramafic dykes, and diverse meteoric waters. Mixing of carbon from several sources, and recycling of older carbonate is likely (Fig. 5.13 A).

In this study, the various carbonate types were characterized in terms of mineralogy, composition, textures, host rock and age of deposition (Fig. 6.7). Strong evidence for diachronous carbonate deposition precludes a strictly paragenetic approach; instead the carbonates were assigned to seven carbonate associations mainly based on host rock. The following is a brief summary of the results presented in terms of carbonate age:

(1) Mesoproterozoic carbonates

This group includes oolite-related mineralized siderite (~1.59 Ga or older, based on low $^{87}Sr/^{86}Sr$), massive packages of mineralized laminated siderite (Lu-Hf age of 1428±3 Ma, Sm-Nd age of 1598±170 Ma) and largely unmineralized *'deep, early'* calcite veins (Lu-Hf age of 1472±20 Ma, Sm-Nd age of 1546±33 Ma, ^{207}Pb-^{206}Pb isochron age of 1585±23 Ma). These data imply early carbonate precipitation between ~1.59 and ~1.55 Ga which temporally correlates with the formation of the RDG, GRV and felsic unit. The GRV-Hiltaba event is in turn related to initial breakup of the supercontinent Columbia. The available geochronology does not allow resolution of what are almost certainly multiple early carbonate generations. For example, calcite veins which crosscut a carbonate-free, 'early, deep' magnetite-apatite-

pyrite-quartz-uraninite assemblage and its host granite/felsic unit (all ~1.59 Ga) could postdate its host rocks by several 10s of Ma. The setting of carbonate deposition (magmatic-hydrothermal, episodic hydrothermal activity with unknown heat sources) is therefore not clear. Unsurprisingly, given the location of the Mesoproterozoic carbonates within the granite, Sr-Nd isotopic data support an origin of carbonate-bearing fluids, or equilibration of such fluids with, the host granite and breccia complex.

A further stage of carbonate (REE-fluorocarbonates) precipitation is thought to have occurred in a period ~1.4-1.1 Ga. While this period overlaps the final stage of Columbia breakup and the start of amalgamation of Rodinia, with potential large-scale tectonic effects, there are currently few known events in the geological record of South Australia which might be correlated with this stage of carbonate deposition. However, a prominent sericitic alteration event, most clearly seen (and dated) in older Olympic Dam mafic and ultramafic rocks, but unknown prior to this work, occurred at 1200-1100 Ma and may be related to this carbonate deposition cycle.

(2) Neoproterozoic (~0.8 Ga) carbonates

Carbonates (mainly Ca-Mg-dominated compositions) formed during the Neoproterozoic period are related to the emplacement of relatively voluminous dolerites and basalts which have been confidently correlated with the regional 827 Ma GDS. The carbonates occur as veins, as alteration of the rock, and as amygdale fillings in these host rocks. Direct dating of carbonates (Sm-Nd age of 888±22 Ma) and associated gangue and accessory minerals suggest these carbonate-bearing assemblages formed not long after dyke emplacement at ~0.82 Ga. Fluids which formed the carbonates have a noticeable Nd isotopic contribution from their host dolerites/basalt but other isotopic signatures ($\delta^{13}C$, $^{87}Sr/^{86}Sr$) are more 'crustal' and reflect input from the host breccia complex. At the regional scale, the Gairdner Dykes mark the disintegration of supercontinent Rodinia.

(3) Ediacaran to Cambrian (~0.64-0.5 Ga) carbonates

The youngest carbonate generation at Olympic Dam are barren carbonates (mostly Ca-Mg dominated) which occur as cement in a conglomerate and sandstone interpreted to have formed at the unconformity which cuts the breccia complex. A late Neoproterozoic/Early Cambrian age for these cements is suggested both by the geology and by Sm-Nd dating (522±83 Ma). Siderite-dolomite associated with structurally late (unbrecciated) but sulfide-bearing barite-fluorite veins were identified as Cambrian in age, based on Sm-Nd dating of both the fluorite and the carbonates. It is suggested that the ~500 Ma carbonate generations may represent reworking of older carbonate generations, including dolomites of the ~630-600 Ma Nuccaleena Dolomite Formation, a cap dolomite related to the Marinoan glacial event. This event also correlates with the final stage of the breakup of Rodinia and early stage of amalgamation of Gondwana.

(4) Carbonates of unclear age

Age constraints for some of the carbonates are poor, e.g. those in mineralized carbonate veins within clastic sediments of the *'bedded facies'*, and some examples found in inferred 1.59 Ga mafic-ultramafic rocks. Their host rocks provide maximum ages of 1.59 Ga (for vein in mafic/ultramafic rocks) or perhaps slightly younger *('bedded facies'*) but the carbonates themselves could be as young as 0.5 Ga. Sm-Nd isotope constraints suggest that some may be as old as 1.59 Ga while others are 0.5 Ga. There is also some evidence that carbonates within inferred 1.59 Ga mafic/ultramafic hosts formed at 0.9-0.8 Ga, like the carbonates in GDS-type dolerites. Much of the siderite within the breccia complex is also of uncertain age. The siderite can form breccia clasts and breccia cement, it is intergrown with other gangue and ore

minerals and often exhibits zoning and mutual replacements with other carbonate types. Robust isochron dating of such heterogeneous material is almost impossible. Nevertheless, it appears that this siderite type is a product of recycling of the early carbonate generations.

This study suggests that carbonate deposition at Olympic Dam occurred episodically over a period of more than 1000 Ma. The local geology at Olympic Dam, and presumably the Stuart Shelf in general, appears to have responded to major geological events which are associated with the amalgamation and breakup of at least three supercontinents (e.g., Columbia, Rodinia and Gondwana). It is unclear if carbonates at other, smaller and simpler IOCG deposits in the Olympic Au-Cu Province have a similarly complex depositional history. While the geological history is shared by all these deposits, Olympic Dam is by far the largest and most complex, and carbonates at Olympic Dam reflect that. It is hoped that this study will encourage further research (including radiometric dating) on carbonate gangue at other IOCG deposits; this would establish similarities and differences which could be used to further refine models of IOCG ore genesis.

References

Agangi, A., Kamenetsky, V.S., McPhie, J., 2010. The role of fluorine in the concentration and transport of lithophile trace elements in felsic magmas: Insights from the Gawler Range Volcanics, South Australia. Chem Geol 273, 314-325.

Allen, S., McPhie, J., Ferris, G., Simpson, C., 2008. Evolution and architecture of a large felsic igneous province in western Laurentia: the 1.6 Ga Gawler Range Volcanics, South Australia. J Volcanol Geoth Res 172, 132-147.

Allen, S.R., McPhie, J., 2002. The Eucarro Rhyolite, Gawler Range Volcanics, South Australia: A >675 km^3, compositionally zoned lava of Mesoproterozoic age. Geological Society of America Bulletin 114, 1592-1609.

Amelin, Y., Zaitsev, A.N., 2002. Precise geochronology of phoscorites and carbonatites: The critical role of U-series disequilibrium in age interpretations. Geochim Cosmochim Ac 66, 2399-2419.

Apukhtina, O.B., Kamenetsky, V.S., Ehrig, K., Kamenetsky, M.B., McPhie, J., Maas, R., Meffre, S., Goemann, K., Rodemann, T., Cook, N.J., Ciobanu, C.L., 2015. Postmagmatic magnetite-apatite assemblage in mafic intrusions: a case study of dolerite at Olympic Dam, South Australia. Contrib Mineral Petr 171, 1-15. **Chapter 3**

Apukhtina, O.B., Kamenetsky, V.S., Ehrig, K., Kamenetsky, M.B., Maas, R., Thomson, J., McPhie, J., Ciobanu, C.L., Cook, N.J., in preparation a. Deep, early mineralization at the Olympic Dam Cu-U-Au-Ag deposit, South Australia. Economic Geology (Scientific Comm). **Chapter 4**

Apukhtina, O.B., Ehrig, K., Kamenetsky, V.S., Kamenetsky, M.B., Goemann, K., Maas, R., McPhie, J., Ciobanu, C.L., Cook, N.J., in preparation b. Carbonates in the Olympic Dam Cu-U-Au-Ag deposit. Part I: Distribution, textures, associations and stable isotope (C, O) signatures. Ore Geology Reviews. **Chapter 5**

Bai, G., Yuan, Z., Wu, C., Zhang, Z., Zheng, L., 1996. Demonstration on the geological features and genesis of the Bayan Obo ore deposit. Beijing: Geological Publishing House, 1-103.

Baker, J., Peate, D., Waight, T., Meyzen, C., 2004. Pb isotopic analysis of standards and samples using a ^{207}Pb-^{204}Pb double spike and thallium to correct for mass bias with a double-focusing MC-ICP-MS. Chem Geol 211, 275-303.

Barfod, G.H., Krogstad, E.J., Frei, R., Albarède, F., 2005. Lu-Hf and PbSL geochronology of apatites from Proterozoic terranes: A first look at Lu-Hf isotopic closure in metamorphic apatite. Geochim Cosmochim Ac 69, 1847-1859.

Barfod, G.H., Otero, O., Albarède, F., 2003. Phosphate Lu-Hf geochronology. Chem Geol 200, 241-253.

Barton, M.D., 2014. Iron oxide (-Cu-Au-REE-P-Ag-U-Co) systems. Treatise on Geochemistry: Amsterdam, Elsevier, 515-541.

Barton, M.D., Johnson, D.A., 2000. Alternative brine sources for Fe-oxide (-Cu-Au) systems: Implications for hydrothermal alteration and metals. Hydrothermal Iron Oxide Copper-Gold & Related Deposits: A Global Perspective 1, 43-60.

Bast, R., Scherer, E.E., Sprung, P., Fischer-Godde, M., Stracke, A., Mezger, K., 2015. A rapid and efficient ion-exchange chromatography for Lu-Hf, Sm-Nd, and Rb-Sr geochronology and the routine isotope analysis of sub-ng amounts of Hf by MC-ICP-MS. Journal of Analytical Atomic Spectrometry 30, 2323-2333.

Bastrakov, E.N., Skirrow, R.G., Didson, G.J., 2007. Fluid evolution and origins of iron oxide Cu-Au prospects in the Olympic Dam district, Gawler Craton, South Australia. Econ Geol 102, 1415-1440.

Bau, M., Möller, P., 1992. Rare earth element fractionation in metamorphogenic hydrothermal calcite, magnesite and siderite. Miner Petrol 45, 231-246.

Baumgartner, J., Dey, A., Bomans, P.H.H., Le Coadou, C., Fratzl, P., Sommerdijk, N.A.J.M., Faivre, D., 2013. Nucleation and growth of magnetite from solution. Nature Materials 12, 310-314.

Baur, M.E., Hayes, J.M., Studley, S.A., Walter, M.R., 1985. Millimetre-scale variations of stable isotope abundances in carbonates from banded iron-formations in the Hamersley Group of Western Australia. Econ Geol 80, 270-282.

Belousova, E.A., Reid, A.J., Griffin, W.L., O'Reilly, S.Y., 2009. Rejuvenation vs. recycling of Archean crust in the Gawler Craton, South Australia: Evidence from U-Pb and Hf isotopes in detrital zircon. Lithos 113, 570-582.

Belperio, A., Flint, R., Freeman, H., 2007. Prominent Hill: a hematite-dominated, iron oxide copper-gold system. Econ Geol 102, 1499-1510.

Best, F.C., 2012. The Petrogenesis and Ni-Cu-PGE Potential of the Dido Batholith, North Queensland, Australia. PhD thesis, University of Tasmania, unpublished.

Betts, P.G., Giles, D., 2006. The 1800–1100Ma tectonic evolution of Australia. Precambrian Research 144, 92-125.

Biczok, J., Hollings, P., Klipfel, P., Heaman, L., Maas, R., Hamilton, M., Kamo, S., Friedman, R., 2012. Geochronology of the North Caribou greenstone belt, Superior Province Canada: Implications for tectonic history and gold mineralization at the Musselwhite mine. Precambrian Research 192, 209-230.

Bizimis, M., Salters, V.M., Dawson, J.B., 2003. The brevity of carbonatite sources in the mantle: evidence from Hf isotopes. Contrib Mineral Petr 145, 281-300.

Black, L., Gulson, B., 1978. The age of the mud tank carbonatite, strangways range, northern territory. BMR Journal of Australian Geology and Geophysics 3, 227-232.

Black, L.P., Kamo, S.L., Allen, C.M., Aleinikoff, J.N., Davis, D.W., Korsch, R.J., Foudoulis, C., 2003. TEMORA 1: A new zircon standard for Phanerozoic U-Pb geochronology. Chem Geol 200, 155-170.

Black, L.P., Kamo, S.L., Allen, C.M., Davis, D.W., Aleinikoff, J.N., Valley, J.W., Mundil, R., Campbell, I.H., Korsch, R.J., Williams, I.S., Foudoulis, C., 2004. Improved $^{206}Pb/^{238}U$ microprobe geochronology by the monitoring of a trace-element-related matrix effect; SHRIMP, ID-TIMS, ELA-ICP-MS and oxygen isotope documentation for a series of zircon standards. Chem Geol 205, 115-140.

Blissett, A.H., Creaser, R.A., Daly, S.J., Flint, R.B., Parker, A.J., 1993. Gawler Range Volcanics, in: Drexel, J.F., Preiss, W.V., Parker A.J. (Eds.), The Geology of South Australia. Vol. 1, The Precambrian, Geological Survey of South Australia, 107-131.

Bookstrom, A.A., 1977. The magnetite deposits of El Romeral, Chile. Econ Geol 72, 1101-1130.

Bouvier, A., Vervoort, J.D., Patchett, P.J., 2008. The Lu-Hf and Sm-Nd isotopic composition of CHUR: Constraints from unequilibrated chondrites and implications for the bulk composition of terrestrial planets. Earth and Planetary Science Letters 273, 48-57.

Brugger, J., Maas, R., Lahaye, Y., McRae, C., Ghaderi, M., Costa, S., Lambert, D., Bateman, R., Prince, K., 2002. Origins of Nd-Sr-Pb isotopic variations in single scheelite grains from Archaean gold deposits, Western Australia. Chem Geol 182, 203-225.

Burke, E.A.J., 2001. Raman microspectrometry of fluid inclusions. Lithos 55, 139-158.

Calver, C., Crowley, J., Wingate, M., Evans, D., Raub, T., Schmitz, M., 2013. Globally synchronous Marinoan deglaciation indicated by U-Pb geochronology of the Cottons Breccia, Tasmania, Australia. Geology 41, 1127-1130.

References

Cannell, J., Davidson, G.J., 1998. A carbonate-dominated copper-cobalt breccia-vein system at the Great Australia Deposit, Mount Isa eastern succession. Econ Geol 93, 1406-1421.

Carr, G.R., Dean, J.A., Suppel, D.W., Heithersay, P.S., 1995. Precise lead isotope fingerprinting of hydrothermal activity associated with Ordovician to Carboniferous metallogenic events in the Lachlan fold belt of New South Wales. Econ Geol 90, 1467-1505.

Charlier, B., Namur, O., Bolle, O., Latypov, R., Duchesne, J.-C., 2015. Fe-Ti-V-P ore deposits associated with Proterozoic massif-type anorthosites and related rocks. Earth-Science Reviews 141, 56-81.

Chen, W.T., Zhou, M.-F., 2012. Paragenesis, stable isotopes, and molybdenite Re-Os isotope age of the Lala Iron-Copper Deposit, Southwest China. Econ Geol 107, 459-480.

Chernyshova, I.V., Hochella Jr, M.F., Madden, A.S., 2007. Size-dependent structural transformations of hematite nanoparticles. 1. Phase transition. Physical Chemistry Chemical Physics 9, 1736-1750.

Cherry, A.R., Kamenetsky, V.S., Ehrig, K., McPhie, J., Kamenetsky, M.B., Ciobanu, C.L., Cook, N.J., in preparation. Petrography and provenance of the bedded sedimentary units within the Olympic Dam deposit.

Chesley, J.T., Halliday, A.N., Kyser, T.K., Spry, P.G., 1994. Direct dating of Mississippi Valley-type mineralization; use of Sm-Nd in fluorite. Econ Geol 89, 1192-1199.

Chew, D.M., Petrus, J.A., Kamber, B.S., 2014. U-Pb LA-ICPMS dating using accessory mineral standards with variable common Pb. Chem Geol 363, 185-199.

Chew, D.M., Sylvester, P.J., Tubrett, M.N., 2011. U-Pb and Th-Pb dating of apatite by LA-ICPMS. Chem Geol 280, 200-216.

Chukhrov, F.V., 1966. Present views on colloids in ore formation. Int Geol Rev 8, 336-345.

Ciobanu, C.L., Wade, B.P., Cook, N.J., Schmidt Mumm, A., Giles, D., 2013. Uranium-bearing hematite from the Olympic Dam Cu–U–Au deposit, South Australia: A geochemical tracer and reconnaissance Pb–Pb geochronometer. Precambrian Research 238, 129-147.

Ciobanu, C.L., Cook, N.J., Ehrig, K., Wade, B.P., Kamenetsky, V.S., 2015. The potential of iron oxides for U-Pb geochronology - examples from the Olympic Dam IOCG deposit, South Australia. SEG conference, Hobart.

Clark, C., Mumm, A.S., Hand, M., Faure, K., 2006. Episodic shear zone associated fluid flow in the Curnamona Province, South Australia. Journal of Geochemical Exploration 89, 69-72.

Conor, C., 2004. Hydraulic Jacking and stopping - an explanation for breccia sedimentation in Mine Area A, Olympic Dam. MESA Journal, 45-50.

Conor, C., Raymond, O., Baker, T., Teale, G., Say, P., Lowe, G., 2010. Alteration and mineralisation in the Moonta-Wallaroo Cu-Au mining field region, Olympic domain, South Australia. Hydrothermal Iron Oxide Copper-Gold and Related Deposits: A Global Perspective 3, 1-24.

Cook, N.J., Ciobanu, C.L., Ehrig, K., 2015. New insights into zonation within the Olympic Dam Cu-U-Au-Ag deposit from the trace element composition of sulfide minerals. SEG conference, Hobart.

Cowley, W., Conor, C., Zang, W., 2003. New and revised Proterozoic stratigraphic units on northern Yorke Peninsula. MESA Journal 29, 46-58.

Cowley, W.M., 1993. Pandurra Formation, in: Drexel, J.F., Preiss, W.V., Park, J.K. (Eds.), The Geology of South Australia. Vol. 1, The Precambrian, Geological Survey of South Australia.

Craig, H., 1953. The geochemistry of the stable carbon isotopes. Geochim Cosmochim Ac 3, 53-92.

Cranswick, E., Network, P.S., 2009. Mashers Fault and the seismicity anticipated to be stimulated by the proposed open pit mine at Olympic Dam, Earthquake engineering in Australia: proceedings of the conference held by the Australian Earthquake Engineering Society in Newcastle, NSW, 11-13.

Creaser, R.A., 1989. The geology and petrology of Middle Proterozoic felsic magmatism of the Stuart Shelf, South Australia. La Trobe University.

Creaser, R.A., Gray, C.M., 1992. Preserved initial $^{87}Sr/^{86}Sr$ in apatite from altered felsic igneous rocks: A case study from the Middle Proterozoic of South Australia. Geochim Cosmochim Ac 56, 2789-2795.

Daly, S.J., Fanning, C.M., Fairclough, M.C., 1998. Tectonic evolution and exploration potential of the Gawler Craton, South Australia. AGSO Journal of Australia Geology and Geophysics 17, 145-168.

Danyushevsky, L., Robinson, P., Gilbert, S., Norman, M., Large, R., McGoldrick, P., Shelley, M., 2011. Routine quantitative multi-element analysis of sulphide minerals by laser ablation ICP-MS: Standard development and consideration of matrix effects. Geochemistry: Exploration, Environment, Analysis 11, 51-60.

Dare, S.S., Barnes, S.-J., Beaudoin, G., 2015. Did the massive magnetite "lava flows" of El Laco (Chile) form by magmatic or hydrothermal processes? New constraints from magnetite composition by LA-ICP-MS. Miner Deposita 50, 607-617.

Davidson, G.J., Paterson, H., Meffre, S., Berry, R.F., 2007. Characteristics and origin of the Oak Dam East breccia-hosted, iron oxide Cu-U-(Au) deposit: Olympic Dam region, Gawler Craton, South Australia. Econ Geol 102, 1471-1498.

Deer, W.A., Howie, R.A., Zussman, J., 1992. An introduction to the rock-forming minerals. Longman London.

Deines, P., Gold, D., 1973. The isotopic composition of carbonatite and kimberlite carbonates and their bearing on the isotopic composition of deep-seated carbon. Geochim Cosmochim Ac 37, 1709-1733.

Diemar, G., 2014. The petrology of hydrothermal REE bearing minerals in the Olympic Dam IOCG deposit support a 1.3 Ga formation. B. Sc. (Hons.) thesis, University of Tasmania, unpublished.

DMITRE Resources and Energy Group, G.o.S.A., 2014. South Australian Resources Information Geoserver, https://sarig.pir.sa.gov.au/Map.

Drexel, J.F., Preiss, W.V., Parker, A.J., 1993. The geology of South Australia, Vol. 1, The Precambrian, Bulletin 54.

Droop, G., 1987. A general equation for estimating Fe^{3+} concentrations in ferromagnesian silicates and oxides from microprobe analyses, using stoichiometric criteria. Mineralogical Magazine 51, 431-435.

Drummond, B., Lyons, P., 2002. Geophysical interpretation of the Central Olympic Cu-Au province. Geoscience Australia.

Dumanska-Słowik, M., Natkaniec-Nowak, L., Wesełucha-Birczynska, A., Gaweł, A., Lankosz, M., Wróbel, P., 2013. Agates from Morocco: Gemmological Characteristics and Proposed Origin. Gems & Gemology 49.

Dymkin, Sokolov, 1961. Colloform segregations of endogenous magnetite in the Kurzhunkul deposit. Geologiya i geofizika 1, 77-85.

Eckstrand, O., Grinenko, L., Krouse, H., Paktunc, A., Schwann, P., Scoates, R., 1989. Preliminary data on sulphur isotopes and Se/S ratios, and the source of sulphur in magmatic sulphides from the Fox River Sill, Molson Dykes and Thompson nickel deposits, northern Manitoba. Current Research Part C, Geological Survey of Canada, Paper, 235-242.

Eggins, S., Woodhead, J., Kinsley, L., Mortimer, G., Sylvester, P., McCulloch, M., Hergt, J., Handler, M., 1997. A simple method for the precise determination of≥ 40 trace elements in geological samples by ICPMS using enriched isotope internal standardisation. Chem Geol 134, 311-326.

Ehrig, K., McPhie, J., Kamenetsky, V.S., 2012. Geology and mineralogical zonation of the Olympic Dam Iron Oxide Cu-U-Au-Ag Deposit, South Australia, in: Hedenquist, J.W., Harris, M., Camus, F. (Eds.), Economic Geology Special Publication 16, pp. 237-267.

References

Eldridge, C., Danti, K., 1994. Low sulfur isotope ratios; high gold values - a closer look at the Olympic Dam Deposit via SHRIMP, Geol Soc Am, Abstr Programs, pp. 489-490.

Fanning, C.M., 2003. Detrital zircon provenance of the Mesoproterozoic Pandurra Formation, South Australia: Gawler Craton zircon population and implications for the Belt Supergroup, Presented at the 2003 GSA Annual Meeting.

Fanning, C.M., Flint, R.B., Parker, A.J., Ludwig, K.R., Blissett, A.H., 1988. Refined Proterozoic evolution of the Gawler Craton, South Australia, through U-Pb zircon geochronology. Precambrian Research 40, 363-386.

Fanning, M., Reid, A.J., Teale, G.S., Teale, G.S., SA, P.I.a.R., 2007. A geochronological framework for the Gawler Craton, South Australia, Adelaide: Primary Industries and Resources SA, 2007.

FitzGerald, D., Milligan, P., Reid, A., 2004. Integrating Euler solutions into 3D geological models-automated mapping of depth to magnetic basement, 2004 SEG Annual Meeting. Society of Exploration Geophysicists.

Foden, J., Marlina A. Elburg, Jon Dougherty-Page, Andrew Burtt, 2006. The Timing and Duration of the Delamerian Orogeny: Correlation with the Ross Orogen and Implications for Gondwana Assembly. The Journal of Geology 114, 189-210.

Fraser, G., McAvaney, S., Neumann, N., Szpunar, M., Reid, A., 2010. Discovery of early Mesoarchean crust in the eastern Gawler Craton, South Australia. Precambrian Research 179, 1-21.

Giles, C.W., 1988. Petrogenesis of the Proterozoic Gawler Range Volcanics, South Australia. Precambrian Research 40-41, 407-427.

Goldstein, S.L., 1988. Decoupled evolution of Nd and Sr isotopes in the continental crust and the mantle. Nature 336, 733-738.

Gole, M.J., Klein, C., 1981. Banded Iron-Formations through Much of Precambrian Time. The Journal of Geology 89, 169-183.

Götze, J., 2002. Potential of cathodoluminescence microscopy and spectroscopy for the analysis of minerals and materials. Anal Bioanal Chem 374, 703-708.

Groves, D.I., Vielreicher, N.M., 2001. The Phalabowra (Palabora) carbonatite-hosted magnetite-copper sulfide deposit, South Africa: an end-member of the iron-oxide copper-gold-rare earth element deposit group? Miner Deposita 36, 189-194.

Groves, D.I., Bierlein, F.P., Meinert, L.D., Hitzman, M.W., 2010. Iron Oxide Copper-Gold (IOCG) Deposits through Earth History: Implications for Origin, Lithospheric Setting, and Distinction from Other Epigenetic Iron Oxide Deposits. Econ Geol 105, 641-654.

Gustafson, L., Compston, W., 1979. Rb-Sr dating of Olympic Dam core samples, Report to Western Mining Corporation, Research School of Earth Sciences. Australian National University 18.

Halpin, J.A., Jensen, T., McGoldrick, P., Meffre, S., Berry, R.F., Everard, J.L., Calver, C.R., Thompson, J., Goemann, K., Whittaker, J.M., 2014. Authigenic monazite and detrital zircon dating from the Proterozoic Rocky Cape Group, Tasmania: Links to the Belt-Purcell Supergroup, North America. Precambrian Research 250, 50-67.

Hand, M., Reid, A., Jagodzinski, L., 2007. Tectonic Framework and Evolution of the Gawler Craton, Southern Australia. Econ Geol Bull Soc 102, 1377-1395.

Harlov, D.E., 2015. Apatite: A Fingerprint for Metasomatic Processes. Elements 11, 171-176.

Harmer, R.E., 2015. Mineralisation of the Phalaborwa Complex and the carbonatite connection in Iron Oxide-Cu-Au-U-REE deposits. PGS Publishing.

Hattori, K.H., Keith, J.D., 2001. Contribution of mafic melt to porphyry copper mineralization: evidence from Mount Pinatubo, Philippines, and Bingham Canyon, Utah, USA. Miner Deposita 36, 799-806.

Hauck, S.A., 1990. Petrogenesis and tectonic setting of middle Proterozoic iron oxide-rich ore deposits: an ore deposit model for Olympic Dam-type mineralization. US Geological Survey Bulletin 1932, 4-39.

Haynes, D.W., 1972. Geochemistry of altered basalts (continental tholeiites) and associated copper deposits. The Australian National University, unpublished.

Haynes, D.W., Cross, K.C., Bills, R.T., Reed, M.H., 1995. Olympic Dam Ore Genesis - a Fluid-Mixing Model. Econ Geol 90, 281-307.

Hayward, N., Skirrow, R., 2010. Geodynamic setting and controls on iron oxide Cu-Au (±U) ore in the Gawler Craton, South Australia. Hydrothermal iron oxide copper-gold and related deposits: A global perspective 3, 105-131.

Hecht, L., Freiberger, R., Gilg, H.A., Grundmann, G., Kostitsyn, Y.A., 1999. Rare earth element and isotope (C, O, Sr) characteristics of hydrothermal carbonates: genetic implications for dolomite-hosted talc mineralization at Göpfersgrün (Fichtelgebirge, Germany). Chem Geol 155, 115-130.

Hitzman, M.W., Oreskes, N., Einaudi, M.T., 1992. Geological characteristics and tectonic setting of Proterozoic iron oxide (Cu-U-Au-REE) deposits. Precambrian Research 58, 241-287.

Hoatson, D.M., Claoué-Long, J.C., Jaireth, S., 2008a. Australian Proterozoic Mafic-Ultramafic Magmatic Events: Sheets 1 and 2 (1:5000000 and 1:10000000Scale Maps). Geoscience Australia, Australia.

Hoatson, D.M., Claoué-Long, J.C., Jaireth, S., 2008b. Guide to Using the 1:5000000Map of the Australian Proterozoic Mafic-Ultramafic Magmatic Events. 140.

Hoatson, D.M., Sun, S.-S., Duggan, M.B., Davies, M.B., Daly, S.J., Purvis, A.C., 2005. Late Archean Lake Harris komatiite, central Gawler Craton, South Australia: geologic setting and geochemistry. Econ Geol 100, 349-374.

Hoefs, J., 1997. Stable isotope geochemistry. Springer.

Huang, Q.-Y., Kamenetsky, V.S., McPhie, J., Ehrig, K., Meffre, S., Maas, R., Apukhtina, O.B., Kamenetsky, M.B., Chambefort, I., Hu, Y., Ling, M., 2015. Neoproterozoic (820 Ma) mafic dykes at Olympic Dam, South Australia: links with the Gairdner Large Igneous Province. Precambrian Research.

Huang, Q.-Y., Kamenetsky, V.S., Ehrig, K., McPhie, J., Maas, R., Kamenetsky, M.B., Apukhtina, O.B., Chambefort, I., in preparation. Alteration of mafic rocks at the Olympic Dam iron oxide Cu-U-Au-Ag deposit. Chem Geol.

Huang, Q.-Y., Kamenetsky, V.S., Ehrig, K., McPhie, J., Maas, R., Kamenetsky, M.B., Apukhtina, O.B., Chambefort, I., 2016. Olivine-phyric basalt at the Olympic Dam Cu-U-Au-Ag deposit: insights into the mantle source and petrogenesis of the Gawler Silicic Large Igneous Province, South Australia. Lithos.

Hunt, J.A., Baker, T., Thorkelson, D.J., 2007. A Review of Iron Oxide Copper-Gold Deposits, with Focus on the Wernecke Breccias, Yukon, Canada, as an Example of a Non-Magmatic End Member and Implications for IOCG Genesis and Classification. Exploration and Mining Geology 16, 209-232.

Ismail, R., Lin, Y., Ciobanu, C.L., Cook, N.J., 2014. The Hillside Cu-Au Deposit, South Australia: A Preliminary Fluid Inclusion Study. Acta Geologica Sinica - English Edition 88, 1454-1456.

Jagodzinski, E.A., 2005. Compilation of SHRIMP U-Pb geochronological data Olympic Domain, Gawler Craton, South Australia, 2001-2003: Geoscience Australia Record 2005/20, 211p.

References

Jagodzinski, E.A., 2014. The age of magmatic and hydrothermal zircon at Olympic Dam. AESC-Abstract-Proceedings Newcastle.

Javoy, M., Pineau, F., Cheminee, J., Kraft, M., 1988. The gas-magma relationship in the 1988 eruption of Oldoinyo Lengai (Tanzania). EOS 69, 1466.

Jochum, K.P., Weis, U., Stoll, B., Kuzmin, D., Yang, Q., Raczek, I., Jacob, D.E., Stracke, A., Birbaum, K., Frick, D.A., Günther, D., Enzweiler, J., 2011. Determination of Reference Values for NIST SRM 610-617 Glasses Following ISO Guidelines. Geostandards and Geoanalytical Research 35, 397-429.

Johnson, J.P., 1993. The geochronology and radiogenic isotope syetematics of the Olympic Dam copper-uranium-gold-silver deposit, South Australia. The Australian National University, unpublished.

Johnson, J.P., Cross, K.C., 1995. U-Pb geochronological constraints on the genesis of the Olympic Dam Cu-U-Au-Ag Deposit, South Australia. Economic Geology & the Bulletin of the Society of Economic Geologists 90, 1046-1063.

Johnson, J.P., McCulloch, M.T., 1995. Sources of mineralising fluids for the Olympic Dam deposit (South Australia): Sm-Nd isotopic constraints. Chem Geol 121, 177-199.

Jonsson, E., Troll, V.R., Högdahl, K., Harris, C., Weis, F., Nilsson, K.P., Skelton, A., 2013. Magmatic origin of giant 'Kiruna-type' apatite-iron-oxide ores in Central Sweden. Scientific Reports 3, 1644.

Kamenetsky, V.S., Ehrig, K., Maas, R., Meffre, S., Kamenetsky, M.B., McPhie, J., Apukhtina, O.B., Huang, Q.-Y., Thompson, J., Ciobanu, C.L., Cook, N.J., 2015. The supergiant Olympic Dam Cu-U-Au-Ag ore deposit: towards a new genetic model. SEG conference, Hobart.

Karathanasis, A.D., 1999. Subsurface Migration of Copper and Zinc Mediated by Soil Colloids. Soil Science Society of America Journal 63, 830-838.

Keith, M., Weber, J., 1964. Carbon and oxygen isotopic composition of selected limestones and fossils. Geochim Cosmochim Ac 28, 1787-1816.

Kendall, B.S., Creaser, R.A., Ross, G.M., Selby, D., 2004. Constraints on the timing of Marinoan "Snowball Earth" glaciation by ^{187}Re-^{187}Os dating of a Neoproterozoic, post-glacial black shale in Western Canada. Earth and Planetary Science Letters 222, 729-740.

Kennedy, M., Mrofka, D., von der Borch, C., 2008. Snowball Earth termination by destabilization of equatorial permafrost methane clathrate. Nature 453, 642-645.

Kholodov, V.N., Butuzova, G.Y., 2008. Siderite formation and evolution of sedimentary iron ore deposition in the Earth's history. Geol. Ore Deposits 50, 299-319.

Kim, S.-T., Mucci, A., Taylor, B.E., 2007. Phosphoric acid fractionation factors for calcite and aragonite between 25 and 75˚C: revisited. Chem Geol 246, 135-146.

Klötzli, U., Klötzli, E., Günes, Z., Kosler, J., 2009. Accuracy of laser ablation U-Pb zircon dating: Results from a test using five different reference zircons. Geostandards and Geoanalytical Research 33, 5-15.

Knipping, J.L., Bilenker, L.D., Simon, A.C., Reich, M., Barra, F., Deditius, A.P., Lundstrom, C., Bindeman, I., Munizaga, R., 2015. Giant Kiruna-type deposits form by efficient flotation of magmatic magnetite suspensions. Geology.

Köhler, I., Konhauser, K.O., Papineau, D., Bekker, A., Kappler, A., 2013. Biological carbon precursor to diagenetic siderite with spherical structures in iron formations. Nature communications 4, 1741.

Krneta, S., Ciobanu, C.L., Cook, N.J., Ehrig, K., Kamenetsky, V.S., 2015. Apatite in the Olympic Dam Fe-Oxide Cu-U-Au-Ag Deposit. Mineral resources in a sustainable world 3.

Li, X.-H., Liu, D., Sun, M., Li, W.-X., Liang, X.-R., Liu, Y., 2004. Precise Sm-Nd and U-Pb isotopic dating of the supergiant Shizhuyuan polymetallic deposit and its host granite, SE China. Geol Mag 141, 225-231.

Li, Z.X., Bogdanova, S.V., Collins, A.S., Davidson, A., De Waele, B., Ernst, R.E., Fitzsimons, I.C.W., Fuck, R.A., Gladkochub, D.P., Jacobs, J., Karlstrom, K.E., Lu, S., Natapov, L.M., Pease, V., Pisarevsky, S.A., Thrane, K., Vernikovsky, V., 2008. Assembly, configuration, and breakup history of Rodinia: A synthesis. Precambrian Research 160, 179-210.

Li, Z.X., Li, X.H., Kinny, P.D., Wang, J., 1999. The breakup of Rodinia: did it start with a mantle plume beneath South China? Earth and Planetary Science Letters 173, 171-181.

Ling, W., Gao, S., Zhang, B., Li, H., Liu, Y., Cheng, J., 2003. Neoproterozoic tectonic evolution of the northwestern Yangtze craton, South China: implications for amalgamation and breakup of the Rodinia Supercontinent. Precambrian Research 122, 111-140.

Lottermoser, B., 1995. Rare-Earth Element Mineralogy of the Olympic Dam Cu-U-Au-Ag deposit, Roxby-Downs, South Australia - Implications for Ore Genesis. Neues Jahrbuch fur Mineralogie-Monatshefte, 371-384.

Maas, R., 1989. Nd-Sr isotope constraints on the age and origin of unconformity-type uranium deposits in the Alligator Rivers Uranium Field, Northern Territory, Australia. Econ Geol 84, 64-90.

Maas, R., Apukhtina, O.B., Kamenetsky, V.S., Ehrig, K., Sprung, P., in preparation b. Carbonates at supergiant Olympic Dam deposit, South Australia. Part II: Trace elements, radiogenic isotopes (Sr, Nd, Pb, Hf) and episodes of carbonate formation. Ore Geology Reviews. **Chapter 6**

Maas, R., Apukhtina, O.B., Kamenetsky, V.S., Ehrig, K., 2015. Olympic Dam Cu-U-Au deposit: $^{87}Sr/^{86}Sr$ in carbonate gangue documents long formation history. Proceedings Goldschmidt 2015, Prague: 1957.

Maas, R., Kamenetsky, M.B., Sobolev, A.V., Kamenetsky, V.S., Sobolev, N.V., 2005. Sr, Nd, and Pb isotope evidence for a mantle origin of alkali chlorides and carbonates in the Udachnaya kimberlite, Siberia. Geology 33, 549-552.

Maas, R., Kamenetsky, V.S., Ehrig, K., Meffre, S., McPhie, J., Diemar, G., 2011. Olympic Dam U-Cu-Au Deposit, Australia: New Age Constraints. Mineralogical Magazine 75.

Maas, R., Kirchenbauer, M., Ehrig, K., Kamenetsky, V.S., Apukhtina, O.B., McPhie, J., Meffre, S., Diemar, G., in preparation a. Isotopic (Nd-Sr-Pb) complexity in the supergiant Olympic Dam IOCG (Cu-Au-U) deposit, Australia: protracted ore formation in response to large-scale tectonic events.

Macmillian, E., Cook, N.J., Ciobanu, C.L., Ehrig, K., Kamenetsky, V.S., Thompson, J., Pring, A., 2015. Evolution of uranium minerals at Olympic Dam, South Australia. SEG conference, Hobart.

Marschik, R., Fontboté, L., 2001. The Candelaria-Punta del Cobre Iron Oxide Cu-Au(-Zn-Ag) Deposits, Chile. Econ Geol 96, 1799-1826.

Marshall, L., Oliver, N.S., Davidson, G., 2006. Carbon and oxygen isotope constraints on fluid sources and fluid-wallrock interaction in regional alteration and iron-oxide-copper-gold mineralisation, eastern Mt Isa Block, Australia. Miner Deposita 41, 429-452.

Mason, M., Thomson, B., Tonkin, D., 1978. Regional stratigraphy of the Beda Volcanics, Backy Point Beds and Pandurra Formation on the southern Stuart Shelf, South Australia. South Aust. Geol. Surv. Q. Geol. Notes 66, 1-9.

McDonough, W.F., Sun, S.s., 1995. The composition of the Earth. Chem Geol 120, 223-253.

References

McInnes, B.I.A., Keays, R.R., Lambert, D.D., Hellstrom, J., Allwood, J.S., 2008. Re-Os geochronology and isotope systematics of the Tanami, Tennant Creek and Olympic Dam Cu-Au deposits. Australian Journal of Earth Sciences 55, 967-981.

McPhie, J., Kamenetsky, V.S., Chambefort, I., Ehrig, K., Green, N., 2011. Origin of the supergiant Olympic Dam Cu-U-Au-Ag deposit, South Australia: Was a sedimentary basin involved? Geology 39, 795-798.

McPhie, J., Orth, K., Kamenetsky, V.S., Kamenetsky, M.B., Ehrig, K., 2016. Characteristics, origin and significance of Mesoproterozoic bedded clastic facies at the Olympic Dam Cu-U-Au-Ag deposit, South Australia. Precambrian Research.

Meffre, S., Ehrig, K., Kamenetsky, V.S., Chambefort, I., Maas, R., McPhie, J., 2010. Pb isotopes at Olympic Dam: constraining sulphide growth. IAGOD processings.

Menard, T., Lesher, C.M., Stowell, H.H., Price, D.P., Pickell, J.R., Onstott, T.C., Hulbert, L., 1996. Geology, genesis, and metamorphic history of the Namew Lake Ni-Cu deposit, Manitoba. Econ Geol 91, 1394-1413.

Meyer, C., 1988a. Ore deposits as guides to geologic history of the Earth. Annual Review of Earth and Planetary Sciences 16, 147.

Meyer, C., 1988b. Proterozoic ore-forming habitats - Tectonic and chemical transitions, Proceedings Volume of the North American Conference on Tectonic Control of Ore Deposits and the Vertical and Horizontal Extent of Ore Systems. University of Missouri-Rolla, 217-235.

Molchan, I.S., Thompson, G.E., Lindsay, R., Skeldon, P., Likodimos, V., Romanos, G.E., Falaras, P., Adamova, G., Iliev, B., Schubert, T.J.S., 2014. Corrosion behaviour of mild steel in 1-alkyl-3-methylimidazolium tricyanomethanide ionic liquids for CO_2 capture applications. RSC Advances 4, 5300-5311.

Monteiro, L.S., Xavier, R., de Carvalho, E., Hitzman, M., Johnson, C., de Souza Filho, C., Torresi, I., 2008. Spatial and temporal zoning of hydrothermal alteration and mineralization in the Sossego iron oxide-copper-gold deposit, Carajás Mineral Province, Brazil: paragenesis and stable isotope constraints. Miner Deposita 43, 129-159.

Morales Ruano, S., Both, R.A., Golding, S.D., 2002. A fluid inclusion and stable isotope study of the Moonta copper-gold deposits, South Australia: evidence for fluid immiscibility in a magmatic hydrothermal system. Chem Geol 192, 211-226.

Mortimer, G.E., Cooper, J.A., Paterson, H.L., Cross, K., Hudson, G.R.T., Uppill, R.K., 1988. Zircon U-Pb Dating in the Vicinity of the Olympic Dam Cu-U-Au Deposit, Roxby Downs, South Australia. Econ Geol 83, 694-709.

Nystroem, J.O., Henriquez, F., 1994. Magmatic features of iron ores of the Kiruna type in Chile and Sweden; ore textures and magnetite geochemistry. Econ Geol 89, 820-839.

O'Neil, J.R., Clayton, R.N., Mayeda, T.K., 1969. Oxygen Isotope Fractionation in Divalent Metal Carbonates. Journal Name: J. Chem. Phys. 51: 5547-58.

O'Reilly, G., 2006. Are Nova Scotia's Carboniferous carbonate-hosted base metal deposits and iron-oxide-copper-gold (IOCG) deposits close cousins. Mining Matters, 2006-2002.

Ohmoto, H., 1972. Systematics of sulfur and carbon isotopes in hydrothermal ore deposits. Econ Geol 67, 551-578.

Oreskes, N., Einaudi, M.T., 1990. Origin of rare-earth element-enriched hematite breccias at the Olympic-Dam Cu-U-Au-Ag Deposit, Roxby Downs, South Australia. Econ Geol 85, 1-28.

Oreskes, N., Einaudi, M.T., 1992. Origin of Hydrothermal Fluids at Olympic Dam: Preliminary Results from Fluid Inclusions and Stable Isotopes. Econ Geol 87, 64-90.

Parak, T., 1975. Kiruna iron ores are not "intrusive-magmatic ores of the Kiruna type". Econ Geol 70, 1242-1258.

Parak, T., 1984. On the magmatic origin of iron ores of the Kiruna type; Discussion. Econ Geol 79, 1945-1949.

Parker, A., Lemon, N., 1982. Reconstruction of the early Proterozoic stratigraphy of the Gawler Craton, South Australia. Journal of the Geological Society of Australia 29, 221-238.

Parker, A.J., 1987. Archaean to middle Proterozoic mineralization of the Gawler Craton (including the Stuart Shelf region), South Australia. Department of Mines and Energy.

Parr, J.M., Stevens, B.P., Carr, G.R., Page, R.W., 2004. Subseafloor origin for Broken Hill Pb-Zn-Ag mineralization, New South Wales, Australia. Geology 32, 589-592.

Paterson, H., 1986. The Acropolis Prospect, Paterson, HL, (Compiler), Basement geology of the Stuart Shelf region, 8th Australian Geological Convention, 17-23.

Paton, C., Woodhead, J.D., Hellstrom, J.C., Hergt, J.M., Greig, A., Maas, R., 2010. Improved laser ablation U-Pb zircon geochronology through robust downhole fractionation correction. Geochemistry, Geophysics, Geosystems 11, pages nos.

Pavlov, N.V., 1961. Magnetite deposits of the Tungusska tectonic Depression on the Siberian Platform. Tr. IGEM Akad. Nauk SSSR 52.

Peng, J.-T., Hu, R.-Z., Burnard, P., 2003. Samarium-neodymium isotope systematics of hydrothermal calcites from the Xikuangshan antimony deposit (Hunan, China): the potential of calcite as a geochronometer. Chem Geol 200, 129-136.

Pin, C., Briot, D., Bassin, C., Poitrasson, F., 1994. Concomitant separation of strontium and samarium-neodymium for isotopic analysis in silicate samples, based on specific extraction chromatography. Analytica Chimica Acta 298, 209-217.

Pin, C., Zalduegui, J.S., 1997. Sequential separation of light rare-earth elements, thorium and uranium by miniaturized extraction chromatography: application to isotopic analyses of silicate rocks. Analytica Chimica Acta 339, 79-89.

Pineau, F., Javoy, M., Allegre, C.J., 1973. Etude systématique des isotopes de l'oxygène, du carbone et du strontium dans les carbonatites. Geochim Cosmochim Ac 37, 2363-2377.

Pollard, P.J., 2006. An intrusion-related origin for Cu-Au mineralization in iron oxide-copper-gold (IOGG) provinces. Miner Deposita 41, 179-187.

Porter, T., 2010. The Carrapateena iron oxide copper gold deposit, Gawler Craton, South Australia: a review, Hydrothermal Iron Oxide Copper-Gold and Related Deposits. A Global Perspective, v. 3, Advances in the Understanding of IOCG Deposits. Porter Geoscience Consultancy Publishing Adelaide, 191-200.

Preiss, W.V., 1987. The Adelaide Geosyncline: Late Proterozoic stratigraphy, sedimentation, palaeontology and tectonics. Department of Mines and Energy.

Ramdohr, P., 1950: Die Erzmineralien und ihre Verwachsungen. Berlin.

Reeder, R.J., Dollase, W.A., 1989. Structural variation in the dolomite-ankerite solid-solution series; an X-ray, Moessbauer, and TEM study. Am Mineral 74, 1159-1167.

Reeve, J.S., Cross, K.C., Smith, R.N., Oreskes, N., 1990. Olympic Dam copper-uranium-gold-silver deposit, in: Hughes, F.E. (Ed.), Geology of the mineral deposits of Australia and Papua New Guinea. Australasian Institute of Mining and Metallurgy, Melbourne, 1009-1035.

Reid, A., Flint, R., Maas, R., Howard, K., Belousova, E., 2009. Geochronological and isotopic constraints on Paleoproterozoic skarn base metal mineralisation in the central Gawler Craton, South Australia. Ore Geology Reviews 36, 350-362.

References

Reid, A.J., Fabris, A., 2015. Influence of Preexisting Low Metamorphic Grade Sedimentary Successions on the Distribution of Iron Oxide Copper-Gold Mineralization in the Olympic Cu-Au Province, Gawler Craton. Econ Geol 110, 2147-2157.

Richards, J., 1986. Lead isotopic signatures: further examination of comparisons between South Africa and Western Australia.

Roberts, D.E., Hudson, G.R.T., 1983. The Olympic Dam copper-uranium-gold deposit, Roxby Downs, South Australia. Econ Geol 78, 799-822.

Rogers, J.J.W., Santosh, M., 2009. Tectonics and surface effects of the supercontinent Columbia. Gondwana Research 15, 373-380.

Rose, C.V., Maloof, A.C., 2010. Testing models for post-glacial 'cap dolostone' deposition: Nuccaleena Formation, South Australia. Earth and Planetary Science Letters 296, 165-180.

Sandeman, H.A., Ootes, L., Cousens, B., Kilian, T., 2014. Petrogenesis of Gunbarrel magmatic rocks: Homogeneous continental tholeiites associated with extension and rifting of Neoproterozoic Laurentia. Precambrian Research 252, 166-179.

Santos, R.V., Clayton, R.N., 1995. Variations of oxygen and carbon isotopes in carbonatites: A study of Brazilian alkaline complexes. Geochim Cosmochim Ac 59, 1339-1352.

SARIG database, https://sarig.pir.sa.gov.au/Map.

Saunders, J.A., 1990. Colloidal transport of gold and silica in epithermal precious-metal systems: Evidence from the Sleeper deposit, Nevada. Geology 18, 757-760.

Saunders, J.A., 1994. Silica and gold textures in bonanza ores of the Sleeper Deposit, Humboldt County, Nevada; evidence for colloids and implications for epithermal ore-forming processes. Econ Geol 89, 628-638.

Scher, H.D., Griffith, E.M., Buckley, W.P., 2014. Accuracy and precision of $^{88}Sr/^{86}Sr$ and $^{87}Sr/^{86}Sr$ measurements by MC-ICPMS compromised by high barium concentrations. Geochemistry, Geophysics, Geosystems 15, 499-508.

Schoene, B., Bowring, S., 2006. U-Pb systematics of the McClure Mountain syenite: thermochronological constraints on the age of the $^{40}Ar/^{39}Ar$ standard MMhb. Contrib Mineral Petr 151, 615-630.

Schwinn, G., Wagner, T., Baatartsogt, B., Markl, G., 2006. Quantification of mixing processes in ore-forming hydrothermal systems by combination of stable isotope and fluid inclusion analyses. Geochim Cosmochim Ac 70, 965-982.

Shebanova, O.N., Lazor, P., 2003. Raman spectroscopic study of magnetite ($FeFe_2O_4$): a new assignment for the vibrational spectrum. Journal of Solid State Chemistry 174, 424-430.

Sillitoe, R.H., Burrows, D.R., 2002. New field evidence bearing on the origin of the El Laco magnetite deposit, Northern Chile. Econ Geol 97, 1101-1109.

Sillitoe, R.H., 2003. Iron oxide-copper-gold deposits: an Andean view. Miner Deposita 38, 787-812.

Skirrow, R.G., Bastrakov, E.N., Baroncii, K., Fraser, G.L., Creaser, R.A., Fanning, C.M., Raymond, O.L., Davidson, G.J., 2007. Timing of iron oxide Cu-Au-(U) hydrothermal activity and Nd isotope constraints on metal sources in the Gawler Craton, South Australia. Econ Geol 102, 1441-1470.

Sláma, J., Košler, J., Condon, D.J., Crowley, J.L., Gerdes, A., Hanchar, J.M., Horstwood, M.S., Morris, G.A., Nasdala, L., Norberg, N., 2008. Plešovice zircon - a new natural reference material for U-Pb and Hf isotopic microanalysis. Chem Geol 249, 1-35.

Smith, M., Coppard, J., Herrington, R., Stein, H., 2007. The Geology of the Rakkurijärvi Cu-(Au) Prospect, Norrbotten: A New Iron Oxide-Copper-Gold Deposit in Northern Sweden. Econ Geol 102, 393-414.

Song, X.-Y., Qi, H.-W., Hu, R.-Z., Chen, L.-M., Yu, S.-Y., Zhang, J.-F., 2013. Formation of thick stratiform Fe-Ti oxide layers in layered intrusion and frequent replenishment of fractionated mafic magma: Evidence from the Panzhihua intrusion, SW China. Geochemistry, Geophysics, Geosystems 14, 712-732.

Sprung, P., Kleine, T., Scherer, E.E., 2013. Isotopic evidence for chondritic Lu/Hf and Sm/Nd of the Moon. Earth and Planetary Science Letters 380, 77-87.

Srivastava, R.K., Rao, N.C., 2007. Petrology, geochemistry and tectonic significance of Paleoproterozoic alkaline lamprophyres from the Jungel Valley, Mahakoshal supracrustal belt, Central India. Miner Petrol 89, 189-215.

Stacey, J.S., Kramers, J.D., 1975. Approximation of terrestrial lead isotope evolution by a two-stage model. Earth and Planetary Science Letters 26, 207-221.

Stevenson, J.S., Jeffery, W.G., 1964. Colloform magnetite in a contact metasomatic iron deposit, Vancouver Island, British Columbia. Econ Geol 59, 1298-1305.

Stipp, S.L.S., Christensen, J., Lakshtanov, L., Baker, J., Waight, T.E., 2006. Rare Earth element (REE) incorporation in natural calcite: upper limits for actinide uptake in a secondary phase. Radiochimica Acta 94, 523-528.

Su, W., Hu, R., Xia, B., Xia, Y., Liu, Y., 2009. Calcite Sm-Nd isochron age of the Shuiyindong Carlin-type gold deposit, Guizhou, China. Chem Geol 258, 269-274.

Sugden, T., Cross, K., 1991. Significance of overprinting fault systems in the Olympic Dam breccia complex. Structural Geology in Mining and Exploration. University of Western Australia. Geology Department and University Extension, 93-98.

Sun, S.s., McDonough, W.F., 1989. Chemical and isotopic systematics of oceanic basalts: implications for mantle composition and processes. Geological Society, London, Special Publications 42, 313-345.

Swain, G., Woodhouse, A., Hand, M., Barovich, K., Schwarz, M., Fanning, C.M., 2005. Provenance and tectonic development of the late Archaean Gawler Craton, Australia; U-Pb zircon, geochemical and Sm-Nd isotopic implications. Precambrian Research 141, 106-136.

Tappert, M.C, Rivard, B., Giles, D., Tappert, R., Mauger, A., 2011. Automated drill core logging using visible and near-infrared reflectance spectroscopy: a case study from the Olympic Dam IOCG deposit, South Australia. Econ Geol 106, 289-296.

Tappert, M.C., Rivard, B., Giles, D., Tappert, R., Mauger, A., 2013. The mineral chemistry, near-infrared, and mid-infrared reflectance spectroscopy of phengite from the Olympic Dam IOCG deposit, South Australia. Ore Geology Reviews 53, 26-38.

Taylor, H.P., Frechen, J., Degens, E.T., 1967. Oxygen and carbon isotope studies of carbonatites from the Laacher See District, West Germany and the Alnö District, Sweden. Geochim Cosmochim Ac 31, 407-430.

Teasdale, J., 1997. Methods for understanding poorly exposed terranes: the interpretive geology and tectonothermal evolution of the western Gawler Craton.

Thompson, J., Goemann, K., Whittaker, J.M., 2014a. Authigenic monazite and detrital zircon dating from the Proterozoic Rocky Cape Group, Tasmania: Links to the Belt-Purcell Supergroup, North America. Precambrian Research 250, 50-67.

Torresi, I., Xavier, R., Bortholoto, D.A., Monteiro, L.S., 2012. Hydrothermal alteration, fluid inclusions and stable isotope systematics of the Alvo 118 iron oxide-copper-gold deposit, Carajás Mineral Province (Brazil): Implications for ore genesis. Miner Deposita 47, 299-323.

References

Treloar, P.J., Colley, H., 1996. Variations in F and Cl contents in apatites from magnetite-apatite ores in northern Chile, and their ore-genetic implications. Mineralogical Magazine 60, 285-302.

Trueman, N.A., 1986. Lead-uranium systematics of the Olympic Dam deposit and Stuart Shelf mineralization: Summary report of U-REE mineralization, Adelaide, Australia. Western Mining Corporation, unpublished group memo.

Turner, W.A., Heaman, L.M., Creaser, R.A., 2003. Sm Nd fluorite dating of Proterozoic low-sulfidation epithermal Au-Ag deposits and U Pb zircon dating of host rocks at Mallery Lake, Nunavut, Canada. Canadian Journal of Earth Sciences 40, 1789-1804.

Uysal, I.T., Zhao, J.-X., Golding, S.D., Lawrence, M.G., Glikson, M., Collerson, K.D., 2007. Sm-Nd dating and rare-earth element tracing of calcite: implications for fluid-flow events in the Bowen Basin, Australia. Chem Geol 238, 63-71.

Veevers, J.J., 2004. Gondwanaland from 650-500 Ma assembly through 320 Ma merger in Pangea to 185-100 Ma breakup: supercontinental tectonics via stratigraphy and radiometric dating. Earth-Science Reviews 68, 1-132.

Vella, L., 1997. Interpretation and modelling, based on petrophysical measurements, of the Wirrda Well potential field anomaly, South Australia. Exploration Geophysics 28, 299-306.

Vervoort, J.D., Patchett, P.J., Blichert-Toft, J., Albarède, F., 1999. Relationships between Lu-Hf and Sm-Nd isotopic systems in the global sedimentary system. Earth and Planetary Science Letters 168, 79-99.

Waight, T., Baker, J., Willigers, B., 2002. Rb isotope dilution analyses by MC-ICPMS using Zr to correct for mass fractionation: towards improved Rb-Sr geochronology? Chem Geol 186, 99-116.

Wang, X.-C., Li, X.-H., Li, W.-X., Li, Z.-X., Liu, Y., Yang, Y.-H., Liang, X.-R., Tu, X.-L., 2008. The Bikou basalts in the north-western Yangtze block, South China: Remnants of 820-810 Ma continental flood basalts? Geological Society of America Bulletin 120, 1478-1492.

Wang, X.-C., Li, X.-H., Li, Z.-X., Liu, Y., Yang, Y.-H., 2010. The Willouran basic province of South Australia: Its relation to the Guibei large igneous province in South China and the breakup of Rodinia. Lithos 119, 569-584.

Watson, T., Taber, S., 1910. Nelsonite, a new rock type; its occurrence, association, and composition. Geological Society of America Bulletin 21, 787.

Wawryk, C., 1989. Strontium and rare earth element geochemistry of barite-fluorite mineralization at Olympic Dam, South Australia. B.Sc. thesis, unpublished.

Webb, A.W., Coats, R.P., 1980. A reassessment of the age of the Beda Volcanics on the Stuart Shelf, South Australia. Department of Mines and Energy. Report Book.

Webb, A., Coats, R., Fanning, C., Flint, R., 1983. Geochronological framework of the Adelaide Geosyncline, Geological Society of Australia Abstracts, 7-9.

Widupp H., Fouet, T., Hodgkison, J., McCuaig, T.C., Miller, J., 2004. A three-dimensional structural interpretation of the Olympic Dam deposit - implications for mine planning and exploration: Hi Tech and World Competitive Mineral Success Stories Around the Pacific Rim. Proceedings of the Pacrim 2004 Conference, Adelaide, 417-426.

Wiedenbeck, M., AllÉ, P., Corfu, F., Griffin, W.L., Meier, M., Oberli, F., Quadt, A.V., Roddick, J.C., Spiegel, W., 1995. Three natural zircon standards for U-Th-Pb, Lu-Hf, trace element and REE analyses. Geostandards Newsletter 19, 1-23.

Wilkinson, J.J., Nolan, J., Rankin, A.H., 1996. Silicothermal fluid: A novel medium for mass transport in the lithosphere. Geology 24, 1059-1062.

Williams, P.J., Barton, M.D., Johnson, D.A., Fontboté, L., De Haller, A., Mark, G., Oliver, N.H., Marschik, R., 2005. Iron oxide copper-gold deposits: Geology, space-time distribution, and possible modes of origin. Econ Geol, 371-405.

Williamson, B.J., Wilkinson, J.J., Luckham, P.F., Stanley, C.J., 2002. Formation of coagulated colloidal silica in high-temperature mineralizing fluids. Mineralogical Magazine 66, 547-553.

Wingate, M.T.D., Campbell, I.H., Compston, W., Gibson, G.M., 1998. Ion microprobe U-Pb ages for Neoproterozoic basaltic magmatism in south-central Australia and implications for the breakup of Rodinia. Precambrian Research 87, 135-159.

Wong, B.L., Morrissey, L.J., Hand, M., Fields, C.E., Kelsey, D.E., 2015. Grenvillian-aged reworking of late Paleoproterozoic crust of the southern North Australian Craton, central Australia: Implications for the assembly of Mesoproterozoic Australia. Precambrian Research 270, 100-123.

Woodhead, J., 2002. A simple method for obtaining highly accurate Pb isotope data by MC-ICP-MS. Journal of Analytical Atomic Spectrometry 17, 1381-1385.

Woodhead, J., Pickering, R., 2012. Beyond 500ka: Progress and prospects in the U-Pb chronology of speleothems, and their application to studies in palaeoclimate, human evolution, biodiversity and tectonics. Chem Geol 322, 290-299.

Wu, C., 2008. Bayan Obo Controversy: Carbonatites versus Iron Oxide-Cu-Au-(REE-U). Resour Geol 58, 348-354.

Zhao, J., McCulloch, M.T., 1993. Sm-Nd mineral isochron ages of Late Proterozoic dyke swarms in Australia: evidence for two distinctive events of mafic magmatism and crustal extension. Chem Geol 109, 341-354.

Zhao, J., McCulloch, M.T., Korsch, R.J., 1994. Characterisation of a plume-related ~800 Ma magmatic event and its implications for basin formation in central-southern Australia. Earth and Planetary Science Letters 121, 349-367.

Appendices

Additional analyses which are not included in chapters 1-6

Carbonates: chemical composition

A total of 113 analyses of *major, minor and trace elements* (45 elements, spot analyses, Table 4.11, has been acquired on 103 carbonate samples using LA-ICPMS at UTas (see Chapter 4) and 82 analyses in 68 samples have been measured by Q-ICPMS in Melbourne (see Chapter 4, analyses on a 10% split of the sample solution, Table A.1). The goal of this investigation at UTas was, firstly, to determine the trace element contents (particularly of Rb, Sr, Sm, Nd, Pb, U, Lu and Hf) in order to choose most suitable samples for an isotope dilution study conducted in Melbourne. Another goal was to compare trace element concentrations in different carbonate types and groups/associations. The results for this investigation and the trace element measurements conducted in Melbourne are very similar (Fig. A.1). Further, the results of the major elements analyzed by LA-ICPMS at UTAS correlate well with the data obtained from the EPMA (see Chapter 5, Table 5.4). In general, carbonates at Olympic Dam show very varying trace element contents between different samples. REY patterns for siderite, calcite and solid solutions of siderite-magnesite-rhodochrosite, dolomite-ankerite (Fig. A.1) cannot be clearly distinguished. In terms of different carbonate associations, most of the groups show different REY patterns than the others (Fig. A.2).

Anhydrite: trace elements, Raman spectroscopy, stable S isotopes

A total of five analyses of *major, minor and trace elements* (28 trace elements, including REE, Table A.1, has been acquired on three anhydrite samples using Q-ICPMS in Melbourne (see Chapter 4, analyses on a 10% split of the sample solution).

Raman spectroscopy study of anhydrite has been conducted on three samples (carefully hand-picked grains have been placed into an epoxy mount for investigation, Fig. A.3 A) Renishaw inVia Raman microscope with Streamline at UTas (CSL, see Chapter 3, excitation wavelength was 532 nm; focussing of the beam was carried out by a 50x object lens, NA 0.75, resulting in a spot size of ~1 μm; spectra recorded from ~100 to 4000 cm^{-1} using a laser power of ~1.5 mW on the sample surface). The aim was to distinguish between the anhydrous anhydrite and H_2O-bearing gypsum. In total 3 samples have been studied; in each sample two different areas have been tested. The spectra for all point measurements revealed almost identical peak positions (five peaks between 400 and 700 cm^{-1}, main peak at ~1000 cm^{-1} and three peaks between 1100 and 1200 cm^{-1}) which entirely overlap with the anhydrite spectra in the rruff database (*www.rruff.info*, Fig. A.3 B). To note, there are no signals in the interval between 3400 to 3700 cm^{-1} which points to the absence of the crystal-bound water molecules. One sample (OD817) has been chosen for Raman mapping in order to study the heterogeneity of anhydrite in BSE images (different brightness between different anhydrite grains and within the fine lamellae within grains, Fig. A.4 A). Thereby, two zones within this sample have been mapped. The Raman maps (Fig. A.4 B-C) revealed differences in the Raman signal as well. Three types of maps have been created on a basis of the shift of one or more peaks or a particular interval of the spectrum. Each map displays different features, namely crystallographic orientation, chemistry and mineral phase distribution (e.g., hematite inclusions inside the anhydrite

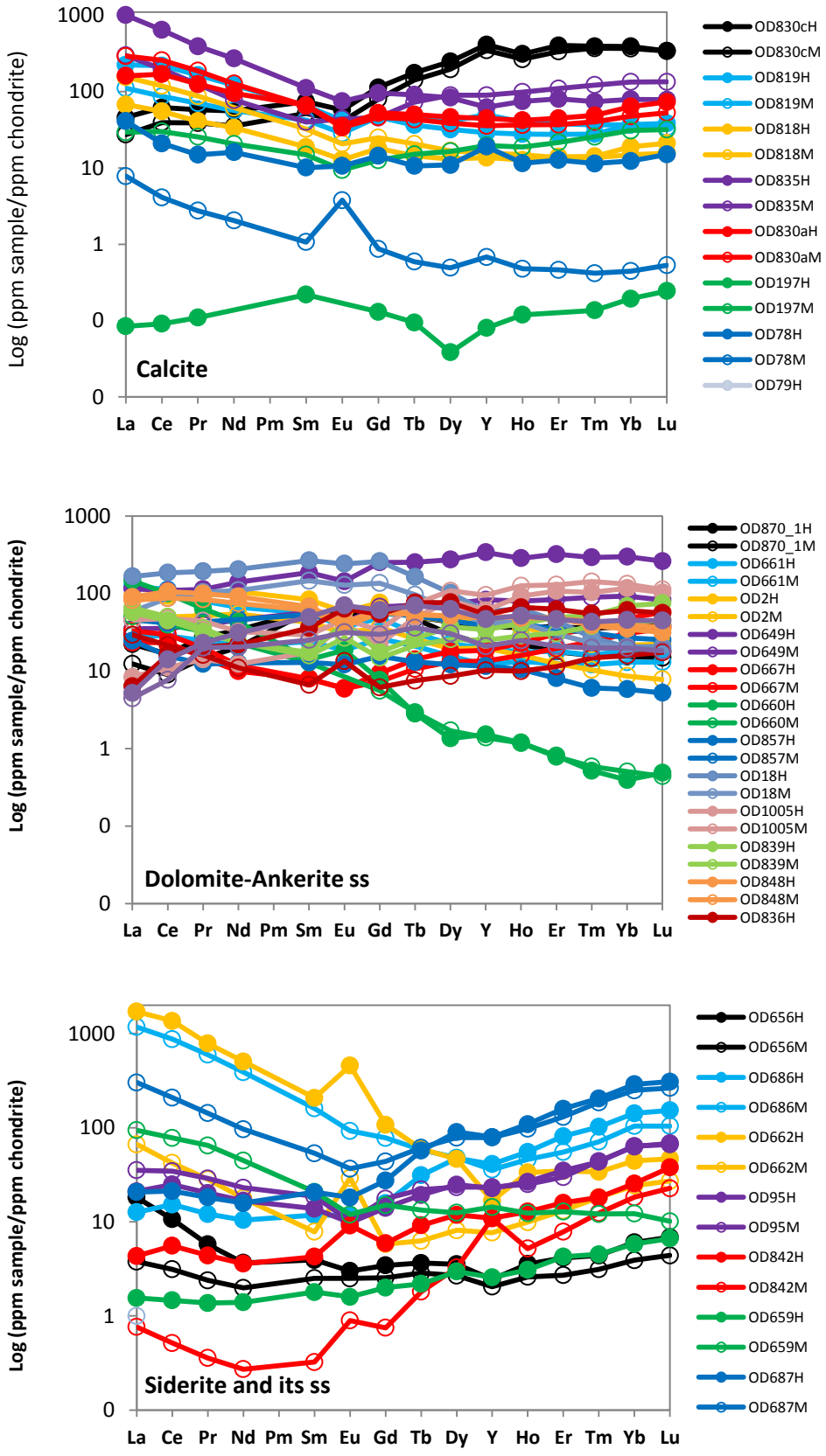

Fig. A.1: Comparison of the trace element data (REY) of carbonates analyzed in Hobart (filled circles, spot analyses, H) and in Melbourne (empty circles (M), 10% split of the sample solution). Note the similarity between most of the patterns for single samples analyzed by diverse techniques. Chondrite data for normalization have been taken from McDonough and Sun (1995). Ss: solid solution.

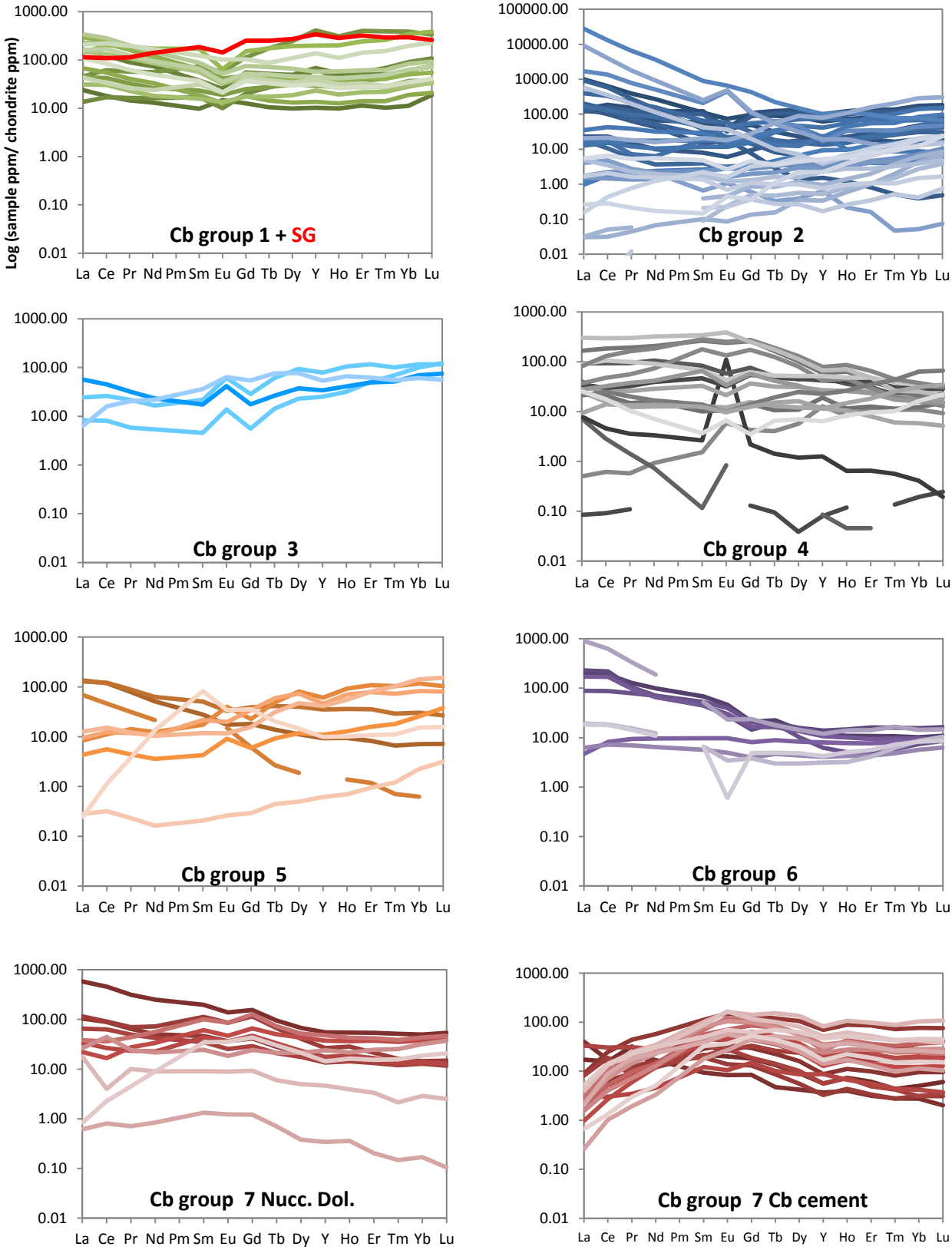

Fig. A.2: REY patterns of carbonates (Cb) ordered after different carbonate associations. See full group names in Chapter 5 and Table 5.2. Note that most of the groups differ from each other; internal heterogeneity within single groups is sometimes observable. Chondrite data for normalization have been taken from McDonough and Sun (1995). Abbr.: carbonate (Cb), Nuccaleena Dolomite-like sediment (Nucc. Dol.), sample of the vein from the Snake Gully prospect (SG).

or ordered along the anhydrite grain boundaries).

Stable isotopes of S (Table A.2) have been performed on a common IRMS instrument at UTas (CSL) on the same set of samples where Raman spectroscopy has been conducted (Fig. A.3 A). Each sample (carefully handpicked and grounded, ~0.12 g) has been treated using a technique (flash combustion, Elementar, vario PyroCube, Germany) where a sample is burned in an excess of oxygen and then converted into SO_2. This measurement provides quantitative data on element content in the samples. The purified gases are then sequentially released into a continuous flow mass spectrometer (Isoprime 100 with IonVantage software) to perform the isotopic measurements of $\delta^{34}S$ (values are reported relative to Vienna Cañon Diablo troilite) in the IRMS. The analytical precision of the $\delta^{34}S$ values, determined by repetitive measurements of three international sulphur standards, is around 0.2 ‰. Prior to this study, no stable isotope data has been done on anhydrite from Olympic Dam. The results of the current study allow distinguishing between the two anhydrite groups with different $\delta^{34}S$ ranges, namely from 16.90 to 16.74‰ for samples OD670 and OD785, and 4.58 to 6.82‰ for sample OD817 (Fig. A.5). Remarkably, the samples with the high $\delta^{34}S$ values are most likely much younger (e.g., one veins crosscuts the GDS dolerite which is ~0.82 Ga, see Chapter 3, Huang et al., 2015) anhydrite generations than the pinkish anhydrite with low $\delta^{34}S$ values which represents the old (~1.59 Ga, see Chapter 6). Nearly same isotopic ranges have been produced by Wawryk (1989) for the early and late barite generations of barite; thereby barite data obtained by (Eldridge and Danti, 1994) for few barite samples entirely close the gap between the older and the younger barite generations on the $\delta^{34}S$ diagram. Thus, this might point to multiple generations of sulfates (e.g., anhydrite, barite) formed at Olympic Dam during its evolution. In contrast to sulfates, the $\delta^{34}S$ values of various sulfides (e.g., pyrite, chalcopyrite, bornite, and chalcocite, Eldridge and Danti, 1994) are negative and do not show any clustering. Altogether, the stable isotope results implies derivation of the S from sediments (including evaporates), granitoids and nearly all other potential S reservoirs (Eckstrand et al., 1989; Hoefs, 1997) shown in Fig. A.5. Therefore, the interpretation of the sparse stable data of S isotopes does not allow a full understanding of the S isotope systematics of the supergiant Olympic Dam deposit at this point of research. However, it is of a great importance to conduct a broad study on the isotopy of different sulfates and sulfides (from a number of different associations found across the deposit) in order to be able to clearly identify of the sulfur reservoirs at Olympic Dam.

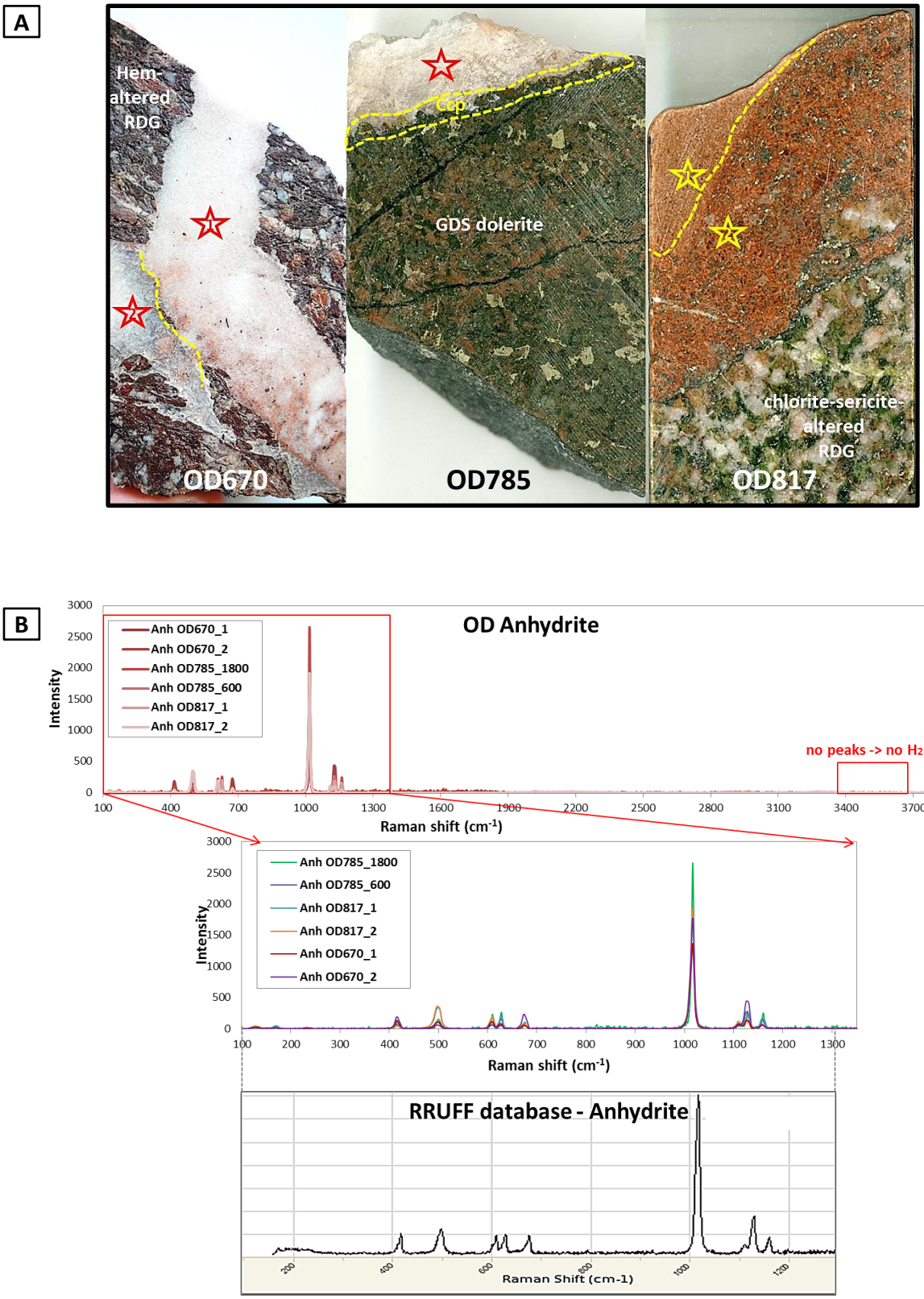

Fig. A.3. (A) Drillcore images of three anhydrite (Anh)-bearing samples (OD670, OD785 and OD817) which have been studied by Raman spectroscopy (see Figs. A.3 B and A.4) and IRMS (stable S isotopes, see Fig. A.4). Note that two of the samples each have two subsamples. (B) Raman spectra for three vein anhydrite (Anh) samples from Olympic Dam (OD) hosted by the granite (either hematite (Hem)- or chlorite-sericite-altered) and the GDS-type dolerites. Note the similarities between the different spectra and the reference anhydrite spectrum from rruff database (www.rruff.info).

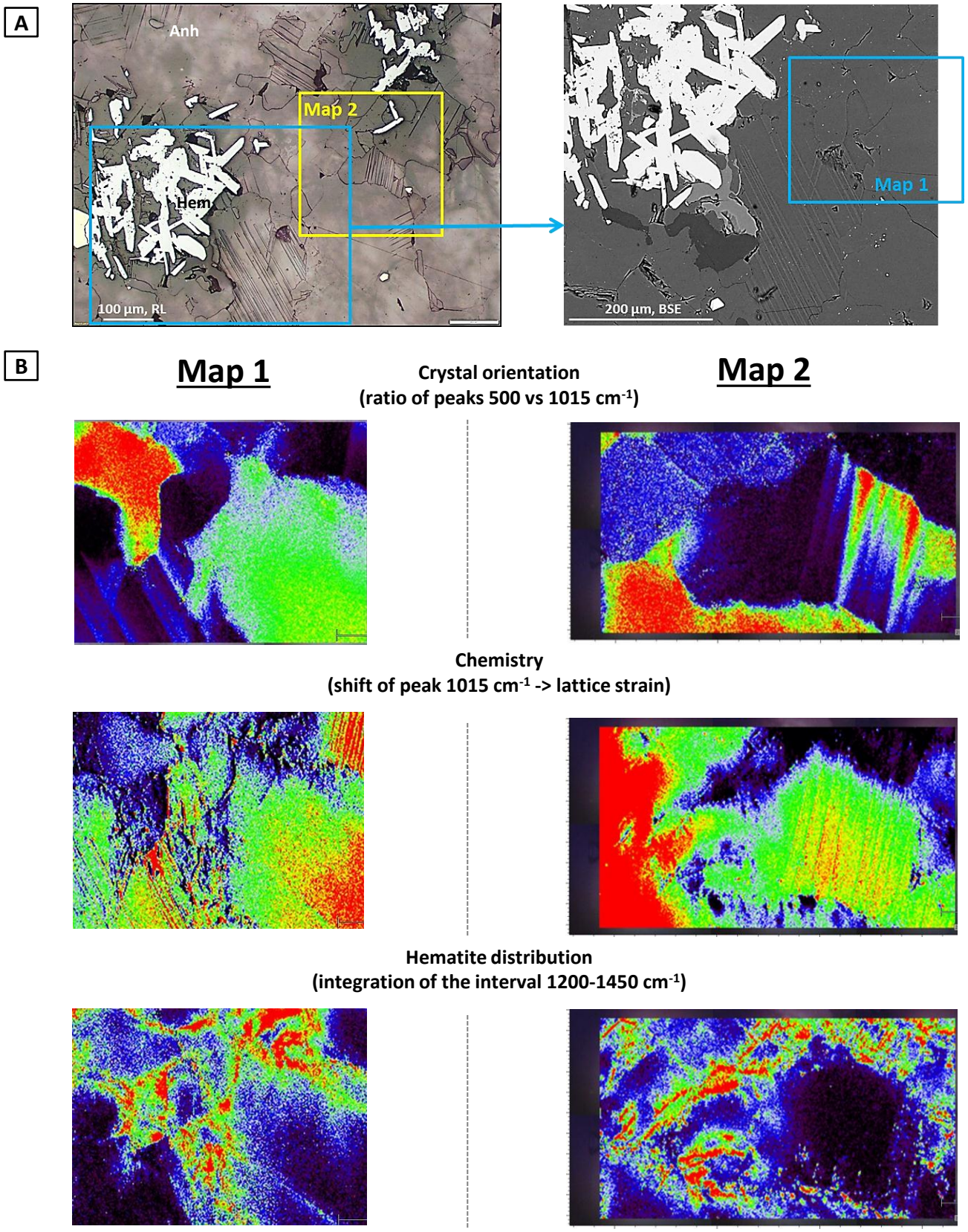

Fig. A.4: (A) TL (//P, on the left side) and BSE (on the right side) images of anhydrite (Anh, OD817) which is intergrown with the hematite (Hem). Note lamellae within anhydrite and differences in the brightness between different anhydrite grains, and fine lamellae within some of the grains. (B) Several maps for the two selected areas in the sample (thin section). The maps show such different features as differences in the crystal orientation, chemically induced differences and hematite distribution within anhydrite grains and on the boundary of some anhydrite grains.

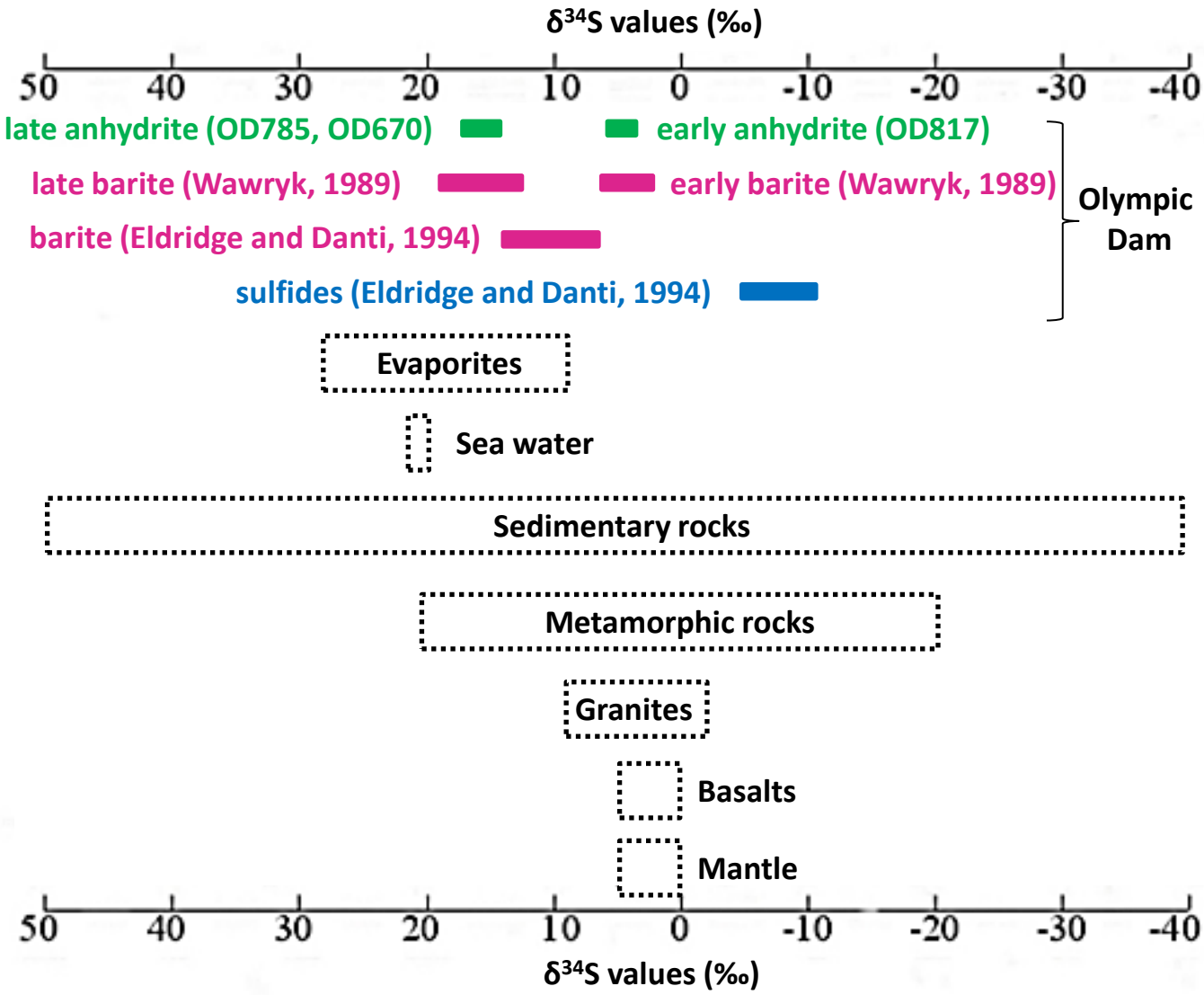

Fig. A.5: Results of the stable isotope ($\delta^{34}S$) study in anhydrite, compared with the literature data for barite (Wawryk, 1989; Eldridge and Danti, 1994) and diverse sulfides (Eldridge and Danti, 1994) from the Olympic Dam deposit. The potential sources of S in sulfates and sulfides at Olympic Dam are sediments and granitoids. All values for potential S reservoirs obtained from Hoefs (1997), except mantle values from Eckstrand et al. (1989).

General abbreviations

$\delta^{18}O$	$^{18}O/^{16}O$ isotopic ratio
$\delta^{13}C$	$^{13}C/^{12}C$ isotopic ratio
$\delta^{34}S$	$^{34}S/^{32}S$ isotopic ratio
BIFs	Banded Iron Formations
BSE	Backscattered electron (image)
CL	Cathodoluminescence (image)
CODES	Council (ARC) Centre of Excellence in Ore Deposits
CSL	Central Science Laboratory
IOA	Iron oxide-apatite (deposits)
IOCG	Iron-oxide copper-gold (deposits)
IPF	Inverse pole figure
IRMS	Isotope Ratio Mass Spectrometer
Fig(s).	Figure(s)
Ga	Billion years
GDS	Gairdner Dyke Swarm
GRV	Gawler Range Volcanics
HREE	Heavy rare earth elements
RL	Reflected light
EBSD	Electron backscatter diffraction
EDS	Energy dispersive x-ray spectrometry
E	East, eastern
EOH	End of drillhole
EPMA	Electron Probe Microanalyzer
LA-ICPMS	Laser Ablation Inductively Coupled Plasma Mass Spectrometer
LIP	Large Igneous Province
LREE	Light rare earth elements
Ma	Million years
MC-ICPMS	Multicollector Inductively Coupled Plasma Mass Spectrometer
N	North, northern
OD	Olympic Dam (deposit)
ODBC	Olympic Dam Breccia Complex
Q-ICPMS	Quadrupole Inductively Coupled Plasma Mass Spectrometer
RDG	Roxby Downs Granite
REE	Rare earth elements
RL	Reflected light
S	South, southern
SEM	Scanning electron microscope
senso lato	in the wide or broad sense
senso stricto	in the strict sense
SLIP	Silicic Large Igneous Province
ss	solid solution(s)
TL	Transmitted light
UTas	University of Tasmania
vol.%	volume percent
V-PDB	Vienna Pee Dee Belemnite
V-SMOW	Vienna Standard Mean Ocean Water
W	West, western
wt%	Weight percent
xP	Crossed polars
//P	Uncrossed polars

Tables

Table 3.1: List of samples from the drillholes RD222 and RU65-8337 which show similar magnetite-apatite-titanite dominated alteration assemblages (veins and massive occurrences) associated with the dolerite and basalt. The numbers in the first column correlates to the numbers in Figs. 3.14-3.15. Abbr: anhydrite (Anh), apatite (Ap), barite (Brt), calcite (Cal), chalcocite (Cc), chalcopyrite (Ccp), chlorite (Chl), dolomite-apatite solid solution (Dol-Ank ss), Fl (fluorite), galena (Gn), hematite (Hem), magnetite (Mt), monazite (Mon), pyrite (Py), sericite (Ser), sphalerite (Sp), titanite (Tit), quartz (Qtz), uraninite (Urn). See location of the drillholes RD222 and RU65-8337 in Fig. 3.1.

#	OD/RX#	Drillhole	Depth/m	Host rock	Mineralogy (vein, alteration)
1	OD422	RD222	759	basalt	Mt-Ap-Cal-Dol Ank ss-Qtz-Ccp-Tit
2	OD423	RD222	769.4	basalt	Mt-Ap-Cal-Qtz-Ccp
3	OD949	RU65-8337	502.3	dolerite	Mt-Ap-Cal-Qtz ore, cut by Qtz-Fl-Ccp
4	RX8152	RU65-8337	505.2	dolerite	Mt-Hem*-Ap-Ccp-Chl-Tit-Ti oxide
5	RX8153	RU65-8337	505.2	dolerite	Mt-Ap-Qtz-Chl-Ser-Urn-Mon-Ccp-Py ore
6	RX8154	RU65-8337	505.5	dolerite	Mt-Ap-Qtz-Chl-Ser-Urn-Mon-Ccp-Py ore
7	RX8155	RU65-8337	507.5	dolerite	Hem*-Ap-Qtz
8	RX8156	RU65-8337	508.1	dolerite	Hem
9	RX8157	RU65-8337	509.2	dolerite	Hem*-Ap-Qtz-Chl
10	RX8162	RU65-8337	513	dolerite	Hem*-Ap-Qtz-Chl-Cal-Anh-Cc-Mon-Tit
11	RX8163	RU65-8337	514	dolerite	-
12	RX8166	RU65-8337	517	dolerite	-
13	RX8168	RU65-8337	518	dolerite	-
14	OD956	RU65-8337	555.5	dolerite	Mt-Hem*-Cal-Anh-Chl-Ccp-Sp-Py-Gn
15	OD957	RU65-8337	561.4	dolerite	Mt-Hem*-Cal-Qtz-Ccp-Sp
16	RX8234	RU65-8337	583.3	dolerite	-
17	RX8235	RU65-8337	584.2	dolerite	-
18	RX8242	RU65-8337	591	dolerite	-
19	RX8246	RU65-8337	595	dolerite	Mt-Qtz-Cal-Chl-Gn-Tit
20	RX8248	RU65-8337	597	dolerite	Mt-Hem*-Ap-Ccp-Gn-Cal-Chl

* possibly former magnetite

Appendices

Table 3.2: Selected major and minor element concentrations (in wt%) of the vein apatite (sample OD422).

Descr.	Si	Fe	Ca	P	Cl	F	O	Total
grain 1 core	1.34	0.11	36.0	15.62	0.48	3.93	36.1	93.6
grain 1	1.14	0.05	36.5	15.77	0.64	3.53	36.3	93.9
grain 1	1.19	0.09	36.4	15.85	0.54	3.85	36.4	94.4
grain 1	1.13	0.06	36.5	16.02	0.55	3.59	36.6	94.4
grain 1 rim	1.03	0.10	36.8	16.07	0.38	4.13	36.6	95.1
grain 2 core	0.68	0.11	37.9	16.90	0.37	3.70	37.7	97.4
grain 2	0.61	0.22	37.8	17.20	0.52	3.72	38.1	98.2
grain 2 rim	0.49	0.05	38.2	17.35	0.24	3.91	38.2	98.4
grain 3 core	0.39	0.18	38.5	17.40	0.28	3.86	38.4	99.0
grain 3	0.61	0.24	38.4	17.31	0.50	3.66	38.5	99.3
grain 3 rim	0.21	0.06	39.0	17.84	0.28	3.96	38.8	100.2

Recalc with REE	Si	Fe	Ca	P	Cl	F	O	La	Ce	Pr	Nd	Total
grain 1 core	1.34	0.11	35.99	15.62	0.48	3.93	36.10	-	-	-	-	93.61
With REE in matrix correction	1.39	0.11	35.47	15.94	0.48	3.71	37.47	1.24	3.40	0.41	1.49	101.09
Difference absolute wt%	0.05	0.00	-0.53	0.32	0.00	-0.22	1.37					
Difference relative %	3.5%	-1.8%	-1.5%	2.0%	0.3%	-5.7%	3.8%					

REE → F interference	La	Ce
	-0.3	1.6
	59.4	59.7
	1.2	3.4
	-0.0061	0.0911

Table 3.3: U-Th-Pb isotopic data for apatite standard OD306 from Acropolis prospect, South Australia.

	Compositional Parmeters								
Sample	Wt. mg (a)	U ppm (b)	Th / U (c)	Pb ppm (d)	$^{206}Pb^*$ x10^{-13} mol (c)	mol% $^{206}Pb^*$ (e)	Pb^*/Pb_c (e)	Pb_c (pg) (e)	$^{206}Pb/^{204}Pb$ (e) (f)
OD306.1	2.380	19.716	4.617	11.758	533.860	0.988	46.419	590.209	1290.534
OD306.2	1.350	16.538	4.820	10.983	261.806	0.953	11.892	1150.225	336.513
OD306.3	4.780	16.393	4.793	10.161	918.014	0.990	56.640	842.714	1550.415
OD306.4	2.850	15.657	4.781	9.670	521.209	0.990	56.793	476.916	1556.369
OD306.5	2.590	16.572	4.882	10.455	503.931	0.986	42.773	618.694	1163.628
OD306.6	2.630	15.072	5.098	10.166	466.244	0.962	15.624	1608.433	424.118

	Radiogenic Isotope Ratios							
	$^{206}Pb/^{204}Pb$ (g)	$^{207}Pb/^{206}Pb$ (g)	% err (h)	$^{207}Pb/^{235}U$ (g)	% err (h)	$^{206}Pb/^{238}U$ (g)	% err (h)	corr. coef.
OD306.1	1.379	0.098	0.077	3.702	0.516	0.273	0.507	0.989
OD306.2	1.423	0.099	0.168	3.837	0.564	0.281	0.542	0.955
OD306.3	1.411	0.098	0.082	3.812	0.521	0.281	0.51	0.988
OD306.4	1.410	0.098	0.057	3.801	0.513	0.280	0.506	0.994
OD306.5	1.436	0.098	0.073	3.820	0.518	0.281	0.509	0.990
OD306.6	1.503	0.099	0.137	3.847	0.528	0.282	0.511	0.966

	Isotopic Ages					
	$^{207}Pb/^{206}Pb$ (i)	± (h)	$^{207}Pb/^{235}U$ (i)	± (h)	$^{206}Pb/^{238}U$ (i)	± (h)
OD306.1	1594.864	1.445	1571.891	4.129	1554.789	7.005
OD306.2	1604.895	3.134	1600.463	4.547	1597.047	7.672
OD306.3	1594.549	1.534	1595.296	4.189	1595.810	7.215
OD306.4	1594.817	1.058	1592.997	4.127	1591.571	7.142
OD306.5	1594.499	1.369	1597.004	4.169	1598.849	7.212
OD306.6	1604.348	2.559	1602.681	4.256	1601.353	7.239

	Sample (Radiogenic + Initial Pb) Isotope Ratios								
	$^{238}U/^{206}Pb$ (j)	% err (h)	$^{207}Pb/^{206}Pb$ (j)	% err (h)	$^{204}Pb/^{206}Pb$ (j)	% err (h)	corr. coef. 8/6-7/6	corr. coef. 8/6-4/6	corr. coef. 7/6-4/6
OD306.1	3.622	0.508	0.109	0.321	0.001	3.353	-0.094	-0.083	0.987
OD306.2	3.391	0.543	0.139	0.476	0.003	1.628	-0.161	-0.153	0.981
OD306.3	3.524	0.511	0.107	0.19	0.001	2.384	-0.066	-0.046	0.961
OD306.4	3.536	0.508	0.107	0.336	0.001	4.187	-0.096	-0.086	0.989
OD306.5	3.505	0.511	0.11	0.336	0.001	3.184	-0.098	-0.088	0.985
OD306.6	3.414	0.509	0.131	0.289	0.002	1.171	-0.105	-0.089	0.978

Table 3.3: Continued.

	Sample (Radiogenic + Initial Pb) Isotope Ratios									
	$^{238}U/^{204}Pb$ (j)	% err (h)	$^{206}Pb/^{204}Pb$ (j)	% err (h)	corr. coef. 8/4-6/4	$^{235}U/^{204}Pb$ (j)	% err (h)	$^{207}Pb/^{204}Pb$ (j)	% err (h)	corr. coef. 5/4-7/4
OD306.1	4830.807	3.432	1333.646	3.353	0.989	35.036	3.432	145.077	3.037	0.989
OD306.2	1159.611	1.793	341.969	1.628	0.954	8.41	1.793	47.625	1.164	0.95
OD306.3	5590.86	2.461	1586.394	2.384	0.978	40.549	2.461	169.933	2.202	0.978
OD306.4	5732.678	4.261	1621.402	4.187	0.993	41.577	4.261	173.401	3.855	0.993
OD306.5	4208.344	3.269	1200.597	3.184	0.988	30.522	3.269	131.956	2.853	0.987
OD306.6	1464.938	1.318	429.065	1.171	0.923	10.625	1.318	56.233	0.89	0.919

Table 3.4: Major (wt%) and trace (ppm) element concentrations for OD422 dolerite.

TiO_2	Al_2O_3	FeOt	MnO	MgO	CaO	Na_2O	K_2O	P_2O_5	Mg#	Li	Be	Sc
2.40	12.70	15.00	0.00	5.67	9.63	2.14	0.42	0.23	0.43	20.10	0.70	38.00

Ti	V	Cr	Mn	Ni	Cu	Zn	Ga	As	Rb	Sr	Y	Zr
1.44	434.00	92.00	0.19	68.00	286.00	102.00	21.00	<0.5	15.60	171.80	32.30	133.00

Nb	Mo	Sb	Cs	Ba	La	Ce	Pr	Nd	Sm	Eu	Gd	Tb
11.90	0.80	0.60	2.32	100.60	12.30	28.70	4.22	20.00	5.50	1.90	6.03	0.97

Dy	Ho	Er	Tm	Yb	Lu	Hf	Ta	Tl	Pb	Th	U
5.81	1.22	3.43	0.48	2.89	0.36	3.90	0.80	0.06	6.00	1.88	0.51

Table 3.5: Sm-Nd, Rb-Sr isotope data for OD422 dolerite, bulk vein and pure vein apatite concentrate.

	OOD422 wr dolerite #	OD422.4 dolerite*	OD422.5 dolerite*	OD422.6 bulk vein	OD422 ap vein apatite
Rb ppm	14.3	14.8	14.5	11.45	1.0
Sr ppm	168	178.0	176.2	54.78	451
$^{87}Rb/^{86}Sr$	0.247	0.240	0.237	0.606	0.0064
$^{87}Sr/^{86}Sr$	0.706399±16	0.707890±16	0.707932±15	0.727767±15	0.734919±22
Sm ppm	5.54	5.19	5.28	10.13	596
Nd ppm	20.48	18.95	19.43	51.00	4788
$^{147}Sm/^{144}Nd$	0.1633	0.165	0.164	0.1199	0.0752
$^{143}Nd/^{144}Nd$	0.512603±12	0.5126174±8	0.5125998±8	0.512019±10	0.511499±8
εNd_{meas}	-0.6	-0.3	-0.6	-12.0	-22.1
$^{87}Sr/^{86}Sr$ (i)	0.70354	0.70511	0.70518	0.72074	0.73485
εNd (i)	2.9	3	2.7	-3.9	-9.1

$^{87}Sr/^{86}Sr$ (i) and εNd (i) are age-corrected to 827 Ma
whole rock powder; * small-scale sampling with dental drill

Table 3.6: Selected major and minor element concentrations (in wt%) of the vein magnetite (sample OD422). Abbr.: core (c), grain (g.), rim (r).

Descr.	Si	Zn	Al	V	Fe	Mn	Mg	Ca	O	Total	Fe^{3+}	Fe^{2+*}	O*	Total*
c. g. 1	2.51	0.04	0.02	<0.017	68.0	0.41	0.13	0.54	22.8	94.3	31.8	36.2	27.3	98.9
c. g. 1	2.55	0.02	<0.01	<0.018	68.2	0.41	0.13	0.52	22.8	94.6	31.8	36.4	27.4	99.2
c. g. 1	2.61	0.02	0.01	<0.017	68.0	0.42	0.14	0.56	22.9	94.6	31.6	36.3	27.4	99.2
c. g. 1	2.71	0.04	0.02	<0.016	67.8	0.41	0.13	0.60	23.0	94.7	31.5	36.4	27.5	99.2
c. g. 1	2.60	0.02	<0.01	<0.017	67.8	0.38	0.15	0.56	22.8	94.4	31.6	36.2	27.3	98.9
c. g. 1	2.61	0.04	0.01	<0.014	67.8	0.41	0.17	0.58	22.9	94.5	31.6	36.2	27.4	99.0
c. g. 1	2.03	0.05	<0.01	<0.013	69.1	0.33	0.16	0.33	22.5	94.4	32.8	36.3	27.2	99.1
c. g. 1	2.31	0.04	0.02	<0.014	68.3	0.36	0.10	0.45	22.6	94.1	32.1	36.3	27.2	98.7
c. g. 1	3.30	0.04	0.08	<0.013	66.4	0.44	0.15	0.72	23.4	94.5	29.9	36.5	27.7	98.8
c. g. 1	3.28	0.04	0.15	<0.013	66.2	0.45	0.15	0.66	23.3	94.2	29.8	36.4	27.6	98.5
c. g. 2	2.16	<0.02	0.07	<0.014	68.8	0.38	0.20	0.50	22.7	94.8	32.6	36.2	27.3	99.5
c. g. 2	2.13	<0.02	0.04	<0.014	68.9	0.37	0.22	0.48	22.6	94.7	32.7	36.1	27.3	99.4
c. g. 2	2.16	0.04	0.04	<0.014	68.7	0.37	0.23	0.50	22.6	94.7	32.7	36.1	27.3	99.4
c. g. 2	2.07	<0.02	0.09	<0.014	68.9	0.33	0.19	0.49	22.6	94.7	32.8	36.1	27.3	99.4
c. g. 2	2.80	<0.02	0.55	<0.014	66.2	0.43	0.22	0.76	23.2	94.2	30.6	35.6	27.6	98.6
c. g. 2	2.65	0.03	0.55	<0.017	66.6	0.35	0.21	0.74	23.1	94.3	30.9	35.6	27.6	98.7
c. g. 2	1.99	0.02	0.19	<0.013	69.0	0.30	0.12	0.51	22.6	94.7	32.8	36.2	27.3	99.4
c. g. 2	1.80	0.03	0.21	<0.014	69.4	0.26	0.13	0.43	22.5	94.7	33.2	36.2	27.2	99.5
r. g. 1	0.98	0.03	0.14	<0.014	71.0	0.15	0.06	0.18	21.8	94.3	34.7	36.3	26.7	99.3
r. g. 1	1.14	<0.02	0.05	<0.014	70.7	0.16	0.07	0.22	21.8	94.2	34.4	36.3	26.7	99.1
r. g. 1	1.06	0.02	0.03	<0.013	70.8	0.17	0.05	0.19	21.7	94.0	34.5	36.3	26.6	99.0
r. g. 1	1.25	0.03	0.06	<0.013	70.7	0.23	0.06	0.21	21.9	94.5	34.3	36.4	26.8	99.4
r. g. 1	0.91	<0.02	0.04	<0.014	70.8	0.19	0.05	0.11	21.5	93.6	34.6	36.1	26.5	98.5
r. g. 1	0.79	<0.02	0.02	<0.014	71.5	0.14	0.07	0.09	21.5	94.2	35.1	36.4	26.6	99.2
r. g. 1	0.99	0.02	0.02	<0.013	71.5	0.20	0.05	0.14	21.8	94.7	34.9	36.6	26.8	99.7
r. g. 2	0.96	0.02	0.04	<0.014	70.8	0.21	0.09	0.13	21.6	93.8	34.7	36.1	26.6	98.8
r. g. 2	0.56	0.03	0.02	<0.013	71.7	0.24	0.02	0.05	21.3	93.9	35.5	36.3	26.4	99.0
r. g. 2	0.70	0.02	<0.01	<0.013	71.2	0.26	0.09	0.15	21.4	93.7	35.2	36.0	26.4	98.8
r. g. 2	0.37	0.03	<0.01	<0.014	72.0	0.22	0.02	0.05	21.2	93.8	35.8	36.2	26.3	99.0
r. g. 2	0.61	0.03	0.02	<0.014	71.5	0.23	0.04	0.10	21.3	93.8	35.3	36.1	26.4	98.9

* values after calculation of Fe^{2+} and Fe^{3+}.

Table 3.7: Selected trace element concentrations (in ppm) for the vein magnetite (sample OD422).

Element	rim	inner core	outer core
Al	314.3	3822	2195
Si	12925	38330	24292
Ca	301.17	6879.7	7696.04
Ti	29.95	166.3	77.41
V	17.45	57.94	29.35
Mn	1868	2723	2315
Fe*	723600	723600	723600
Sr	1.25	14.45	7.52
Zr	0.30	4.00	1.21
Ba	1.43	36.41	9.40
La	2.33	76.85	127.18
Ce	4.46	142.46	238.98
Nd	1.79	50.87	76.61
Sm	0.26	7.65	7.07
Gd	0.27	5.30	4.55
Dy	0.19	3.10	1.69
Yb	0.08	1.23	1.22
U	0.37	7.79	9.69

* ideal Fe concentration

Table 3.8: Selected trace element concentrations (in ppm) for the vein apatite (sample OD422). Table includes a selection of elements.
*Ideal Ca concentration. Abbr.: grain (gr.).

Descr.	Si	P	Ca*	Sr	Y	La	Ce	Pr	Nd	Sm	Eu	Gd	Tb	Dy	Ho	Er	Tm	Yb	Lu
gr. 1	6887.66	194470	397400	222.78	1601.66	7358.77	17036.75	1697.79	5669.10	671.43	53.46	494.86	56.46	300.30	56.67	146.49	16.20	82.03	7.77
gr. 1	10310.14	192049	397400	237.69	2038.12	10895.98	26341.08	2758.58	9217.94	1144.09	66.88	759.92	84.60	439.99	81.08	207.54	23.88	117.37	10.18
gr. 1	11554.90	190384	397400	227.66	3067.77	10936.02	28189.19	3120.73	10726.44	1422.47	67.35	1009.58	116.11	618.67	114.31	294.69	33.75	165.99	14.52
gr. 1	5983.14	195727	397400	236.15	1554.83	6381.40	16825.78	1857.42	6629.23	819.41	82.46	566.16	62.70	326.69	59.31	147.08	16.07	75.89	7.59
gr. 1	5806.58	195780	397400	287.12	1156.66	6019.79	15677.85	1787.31	6535.99	835.76	136.30	552.72	59.69	302.78	51.65	122.98	12.56	55.08	4.96
gr. 1	6241.42	194626	397400	481.90	773.85	5947.82	9445.77	792.19	2379.01	298.37	114.79	223.43	28.46	158.75	28.28	71.68	7.55	31.24	2.51
gr. 1	4608.45	196850	397400	367.39	1217.59	4872.53	9748.31		2920.93	368.49	78.95	286.02	35.92	203.59	39.12	102.90	11.38	50.70	4.44
gr. 1	7258.36	196165	397400	228.98	1197.64	5121.14	13554.09	1493.52	5310.59	638.30	76.38	450.96	48.59	250.18	45.95	113.33	11.91	54.64	5.36
gr. 1	14136.93	188346	397400	200.81	4496.11	12403.53	34017.82	4113.99	14894.72	2186.84	71.04	1575.70	179.20	946.62	172.82	453.15	51.57	244.10	19.02
gr. 1	11000.30	191490	397400	241.31	2142.21	11318.92	27160.10	2856.18	9423.53	1164.21	70.82	782.88	86.50	458.73	83.74	218.37	24.95	119.76	9.79
gr. 2	8781.22	194214	397400	369.76	867.72	6462.63	12934.02	1225.24	3919.70	459.59	71.54	310.06	34.25	182.56	32.95	82.01	8.81	38.75	3.50
gr. 2	3842.67	198180	397400	716.26	996.92	5994.64	8193.92	638.57	1955.93	282.45	69.75	256.47	33.27	189.10	35.06	90.68	10.01	51.82	5.75
gr. 2	6794.38	193302	397400	658.59	665.75	7824.78	11235.23	868.34	2399.28	267.00	85.00	194.26	23.71	128.62	23.09	57.45	6.16	24.55	2.07
gr. 2	14812.63	191835	397400	457.67	869.09	5068.31	8885.94	777.36	2389.83	296.86	60.15	226.78	27.69	156.90	29.18	74.99	7.73	32.78	2.72
gr. 2	5409.53	195854	397400	243.05	975.07	7028.18	15444.71	1548.83	5105.72	588.32	69.42	380.28	41.92	217.29	38.37	95.88	10.31	47.88	4.31
gr. 2	6345.86	196546	397400	652.88	595.36	7161.01	10095.11	775.06	2160.67	241.57	82.21	174.73	21.38	118.15	20.85	52.10	5.62	23.36	1.89
gr. 3	9302.05	190244	397400	241.02	1651.70	9811.31	21929.00	2188.87	7315.98	891.55	55.00	607.65	67.87	351.33	64.32	163.87	18.54	86.87	7.70
gr. 3	7087.47	195826	397400	306.31	1046.92	6425.83	13611.66	1351.09	4448.88	542.57	63.60	366.41	41.87	221.38	39.52	101.85	11.15	50.60	4.58
gr. 3	12981.35	189544	397400	597.50	564.87	6677.36	9621.34	751.69	2094.45	240.41	81.80	173.21	20.66	111.70	20.61	50.59	5.28	21.29	1.66
gr. 3	5438.08	196488	397400	614.81	659.04	6433.20	8794.01	677.58	1951.71	241.93	68.39	193.73	23.70	129.76	23.60	58.88	6.30	30.98	3.11
gr. 3	4416.84	197442	397400	650.80	674.12	6464.54	8521.27	638.14	1841.07	238.59	71.27	195.80	24.67	133.94	24.48	60.89	6.85	33.07	3.49
gr. 3	4329.23	196244	397400	606.55	858.64	5449.48	7858.47	633.63	1937.03	271.99	73.64	234.36	29.80	164.26	31.10	79.34	8.93	45.19	4.89
gr. 3	4163.76	196877	397400	570.23	823.09	5742.38	8146.08	634.88	1891.41	254.04	83.24	217.52	27.61	154.94	28.88	73.86	8.11	39.86	4.02
gr. 3	5062.48	195565	397400	427.40	736.75	5569.30	8918.08	748.78	2261.46	288.59	91.33	224.75	26.95	143.98	25.96	63.85	6.72	29.64	2.44
gr. 3	5610.12	193934	397400	281.63	805.69	7261.52	15407.10	1529.22	4970.30	578.31	75.66	361.36	38.94	197.55	34.51	84.54	9.08	39.49	3.43
gr. 3	8525.55	194652	397400	238.10	1476.62	9585.56	21140.47	2122.85	7049.45	862.75	60.48	569.25	62.73	324.36	57.67	149.13	16.75	77.71	6.61

Table 3.8: Selected trace element concentrations (in ppm) for the vein apatite (sample OD422).
*Ideal Ca concentration. Abbr.: grain (gr.).

Descr.	Si	P	Ca*	Sr	Y	La	Ce	Pr	Nd	Sm	Eu	Gd	Tb	Dy	Ho	Er	Tm	Yb	Lu
gr. 4	8418.56	190369	397400	281.84	1394.62	8288.85	18764.62	1850.99	6124.40	739.27	61.31	507.02	57.16	299.07	53.72	136.36	15.51	74.46	6.39
gr. 4	6042.48	192245	397400	307.19	926.91	5816.39	12034.43	1162.01	3768.77	449.18	61.55	310.95	36.19	189.49	34.75	87.01	9.45	43.26	3.99
gr. 4	5263.23	195674	397400	294.89	891.54	6613.23	13675.38	1335.32	4307.70	513.04	77.01	345.57	38.85	204.99	36.46	91.59	9.08	39.87	3.37
gr. 4	5092.08	194993	397400	357.17	924.29	5523.23	11496.18	1122.72	3692.10	450.86	94.04	308.84	35.40	188.94	34.54	86.81	9.31	41.42	3.60
gr. 4	5422.89	196569	397400	211.37	1284.65	4888.20	13721.59	1615.71	6094.04	794.36	102.34	543.45	57.07	291.75	50.60	125.43	13.08	59.70	5.36
gr. 5	13530.80	189940	397400	354.75	1072.25	6383.48	12747.71	1198.88	3786.96	447.61	72.73	309.32	36.65	201.27	36.88	94.17	10.52	46.75	4.21
gr. 6	8765.83	192922	397400	246.88	1274.11	8873.65	19324.40	1912.52	6246.33	741.31	59.77	492.97	53.50	279.29	50.37	125.49	14.15	66.48	5.75
gr. 6	4958.89	193753	397400	381.68	790.93	6035.20	11579.94	1088.30	3432.29	397.82	67.05	273.28	30.62	163.31	29.41	74.63	7.84	34.52	3.11
gr. 6	5873.44	193816	397400	485.54	717.46	6070.17	10327.21	899.91	2709.42	317.03	71.04	222.08	26.03	141.32	25.35	63.88	6.67	30.13	2.48
gr. 6	6636.76	195076	397400	601.35	686.19	6198.46	8916.96	700.06	2028.69	248.06	71.89	194.98	23.42	133.06	23.90	60.58	6.69	30.32	2.79
gr. 6	4285.37	196603	397400	673.31	994.12	6109.77	8439.14	662.65	2014.97	288.29	71.36	258.21	33.38	188.03	34.63	90.01	10.12	50.09	5.42
gr. 6	5044.59	197347	397400	628.81	1055.75	5253.99	8017.70	672.97	2139.71	309.30	65.78	279.85	35.10	197.19	37.23	96.35	11.32	57.37	6.30
gr. 6	4881.25	195296	397400	638.46	906.29	5959.04	8613.47	690.40	2098.53	285.79	68.67	246.77	30.74	171.06	32.18	80.58	9.14	45.49	4.86
gr.7	9846.30	192439	397400	228.71	1680.97	10275.90	22694.10	2263.91	7496.99	914.52	54.25	624.17	68.48	362.27	66.05	170.17	19.03	91.66	7.83
gr.7	24514.54	188698	397400	564.23	694.53	6676.58	10049.96	811.43	2348.96	275.93	76.60	209.38	24.96	135.93	24.80	59.24	6.39	28.82	2.56
gr.7	9423.26	195370	397400	674.61	815.07	5476.48	7593.49	600.01	1848.36	263.40	59.20	227.68	28.85	161.51	29.18	75.29	8.24	42.05	4.53
gr.7	4478.37	195754	397400	698.80	807.01	6106.17	8025.68	609.33	1829.39	254.92	58.89	225.48	28.59	158.77	29.16	75.38	8.33	42.77	4.59
gr.7	4655.52	197110	397400	671.63	986.85	5498.28	7951.38	650.48	2038.97	301.05	61.34	263.34	33.38	189.14	34.95	90.89	10.42	53.39	5.71
gr.7	14831.63	193028	397400	639.46	655.87	5802.15	7936.88	609.80	1770.91	234.14	68.79	187.32	24.09	130.83	23.80	59.75	6.60	32.96	3.45
gr.7	8055.35	194122	397400	266.23	1425.50	8180.08	18525.06	1883.58	6298.83	768.92	65.04	526.26	58.43	298.67	54.85	140.94	15.70	74.29	6.52

Table 3.9: Major and minor element concentrations (in wt%) of the vein calcite (sample OD422).

Description	Fe	Mn	Mg	Ca	Si
grain 1	2.38	1.88	0.44	34.4	0.36
grain 2	2.62	1.18	0.61	34.9	0.02
grain 3	1.06	2.42	0.31	35.1	0.02

Table 3.10: U-Pb dating of the vein apatite (sample OD422).

^{207}Pb cor ^{206}Pb/^{238}U age		^{206}Pb/^{238}U		^{207}Pb/^{206}Pb		Pb	Th	U
Ma	+/-1 ster	ratio	+/-1 RSE	ratio	+/-1 RSE	ppm	ppm	ppm
845	11.3	0.1393	1.4%	0.0630	3.0%	3.0	83.1	50.4
836	18.4	0.1381	2.2%	0.0645	5.1%	1.6	55.3	19.4
827	14.6	0.1367	1.8%	0.0656	4.1%	2.4	80.9	31.2
818	8.9	0.1351	1.1%	0.0656	1.8%	4.8	31.6	140.0
802	10.5	0.1325	1.3%	0.0659	2.1%	3.6	35.0	100.2
813	11.2	0.1345	1.4%	0.0662	2.6%	3.8	117.8	58.5
806	8.4	0.1333	1.1%	0.0663	1.7%	6.0	46.3	174.6
839	15.3	0.1389	1.9%	0.0665	3.8%	2.3	84.1	26.2
798	10.3	0.1319	1.3%	0.0667	2.1%	3.8	55.5	94.5
828	11.4	0.1372	1.4%	0.0671	2.7%	2.6	29.0	67.8
822	15.4	0.1361	1.9%	0.0671	4.6%	2.1	77.7	22.0
844	14.6	0.1398	1.8%	0.0672	3.3%	1.7	29.7	34.6
815	7.7	0.1349	1.0%	0.0674	1.2%	9.2	60.6	276.1
804	15.3	0.1331	1.9%	0.0674	4.6%	2.2	82.8	23.3
798	13.7	0.1320	1.7%	0.0676	3.6%	1.8	47.0	34.0
819	10.4	0.1357	1.3%	0.0677	2.1%	4.6	93.3	98.1
829	15.0	0.1374	1.8%	0.0680	4.0%	1.9	60.2	24.1
814	14.6	0.1349	1.8%	0.0682	4.6%	1.8	60.2	24.2
810	14.4	0.1343	1.8%	0.0685	4.2%	2.0	73.6	23.6
802	8.0	0.1328	1.0%	0.0686	1.3%	8.5	58.0	251.7
828	8.2	0.1374	1.0%	0.0688	1.3%	7.7	43.8	224.4
825	10.9	0.1370	1.3%	0.0688	2.7%	4.0	128.9	54.7
822	14.3	0.1363	1.8%	0.0689	3.8%	2.0	64.3	27.3
817	8.5	0.1355	1.1%	0.0691	1.5%	6.0	48.7	175.4
800	13.9	0.1327	1.8%	0.0696	4.4%	2.3	77.5	27.7
814	14.2	0.1352	1.8%	0.0699	3.7%	2.7	94.1	31.4
800	10.7	0.1329	1.4%	0.0702	2.5%	3.1	49.9	76.4
830	13.4	0.1379	1.6%	0.0704	3.7%	2.9	107.4	31.5
824	14.3	0.1370	1.8%	0.0704	3.2%	3.2	112.4	37.8
810	14.1	0.1346	1.8%	0.0706	3.9%	1.9	56.7	28.3
827	9.8	0.1375	1.2%	0.0707	1.8%	4.1	33.0	111.0
852	16.2	0.1420	1.9%	0.0713	4.7%	1.5	42.3	21.0
830	14.3	0.1382	1.8%	0.0721	3.0%	2.9	99.1	33.3
826	15.7	0.1376	1.9%	0.0722	3.8%	1.7	52.1	24.4
802	16.4	0.1336	2.1%	0.0723	4.2%	2.1	76.9	22.7
799	18.4	0.1331	2.3%	0.0727	4.4%	1.5	50.9	19.8
818	18.5	0.1365	2.3%	0.0734	4.8%	1.4	48.7	18.2
817	17.1	0.1365	2.1%	0.0750	4.4%	1.0	19.0	21.7
848	17.9	0.1421	2.1%	0.0760	4.8%	1.3	38.6	17.0
799	14.7	0.1336	1.9%	0.0764	4.0%	2.0	67.8	25.1
833	17.5	0.1396	2.1%	0.0768	4.4%	2.4	87.0	22.4
826	17.1	0.1387	2.1%	0.0782	3.8%	2.0	65.0	22.1
816	17.7	0.1369	2.2%	0.0783	4.5%	2.4	97.8	17.2
828	19.0	0.1392	2.3%	0.0796	4.8%	1.3	36.6	18.8
848	19.3	0.1427	2.3%	0.0798	5.7%	1.9	63.9	22.1
808	10.3	0.1359	1.3%	0.0802	2.1%	3.7	34.6	99.3
836	15.1	0.1407	1.8%	0.0804	3.6%	1.8	52.5	25.8
816	14.9	0.1384	1.8%	0.0870	3.6%	3.0	102.8	30.6
833	19.8	0.1414	2.4%	0.0874	4.0%	2.1	66.2	25.2

Table 3.10: Continued.

^{207}Pb cor ^{206}Pb/^{238}U age		^{206}Pb/^{238}U		^{207}Pb/^{206}Pb		Pb	Th	U
Ma	+/-1 ster	ratio	+/-1 RSE	ratio	+/-1 RSE	ppm	ppm	ppm
850	18.3	0.1452	2.2%	0.0911	4.1%	1.4	26.5	25.6
816	11.0	0.1404	1.4%	0.0982	2.4%	4.8	34.2	114.2
847	22.3	0.1475	2.6%	0.1075	4.9%	1.4	40.1	16.9
809	18.3	0.1410	2.3%	0.1086	4.4%	2.5	82.2	26.0
824	17.5	0.1447	2.1%	0.1149	3.7%	1.2	17.0	20.6
816	17.4	0.1458	2.1%	0.1279	3.7%	2.1	65.0	19.5
817	11.5	0.1359	1.4%	0.0706	3.3%	3.9	126.3	51.1
815	17.3	0.1365	2.1%	0.0764	5.4%	1.4	40.7	21.0
822	15.5	0.1391	1.9%	0.0854	4.0%	2.0	22.3	45.3
808	11.9	0.1344	1.5%	0.0719	3.2%	2.7	59.6	50.5
831	17.8	0.1390	2.2%	0.0749	5.1%	1.4	41.4	21.8
807	7.5	0.1334	0.9%	0.0662	1.7%	7.8	90.7	211.0
824	18.9	0.1370	2.3%	0.0701	6.0%	1.4	38.8	21.3
823	20.8	0.1421	2.5%	0.1011	5.3%	1.2	13.9	28.2
830	19.0	0.1382	2.3%	0.0712	5.1%	1.4	33.4	22.7
820	20.4	0.1367	2.5%	0.0728	5.4%	2.3	86.3	25.1
821	19.4	0.1393	2.4%	0.0875	6.2%	1.3	34.8	18.6
815	17.6	0.1353	2.2%	0.0701	4.9%	2.6	90.0	26.6
818	7.2	0.1355	0.9%	0.0677	1.6%	7.5	60.0	209.8
808	16.3	0.1353	2.0%	0.0764	4.6%	1.8	41.9	32.0
821	12.7	0.1361	1.6%	0.0682	3.8%	3.2	81.0	54.9
835	25.6	0.1390	3.1%	0.0710	7.8%	1.9	64.9	20.5
808	10.6	0.1339	1.3%	0.0688	3.0%	4.2	93.3	85.0

Table 3.11: U-Pb dating of titanite (sample OD422).

^{207}Pb cor ^{206}Pb/^{238}U age		^{206}Pb/^{238}U		^{207}Pb/^{206}Pb		Pb	Th	U
Ma	+/-1 ster	ratio	+/-1 RSE	ratio	+/-1 RSE	ppm	ppm	ppm
822	21.3	0.1389	2.6%	0.0834	6.0%	1.1	33.3	12.0
875	31.7	0.1460	3.7%	0.0722	8.5%	0.8	26.2	6.5
858	20.5	0.1439	2.4%	0.0760	5.5%	1.2	25.8	18.3
863	25.4	0.1466	3.0%	0.0866	5.0%	1.4	41.6	14.9
844	25.4	0.1499	3.0%	0.1230	5.8%	1.2	19.7	16.2
828	28.1	0.1391	3.4%	0.0789	7.5%	0.6	17.1	7.4
892	32.1	0.1570	3.6%	0.1144	6.3%	0.6	13.1	6.9
885	26.8	0.1546	3.0%	0.1088	6.3%	0.8	16.2	9.1
830	25.3	0.1481	3.0%	0.1270	5.0%	1.5	36.8	14.9
825	30.8	0.1462	3.7%	0.1214	7.3%	0.8	23.7	6.5
811	26.3	0.1386	3.3%	0.0934	5.4%	1.2	37.9	10.9
823	20.7	0.1374	2.5%	0.0733	5.7%	2.2	78.8	17.8
822	20.5	0.1406	2.5%	0.0941	4.6%	2.7	96.4	19.9
871	22.5	0.1480	2.6%	0.0869	4.9%	1.8	60.5	14.8
826	19.7	0.1424	2.4%	0.1004	4.7%	2.1	63.2	20.9

Table 4.1: Summary of samples (listed only a selection of samples from drillhole RD2773) and applied analyses.

#	Depth (m)	OD/RX#	Host rock(s)	Grain size of mineralization	U-Pb dating	Sr	Sm-Nd
1	1998.1	OD814	RDG	fine-grained	Ap, Urn		
2	1998.1	RX7986	FU	fine-grained	Hem, Urn		
3	1998.1	RX7987	FU	-	Hem, Urn		
4	2010.5	OD201	FU	-	Zrn		
5	2012.2	OD815	FU, RDG	fine-grained	Zrn		
6	2013.8	OD816	FU, RDG	-	Zrn		
7	2036.3	OD817	RDG	fine-grained (with Anh)			
8	2036.7	OD818	FU, RDG	fine-grained (with Anh)		Cal	
9	2051.3	OD819	FU	fine-grained		Cal	Cal
10	2069.1	OD820	FU	fine-grained	Zrn		FU
11	2083.2	OD821	FU	fine-grained			
12	2092.8	OD823	FU, RDG	fine-grained			
13	2098.9	OD824	FU	fine-grained			
14	2149.7	OD825	FU	fine-grained	Zrn		
15	2179.2	OD826	FU	fine-grained		Cal	Cal
16	2182.4	OD827	FU	coarse-grained		Cal	Cal
17	2189.1	OD828	FU	coarse-grained			
18	2206.1	OD85	FU	-	Zrn		
19	2208.5	OD829	FU	fine-grained		Cal	Cal
20	2238.4	OD830a	FU	coarse-grained		Cal	Cal
21	2249.3	OD86	FU	-	Zrn		
22	2294.5	OD830b	FU	coarse-grained			
23	2311.5	OD830c	FU	coarse-grained		Cal	

Abbr.: anhydrite (Anh), apatite (Ap), calcite (Cal), felsic unit (FU), hematite (Hem), uraninite (Urn), zircon (Zrn).

Table 4.2: U-Pb dating of zircon in felsic unit.

OD#	^{207}Pb cor $^{206}Pb/^{238}U$ age		$^{206}Pb/^{238}U$		$^{207}Pb/^{206}Pb$		Pb	Th	U
	Ma	+/-1 ster	ratio	+/-1 RSE	ratio	+/-1 RSE	ppm	ppm	ppm
	used in age calculation:								
OD201	1546	34.0	0.2710	0.02	0.0956	0.01	77.1	225.0	826.9
OD85	1550	19.0	0.2719	0.01	0.0959	0.01	149.4	1231.1	1056.7
OD816	1567	17.9	0.2752	0.01	0.0970	0.01	42.0	174.7	471.4
OD816	1582	28.0	0.2781	0.02	0.0980	0.02	21.2	139.0	159.8
OD820	1589	16.2	0.2796	0.01	0.0976	0.01	51.7	300.9	466.4
OD816	1590	15.0	0.2798	0.01	0.0979	0.01	68.4	424.5	664.8
OD816	1592	16.3	0.2801	0.01	0.0982	0.01	56.6	430.6	520.5
OD816	1594	14.5	0.2805	0.01	0.0985	0.01	55.6	302.6	537.0
OD816	1600	49.6	0.2817	0.03	0.0979	0.01	35.8	129.9	431.5
OD816	1605	15.3	0.2828	0.01	0.0990	0.01	59.4	298.0	590.7
OD816	1607	15.5	0.2831	0.01	0.0986	0.01	64.2	461.6	501.1
OD816	1607	17.0	0.2831	0.01	0.0990	0.01	71.8	402.4	757.6
OD816	1609	15.0	0.2834	0.01	0.0984	0.01	79.6	457.2	695.5
OD816	1611	15.7	0.2838	0.01	0.0991	0.01	90.7	514.9	774.3
OD816	1611	20.2	0.2839	0.01	0.0992	0.01	44.2	195.5	384.7
OD816	1611	14.8	0.2840	0.01	0.0993	0.01	58.2	371.6	522.3
OD820	1612	14.9	0.2841	0.01	0.0981	0.01	51.9	351.4	462.8
OD816	1614	20.6	0.2844	0.01	0.0976	0.01	53.6	294.2	437.2
OD816	1615	17.3	0.2848	0.01	0.0990	0.01	80.8	373.2	710.6
OD816	1617	17.5	0.2851	0.01	0.0987	0.01	52.8	312.2	435.9
OD816	1617	15.7	0.2851	0.01	0.0993	0.01	71.6	367.5	650.4
OD816	1618	19.4	0.2855	0.01	0.1002	0.01	65.7	404.5	521.5
OD820	1619	17.7	0.2855	0.01	0.0979	0.01	77.4	402.6	649.9
OD820	1623	17.8	0.2863	0.01	0.0994	0.01	68.4	338.5	588.3
OD816	1550	14.7	0.2724	0.01	0.0981	0.01	117.4	1163.1	951.8
OD85	1493	21.0	0.2613	0.01	0.0952	0.01	103.6	820.5	991.4
OD816	1508	21.6	0.2644	0.01	0.0970	0.01	69.5	320.7	837.6
OD816	1416	15.4	0.2469	0.01	0.0941	0.01	104.3	749.1	1215.8
OD201	1493	22.3	0.2619	0.02	0.0978	0.01	88.8	668.1	655.1
	not used in age calculation:								
OD816	1377	13.9	0.2407	0.01	0.0968	0.01	83.8	498.6	881.9
OD825	1306	14.8	0.2274	0.01	0.0948	0.01	85.4	774.4	943.4
OD85	1291	12.9	0.2251	0.01	0.0966	0.01	94.0	161.8	1324.3
OD85	1285	17.0	0.2245	0.01	0.0983	0.01	286.1	3421.9	2101.4
OD85	1201	11.3	0.2088	0.01	0.0963	0.01	101.9	1230.9	1140.5
OD816	1060	14.8	0.1821	0.01	0.0903	0.01	147.8	751.9	2841.0
OD816	1029	11.6	0.1764	0.01	0.0890	0.01	121.9	515.4	2351.3
OD201	1046	12.6	0.1799	0.01	0.0919	0.01	117.5	718.1	1742.9
OD85	1093	11.7	0.1897	0.01	0.0979	0.01	181.2	1828.5	1969.0
OD86	1148	14.0	0.2024	0.01	0.1089	0.01	253.0	3040.6	2053.7

Table 4.2: Continued.

OD#	^{207}Pb cor ^{206}Pb/^{238}U age		^{206}Pb/^{238}U		^{207}Pb/^{206}Pb		Pb	Th	U
	Ma	+/-1 ster	ratio	+/-1 RSE	ratio	+/-1 RSE	ppm	ppm	ppm
OD816	935	48.8	0.1600	0.05	0.0908	0.01	300.4	485.3	5276.4
OD825	935	13.8	0.1603	0.02	0.0920	0.01	141.5	1232.6	2246.2
OD201	919	16.2	0.1572	0.02	0.0910	0.01	248.9	2650.1	3311.7
OD825	1556	109.3	0.3028	0.07	0.1826	0.02	315.3	2096.8	1713.3
OD825	1473	66.5	0.2805	0.05	0.1658	0.02	400.6	2198.3	2242.1
OD825	791	13.0	0.1335	0.02	0.0845	0.01	134.1	2897.7	2023.4
OD816	1066	80.7	0.1891	0.08	0.1161	0.03	355.2	1830.8	3861.5
OD201	836	14.2	0.1429	0.02	0.0922	0.01	154.6	1380.6	2558.3
OD816	701	13.3	0.1176	0.02	0.0813	0.01	171.8	1123.5	4584.2
OD85	893	12.2	0.1544	0.01	0.1005	0.01	266.1	3883.5	3631.3
OD85	823	13.1	0.1410	0.02	0.0952	0.01	146.1	1982.1	2622.6
OD85	770	11.3	0.1309	0.02	0.0903	0.01	213.2	3085.6	3807.3
OD85	603	31.5	0.1009	0.05	0.0831	0.01	208.7	3942.9	6497.2
OD86	1132	41.8	0.2619	0.04	0.3115	0.03	776.3	3491.2	3070.0
OD85	377	7.2	0.0617	0.02	0.0734	0.01	226.3	4935.3	11376.5
OD85	953	44.3	0.2214	0.05	0.3126	0.02	1614.4	14584.3	8548.8
OD815	400	6.3	0.0662	0.02	0.0814	0.01	289.0	5273.6	11011.9
OD85	743	26.4	0.1427	0.04	0.1843	0.03	531.3	6475.3	5149.3
OD85	805	89.3	0.1938	0.11	0.3340	0.01	3077.0	83834.9	21157.8
OD85	775	15.9	0.1612	0.02	0.2394	0.01	879.3	2606.4	7962.4
OD825	6810	207.2	1.8758	0.06	0.2769	0.01	9450.4	8170.9	6281.6
OD85	5561	39.5	1.3696	0.09	0.3560	0.02	2382.4	911.4	1522.7
OD85	4762	164.6	1.0933	0.11	0.3819	0.01	4867.5	6032.7	4426.4
OD85	2962	175.3	0.6763	0.05	0.3446	0.01	1790.1	1118.4	2705.5
OD85	2580	397.4	0.5581	0.14	0.2813	0.03	6364.4	4779.7	6768.9
OD85	1875	129.5	0.4521	0.07	0.3504	0.02	3921.9	8071.8	10004.0
OD85	1388	36.6	0.3244	0.03	0.3204	0.01	1802.8	3073.2	6689.2
OD85	1362	66.5	0.3040	0.05	0.2875	0.02	1293.6	6449.4	4902.6
OD85	4097	393.1	0.8879	0.04	0.4050	0.00	7902.3	12757.8	9051.6
OD201	1877	76.9	0.3402	0.04	0.1205	0.02	67689.6	1596048.1	47972.9
OD825	1374	22.0	0.2413	0.02	0.1007	0.01	45037441.7	886142903.2	62417866.8
OD825	1521	30.2	0.2740	0.02	0.1196	0.03	59436.0	1164633.3	58422.9
OD825	1518	40.0	0.2807	0.03	0.1415	0.02	163049.6	3791464.4	142329.9

Only concordant analyses are reported in this table.

Table 4.3: U-Pb dating of apatite.

^{207}Pb cor ^{206}Pb/^{238}U age		^{206}Pb/^{238}U		^{207}Pb/^{206}Pb		Pb	Th	U
Ma	**+/-1 ster**	**ratio**	**+/-1 RSE**	**ratio**	**+/-1 RSE**	**ppm**	**ppm**	**ppm**
used in age calculation:								
1535	19.2	0.2723	1.3%	0.1061	1.6%	3.9	20.1	48.0
1549	21.7	0.2742	1.4%	0.1045	2.2%	2.4	12.2	28.6
1549	22.9	0.2784	1.5%	0.1170	2.2%	2.7	19.7	29.1
1555	41.9	0.2807	2.8%	0.1207	2.3%	8.2	29.1	98.6
1557	20.5	0.2820	1.3%	0.1237	2.5%	3.8	31.8	35.4
1557	16.7	0.2864	1.1%	0.1365	1.3%	5.8	51.1	48.5
1557	47.4	0.3106	3.1%	0.2024	2.7%	4.7	18.5	33.9
1557	43.1	0.2959	2.8%	0.1634	3.1%	5.9	21.7	50.3
1558	21.6	0.2890	1.4%	0.1435	1.6%	4.9	19.9	49.4
1559	37.1	0.2982	2.3%	0.1689	3.7%	2.4	10.9	19.1
1565	16.5	0.2808	1.1%	0.1153	1.3%	4.2	18.9	48.4
1569	20.6	0.2930	1.3%	0.1491	1.3%	5.0	17.7	47.8
1570	33.1	0.2823	2.2%	0.1172	2.3%	3.6	11.8	41.2
1573	31.1	0.2873	2.0%	0.1304	2.7%	3.1	10.8	35.9
1573	17.7	0.2822	1.1%	0.1150	1.2%	4.4	20.8	48.7
1573	21.3	0.2845	1.4%	0.1219	1.9%	4.0	16.5	42.5
1576	22.8	0.2825	1.5%	0.1144	1.9%	4.4	20.8	48.9
1576	35.2	0.2911	2.3%	0.1396	2.8%	3.6	17.3	35.0
1576	34.9	0.3043	2.2%	0.1759	2.5%	3.8	15.0	30.5
1577	22.2	0.2918	1.4%	0.1413	1.8%	4.1	12.6	40.5
1578	16.5	0.2863	1.1%	0.1249	1.2%	4.7	19.9	50.7
1580	20.2	0.2790	1.3%	0.1016	1.7%	3.2	12.4	43.4
1581	20.0	0.2786	1.3%	0.0996	1.9%	4.2	19.5	49.8
1583	16.4	0.2800	1.1%	0.1028	1.4%	4.1	20.4	49.4
1584	19.1	0.2854	1.2%	0.1187	1.4%	4.4	17.7	50.0
1585	29.3	0.2897	1.8%	0.1310	4.0%	2.8	12.5	27.2
1587	18.9	0.2845	1.2%	0.1144	1.4%	3.9	18.9	45.6
1588	16.5	0.2805	1.1%	0.1013	1.3%	4.1	17.2	51.1
1589	20.1	0.2832	1.3%	0.1097	1.6%	4.2	15.7	48.9
1593	16.3	0.2853	1.0%	0.1138	1.4%	4.2	18.6	48.5
1596	21.1	0.2888	1.3%	0.1221	2.0%	4.8	17.7	49.3
1597	33.7	0.2973	2.1%	0.1457	2.3%	3.9	11.3	41.5
1598	18.8	0.2832	1.2%	0.1046	1.5%	3.7	15.8	46.3
1600	34.1	0.3080	2.1%	0.1737	3.5%	3.9	15.0	36.2
1601	17.5	0.2885	1.1%	0.1183	1.3%	4.5	19.6	49.7
1603	27.8	0.2954	1.8%	0.1375	2.0%	4.7	18.5	48.9
1604	20.7	0.2845	1.3%	0.1053	1.4%	4.1	16.2	50.2
1606	26.9	0.2849	1.7%	0.1053	1.8%	3.2	14.6	41.8
1608	18.8	0.2862	1.2%	0.1080	1.5%	6.9	61.0	67.2
1610	20.6	0.2851	1.3%	0.1036	1.8%	3.1	20.8	34.4
1611	27.9	0.2892	1.8%	0.1155	1.8%	3.5	14.0	41.5
1613	40.8	0.2870	2.5%	0.1076	5.5%	3.9	35.4	40.3

Table 4.3: Continued.

^{207}Pb cor $^{206}Pb/^{238}U$ age		$^{206}Pb/^{238}U$		$^{207}Pb/^{206}Pb$		Pb	Th	U
Ma	**+/-1 ster**	**ratio**	**+/-1 RSE**	**ratio**	**+/-1 RSE**	**ppm**	**ppm**	**ppm**
1614	43.2	0.2978	2.7%	0.1385	3.5%	3.6	8.8	37.4
1621	41.0	0.2969	2.5%	0.1319	3.7%	2.9	28.7	24.3
1623	21.7	0.3006	1.3%	0.1411	2.1%	9.1	49.6	76.5
1624	21.4	0.2911	1.3%	0.1138	1.8%	4.3	19.0	49.2
not used in age calculation:								
1631	30.0	0.2904	1.9%	0.1079	2.3%	3.9	29.1	36.8
1655	38.4	0.2939	2.3%	0.1052	4.2%	1.4	10.2	15.2
1638	43.8	0.3250	2.5%	0.1978	4.5%	2.0	11.1	12.4
1676	46.5	0.3030	2.8%	0.1202	3.3%	2.8	9.6	31.7
1815	54.5	0.3964	2.9%	0.2741	3.0%	3.2	49.9	7.1
2416	28.1	0.4571	1.1%	0.1611	1.0%	8.3	18.3	49.4
1870	43.9	0.4661	2.1%	0.3751	2.1%	6.1	6.1	20.7
2037	49.4	0.3966	2.4%	0.1820	1.9%	4.3	12.8	27.5
2203	106.7	0.5332	4.5%	0.3612	3.2%	13.6	14.7	41.6
2261	67.1	0.4842	2.9%	0.2642	1.7%	7.4	9.8	31.6
2431	46.8	0.4770	1.8%	0.1934	1.6%	7.3	15.0	39.0
2484	70.5	0.4821	2.6%	0.1852	1.3%	7.5	19.3	37.2
2532	70.0	0.5111	2.5%	0.2207	2.5%	7.4	10.5	35.0
3268	280.6	0.7729	5.6%	0.3950	2.0%	2.9	4.3	7.3
6520	476.0	1.8363	13.5%	0.2670	1.6%	29.2	9.0	126.2
6614	145.3	1.8577	3.9%	0.2427	1.9%	23.0	12.5	27.4
0	83737.5	146.2344	8.9%	0.6719	0.7%	2956.7	7.3	18.2
0	151.0	1.1814	2.3%	0.3529	1.3%	15.9	7.5	21.0
1353	28.3	0.2493	2.1%	0.1410	2.2%	3.9	13.9	45.8
1498	85.7	0.3274	5.9%	0.2725	1.5%	18.7	50.3	143.9
1718	48.0	0.3644	2.7%	0.2505	2.8%	2.2	6.1	13.1
2561	161.2	0.5391	5.8%	0.2577	1.4%	9.5	32.9	40.6
2316	113.7	0.4690	4.7%	0.2184	2.4%	2.8	9.5	15.7
1675	45.5	0.3127	2.8%	0.1478	1.6%	4.7	15.6	46.1
1200	63.5	0.2382	5.4%	0.2018	3.9%	5.8	18.7	71.8
1662	34.7	0.3143	2.1%	0.1582	2.1%	5.6	14.2	53.4
1730	91.9	0.3404	5.4%	0.1907	3.2%	11.4	31.4	81.4
1878	40.1	0.3533	2.1%	0.1527	2.7%	5.0	14.2	43.5
1047	72.4	0.2024	7.2%	0.1834	2.4%	89.7	54.0	1753.1
618	18.8	0.1202	3.1%	0.1955	1.1%	54.7	216.6	1004.0

Table 4.4: U-Pb dating of uraninite.

OD#	^{207}Pb cor $^{206}Pb/^{238}U$ age		$^{206}Pb/^{238}U$		$^{207}Pb/^{206}Pb$		Pb	Th
	Ma	+/-1 ster	ratio	+/-1 RSE	ratio	+/-1 RSE	ppm	ppm
used in age calculation:								
RX7986	2058	85.2	0.3762	0.0	0.0974	0.0	45472	14134
RX7986	1917	64.8	0.3463	0.0	0.0974	0.0	52934	20167
RX7986	1618	71.7	0.2852	0.0	0.0977	0.0	102236	1384
RX7986	1982	78.2	0.3600	0.0	0.0977	0.0	61918	24444
RX7986	1880	59.5	0.3387	0.0	0.0978	0.0	50766	10996
RX7986	1812	50.4	0.3246	0.0	0.0978	0.0	54509	17469
RX7986	1720	66.1	0.3057	0.0	0.0978	0.0	60519	27965
RX7986	1695	56.4	0.3007	0.0	0.0979	0.0	48645	9698
RX7986	1645	37.2	0.2907	0.0	0.0979	0.0	42910	13187
RX7986	1912	81.7	0.3453	0.0	0.0980	0.0	46892	19089
RX7986	1708	70.6	0.3034	0.0	0.0980	0.0	58575	8716
RX7986	1776	55.8	0.3172	0.0	0.0980	0.0	50044	7278
RX7986	1609	40.7	0.2834	0.0	0.0981	0.0	39609	10555
RX7986	1865	46.4	0.3356	0.0	0.0981	0.0	48542	12144
RX7986	1813	49.3	0.3248	0.0	0.0981	0.0	52163	21007
RX7986	1838	160.4	0.3299	0.1	0.0982	0.0	100741	14898
RX7986	1915	77.6	0.3459	0.0	0.0982	0.0	53287	28441
RX7986	1807	45.7	0.3235	0.0	0.0982	0.0	51416	25313
RX7986	1690	86.4	0.2997	0.1	0.0982	0.0	58817	10539
RX7986	1927	70.7	0.3485	0.0	0.0982	0.0	65110	12148
RX7986	1670	58.8	0.2957	0.0	0.0982	0.0	49135	10031
RX7986	1655	45.9	0.2928	0.0	0.0982	0.0	56494	18393
RX7986	1966	50.2	0.3565	0.0	0.0983	0.0	55232	1742
RX7986	2164	110.1	0.3989	0.0	0.0983	0.0	77518	10689
RX7986	1573	144.2	0.2767	0.1	0.0983	0.0	78290	5979
RX7986	1619	40.6	0.2854	0.0	0.0983	0.0	50685	9401
RX7986	1771	82.1	0.3161	0.0	0.0983	0.0	87037	13576
RX7986	1904	102.7	0.3436	0.1	0.0983	0.0	112769	1731
RX7986	2027	82.4	0.3696	0.0	0.0984	0.0	123081	17241
RX7986	2045	76.2	0.3733	0.0	0.0984	0.0	55331	27967
RX7986	1852	125.0	0.3327	0.1	0.0984	0.0	91685	23411
RX7986	1563	25.5	0.2749	0.0	0.0985	0.0	80200	2327
RX7986	1581	39.2	0.2782	0.0	0.0985	0.0	43978	10550
RX7986	2137	88.3	0.3931	0.0	0.0985	0.0	51679	4480
RX7986	1901	84.4	0.3430	0.0	0.0985	0.0	52112	7944
RX7986	1884	57.6	0.3394	0.0	0.0985	0.0	63983	32874
RX7986	1917	62.5	0.3463	0.0	0.0985	0.0	67026	17347
RX7986	1629	43.1	0.2875	0.0	0.0985	0.0	46852	12726
RX7986	2575	295.0	0.4911	0.1	0.0985	0.0	99611	8023
RX7986	2166	66.9	0.3993	0.0	0.0985	0.0	66784	20519
RX7986	1940	172.8	0.3512	0.1	0.0986	0.0	87648	13396

Table 4.4: Continued.

OD#	^{207}Pb cor $^{206}Pb/^{238}U$ age Ma	+/-1 ster	$^{206}Pb/^{238}U$ ratio	+/-1 RSE	$^{207}Pb/^{206}Pb$ ratio	+/-1 RSE	Pb ppm	Th ppm
RX7986	1580	37.5	0.2780	0.0	0.0986	0.0	53606	14942
RX7986	1882	57.2	0.3390	0.0	0.0986	0.0	57704	15826
RX7986	1559	93.7	0.2743	0.1	0.0986	0.0	66794	3938
RX7986	1950	90.3	0.3533	0.0	0.0986	0.0	121868	10364
RX7986	2007	65.0	0.3653	0.0	0.0986	0.0	55581	24867
RX7986	1835	61.4	0.3292	0.0	0.0988	0.0	55414	21829
RX7986	1781	42.7	0.3182	0.0	0.0989	0.0	55781	15388
RX7986	1754	50.4	0.3126	0.0	0.0989	0.0	55872	21561
RX7986	1880	59.3	0.3386	0.0	0.0989	0.0	54260	22324
RX7986	1575	44.7	0.2772	0.0	0.0989	0.0	44276	12926
RX7986	1600	66.5	0.2819	0.0	0.0990	0.0	80490	11344
RX7986	2112	69.3	0.3876	0.0	0.0990	0.0	66324	9371
RX7986	1689	86.2	0.2994	0.1	0.0990	0.0	108563	13758
RX7986	1831	67.4	0.3285	0.0	0.0991	0.0	118537	22295
RX7986	1983	64.0	0.3602	0.0	0.0991	0.0	56853	22023
RX7986	1364	54.5	0.2390	0.0	0.0991	0.0	82257	11579
RX7986	1804	42.1	0.3230	0.0	0.0992	0.0	109524	2848
RX7986	2067	65.4	0.3781	0.0	0.0992	0.0	60446	37122
RX7986	2018	95.6	0.3676	0.0	0.0992	0.0	102633	17888
RX7986	1633	54.5	0.2883	0.0	0.0992	0.0	57592	21980
RX7986	1609	67.1	0.2835	0.0	0.0992	0.0	68864	17486
RX7986	1729	118.8	0.3076	0.1	0.0993	0.0	111961	19659
RX7986	1599	60.3	0.2818	0.0	0.0994	0.0	77249	3982
RX7986	1676	39.5	0.2969	0.0	0.0994	0.0	58152	8034
RX7987	1687	77.0	0.2991	0.0	0.0961	0.0	86568	7190
RX7987	1578	76.0	0.2773	0.0	0.0969	0.0	75992	29464
RX7987	1757	48.9	0.3134	0.0	0.0969	0.0	51469	7153
RX7987	2047	71.6	0.3737	0.0	0.0971	0.0	69754	14764
RX7987	2018	94.9	0.3675	0.0	0.0972	0.0	53851	6484
RX7987	1782	42.9	0.3183	0.0	0.0975	0.0	55170	9570
RX7987	1848	36.7	0.3321	0.0	0.0975	0.0	60783	8025
RX7987	1916	57.5	0.3461	0.0	0.0975	0.0	43717	16124
RX7987	1906	48.3	0.3440	0.0	0.0975	0.0	69657	12643
RX7987	1985	60.4	0.3606	0.0	0.0976	0.0	59335	12169
RX7987	1699	43.8	0.3016	0.0	0.0976	0.0	47498	10340
RX7987	1593	78.4	0.2802	0.1	0.0978	0.0	108096	25221
RX7987	2033	67.3	0.3709	0.0	0.0978	0.0	59484	15303
RX7987	1890	70.5	0.3406	0.0	0.0978	0.0	68271	22355
RX7987	2076	71.6	0.3799	0.0	0.0980	0.0	67101	3075
RX7987	1597	42.3	0.2811	0.0	0.0980	0.0	49162	13250
RX7987	1929	57.8	0.3489	0.0	0.0981	0.0	61549	21974
RX7987	2055	49.6	0.3755	0.0	0.0981	0.0	66038	15897

Table 4.4: Continued.

OD#	^{207}Pb cor $^{206}Pb/^{238}U$ age		$^{206}Pb/^{238}U$		$^{207}Pb/^{206}Pb$		Pb	Th
	Ma	+/-1 ster	ratio	+/-1 RSE	ratio	+/-1 RSE	ppm	ppm
RX7987	1735	47.5	0.3088	0.0	0.0982	0.0	54545	13490
RX7987	1639	110.4	0.2895	0.1	0.0982	0.0	54407	8638
RX7987	1952	141.3	0.3537	0.1	0.0982	0.0	113730	10701
RX7987	1591	80.6	0.2800	0.1	0.0982	0.0	52391	20772
RX7987	1818	93.3	0.3259	0.1	0.0982	0.0	119301	24929
RX7987	1534	43.3	0.2696	0.0	0.0983	0.0	45656	15121
RX7987	1584	89.9	0.2787	0.1	0.0983	0.0	53260	10121
RX7987	1821	81.1	0.3263	0.0	0.0984	0.0	109250	15207
RX7987	1984	67.0	0.3604	0.0	0.0985	0.0	85827	24993
RX7987	1702	86.3	0.3021	0.1	0.0986	0.0	85619	9086
RX7987	1994	49.7	0.3624	0.0	0.0987	0.0	61141	14344
RX7987	2043	72.9	0.3730	0.0	0.0987	0.0	60706	21658
RX7987	1758	61.8	0.3135	0.0	0.0988	0.0	48284	9594
RX7987	1990	67.9	0.3616	0.0	0.0989	0.0	72934	20713
RX7987	1770	76.0	0.3159	0.0	0.0990	0.0	109627	24553
RX7987	1808	49.0	0.3237	0.0	0.0993	0.0	64320	10627
RX7987	1917	57.1	0.3463	0.0	0.0994	0.0	52783	13473
OD814	2049	64.7	0.3742	0.0	0.0968	0.0	57448	2590
OD814	1839	54.9	0.3302	0.0	0.0971	0.0	72109	1651
OD814	1684	47.3	0.2986	0.0	0.0972	0.0	65165	1963
OD814	1591	44.1	0.2799	0.0	0.0973	0.0	44121	0
OD814	2038	60.5	0.3718	0.0	0.0977	0.0	70863	0
OD814	1665	54.8	0.2947	0.0	0.0977	0.0	50311	995
OD814	1812	45.0	0.3247	0.0	0.0978	0.0	72693	2408
OD814	1976	55.5	0.3588	0.0	0.0978	0.0	63142	993
OD814	2102	60.2	0.3855	0.0	0.0978	0.0	67366	0
OD814	1589	85.9	0.2794	0.1	0.0979	0.0	58517	606
OD814	1580	57.3	0.2779	0.0	0.0979	0.0	89485	4085
OD814	1675	65.1	0.2967	0.0	0.0979	0.0	42686	2231
OD814	1716	123.4	0.3049	0.1	0.0980	0.0	19678	18615
OD814	1695	72.6	0.3008	0.0	0.0980	0.0	100279	2157
OD814	1614	43.3	0.2845	0.0	0.0980	0.0	61831	0
OD814	1735	49.1	0.3088	0.0	0.0980	0.0	49414	0
OD814	1887	71.3	0.3402	0.0	0.0981	0.0	61598	1215
OD814	2000	58.0	0.3638	0.0	0.0981	0.0	70003	1495
OD814	1827	55.3	0.3277	0.0	0.0981	0.0	65360	1280
OD814	1925	51.8	0.3479	0.0	0.0981	0.0	61534	0
OD814	1816	45.2	0.3254	0.0	0.0981	0.0	64230	0
OD814	1826	82.0	0.3274	0.0	0.0982	0.0	100158	67
OD814	1866	74.3	0.3357	0.0	0.0982	0.0	57844	2734
OD814	1570	45.9	0.2761	0.0	0.0983	0.0	45285	346
OD814	1597	91.1	0.2810	0.1	0.0983	0.0	95256	0

Table 4.4: Continued.

OD#	^{207}Pb cor $^{206}Pb/^{238}U$ age		$^{206}Pb/^{238}U$		$^{207}Pb/^{206}Pb$		Pb	Th
	Ma	+/-1 ster	ratio	+/-1 RSE	ratio	+/-1 RSE	ppm	ppm
OD814	1891	72.6	0.3409	0.0	0.0983	0.0	71710	288
OD814	1903	59.2	0.3434	0.0	0.0983	0.0	68410	323
OD814	1811	68.2	0.3243	0.0	0.0984	0.0	79634	2649
OD814	1672	95.5	0.2961	0.1	0.0985	0.0	73304	3462
OD814	1742	59.8	0.3102	0.0	0.0986	0.0	63497	1047
OD814	1909	63.1	0.3446	0.0	0.0986	0.0	69103	1298
OD814	1644	41.9	0.2904	0.0	0.0987	0.0	54082	332
OD814	1866	57.7	0.3357	0.0	0.0987	0.0	61332	1068
OD814	1980	56.4	0.3596	0.0	0.0987	0.0	71367	0
OD814	1946	46.9	0.3523	0.0	0.0988	0.0	59391	2127
OD814	2015	57.4	0.3670	0.0	0.0988	0.0	74408	3693
OD814	1605	55.8	0.2827	0.0	0.0988	0.0	72693	1589
OD814	1846	55.3	0.3315	0.0	0.0988	0.0	65697	0
OD814	1822	45.5	0.3266	0.0	0.0989	0.0	67057	0
OD814	1606	78.5	0.2830	0.1	0.0989	0.0	62855	265
OD814	1534	65.9	0.2697	0.0	0.0989	0.0	101729	0
OD814	1632	74.9	0.2881	0.0	0.0990	0.0	112974	2502
OD814	1591	68.0	0.2803	0.0	0.0991	0.0	74832	3376
OD814	1597	71.7	0.2812	0.0	0.0991	0.0	73490	3272
OD814	1842	99.5	0.3308	0.1	0.0991	0.0	129184	0
OD814	1586	45.3	0.2794	0.0	0.0992	0.0	53195	0
OD814	1779	42.3	0.3177	0.0	0.0993	0.0	56734	0

Table 4.4: Continued.

OD#	^{207}Pb cor ^{206}Pb/^{238}U age		^{206}Pb/^{238}U		^{207}Pb/^{206}Pb		Pb	Th
	Ma	+/-1 ster	ratio	+/-1 RSE	ratio	+/-1 RSE	ppm	ppm
not used in age calculation:								
RX7986	2101	82.2	0.3854	0.0	0.1019	0.0	57999	4193
RX7986	2026	71.6	0.3693	0.0	0.1020	0.0	128948	7727
RX7986	1978	66.9	0.3591	0.0	0.1002	0.0	52284	19902
RX7986	1951	65.1	0.3534	0.0	0.1041	0.0	48540	26920
RX7986	1939	35.3	0.3510	0.0	0.1024	0.0	68065	11425
RX7986	1893	70.6	0.3413	0.0	0.1036	0.0	52165	38079
RX7986	1887	45.3	0.3401	0.0	0.1060	0.0	52580	3192
RX7986	1877	46.4	0.3380	0.0	0.1106	0.0	61056	4433
RX7986	1858	36.0	0.3342	0.0	0.1114	0.0	67760	4643
RX7986	1827	100.8	0.3276	0.1	0.1005	0.0	121118	18818
RX7986	1792	44.6	0.3204	0.0	0.1090	0.0	53590	8680
RX7986	1647	35.5	0.2910	0.0	0.1007	0.0	43085	4578
RX7986	1563	48.2	0.2770	0.0	0.1047	0.0	43216	9223
RX7986	1754	92.0	0.3127	0.1	0.1000	0.0	100198	23540
RX7986	1742	40.9	0.3122	0.0	0.1119	0.0	81158	3663
RX7986	1732	199.2	0.3082	0.1	0.1018	0.0	139103	6466
RX7986	1693	102.0	0.3004	0.1	0.1029	0.0	63791	33269
RX7986	1678	59.8	0.2973	0.0	0.1025	0.0	92332	11310
RX7986	1650	126.6	0.2918	0.1	0.1010	0.0	122717	22839
RX7986	1477	26.7	0.2574	0.0	0.0923	0.0	48692	1525
RX7987	1538	99.3	0.2713	0.1	0.1010	0.0	91956	10029
RX7987	2046	84.3	0.3734	0.0	0.1031	0.0	71162	16269
RX7987	1937	47.1	0.3506	0.0	0.1033	0.0	63947	15847
RX7987	1920	36.9	0.3469	0.0	0.1073	0.0	82100	27619
RX7987	1714	41.2	0.3070	0.0	0.1117	0.0	50759	13639
RX7987	1823	33.2	0.3269	0.0	0.1031	0.0	73747	25509
RX7987	1807	55.7	0.3234	0.0	0.1048	0.0	46503	13668
RX7987	1773	66.1	0.3165	0.0	0.1016	0.0	59161	10167
OD814	1786	53.4	0.3192	0.0	0.1071	0.0	63292	0
OD814	1740	90.5	0.3098	0.1	0.1044	0.0	95529	5006
OD814	1850	30.7	0.3323	0.0	0.1106	0.0	59763	0
OD814	1939	51.2	0.3509	0.0	0.1097	0.0	42642	938
OD814	1648	77.5	0.2913	0.0	0.1012	0.0	29475	0
OD814	1593	96.8	0.2811	0.1	0.1004	0.0	101876	2088

Table 4.5: U-Pb dating of hematite.

OD#	^{207}Pb cor ^{206}Pb/^{238}U age Ma	+/-1 ster	^{206}Pb/^{238}U ratio	+/-1 RSE	^{207}Pb/^{206}Pb ratio	+/-1 RSE	Pb ppm	Th ppm	U ppm
used in age calculation:									
RX7986	1438	89.6	0.2731	0.1	0.1642	0.10	0.4	0.0	4.4
RX7986	1518	51.5	0.2959	0.0	0.1845	0.04	0.6	0.0	5.2
RX7986	1525	58.9	0.2686	0.0	0.1003	0.05	0.7	0.0	9.3
RX7986	1527	109.4	0.2824	0.1	0.1412	0.08	0.2	0.0	2.4
RX7986	1528	23.1	0.2700	0.0	0.1030	0.01	51.3	32.8	735.4
RX7986	1538	34.3	0.2701	0.0	0.0977	0.02	3.1	0.0	42.3
RX7986	1542	117.7	0.2712	0.1	0.0988	0.01	38.4	16.0	524.0
RX7986	1547	32.4	0.2764	0.0	0.1122	0.02	2.0	0.0	26.5
RX7986	1551	58.1	0.2784	0.0	0.1158	0.05	0.3	0.0	4.4
RX7986	1557	62.3	0.2734	0.0	0.0972	0.07	0.5	0.0	6.0
RX7986	1557	28.0	0.2735	0.0	0.0975	0.01	16.3	4.0	225.4
RX7986	1562	84.9	0.2774	0.1	0.1069	0.02	64.7	8.7	869.1
RX7986	1562	40.0	0.3471	0.0	0.2851	0.02	1.5	0.1	8.2
RX7986	1563	41.5	0.2763	0.0	0.1025	0.01	263.4	32.2	4003
RX7986	1565	59.2	0.3420	0.0	0.2728	0.03	0.9	0.0	5.5
RX7986	1565	38.6	0.2757	0.0	0.0999	0.01	40.7	42.9	490.0
RX7986	1565	32.1	0.2757	0.0	0.0997	0.01	36.0	35.0	511.0
RX7986	1569	45.0	0.3160	0.0	0.2098	0.02	2.5	0.2	18.3
RX7986	1569	60.5	0.2761	0.0	0.0986	0.07	0.5	1.0	5.3
RX7986	1574	28.9	0.2814	0.0	0.1125	0.01	5.4	0.0	73.9
RX7986	1582	36.0	0.3602	0.0	0.3033	0.02	2.5	0.1	12.6
RX7986	1584	24.9	0.2789	0.0	0.0989	0.01	28.0	34.6	383.3
RX7986	1585	29.2	0.2794	0.0	0.0999	0.02	4.8	0.0	70.0
RX7986	1586	36.2	0.2919	0.0	0.1369	0.02	1.9	0.0	19.7
RX7986	1587	51.0	0.2987	0.0	0.1549	0.04	0.6	0.0	5.0
RX7986	1589	38.0	0.2795	0.0	0.0975	0.01	8.7	15.9	118.0
RX7986	1591	53.3	0.3373	0.0	0.2498	0.02	1.4	0.0	8.9
RX7986	1593	27.4	0.2804	0.0	0.0987	0.01	38.6	32.4	537.8
RX7986	1596	26.4	0.2810	0.0	0.0987	0.01	18.0	4.3	265.2
RX7986	1596	67.5	0.3041	0.0	0.1650	0.04	0.4	0.0	3.4
RX7986	1597	88.7	0.2811	0.1	0.0983	0.11	0.2	0.2	1.8
RX7986	1597	35.8	0.2830	0.0	0.1044	0.01	41.7	48.3	562.7
RX7986	1598	50.1	0.2828	0.0	0.0988	0.06	26.7	0.8	358.4
RX7986	1600	139.3	0.2859	0.1	0.1113	0.12	0.2	0.1	2.4
RX7986	1603	61.2	0.2889	0.0	0.1187	0.05	0.5	0.0	6.1
RX7986	1603	51.6	0.2937	0.0	0.1323	0.04	0.8	0.0	7.7
RX7986	1605	41.6	0.3061	0.0	0.1660	0.01	28.8	4.8	270.5
RX7986	1606	36.0	0.3097	0.0	0.1748	0.02	3.5	0.0	31.7
RX7986	1607	20.4	0.2832	0.0	0.0994	0.01	68.3	122.8	897.3
RX7986	1608	54.7	0.2963	0.0	0.1374	0.05	0.9	0.1	10.2
RX7986	1612	47.6	0.2909	0.0	0.1196	0.03	1.2	0.1	14.3

Table 4.5: Continued.

OD#	^{207}Pb cor $^{206}Pb/^{238}U$ age	+/-1	$^{206}Pb/^{238}U$	+/-1	$^{207}Pb/^{206}Pb$	+/-1	Pb	Th	U
	Ma	ster	ratio	RSE	ratio	RSE	ppm	ppm	ppm
RX7986	1613	93.5	0.3789	0.1	0.3264	0.04	1.1	0.0	5.0
RX7986	1617	31.9	0.3099	0.0	0.1698	0.02	2.7	0.1	21.9
RX7986	1624	37.3	0.3343	0.0	0.2268	0.02	4.3	0.5	27.0
RX7986	1627	49.3	0.2870	0.0	0.0989	0.02	5.2	0.9	74.8
RX7986	1634	71.9	0.2884	0.0	0.0993	0.02	2.6	0.2	36.5
RX7986	1636	42.5	0.3463	0.0	0.2486	0.03	2.4	0.2	14.3
RX7986	1642	55.9	0.3029	0.0	0.1381	0.03	1.3	0.0	14.3
RX7986	1661	65.6	0.2940	0.0	0.0989	0.01	38.1	2.4	489.0
RX7986	1685	78.9	0.4321	0.0	0.3910	0.03	0.9	0.0	2.5
RX7987	1517	77.9	0.2680	0.1	0.1031	0.08	0.2	0.0	2.1
RX7987	1561	46.2	0.2836	0.0	0.1261	0.01	15.8	14.6	172.1
RX7987	1571	48.6	0.3107	0.0	0.1957	0.03	2.6	0.5	19.1
RX7987	1576	60.1	0.2777	0.0	0.0996	0.02	33.2	18.6	420.3
RX7987	1577	86.4	0.3088	0.1	0.1874	0.09	0.2	0.0	1.9
RX7987	1581	27.6	0.2821	0.0	0.0989	0.07	62.5	84.8	791.2
RX7987	1614	45.0	0.2846	0.0	0.0998	0.01	47.4	24.5	596.9
RX7987	1614	92.2	0.3219	0.1	0.2020	0.07	0.2	0.2	1.7
RX7987	1616	154.1	0.3648	0.1	0.2973	0.10	0.1	0.0	0.5
RX7987	1653	148.7	0.3280	0.1	0.1978	0.10	0.1	0.0	0.7
not used in age calculation:									
RX7986	1235	41.8	0.2158	0.04	0.0998	0.01	72.8	9.1	1434
RX7986	1353	86.8	0.2380	0.07	0.1029	0.01	122.2	24.8	1913
RX7986	1386	194.3	0.2423	0.15	0.0970	0.04	4.4	0.4	68.4
RX7986	1757	76.1	0.3133	0.04	0.0983	0.05	0.5	0.0	5.9
RX7986	1866	79.0	0.3357	0.04	0.1133	0.04	0.5	0.0	5.3
RX7987	1348	21.8	0.2358	0.02	0.0981	0.01	3148.1	5113.0	47500
RX7987	1780.8	83.5881	0.3	0.05	0.1	0.07	0.1	0.0	1.23426

Table 4.6: Trace element concentrations (in ppm) of apatite. Note that sample OD846 has been interpreted to contain the early mineralization as well. Table includes a selection of elements. *Ideal Ca concentration.

OD#	Li	Na	Mg	Si	P	Ca*	Mn	Fe	Zn	Ga	Ge	As	Sr	Y
OD826A-ap	2.31	1342	61	2275	196316	397400	110	500	1.66	12.19	7.03	111	411	1510
OD826A-ap	3.19	1312	64	2127	197259	397400	97	519	3026.95	12.70	9.03	105	426	1548
OD826A-ap	4.91	1377	57	2233	199017	397400	121	596	3.77	13.17	7.39	115	423	1525
OD826A-ap	5.38	1011	391	24288	191091	397400	99	3246	1638.95	13.91	4.13	68	387	813
OD826A-ap	2.03	1289	63	2260	198110	397400	88	573	10.17	12.21	7.98	99	411	1440
OD826A-ap	3.70	1431	58	2341	197566	397400	110	546	9.57	11.58	7.61	102	436	1487
OD826A-ap	2.04	1207	57	2159	201393	397400	130	382	1.82	10.11	6.65	109	478	1317
OD826A-ap	2.61	1370	54	2332	198937	397400	113	425	4.17	12.44	9.01	122	457	1549
OD826A-ap	3.64	1263	49	37044	191336	397400	112	1406	3.61	11.95	8.51	139	444	1423
OD826A-ap	2.89	1402	58	2640	197687	397400	124	1050	10.81	12.84	10.51	118	415	1550
OD826A-ap	2.30	1158	58	2317	193762	397400	490	548	2.54	11.02	7.11	139	408	1480
OD826A-ap	3.49	1178	57	2338	197429	397400	120	471	2.88	10.60	7.03	110	391	1412
OD826A-ap	2.29	1282	77	2335	196092	397400	800	1046	1.23	11.78	8.81	112	392	1446
OD826A-ap	2.15	1452	55	2732	197566	397400	91	478	5.34	12.42	8.30	112	431	1588
OD826A-ap	2.75	1312	54	2439	198930	397400	92	443	3.36	11.99	7.79	125	408	1501
OD826A-ap	2.62	1454	62	2661	198996	397400	98	592	6.16	13.51	12.42	117	417	1716
OD826A-ap	3.02	1346	61	51194	181907	397400	108	13655	4.02	12.78	8.41	125	425	1609
OD826A-ap	2.09	1220	66	2371	198620	397400	123	871	6.00	12.34	8.92	88	437	1597
OD826A-ap	5.09	1148	104	24207	189418	397400	354	4208	3.94	11.47	9.11	132	468	1469
OD826A-ap	3.28	893	85	10501	195211	397400	132	1636	2.50	9.79	8.03	138	468	1335
OD826A-ap	4.19	1285	67	5732	195912	397400	104	6864	1.83	12.82	9.06	127	452	1532
OD826A-ap	4.53	1224	56	20428	191613	397400	107	1360	2.20	12.43	8.10	157	441	1603
OD826A-ap	5.58	1186	47	9350	195000	397400	106	1632	2.31	11.77	8.80	222	403	1510
OD826A-ap	4.93	1403	65	21280	189487	397400	121	5860	1.93	12.46	7.97	172	445	1589
OD826A-ap	3.02	1152	66	2457	194836	397400	85	447	1.19	12.96	8.94	105	420	1506
OD826A-ap	2.86	1215	57	1997	198761	397400	109	378	2.13	12.36	9.12	115	464	1427
OD826A-ap	3.36	1072	49	1680	194167	397400	105	385	6.04	14.32	8.80	93	434	1351
OD826A-ap	3.38	1053	47	1927	199400	397400	170	370	0.64	11.47	8.33	103	552	1318
OD826A-ap	3.74	1156	58	2049	196532	397400	99	426	0.92	12.52	9.60	116	449	1478
OD826A-ap	3.90	1296	56	2351	197582	397400	99	515	3.32	12.72	11.64	110	416	1455
OD826A-ap	1.49	772	29	960	195803	397400	126	2552	18.26	6.30	4.38	59	436	768
OD826A-ap	3.59	1098	60	2131	197740	397400	90	433	1.25	11.59	8.06	106	427	1388
OD826A-ap	1.67	1378	66	2140	196486	397400	91	433	1.42	11.98	8.42	106	420	1529
OD826A-ap	2.43	1387	70	2768	195629	397400	277	688	6.07	13.71	9.46	100	431	1699

Table 4.6: Continued.

OD#	Li	Na	Mg	Si	P	Ca*	Mn	Fe	Zn	Ga	Ge	As	Sr	Y
OD826A-ap	1.04	1428	77	2872	197563	397400	99	481	1.33	14.01	9.87	96	445	1807
OD826A-ap	1.58	1543	67	8676	190185	397400	124	1058	0.12	12.34	9.18	108	436	1530
OD826A-ap	3.37	1048	27	1712	195395	397400	124	344	16.07	9.63	6.92	78	360	1344
OD826A-ap	2.66	851	24	1746	193567	397400	133	254	12.79	7.21	5.80	66	397	1039
OD826A-ap	2.10	694	49	2548	198185	397400	129	688	11.15	8.94	5.98	55	394	741
OD826A-ap	1.15	498	67	3616	197025	397400	118	475	6.44	3.92	3.46	108	547	650
OD826A-ap	2.51	732	53	2447	196606	397400	71	462	8.12	6.50	5.34	57	479	866
OD829-ap	2.30	1126	59	1970	193252	397400	96	533	2.92	10.82	6.38	108	422	1447
OD829-ap	4.39	1414	61	2471	198884	397400	112	635	4.61	12.43	9.21	128	438	1637
OD829-ap	3.45	1452	55	1914	197719	397400	181	533	6.43	10.41	7.45	118	408	1352
OD829-ap	3.88	1189	49	1664	199620	397400	129	651	4.25	9.14	6.49	102	418	1174
OD829-ap	2.47	1487	64	2241	197136	397400	122	542	7.51	12.90	8.63	119	408	1542
OD829-ap	4.20	1352	49	1882	202961	397400	162	463	10.92	10.80	6.50	112	466	1266
OD829-ap	1.84	1424	59	2109	199869	397400	111	480	3.82	11.82	8.51	125	431	1447
OD829-ap	3.21	1599	62	2171	200654	397400	127	430	7.72	11.72	8.70	117	425	1513
OD829-ap	0.92	1517	75	2473	202293	397400	95	462	0.70	12.73	8.56	131	436	1606
OD829-ap	1.37	1311	60	1990	199956	397400	85	354	1.35	10.59	7.88	107	380	1319
OD829-ap	2.81	1787	85	2455	199012	397400	104	631	5.76	13.37	9.49	131	408	1688
OD829-ap	1.91	1434	80	2456	199796	397400	92	487	1.72	12.64	8.36	120	432	1645
OD829-ap	2.94	2192	70	2018	197927	397400	96	615	16.35	11.59	9.19	108	421	1320
OD829-ap	4.32	1768	59	1925	202282	397400	96	412	77.49	11.97	7.52	125	417	1543
OD829-ap	3.22	1371	44	3263	197247	397400	88	306	69.40	10.00	7.00	107	396	1399
OD829-ap	3.79	1548	58	2265	197424	397400	77	356	57.93	11.72	7.59	112	422	1556
OD829-ap	3.30	1225	54	2969	195731	397400	103	448	39.93	14.96	11.81	108	415	1402
OD829-ap	3.29	3335	24	1967	199151	397400	100	494	62.76	11.80	9.80	103	379	1624
OD829-ap	1.10	874	10	364	202555	397400	287	84	11.30	1.88	0.59	25	609	555
OD829-ap	4.03	1414	33	1163	201712	397400	116	1577	50.36	7.59	6.03	104	370	962
OD829-ap	3.07	1364	23	1663	198719	397400	135	351	22.58	7.01	5.49	114	368	1088
OD829-ap	3.88	1373	27	1371	200450	397400	99	448	15.89	7.60	4.15	81	321	952
OD829-ap	2.59	1300	42	1875	199224	397400	94	1172	5.75	10.16	6.70	105	371	1282
OD829-ap	3.92	1600	45	2426	199396	397400	113	409	10.89	10.87	7.84	108	396	1714
OD829-ap	7.19	986	4088	18144	189406	397400	783	27580	145.50	19.56	5.10	79	340	962
OD829-ap	2.91	784	17	801	202867	397400	118	1583	12.07	4.79	4.33	55	305	734
OD829-ap	2.89	1349	39	1943	197385	397400	102	297	14.75	10.31	6.37	85	364	1272
OD829-ap	3.20	1470	121	2148	200848	397400	89	437	15.72	10.21	6.59	86	358	1278

Table 4.6: Continued.

OD#	Li	Na	Mg	Si	P	Ca*	Mn	Fe	Zn	Ga	Ge	As	Sr	Y
OD829-ap	2.68	1349	62	2093	200404	397400	90	391	3.39	11.22	7.12	116	398	1429
OD829-ap	4.06	1755	50	2220	197631	397400	110	489	6.36	11.65	8.71	108	384	1450
OD829-ap	1.87	908	59	1440	200900	397400	96	895	3.22	8.73	5.63	81	348	1121
OD829-ap	1.12	1309	62	2403	201970	397400	86	429	2.95	13.95	8.11	121	419	1550
OD829-ap	1.58	695	50	1076	194156	397400	1084	2116	4.45	5.48	2.56	57	278	695
OD829-ap	3.59	1381	61	2163	199255	397400	90	494	8.09	11.35	6.94	104	415	1341
OD829-ap	2.61	1347	59	2110	200991	397400	90	407	4.21	10.55	7.54	117	417	1371
OD829-ap	3.69	1233	76	2389	202171	397400	89	443	10.85	12.95	9.07	110	403	1509
OD829-ap	3.10	1201	67	2380	201035	397400	87	409	13.48	11.79	8.85	112	411	1530
OD829-ap	3.37	1186	60	2255	197461	397400	87	385	11.55	12.11	9.27	109	404	1482
OD829-ap	4.16	1328	54	2158	200598	397400	92	368	14.64	12.38	7.65	119	405	1486
OD829-ap	3.93	1313	41	14802	194816	397400	95	1027	15.52	10.44	7.62	88	376	1254
OD829-ap	3.92	1476	63	2560	199549	397400	103	542	20.89	12.16	7.85	96	418	1618
OD829-ap	4.72	1224	46	1973	199067	397400	98	529	21.50	11.70	7.57	90	398	1351
OD829-ap	4.58	1919	60	2275	199875	397400	97	1690	9.38	11.95	7.12	99	413	1618
OD829-ap	3.38	1601	71	2554	199300	397400	102	539	12.07	13.26	8.32	96	417	1671
OD829-ap	2.90	1416	59	1977	201692	397400	94	458	11.64	11.43	7.88	106	402	1350
OD829-ap	2.75	1391	54	2018	199092	397400	109	404	11.70	11.95	7.47	105	415	1454
OD829-ap	3.61	1322	41	1710	203195	397400	106	391	13.09	9.25	6.58	85	366	1131
OD829-ap	3.65	1184	50	1709	202942	397400	108	364	12.21	10.49	7.56	96	412	1387
OD829-ap	3.71	1230	62	2434	201605	397400	84	472	4.81	12.78	9.02	120	418	1539
OD829-ap	3.55	1234	59	2403	201435	397400	88	424	8.59	12.92	9.06	112	416	1493
OD829-ap	3.98	1139	58	2291	200604	397400	104	762	4.40	11.40	9.71	110	425	1596
OD829-ap	5.79	1317	61	2507	199485	397400	90	384	7.30	13.04	9.18	120	429	1675
OD829-ap	4.52	1006	57	4244	194926	397400	112	497	5.80	11.02	6.52	95	432	1464
OD829-ap	4.28	1120	42	2852	197772	397400	143	426	12.52	9.70	6.68	93	426	1188
OD829-ap	2.80	1209	51	4774	198515	397400	113	3382	10.64	11.42	7.44	103	387	1308
OD829-ap	5.17	1337	46	2516	200553	397400	99	569	14.24	11.95	7.75	101	400	1466
OD829-ap	3.45	1024	25	1813	201380	397400	100	355	24.77	8.20	5.14	76	342	1128
OD829-ap	4.82	1337	57	2416	194699	397400	90	460	30.92	12.85	9.02	107	409	1609
OD829-ap	4.58	1406	57	2456	200663	397400	98	442	17.16	11.55	8.56	107	403	1496
OD829-ap	3.97	1393	73	2402	202512	397400	93	439	9.14	14.21	10.08	115	417	1609
OD829-ap	3.29	1372	78	2206	197508	397400	90	519	9.96	12.63	7.58	106	408	1623
OD829-ap	4.22	1169	61	2347	198618	397400	90	400	8.37	11.68	8.32	97	409	1493
OD829-ap	4.81	1371	68	2143	201593	397400	93	474	3.11	11.84	9.77	128	428	1543

Table 4.6: Continued.

OD#	Li	Na	Mg	Si	P	Ca*	Mn	Fe	Zn	Ga	Ge	As	Sr	Y
OD829-ap	3.21	1348	77	2708	202166	397400	91	512	1.87	13.83	10.59	106	431	1720
OD829-ap	2.43	1409	90	2806	197903	397400	96	455	5.33	13.54	8.81	105	414	1700
OD829-ap		1455	74	2628	200448	397400	86	441		13.00	8.68	116	420	1596
OD829-ap	0.68	1468	71	2438	199936	397400	82	458	1.98	12.47	8.88	128	405	1510
OD829-ap	2.01	1419	67	2421	201353	397400	85	475	3.21	12.37	8.88	123	413	1477
OD829-ap	4.04	1491	64	2358	201656	397400	124	473	7.05	13.29	8.37	117	443	1645
OD829-ap	4.65	1397	66	2333	199329	397400	106	445	6.92	12.39	9.15	108	421	1539
OD829-ap	3.06	1404	65	2357	202458	397400	100	398	6.24	12.19	9.73	103	415	1539
OD829-ap	3.97	1401	80	2473	201577	397400	103	521	8.43	12.30	8.78	90	434	1619
OD829-ap	5.32	1314	38	2112	200972	397400	98	346	17.30	12.49	8.92	95	394	1681
OD829-ap	4.28	1580	65	2433	198083	397400	105	540	10.02	13.59	9.77	90	432	1700
OD829-ap	2.92	1469	66	2401	200994	397400	104	568	7.33	13.62	9.91	104	418	1605
OD829-ap	2.23	1399	67	2247	202613	397400	104	405	3.57	12.61	8.64	116	414	1516
OD829-ap	4.29	1345	65	2271	200405	397400	102	597	10.50	12.18	8.44	95	418	1577
OD829-ap	4.68	1365	50	2322	202039	397400	100	402	13.67	12.40	8.80	111	399	1693
OD846-ap	0.24	481	15	3065	197541	397400	36	601	1.44	17.88	13.14	238	326	1671
OD846-ap	0.33	467	199	4989	198164	397400	1116	10993	2.84	14.54	11.83	234	315	1450
OD846-ap	1.01	410	16	1494	198479	397400	34	803	1.33	7.58	6.65	119	519	1037
OD846-ap	2.27	530	144	7974	187582	397400	39	1462	0.95	14.09	12.40	168	339	1363
OD846-ap	0.74	531	97	3296	196085	397400	54	3257	5.05	15.28	10.75	195	526	1520
OD846-ap	0.61	688	14	3511	196538	397400	49	3196	0.80	19.09	14.56	221	406	1801
OD846-ap	3.89	570	1402	10078	193182	397400	237	25680	56.87	12.55	5.73	163	457	1077
OD846-ap	3.13	332	756	7788	196071	397400	154	31978	34.25	8.16	3.95	149	492	943
OD846-ap	2.01	293	728	5701	192841	397400	131	18295	25.70	5.84	2.75	135	388	826
OD846-ap	1.59	563	169	4461	196896	397400	75	6753	11.50	15.75	11.15	222	396	1440
OD846-ap	0.92	745	134	2155	195437	397400	57	2404	4.26	8.74	6.11	153	528	1059
OD846-ap	1.99	676	485	4913	195006	397400	114	23146	21.13	9.13	7.49	165	584	1109
OD846-ap	3.28	818	1073	8509	193752	397400	198	27193	49.06	12.47	6.38	166	560	1083
OD846-ap	3.11	564	1093	8015	194036	397400	179	41441	45.87	12.43	5.94	154	458	1069
OD846-ap	4.81	574	1469	11266	201446	397400	230	49290	59.75	13.36	6.13	155	423	1003
OD846-ap	2.36	486	697	6397	191573	397400	129	23619	27.15	8.20	4.16	135	569	914
OD846-ap	9.01	588	2972	19998	192975	397400	431	52907	148.62	17.28	5.50	166	842	937
OD846-ap	0.50	457	31	1635	194791	397400	37	1286	3.93	6.70	7.49	148	609	957
OD846-ap	1.08	310	296	4174	190699	397400	89	35966	33.98	7.94	4.62	110	311	900
OD846-ap	1.34	831	337	4137	191999	397400	87	32181	15.40	10.10	6.38	164	519	1097

Table 4.6: Continued.

OD#	Li	Na	Mg	Si	P	Ca*	Mn	Fe	Zn	Ga	Ge	As	Sr	Y
OD846-ap	1.31	641	183	3744	194764	397400	63	29109	6.64	11.25	7.94	216	422	1286
OD846-ap	0.86	682	30	2708	193851	397400	43	803	2.09	11.93	8.20	202	440	1314
OD846-ap	1.01	673	153	2824	190054	397400	62	3638	7.22	9.96	8.11	194	488	1237
OD846-ap	0.77	680	89	2864	193682	397400	57	17565	9.47	9.67	5.95	201	450	1256
OD846-ap	0.78	511	228	5243	193732	397400	65	72624	95.28	7.72	4.73	135	423	893
OD846-ap	1.05	620	150	2994	191382	397400	56	3167	12.11	8.15	5.51	149	471	1064
OD846-ap	1.61	643	381	4591	190934	397400	96	8148	22.16	8.65	5.55	119	552	1022
OD846-ap	0.87	429	20	1350	189349	397400	36	484	3.67	5.82	3.97	116	399	987
OD846-ap	0.36	594	19	1550	195948	397400	68	29992	9.58	7.08	4.63	128	323	881
OD846-ap	0.65	624	15	1623	195480	397400	49	3725	9.10	9.55	6.27	137	364	1023
OD846-ap	0.96	856	25	2825	191170	397400	49	1073	1.48	14.60	11.61	230	448	1516
OD846-ap	0.72	557	166	2436	190974	397400	69	3205	22.47	8.58	6.11	150	457	1111
OD846-ap	0.64	772	17	2072	191465	397400	45	1155	3.93	8.44	6.96	169	393	1136
OD846-ap	0.33	686	20	4606	191585	397400	52	1163	30.45	8.47	6.54	147	750	1079
OD846-ap	0.19	575	12	1444	189696	397400	45	1194	2.42	6.93	5.51	135	712	932
OD846-ap		558	16	1646	193075	397400	54	464	8.53	7.21	6.07	125	416	901
OD846-ap	0.31	596	81	2106	193996	397400	59	36937	25.21	8.04	6.32	127	370	944
OD846-ap	0.30	382	16	1228	187362	397400	103	534	7.61	5.42	4.94	93	284	786
OD846-ap	5.00	556	1626	10838	191542	397400	252	62562	89.22	12.41	6.11	121	401	872
OD846-ap	3.90	562	1231	9563	183908	397400	219	24042	69.23	11.62	6.42	131	442	958

Table 4.6: Continued.

OD#	La	Ce	Pr	Nd	Sm	Eu	Eu	Gd	Tb	Dy	Ho	Er	Tm	Yb	Lu	Th	U	Pb(tot)
OD826A-ap	1789	4918	601	2323	376	31	31	324	42	251	50	138	18	104	14	49	42	19
OD826A-ap	1806	4963	608	2329	384	31	31	326	42	253	51	139	18	106	14	54	47	21
OD826A-ap	1921	5069	631	2420	397	34	33	332	43	249	49	135	18	103	13	52	43	21
OD826A-ap	918	2494	312	1246	230	24	23	203	25	140	26	70	9	51	7	27	22	143
OD826A-ap	1669	4556	560	2158	357	29	29	300	40	233	46	130	17	98	13	50	43	20
OD826A-ap	1678	4608	567	2188	363	29	29	309	41	233	47	135	17	102	13	54	48	21
OD826A-ap	1419	3840	475	1850	317	26	25	274	36	208	43	116	16	88	12	49	40	16
OD826A-ap	1831	4984	606	2351	383	31	31	322	43	250	49	137	18	107	14	61	50	17
OD826A-ap	1597	4353	535	2071	345	29	30	298	40	229	45	127	17	99	13	61	47	24
OD826A-ap	1859	5046	617	2372	389	31	31	327	43	248	49	139	18	105	14	60	50	19
OD826A-ap	1584	4316	531	2064	340	29	28	299	40	231	47	134	17	104	15	53	44	40
OD826A-ap	1521	4178	512	2002	339	27	28	290	38	221	44	126	17	98	13	47	41	30
OD826A-ap	1614	4371	541	2107	349	28	28	302	40	230	47	130	17	99	13	56	47	25
OD826A-ap	1866	5119	618	2376	391	30	30	329	44	258	52	145	19	111	14	68	55	20
OD826A-ap	1722	4694	567	2199	358	30	30	306	41	236	48	136	17	105	14	54	46	17
OD826A-ap	2032	5518	668	2584	427	34	34	368	48	277	56	155	20	118	15	72	55	23
OD826A-ap	1914	5109	632	2420	406	32	31	339	44	260	52	147	19	112	15	68	51	32
OD826A-ap	1785	4844	592	2290	381	29	29	331	44	255	51	146	19	111	14	67	59	25
OD826A-ap	1675	4514	547	2124	360	28	27	307	40	238	47	134	17	102	13	65	55	23
OD826A-ap	1372	3732	463	1804	313	25	25	276	36	213	43	121	16	91	12	50	41	18
OD826A-ap	1794	4890	597	2284	379	30	30	321	42	245	49	139	18	108	14	60	49	24
OD826A-ap	1838	4985	609	2375	391	32	31	333	44	257	52	144	19	111	15	67	51	38
OD826A-ap	1623	4543	556	2184	367	29	29	319	42	245	49	136	18	107	14	61	48	23
OD826A-ap	1778	4847	594	2302	383	31	31	332	44	255	51	144	19	112	14	68	54	22
OD826A-ap	1882	5214	624	2391	385	31	32	319	42	247	49	139	18	106	14	48	44	15
OD826A-ap	1747	4816	580	2244	362	31	31	307	40	230	46	131	16	100	13	40	35	14
OD826A-ap	1813	4977	595	2286	366	33	33	304	39	225	44	127	16	92	12	41	37	13
OD826A-ap	1614	4399	539	2071	343	31	30	297	38	216	43	121	15	91	12	39	36	14
OD826A-ap	1787	4920	594	2284	369	31	30	307	41	239	48	134	18	102	14	42	40	14
OD826A-ap	1869	5071	612	2354	380	32	32	312	41	235	47	133	17	101	13	44	37	15
OD826A-ap	800	2199	276	1102	191	18	19	177	22	126	25	69	8	51	7	17	15	75
OD826A-ap	1632	4496	553	2134	349	29	30	296	39	225	45	128	17	98	13	34	33	16
OD826A-ap	1725	4755	584	2256	372	29	29	319	41	246	49	140	18	105	14	53	49	19
OD826A-ap	1937	5249	638	2450	415	31	32	353	47	277	55	155	21	119	15	76	63	29
OD826A-ap	2043	5552	669	2589	431	33	32	370	50	292	58	167	22	126	17	80	67	29
OD826A-ap	1755	4890	589	2291	377	29	29	323	42	244	49	139	18	110	14	54	52	18

Table 4.6: Continued.

OD#	La	Ce	Pr	Nd	Sm	Eu	Eu	Gd	Tb	Dy	Ho	Er	Tm	Yb	Lu	Th	U	Pb(tot)
OD826A-ap	1278	3519	435	1704	286	24	24	263	35	210	42	121	16	94	13	45	37	46
OD826A-ap	972	2699	341	1347	234	19	20	216	28	167	34	95	12	71	10	32	29	36
OD826A-ap	1173	3011	366	1424	244	23	23	196	24	127	24	64	8	46	6	48	33	11706
OD826A-ap	584	1529	193	788	150	17	17	141	18	102	21	54	7	44	7	15	13	321
OD826A-ap	884	2470	311	1252	224	22	23	200	26	145	27	77	10	56	7	30	25	11078
OD829-ap	1665	4644	563	2186	359	29	28	301	40	226	46	131	17	102	13	46	42	17
OD829-ap	1910	5207	635	2430	403	32	32	338	45	262	52	149	19	111	15	63	54	27
OD829-ap	1537	4228	524	2003	330	27	28	282	37	218	44	123	16	95	12	37	36	16
OD829-ap	1370	3754	468	1821	311	28	27	266	34	196	38	105	13	81	11	32	28	15
OD829-ap	1808	4976	603	2342	381	31	29	329	42	249	49	140	18	107	14	51	42	18
OD829-ap	1496	4130	507	1951	319	27	28	275	36	203	42	114	15	89	11	36	30	13
OD829-ap	1751	4803	584	2265	358	30	29	312	40	235	47	131	17	99	14	48	43	16
OD829-ap	1699	4604	564	2181	355	28	28	304	41	241	49	137	18	105	14	51	46	20
OD829-ap	1863	5028	617	2383	393	31	31	333	44	257	52	146	19	111	15	56	51	18
OD829-ap	1514	4122	508	1971	332	27	28	292	37	216	43	121	16	91	12	46	42	17
OD829-ap	1993	5364	656	2513	406	32	32	346	45	264	54	153	20	119	15	61	57	21
OD829-ap	1895	5165	630	2428	396	31	30	341	44	260	54	148	19	113	15	59	53	20
OD829-ap	1844	5095	623	2372	395	31	31	328	40	226	45	120	15	91	12	54	47	27
OD829-ap	1705	4653	574	2240	370	29	28	319	43	247	49	142	18	108	14	52	46	23
OD829-ap	1494	4094	516	1993	335	27	27	300	40	231	46	127	17	97	12	52	47	19
OD829-ap	1720	4728	578	2213	370	29	29	312	43	249	50	143	18	107	14	56	49	20
OD829-ap	2407	6573	779	3001	462	34	34	358	44	240	46	125	16	92	12	64	46	19
OD829-ap	1699	4591	571	2207	368	29	30	325	43	260	52	145	19	110	15	63	53	22
OD829-ap	159	546	86	425	114	10	10	126	17	96	18	48	6	33	4	7	4	5
OD829-ap	1126	3114	390	1533	263	23	22	232	29	164	31	85	11	63	8	32	25	11
OD829-ap	991	2707	342	1368	245	19	19	221	30	174	35	98	12	72	10	33	26	15
OD829-ap	1072	2916	363	1423	243	20	20	213	27	159	31	84	11	63	9	30	24	12
OD829-ap	1446	3898	486	1877	316	25	25	270	37	210	42	117	15	87	11	45	37	15
OD829-ap	1683	4596	565	2180	368	29	29	325	44	267	55	156	20	122	16	54	46	20
OD829-ap	1080	2922	366	1437	245	21	21	216	28	162	32	87	11	66	9	33	28	15
OD829-ap	713	1957	250	1005	185	16	16	168	22	122	24	65	8	47	6	23	16	12
OD829-ap	1427	3849	477	1846	306	24	24	268	35	208	41	116	15	87	11	43	35	15
OD829-ap	1511	4114	501	1905	319	25	26	272	36	206	42	115	15	87	11	45	38	18
OD829-ap	1718	4675	572	2182	357	28	28	302	39	228	46	129	16	99	13	45	40	20
OD829-ap	1842	4957	601	2305	374	29	30	317	40	234	47	131	17	96	13	49	39	18
OD829-ap	1260	3448	429	1670	277	24	25	243	32	185	36	101	13	76	10	28	26	10

Table 4.6: Continued.

OD#	La	Ce	Pr	Nd	Sm	Eu	Eu	Gd	Tb	Dy	Ho	Er	Tm	Yb	Lu	Th	U	Pb(tot)
OD829-ap	1913	5194	629	2420	387	31	31	326	43	251	50	143	18	108	15	50	43	16
OD829-ap	780	2132	265	1045	182	16	16	161	22	119	23	61	8	46	6	20	16	32
OD829-ap	1649	4405	543	2082	332	27	26	290	37	214	44	121	16	91	12	43	36	14
OD829-ap	1728	4633	569	2165	352	27	28	298	38	219	45	123	16	94	12	42	37	15
OD829-ap	1840	5029	608	2337	377	31	30	316	42	238	49	137	18	104	14	49	42	17
OD829-ap	1790	4839	592	2268	371	29	29	314	41	244	49	137	18	108	14	47	41	18
OD829-ap	1765	4851	586	2258	364	30	30	307	41	239	48	135	18	103	13	46	39	18
OD829-ap	1779	4813	593	2262	366	30	30	315	41	238	48	134	18	103	14	45	42	18
OD829-ap	1517	4072	508	1956	322	27	27	272	35	205	41	115	15	86	11	37	36	27
OD829-ap	1855	5044	615	2369	397	29	30	336	45	261	53	147	20	114	15	64	55	35
OD829-ap	1620	4452	543	2088	342	28	27	297	38	217	44	123	16	89	12	44	39	31
OD829-ap	1771	4777	590	2274	379	28	29	329	44	262	53	149	19	121	15	73	58	536
OD829-ap	1959	5278	646	2477	408	31	31	355	47	273	55	153	20	119	15	79	64	35
OD829-ap	1632	4425	543	2096	337	28	28	287	38	215	44	123	16	92	12	37	33	14
OD829-ap	1769	4757	580	2241	362	30	30	304	40	231	47	132	17	102	13	41	35	16
OD829-ap	1317	3601	445	1735	284	25	25	243	33	188	38	103	13	78	10	32	26	15
OD829-ap	1473	4021	496	1918	315	26	27	277	38	222	45	128	16	98	13	37	32	14
OD829-ap	1876	5119	619	2378	385	31	32	324	43	248	51	142	18	108	14	47	41	16
OD829-ap	1844	5007	611	2352	382	31	31	318	42	240	49	138	18	105	14	45	39	17
OD829-ap	1699	4645	575	2222	363	29	30	323	42	250	51	144	19	112	15	47	48	18
OD829-ap	1886	5231	632	2428	398	32	32	341	46	270	54	154	20	119	15	66	56	34
OD829-ap	1705	4704	572	2184	359	29	28	295	39	230	49	130	17	101	12	52	49	19
OD829-ap	1326	3724	461	1815	299	23	24	257	34	191	38	108	14	81	10	37	37	19
OD829-ap	1582	4281	525	2037	325	26	27	279	36	211	42	118	15	89	12	39	37	32
OD829-ap	1757	4748	581	2245	368	29	30	312	41	239	47	134	17	101	13	60	51	22
OD829-ap	1229	3358	421	1643	278	23	23	241	32	185	36	101	13	76	10	44	36	17
OD829-ap	1866	5211	630	2420	388	30	32	341	44	263	54	144	19	110	14	69	58	27
OD829-ap	1731	4763	580	2253	371	28	28	316	41	240	48	135	18	104	14	53	49	24
OD829-ap	1997	5431	664	2561	417	32	32	350	46	258	53	146	19	111	14	61	49	21
OD829-ap	1762	4834	586	2267	374	29	29	326	44	258	52	148	19	113	15	61	52	22
OD829-ap	1707	4718	566	2207	363	29	29	314	42	241	49	133	18	103	13	60	51	21
OD829-ap	1767	4827	591	2290	375	30	29	319	43	243	50	140	18	105	14	52	48	18
OD829-ap	1982	5401	656	2561	416	33	32	360	47	280	56	155	20	120	16	66	55	20
OD829-ap	1892	5240	640	2466	408	30	31	347	47	269	54	154	20	118	15	59	49	19
OD829-ap	1817	4954	606	2348	382	29	29	324	43	253	52	144	19	109	15	54	51	17
OD829-ap	1769	4877	591	2279	372	29	29	314	41	241	48	139	18	104	14	51	47	17

Table 4.6: Continued.

OD#	La	Ce	Pr	Nd	Sm	Eu	Eu	Gd	Tb	Dy	Ho	Er	Tm	Yb	Lu	Th	U	Pb(tot)
OD829-ap	1753	4826	584	2255	366	29	29	307	40	234	47	133	18	103	14	47	45	16
OD829-ap	1836	5082	615	2382	383	31	31	340	45	267	53	148	20	115	15	67	57	23
OD829-ap	1762	4838	592	2278	379	30	29	322	43	246	50	139	18	106	14	61	53	21
OD829-ap	1793	4859	593	2288	374	28	29	318	42	243	50	138	18	106	14	57	51	20
OD829-ap	1869	5023	610	2324	385	30	30	333	44	261	52	147	19	113	14	77	63	28
OD829-ap	1814	4881	604	2358	395	30	30	340	46	270	54	154	20	120	16	62	52	22
OD829-ap	1886	5168	616	2399	397	31	31	340	46	272	53	154	20	119	15	78	66	27
OD829-ap	1845	5128	618	2376	390	30	30	328	44	254	51	146	19	114	14	61	53	21
OD829-ap	1717	4713	581	2236	368	29	29	307	41	241	48	137	18	105	14	49	46	31
OD829-ap	1762	4794	600	2259	376	28	29	325	43	252	50	140	18	108	14	61	53	21
OD829-ap	1757	4744	583	2247	371	30	30	329	44	260	53	154	20	124	17	56	46	41
OD846-ap	1898	6548	874	3517	531	39	38	396	49	272	54	157	21	133	19	88	16	11
OD846-ap	1649	5434	718	2860	436	34	35	334	41	234	46	132	17	109	17	73	16	10
OD846-ap	690	2551	372	1614	294	31	31	327	36	184	34	90	11	69	10	61	8	8
OD846-ap	1499	5217	690	2859	445	33	32	354	41	225	44	124	16	94	13	105	16	13
OD846-ap	1702	5792	773	3145	493	39	39	402	48	262	51	139	18	109	15	127	21	16
OD846-ap	2371	7698	985	3905	562	41	41	423	52	293	58	166	21	129	18	147	31	18
OD846-ap	971	2843	374	1550	281	32	31	271	35	187	36	96	12	70	10	115	34	11
OD846-ap	527	1574	213	933	211	28	28	233	30	159	31	81	10	57	8	36	8	7
OD846-ap	387	1168	159	705	160	20	20	185	24	134	26	69	9	50	7	30	5	6
OD846-ap	1675	5300	692	2794	427	38	38	352	44	246	47	135	17	105	15	94	26	14
OD846-ap	1038	2906	369	1502	320	42	42	323	38	196	36	94	11	67	9	63	14	11
OD846-ap	1078	3092	397	1607	307	38	37	297	36	196	37	97	12	71	10	63	15	11
OD846-ap	1171	3285	414	1657	311	38	39	308	37	197	37	96	12	71	10	66	16	12
OD846-ap	1035	2991	385	1515	264	29	29	251	31	178	34	93	12	70	10	54	18	12
OD846-ap	976	2859	369	1485	253	27	27	244	31	171	33	87	11	65	9	55	15	12
OD846-ap	713	2047	270	1123	240	32	31	262	32	167	30	80	10	59	8	48	10	9
OD846-ap	840	2522	338	1417	278	33	32	289	33	173	32	83	10	61	8	51	12	14
OD846-ap	648	2360	346	1532	332	42	41	367	40	188	32	85	11	65	9	76	8	10
OD846-ap	671	2090	278	1126	212	25	24	210	27	147	28	76	9	56	8	41	7	9
OD846-ap	1222	3406	431	1705	338	44	44	332	39	201	37	98	12	72	10	69	17	12
OD846-ap	1195	3617	484	2007	363	38	38	324	40	221	42	115	15	85	12	70	17	12
OD846-ap	1496	4617	599	2378	385	37	38	327	42	229	43	119	15	93	13	93	22	14
OD846-ap	1204	3541	467	1914	336	35	35	308	38	215	40	112	14	83	12	70	17	11
OD846-ap	1176	3492	465	1920	347	38	38	324	40	222	41	114	14	85	12	75	17	12
OD846-ap	673	1966	258	1076	246	34	34	253	31	162	30	78	9	55	8	46	11	17

Table 4.6: Continued.

OD#	La	Ce	Pr	Nd	Sm	Eu	Eu	Gd	Tb	Dy	Ho	Er	Tm	Yb	Lu	Th	U	Pb(tot)
OD846-ap	1009	2884	372	1530	315	39	40	320	38	200	36	95	11	71	10	66	14	11
OD846-ap	1011	2840	363	1467	328	48	48	340	40	200	35	91	11	64	9	73	18	11
OD846-ap	801	2314	306	1280	281	39	38	300	35	186	33	87	11	64	9	61	12	9
OD846-ap	871	2405	309	1227	245	31	30	219	27	147	29	77	10	56	8	43	12	9
OD846-ap	1190	3349	426	1681	310	38	38	276	33	178	33	91	11	67	10	60	19	11
OD846-ap	1892	5700	731	2886	444	42	43	372	46	257	50	135	18	109	15	106	28	16
OD846-ap	981	2833	373	1512	298	36	37	291	37	197	36	98	12	72	10	61	15	12
OD846-ap	1202	3406	429	1716	303	31	32	265	32	186	36	100	13	75	11	56	15	9
OD846-ap	1133	3225	417	1677	312	36	36	281	34	191	36	96	12	72	10	57	16	10
OD846-ap	837	2472	327	1343	276	34	35	294	33	171	31	82	10	59	8	52	12	9
OD846-ap	970	2752	351	1406	261	31	31	222	28	153	29	80	10	58	8	46	14	8
OD846-ap	961	2693	342	1352	292	40	40	273	33	171	31	84	10	59	8	52	16	11
OD846-ap	734	2183	290	1190	241	29	31	215	25	134	26	67	8	52	7	38	10	6
OD846-ap	907	2536	324	1299	250	30	31	232	28	154	29	77	10	57	8	49	14	14
OD846-ap	945	2682	340	1373	252	30	30	243	31	169	32	86	11	61	9	56	14	14

Table 4.7: Trace element concentrations (in ppm) of magnetite. Table includes a selection of elements. *Ideal Fe concentration.

OD#	Al	Si	P	Ca	Sc	Ti	V	Mn	Fe*	Cu	Zn	Th	U	Pb(tot)
OD829-mt	58	224		128	0.17	395	94	319	723600	0.83	31	0.00		0.03
OD829-mt	98	509	14	1636	0.57	568	100	451	723600		79	0.03	0.02	0.39
OD829-mt	253	179	12	127	1.14	824	101	333	723600	7.89	227	0.01	0.02	0.01
OD829-mt	341	148	2	552	1.01	702	99	380	723600	0.65	241	0.01	0.02	0.90
OD829-mt	267	310	35		0.56	749	101	381	723600	1.70	228		0.00	0.16
OD829-mt	140	179	48		0.40	452	98	325	723600	1.00	100	0.00	0.02	0.62
OD829-mt	466	118	26	511	0.76	765	103	366	723600	0.45	544	0.00	0.00	0.11
OD829-mt	237	286	136	119	0.69	713	99	354	723600	0.91	220	0.00	0.00	0.43
OD829-mt	55	245	21	559	0.50	280	87	328	723600		30	0.01	0.00	0.97
OD829-mt	363	428	5		1.25	1028	101	313	723600	0.09	371	0.00	0.00	0.02
OD829-mt	528	24		248	2.51	1447	102	333	723600		456	0.00	0.01	0.05
OD829-mt	378	277	11	56	1.36	1125	103	347	723600	0.25	391	0.02		0.02
OD829-mt	84	555	18	61	0.47	630	92	280	723600		41	0.00	0.01	3.86
OD829-mt	94	118	5		0.44	731	98	310	723600	0.45	35	0.01	0.04	0.80
OD829-mt	161	33	4		1.22	969	107	307	723600		153	0.00	0.00	0.01
OD829-mt	386	272	26	2012	2.16	1039	102	483	723600	0.36	341	0.00	0.01	6.02
OD829-mt	423	399	12		3.03	1149	101	330	723600	0.07	289	0.00	0.01	0.17
OD829-mt	292	123		91	1.28	994	96	322	723600		293	0.00	0.01	0.15
OD829-mt	131	143	1		0.36	638	98	333	723600	0.42	37	0.00	0.01	0.10
OD829-mt	238	374			0.90	822	102	327	723600		235		0.01	0.12
OD829-mt	203	191		127	0.52	849	98	318	723600	0.01	178	0.05	0.03	0.03
OD829-mt	846	1125	2	128	1.24	625	95	357	723600	0.34	68	0.00	0.02	0.16
OD829-mt	155	284	25		0.47	639	100	318	723600	0.11	131	0.00		0.03
OD829-mt	286	394			0.46	598	97	324	723600		45	0.00	0.01	0.05
OD829-mt	109	411		220	1.21	788	101	305	723600	0.09	55	0.03	0.02	0.26
OD829-mt	50	141	19		0.54	480	92	274	723600	0.57	24	0.00		0.25
OD829-mt	127	528	5	124	1.31	420	65	339	723600	0.27	88	0.00	0.02	1.94
OD829-mt	135	189		226	0.71	791	101	316	723600		86	0.03	0.02	0.11
OD829-mt	75	314	8		0.32	423	100	307	723600	3.81	33	0.00		0.14
OD829-mt	36	208		3394	2.09	98	91	631	723600		29	0.02	0.02	2.43
OD829-mt	44	273	281	748	0.08	587	101	343	723600	0.56	35	0.02	0.03	2.40
OD829-mt	152	246	8	524	0.64	768	98	328	723600	0.41	117	0.00	0.00	0.47
OD829-mt	175			122	0.88	969	101	314	723600	0.53	145	0.00	0.02	0.05
OD829-mt	1411	2617	10		2.89	634	96	300	723600	4.85	39	0.03	0.19	10.11
OD829-mt	72	272		69	0.20	624	93	279	723600	0.26	31	0.01	0.01	0.16
OD829-mt	322	219		159	1.65	985	103	328	723600	0.06	350	0.01	0.00	0.27

Table 4.7: Continued.

OD#	Al	Si	P	Ca	Sc	Ti	V	Mn	Fe*	Cu	Zn	Th	U	Pb(tot)
OD829-mt	705	862	16		0.59	814	96	330	723600	0.58	229	0.01	0.02	0.04
OD826A-mt	1589	439		1881	1.35	0	0	120	723600	0.85	6	0.14	0.36	1.58
OD826A-mt	1577	310		4374	2.85	1	2	293	723600	0.06	7	0.09	1.28	1.56
OD826A-mt	1836	525		4906	4.26	4	2	309	723600	6.41	8	0.17	3.16	39.78
OD826A-mt	1743	592	1	3074	1.37	0	0	270	723600	0.07	4	0.05	0.81	0.90
OD826A-mt	1254	287		1227	1.13	31	1	118	723600	0.21	3	0.07	0.42	1.12
OD826A-mt	353	69	31	1598	5.13	1	2	277	723600	0.02	11	0.06	0.56	4.94
OD826A-mt	170	318		1866	0.66		0	21	723600	0.42	6	0.00	0.07	1.31
OD826A-mt	278	216	8	3332	3.03	0	1	256	723600		1	0.03	0.18	1.24
OD826A-mt	922	167	24	435	22.30	0	2	76	723600	0.15	1	0.21	0.82	0.54
OD826A-mt	901	371	13	76	18.96	3	2	58	723600	0.50	9	0.94	1.13	59.78
OD826A-mt	1322	298		1312	2.55	0	0	75	723600	0.67	1	0.04	1.33	1.58
OD826A-mt	1399	648		3721	4.40	5	3	774	723600	2.32	31	0.09	2.53	108.95
OD826A-mt	1554	298		79	2.75	22	2	198	723600	0.46	1	0.11	0.65	1.16
OD826A-mt	2106	606	7	5431	7.48	12	4	458	723600	4.14	7	0.07	0.81	117.26
OD826A-mt	1685	676	7	1599	4.05	7	3	403	723600	1.55	20	0.05	0.87	35.87
OD826A-mt	1988	323	11	51	16.07	54	4	4	723600	0.24		0.07	0.39	2.36
OD826A-mt	2063	66	11		15.06	35	1	4	723600	0.41	1	0.09	0.56	5.02
OD826A-mt	1079	516		4428	5.73	4	0	294	723600	22.63	10	0.09	2.00	2.64
OD826A-mt	589	568	11	3694	2.43	6	1	532	723600	17.61	6	0.00	0.57	17.38
OD826A-mt	926	259		21	4.45	6	3	41	723600	0.39	10	0.27	0.66	5.36
OD826A-mt	618	167	8	219	11.70	0	2	22	723600	0.02	0	0.10	0.62	0.38
OD826A-mt	834	50	15		19.74		1	59	723600		3	0.01	0.50	1.03
OD826A-mt	751	529	38	809	1.26		1	235	723600	1.44	142	0.01	2.62	14.91
OD826A-mt	1181	314		2816	16.70	1	1	456	723600	9.82	2	0.34	0.83	1.19

Table 4.8: Trace element concentrations (in ppm) of hematite. Table includes a selection of elements. *Ideal Fe concentration.

OD#	Al	Si	Ca	Sc	Ti	V	Fe*	Cu	As	Sb	W	Th	U	Pb(tot)
OD829-hm	323	567	107	5.50	1053	97	699400	2.21	14.01	3.92	1.68	0.34	0.76	22.92
OD829-hm	367	309		0.96	860	107	699400		8.32	1.21	0.19	0.08	0.15	1.69
OD829-hm	1357	339	186	160.06	1630	16	699400	1.55	11.09	2.95	2.96	0.73	1.87	4.48
OD829-hm	154	353		1.96	368	87	699400	0.33	12.76	2.13	0.57	0.07	0.37	3.75
OD829-hm	1347	3749	3182	9.64	2241	107	699400	5.61	21.97	6.97	7.12	3.13	3.39	51.39
OD829-hm	952	705	476	2.10	789	109	699400	3.00	46.59	41.52	1.27	0.18	1.46	1.59
OD829-hm	1117	646	362	2.09	1029	127	699400		78.36	68.07	1.22	0.14	2.83	3.77
OD829-hm	1000	402	310	4.04	1228	98	699400	18.01	31.06	25.07	1.20	0.08	1.61	1.62
OD829-hm	1233	621	260	4.43	1262	124	699400	10.47	34.29	24.04	3.56	0.13	2.86	2.66
OD829-hm	1484	1185	52	31.13	1040	56	699400	2.65	38.96	12.19	48.91	3.83	9.35	43.69
OD829-hm	918	244	84	12.31	1731	47	699400	0.02	5.69	2.09	14.83	3.24	6.55	14.03
OD829-hm	1155	1021	111	5.09	382	40	699400	2.66	3.96	1.47	2.16	4.77	0.86	6.56
OD829-hm	1318	697		5.83	274	37	699400	0.88	2.87	0.68	4.96	0.26	0.82	4.00
OD829-hm	1133	666		6.76	786	31	699400	1.42	1.55	0.64	2.26	0.69	1.01	6.54
OD829-hm	855	310	136	18.83	5728	31	699400	2.49	8.66	2.50	3.27	1.42	3.06	42.51
OD829-hm	455	178	72	0.65	888	100	699400		5.25	0.82	0.12	0.00	0.03	0.55
OD829-hm	406	243	220	0.97	971	93	699400	0.51	5.23	0.70	0.68	0.05	0.23	1.28
OD829-hm	481	514	111	2.95	1165	89	699400	5.56	4.65	1.67	2.01	0.83	1.31	1.94
OD829-hm	386	380	735	1.03	908	67	699400	4.59	11.03	5.89	1.00	0.04	0.81	1.84
OD829-hm	372	277	8	1.99	900	32	699400	0.90	4.43	0.82	3.63	0.08	0.44	0.95
OD829-hm	889	457	105	6.63	669	33	699400	0.27	2.98	0.53	3.61	0.57	0.67	4.99
OD829-hm	11151	15515		27.74	7935	30	699400	2.20	10.39	2.50	6.07	0.87	2.96	37.30
OD829-hm	1948	2737	2342	8.47	5033	35	699400	2.05	15.33	2.17	6.70	0.75	2.55	20.46
OD829-hm	988	1325	657	22.41	1140	59	699400	51.30	70.65	33.04	18.14	2.38	6.09	87.86
OD829-hm	765	586	1858	1.86	376	47	699400	1.95	12.84	3.62	2.82	0.26	0.64	8.28
OD829-hm	980	575		4.39	635	117	699400	0.73	42.65	22.44	0.88	0.12	0.56	1.02

Table 4.8: Continued.

OD#	Al	Si	Ca	Sc	Ti	V	Fe*	Cu	As	Sb	W	Th	U	Pb(tot)
OD829-hm	1156	540	10	1.72	360	42	699400	3.00	8.71	3.89	2.80	0.06	0.37	3.31
OD829-hm	1172	554		13.37	1327	38	699400	1.39	6.17	2.01	18.43	3.60	6.55	14.48
OD829-hm	452	463	137	6.95	1402	91	699400	4.17	13.10	4.39	6.85	1.98	3.75	7.83
OD829-hm	397	20	52	0.46	549	100	699400	0.27	1.54	0.27	0.01	0.03	0.03	0.11
OD826A-hm	173		3990	1.38	8	1	699400	0.98	1.47	0.25	32.31	0.00	0.14	0.47
OD826A-hm	335	215	128	2.68		1	699400		0.31	0.05	32.94	0.01	0.12	0.43
OD826A-hm	254	132	44	3.07	4	1	699400	6.39	4.99	2.01	12.32	0.14	1.36	18.98
OD826A-hm	1131	369	239	6.65	11	3	699400	3.14	9.17	1.92	91.80	0.31	3.90	5.20
OD826A-hm	1668	17	21	0.86	1	0	699400		5.99	1.45	0.93	0.04	0.66	0.97
OD826A-hm	901	539	41	25.25	33	3	699400	1.93	10.79	2.81	92.47	0.43	8.26	43.09
OD826A-hm	2586	1638	1487	2.56	5	1	699400	1.75	32.13	7.79	7.19	0.14	1.35	42.20
OD826A-hm	1478	408	694	1.93	8	2	699400	75.14	23.87	5.60	20.62	0.09	1.66	27.10
OD826A-hm	356	355		2.71	5	2	699400	17.40	5.64	0.60	32.46	0.04	0.73	3.40
OD826A-hm	680	235	2022	7.95	201	25	699400	10.90	15.92	4.49	133.73	0.26	2.77	98.29
OD826A-hm	875	68		26.20	28	12	699400	5.36	4.32	2.09	112.51	0.23	2.25	3.38
OD826A-hm	717	318	174	13.61	30	10	699400	1.48	16.55	4.14	219.62	0.19	1.56	5.88
OD826A-hm	1175	402		37.69	34	5	699400	2.38	17.01	5.74	64.15	0.38	2.97	7.85
OD826A-hm	1726	544	336	52.88	10	5	699400	4.09	12.84	4.94	43.55	0.73	2.09	5.27
OD826A-hm	1684	1742	1289	36.74	31	8	699400	8.53	38.95	5.03	143.14	0.66	24.19	44.23
OD826A-hm	663	575	393	11.83	6	1	699400	35.56	5.63	1.26	22.40	0.24	8.07	39.38
OD826A-hm	1709	339		1.70	1	0	699400	0.10	12.00	2.67	2.48	0.06	1.35	2.00
OD826A-hm	137	9	78	1.46	1	0	699400		0.54	0.11	0.39	0.01	0.02	1.06
OD826A-hm	236	55	371	2.37		2	699400	1.28	1.86	0.25	58.88	0.00	0.32	2.15
OD826A-hm	215	70		2.25	0	0	699400		0.76	0.08	0.46	0.02	0.10	0.17
OD826A-hm	1611	45	60	10.03	51	3	699400	0.54	1.82	0.61	10.81	0.08	0.52	10.61
OD826A-hm	1763	146	1115	8.00	31	3	699400	1.50	5.74	0.86	14.25	0.07	0.90	34.11

Table 4.8: Continued.

OD#	Al	Si	Ca	Sc	Ti	V	Fe*	Cu	As	Sb	W	Th	U	Pb(tot)
OD826A-hm	509	531	38	8.23	9	2	699400	6.82	16.74	2.93	36.32	0.05	7.89	9.08
OD826A-hm	497	235	73	7.17	47	3	699400	16.69	5.76	2.02	40.55	0.12	4.87	3.71
OD826A-hm	460	402	4	5.11	29	5	699400	17.31	26.81	3.55	41.34	0.22	3.46	130.39
OD826A-hm	1404	293	74	4.04	92	4	699400	10.04	83.50	37.50	19.44	0.12	1.69	16.94
OD826A-hm	874	232	283	3.58	2	0	699400	107.65	77.67	22.82	4.69	0.02	1.20	4.41
OD826A-hm	891	1100	2216	3.67	30	3	699400	63.53	56.86	20.93	39.12	0.06	1.58	14.00
OD826A-hm	656	167	38	4.82	994	30	699400	1.05	3.62	0.70	36.60	0.06	0.43	5.12
OD826A-hm	994	779	775	2.81	32	2	699400	99.60	76.84	31.78	26.29	0.09	1.95	47.08
OD826A-hm	288	72		0.73	23	1	699400	56.40	19.14	1.57	30.22	0.19	1.02	24.36
OD826A-hm	295	206	81	1.33	4	2	699400	0.23	1.23	0.16	42.24	0.01	0.15	0.20
OD826A-hm	565	282		3.61	20	5	699400	0.06	7.29	1.39	47.44	0.02	1.16	2.14

Table 4.9: Trace element concentrations (in ppm) of pyrite. Table includes a selection of elements. *Ideal Fe concentration.

RX#	Descr.	Ti	Mn	Fe*	Co	Ni	Cu	Zn	As	Se	Ag	Au	Pb(tot)
RX7986 py	euhedral	1.42	2.14	465500	50.44	3.10	1.04	0.19	108.08	2.10	0.02	0.04	12.21
RX7986 py	euhedral	1.25	9.80	465500	56.55	0.09	1.34	0.39	776.33	4.47		0.12	0.09
RX7986 py	euhedral	0.67	0.03	465500	191.55	217.66	8.94	0.64	18.23	42.08			0.21
RX7986 py	euhedral	0.29	0.23	465500	247.51	201.04	496.87		4.04	49.36	0.00	0.03	0.16
RX7986 py	euhedral	0.09	0.58	465500	1907.23	9.64	3.92	0.03	2925.77	7.93	0.01	2.03	0.27
RX7986 py	euhedral	0.76		465500	1737.64	18.09	5.74	0.60	2554.66	8.93		1.01	0.20
RX7986 py	euhedral	1.02	0.18	465500	81.39	0.44	0.77	0.59	733.90	2.63	0.01	0.17	0.36
RX7986 py	euhedral	1.64	0.91	465500	968.75	7.20	8.34	0.15	1405.90	7.93	0.03	0.56	2.66
RX7986 py	euhedral	92.19	4.38	465500	1091.69	159.89	112.53	1.06	71.46	43.23	3.07	0.04	61.34
RX7986 py	euhedral		0.14	465500	2066.68	255.47	1.67	0.23	7.05	52.89	0.03		0.06
RX7986 py	euhedral	0.65	0.05	465500	6283.97	22.71	0.35	0.53	4.79	36.94		0.00	0.70
RX7986 py	euhedral	0.61	32.38	465500	15854.10	12.81	458.38	3.30	5.95	51.65	0.54	0.13	2.61
RX7986 py	euhedral	2.68	0.56	465500	9453.50	18.78	22.62	0.14	21.15	42.61	0.12		6.21
RX7986 py	euhedral	55.39	51.82	465500	3016.92	192.00	11.27	0.35	657.55	35.25	2.91	0.16	95.30
RX7986 py	euhedral			465500	3156.68	6.70	1.87		3.63	28.31	0.07	0.01	0.77
RX7986 py	euhedral	1.07	4.55	465500	7797.13	12.61	16.38	2.40	37.58	39.75	0.53	0.08	3.55
RX7986 py	euhedral	1.78	7.23	465500	10525.38	43.02	4.60	1.42	25.08	77.17	0.02	0.03	1.37
RX7986 py	euhedral	1.80	23.29	465500	8325.31	136.62	545.06	5.40	6.91	57.25	0.16	0.03	3.75
RX7986 py	euhedral	1.15	3.43	465500	5379.35	35.36	3.36	0.11	6.28	30.05	0.01	0.00	0.13
RX7986 py	euhedral	1.23	27.23	465500	7943.24	80.38	128.82	5.45	5.13	59.40	0.05		0.40
RX7986 py	euhedral	0.30	1.12	465500	11378.48	10.85	0.65	0.16	24.44	40.41		0.01	0.15
RX7986 py	euhedral	0.80	5.72	465500	13759.94	13.05	5.42	1.00	5.85	47.02			0.12
RX7986 py	euhedral	0.77	0.95	465500	14333.21	28.58	4.08	0.21	3.72	52.44		0.02	0.21
RX7986 py	euhedral	1.08	34.14	465500	13415.49	14.98	3.04		16.99	53.41		0.02	0.23
RX7986 py	euhedral	0.79	3.88	465500	8422.91	21.72	5.48	0.94	53.77	33.90	1.55	0.08	8.74
RX7986 py	euhedral	17.56	1824.02	465500	1602.92	58.01	29.08	0.25	500.25	12.57	1.01	0.11	14.39
RX7986 py	euhedral	0.45	0.45	465500	9925.27	18.99	0.52	0.54	4.31	47.55	0.27		1.18
RX7986 py	euhedral		0.04	465500	9926.24	11.89	0.17	0.30	5.79	51.06	0.01		0.01
RX7986 py	euhedral	1.27	0.81	465500	3473.19	184.81	0.68	0.46	286.38	51.24	0.03	0.03	0.31
RX7986 py	euhedral	0.38	13.16	465500	12714.07	101.37	133.37	2.90	6.39	55.87	0.00	0.01	0.64
RX7986 py	euhedral	1.89	9.57	465500	5069.18	127.17	0.79	0.97	171.12	49.41	0.17	0.03	8.83
RX7987 py	subrounded		0.19	465500	42.07	41.43	0.79	0.42	2.70	67.56	0.00		0.02
RX7987 py	subrounded	0.14		465500	17.58	84.37	0.28	0.64	9.27	68.00	0.04	0.01	0.02
RX7987 py	subrounded	1.36	0.08	465500	14.75	115.84	0.28	0.55	15.12	68.22	0.01	0.01	0.00
RX7987 py	subrounded	0.35	0.05	465500	17.40	111.65	0.15	0.14	3.27	97.24	0.01		0.01
RX7987 py	subrounded			465500	29.58	147.19	0.44	0.43	3.00	90.15		0.01	0.01
RX7987 py	subrounded	0.55		465500	48.60	152.94	0.52	0.24	4.19	103.16	0.00	0.02	0.19
RX7987 py	subrounded	25.73	23.33	465500	82.03	52.48	114.47	0.82	14.03	42.87	0.04	0.01	5.30
RX7987 py	subrounded		0.59	465500	150.59	159.97	10.81	0.31	25.27	52.07	0.42	0.18	2.62
RX7987 py	subrounded	0.14	0.15	465500	29.56	246.97			2.20	42.85	0.00		0.76
RX7987 py	subrounded	1.19		465500	25.57	131.88	0.06		2.26	53.13	0.02	0.00	0.21
RX7987 py	subrounded	1.19	0.74	465500	28.08	84.83	0.42	0.08	2.75	57.13	0.01	0.01	0.10
RX7987 py	subrounded			465500	33.16	86.90		0.48	3.44	50.88			0.74
RX7987 py	subrounded		0.18	465500	36.56	105.25		0.38	2.89	59.99		0.00	0.40
RX7987 py	subrounded			465500	29.11	75.80	0.28	0.05	2.27	54.04			0.02
RX7987 py	subrounded	0.82		465500	112.37	226.91	0.20	0.32	2.43	47.15	0.01		0.18
RX7987 py	subrounded	0.39	0.02	465500	44.55	263.46	0.02		2.21	48.35	0.06	0.00	0.01
RX7987 py	subrounded		0.23	465500	42.82	104.38	0.84	0.33	1.89	39.60	0.01		0.06
RX7987 py	subrounded	3.59		465500	29.58	91.86	1.26	0.22	5.00	46.30	0.16	0.05	3.12
RX7987 py	subrounded	0.64	0.01	465500	65.77	273.75	0.68	0.26	2.01	42.90			0.02
RX7987 py	subrounded		0.12	465500	20.42	120.81	0.04	0.25	2.96	48.55		0.00	0.00
RX7987 py	subrounded			465500	25.96	90.26	0.24	0.04	2.73	33.81			0.12
RX7987 py	subrounded	0.25	0.22	465500	36.28	96.48	5.49	0.23	31.42	49.58	0.02		0.05
RX7987 py	subrounded	1.91	1.28	465500	39.54	107.15	1.11	0.70	22.16	48.71	0.04		0.07
RX7987 py	subrounded	2.43	0.77	465500	313.22	808.09	0.70	0.45	5.72	34.45	0.01	0.02	0.16

Table 4.9: Continued.

RX#	Descr.	Ti	Mn	Fe*	Co	Ni	Cu	Zn	As	Se	Ag	Au	Pb(tot)
RX7987 py	subrounded	0.70		465500	678.10	358.05	0.30	0.15	2.35	25.85	0.01	0.01	0.04
RX7987 py	subrounded	0.54	0.41	465500	199.67	99.18	0.11	0.62	1.24	56.96			0.66
RX7987 py	subrounded	0.39	0.22	465500	143.93	80.41		0.29	1.06	59.42	0.01	0.00	1.48
RX7987 py	subrounded	0.97		465500	168.92	197.94		0.38	2.15	63.42	0.00		0.00
RX7987 py	subrounded	0.88	0.50	465500	115.56	269.83	0.15	0.21	1.48	42.75		0.00	0.02
RX7987 py	subrounded		0.94	465500	177.37	314.80		0.46	2.03	54.30	0.00	0.00	0.05
RX7987 py	subrounded	0.63	0.32	465500	109.92	209.65		0.58	2.19	56.19	0.02		0.01
RX7987 py	subrounded		0.21	465500	36.02	392.35	0.16		5.42	42.08	0.02	0.01	0.02
RX7987 py	subrounded	0.10	0.03	465500	12.10	102.74		0.40	2.39	44.41	0.03	0.01	0.26
RX7987 py	subrounded	1.55	0.05	465500	26.93	394.23	0.29		15.30	35.28	0.00		0.00
RX7987 py	subrounded	1.00	0.12	465500	47.60	624.68	0.21	0.13	12.48	29.70			0.35
RX7987 py	subrounded	1.28	1.00	465500	457.79	332.11	4.72		27.54	39.41	1.14	0.05	8.36
RX7987 py	subrounded	0.66	0.57	465500	220.21	951.01	0.07	0.72	16.32	48.19	0.00	0.02	0.02
RX7987 py	subrounded	1.69	0.12	465500	43.82	484.36			12.71	32.32	0.00	0.02	0.17
RX7987 py	subrounded			465500	310.63	1248.25	0.22	0.03	18.50	46.20	0.07		1.41
RX7987 py	subrounded	1.15		465500	4474.71	12.60			11.30	30.96		0.00	0.00
RX7987 py	subrounded	1.46		465500	2269.55	44.68		0.26	7.71	31.27	0.00	0.01	0.01
RX7987 py	subrounded	0.69		465500	4060.60	34.24	0.80	0.38	9.97	27.38	0.00	0.00	0.00
RX7987 py	subrounded	0.14	0.12	465500	5254.96	33.50		0.10	14.55	24.95			0.00
RX7987 py	subrounded	0.19	0.60	465500	4088.14	26.34		0.35	22.36	24.64			0.01
RX7987 py	subrounded	0.96		465500	6721.72	10.53			21.62	39.07	0.00		0.26
RX7987 py	subrounded	0.95	0.41	465500	7558.54	17.82	1.76	0.21	21.91	37.64	0.01	0.01	0.03
RX7987 py	subrounded	1.05	0.19	465500	9647.96	9.35	0.27	0.15	38.84	26.46	0.43	0.00	0.01
RX7987 py	subrounded	0.33	0.30	465500	12155.11	5.48			35.09	23.15		0.01	0.01
RX7987 py	subrounded	2.11	0.33	465500	19287.47	7.75	0.50	0.35	80.08	30.89			0.00
RX7987 py	subrounded	1.25	0.33	465500	14746.93	6.59			84.13	30.03		0.00	0.01
RX7987 py	subrounded	0.47	0.04	465500	9361.58	4.20	0.17		71.52	17.11			0.03
RX7987 py	subrounded	0.55		465500	15824.24	5.18			50.09	33.13	0.00	0.01	0.01
RX7987 py	subrounded	1.00	0.17	465500	16370.01	8.36			54.65	34.14	0.02	0.01	0.00
RX7987 py	subrounded	0.97	0.85	465500	8363.02	8.61	0.78	0.20	16.81	23.84	0.02		0.12
RX7987 py	subrounded		0.20	465500	9067.65	3.85			17.12	25.17	0.00	0.00	0.03
RX7987 py	subrounded	0.86	0.07	465500	10242.86	2.97		0.21	19.66	25.33		0.00	0.05
RX7987 py	subrounded	1.78	1.55	465500	8631.31	15.50	3.59	0.28	43.40	27.28	0.02	0.05	0.48
RX7987 py	subrounded	1.17	1.03	465500	9995.10	3.16	8.45	0.50	25.12	18.68	0.16	0.03	1.00
RX7987 py	subrounded	0.97	4.18	465500	6602.86	3.52	21.71	1.07	10.58	16.55	0.46	0.03	0.42
RX7987 py	subrounded	0.07		465500	1897.13	85.56	0.10	0.40	11.56	16.10	0.03		0.02
RX7987 py	subrounded	0.78	0.52	465500	445.89	946.34	0.18	0.48	10.48	40.02	0.02	0.00	0.01
RX7987 py	subrounded	0.67		465500	135.84	1838.45	0.31		11.50	53.36		0.01	0.00
RX7987 py	subrounded	0.35	0.17	465500	3102.22	225.57		0.02	28.40	14.32			0.01
RX7987 py	subrounded	1.42	0.16	465500	2441.52	500.94	129.29	0.15	41.11	25.82			0.01
RX7987 py	subrounded	0.43	1.81	465500	1294.74	117.15	1492.63		19.87	12.42	0.04	0.02	1.60
RX7987 py	subrounded	0.47	0.52	465500	5305.77	18.09	0.32	0.36	16.13	36.57	0.04	0.00	0.16
RX7987 py	subrounded	0.21	0.09	465500	5512.58	12.93	9.30	0.36	8.85	20.80	0.16	0.02	1.69
RX7987 py	subrounded	0.37		465500	7011.34	7.79	1.15	0.16	4.24	21.53	0.01		0.04
RX7987 py	subrounded	1.24		465500	362.31	135.64		0.24	0.78	30.86		0.02	0.02
RX7987 py	subrounded	1.42		465500	95.59	489.51		0.07	1.04	39.81		0.01	0.00
RX7987 py	subrounded	1.38		465500	118.01	888.51		0.67	1.24	48.62			0.02
RX7987 py	subrounded		0.85	465500	38.87	12.86			5.63	44.31	0.02	0.00	0.02
RX7987 py	subrounded	0.87	0.02	465500	55.96	17.57	0.27		5.69	32.11		0.01	0.10
RX7987 py	subrounded			465500	1308.19	11.23	0.38		42.86	6.39			0.21
RX7987 py	subrounded	1.25	0.33	465500	2457.55	36.13		0.36	1.18	37.67	0.01	0.02	0.17
RX7987 py	subrounded	1.57	0.22	465500	3080.80	16.00	0.29	0.26	2.45	20.16			0.01
RX7987 py	subrounded	0.37	0.03	465500	21882.00	5.50			8.07	29.19	0.02		0.01
RX7987 py	subrounded	0.70		465500	2745.77	159.71	0.41	0.19	3.91	32.57	0.06	0.00	0.05
RX7987 py	subrounded	0.48	0.01	465500	1512.19	271.03	0.08	0.18	1.75	41.80			0.10
RX7987 py	subrounded	0.48	0.31	465500	1916.21	400.09	0.32	0.11	3.28	50.55	0.01	0.00	0.01
RX7987 py	subrounded	3.40	0.43	465500	525.57	118.47		0.30	9.97	16.13	0.09		0.54
RX7987 py	subrounded			465500	3711.55	26.03	0.66	0.44	7.63	23.35	0.02	0.01	0.01

Table 4.9: Continued.

RX#	Descr.	Ti	Mn	Fe*	Co	Ni	Cu	Zn	As	Se	Ag	Au	Pb(tot)
RX7987 py	subrounded	1.23		465500	4474.57	32.27			10.09	31.48	0.01	0.01	0.01
RX7987 py	subrounded	1.62		465500	4565.04	63.00		0.17	11.25	30.75	0.01	0.00	0.02
RX7987 py	subrounded	1.49	0.22	465500	4931.54	42.71	0.32	0.15	12.43	33.63			0.01
RX7987 py	subrounded	0.70	0.89	465500	8344.95	42.26	0.20	0.54	18.70	29.53	0.01	0.01	0.00
RX7987 py	subrounded	0.57		465500	7294.19	51.48	0.09	0.47	17.72	31.03			0.00
RX7987 py	subrounded		0.00	465500	10012.94	40.65		1.68	18.75	32.75		0.02	0.78
RX7987 py	subrounded	1.01		465500	7450.28	35.34	0.66	0.28	15.72	31.69	0.01		0.01
RX7987 py	subrounded	0.75		465500	5868.20	20.45	0.09	0.12	16.93	39.36			0.01
RX7987 py	subrounded	1.97	0.41	465500	6316.40	22.07	0.02	0.01	13.75	30.53		0.00	0.01
RX7987 py	subrounded	0.26		465500	689.67	94.48	1.00	0.47	55.93	37.65	0.08	0.06	4.49
RX7987 py	subrounded	0.84	0.64	465500	518.93	103.28	12.99		104.86	40.89		0.04	0.07
RX7987 py	subrounded	0.26	0.25	465500	953.34	80.65	370.20	0.51	220.03	30.83	0.04	0.01	0.06
RX7987 py	subrounded	1.11		465500	527.01	99.03	13.17		105.03	34.78		0.01	0.03
RX7987 py		1.03	0.36	465500	910.00	2.53		0.33	3.17	21.24		0.01	0.01
RX7987 py		1.70	0.51	465500	347.42	0.59	0.24	0.01	0.13	16.80	0.01		0.00
RX7987 py		0.59		465500	450.35	0.85	0.28	0.68	0.32	23.32	0.03		0.01
RX7987 py		0.04	0.49	465500	600.79	1.72		0.28	0.76	23.87	0.01		0.01
RX7987 py		0.95	0.76	465500	967.09	1.78	0.30	0.04	1.30	24.04		0.00	0.00
RX7987 py		0.67	0.23	465500	570.85	4.17	122.99	0.30	2.06	26.36	5.20	0.63	0.12
RX7987 py		0.56	0.37	465500	530.08	3.65	99.01	0.04	1.94	29.67	0.50	0.46	0.07
RX7987 py		0.22	0.20	465500	576.86	3.63	56.02	0.01	1.01	29.46	0.76	0.08	0.12
RX7987 py		0.42		465500	704.73	2.08	0.51	0.34	0.36	24.44	0.05	0.00	0.00
RX7987 py		1.52	0.06	465500	1255.14	3.80	2.10		0.43	27.29	0.06	0.03	0.09
RX7987 py				465500	1744.56	3.33	4.00	1.05	1.02	24.67	0.08	0.03	0.06
RX7987 py		1.36	0.79	465500	2160.30	6.38	0.53	0.56	9.13	33.20		0.01	0.01
RX7987 py			0.67	465500	1932.87	10.63	0.02	0.11	28.82	28.17	0.01	0.01	0.01
RX7987 py				465500	2995.85	24.94	2.15	0.23	92.89	25.82	0.09	0.05	0.01
RX7987 py		1.66	0.19	465500	1006.67	2.33	0.87	0.93	0.90	32.32	0.00	0.02	0.22
RX7987 py		0.57	0.76	465500	1035.41	3.18	0.63	0.14	10.81	36.93	1.55	0.12	2.05
RX7987 py			0.36	465500	829.16	1.92	0.60	0.58	0.42	24.68	0.01		0.03
RX7987 py		1.53	5.09	465500	1205.40	2.16	0.88	0.36	0.17	31.36	0.03		0.21
RX7987 py		1.27		465500	1382.59	2.55	0.04	0.07	0.32	27.26		0.00	0.03
RX7987 py		0.60	0.60	465500	1753.59	2.89	1.39	0.20	0.99	32.07	0.50	0.01	1.04
RX7987 py		1.84	0.25	465500	1210.78	2.93		0.17	0.32	27.45	0.00		0.00
RX7987 py			0.94	465500	1507.73	160.46		0.64	152.43	31.88		0.02	0.01
RX7987 py		1.91	0.16	465500	1101.07	2.07		0.68	0.52	32.68		0.01	0.01
RX7987 py		0.38		465500	1128.56	3.27	0.02	0.21	0.89	29.32	0.01		0.00
RX7987 py		2.25	0.38	465500	762.40	3.18	0.37		4.42	28.09			0.00
RX7987 py		0.63	0.42	465500	656.48	4.07	0.04		0.67	29.88		0.01	0.00
RX7987 py		0.58	0.28	465500	1097.66	2.99	0.42	0.36	0.26	28.61	0.00	0.01	0.01
RX7987 py		0.73		465500	612.83	2.48	0.81		0.93	27.66	0.02	0.01	0.01
RX7987 py			14.43	465500	1383.91	3.19	521.71	1.09	13.83	24.54	0.66	0.14	0.25
RX7987 py				465500	14.86	913.61	2.12	0.66	0.61	29.82	0.01		0.17
RX7987 py		0.30	0.04	465500	452.34	403.97	1.51	0.68	1.97	22.28			0.02
RX7987 py		1.28	0.08	465500	754.38	133.77	0.25	0.25	2.17	21.57	0.01		0.08
RX7987 py		1.11	0.33	465500	1888.00	26.49	0.44	0.52	3.45	25.67		0.02	0.03
RX7987 py		1.08	0.80	465500	2498.23	88.64	159.25	0.35	3.63	42.73	0.01	0.02	0.01
RX7987 py		1.89	0.10	465500	3228.81	132.36		0.21	6.17	32.33	0.01	0.00	0.01
RX7987 py		1.16	0.38	465500	189.10	647.15			3.12	32.80		0.01	0.05
RX7987 py		0.34	0.26	465500	24.10	230.10		0.15	1.16	28.30			0.01
RX7987 py		0.68	0.86	465500	51.60	226.84	1.12	1.10	8.95	26.66	0.02	0.02	2.51
RX7987 py		1.02	0.14	465500	8.17	1001.17		0.95	0.76	24.61			0.05
RX7987 py		1.02	1.18	465500	14113.77	6.92	0.46	1.54	72.53	18.53	0.47	0.06	1.30
RX7987 py		0.77	1.42	465500	12439.08	5.15	0.29	0.30	56.05	22.07	0.01		0.02
RX7987 py		0.94	0.36	465500	4980.91	35.08	0.77	0.16	13.92	23.71	0.01	0.01	0.08
RX7987 py		0.21	0.20	465500	4864.39	30.28	0.08	0.04	11.48	24.52	0.01		0.02
RX7987 py		3.90	0.62	465500	4581.19	27.46	1.22	0.17	11.04	27.44	0.19	0.00	2.39
RX7987 py		1.49	0.59	465500	6240.67	24.53	0.73		16.45	22.73	0.06	0.01	0.89

Table 4.9: Continued.

RX#	Ti	Mn	Fe*	Co	Ni	Cu	Zn	As	Se	Ag	Au	Pb(tot)
RX7987 py	1.31	0.44	465500	1325.45	114.82	0.57	0.12	9.39	42.79	0.01	0.01	0.03
RX7987 py	0.28		465500	1048.61	127.64	0.18	0.26	9.11	37.03		0.01	0.17
RX7987 py	1.19		465500	862.51	140.80		0.24	10.44	43.11			0.03
RX7987 py	0.23	1.68	465500	337.05	443.27	1.63	0.09	34.43	34.43	0.15	0.08	0.15
RX7987 py	0.16	0.16	465500	287.06	681.26	0.32		57.15	53.40	0.05	0.03	0.39
RX7987 py	1.60		465500	237.31	582.77	0.24		59.27	62.08			0.02
RX7987 py	1.78		465500	12.21	64.54	0.46		8.77	38.07			0.05
RX7987 py			465500	11.69	36.55		0.06	5.66	39.68			0.00
RX7987 py	0.24	0.22	465500	14.44	36.28		0.78	6.86	38.28			0.00
RX7987 py	2.23	0.16	465500	58.06	113.16	1.58	0.08	16.76	44.60	0.01	0.03	0.06
RX7987 py	1.43	0.36	465500	31.35	216.30	0.57	0.01	6.78	36.73		0.01	0.01
RX7987 py	0.41		465500	34.61	159.86	0.51		6.52	28.18	0.02	0.00	0.97
RX7987 py	0.55	0.70	465500	85.35	337.53	1.08		12.28	28.03	0.26	0.01	2.89
RX7987 py	1.38	0.86	465500	136.64	13.49	0.98	0.41	6.69	34.87		0.00	0.55
RX7987 py	0.48	0.48	465500	359.82	51.21		0.01	6.60	27.39	0.01		0.98
RX7987 py	2.04		465500	3714.94	29.63	0.42		30.14	18.49			0.20
RX7987 py	0.77		465500	4265.04	39.90	0.43	0.12	29.91	15.72	0.02	0.00	0.51
RX7987 py	1.38	0.01	465500	488.23	12.78	0.27	0.27	2.32	42.70	0.00	0.01	0.04
RX7987 py		0.54	465500	308.24	16.98	0.70	0.49	2.09	39.30	0.03	0.02	0.01
RX7987 py		0.11	465500	1025.27	37.78	1.53	0.30	7.13	37.79	0.06		2.21
RX7987 py		2.17	465500	2595.89	67.92	490.36	0.52	6.94	32.82	0.03	0.02	0.07
RX7987 py	0.40	3.81	465500	1759.14	88.44	5.61	0.57	7.03	35.70	0.02	0.01	2.82
RX7987 py	0.24	0.47	465500	48.68	36.35		0.21	5.94	32.55			0.01
RX7987 py	0.19	0.10	465500	24.58	51.67	0.28	0.18	4.52	32.41			0.02
RX7987 py	1.63	0.16	465500	32.48	82.95	1.97	0.05	9.15	39.27			0.00
RX7987 py			465500	77.75	80.15			9.82	47.91			0.01
RX7987 py		0.56	465500	13088.60	34.90	112.06	0.86	84.34	27.72	0.01		0.00
RX7987 py		0.15	465500	144.86	42.48	0.28	0.10	4.71	29.14	0.01	0.00	0.01
RX7987 py	1.06		465500	211.01	430.52	0.19	0.33	4.55	39.68			0.01
RX7987 py	1.64	0.05	465500	149.74	169.41	0.32	0.15	4.48	42.17		0.00	0.11
RX7987 py	1.71		465500	122.76	34.13	0.00	0.51	30.57	39.98	0.01		0.01
RX7987 py	0.20	0.51	465500	593.78	16.96	0.24	0.16	19.42	25.28		0.00	0.45
RX7987 py	2.46		465500	61.05	1119.19	0.06	0.23	10.63	57.61	0.01	0.01	0.14

Table 4.10: Trace element concentrations (in ppm) of chalcopyrite. Table includes a selection of elements. *Ideal Cu concentration.

RX#	Fe	Cu*	Zn	Se	Ag	Pb(tot)	Bi
RX7986A	280856.91	346300	21.05	225.82	5.33	3.04	2.22
RX7986A	279274.38	346300	27.87	46.79	4.61	3.32	1.89
RX7986A	282259.41	346300	27.85	24.66	4.54	3.84	1.40
RX7986A	279409.52	346300	18.95	42.21	4.75	1.90	0.98
RX7986A	289602.51	346300	22.72	31.52	5.23	9.53	4.65
RX7986A	265406.74	346300	20.78	22.56	4.82	6.34	3.00
RX7986A	282446.44	346300	55.04	23.11	6.10	14.67	3.01
RX7986A	290799.54	346300	18.86	34.02	5.09	6.90	4.37
RX7986A	292182.61	346300	28.85	57.76	5.48	3.96	4.18
RX7986A	278112.21	346300	26.09	61.70	4.50	7.87	4.28
RX7986A	283440.00	346300	24.41	25.56	20.71	1.09	2.26
RX7986A	273138.05	346300	16.50	42.74	3.15	0.18	<0.04
RX7986A	284827.95	346300	25.45	54.45	3.12	0.64	0.23
RX7986A	289852.01	346300	24.00	29.24	9.42	11.62	0.31
RX7986A	287793.85	346300	26.13	32.77	3.17	0.54	0.33
RX7986A	289009.50	346300	20.28	44.01	3.36	0.64	0.46
RX7986A	291272.22	346300	24.26	38.27	3.56	0.64	0.47
RX7986A	289233.31	346300	21.19	66.83	4.00	2.54	1.24
RX7986A	283128.00	346300	22.75	43.47	3.43	0.61	0.40
RX7986A	275616.65	346300	22.57	46.68	3.45	0.83	0.70
RX7986A	290178.83	346300	15.29	38.56	3.96	0.90	0.32
RX7986A	286174.98	346300	19.23	47.13	2.99	0.63	0.49
RX7986A	298055.25	346300	28.78	24.55	4.00	2.30	1.32
RX7986A	280427.40	346300	23.92	69.20	3.44	0.93	0.35
RX7986A	286102.03	346300	20.98	61.44	3.03	0.38	0.19
RX7986A	294420.19	346300	24.95	48.40	3.52	0.45	0.31
RX7986A	280805.28	346300	24.17	46.06	3.93	1.39	0.88
RX7986A	289908.79	346300	24.76	56.10	3.55	0.40	0.22
RX7986A	298142.08	346300	33.37	73.84	4.69	11.82	3.30
RX7986A	289259.63	346300	23.15	51.61	3.46	1.00	0.27
RX7986A	277338.34	346300	23.27	49.87	3.34	0.37	0.35
RX7986A	291351.24	346300	23.67	56.47	5.12	12.32	4.82
RX7986A	287009.62	346300	26.35	42.27	4.09	1.40	0.86

Table 4.11: Trace element concentrations (in ppm, spot analyses) of the early calcite (gr. 1) and all other carbonate associations at Olympic Dam. Table includes a selection of elements (Rb, Sr, REY). Abbr.: calcite (Cal), carbonate (Cb), dolomite-ankerite ss (Dol-Ank ss), group (Gr.), siderite and its solid solution (Sid), Snake Gully (SG).

OD#	Gr.	Cb type	Sr	Rb	La	Ce	Pr	Nd	Sm	Eu	Gd	Tb	Dy	Y	Ho	Er	Tm	Yb	Lu
814	1	Cal	55	0.10	38.91	75.74	8.36	31.84	5.56	1.43	11.10	1.86	12.12	108.03	2.89	8.92	1.21	10.18	1.81
818	1	Cal	226	0.14	16.04	33.69	3.80	14.84	2.77	0.72	3.59	0.52	3.21	21.41	0.69	2.24	0.35	2.87	0.52
819	1	Cal	113		52.86	133.86	15.23	55.38	9.57	2.37	9.26	1.31	7.87	45.60	1.51	4.42	0.69	5.79	0.94
821	1	Cal	62	0.06	35.19	81.17	10.13	39.95	8.38	1.83	9.55	1.40	8.45	57.11	1.62	4.89	0.65	4.91	0.80
823	1	Cal	105	117.09	5.68	11.08	1.35	5.85	1.45	0.83	2.52	0.38	2.45	16.21	0.54	1.82	0.25	1.98	0.47
824a	1	Cal	180	0.12	3.22	10.38	1.52	7.47	2.51	0.56	4.04	0.98	8.51	98.83	2.30	8.94	1.69	14.63	2.66
826	1	Cal	70	0.09	10.33	20.50	2.44	11.09	4.63	1.18	8.55	1.37	8.37	62.68	1.71	5.30	0.72	5.81	0.99
827 pink	1	Cal	122	0.11	25.29	51.82	5.82	22.27	5.44	1.21	7.32	1.18	7.32	49.75	1.44	4.44	0.69	5.72	0.99
828	1	Cal	101	0.16	81.06	174.22	18.62	67.61	12.97	2.95	14.94	2.59	16.26	90.27	3.17	9.79	1.54	13.16	2.28
829	1	Cal	130	0.10	33.83	124.76	17.79	78.75	25.33	3.66	30.41	6.29	47.93	313.53	11.01	38.97	6.41	54.15	9.61
830a	1	Cal	100		38.04	103.50	11.62	43.11	9.76	1.99	10.44	1.80	11.37	70.10	2.30	7.17	1.20	9.78	1.79
830b orange	1	Cal	57		7.43	18.72	2.13	8.83	2.35	0.76	3.50	0.63	4.57	36.50	1.06	3.45	0.54	4.43	0.84
830b white	1	Cal	75	0.08	10.44	26.04	3.03	12.25	3.46	1.07	4.98	1.00	7.61	59.11	1.81	6.03	1.01	9.63	1.83
830c pink	1	Cal	69	0.07	70.18	147.02	15.19	52.35	8.43	1.83	8.85	1.49	10.04	62.66	2.10	6.85	1.01	8.02	1.35
830c white	1	Cal	176	0.30	10.86	37.77	5.35	25.73	10.93	3.24	22.56	6.34	60.75	646.30	16.93	64.26	9.68	62.54	8.34
835	2	Cal	129	0.86	237.63	392.58	36.39	122.59	16.50	4.19	19.04	3.27	20.47	97.58	4.07	12.84	1.82	12.95	1.92
661	2	Dol-Ank ss	36	0.29	29.60	68.83	7.61	30.17	8.55	2.15	9.89	1.14	5.70	28.64	1.00	2.98	0.41	3.22	0.48
660	2	Dol-Ank ss	14	0.18	34.79	61.40	5.93	18.18	2.08	1.05	1.52	0.10	0.33	2.39	0.06	0.13	0.01		0.01
689	2	Sid	0		0.40	1.27	0.15	0.70	0.20	0.04	0.22	0.04	0.24	1.19	0.05	0.17	0.03	0.27	0.04
690	2	Sid	1	0.07	0.04	0.26	0.07	0.53	0.33	0.09	0.64	0.14	1.40	6.97	0.39	1.68	0.34	3.32	0.59
664	2	Sid	1		0.06	0.17	0.02	0.08	0.02	0.03	0.07	0.04	0.54	3.49	0.22	0.99	0.27	3.28	0.58
652	2	Sid	3	0.53	1.30	4.04	0.49	2.59	0.71	0.15	0.91	0.13	1.09	8.15	0.31	1.28	0.24	2.23	0.58
675	2	Sid	71	4.19	219.75	362.45	25.73	65.86	5.55	1.08	2.87	0.30	1.61	5.63	0.32	1.29	0.26	2.79	0.54
676	2	Sid	6	2.81	48.10	85.98	7.27	23.16	3.82	0.67	3.25	0.57	4.11	25.38	0.99	3.72	0.64	4.95	0.75

Table 4.11: Continued.

OD#	Gr.	Cb type	Sr	Rb	La	Ce	Pr	Nd	Sm	Eu	Gd	Tb	Dy	Y	Ho	Er	Tm	Yb	Lu
656	2	Sid	16	4.21	4.31	6.53	0.53	1.67	0.58	0.17	0.68	0.13	0.87	3.84	0.19	0.66	0.11	1.01	0.17
666	2	Sid	13	0.26	93.73	203.30	20.41	71.10	9.61	3.27	6.21	0.66	3.82	20.82	0.83	3.36	0.64	5.98	1.02
680	2	Sid	15	2.83	39.52	80.27	9.20	37.74	6.50	1.25	4.68	0.56	3.89	29.18	1.01	3.82	0.70	7.08	1.77
665	2	Sid	32	0.53	3.12	10.46	0.67	3.03	2.68	2.40	11.04	2.25	17.64	118.09	3.75	10.97	1.61	10.37	1.49
657	2	Sid	15	2.43	4.05	10.73	1.63	8.03	2.62	0.99	3.82	0.47	3.04	37.50	0.54	1.63	0.21	1.38	0.19
844	2	Sid	14	0.13	8.41	26.08	3.59	14.67	4.38	0.85	4.39	1.25	10.30	35.02	2.43	8.80	1.39	14.22	2.41
657	2	Sid	10	0.15	0.23	1.08	0.20	1.18	0.40	0.18	0.68	0.13	0.86	5.18	0.20	0.66	0.10	0.75	0.13
654	2	Sid	5	0.51	0.29	1.23	0.19	1.03	0.32	0.09	0.63	0.17	1.65	14.79	0.53	2.06	0.37	2.91	0.57
654	2	Sid	3	0.09	0.40	1.36	0.21	1.05	0.36	0.16	0.55	0.12	0.98	5.03	0.24	0.74	0.14	1.34	0.26
659	2	Sid	2	0.12	0.37	0.90	0.13	0.59	0.27	0.09	0.40	0.08	0.73	4.04	0.17	0.68	0.11	0.97	0.16
665	2	Sid	0	0.01	0.96	2.97	0.26	1.07	0.10	0.06	0.12	0.01	0.10	1.00	0.01	0.03	0.00	0.01	0.00
687	2	Sid	6	0.46	4.90	13.01	1.69	7.51	3.05	1.02	5.46	2.06	22.09	124.56	5.93	25.33	5.05	46.83	7.56
1001	2	Sid	1		0.01	0.02	0.00	0.04	0.01	0.00	0.03	0.01	0.09	0.53	0.03	0.16	0.05	0.72	0.16
673	2	Sid	1		0.01	0.03	0.01	0.06	0.06	0.03	0.17	0.03	0.29	1.50	0.08	0.32	0.09	0.89	0.21
674	2	Sid	1	0.03		0.00			0.01	0.01	0.10	0.02	0.14	0.82	0.04	0.16	0.04	0.49	0.09
834	2	Sid	5	0.98	1.18	2.15	0.21	0.78	0.25	0.07	0.26	0.06	0.39	3.59	0.15	0.44	0.08	0.62	0.12
674	2	Sid	0		0.00	0.00	0.00		0.03	0.01	0.07	0.01	0.07	0.27	0.01	0.06	0.01	0.08	0.02
836	3	Dol-Ank ss	90		1.50	9.85	1.89	10.15	5.33	3.58	10.77	2.74	18.90	84.15	3.63	10.01	1.36	10.17	1.38
839	3	Dol-Ank ss	48	0.78	13.49	27.53	2.97	10.72	2.58	2.34	3.49	0.95	9.16	53.84	2.25	7.89	1.28	10.94	1.84
837	3	Dol-Ank ss	27	0.07	5.74	15.99	2.01	7.67	3.22	3.46	5.70	2.20	23.12	123.67	5.75	18.72	2.47	18.24	2.89
838	3	Dol-Ank ss	45	0.54	1.97	4.93	0.54	2.56	0.68	0.77	1.12	0.52	5.62	39.51	1.73	8.14	1.71	16.22	3.01
18	4	Dol-Ank ss	43	0.10	19.33	79.30	15.03	84.91	42.15	14.05	54.87	6.87	32.04	124.08	4.73	10.45	1.10	5.81	0.77
113	4	Dol-Ank ss	56	0.28	72.14	182.59	27.93	149.98	50.61	22.07	49.86	6.40	27.78	105.55	3.85	7.76	0.65	4.13	0.51
7	4	Dol-Ank ss	20		6.53	19.79	3.51	20.04	9.72	1.91	11.45	1.51	8.16	35.86	1.43	3.72	0.43	2.88	0.38
95	4	Sid	4	0.21	4.98	15.27	1.87	7.38	2.04	0.55	2.80	0.70	6.11	35.53	1.45	5.59	1.07	10.38	1.63
857	4	Sid	10		6.04	10.84	0.97	2.97	0.54	0.37	0.69	0.23	1.72	10.01	0.46	1.55	0.25	2.34	0.54

Table 4.11: Continued.

OD#	Gr.	Cb type	Sr	Rb	La	Ce	Pr	Nd	Sm	Eu	Gd	Tb	Dy	Y	Ho	Er	Tm	Yb	Lu
656	2	Sid	16	4.21	4.31	6.53	0.53	1.67	0.58	0.17	0.68	0.13	0.87	3.84	0.19	0.66	0.11	1.01	0.17
666	2	Sid	13	0.26	93.73	203.30	20.41	71.10	9.61	3.27	6.21	0.66	3.82	20.82	0.83	3.36	0.64	5.98	1.02
680	2	Sid	15	2.83	39.52	80.27	9.20	37.74	6.50	1.25	4.68	0.56	3.89	29.18	1.01	3.82	0.70	7.08	1.77
665	2	Sid	32	0.53	3.12	10.46	0.67	3.03	2.68	2.40	11.04	2.25	17.64	118.09	3.75	10.97	1.61	10.37	1.49
657	2	Sid	15	2.43	4.05	10.73	1.63	8.03	2.62	0.99	3.82	0.47	3.04	37.50	0.54	1.63	0.21	1.38	0.19
844	2	Sid	14	0.13	8.41	26.08	3.59	14.67	4.38	0.85	4.39	1.25	10.30	35.02	2.43	8.80	1.39	14.22	2.41
657	2	Sid	10	0.15	0.23	1.08	0.20	1.18	0.40	0.18	0.68	0.13	0.86	5.18	0.20	0.66	0.10	0.75	0.13
654	2	Sid	5	0.51	0.29	1.23	0.19	1.03	0.32	0.09	0.63	0.17	1.65	14.79	0.53	2.06	0.37	2.91	0.57
654	2	Sid	3	0.09	0.40	1.36	0.21	1.05	0.36	0.16	0.55	0.12	0.98	5.03	0.24	0.74	0.14	1.34	0.26
659	2	Sid	2	0.12	0.37	0.90	0.13	0.59	0.27	0.09	0.40	0.08	0.73	4.04	0.17	0.68	0.11	0.97	0.16
665	2	Sid	0	0.01	0.96	2.97	0.26	1.07	0.10	0.06	0.12	0.01	0.10	1.00	0.01	0.03	0.00	0.01	0.00
687	2	Sid	6	0.46	4.90	13.01	1.69	7.51	3.05	1.02	5.46	2.06	22.09	124.56	5.93	25.33	5.05	46.83	7.56
1001	2	Sid	1		0.01	0.02	0.00	0.04	0.01	0.00	0.03	0.01	0.09	0.53	0.03	0.16	0.05	0.72	0.16
673	2	Sid	1		0.01	0.03	0.01	0.06	0.06	0.03	0.17	0.03	0.29	1.50	0.08	0.32	0.09	0.89	0.21
674	2	Sid	1	0.03		0.00			0.01	0.01	0.10	0.02	0.14	0.82	0.04	0.16	0.04	0.49	0.09
834	2	Sid	5	0.98	1.18	2.15	0.21	0.78	0.25	0.07	0.26	0.06	0.39	3.59	0.15	0.44	0.08	0.62	0.12
674	2	Sid	0		0.00	0.00	0.00		0.03	0.01	0.07	0.01	0.07	0.27	0.01	0.06	0.01	0.08	0.02
836	3	Dol-Ank ss	90		1.50	9.85	1.89	10.15	5.33	3.58	10.77	2.74	18.90	84.15	3.63	10.01	1.36	10.17	1.38
839	3	Dol-Ank ss	48	0.78	13.49	27.53	2.97	10.72	2.58	2.34	3.49	0.95	9.16	53.84	2.25	7.89	1.28	10.94	1.84
837	3	Dol-Ank ss	27	0.07	5.74	15.99	2.01	7.67	3.22	3.46	5.70	2.20	23.12	123.67	5.75	18.72	2.47	18.24	2.89
838	3	Dol-Ank ss	45	0.54	1.97	4.93	0.54	2.56	0.68	0.77	1.12	0.52	5.62	39.51	1.73	8.14	1.71	16.22	3.01
18	4	Dol-Ank ss	43	0.10	19.33	79.30	15.03	84.91	42.15	14.05	54.87	6.87	32.04	124.08	4.73	10.45	1.10	5.81	0.77
113	4	Dol-Ank ss	56	0.28	72.14	182.59	27.93	149.98	50.61	22.07	49.86	6.40	27.78	105.55	3.85	7.76	0.65	4.13	0.51
7	4	Dol-Ank ss	20		6.53	19.79	3.51	20.04	9.72	1.91	11.45	1.51	8.16	35.86	1.43	3.72	0.43	2.88	0.38
95	4	Sid	4	0.21	4.98	15.27	1.87	7.38	2.04	0.55	2.80	0.70	6.11	35.53	1.45	5.59	1.07	10.38	1.63
857	4	Sid	10		6.04	10.84	0.97	2.97	0.54	0.37	0.69	0.23	1.72	10.01	0.46	1.55	0.25	2.34	0.54

Table 4.11: Continued.

OD#	Gr.	Cb type	Sr	Rb	La	Ce	Pr	Nd	Sm	Eu	Gd	Tb	Dy	Y	Ho	Er	Tm	Yb	Lu
2	4	Dol-Ank ss	15	0.08	22.22	56.95	8.77	48.44	12.35	3.27	15.20	1.83	10.92	76.96	1.97	4.94	0.55	3.71	0.55
197	4	Cal	33		0.02	0.06	0.01	0.06	0.03		0.03	0.00	0.01	0.13	0.01		0.00	0.04	0.01
199	4	Cal	125		0.12	0.38	0.05	0.43	0.23	0.33	0.85	0.15	1.41	20.05	0.46	1.87	0.27	1.73	0.23
82	4	Cal	57		1.72	1.75	0.13	0.35	0.02	0.05				0.13	0.00	0.01			
79	4	Cal	318		1.88	2.82	0.33	1.67	0.39	6.26	0.44	0.05	0.29	1.97	0.04	0.10	0.01	0.06	0.00
78	4	Cal	108		9.69	12.83	1.38	6.90	1.49	0.60	2.86	0.38	2.69	29.90	0.63	2.03	0.28	1.99	0.37
857	4	Dol-Ank ss	91	1.51	5.86	9.57	1.14	5.81	1.92	0.68	3.10	0.47	2.98	18.16	0.58	1.29	0.15	1.05	0.13
848	4	Dol-Ank ss	44	0.40	21.41	64.91	9.24	41.84	10.02	2.39	12.28	1.91	12.74	81.24	2.64	7.75	0.96	5.66	0.77
857	4	Dol-Ank ss	121	7.74	7.74	16.09	2.39	13.46	4.88	1.21	7.32	1.15	7.65	42.70	1.42	4.00	0.49	3.08	0.45
868_2	4	Dol-Ank ss	48	0.30	8.75	29.33	5.17	34.14	26.33	7.56	34.67	4.53	19.78	65.92	2.50	4.74	0.49	2.52	0.32
18	4	Dol-Ank ss	56	2.27	39.31	113.33	17.88	93.72	39.51	13.57	51.73	5.93	25.03	93.20	3.45	7.13	0.67	3.28	0.51
857	4	Dol-Ank ss	56	2.04	8.23	18.40	3.03	17.83	6.89	1.82	10.87	1.73	11.23	66.18	2.17	6.27	0.76	4.59	0.69
1005	5	Dol-Ank ss	160	0.22	1.99	6.82	1.31	6.23	2.58	2.23	4.48	1.77	19.88	94.84	5.05	17.29	2.55	18.36	2.54
847	5	Cal	304		31.72	72.67	7.29	23.08	4.09	0.98	3.57	0.50	2.75	14.66	0.52	1.31	0.16	1.09	0.18
847	5	Cal	233	0.15	30.56	74.47	8.18	28.74	7.49	1.84	7.76	1.48	9.79	55.06	1.96	5.68	0.72	5.05	0.66
842	5	Dol-Ank ss	76	0.34	1.03	3.41	0.41	1.35	0.63	0.51	1.18	0.33	2.92	17.10	0.70	2.54	0.45	4.03	0.93
847	5	Dol-Ank ss	19	0.19	2.22	7.56	1.10	5.03	3.19	1.11	6.83	2.15	18.07	71.90	3.86	12.55	1.80	13.50	1.98
89	5	Sid	11		0.06	0.70	0.35	6.02	12.21	1.92	7.04	0.73	3.56	15.40	0.55	1.72	0.27	2.46	0.39
686	5	Sid	6	0.62	2.99	9.35	1.12	4.76	1.75	0.66	3.14	1.12	11.67	64.48	3.02	12.96	2.52	23.26	3.76
842	5	Sid	6	0.26	0.07	0.20	0.02	0.07	0.03	0.01	0.06	0.02	0.12	0.97	0.04	0.15	0.03	0.36	0.08
847	5	Dol-Ank ss	33		16.34	28.31	2.91	10.00		0.84	1.21	0.10	0.46		0.08	0.19	0.02		
813	5	Cal	39	0.15	50.31	136.24	18.19	79.50	18.23	5.72	20.54	3.15	26.79	218.29	6.07	22.77	3.80	34.62	5.65
874_1	7	Dol-Ank ss	149	232.09	138.19	279.05	29.20	114.38	29.01	7.74	30.93	3.42	16.55	86.50	2.98	8.59	1.26	8.17	1.32
884_2	7	Dol-Ank ss	65	91.27	24.65	54.61	5.96	23.90	6.86	2.04	8.23	1.01	5.04	23.52	0.97	2.43	0.34	2.26	0.36
875_2	7	Dol-Ank ss	59	38.27	27.44	55.35	6.48	33.21	16.74	4.80	22.97	2.39	10.04	41.68	1.55	3.43	0.39	2.29	0.36
883	7	Dol-Ank ss	61	42.83	15.50	38.60	4.59	18.96	5.13	1.43	5.78	0.75	4.30	21.35	0.79	2.12	0.29	2.14	0.29

Table 4.11: Continued.

OD#	Gr.	Cb type	Sr	Rb	La	Ce	Pr	Nd	Sm	Eu	Gd	Tb	Dy	Y	Ho	Er	Tm	Yb	Lu
880_2	7	Dol-Ank ss	56	42.71	8.06	16.20	2.16	10.75	6.50	2.03	9.29	1.19	5.75	27.68	1.02	2.65	0.33	2.17	0.31
870_1	7	Dol-Ank ss	50	12.97	5.26	10.14	2.53	15.42	9.04	2.63	13.05	1.81	10.59	58.53	1.99	5.97	0.87	6.36	0.94
876	7	Dol-Ank ss	43	7.08	4.09	9.60	2.98	5.15	3.17	1.12	3.59	0.48	2.25	8.85	0.40	0.97	0.11	0.73	0.15
882_3	7	Dol-Ank ss	48	2.64	9.09	22.20	4.04	25.39	14.89	4.82	25.14	2.63	12.75	75.54	2.35	6.70	0.95	7.12	1.15
881_2	7	Dol-Ank ss	55	1.08	6.26	26.99	2.26	10.79	3.62	1.04	4.79	0.76	5.27	37.65	1.18	3.91	0.62	4.88	0.91
878	7	Dol-Ank ss	68	0.58	9.51	10.53	2.05	8.03	1.39	0.47	1.68	0.17	1.03	5.76	0.22	0.51	0.07	0.39	0.05
882_1	7	Dol-Ank ss	37	0.12	0.92	3.87	0.84	5.80	4.24	1.91	5.92	0.81	3.94	13.71	0.61	1.59	0.20	1.50	0.24
874_2	7	Dol-Ank ss	31	0.08	1.94	11.49	0.74	5.59	4.93	1.46	6.60	0.94	5.83	27.56	1.03	2.67	0.43	2.50	0.49
873_2	7	Dol-Ank ss	26		0.77	7.17	1.01	6.52	3.03	1.57	3.71	0.51	2.50	8.75	0.40	0.78	0.10	0.67	0.09
882_2	7	Dol-Ank ss	52		4.23	2.44	0.93	4.20	1.35	0.50	1.85	0.21	1.23	7.27	0.21	0.54	0.05	0.52	0.06
881_2	7	Dol-Ank ss	148	2.01	0.20	1.38	0.42	3.68	5.07	2.01	8.64	1.09	5.28	22.57	0.89	2.45	0.39	2.98	0.51
885	7	Dol-Ank ss	29	1.15	7.87	18.62	2.88	12.41	6.96	2.32	10.91	1.70	8.10	25.84	1.36	3.93	0.70	6.18	1.02
882_2	7	Dol-Ank ss	88		0.14	0.49	0.07	0.40	0.20	0.07	0.24	0.03	0.09	0.53	0.02	0.03	0.00	0.03	0.00
427	7	Dol-Ank ss	57		2.12	15.08	4.08	25.97	16.60	8.55	26.10	4.33	25.95	109.59	4.86	13.70	1.78	12.46	1.86
885	7	Dol-Ank ss	26	0.20	0.76	5.36	1.15	7.32	2.83	0.78	2.61	0.31	1.38	5.14	0.24	0.54	0.07	0.48	0.08
870_2	7	Dol-Ank ss	47	1.69	0.70	1.86	0.32	1.84	1.81	0.59	2.97	0.37	2.12	13.71	0.36	0.89	0.11	0.59	0.09
874_2	7	Dol-Ank ss	60	0.66	0.16	0.82	0.28	2.40	4.80	2.06	10.47	1.59	7.81	26.50	1.21	2.99	0.37	2.63	0.38
870_2	7	Dol-Ank ss	26	0.13	0.23	1.65	0.55	5.74	7.62	2.47	12.66	1.85	9.06	31.62	1.45	3.62	0.46	3.35	0.45
884_1	7	Dol-Ank ss	40		0.65	3.13	0.72	5.99	5.83	2.99	8.79	1.28	6.06	20.14	0.92	2.27	0.30	1.94	0.31
878	7	Dol-Ank ss	21		0.45	3.19	0.90	6.41	8.31	3.97	17.09	2.83	14.12	42.00	2.33	5.78	0.81	6.15	0.94
875_1	7	Dol-Ank ss	105	0.02	0.73	6.53	1.60	11.74	10.21	6.90	20.43	3.04	14.45	54.95	2.14	4.77	0.59	4.04	0.56
425	7	Dol-Ank ss	55	0.19	0.37	2.46	0.67	6.04	7.30	3.31	9.96	1.45	7.88	37.28	1.51	4.39	0.63	4.20	0.64
876	7	Dol-Ank ss	31		0.55	4.33	1.34	10.48	12.11	5.87	19.54	2.83	13.73	45.96	2.19	5.32	0.64	4.56	0.71
870_2	7	Dol-Ank ss	41		0.06	0.62	0.18	1.69	2.66	1.53	8.99	1.35	6.20	22.22	0.94	2.11	0.24	1.71	0.26
885	7	Dol-Ank ss	319		0.48	5.46	1.67	10.65	5.70	3.20	9.00	1.87	11.44	52.07	1.99	5.04	0.65	4.37	0.60
882_1	7	Dol-Ank ss	103	0.03	0.93	8.22	2.26	16.08	14.84	9.06	28.01	5.54	33.15	128.87	5.85	15.57	2.17	17.19	2.66

Table 4.11: Continued.

OD#	Gr.	Cb type	Sr	Rb	La	Ce	Pr	Nd	Sm	Eu	Gd	Tb	Dy	Y	Ho	Er	Tm	Yb	Lu
873_1	7	Dol-Ank ss	139	0.07	0.97	8.22	2.07	13.54	13.09	9.34	23.33	3.65	19.92	81.33	3.34	8.32	1.06	6.76	0.92
886_1 fawn	7	Dol-Ank ss	274	0.10	1.23	8.68	2.13	14.35	7.34	3.94	12.17	2.53	15.50	73.34	2.82	7.46	1.06	7.50	1.10
649	SG	Dol-Ank ss	30	0.27	27.27	66.88	10.52	63.74	27.51	8.10	50.01	9.12	67.37	534.20	15.58	51.38	7.22	48.26	6.44
667	-	Dol-Ank ss	23	0.54	5.51	14.25	1.38	4.60	1.18	0.34	1.87	0.51	4.39	29.10	1.25	4.82	0.86	7.54	1.41
671	-	Dol-Ank ss	262		28.39	95.15	11.80	44.80	14.89	1.80	17.20	3.82	26.48	116.85	5.42	18.54	2.92	23.70	3.64
671	-	Dol-Ank ss	90	0.09	34.11	113.83	14.29	55.33	18.03	2.22	21.66	4.52	32.55	158.65	6.72	22.08	3.40	28.32	4.51

Table 4.12: Sr-Nd isotopes of calcite, anhydrite and felsic unit.

Sample	Sample#	Rb ppm	Sr ppm	$^{87}Rb/^{86}Sr$	$^{87}Sr/^{86}Sr$	Sm ppm	Nd ppm	$^{147}Sm/^{144}Nd$	$^{143}Nd/^{144}Nd$	εNd_{meas}
Calcite	OD818	2.5	139.6	0.052	0.723206	4.78	28.17			
Calcite	OD819	0.5	97.5	0.015	0.717110	6.27	25.78	0.1502	0.511937	-13.7
Calcite	OD826_1	0.1	97.5	0.004	0.710388	5.77	18.77	0.1854	0.512349	-5.6
Calcite	OD826_2	0.1	84.1	0.005	0.712175	5.55	16.94	0.1980	0.512459	-3.5
Calcite	OD827_1	0.1	93.2	0.003	0.710819	3.53	17.72	0.1206	0.511684	-18.6
Calcite	OD827_2	0.2	83.8	0.006	0.713625	3.90	18.69	0.1264	0.511714	-18.0
Calcite	OD829_1	0.1	107.4	0.003	0.712044	18.85	67.83	0.1675	0.512150	-9.5
Calcite	OD829_2	0.1	103.7	0.003	0.711527	25.62	93.80	0.1644	0.512100	-10.5
Calcite	OD830a	0.02	87.5	0.001	0.710094	9.64	58.00	0.1001	0.511458	-23.0
Calcite	OD830c_1 white	0.1	165.8	0.002	0.716610	7.67	16.13			
Calcite	OD830c_2 pink	0.4	85.7	0.014	0.711096	7.23	41.20	0.1061	0.511511	-22.0
Calcite	OD830c_3 white	0.3	156.3	0.005	0.718297	8.78	19.92	0.2640	0.513100	-9.0
Anhydrite	OD817_1	0.03	1690.0	0.0001	0.720432	5.97	45.08	0.0793	0.511259	-26.9
Anhydrite	OD817_2	0.9	1424.5	0.0019	0.718045	5.60	42.93	0.0783	0.511226	-27.5
Felsic unit	OD820.3	139.7	9.0	49.883	1.790358	3.63	20.74	0.105771	0.511495	-22.3
Felsic unit	OD820.5	173.9	8.8	65.294	2.117096	4.36	25.40	0.103536	0.511477	-22.6

Table 4.12: Continued. $^{87}Sr/^{86}Sr$ (i) and εNd (i) are age-corrected to1593 Ma.

Sample	Sample#	age, Ma	$^{87}Sr/^{86}Sr$ (i)	$^{143}Nd/^{144}Nd$ (i)	εNd (i)
Calcite	OD818		0.72321		
Calcite	OD819	**1593**	0.71677	0.510364	-4.2
Calcite	OD826_1	**1593**	0.71031	0.510407	-3.4
Calcite	OD826_2	**1593**	0.71207	0.510385	-3.8
Calcite	OD827_1	**1593**	0.71074	0.510421	-3.1
Calcite	OD827_2	**1593**	0.71350	0.510390	-3.7
Calcite	OD829_1	**1593**	0.71198	0.510395	-3.6
Calcite	OD829_2	**1593**	0.71147	0.510378	-3.9
Calcite	OD830a	**1593**	0.71008	0.510410	-3.3
Calcite	OD830c_1 white	**1593**	0.71657		
Calcite	OD830c_2 pink	**1593**	0.71077	0.510400	-3.5
Calcite	OD830c_3 white	**1593**	0.71818	0.510335	-4.8
Anhydrite	OD817_1	**1593**	0.72043	0.510429	-2.9
Anhydrite	OD817_2	**1593**	0.71800	0.510406	-3.4
Felsic unit	OD820.3	**1593**	0.66943	0.510387	-3.7
Felsic unit	OD820.5	**1593**	0.64987	0.510393	-3.6

Appendices

Table 5.1: List of all carbonate-bearing samples covered in this study, with group number, drillhole number; depth; carbonate types. Carbonate types in *italic* mean that the composition has been established using EDS, whereas composition of all other carbonate types has been measured using EPMA. A separate column lists REE-fluorocarbonate types which have been observed to be associated with the Ca-Fe-Mg-Mn carbonates. The composition of the REE-fluorocarbonates has been determined only by EDS.
Abbr.: basalt (Bast), bastnäsite (Bast), calcite (Cal), carbonate (Cb), coarse-grained (cg.), conglomerate (congl.), dolerite (Dol), dolomite-ankerite solid solution (Dol-Ank ss), felsic unit (FU), fine-grained (fg.), group (Gr.), laminated (lam.), Nuccaleena Dolomite-like sediment (ND), picrite (Pic), sediment (sed.), siderite (Sid), siderite solid solution (Sid ss), synchysite (Syn). *Sample OD649 has been collected at Snake Gully prospect.

OD#	Drillhole	Depth	Lithology	Gr. #	Ca-Fe-Mg-Mn Cb	Ca-Fe-Mg-Mn Cb texture	REE-F Cb
OD814	RD2773	1998.1	RDG	1	Cal	isolated grains	*Syn-Bast ss*
OD815	RD2773	2012.2	FU, RDG	1	*Cal*	-	
OD816	RD2773	2013.8	FU, RDG	1	*Cal*	inclusions in Py	
OD817	RD2773	2036.3	RDG	1	*Cal*	vein	*Bast or Syn*
OD818	RD2773	2036.7	FU, RDG	1	Cal, *Dol-Ank ss*	vein	
OD819	RD2773	2051.3	FU	1	Cal	vein	
OD820	RD2773	2069.1	FU	1	*Cal*	vein	
OD821	RD2773	2083.2	FU	1	Cal	vein	
OD823	RD2773	2092.8	FU, RDG	1	Cal	dissem. grains in a host rocks	
OD824	RD2773	2098.9	FU	1	Cal	vein	
OD826	RD2773	2179.2	FU	1	Cal	vein	
OD827	RD2773	2182.4	FU	1	Cal, *Sid*	vein	
OD828	RD2773	2189.1	FU	1	Cal, *Sid*	vein	
OD829	RD2773	2208.5	FU	1	Cal	vein	*Syn?*
OD830A	RD2773	2238.4	FU	1	Cal	vein	*Syn*
OD830B	RD2773	2294.5	FU	1	Cal	vein	*Syn*
OD830C	RD2773	2311.5	FU	1	Cal	vein	*Syn*
OD193	RD2773	1172.1	fg. breccia	2	Cal	vein	
OD650	RD1171	450.6	fg. breccia	2	Sid	matrix	*Bast*
OD651	RD1171	471	fg. breccia	2	Sid	matrix	*Bast, Syn*
OD652	RD1171	776.7	cg. breccia	2	Sid, *Sid ss*	matrix (Sid), void (Sid ss)	*Bast*
OD653	RD1171	792.2	fg. breccia	2	Sid	matrix	*Bast*
OD654	RD1171	795.4	fg. breccia	2	Sid, Sid ss	matrix, vein	*Bast*
OD655	RD1171	839.3	cg. breccia	2	Sid, *Sid ss*	matrix (Sid II, Sid ss), clast (Sid II)	*Bast*
OD656	RD1172	571.5	cg. breccia	2	Sid, Sid ss	vein	
OD657	RD1172	572.5	fg. breccia	2	Sid, Sid ss	vein	
OD658	RD1172	668	fg. breccia	2	Sid, *Sid ss*	matrix (Sid I), vein (Sid II, Sid ss)	*Bast*
OD659	RD1705	493.8	fg. breccia	2	Sid, *Sid ss*	matrix&vein (Sid ss), clast (Sid)	
OD660	RD2016	622.3	fg. breccia	2	Dol-Ank ss	vein	
OD661	RD2063	680.3	fg. breccia	2	Dol-Ank ss	vein	
OD662	RD2143	542.1	fg. breccia	2	Sid	vein, clast	*Bast*
OD664	RD2143	703.3	cg. breccia	2	Sid, *Sid ss*	vein (Sid II, Sid ss), clast (Sid I), matrix (Sid)	*Bast*

Table 5.1: Continued.

OD#	Drillhole	Depth	Lithology	Gr. #	Ca-Fe-Mg-Mn Cb	Ca-Fe-Mg-Mn Cb texture	REE-F Cb
OD665	RD2143	787.6	cg. breccia	2	Dol-Ank ss, *Sid*	matrix (Sid II, Dol-Ank ss), clast (Sid I)	*Bast*
OD666	RD2143	801.5	fg. breccia	2	Sid	matrix, vein, clast, void	
OD669	RD2319	788.9	cg. breccia	2	Dol-Ank ss, *Sid ss*	vein (Dol-Ank ss, Sid)	
OD672	RD2384	700.8	cg. breccia	2	*Dol-Ank ss*	vein	
OD673	RD2681	716.2	cg. breccia	2	Cal, Sid	matrix	
OD674	RD2681	718.3	cg. breccia	2	Sid ss	matrix	
OD675	RD2681	731.8	fg. breccia	2	Sid, *Sid ss*	matrix (Sid, Sid ss), clast (Sid)	*Bast, Syn*
OD676	RD2687A	466.5	cg. breccia	2	Sid	matrix	
OD677	RD2687A	519.3	fg. breccia	2	Sid ss	vein	
OD680	RD2715	352.6	fg. breccia	2	Sid ss	matrix, clast (?)	*Bast*
OD681	RD2715	547.4	fg. breccia	2	Sid	matrix, void	*?*
OD682	RD2715	770.8	cg. breccia	2	Sid	clast	
OD683	RD2715	771.8	cg. breccia	2	Sid	matrix	*Bast*
OD687	RD2715	855.7	cg. breccia	2	Sid ss	matrix	*Bast, Syn*
OD688	RD2716	602.4	fg. breccia	2	Sid ss	matrix, vein	
OD689	RD2716	639.8	cg. breccia	2	Sid ss	vein, clast	
OD690	RD2717	664.2	cg. breccia	2	Sid, Sid ss	matrix, clast, voids, vein	
OD812	RD2773	1904.2	cg. breccia	2	Cal	1 euhedral grain	
OD833	RD2786A	1614.5	cg. breccia	2	Sid ss	vein, matrix	
OD834	RD2786A	1716.2	cg. breccia	2	Sid	isolated grains	*Bast, Syn*
OD835	RD2786A	1753.2	fg. breccia	2	Cal (vein), *Sid (matrix)*	vein, matrix	*Bast, Syn*
OD843	RU65-8230	101.1	cg. breccia	2	Sid ss	vein, void filling	
OD844	RU65-8230	365.2	fg. breccia	2	Dol-Ank, Sid, Sid ss	matrix (Sid), void (Dol-Ank ss, Sid ss)	*Bast*
OD845	RU65-8230	372.5	fg. breccia	2	*Sid, Sid ss*	matrix	
OD846	RU65-8230	405.7	cg. breccia	2	*Cal, Dol-Ank ss*	aggregates?	*Syn*
OD923	RU65-7938	421	fg. breccia	2	-	vein	
OD932	RU65-7938	621.3	cg. breccia	2	*Dol-Ank ss, Sid ss*	vein	
OD937	RU65-8333	468.8	fg. breccia	2	*Cal*	vein	
OD944	RU65-8337	330	fg. breccia	2	-	vein	
OD948	RU65-8337	495.6	fg. breccia	2	Dol-Ank ss, Sid ss	vein	
OD967	RD635	371	fg. breccia	2	Dol-Ank ss	vein	
OD969	RU65-3776	337.2	fg. breccia	2	Dol-Ank ss, Sid ss	vein	
OD237	RD1939A	540.5	oolite	2	Sid	matrix	
OD1001	hand grabed		oolite	2	Sid	matrix, ooids	
OD1002	hand grabed		oolite	2	Sid	matrix, ooids	
OD1007	RU65-8337	69.3	oolite	2			
OD1035	hand grabed		oolite	2			
OD1036	hand grabed		oolite	2			
OD1037	RU31-809	116.9	oolite	2			
OD1038	RD1939A	590.5	oolite	2			
OD1039	RD1939A	719.5	oolite	2			

Table 5.1: Continued.

OD#	Drillhole	Depth	Lithology	Gr. #	Ca-Fe-Mg-Mn Cb	Ca-Fe-Mg-Mn Cb texture	REE-F Cb
OD836	RD2786A	1796.2	red sed.	3	Dol-Ank ss, *Sid*, *Cal*	vein	
OD837	RD2786A	1847.8	red sed.	3	Cal, Dol-Ank ss	vein	
OD838	RD2786A	1895.8	red sed.	3	Dol-Ank ss	vein	
OD839	RD2786A	1896.5	red sed.	3	Dol-Ank ss, Sid ss	vein	
OD840	RD2786A	1937.8	red sed.	3	Dol-Ank ss	vein	
OD131	RD1627	650.4	green sed.	3	Dol-Ank ss, *Cal*	vein	
OD132	RD1627	738.4	green sed.	3	Dol-Ank ss, *Cal*	vein	
OD187	RD2821	627.9	green sed.	3	Dol-Ank ss, Sid ss	vein	
OD226	RD1624	584.2	green sed.	3	Dol-Ank ss, *Sid*	vein	
OD7	RD2570	764.4	Pic	4	Dol-Ank ss	vein	
OD24C	RD3008	406.2	Pic	4	Dol-Ank ss	vein	
OD28B	RD3008	688.4	Pic	4	Dol-Ank ss	vein	
OD494	RD3564	368.9	Pic	4	Dol-Ank ss	vein	
OD571	RD6	333	Pic	4	Dol-Ank ss, *Sid ss*, *Cal*	vein	
OD647	RD3008	397.2	Pic	4	*Dol-Ank ss*	vein	
OD868	RD1756	342	Pic	4	Dol-Ank ss, *Sid ss*	vein	
OD968	RD635	371.6	Pic	4	Dol-Ank ss	vein	
OD2	RU39-5426	224.4	Bas	4	Dol-Ank ss	vein	
OD6	RU39-5426	195.6	Bas	4	Cal	vein on brecciated mafic dyke	
OD16	RD2744	761.4	Bas	4	Dol-Ank ss, Sid ss	vein in GRA & mafic dyke	
OD17	RD2744	808.9	Bas	4	Dol-Ank ss, *Sid ss*	vein, matrix	*Bast*
OD18	RD2744	821.2	Bas	4	Dol-Ank ss	vein	
OD78	RD2773	1255.2	Bas	4	Cal	vein	
OD82	RD2773	1331.7	Bas	4	Cal	vein	
OD87	RD2678	565.5	Bas	4	Sid	void filling	
OD90	RD2715	804.8	Bas	4	Sid ss, *Dol-Ank ss*	void filling	
OD92	RD2715	811.8	Bas	4	*Sid ss*	void filling and vein	
OD93	RD2715	819.8	Bas	4	*Sid ss*	void filling and vein	
OD95	RD2715	836.3	Bas	4	Sid ss	vein on brecciated mafic dyke	
OD96	RD2715	852.4	Bas	4	Dol-Ank ss	vein	
OD99	RD1500	651.3	Bas	4	Sid ss, *Dol-Ank ss*	vein	
OD102	RD2018B	812.8	Bas	4	Dol-Ank ss	vein	
OD106	RD2031W1	889.1	Bas	4	Dol-Ank ss	vein	
OD111	RD271	649	Bas	4	Dol-Ank ss	vein	
OD112	RD271	649.2	Bas	4	Dol-Ank ss, *Cal*	vein	*Syn*
OD113	RD271	650	Bas	4	Dol-Ank ss	vein	
OD114	RD271	650.5	Bas	4	Cal	vein	
OD116	RD271	652.7	Bas	4	Cal, *Dol-Ank ss*	vein	
OD117	RD271	657.4	Bas	4	Dol-Ank ss	vein	

Table 5.1: Continued.

OD#	Drillhole	Depth	Lithology	Gr. #	Ca-Fe-Mg-Mn Cb	Ca-Fe-Mg-Mn Cb texture	REE-F Cb
OD134	RD1763	864.5	Bas	4	Dol-Ank ss	vein	
OD135	RD1745	769.6	Bas	4	Dol-Ank ss	vein	
OD196	RD2773	1247.8	Bas	4	*Cal*	vein	
OD197	RD2773	1248.5	Bas	4	Cal	vein	
OD199	RD2773	1329.2	Bas	4	Cal	vein	
OD421	RD222	751	Bas	4	*Cal*	vein	
OD423	RD222	769.4	Bas	4	Cal	vein	
OD502	RD1625	520	Bas	4	Dol-Ank ss	vein	
OD604	RD2821	605	Bas	4	Dol-Ank ss	vein	
OD663	RD2143	690.7	Bas	4	Sid ss	vein	*Bast*
OD678	RD2687A	630.6	Bas	4	*Sid ss*	vein	*Bast*
OD679	RD2687A	631.3	Bas	4	Dol-Ank ss, Sid ss	vein, matrix	
OD684	RD2715	839.2	Bas	4	Sid ss	vein	
OD685	RD2715	851.3	Bas	4	Dol-Ank ss, *Sid ss*	vein	*Bast, Syn*
OD806	RD2773	1263.1	Bas	4	Cal	vein	
OD809	RD2773	1333.6	Bas	4	Cal	vein	
OD811	RD2773	1364.3	Bas	4	Cal	vein	
OD858	RU39-5426	239.5	Bas	4	Dol-Ank ss	vein	
OD906	RD2715	810.1	Bas	4	Sid ss	vein	
OD911	RD2715	834.2	Bas	4	Sid ss	vein	
OD914	RD2715	852.6	Bas	4	Dol-Ank ss	vein	
OD931	RU65-7938	573.8	Bas	4	Cal	vein	
OD938	RU65-8333	469.8	Bas	4	no	vein	
OD945	RU65-8337	337.6	Bas	4	Dol-Ank ss, *Sid ss*	vein	
OD949	RU65-8337	502.3	Bas	4	Dol-Ank ss	vein	
OD950	RU65-8337	504.9	Bas	4	Dol-Ank ss, Sid ss	vein	
OD79	RD2773	1270.6	Bas, Dol	4	Cal	vein	
OD186	RD2821	607.7	Dol	4	Dol-Ank ss	vein	
OD422	RD222	759	Dol	4	Cal	vein	
OD785	RU65-8228	418.7	Dol	4	*Cal*	vein	
OD800	RU65-8230	554.7	Dol	4	Cal	vein	
OD848	RU65-8230	528.7	Dol	4	Dol-Ank ss, *Cal*	vein	
OD852	RU65-8230	596.1	Dol	4	Cal	vein	
OD853	RU65-8230	603.2	Dol	4	Cal, Dol-Ank ss	vein	
OD857	RU39-5426	237.8	Dol	4	Dol-Ank ss, Sid ss	vein	
OD904	RD2715	800.8	Dol	4	-	vein	
OD929	RU65-7938	561.1	Dol	4	Cal	vein	
OD930	RU65-7938	563.8	Dol	4	-	vein	
OD939	RU65-8333	470.1	Dol	4	-	vein	
OD956	RU65-8337	555.5	Dol	4	Cal, Sid	vein	
OD957	RU65-8337	561.4	Dol	4	Cal	vein	

Table 5.1: Continued.

OD#	Drillhole	Depth	Lithology	Gr. #	Ca-Fe-Mg-Mn Cb	Ca-Fe-Mg-Mn Cb texture	REE-F Cb
OD89	RD2678	600.3	massive vein	5	Sid	vein	
OD686	RD2715	855.3	massive vein	5	Sid ss	vein	*Bast, Syn*
OD691	RU31-6016	346.6	massive vein	5	*Dol-Ank ss*	vein	
OD692	RU36-7731	237.5	massive vein	5	-	vein	
OD798	RU65-8230	495.5	massive vein	5	Dol-Ank ss, *Cal*	vein 1 (Dol-Ank ss) & 2 (Cal)	
OD813	RD2773	1990.1	massive vein	5	Cal	vein	
OD831	RD2786A	1600.5	massive vein	5	Sid	vein	
OD841	RD2786A	1948.9	massive vein	5	Dol-Ank ss	vein	
OD842	RD2786A	2160.4	massive vein	5	Dol-Ank ss, Sid ss	vein	
OD847	RU65-8230	495.3	massive vein	5	Cal, Dol-Ank ss	vein	
OD933	RU65-8333	16.9	massive vein	5	*Sid*	vein	
OD1005	hand picked		massive vein	5	Dol-Ank ss	vein	*Bast*
OD1006	RU36-8834	69.3	lam. Cb	6	Sid	alternating bands	
OD1008	RU36-8834	64.6	lam. Cb	6	*Sid, Sid ss*		*Bast*
OD1042	RU36-8834	43.5	lam. Cb	6	*Sid, Sid ss*		
OD1043	RU36-8834	46.2	lam. Cb	6	*Sid, Sid ss*		
OD1044	RU36-8834	50.4	lam. Cb	6	*Sid, Sid ss*		
OD1045	RU36-8834	62.2	lam. Cb	6	*Sid, Sid ss*		
OD1046	RU36-8834	69	lam. Cb	6	*Sid, Sid ss*		
OD1047	RU36-8834	70.2	lam. Cb	6	*Sid, Sid ss*		
OD1048	RU36-8834	71.4	lam. Cb	6	*Sid, Sid ss*		
OD1049	RU36-8834	76.9	lam. Cb	6	*Sid, Sid ss*		
OD1050	RU36-8771	105	lam. Cb	6	*Sid, Sid ss*		
OD1051	RU36-8771	108.5	lam. Cb	6	*Sid, Sid ss*		

Table 5.1: Continued.

OD#	Drillhole	Depth	Lithology	Gr. #	Ca-Fe-Mg-Mn Cb	Ca-Fe-Mg-Mn Cb texture	REE-F Cb
OD425	RD3564	364.1	congl.	7	Dol-Ank ss	matrix	
OD427	RD3554	368.5	congl.	7	Cal, Dol-Ank ss	matrix	
OD870	RD1398	340.4	congl., ND	7	Dol-Ank ss, *Dol*	vein	
OD873	RD1629	329.6	congl.	7	Dol-Ank ss	matrix, vein	
OD874	RD1629	329.8	congl., ND	7	Dol-Ank ss, *Dol?*	vein	
OD875	RD1810	334.6	congl., ND	7	Dol-Ank ss, *Dol*, *Sid*	matrix, vein	
OD876	RD1810	334.8	congl., sandstone	7	Cal, Dol-Ank ss, *Sid*	matrix	
OD878	RD1913	382.6	sandstone	7	Dol-Ank ss (matrix, clasts), Dol (ND)	clast, matrix	
OD880	RD1963	335.2	congl., ND	7	Dol	sediment	
OD881	RD2020	332.9	congl., ND	7	Dol, Dol-Ank ss	vein (Dol-Ank ss), sediment (Dol)	
OD882	RD2965	365.7	congl., ND	7	Dol, Dol-Ank ss	sediment, vein	
OD883	RD2972	385	ND	7	Dol	sedimet	
OD884	RD2972	385.1	congl., ND	7	Dol, Dol-Ank ss	sediment	
OD885	RD2972	387	congl.	7	*Dol-Ank ss*	matrix	
OD886	RD2972	388	congl.	7	Dol-Ank ss	matrix	
OD667	RD2319	760.1	unbrecciated RDG	-	Dol-Ank ss	vein	*Syn*
OD670	RD2322	944.5	unbrecciated RDG	-	Dol-Ank ss	vein	
OD671	RD2384	683.5	unbrecciated RDG	-	Dol-Ank ss, *Cal*	vein	*Syn*
OD649*	SGD5	737	granite	-	Dol-Ank ss	vein	

Table 5.2: Characteristics and classification of carbonates in samples from Olympic Dam (associations/groups 1-7). Note broad variation in mineralogy of sulfides and other minerals associated with carbonates from within each group. The range of stable isotopic compositions in each group is indicated. Carbonate 'types' given in parentheses are relatively rare. Abbr.: solid solution (ss).

Gr. #	Group Name	Carbonate texture(s)	Carbonate type(s)	Associated minerals		C-O isotope range		
				sulfides	other minerals	# analyses	$\delta^{13}C$ ‰	$\delta^{18}O$ ‰
1	Coarse-grained calcite veins in weakly-brecciated granite and rhyolite	veins	calcite	pyrite, chalcopyrite, sphalerite, galena	quartz, barite, fluorite, hematite	18	-4.1 to -3.5	9.4 to 12
2	Carbonates in strongly-brecciated granite	matrix, clasts, oolites, voids	siderite, siderite *ss*, REE-fluorocarbonate (dolomite-ankerite *ss*, calcite)	pyrite, marcasite, chalcopyrite, sphalerite, galena, bornite, Co-sulfides	monazite, apatite, quartz, barite (-celestite), fluorite, anhydrite, magnetite, hematite, Bi-Ag-Pb-Te-Se minerals, U-minerals, chlorite	12	-5.3 to -2.8	10.5 to 16.9
3	Carbonate veins in bedded sediments	veins	dolomite-ankerite *ss*, calcite, (siderite, siderite *ss*)	chalcopyrite, galena, bornite, fahlore	barite, fluorite, anhydrite, quartz, hematite	4	-4.7 to -3.4	10.3 to 12.7
4	Carbonates in mafic and ultramafic igneous rocks	alteration, veins, voids	dolomite-ankerite ss, calcite, (siderite, siderite *ss*)	pyrite, chalcopyrite, sphalerite, galena, bornite, fahlore, chalcocite, Co-sulfides	apatite, titanite, Ti-oxides, quartz, chlorite, barite, fluorite, anhydrite, hematite, magnetite, sericite, altaite, zeolites	28	-6.5 to -2	10.3 to 20.9
5	Massive barite-fluorite-dominated veins (with minor carbonate)	veins, voids (in groups 2 & 4)	dolomite-ankerite *ss*, siderite, siderite *ss*, REE-fluorocarbonate	pyrite, chalcopyrite, bornite, chalcocite, fahlore, Co-sulfides, löllingite	barite, fluorite, hematite, gold, Bi-Ag-Pb-Se-Te alloys, U-REE minerals	10	-4.9 to -3.9	11.0 to 16.0
6	Laminated siderite	alternating layers	siderite *ss*, REE-fluorocarbonate	pyrite, chalcopyrite, sphalerite, galena	barite, fluorite, quartz, hematite, monazite, U-minerals	2	-3.2 to -3.1	15.1 to 15.2
7	Carbonate matrix in a conglomerate-breccia and sandstone	matrix	dolomite-ankerite ss, (calcite, siderite)	chalcopyrite, bornite	barite	4	-5.8 to -3.8	11.4 to 13.7

Table 5.3: Results of the EPMA study of carbonates from Olympic Dam. Abbr.: group (Gr.). *Sample OD649 has been collected at Snake Gully (SG) prospect. Element concentrations are in wt%.

OD #	Gr.#	Fe	Mn	Mg	Ca	Si	C	O	Total
814	1	0.52	6.31	0.04	32.39	0.02	11.94	46.78	97.99
823	1	0.41	2.23	0.00	36.47	0.01	12.03	47.39	98.53
818	1	0.67	2.10	0.01	36.03	0.00	12.05	47.31	98.18
823	1	0.80	1.30	0.01	36.65	0.02	12.07	47.43	98.30
821	1	0.31	2.64	0.04	36.01	0.00	12.04	47.33	98.37
814	1	1.18	6.02	0.49	31.92	0.01	11.92	46.93	98.46
826	1	1.01	2.18	0.01	35.66	0.00	12.04	47.24	98.15
830a	1	0.93	2.02	0.01	35.75	0.00	12.06	47.26	98.04
827	1	0.79	1.56	-0.01	36.44	-0.01	12.06	47.35	98.19
827	1	0.16	2.27	0.01	36.69	0.00	12.03	47.42	98.59
828	1	0.69	2.72	0.02	35.60	0.01	12.02	47.25	98.31
819	1	0.19	0.70	0.04	38.17	0.02	12.07	47.68	98.86
819	1	0.74	2.82	0.08	35.27	0.00	12.04	47.23	98.17
817	1	0.45	1.07	-0.01	37.44	0.00	12.06	47.53	98.55
828	1	0.78	1.94	0.02	36.29	0.00	12.04	47.35	98.42
830b	1	0.40	2.54	0.05	36.95	0.01	11.95	47.49	99.39
830b	1	0.51	2.53	0.07	36.18	0.01	12.01	47.37	98.68
829	1	0.92	3.53	0.03	34.30	0.01	12.03	47.06	97.87
830c	1	0.74	2.50	0.05	35.34	0.00	12.07	47.23	97.92
830c	1	0.65	1.47	-0.01	36.77	0.00	12.06	47.42	98.37
818	1	0.45	2.04	0.01	36.44	0.00	12.05	47.37	98.35
819	1	0.71	2.73	0.01	35.49	0.01	12.03	47.24	98.23
824a	1	0.41	1.84	0.01	36.70	0.01	12.05	47.43	98.44
818	1	0.44	1.95	0.02	36.47	0.01	12.06	47.40	98.34
948	2	31.48	9.73	3.95	0.32	0.00	10.92	43.67	100.06
948	2	10.48	4.91	4.66	20.22	0.08	11.89	47.34	99.59
654	2	29.51	4.81	7.99	0.07	0.00	11.49	45.75	99.63
812	2	1.64	2.66	0.21	34.66	0.04	12.00	47.24	98.45
193	2	-0.02	0.07	-0.01	39.49	0.01	12.04	47.87	99.45
651	2	45.09	1.84	0.30	0.27	0.00	10.46	41.62	99.58
237	2	45.54	1.14	0.58	0.22	0.01	10.48	41.78	99.74
677	2	43.71	3.37	0.07	0.44	0.00	10.44	41.53	99.55
650	2	45.27	1.86	0.06	0.08	0.02	10.46	41.46	99.19
844	2	12.52	4.43	4.42	19.96	0.02	11.76	47.11	100.22
844	2	11.58	3.95	4.40	20.39	0.01	11.87	47.15	99.35
844	2	32.35	5.77	5.77	0.49	0.03	11.15	44.68	100.26
833	2	43.75	3.77	0.16	0.06	0.02	10.42	41.56	99.74
683	2	46.89	0.06	0.39	0.54	0.01	10.44	41.74	100.07
688	2	42.63	3.33	0.48	0.33	0.01	10.54	41.72	99.03
688	2	37.12	4.15	3.87	0.03	0.02	10.93	43.54	99.66
682	2	45.89	0.79	0.13	0.18	0.15	10.50	41.67	99.30

Table 5.3: Continued.

OD #	Gr.#	Fe	Mn	Mg	Ca	Si	C	O	Total
1001	2	47.38	0.76	0.02	0.13	0.02	10.36	41.49	100.17
1002	2	46.83	0.91	0.00	0.00	0.03	10.41	41.44	99.62
669	2	7.71	1.50	8.73	20.35	0.02	12.36	49.46	100.12
669	2	0.62	1.23	12.69	20.74	0.03	12.94	51.68	99.93
689	2	44.74	3.46	0.03	0.16	0.02	10.36	41.52	100.29
676	2	0.65	0.05	0.00	53.56	0.00	10.95	50.75	115.96
676	2	45.50	1.68	0.05	0.05	0.01	10.45	41.44	99.19
662	2	46.20	0.94	0.19	0.36	0.00	10.43	41.58	99.70
659	2	44.13	3.23	0.03	0.05	0.00	10.44	41.43	99.32
659	2	36.35	6.50	3.15	0.14	0.01	10.79	43.19	100.13
660	2	0.85	2.36	11.53	20.67	0.00	12.86	51.03	99.31
690	2	45.54	2.68	0.11	0.02	0.01	10.36	41.53	100.25
664	2	46.62	1.40	0.17	0.17	0.00	10.37	41.57	100.30
681	2	45.42	0.13	0.82	0.61	0.01	10.55	41.94	99.47
680	2	43.83	2.74	0.49	0.07	0.02	10.50	41.71	99.36
654	2	45.22	0.40	1.42	0.23	0.00	10.56	42.23	100.06
652	2	46.19	1.45	0.13	0.01	0.00	10.41	41.48	99.68
655	2	44.86	1.28	1.05	0.30	0.00	10.51	42.05	100.05
657	2	35.34	7.22	2.28	0.39	0.00	10.82	42.71	98.75
657	2	25.71	7.63	9.32	0.06	0.00	11.54	46.51	100.79
687	2	38.97	6.68	0.62	1.04	-0.02	10.52	41.94	99.75
674	2	43.69	3.94	0.17	0.34	0.02	10.40	41.62	100.17
674	2	38.35	4.10	3.46	0.19	0.00	10.81	43.34	100.26
673	2	0.17	0.00	-0.01	39.48	0.02	12.03	47.87	99.55
673	2	45.49	1.24	0.70	0.22	0.00	10.47	41.85	99.98
656	2	29.18	7.19	7.13	0.30	0.02	11.30	45.39	100.51
656	2	36.19	6.46	2.95	0.27	0.14	10.81	43.26	100.09
653	2	48.99	1.52	0.17	0.11	0.04	10.17	41.77	102.77
666	2	47.18	0.73	0.08	0.02	0.01	10.39	41.48	99.88
666	2	46.40	0.78	0.02	0.19	0.00	10.44	41.42	99.25
834	2	43.20	4.34	0.27	0.09	0.01	10.42	41.61	99.93
835	2	0.67	0.72	0.00	37.49	0.00	12.07	47.53	98.48
843	2	39.53	5.94	0.75	0.23	0.60	10.64	42.66	100.35
844	2	46.27	1.21	0.24	0.06	0.15	10.43	41.76	100.12
675	2	44.67	2.65	0.47	0.30	0.02	10.42	41.78	100.30
1001	2	46.46	1.49	0.03	0.05	0.01	10.39	41.47	99.89
661	2	0.26	1.35	12.45	20.90	0.00	12.97	51.54	99.45
661	2	10.08	3.84	6.21	20.13	0.01	11.99	48.08	100.34
658	2	46.03	1.42	0.17	0.14	0.01	10.42	41.55	99.74
661	2	0.19	1.48	12.50	20.88	0.00	12.96	51.57	99.58
661	2	9.65	2.30	6.89	20.31	0.00	12.15	48.45	99.74
675	2	44.81	2.12	0.48	0.35	0.00	10.45	41.75	99.95
665	2	46.29	1.54	0.02	0.42	0.00	10.37	41.53	100.18

Table 5.3: Continued.

OD #	Gr.#	Fe	Mn	Mg	Ca	Si	C	O	Total
665	2	33.96	2.32	7.37	0.07	0.00	11.31	45.42	100.46
665	2	46.82	1.37	0.02	0.43	0.01	10.34	41.56	100.54
835	2	0.63	1.30	0.00	37.02	0.00	12.06	47.46	98.48
659	2	39.47	3.24	2.47	0.43	0.02	10.80	42.83	99.25
659	2	40.02	7.27	0.04	0.16	-0.01	10.44	41.48	99.39
669	2	8.46	2.14	7.86	20.53	0.01	12.23	49.01	100.25
969	2	32.64	7.73	4.98	0.10	0.01	10.98	44.20	100.64
969	2	36.03	6.55	3.38	0.24	0.00	10.80	43.33	100.33
969	2	12.70	3.70	4.57	20.64	0.00	11.75	47.27	100.64
969	2	31.43	6.82	6.45	0.05	0.01	11.15	44.98	100.90
969	2	36.10	7.20	2.45	0.23	0.00	10.76	42.81	99.55
658_1	2	45.73	1.21	0.04	0.15	0.01	10.47	41.44	99.06
658_2	2	52.85	1.86	0.50	0.22	0.04	9.84	42.38	107.69
675	2	45.98	1.16	-0.01	0.05	0.00	10.45	41.37	99.01
967	2	0.07	1.83	12.15	21.03	0.00	12.94	51.41	99.42
673	2	46.43	0.86	0.02	0.11	0.04	10.44	41.47	99.37
673	2	46.43	1.44	0.00	0.01	0.01	10.39	41.43	99.71
131	3	0.00	4.77	10.37	20.37	0.03	12.78	50.42	98.73
839	3	8.06	2.46	7.29	20.36	0.01	12.29	48.70	99.17
839	3	39.57	2.64	2.19	1.87	0.01	10.75	42.94	99.98
131	3	0.86	1.15	11.75	21.93	0.04	12.86	51.38	99.96
226	3	3.05	3.07	10.56	20.01	0.02	12.64	50.41	99.75
226	3	9.31	2.83	7.20	20.42	0.00	12.11	48.63	100.49
838	3	10.27	2.55	6.42	20.11	0.01	12.10	48.18	99.64
837	3	4.70	1.96	9.93	20.89	0.00	12.53	50.18	100.18
837	3	0.77	1.24	0.10	36.66	0.01	12.08	47.47	98.32
839	3	7.96	2.46	7.70	20.73	0.01	12.24	48.97	100.07
839	3	7.89	2.69	7.81	20.66	0.00	12.22	49.00	100.28
836	3	7.54	3.75	7.29	20.39	0.00	12.20	48.69	99.86
840	3	7.29	3.64	7.51	20.73	0.04	12.20	48.90	100.30
838	3	8.30	1.97	7.87	20.45	0.00	12.27	49.00	99.86
187	3	28.28	9.74	5.77	0.45	0.02	11.17	44.69	100.11
187	3	22.14	5.28	12.32	0.80	0.02	11.98	48.24	100.77
187	3	4.22	2.08	10.55	20.60	0.01	12.56	50.46	100.48
679	4	32.04	9.10	3.59	0.48	0.06	10.92	43.54	99.73
679	4	24.86	7.75	9.32	0.46	0.01	11.59	46.58	100.57
853	4	2.89	3.56	9.59	20.45	0.00	12.62	49.96	99.06
853	4	0.61	2.76	0.23	35.32	0.00	12.04	47.32	98.30
809	4	0.09	0.03	0.00	39.60	0.03	12.02	47.91	99.68
806	4	0.02	0.00	-0.01	39.12	0.07	12.08	47.87	99.16
806	4	0.02	0.02	-0.01	39.47	0.04	12.04	47.89	99.48
806	4	0.00	-0.02	-0.01	39.40	0.04	12.06	47.88	99.34
800	4	0.60	0.15	0.33	37.93	0.78	12.12	48.74	100.65

Table 5.3: Continued.

OD #	Gr.#	Fe	Mn	Mg	Ca	Si	C	O	Total
684	4	37.19	7.79	1.61	0.09	0.02	10.63	42.36	99.69
684	4	25.29	7.48	9.31	0.07	0.03	11.60	46.52	100.30
811	4	0.09	0.08	0.02	38.97	0.03	12.07	47.82	99.07
422	4	2.38	1.88	0.44	34.44	0.36	12.03	47.72	99.25
422	4	2.62	1.18	0.61	34.87	0.02	12.02	47.46	98.77
422	4	1.06	2.42	0.31	35.05	0.02	12.05	47.34	98.26
858	4	9.97	3.16	5.91	20.74	0.10	12.03	48.12	100.04
858	4	5.19	3.67	8.59	20.71	0.03	12.37	49.47	100.02
17	4	10.45	6.16	4.17	20.28	0.07	11.78	47.09	100.00
17	4	10.57	6.05	3.56	21.08	0.03	11.73	46.85	99.87
17	4	10.16	6.17	4.02	20.46	0.23	11.81	47.24	100.09
17	4	10.07	5.72	3.89	20.31	0.70	11.90	47.73	100.32
134	4	1.62	3.36	10.91	20.34	0.09	12.72	50.74	99.78
87	4	40.49	3.03	2.17	0.85	0.01	10.70	42.77	100.02
112	4	7.29	3.34	7.25	20.90	0.10	12.23	48.87	99.98
117	4	6.91	3.09	7.33	20.70	0.30	12.32	49.13	99.77
857	4	7.96	2.88	6.31	22.36	0.05	12.12	48.54	100.22
857	4	9.42	5.64	4.25	21.11	0.21	11.87	47.44	99.94
857	4	10.24	5.92	3.98	20.28	0.55	11.86	47.59	100.40
114	4	0.33	1.56	0.23	36.77	0.06	12.08	47.62	98.64
132	4	2.49	2.00	10.69	21.15	0.01	12.71	50.64	99.68
132	4	2.71	1.83	10.61	20.97	0.06	12.73	50.64	99.54
99	4	37.45	5.92	1.75	0.98	0.02	10.71	42.57	99.40
99	4	30.37	7.08	6.22	0.16	0.01	11.23	44.85	99.92
16	4	10.03	5.40	4.89	20.51	0.02	11.85	47.44	100.14
16	4	38.82	3.33	3.78	0.10	0.03	10.84	43.54	100.44
96	4	5.15	3.30	8.69	20.54	0.01	12.43	49.49	99.61
102	4	1.58	3.49	10.68	20.54	0.02	12.70	50.57	99.59
102	4	5.53	2.65	8.73	20.80	0.03	12.43	49.56	99.74
102	4	4.30	3.45	8.64	21.31	0.08	12.44	49.66	99.88
106	4	5.76	2.53	9.07	20.40	0.00	12.44	49.64	99.84
116	4	0.44	1.52	0.21	36.25	0.02	12.12	47.48	98.04
6	4	0.47	1.94	0.33	35.48	0.10	12.13	47.52	97.98
6	4	0.65	2.03	0.33	35.28	0.23	12.13	47.65	98.29
186	4	5.55	4.18	7.92	20.43	0.01	12.34	49.05	99.47
423	4	0.60	3.31	0.27	34.65	0.02	12.04	47.26	98.16
848	4	6.25	2.82	8.71	20.62	0.01	12.35	49.49	100.25
868	4	12.15	3.07	5.24	19.94	0.00	11.91	47.51	99.81
857	4	8.49	2.58	7.24	20.89	0.20	12.18	48.97	100.56
685	4	4.79	2.25	9.28	21.00	0.03	12.51	49.88	99.73
663	4	40.99	4.56	1.09	0.19	0.05	10.58	42.11	99.58
785	4	0.01	0.00	-0.02	28.53	-0.01	13.19	46.52	88.22
95	4	35.07	8.79	1.12	2.17	0.01	10.60	42.45	100.19

Table 5.3: Continued.

OD #	Gr.#	Fe	Mn	Mg	Ca	Si	C	O	Total
197	4	0.02	0.23	-0.01	38.93	0.01	12.07	47.78	99.03
199	4	0.05	0.05	0.00	39.45	0.01	12.04	47.86	99.46
90	4	36.34	7.22	2.20	0.31	0.01	10.74	42.70	99.50
82	4	-0.02	0.03	-0.01	39.63	0.00	12.03	47.87	99.54
113	4	7.15	2.70	8.04	20.46	0.00	12.31	49.10	99.77
79	4	0.07	0.06	-0.01	39.03	0.01	12.07	47.78	99.00
78	4	0.04	0.08	0.01	39.08	0.00	12.07	47.80	99.08
2	4	2.00	2.12	10.93	21.27	-0.01	12.73	50.78	99.82
18	4	8.77	4.28	6.23	20.39	0.00	12.06	48.12	99.85
18	4	12.69	6.67	3.02	19.70	0.01	11.59	46.30	99.98
7	4	4.38	3.89	8.74	20.53	0.00	12.45	49.50	99.48
857	4	8.48	2.54	7.67	20.45	0.00	12.20	48.90	100.24
857	4	33.53	4.31	6.31	0.12	0.01	11.19	44.88	100.35
906	4	28.73	9.80	5.29	0.88	0.00	11.10	44.48	100.27
494	4	5.10	0.48	10.42	21.04	0.01	12.61	50.47	100.14
968	4	1.45	1.68	11.70	20.53	0.00	12.87	51.09	99.31
968	4	6.72	5.19	7.07	20.24	0.00	12.15	48.55	99.93
90	4	36.04	7.97	2.00	0.24	0.01	10.70	42.58	99.55
92	4	33.53	9.76	2.56	0.76	0.01	10.72	43.01	100.36
99	4	29.97	7.13	6.50	0.27	0.00	11.24	45.01	100.12
848	4	7.66	2.58	5.53	23.43	0.03	12.12	48.26	99.61
196	4	0.13	1.12	0.09	37.46	0.02	12.09	47.60	98.51
24C	4	1.78	3.47	10.31	20.66	0.01	12.69	50.38	99.30
571	4	6.59	2.21	8.43	20.54	-0.01	12.40	49.32	99.49
571	4	10.50	1.83	7.04	20.26	0.01	12.11	48.53	100.28
571	4	4.68	3.30	9.42	20.03	0.01	12.49	49.79	99.73
571	4	5.21	2.58	9.32	20.48	0.00	12.47	49.79	99.86
929	4	0.08	0.88	0.05	38.09	0.00	12.06	47.66	98.83
852	4	0.83	0.39	1.01	36.52	0.95	12.16	49.08	100.94
931	4	0.01	0.03	-0.01	39.52	0.00	12.04	47.86	99.45
931	4	0.92	2.58	0.08	35.37	0.00	12.03	47.25	98.24
950	4	29.92	6.72	5.93	0.74	0.02	11.27	44.77	99.36
950	4	9.44	4.64	5.22	21.31	0.00	11.91	47.74	100.25
949	4	10.02	5.03	4.28	21.24	0.00	11.85	47.21	99.62
956	4	0.01	0.02	-0.01	39.52	0.03	12.04	47.89	99.50
911	4	36.91	7.32	1.96	0.23	0.02	10.68	42.57	99.70
914	4	3.82	2.02	9.96	21.03	0.01	12.61	50.23	99.67
604	4	9.09	2.61	6.12	21.46	0.00	12.11	48.22	99.61
604	4	8.16	1.50	8.29	20.46	-0.01	12.32	49.21	99.91
945	4	35.97	6.58	2.87	0.65	0.01	10.79	43.12	99.99
945	4	13.13	4.11	3.79	20.01	0.02	11.75	46.77	99.58
28B	4	7.67	4.09	6.93	20.67	0.02	12.14	48.56	100.07
957	4	1.47	1.12	0.14	36.43	0.00	12.03	47.44	98.64

Table 5.3: Continued.

OD #	Gr.#	Fe	Mn	Mg	Ca	Si	C	O	Total
197	4	0.02	0.23	-0.01	38.93	0.01	12.07	47.78	99.03
199	4	0.05	0.05	0.00	39.45	0.01	12.04	47.86	99.46
90	4	36.34	7.22	2.20	0.31	0.01	10.74	42.70	99.50
82	4	-0.02	0.03	-0.01	39.63	0.00	12.03	47.87	99.54
113	4	7.15	2.70	8.04	20.46	0.00	12.31	49.10	99.77
79	4	0.07	0.06	-0.01	39.03	0.01	12.07	47.78	99.00
78	4	0.04	0.08	0.01	39.08	0.00	12.07	47.80	99.08
2	4	2.00	2.12	10.93	21.27	-0.01	12.73	50.78	99.82
18	4	8.77	4.28	6.23	20.39	0.00	12.06	48.12	99.85
18	4	12.69	6.67	3.02	19.70	0.01	11.59	46.30	99.98
7	4	4.38	3.89	8.74	20.53	0.00	12.45	49.50	99.48
857	4	8.48	2.54	7.67	20.45	0.00	12.20	48.90	100.24
857	4	33.53	4.31	6.31	0.12	0.01	11.19	44.88	100.35
906	4	28.73	9.80	5.29	0.88	0.00	11.10	44.48	100.27
494	4	5.10	0.48	10.42	21.04	0.01	12.61	50.47	100.14
968	4	1.45	1.68	11.70	20.53	0.00	12.87	51.09	99.31
968	4	6.72	5.19	7.07	20.24	0.00	12.15	48.55	99.93
90	4	36.04	7.97	2.00	0.24	0.01	10.70	42.58	99.55
92	4	33.53	9.76	2.56	0.76	0.01	10.72	43.01	100.36
99	4	29.97	7.13	6.50	0.27	0.00	11.24	45.01	100.12
848	4	7.66	2.58	5.53	23.43	0.03	12.12	48.26	99.61
196	4	0.13	1.12	0.09	37.46	0.02	12.09	47.60	98.51
24C	4	1.78	3.47	10.31	20.66	0.01	12.69	50.38	99.30
571	4	6.59	2.21	8.43	20.54	-0.01	12.40	49.32	99.49
571	4	10.50	1.83	7.04	20.26	0.01	12.11	48.53	100.28
571	4	4.68	3.30	9.42	20.03	0.01	12.49	49.79	99.73
571	4	5.21	2.58	9.32	20.48	0.00	12.47	49.79	99.86
929	4	0.08	0.88	0.05	38.09	0.00	12.06	47.66	98.83
852	4	0.83	0.39	1.01	36.52	0.95	12.16	49.08	100.94
931	4	0.01	0.03	-0.01	39.52	0.00	12.04	47.86	99.45
931	4	0.92	2.58	0.08	35.37	0.00	12.03	47.25	98.24
950	4	29.92	6.72	5.93	0.74	0.02	11.27	44.77	99.36
950	4	9.44	4.64	5.22	21.31	0.00	11.91	47.74	100.25
949	4	10.02	5.03	4.28	21.24	0.00	11.85	47.21	99.62
956	4	0.01	0.02	-0.01	39.52	0.03	12.04	47.89	99.50
911	4	36.91	7.32	1.96	0.23	0.02	10.68	42.57	99.70
914	4	3.82	2.02	9.96	21.03	0.01	12.61	50.23	99.67
604	4	9.09	2.61	6.12	21.46	0.00	12.11	48.22	99.61
604	4	8.16	1.50	8.29	20.46	-0.01	12.32	49.21	99.91
945	4	35.97	6.58	2.87	0.65	0.01	10.79	43.12	99.99
945	4	13.13	4.11	3.79	20.01	0.02	11.75	46.77	99.58
28B	4	7.67	4.09	6.93	20.67	0.02	12.14	48.56	100.07
957	4	1.47	1.12	0.14	36.43	0.00	12.03	47.44	98.64

Table 5.3: Continued.

OD #	Gr.#	Fe	Mn	Mg	Ca	Si	C	O	Total
111	4	7.85	3.49	6.95	20.40	0.41	12.22	49.01	100.34
111	4	9.39	3.34	6.71	20.42	0.00	12.07	48.37	100.30
17	4	10.05	5.54	4.87	19.90	0.07	11.89	47.40	99.73
17	4	10.01	6.40	3.96	20.72	0.07	11.77	47.05	100.00
135	4	4.30	3.25	9.15	20.53	0.09	12.51	49.82	99.65
685	4	4.97	2.76	9.14	20.67	0.01	12.47	49.74	99.77
502	4	3.03	6.56	7.91	20.05	0.07	12.39	49.08	99.11
686	5	40.78	5.63	0.62	0.90	0.03	10.46	42.01	100.43
686	5	36.87	7.41	2.57	0.17	0.03	10.67	42.96	100.68
686	5	20.09	8.29	11.94	0.40	0.03	11.93	48.00	100.68
831	5	44.34	2.36	0.54	0.15	0.04	10.49	41.79	99.71
841	5	5.59	3.95	8.21	20.19	0.01	12.37	49.16	99.46
798	5	5.75	2.60	9.20	20.53	0.00	12.41	49.73	100.22
798	5	9.71	7.17	3.91	20.33	0.02	11.76	46.90	99.81
813	5	0.15	0.65	0.01	37.66	0.02	12.12	47.60	98.21
686	5	34.81	11.16	0.74	0.38	0.00	10.54	41.93	99.56
686	5	22.65	8.21	10.30	0.35	0.01	11.74	47.09	100.35
847	5	1.03	2.29	0.05	35.64	0.00	12.03	47.27	98.31
89	5	38.89	3.92	1.88	1.77	0.00	10.70	42.75	99.91
1005	5	9.31	4.18	6.39	20.19	0.00	12.02	48.17	100.26
847	5	5.11	2.86	9.38	20.35	0.00	12.46	49.80	99.97
847	5	1.04	2.42	0.08	35.29	-0.01	12.04	47.22	98.09
842	5	8.85	2.52	7.37	20.36	0.00	12.19	48.72	100.00
842	5	37.78	4.00	3.56	0.12	0.01	10.88	43.38	99.73
841	5	6.03	1.14	9.79	20.69	0.00	12.50	50.05	100.19
933	5	33.40	8.45	3.43	0.06	0.02	10.88	43.34	99.59
933	5	44.06	3.58	0.13	0.05	0.02	10.41	41.54	99.80
1006	6	42.39	4.89	0.14	0.07	0.01	10.44	41.53	99.47
1006	6	41.52	5.22	0.27	0.13	0.02	10.49	41.61	99.26
1006	6	42.73	4.11	0.01	0.39	0.02	10.46	41.50	99.22
873	7	5.95	2.50	8.70	20.77	0.00	12.40	49.51	99.85
870	7	0.17	4.03	10.70	20.50	0.09	12.81	50.69	98.99
870	7	10.66	2.76	6.38	20.20	0.01	12.03	48.17	100.20
870	7	7.72	1.24	8.82	20.42	0.01	12.37	49.51	100.09
870	7	-0.01	2.84	11.48	20.85	0.01	12.89	51.05	99.11
870	7	0.11	0.06	12.92	22.27	0.01	12.97	52.00	100.33
875	7	7.21	3.25	7.58	20.49	0.00	12.26	48.87	99.67
874	7	-0.02	5.99	9.79	20.29	-0.01	12.68	50.05	98.76
874	7	10.04	2.38	6.56	19.90	0.09	12.15	48.32	99.45
873	7	0.08	0.23	12.92	21.50	0.02	13.03	51.91	99.68
880	7	0.10	3.53	11.11	20.89	0.06	12.81	50.91	99.40
878	7	0.07	0.01	13.18	21.92	0.01	13.00	52.08	100.26
878	7	9.26	2.53	7.53	20.26	0.00	12.14	48.79	100.51

Table 5.3: Continued.

OD #	Gr.#	Fe	Mn	Mg	Ca	Si	C	O	Total
876	7	0.55	4.49	10.61	20.43	0.00	12.72	50.51	99.32
876	7	7.40	4.23	7.42	20.18	0.01	12.17	48.73	100.14
876	7	0.37	0.87	-0.01	38.09	0.00	12.04	47.63	98.99
875	7	0.03	3.39	11.24	20.99	0.03	12.82	50.96	99.46
881	7	4.66	2.20	9.39	20.68	0.02	12.56	49.89	99.38
881	7	0.08	1.47	12.06	21.59	0.00	12.93	51.44	99.57
882	7	0.24	0.22	13.05	21.43	-0.01	13.01	51.93	99.87
882	7	6.56	2.89	8.15	20.67	0.00	12.33	49.20	99.80
882	7	4.61	2.56	9.62	20.74	0.01	12.50	50.00	100.04
882	7	0.01	-0.02	13.36	22.24	0.00	12.96	52.21	100.76
882	7	1.13	3.07	11.08	20.62	0.03	12.77	50.81	99.53
882	7	4.25	2.77	10.11	20.20	0.00	12.54	50.17	100.05
882	7	13.91	3.04	4.02	20.21	0.01	11.75	46.90	99.83
884	7	0.05	1.37	12.39	20.81	0.01	13.00	51.52	99.16
884	7	6.67	2.89	8.25	20.54	0.00	12.33	49.23	99.91
883	7	0.25	1.19	11.94	20.84	0.56	13.03	51.94	99.75
886	7	11.28	3.25	5.22	20.51	0.00	11.93	47.59	99.79
427	7	7.43	3.53	7.19	20.46	0.01	12.23	48.66	99.52
427	7	11.72	1.93	5.90	20.80	0.01	11.97	48.01	100.33
425	7	7.08	3.49	7.72	20.28	0.01	12.27	48.91	99.75
427	7	0.19	0.95	0.00	37.54	0.01	12.10	47.55	98.34
425	7	7.32	3.43	7.49	20.40	0.00	12.25	48.79	99.68
425	7	3.92	2.27	9.97	20.64	0.00	12.61	50.17	99.57
427	7	4.91	2.43	9.33	20.81	0.01	12.49	49.87	99.86
427	7	13.31	5.49	3.31	19.66	0.00	11.63	46.43	99.83
886	7	13.27	3.67	4.43	20.07	0.01	11.75	47.11	100.30
886	7	9.33	3.05	7.10	20.25	0.01	12.10	48.58	100.42
885	7	6.23	3.32	8.33	20.50	0.00	12.33	49.26	99.96
885	7	13.53	2.81	4.49	20.59	0.00	11.76	47.21	100.40
870	7	0.41	1.93	11.69	21.04	0.01	12.91	51.18	99.17
870	7	3.60	2.55	10.06	20.51	0.02	12.62	50.22	99.58
870	7	10.07	2.95	6.13	20.16	-0.01	12.08	48.01	99.41
870	7	9.65	2.10	6.83	20.18	0.01	12.19	48.41	99.36
870	7	10.77	3.39	6.05	20.35	0.00	11.95	48.02	100.54
874	7	0.26	3.99	10.45	20.92	0.04	12.78	50.55	98.98
873	7	0.45	0.17	12.59	21.51	0.02	13.01	51.74	99.48
873	7	8.61	2.91	6.88	20.64	0.01	12.17	48.52	99.73

Table 5.3: Continued.

OD #	Gr.#	Fe	Mn	Mg	Ca	Si	C	O	Total
649*	SG	2.72	0.99	11.31	20.96	0.01	12.78	50.94	99.72
670	-	0.86	2.56	11.50	20.39	0.08	12.86	51.06	99.31
670	-	1.42	2.70	11.22	20.29	0.07	12.81	50.88	99.39
670	-	1.28	3.13	10.83	20.41	0.02	12.79	50.64	99.09
670	-	1.76	2.88	10.83	20.02	0.35	12.80	50.97	99.60
667	-	0.77	1.66	12.29	20.72	0.00	12.90	51.42	99.75
671	-	1.67	3.14	10.99	20.17	0.00	12.75	50.66	99.39
671	-	1.58	3.20	10.98	20.26	0.01	12.75	50.67	99.45
670	-	2.79	3.66	10.23	19.65	0.05	12.66	50.23	99.28

Table 5.4: Results of the IRMS study (in ‰) on carbonates from Olympic Dam. Abbr.: carbonate (Cb), group (Gr.), calcite (Cal), siderite (Sid), dolomite-ankerite solid solution (Dol-Ank ss).

OD#	Gr.#	Cb type	dominant Cb	δ^{13}C V-PDB	δ^{18}O V-SMOW
OD829	1	Cal	Cal	-4.1	10.1
				-4.1	10.1
OD830C	1	Cal	Cal	-4.1	9.4
				-3.9	10.4
OD826	1	Cal	Cal	-4.0	12.0
				-3.9	11.3
OD830A	1	Cal	Cal	-4.0	10.5
				-3.8	11.4
OD827	1	Cal	Cal	-3.9	10.2
				-3.8	10.5
OD828	1	Cal, Sid	Cal	-3.8	10.8
				-3.8	11.1
OD819	1	Cal	Cal	-3.5	10.7
				-3.6	10.4
OD830B	1	Cal	Cal	-4.0	11.2
				-4.1	10.7
OD818	1	Cal, Dol-Ank ss	Cal	-4.0	11.1
				-4.1	10.9
OD193	2	Cal	Cal	-5.3	13.4
				-5.3	13.4
OD656	2	Sid, Sid ss	ca. 1:1 (mix)	-4.0	15.4
				-3.3	16.9
OD659	2	Sid, Sid ss	ca. 1:1 (mix)	-3.0	14.5
				-2.8	13.8
OD834	2	Sid	Sid	-4.3	12.1
				-4.4	12.0
OD835	2	Cal, Sid	Cal	-3.7	11.1
				-3.8	10.5
OD1001	2	Sid	Sid	-3.2	11.9
				-3.0	11.6
OD836	3	Dol-Ank ss, Sid, Cal	Dol-Ank ss	-3.4	12.5
				-3.6	12.7
OD838	3	Dol-Ank ss	Dol-Ank ss	-4.3	10.3
				-4.7	11.6
OD197	4	Cal	Cal	-5.4	16.0
				-5.4	15.0
OD16	4	Dol-Ank ss, Sid	Dol-Ank ss	-2.5	13.4
				-2.5	13.3

Table 5.4: Continued.

OD#	Gr.#	Cb type	dominant Cb	δ^{13}C V-PDB	δ^{18}O V-SMOW
OD78	4	Cal	Cal	-4.8	13.2
				-4.8	12.8
OD90	4	Sid ss, Dol-Ank ss	Sid ss	-2.9	14.6
OD96	4	Dol-Ank ss	Dol-Ank ss	-3.6	18.4
				-3.5	18.5
OD18	4	Dol-Ank ss	Dol-Ank ss	-2.7	15.7
				-2.7	15.4
OD2	4	Dol-Ank ss	Dol-Ank ss	-2.3	20.8
				-2.3	20.6
OD106	4	Dol-Ank ss	Dol-Ank ss	-2.2	18.0
				-2.2	18.2
OD82	4	Cal	Cal	-5.5	16.9
				-5.1	17.7
OD806	4	Cal	Cal	-4.0	12.7
				-4.3	12.5
OD95	4	Sid ss	Sid ss	-3.8	16.1
				-3.7	15.9
OD848	4	Dol-Ank ss, Cal	Cal	-6.5	16.9
				-6.4	17.0
OD853	4	Cal, Dol-Ank ss	ca. 1:1 (mix)	-2.6	17.5
				-2.5	17.8
OD186	4	Dol-Ank ss	Dol-Ank ss	-2.0	20.9
				-2.4	19.8
OD79	4	Cal	Cal	-4.8	10.3
OD686	5	Sid ss	Sid ss	-4.0	13.0
				-4.1	13.6
OD831	5	Sid	Sid	-4.9	11.5
				-4.6	11.0
OD841	5	Dol-Ank ss	Dol-Ank ss	-4.0	13.7
				-4.0	13.6
OD842	5	Sid	Sid	-4.1	16.0
				-4.1	15.8
OD847	5	Cal, Dol-Ank ss	ca. 1:1 (mix)	-3.9	13.5
				-3.9	13.7
OD1006	6	Sid ss	Sid ss	-3.2	15.2
				-3.1	15.1
OD425	7	Dol-Ank ss	Dol-Ank ss	-3.8	13.7
				-3.9	13.6

Table 5.4: Continued.

OD#	Gr.#	Cb type	dominant Cb	$\delta^{13}C$ V-PDB	$\delta^{18}O$ V-SMOW
OD873	7	Dol-Ank ss	Dol-Ank ss	-5.8	12.6
				-5.8	12.4
OD886	7	Dol-Ank ss	Dol-Ank ss	-4.7	12.0
				-4.7	11.4
OD885	7	Dol-Ank ss	Dol-Ank ss	-4.2	12.8
				-4.2	12.7
OD875	7	Dol	Dol	-4.2	19.1
				-4.2	19.0
OD870	7	Dol	Dol	-3.6	24.3
				-3.7	24.2

Table 6.1: All Rb-Sr and Sm-Nd isotopic data for Olympic Dam carbonates.

OD #	fraction #	drillhole	depth, m	mineral	Rb ppm	Sr ppm	$^{87}Rb/^{86}Sr$	$^{87}Sr/^{86}Sr$	Sm ppm	Nd ppm	$^{147}Sm/^{144}Nd$	$^{143}Nd/^{144}Nd$	εNd	age t, Ma	$^{87}Sr/^{86}Sr_t$	$εNd_t$
assoc. 1 carbonates in felsic unit																
OD 817.1		RD2773	2036.3	Anh	0.03	1,690	0.00006	0.720432	6.03	45.91	0.0793	0.511259	-26.7	1593	0.72043	-2.9
OD 817.2		RD2773	2036.3	Anh	0.93	1,424	0.0019	0.718045	5.35	41.25	0.0783	0.511226	-27.4	1593	0.71800	-3.4
OD 818	11	RD2773	2036.7	Cal	2.49	139.6	0.052	0.723206	4.78	28.17	0.1026					
OD 819	12	RD2773	2051.3	Cal	0.50	97.5	0.015	0.717110	6.44	25.91	0.1502	0.511937	-13.5	1593	0.71677	-4.2
OD 826	47	RD2773	2179.2	Cal	0.12	97.5	0.0037	0.710388	5.54	18.03	0.1854	0.512349	-5.5	1593	0.71031	-3.3
OD 826.2		RD2773	2179.2	Cal	0.13	84.06	0.0046	0.712175	5.49	16.76	0.1980	0.512459	-3.3	1593	0.71207	-3.8
OD 827	41	RD2773	2182.4	Cal	0.11	93.2	0.0035	0.710819	3.42	17.10	0.1206	0.511684	-18.5	1593	0.71074	-3.1
OD 827.2		RD2773	2182.4	Cal	0.16	83.80	0.0057	0.713625	3.91	18.66	0.1264	0.511714	-17.9	1593	0.71350	-3.7
OD 829	42	RD2773	2208.5	Cal	0.11	107.4	0.0030	0.712044	19.80	71.35	0.1675	0.512150	-9.4	1593	0.71198	-3.6
OD 829.2		RD2773	2208.5	Cal	0.10	103.7	0.0027	0.711527	26.56	97.51	0.1644	0.512100	-10.3	1593	0.71147	-3.9
OD 830A	13	RD2773	2238.4	Cal	0.02	87.5	0.0008	0.710094	8.99	54.22	0.1001	0.511458	-22.9	1593	0.71008	-3.3
OD 830C.1	24	RD2773	2294.5	Cal	0.11	165.8	0.0020	0.716610	7.67	16.13	0.2876			1593	0.71657	
OD 830C.2		RD2773	2294.5	Cal	0.42	85.67	0.0143	0.711096	7.04	40.09	0.1061	0.511511	-21.8	1593	0.71077	-3.5
OD 830C.3		RD2773	2294.5	Cal	0.27	156.3	0.0050	0.718297	9.18	20.99	0.2640	0.513100	9.2	1593	0.71818	-4.7

Table 6.1: Continued.

OD #	fraction #	drillhole	depth, m	mineral	Rb ppm	Sr ppm	$^{87}Rb/^{86}Sr$	$^{87}Sr/^{86}Sr$	Sm ppm	Nd ppm	$^{147}Sm/^{144}Nd$	$^{143}Nd/^{144}Nd$	εNd	age t, Ma	$^{87}Sr/^{86}Sr_t$	$εNd_t$
assoc. 2 carbonates in granite-dominated breccia																
OD 193	5	RD2773	1172.1	Cal	0.01	39.0	0.0006	0.719175	2.90	20.39	0.0858	0.511445	-23.1	1593	0.71916	-0.6
OD 667	8	RD2319	760.1	Dol-Ank	0.22	13.4	0.0466	0.716395	1.19	5.39	0.1335			1593	0.71535	
OD 835	14	RD2786A	1753.2	Cal	0.15	84.8	0.0050	0.712139	5.83	35.28	0.0998	0.511451	-23.0	1593	0.71203	-3.4
OD 656	19	RD1172	571.5	Sid	3.74	6.2	1.750	0.751560	0.37	0.91	0.2459			1593	0.71224	
OD 687	27	RD2715	855.7	Sid	0.72	4.2	0.497	0.723364	7.90	43.99	0.1086			1593	0.71220	
OD 674	33	RD2681	718.3	Sid	20.61	20.6	2.890	0.752411	2.71	8.08	0.2029			1593	0.68748	
OD 665	58	RD2143	787.6	Sid	11.21	321.1	0.1009	0.723039	9.93	45.27	0.1324	0.512518	-2.2	1593	0.72077	10.9
OD 659	6	RD1705	493.8	Sid	1.66	11.7	0.4101	0.722635	3.07	20.43	0.0909			1593		
OD 661	7	RD2063	680.3	Dol-Ank	0.09	17.6	0.0141	0.729437	3.53	9.69	0.2202	0.512019	-11.9	1593	0.72912	-16.9
OD 660	29	RD2016	622.3	Dol-Ank	0.71	520.5	0.0039	0.715620	1.73	10.29	0.1014	0.511306	-25.8	1593	0.71553	-6.5
OD 662	34	RD2143	542.1	Sid	0.14	10.0	0.0416	0.710679	1.16	8.14	0.0862			1593		
OD 675	59	RD2681	731.8	Sid	0.06	109.5	0.0017	0.713897	483	3236	0.0903			1593	0.71386	
OD 1001	55	underground grab sample		Sid, oolite	0.57	213.9	0.0077	0.708831	14.53	89.43	0.0981	0.511421	-23.6	1593	0.70866	-3.6
assoc. 3 carbonates in green sandstone																
OD 226.6 vein		RD1624	584.2	Dol-Ank	1.73	122.4	0.0408	0.718450	5.06	20.27	0.1508	0.511909	-14.1	1593	0.71753	-4.8
OD 187	21	RD2821	627.9	Dol-Ank, (Sid-Mag)	0.36	139.2	0.0075	0.736650	3.65	8.97	0.2460	0.513012	7.5	1593	0.73648	-2.8
assoc. 3 carbonates in red sandstone																
OD 836	39	RD2786A	1796.2	Dol-Ank	0.11	80.8	0.0038	0.70769	0.94	4.79	0.1187	0.511711	-17.9	1593	0.70760	-2.2
OD 839	40	RD2786A	1896.5	Dol-Ank	0.50	210.1	0.0068	0.71132	2.25	10.59	0.1281	0.511485	-22.3	1593	0.71117	-8.5
OD 837	45	RD2786A	1847.8	Dol-Ank	0.17	557.5	0.0009	0.72280	4.14	14.10	0.1773	0.511418	-23.6	1593	0.72278	-19.9

Table 6.1: Continued.

OD #	fraction #	drillhole	depth, m	mineral	Rb ppm	Sr ppm	$^{87}Rb/^{86}Sr$	$^{87}Sr/^{86}Sr$	Sm ppm	Nd ppm	$^{147}Sm/^{144}Nd$	$^{143}Nd/^{144}Nd$	εNd	age t, Ma	$^{87}Sr/^{86}Sr_t$	$εNd_t$
assoc. 4 carbonates in basalt (~1590 Ma)																
OD 95	1	RD2715	836.3	Sid	0.37	24.1	0.0450	0.72404	3.79	14.74	0.1551	0.511962	-13.0	1593	0.72303	-4.7
OD 18	3	RD2744	821.2	Dol-Ank	0.22	56.1	0.0112	0.72246	26.36	61.94	0.2570	0.512163	-9.1	1593	0.72221	-21.6
OD 106	4	RD2031W1	889.1	Dol-Ank	4.30	66.1	0.1880	0.72121	18.91	58.57	0.1950	0.511994	-12.4	1593	0.71698	-12.2
OD 806	10	RD2773	1263.1	Cal	0.02	123.3	0.0006	0.72064	0.68	3.77	0.1088	0.512284	-6.7	1593	0.72063	11.1
OD 684	35	RD2715	839.2	Sid	2.91	17.1	0.491	0.72864	14.43	60.75	0.1437			1593	0.71761	
OD 197	20	RD2773	1248.5	Cal	0.03	34.6	0.0028	0.72006	2.05	8.72	0.1422	0.511754	-17.1	1593	0.72000	-6.1
OD 16	22	RD2744	761.4	Dol-Ank	0.30	109.3	0.0081	0.71639	46.82	59.65	0.4740	0.512569	-1.2	1593	0.71621	-58.2
OD 78	23	RD2773	1255.2	Cal	0.08	58.4	0.0041	0.72454	0.16	0.94	0.1030			1593	0.72444	
OD 134	26	RD1763	864.5	Dol-Ank	0.10	58.7	0.0047	0.72063	4.81	36.36	0.0800			1593	0.72052	
OD 2	28	RU39-5426	224.4	Dol-Ank	0.19	226.9	0.0024	0.72964	5.74	22.63	0.1531	0.512538	-1.8	1593	0.72959	7.0
OD 102	49	RD2018B	812.8	Dol-Ank	0.27	103.5	0.0074	0.71611	2.10	5.71	0.2225	0.512221	-8.0	1593	0.71595	-13.5
OD 114	50	RD271	650.5	Cal	1.56	15.0	0.3007	0.72521	0.30	1.00	0.1815			1593	0.71845	
OD 82	51	RD2773	1331.7	Cal	77.86	150.8	1.492	0.73940	0.28	5.89	0.0288			1593	0.70587	
OD 199	53	RD2773	1329.2	Cal	0.38	89.0	0.0122	0.72186	0.06	0.21	0.1728			1593	0.72159	
OD 914.6		RD2715	852.6	Dol-Ank	2.36	13.3	0.514	0.727686	10.56	32.77	0.1963	0.512599	-0.6	1593	0.71613	-0.7
OD 906		RD2715	810.1	Sid	1.36	431.0	0.0092	0.718387						1593	0.71818	
assoc. 4 carbonates in picrite (~1590 Ma)																
OD 868	43	RD1756	342	Dol-Ank	2.70	40.4	0.193	0.719914	25.63	35.8	0.4337			1593	0.71557	
OD 494.6		RD3564	368.9	Dol-Ank	3.09	109.13	0.0819	0.713336	13.40	58.49	0.1383	0.512126	-9.8	1593	0.71149	2.0
assoc. 4 carbonates dolerites (~825 Ma)																
OD 857	30	RU39-5426	238	Dol-Ank	6.23	131.6	0.137	0.72488	7.57	20.21	0.2263	0.512851	4.3	827	0.72330	1.1
OD 852	31	RU65-8230	596	Cal	0.17	62.1	0.0079	0.71872	6.38	18.67	0.2064	0.512746	2.3	827	0.71863	1.2
OD 848	15	RU65-8230	529	Dol-Ank	0.22	72.3	0.0088	0.72329	9.00	34.25	0.1590			827	0.72319	
OD 186	46	RD2821	608	Dol-Ank	1.07	30.2	0.1025	0.72601	3.93	51.84	0.0458	0.511804	-16.1	827	0.72482	-0.2
OD 79	48	RD2773	1271	Cal	0.65	262.6	0.0072	0.71925						827	0.71916	

Table 6.1: Continued.

OD #	fraction #	drillhole	depth, m	mineral	Rb ppm	Sr ppm	$^{87}Rb/^{86}Sr$	$^{87}Sr/^{86}Sr$	Sm ppm	Nd ppm	$^{147}Sm/^{144}Nd$	$^{143}Nd/^{144}Nd$	εNd	age t, Ma	$^{87}Sr/^{86}Sr_t$	$εNd_t$
assoc. 5 carbonates in massive barite-fluorite-siderite veins																
OD 686	9	RD2715	855	Sid	2.97	7.0	1.227	0.73561	23.73	177.7	0.0808			500	0.72702	
OD 831	25	RD2786A	1601	Sid	0.06	2.0	0.0852	0.74123	0.03	0.08	0.1979			500	0.74063	
OD 842	2	RD2786A	2160	Sid	0.08	46.8	0.0048	0.75229	0.05	0.12	0.2334			500	0.75225	
OD 1005	32	underground grab sample		Dol-Ank	2.72	688.0	0.0114	0.71523	5.04	17.07	0.1782	0.511358	-24.8	500	0.71515	-23.7
OD 841	54	RD2786A	1949	Dol-Ank	0.02	45.8	0.0016	0.72553	0.08	0.2	0.2200			500	0.72552	
assoc. 6 laminated carbonate																
OD 1006_ core	36	RU36-8834	69	Sid	0.34	79.6	0.0124	0.72297	6.34	52.97	0.0722	0.511182	-28.2	1593	0.72269	-3.0
OD 1006_ rim1	37	RU36-8834	69	Sid	0.02	4.4	0.0146	0.71674	0.97	5.61	0.1046			1593	0.71641	
OD 1006_ rim2	38	RU36-8834	69	Sid	0.03	39.8	0.0018	0.71784	0.92	4.91	0.1137	0.511425	-23.5	1593	0.71780	-6.7
OD 1045		RU36-8834	62.2	Sid	0.075	18.66	0.0115	0.71772	4.07	27.27	0.0901	0.511380	-24.4	1593	0.71746	-2.8
OD 1047		RU36-8834	70.2	Sid	0.087	4.98	0.0503	0.71902	6.95	37.51	0.1118	0.511503	-22.0	1593	0.71789	-4.8
OD 1048		RU36-8834	71.4	Sid	0.189	13.27	0.0411	0.72383	4.54	29.20	0.0938	0.511272	-26.5	1593	0.72291	-5.6
OD 1050		RU36-8771	105	Sid	0.053	6.75	0.0227	0.71680	1.43	4.51	0.1913	0.512412	-4.2	1593	0.71628	-3.3
OD 1051		RU36-8771	108.5	Sid	0.080	2.86	0.0804	0.71678	0.78	3.07	0.1526	0.511968	-12.9	1593	0.71497	-4.1
OD 1008		RU36-8834	64.6	Sid	0.029	15.88	0.0052	0.71475	5.64	36.00	0.0946	0.511367	-24.6	1593	0.71464	-3.9
OD 1008_1		RU36-8834	64.6	Sid	0.11	7.64	0.0426	0.71843	0.61	3.08	0.1207	0.511624	-19.6	1593	0.71747	-4.2
OD 1008_3		RU36-8834	64.6	Sid	0.068	4.67	0.0423	0.71649	0.51	2.34	0.1313	0.511708	-18.0	1593	0.71554	-4.8
OD 1008_4		RU36-8834	64.6	Sid	0.076	4.63			0.59	2.93	0.1218	0.511637	-19.4	1593		-4.2
OD 1008_8		RU36-8834	64.6	Sid	0.059	3.35	0.0513	0.71519						1593	0.71404	
OD 1008_10		RU36-8834	64.6	Sid	0.060	3.61	0.0482	0.71577	0.52	2.43	0.1287	0.511712	-17.9	1593	0.71469	-4.2

Table 6.1: Continued.

OD #	fraction #	drillhole	depth, m	mineral	Rb ppm	Sr ppm	$^{87}Rb/^{86}Sr$	$^{87}Sr/^{86}Sr$	Sm ppm	Nd ppm	$^{147}Sm/^{144}Nd$	$^{143}Nd/^{144}Nd$	εNd	age t, Ma	$^{87}Sr/^{86}Sr_t$	$εNd_t$
assoc. 7 carbonate matrix in conglomerate at unconformity																
OD 425	57	RD3564	364	Dol-Ank	0.85	59.0	0.0418	0.72327	6.07	9.76	0.3752	0.512151	-9.3	500	0.72298	-20.8
OD 886_1 fawn	17	RD2972	388	Dol-Ank	0.07	411.8	0.0005	0.71990	3.67	9.31	0.2377	0.511733	-17.5	500	0.71990	-20.2
OD 886_2		RD2972	388	Dol-Ank					6.63	11.50	0.3482	0.511883	-14.6	500		-24.3
OD 886_3		RD2972	388	Dol-Ank					5.88	10.40	0.3411	0.511819	-15.8	500		-25.1
OD 873_1	60	RD1629	330	Dol-Ank	0.07	144.0	0.0014	0.71618	9.58	10.55	0.5484	0.512624	-0.1	500	0.71617	-22.7
OD 873_2		RD1629	329.6	Dol-Ank					13.21	15.08	0.5290	0.512580	-1.0	500		-22.3
OD 873_3		RD1629	329.6	Dol-Ank					14.31	16.89	0.5116	0.512550	-1.6	500		-21.8

abbreviations: cal=calcite, dol=dolomite, ank=ankerite, sid=siderite and its solid solution, anh=anhydrite

OD830A and C are from different depths of same drillcore; OD830C1,2,3 refer to different sub-samples of calcite

OD1006 core and rim1, rim 2 refer to siderite in a breccia clast and in siderite overgrowths, respectively, see Apukhtina et al. (in preparation b)

OD1008 is a large chip of siderite; OD1008.1 to .10 are spot samples obtained by micro-drilling of siderite elsewhere in OD1008

Sm-Nd concentrations and Sm/Nd ratio by isotope dilution, external precision ±0.2%

Rb-Sr concentrations and Rb/Sr ratios from trace element data for the sample solutions, see text for details

Typical within-run precision(2se) is ±0.000020 ($^{87}Sr/^{86}Sr$) and ±0.000012 ($^{143}Nd/^{144}Nd$)

Table 6.2: U-Th-Pb isotope data for Olympic Dam carbonates (associations 1 and 6). Abbr.: anhydrite (Anh), calcite (Cal), siderite (Sid).

OD#	drillhole	depth, m	mineral	U ppm	Th ppm	Pb ppm	$^{238}U/^{204}Pb$	$^{232}Th/^{204}Pb$	$^{206}Pb/^{204}Pb$	$^{207}Pb/^{204}Pb$	$^{208}Pb/^{204}Pb$
assoc. 1 carbonates in felsic unit											
OD826	RD2773	2179.2	Cal pink	0.09	0.14	9.2	0.63	0.98	18.420	15.728	36.965
OD827	RD2773	2182.4	Cal pink	0.08	0.04	12.1	0.42	0.20	17.947	15.660	36.734
OD829	RD2773	2208.5	Cal white	0.09	0.09	6.4	0.87	0.96	18.294	15.681	37.355
OD830.1	RD2773	2238.4	Cal pink	0.23	0.03	14.2	1.01	0.12	19.098	15.768	36.927
OD830.2	RD2774	2238	Cal white	0.03	0.01	17.3	0.10	0.04	24.640	16.391	39.079
OD817.1	RD2773	2036.3	Anh, fine-grained, with apatite	0.81	0.07	8.6	16.14	1.51	109.653	24.649	62.897
assoc. 6 laminated carbonate											
OD1045	RU36-8834	62.2	Sid	5.18	0.25	61.7	5.25	0.260	19.248	15.685	36.376
OD1047	RU36-8834	70.2	Sid	13.83	0.90	48.8	17.93	1.202	19.954	15.779	36.418
OD1048	RU36-8834	71.4	Sid	165.64	1.22	89.4	116.38	0.884	19.667	15.751	36.300
OD1050	RU36-8771	105	Sid	0.55	0.02	148.1	0.22	0.009	16.664	15.506	36.202
OD1051	RU36-8771	108.5	Sid	0.37	0.02	79.1	0.28	0.017	16.853	15.522	36.210
OD1008	RU36-8834	64.6	Sid	11.22	0.32	60.5	11.53	0.342	19.019	15.661	36.301
OD1008.1	RU36-8834	64.6	Sid	2.06	0.03	27.2	4.70	0.082	18.868	15.740	36.345
OD1008.3	RU36-8834	64.6	Sid	1.04	0.02	31.3	2.05	0.039	18.328	15.694	36.313
OD1008.4	RU36-8834	64.6	Sid	2.41	0.03	30.6	4.89	0.056	18.816	15.723	36.331
OD1008.8	RU36-8834	64.6	Sid	2.06	0.02	32.1	3.96	0.044	18.449	15.692	36.301
OD1008.10	RU36-8834	64.6	Sid	0.99	0.01	30.5	2.00	0.029	18.618	15.730	36.329

U-Th-Pb concentrations and U/Pb-Th/Pb ratios from trace element data for the sample solutions, see text for details
Typical within-run precision (2se) for Pb isotope ratios is ±0.001 for $^{206}Pb/^{204}Pb$ and $^{207}Pb/^{204}Pb$, and ±0.003 for $^{208}Pb/^{204}Pb$

Table 6.3: Lu-Hf isotope data for Olympic Dam carbonates (associations 1 and 6).

sample	core	depth, m	ppb Lu	2sd%	ppb Hf	2sd%	$^{176}Lu/^{177}Hf$	2sd%	$^{176}Hf/^{177}Hf$	2sd%	rho	molar	model age
assoc. 1 calcite													
OD826	RD2773	2179.2	1296	0.6	1.09	0.7	1496	0.8	43.03	0.6	-0.01	46.40	1.510
OD826.2*	RD2773	2179.2	772	0.3	0.96	0	262.41	0.3	7.32	0.1	-0.01	13.30	1.418
OD827.2*	RD2773	2182.4	633	0.4	0.54	0.2	926.7	0.4	25.39	0.2	-0.01	21.50	1.432
OD829	RD2773	2208.5	5686	3.4	4.25	2	9633	3.5	271	1.6	-0.04	174.10	1.487
OD829.2	RD2773	2208.5	8248	1.3	6.13	0.2	9232	1.3	258	0.1	0.04	113.60	1.477
OD830C1.2	RD2773	2294.5	1106	0.5	0.91	0	1996	0.6	58.0	0.2	0.03	34.60	1.528
OD830C2	RD2773	2294.5	6729	4.2	5.71	0.7	26137	4.2	847	0.5	0.04	265.50	1.707
OD830C2.2*	RD2773	2294.5	5636	2.0	3.94	0.1	2831	2.0	70.9	0.1	0.01	91.20	1.320
assoc. 6 siderite													
1008.2	RU36-8834	64.6	99.4	0.4	0.94	0.2	16.71	0.5	0.8753	0.2	-0.02	13.70	1.870
1045.2	RU36-8834	62.2	230.6	0.3	0.53	0.2	98.46	0.4	3.546	0.2	0.09	7.64	1.747
1047	RU36-8834	70.2	222.3	0.3	2.07	0.05	16.59	0.3	0.7563	0.07	0.02	90.48	1.511
1047.2	RU36-8834	70.2	120.4	0.2	1.88	0.02	9.536	0.2	0.5547	0.06	0.00	31.91	1.512
1048	RU36-8834	71.4	201.6	0.2	5.90	0.04	4.976	0.2	0.4246	0.06	0.00	294.46	1.517
1048.2	RU36-8834	71.4	92.6	0.2	6.90	0.03	1.928	0.2	0.3494	0.05	0.00	165.44	1.851
1050.2	RU36-8771	105	166.8	0.5	0.48	0.1	65.67	0.5	2.115	0.2	0.02	7.82	1.475
1051	RU36-8771	108.5	7.0	0.2	0.062	0.05	17.15	0.2	0.7339	0.08	0.11	2.59	1.394
1051.2	RU36-8771	108.5	1686	0.3	9.86	0.1	27.68	0.3	1.047	0.1	0.00	151.83	1.460

suffix .2 denotes second digestion for same powder; * marks digestions affected by sample loss during dissolution

Lu and Hf ppb measured by isotope dilution; molar sample/blank ratio, see text for details; note that data have not been corrected for blank

Lu-Hf model ages are 2-point model ages calculated with a common Hf anchor composition of $^{176}Lu/^{177}Hf = 0.015$, $^{176}Hf/^{177}Hf = 0.28216$

Table A.1: Major, minor and trace elements (in ppm) of solution analyses of carbonates performed on Q-ICPMS at University of Melbourne. Table includes a selection of elements.

mineral	OD#	Rb	Sr	Y	La	Ce	Pr	Nd	Sm	Eu	Gd	Tb	Dy	Ho	Er	Tm	Yb	Lu	Hf	Pb	Th	U
carbonate	95	0.37	24.1	37	8.362	21.084	2.672	10.501	2.758	0.571	3.502	0.795	5.735	1.367	4.770	1.088	10.119	1.672	0.00	5.5	0.0	5.2
carbonate	842	0.08	46.8	17	0.181	0.316	0.033	0.124	0.048	0.050	0.149	0.065	0.803	0.284	1.254	0.306	2.938	0.559	0.00	1.5	0.0	0.0
carbonate	18	0.22	56.1	65	13.859	53.463	9.656	50.049	21.622	7.218	27.033	3.485	15.198	2.333	4.802	0.571	3.268	0.433	0.00	1.9	0.2	0.0
carbonate	106	4.30	66.1	149	23.074	65.205	9.586	42.612	14.023	6.007	20.920	3.642	21.667	4.441	11.024	1.411	8.034	1.163	0.01	2.4	0.1	4.7
carbonate	193	0.01	39.0	27	53.650	72.544	6.598	21.141	3.036	0.593	2.800	0.531	3.663	0.909	2.939	0.517	3.902	0.610	0.00	0.1	0.0	0.0
carbonate	659	1.66	11.7	23	22.221	47.663	6.008	20.434	3.068	0.671	2.992	0.482	3.066	0.674	2.049	0.299	1.970	0.249	0.05	138.2	0.8	39.7
carbonate	661	0.09	17.6	19	6.765	17.494	2.286	9.660	3.540	1.050	5.199	0.758	3.854	0.728	1.977	0.300	2.090	0.321	0.00	2.5	0.2	18.9
carbonate	667	0.22	13.4	21	7.812	18.109	1.841	5.386	1.185	0.332	1.461	0.384	3.232	0.872	3.125	0.588	4.882	0.873	0.00	0.8	0.2	1.0
carbonate	686	2.97	7.0	56	277.805	533.662	55.279	177.711	23.735	5.205	15.496	2.091	11.775	2.504	8.793	1.751	16.773	2.562	0.03	4.4	1.4	10.4
carbonate	806	0.02	123.3	5	4.519	8.256	0.947	3.864	0.690	0.263	0.808	0.118	0.706	0.159	0.462	0.068	0.485	0.086	0.01	1.0	0.0	0.0
carbonate	818	2.49	139.6	25	36.623	72.738	8.106	28.166	4.781	1.164	4.947	0.744	4.113	0.808	2.190	0.337	2.382	0.385	0.00	10.7	0.2	2.7
carbonate	819	0.50	97.5	78	26.226	53.041	6.533	25.780	6.269	1.600	9.287	1.606	10.107	2.169	6.087	0.903	5.913	0.833	0.00	11.6	0.1	0.3
carbonate	830A	0.02	87.5	56	69.086	157.471	17.349	58.004	9.643	1.907	9.122	1.564	9.475	1.992	5.892	0.990	7.660	1.295	0.00	7.3	0.0	0.0
carbonate	835	0.15	84.8	141	70.433	120.190	11.600	35.435	5.905	2.470	9.100	2.612	21.969	5.384	17.531	3.011	21.459	3.299	0.01	3.4	0.1	0.5
carbonate	848	0.22	72.3	76	19.450	53.427	7.813	34.247	9.000	2.118	11.196	1.941	12.554	2.767	7.642	1.084	6.337	0.909	0.00	10.9	0.0	0.0
carbonate	*649*	0.32	13.2	130	8.293	21.830	3.655	20.916	8.498	2.391	13.357	2.555	18.079	4.349	13.445	2.213	14.925	2.032	0.00	1.0	0.2	0.0
carbonate	886_1 fawn	0.07	411.8	33	1.055	4.720	1.859	9.326	3.731	1.778	5.889	1.308	7.493	1.351	3.361	0.488	3.205	0.448	0.01	1.6	0.0	0.0
carbonate	870_1	3.01	29.3	34	2.928	5.506	1.374	9.280	8.766	2.962	14.728	1.707	7.288	1.212	2.846	0.392	2.474	0.366	0.05	3.6	1.2	0.4
carbonate	656	3.74	6.2	3	0.894	1.918	0.221	0.907	0.373	0.141	0.507	0.103	0.660	0.142	0.434	0.077	0.629	0.108	0.04	4.8	0.7	8.6
carbonate	197	0.03	34.6	31	6.960	18.354	2.366	9.409	2.201	0.530	2.516	0.544	4.053	1.026	3.452	0.634	4.976	0.784	0.00	0.1	0.0	0.0
carbonate	187	0.36	139.2	1	1.280	3.149	0.463	1.990	0.440	-0.195	0.368	0.047	0.218	0.037	0.087	0.013	0.079	0.011	0.00	0.4	0.0	0.0
carbonate	16	0.30	109.3	109	2.451	20.661	6.403	53.046	42.068	13.072	39.666	4.981	24.672	4.428	11.300	1.627	10.748	1.536	0.00	2.6	0.1	0.1
carbonate	78	0.08	58.4	1	1.849	2.514	0.255	0.936	0.159	0.213	0.173	0.021	0.121	0.026	0.074	0.010	0.072	0.013	0.00	0.6	0.0	0.0
carbonate	830c white	0.11	165.8	545	6.474	24.096	3.605	16.134	7.672	2.290	15.889	5.098	48.285	14.524	53.613	9.132	58.981	8.385	0.01	8.8	0.0	0.0
carbonate	831	0.06	2.0	3	0.115	0.207	0.022	0.081	0.027	0.009	0.081	0.036	0.371	0.118	0.538	0.163	1.963	0.419	0.00	1.3	0.0	0.0
carbonate	134	0.10	58.7	18	66.255	117.385	11.852	36.362	4.815	1.750	3.955	0.703	3.843	0.728	1.851	0.264	1.677	0.246	0.14	24.0	1.1	19.9
carbonate	687	0.72	4.2	123	71.548	127.550	13.233	43.988	7.901	2.059	8.722	2.207	19.258	5.315	20.777	4.575	40.097	6.501	0.01	4.9	0.5	18.8
carbonate	2	0.19	226.9	31	11.884	30.426	4.810	24.853	6.299	1.738	7.265	0.935	4.780	0.876	1.999	0.255	1.385	0.192	0.01	2.9	0.0	0.0
carbonate	660	0.71	520.5	2	11.973	24.319	3.029	10.517	1.897	-0.294	1.108	0.106	0.419	0.064	0.125	0.014	0.081	0.011	0.03	2.4	0.1	0.5
carbonate	857	6.23	131.6	61	10.811	25.481	4.018	21.065	7.918	2.372	11.135	1.849	10.975	2.202	5.540	0.770	4.309	0.621	0.00	15.8	0.0	1.5
carbonate	852	0.17	62.1	53	9.568	24.910	3.884	19.176	6.604	2.624	8.843	1.494	8.929	1.817	4.551	0.616	3.246	0.469	0.00	21.4	0.0	0.0
carbonate	1005	2.72	688.0	149	10.779	29.121	4.120	14.692	4.309	2.625	6.710	2.660	26.606	6.867	20.687	3.516	21.388	2.770	0.11	2.7	1.0	57.0
carbonate	674	20.61	20.6	14	9.326	19.540	2.237	8.081	2.707	0.815	4.747	0.623	3.191	0.584	1.608	0.281	1.729	0.296	0.04	3.8	5.8	25.3
carbonate	662	0.14	10.0	12	15.734	25.829	2.620	8.142	1.159	1.646	1.154	0.226	1.999	0.542	2.103	0.449	3.904	0.666	0.00	2.1	0.1	5.5
carbonate	684	2.91	17.1	37	43.408	103.651	14.016	60.746	14.427	3.487	13.099	1.684	7.852	1.311	3.541	0.685	6.337	1.049	0.01	3.6	0.4	0.9
carbonate	1006_ core	0.34	79.6	19	213.292	383.332	30.913	85.706	7.709	1.308	4.705	0.647	3.518	0.763	2.271	0.412	2.304	0.363	0.00	33.1	1.4	9.1

Table A.1: Continued.

mineral	OD#	Rb	Sr	Y	La	Ce	Pr	Nd	Sm	Eu	Gd	Tb	Dy	Ho	Er	Tm	Yb	Lu	Hf	Pb	Th	U
carbonate	1006_ rim1	0.02	4.4	5	4.559	11.259	1.419	5.613	0.973	0.193	0.757	0.108	0.738	0.176	0.659	0.153	1.389	0.258	0.01	27.3	0.1	0.6
carbonate	1006_ rim2	0.03	39.8	7	4.314	11.073	1.325	5.007	0.953	0.034	0.980	0.179	1.192	0.277	0.899	0.178	1.333	0.213	0.00	62.9	0.1	8.2
carbonate	836	0.11	80.8	16	6.961	13.183	1.494	5.042	0.982	0.758	1.225	0.271	2.123	0.544	1.828	0.364	2.554	0.429	0.00	4.2	0.0	0.3
carbonate	839	0.50	210.1	39	15.525	30.588	3.288	10.717	2.336	1.506	2.949	0.775	6.306	1.555	4.899	0.936	6.729	1.116	0.00	4.9	0.0	0.1
carbonate	827	0.11	93.2	38	21.921	44.289	4.905	17.722	3.534	0.796	4.646	0.792	4.942	1.074	3.089	0.476	3.138	0.495	0.00	11.1	0.0	0.1
carbonate	829	0.11	107.4	197	35.592	120.428	16.777	67.831	18.846	2.686	21.283	4.574	31.718	7.278	22.792	3.920	29.439	5.083	0.01	5.9	0.0	0.0
carbonate	868	2.70	40.4	65	9.438	32.302	6.169	35.751	25.628	7.875	34.509	5.064	20.653	2.664	4.802	0.533	2.896	0.346	0.03	3.1	0.4	4.2
carbonate	837	0.17	557.5	91	15.222	36.902	4.377	14.615	4.463	2.370	5.844	1.843	15.928	3.971	11.900	1.792	12.131	1.894	0.01	1.5	0.0	0.0
carbonate	186	1.07	30.2	58	11.451	20.533	14.939	53.067	4.048	1.946	7.667	1.105	7.500	1.744	4.423	0.582	3.183	0.488	0.04	2.8	0.1	0.7
carbonate	826	0.12	97.5	66	18.096	40.653	4.804	18.769	5.768	1.469	9.265	1.625	9.551	1.973	5.553	0.888	6.513	1.125	0.00	9.2	0.0	0.0
carbonate	79	0.65	262.6	5	6.070	11.167	35.208	116.904	1.316	2.575	4.622	0.187	1.862	0.400	0.301	0.038	0.205	0.027	0.05	54.5	0.0	0.1
carbonate	102	0.27	103.5	30	4.388	10.113	1.368	5.879	2.176	1.835	3.544	0.778	5.264	1.120	2.838	0.380	2.423	0.350	0.01	1.5	0.0	0.0
carbonate	114	1.56	15.0	1	0.539	1.368	0.207	1.003	0.303	0.118	0.345	0.051	0.274	0.050	0.114	0.015	0.083	0.011	0.00	0.6	0.0	0.0
carbonate	82	77.86	150.8	1	10.248	11.759	1.910	5.888	0.278	0.148	0.334	0.034	0.220	0.042	0.092	0.014	0.096	0.017	0.20	0.8	0.3	0.5
carbonate	199	0.38	89.0	4	0.139	0.271	0.046	0.206	0.065	0.070	0.181	0.038	0.332	0.105	0.391	0.070	0.521	0.095	0.00	0.2	0.0	0.0
carbonate	841	0.02	45.8	2	0.425	0.696	0.071	0.223	0.083	0.008	0.125	0.039	0.342	0.088	0.297	0.056	0.505	0.092	0.00	0.4	0.0	0.2
carbonate	1001	0.57	213.9	177	81.748	203.184	24.722	91.054	14.849	4.307	15.051	1.795	10.156	2.424	7.894	1.419	11.247	2.049	0.00	4.3	10.3	3.7
carbonate	875	18.50	44.1	19	27.889	49.705	5.346	21.866	7.642	2.106	9.562	1.062	4.369	0.698	1.576	0.208	1.261	0.187	0.72	2.5	2.6	0.7
carbonate	425	0.85	59.0	36	4.058	11.999	1.985	10.150	6.343	3.265	9.284	1.599	8.365	1.496	3.710	0.536	3.528	0.512	0.02	0.8	0.4	0.3
carbonate	665	11.21	321.1	40	30.431	75.881	10.628	47.042	10.416	2.410	9.435	1.305	7.318	1.480	3.996	0.592	3.683	0.543	4.32	10.7	1.9	0.5
carbonate	675	0.06	109.5	83	3048.062	7469.431	905.714	3236.351	483.952	111.619	265.896	19.642	51.383	5.019	7.020	0.692	4.019	0.519	-0.01	10.4	0.1	94
carbonate	873	0.07	144.0	56	0.865	7.218	1.833	11.444	10.409	7.927	17.652	2.973	14.691	2.421	5.509	0.719	4.094	0.513	0.01	1.1	0.0	0.1
carbonate	226	1.76	122.14		14.63	38.03	5.03	20.84	5.23	1.94	6.24	1.00	5.57	1.01	2.43	0.31	1.98	0.28		7.77	0.33	0.51
carbonate	914	2.41	13.2		19.84	55.90	7.93	33.76	10.98	2.66	11.75	2.32	13.77	2.60	6.79	0.99	6.34	0.83		1.36	0.11	0.15
carbonate	494	3.08	109.0		65.56	128.19	15.16	60.19	13.81	1.90	11.12	1.43	6.53	1.06	2.49	0.34	2.14	0.28		4.83	0.53	1.50
carbonate	1008	29	14,584	15,323	48,980	114,758	12,091	46,555	7,035	1,225	4,599	539	2,936	619	1,782	273	1,734	278	1.64	60,489	322	11,216
carbonate	1045	75	16,042	19,922	54,502	133,055	9,819	32,790	4,317	845	3,984	589	3,540	835	2,662	405	2,658	413	2.91	61,713	248	5,182
carbonate	1047	87	4,919	6,768	20,924	53,677	7,520	33,020	6,076	1,181	3,979	383	1,586	288	828	150	1,253	219	2.80	48,776	898	13,834
carbonate	1048	189	12,576	11,283	40,522	103,908	9,182	30,591	4,619	956	3,335	505	2,700	569	1,549	245	1,638	230	8.38	89,428	1,217	165,642
carbonate	1050	53	6,531	9,437	1,111	4,992	894	4,517	1,487	472	1,818	310	2,034	439	1,267	207	1,499	234	1.45	148,073	22	548
carbonate	1051	80	2,911	5,903	1,478	4,429	661	3,022	756	230	965	163	1,038	241	716	124	964	160	1.25	79,115	21	373

Table A.1: Continued.

mineral	OD#	Rb	Sr	Y	La	Ce	Pr	Nd	Sm	Eu	Gd	Tb	Dy	Ho	Er	Tm	Yb	Lu	Hf	Pb	Th	U
carbonate	826_2	0.13	84.06	64.21	16.50	36.44	4.28	16.94	5.55	1.43	9.37	1.64	9.51	1.96	5.41	0.83	5.93	0.98	0.02	9.23	0.14	0.09
carbonate	827 _2	0.16	83.80	40.27	22.83	46.97	5.20	18.69	3.90	0.90	5.14	0.91	5.63	1.21	3.48	0.56	4.01	0.66	0.01	12.06	0.04	0.08
carbonate	829_2	0.10	103.7	245.77	49.97	167.1	23.18	93.80	25.62	3.61	29.06	6.15	42.07	9.68	29.69	5.01	37.08	6.23	0.07	6.41	0.09	0.09
carbonate	830c_2	0.42	85.67	51.15	48.53	111.4	12.17	41.20	7.23	1.55	7.44	1.34	8.31	1.79	5.29	0.89	6.79	1.14	0.01	14.24	0.03	0.23
carbonate	830c_3	0.27	156.3	436.27	9.00	31.68	4.58	19.92	8.78	2.57	16.54	5.06	45.81	13.27	46.69	7.88	51.20	7.18	0.07	17.27	0.01	0.03
carbonate	1008_1	113	7,643	5,310	2,211	5,799	740	3,122	622	151	658	111	860	206	745	153	1,309	226	7	27,181	35	2,057
carbonate	1008_2	75	5,368	5,708	2,025	4,805	666	2,803	567	143	757	118	839	218	773	153	1,263	217	4	30,418	18	1,152
carbonate	1008_3	68	4,669	6,309	1,646	4,385	596	2,352	529	140	667	120	897	240	824	159	1,304	221	5	31,306	19	1,044
carbonate	1008_4	76	4,626	5,841	2,399	5,961	764	3,315	623	156	684	122	868	223	789	157	1,297	223	6	30,572	27	2,408
carbonate	1008_5	58	3,726	5,564	1,751	4,300	549	2,247	491	123	591	111	796	213	762	154	1,320	227	4	33,500	19	2,131
carbonate	1008_6	63	3,702	5,957	2,064	5,385	756	3,028	589	146	670	120	840	230	818	167	1,416	240	4	30,902	18	1,178
carbonate	1008_7	58	3,190	6,498	1,748	4,800	593	2,547	551	143	663	126	902	241	842	165	1,354	230	4	31,077	14	1,077
carbonate	1008_8	59	3,346	5,982	3,016	7,250	885	3,454	684	167	743	140	876	233	774	152	1,233	211	3	32,094	22.0	2,057
carbonate	1008_9	62	3,455	5,750	1,800	4,675	615	2,558	545	137	644	112	820	213	773	155	1,353	226	4	32,312	26.7	1,988
carbonate	1008_10	60	3,612	6,066	1,856	4,672	660	2,784	614	145	680	120	864	232	836	166	1,415	238	3	30,542	13.9	988
anhydrite	817_1	0.03	1,690	12.38	62.64	122.2	13.22	45.08	5.97	0.81	4.33	0.50	2.28	0.40	0.91	0.11	0.55	0.07	0.00	8.60	0.07	0.81
anhydrite	817_2	0.93	1,424	16.40	63.95	124.3	12.94	42.93	5.60	0.92	4.06	0.55	2.92	0.59	1.56	0.21	1.21	0.16	0.02	39.26	6.49	123.7
anhydrite	670_1	1.83	1,454	0.85	16.05	26.14	2.34	7.02	0.99	0.15	0.71	0.07	0.25	0.04	0.07	0.01	0.05	0.01	0.02	0.39	0.84	1.00
anhydrite	670_2	0.05	1,326	0.10	0.67	1.17	0.12	0.45	0.06	0.01	0.07	0.01	0.03	0.00	0.01	0.00	0.00	0.00	0.00	0.04	0.00	0.02
anhydrite	785	0.02	2,207	0.21	0.13	0.30	0.06	0.33	0.15	0.07	0.20	0.02	0.06	0.01	0.01	0.00	0.00	0.00	0.00	0.24	0.00	0.02

Table A.2: Results of the stable isotope ($\delta^{34}S$, in ‰) analysis of anhydrite. CDT: Canyon Diablo Troilite.

OD#	**$\delta^{34}S_{CDT}$**
00670-1	16.74
00670-2	16.89
00785	16.90
00817-1	6.82
00817-2	4.58